Journal of
Cardiovascular Development and Disease

Leaders in Cardiovascular Research

A Special Issue Dedicated to Professor Adriana Gittenberger-De Groot

Edited by
Monique R. M. Jongbloed and Robert E. Poelmann

Printed Edition of the Special Issue Published in
Journal of Cardiovascular Development and Disease

www.mdpi.com/journal/jcdd

MDPI

Leaders in Cardiovascular Research: A Special Issue Dedicated to Professor Adriana Gittenberger-De Groot

Leaders in Cardiovascular Research: A Special Issue Dedicated to Professor Adriana Gittenberger-De Groot

Editors

Monique R. M. Jongbloed
Robert E. Poelmann

MDPI • Basel • Beijing • Wuhan • Barcelona • Belgrade • Manchester • Tokyo • Cluj • Tianjin

MDPI

Editors

Monique R. M. Jongbloed
Leiden University Medical Center
The Netherlands

Robert E. Poelmann
Leiden University Medical Center
The Netherlands

Editorial Office
MDPI
St. Alban-Anlage 66
4052 Basel, Switzerland

This is a reprint of articles from the Special Issue published online in the open access journal *Journal of Cardiovascular Development and Disease* (ISSN 2308-3425) (available at: https://www.mdpi.com/journal/jcdd/special_issues/Adriana_Gittenberger_de_Groot).

For citation purposes, cite each article independently as indicated on the article page online and as indicated below:

LastName, A.A.; LastName, B.B.; LastName, C.C. Article Title. *Journal Name* **Year**, *Volume Number*, Page Range.

ISBN 978-3-0365-4047-4 (Hbk)
ISBN 978-3-0365-4048-1 (PDF)

Cover image courtesy of Hogers et al. Circ Res 1997

Contents

Journal of
Cardiovascular
Development and Disease

MDPI

Editorial

Introduction to Special Issue "Leaders in Cardiovascular Research, Dedicated to the Memory of Professor Adriana Gittenberger-de Groot"

Edi Gittenberger [1], Robert E. Poelmann [2,3] and Monique R. M. Jongbloed [3,4,*]

[1] Naturalis Biodiversity Center, 2333 CR Leiden, The Netherlands; egittenberger@yahoo.com
[2] Institute of Biology, University of Leiden, 2333 BE Leiden, The Netherlands; r.e.poelmann@lumc.nl
[3] Department of Cardiology, Leiden University Medical Center, 2333 ZA Leiden, The Netherlands
[4] Department of Anatomy & Embryology, Leiden University Medical Center, 2333 ZA Leiden, The Netherlands
* Correspondence: m.r.m.jongbloed@lumc.nl

Abstract: This Introduction provides both a short reflection on the scientific career of Adriana Gittenberger-de Groot and an overview of the papers that form the basis of this Special Issue giving them a proper perspective. The papers have as a central focus the outflow tract, and include contributions on development and pathology of the ventricles including AV valves, as well as developmental and pathomorphological aspects of the great arteries including semilunar valves and coronary arteries.

Keywords: cardiovascular development; outflow tract; endocardial cushions; semilunar valves; bicuspid aortic valve; neural crest; aortic wall; coronary arteries; cardiovascular pathogenesis; arterial duct

Citation: Gittenberger, E.; Poelmann, R.E.; Jongbloed, M.R.M. Introduction to Special Issue "Leaders in Cardiovascular Research, Dedicated to the Memory of Professor Adriana Gittenberger-de Groot". *J. Cardiovasc. Dev. Dis.* **2022**, *9*, 92. https://doi.org/10.3390/jcdd9040092

Received: 6 March 2022
Accepted: 18 March 2022
Published: 23 March 2022

1. Introduction: Marriage, Medicine and Malacology, Three in One [E.G.]

It was really a surprise, the Festschrift of the Netherlands Malacological Society to commemorate my 65th birthday in 2008. Even more so was the first contribution, written by Adriana C. Gittenberger—de Groot: 'Marriage and malacology, an adventurous combination'. Adri described the initial 40 years of our living together. She explained why she decided to aim at a career in medical research instead of a clinical specialisation with more restrictions for travelling. She enjoyed our adventurous snail hunting expeditions to the Alps, the Balkans and eventually the Himalaya. After decades of optimal togetherness, life has changed dramatically. Hesitantly, I have accepted the invitation of the editors of this journal to write some introductory sentences. I should have asked her opinion in advance.

Adri was an enthusiastic, tenacious scientist, who believed in serendipity where I noticed her natural talent. Prostaglandin brought her the first breakthrough in research, what resulted in our first visit to the USA. Over the years I learned that the ductus arteriosus is more than a remarkable vessel with programmed arteriosclerosis. Adri was an excellent teacher, who loved to lecture. When we went out to a restaurant for diner after work, she often used the serviette inappropriately to illustrate her most recent ideas about subjects such as the 'pulmonary push'. "Can you still follow me?", she could ask after a while, recognizing the near-invisible negative muscle contractions in my face, "no, I see, I'm sorry, but may I nevertheless go on?" And she continued while I waved the waiter away. Over the years her work had become too complicated for me to follow in detail, in particular when anatomy and histology were complemented by gene expression patterns. Our discussions often moved away from the world (Figure 1) of science to the world of scientists, medical scientists in particular.

Figure 1. "The Gittenbergers ruling the globe". Prof. Dr. Adriana C. Gittenberger-de Groot with her husband Prof. Dr. Edi Gittenberger.

Medical doctors should decide what kind of pills should be described for the patient, medical scientists should decide what alternatives are still possible without neglecting the publications of competitive working groups. Adri studied the literature irrespective of the authors. She wanted to know how heart and vessels develop in the first place. She considered a dogmatic nomenclature of everything a secondary problem and occasionally even a hindrance for a better understanding. Only rarely she entered the semantic boxing ring that some colleagues seemed to enjoy.

Only once, our scientific ways converged in a joint paper, about Nodal, a chirality-related gene both relevant in heart development and in coiling direction of snail shells [1]. When Nature brought the same message a few years later, we were both annoyed, since that journal had considered our manuscript 'too specialistic'.

Being out in the field, walking, looking, listening, Adri enjoyed it very much. Despite her vertigo, she eventually loved the mountains, even after a frightening experience during our very first hiking tour in Austria, when we had to use a short iron cable and a short metal ladder to reach the mountain cabin. Bird-watching became one of our favourite hobbies. Adri understood the remarkable aberration of biologists such as me, people that may acquire a feeling of happy excitement after a vague view of a bird that might be, yes, indeed (!), the very rare yellow-tailed warbler according to the field guide. While peering at it, she joined in the discussion about dots or stripes.

Adri enjoyed snail hunting, in particular the inhabitants of rock-faces and, indeed, she discovered the beautiful Greek species that I described as Albinaria adrianae (Figure 2).

When our youngest son learned scuba-diving, she followed him and urged me to do the same. In vain I referred to the evolutionary origin of terrestrial life and the unnatural behaviour of swimming. She stayed firm and arranged lessons how to swim first and scuba diving shortly afterwards. A full and wonderful dimension was added to our lives. Whenever possible we combined our journeys, holidays, conferences, with scuba diving. That is why we were in Bonaire early in 2020. An unforgettable recent experience were six joint excursions to the Kingdom of Bhutan, where I was invited to start an inventory of the molluscan fauna. Adri was immediately enthusiastic. She appreciated the atmosphere, the people, nature, the blooming rhododendrons high in the Himalaya. Never ever she protested when we had to adapt to non-European circumstances, on the contrary. Back in the capital we indulged in a hamburger with pommes frites, always together.

"The future is bright." was her last sentence in the Festschrift in 2008. She was right. After that year, 12 wonderful years followed. A few more, she had hoped, grateful for the past.

Figure 2. *Albinaria adrianae.* Courtesy of Guido T. Poppe and Philippe Poppe.

2. The Special Issue: The (Bio)medical Legacy of Adriana Gittenberger-de Groot

In the JCDD issue "Leaders in Cardiovascular Research, a Special Issue dedicated to the memory of Professor Adriana Gittenberger-de Groot", committed to Adriana's extensive career, we see a reflection of the versatility of subjects that have been explored by dedicated researchers, driven by the desire to ultimately solve part of the puzzle that encompasses the mechanism of development of structural heart disease, affecting so many patients worldwide [2]. Many mismatches in cardiovascular development particularly result in ventricular septal defects and in outflow tract malformations, that showed a continued presence in Adriana's work. Furthermore, late onset of specific disease processes such as aneurysm of the ascending aorta associated with bicuspid aortic valve [3], might find their origin during embryonic development justifying the inclusion in the category "congenital heart disease".

The majority of congenital cardiac malformations involve ventricular and outflow tract septation with the participation of many interacting cellular players (Figure 3) such as the first/second heart field, neural crest, myocardium, endocardium, epicardium and endoderm. Concentrating on ventricles and outflow tract in development, molecular genetics, pathology and patient management, all these aspects can be encountered in this Special Issue. Several groups of papers can be discerned, dealing with cardiac (mal)development as well as with the aortic valve and the main arteries such as aorta, coronary arterial branches and ductus arteriosus.

OFT and ventricular myocardium—developmental, molecular and genetic aspects. A review paper by Sendra et al. [5] discusses the complexity of heart progenitor cells important to understand congenital heart defects. Three key aspects in early development are important, dealing with 1. the segregation of endocardial and first and second heart field myocardial lineages, 2. the signalling cues that drive differentiation and 3. the transcriptional heterogeneity of cardiomyocyte progenitors. Novel approaches such as single cell transcriptomics (see also Peterson et al. [6]), lineage tracing (see also Stefanovic et al. [7] and Johnson et al. [8] and epigenomics (see also Grunert et al. [9], live imaging and functional analyses will transform our understanding of congenital anomalies.

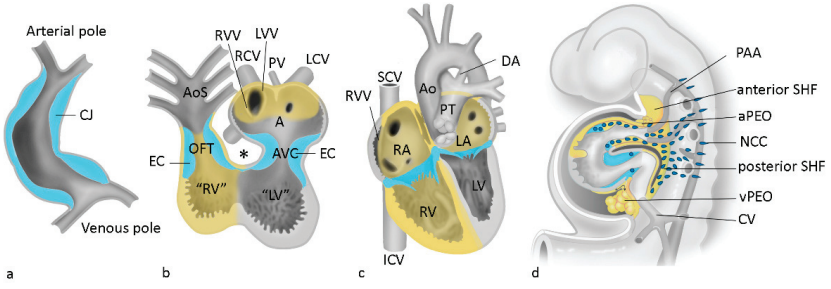

Figure 3. Cardiac development: Contributions from the second heart field and neural crest cells. Panels (**a**–**c**) reflect successive stages of development. Panel (**d**) represents a lateral view showing the migration path of neural crest cells (NCC). A: common atrium, Ao: aorta, AoS: aortic sac, AVC: atrioventricular canal, CJ: cardiac jelly, CV: cardinal vein, DA: ductus arteriosus, EC: endocardial cushions, ICV: inferior vena cava, LA: left atrium, LCV: left cardinal vein, LV: left ventricle, LVV: left venous valve, NCC: neural crest cells, OFT: outflow tract, PAA: pharyngeal arch artery, PEO: pro-epicardial organ, PT: pulmonary trunk, PV: pulmonary vein, RA: right atrium, RCV: right cardinal vein, RV: right ventricle, RVV: right venous valve, SCV: superior vena cava, SHF: second heart field. * inner curvature of the looping heart. Derived with permission from Gittenberger-de Groot et al. [4].

The development of new techniques also opened avenues for more in-depth investigation of signalling and inducing factors involved in the development of congenital and structural heart disease and their roles at other levels of interactions. Cardiac lineage tracing is further explored by Peterson et al. [6]. They show the value of chicken-quail chimeras [10] and retroviral labelling [11]. Furthermore, they elaborate on genetic lineage tracing markers for first and second heart field, myocardium, neural crest, epicardium, and endothelium. Finally, DNA barcoding allows for complex labelling methods incorporating also CRISPR-Cas9 based approaches. The cellular contributions to the conotruncal area are reviewed by Stefanovic et al. [7]. These authors take into account the many cell types responsible for proper heart formation and the consequences of deregulation of transcription factors such as Isl1 and FGF10 for myocardial cells, BMP and T-box factors for endocardium, and Wnt1 and FGF8 for cardiac neural crest cells. Cardiac anomalies are known to be related to complex signalling defects including retinoic acid, Hox transcription factors or chromosomal syndromes. The transcription factor AP-2α (Johnson et al. [8]) is expressed in several tissues during development including pharyngeal ectoderm and cardiac neural crest. Deficient mice present with complex anomalies such as double outlet right ventricle (DORV) and transposition of the great arteries (TGA).

At the molecular and genetic level many cascades have been investigated. The TGFbeta constitute an important family of regulating factors. Chakrabarti et al. [12] relay the requirement of TGFβ3 for cardiovascular development as investigated in a mouse model. The diverse phenotypes were present in about two thirds of null mice, including (right) ventricular myocardium, OFT septal and alignment defects, abnormal aortic and pulmonary walls and thickened semilunar or AV valves. In vitro and biochemical studies indicated that TGFβ3 was required for collagen matrix reorganization involving SMAD and MAP-kinase dependent pathways.

Leung et al. [13] investigated the cardiomyocyte specific role of the small GTPase Rac1 in the ventricular wall in Nkx2.5 transgenic mice. Rac1 deficiency impairs cardiomyocyte elongation and organization as well as proliferative growth, implicating a role of Rac1 in OFT alignment and compaction of the myocardium.

From a genetic point of view, Grunert et al. [9] correlated genetic and epigenetic differences in Tetralogy of Fallot, studying monozygotic twins. They performed genome-wide high-throughput sequencing of twin pairs with TOF. DNA methylation changes in regulatory regions of cardiac-relevant genes were demonstrated.

The cardiac valves—developmental, pathomorphological and clinical aspects. Epicardial derived ells (EPDCs) are relevant for pathogenesis of myxomatous valve disease, as was demonstrated by Wolters et al. [14] who reviewed critical events in the development of the atrioventricular junction, including the role of the epicardium in the development of the AV valves. The parietal AV cushions receive a contribution from epicardium-derived cells (EPDCs) in concordance with results indicated by Gittenberger-de Groot et al. in a chick model [15].

Poelmann et al. [16] described endocardial cushion formation in crocodiles and their role in semilunar valve development. Reptiles in general end up with two aortas besides the pulmonary trunk, while all three main trunks show a bicuspid semilunar valve. It is postulated that "missing the third leaflet" might be related to lack of neural crest or epicardial derived cells.

Zwanenburg et al. [17] searched for predictors of adverse human left ventricular development caused by fetal aortic stenosis using fetal ultrasound. Speckle-tracking recordings were performed to assess myocardial strain. After pregnancy termination. The degree of reduction in myocardial deformation corresponded to the amount of pathological endocardial fibrosis, indicating myocardial deformation on fetal ultrasound as a potential marker for left ventricular structural damage.

Kruithof et al. [18] investigated semilunar aortic valve disease, both regurgitant and stenotic. They demonstrated the occurrence of superimposed tissue in human samples. The regurgitant valve showed this in the free edge, leading to a thicker valve, while the stenotic valve showed this on the aortic face. These highly active areas are populated by myofibroblasts within a varied extracellular matrix that is collagen-rich in the stenotic valve. Çelik et al. [19] studied a patient cohort with bicuspid semilunar aorta valve associated with aortopathy leading to dilation, aneurysm and eventually dissection. Prevalence, predictors and outcome (1–20 years) of 48 patients were analysed. Grewal et al. [20] described earlier the association of BAV with aortopathy as a developmental maturation defect of the aortic root. A second contribution to this Issue by Çelik and colleagues [21] described the impact of intervention in severe but asymptomatic aortic stenosis by valve replacement and long-term survival. Survival rates after valve replacement surgery were significantly higher after 1–10 years follow-up.

Thoracic aorta—histopathomorphological and (patho)developmental) aspects. Grewal et al. [22] reported on the histological structure of the aortic wall in patients with an acute type A aortic dissection (TAAD) showing elastin pathology, mucoid accumulation, and smooth muscle cell nucleic loss in overall medial degeneration while also associated with a thinner intimal layer. The authors hypothesize a developmental defect caused by a multiple hit including a tear in the intima, a diseased media and progression towards the vasa vasorum.

Thiene et al. [23] reviewed the aorta as an organ that deteriorates with age. They investigated many types of pathology in humans and brought also the possibility of an allograft approach in sheep. The aorta with its lamellar units consists of elastic fibres in a collagen-rich extracellular matrix interspersed with smooth muscle cells. Pathology may require replacement sometimes including failing valves. There may be congenital defects such as bicuspid semilunar valve and isthmus coarctation, genetic defects such as Marfan and William syndromes, degenerative diseases and trauma. Antigenicity may prevent the replacement of a sickened aorta using homografts from donors. After proper decellularization and implantation in sheep, endogenous cell repopulation was shown in both the valve and aortic wall without structural deterioration.

Another defect of the aorta relates to the right-sided aortic arch, an early developmental defect in remodelling of the pharyngeal arch arteries [24]. Van Rosendael et al. [25] relay a malformation found in adult patients associated with the branchpoint of an aberrant left subclavian artery (arteria lusoria) from the right-sided aortic arch. In this configuration a Kommerell's diverticulum and persisting ductus arteriosus form a vascular ring which may result in (symptomatic) esophageal or tracheal compression. Serial follow-up is warranted in adult patients with Kommerell's diverticulum with small size and no symptoms,

eventually leading to surgical intervention in patient who become symptomatic or show significant increase in diameter of the diverticulum.

Coronary arteries—The Leiden Convention Coronary Coding System and late follow up after surgery for transposition of the great arteries. Another highlight of Gittenberger-de Groot's research comprised the early formation of the coronary vasculature [26] and the branching pattern of the coronary arteries (Gittenberger-de Groot et al. 2018 [27]). In this Special Issue cardiovascular thoracic surgeon Prof. Dr. Mark Hazekamp [28] stresses the value of an unequivocal and simple coronary coding system developed by Adriana, called the Leiden Convention. This can be used in hearts with congenital heart disease (CHD), such as transposition of the great arteries (TGA), independent of their relative anatomical position which can vary in different forms of congenital heart disease. A recent adjustment of this system to facilitate its use in imaging modalities, facilitates communication between paediatric cardiologists and paediatric heart surgeons [29]. This is further explored by Katekaru-Tokeshi et al. [30] studying patients with a single coronary artery. The Lipton classification (not intended for structural heart diseases) has also been applied but in complex CHD the Leiden Convention is better applicable. In pulmonary atresia the use of both systems is limited.

Due to advancements in surgical and interventional treatments, an increasing number of patients with CHD reaches the adult age. Engele et al. [31] systematically reviewed the follow-up into adulthood of a patient population with TGA that received an arterial switch operation with coronary transfer in early life. Anatomical high-risk features found by coronary computed tomography included stenosis, acute angulation, kinking and an interarterial course. An individualized coronary follow-up strategy is advisable, at least until significant duration of follow-up is available.

Arterial duct. During her life, Adriana studied the influence of prostaglandins on the ductal integrity as clinical reports brought devastating effects on the survival rate of treated neonates [32]. Following her initial reports the pharmaceutical industry lowered the recommended dose promptly, resulting in the expected positive outcome. In addition, later on, the arterial duct kept her interest [33,34].

In the current special issue, Saito et al. [35] performed transcriptome analysis of the arterial duct and demonstrate differential gene expression patterns between the closing and the patent ductus arteriosus, building on the earliest research projects of Adriana Gittenberger-de Groot [36]. The patent ductus exhibited aorta-like elastic lamellae and a poorly developed intimal thickening. Neural crest-related genes including JAG1 and the protein calponin were highly expressed in the tunica intima and media of the closing ductus but not in the patent one. Second-heart field related genes such as ISL1 on the other hand were enriched in the patent ductus sample indicating participation of another cell lineage. Fedrigo et al. [37] reported another clinical phenomenon of the developing ductus, being premature closure causing sudden intrauterine death. Abnormal ductal remodelling showed lack of intimal cushions, cystic medial necrosis and smooth muscle cell apoptosis as pathological substrates.

In conclusion the legacy of Adriana Gittenberger-de Groot (Figure 4) combines the importance of proper knowledge of embryonic development not only for explaining congenital cardiac malformations, but also for late onset clinical issues such as the onset of arteriosclerosis and the repair of myocardial infarction. The content of this special issue reflects the versatility of Adriana's career, during which she worked with remarkable scientists and made many friends, many of whom made a contribution to this special issue. Her creativity, combined with her intellectual spirit and passion for research allowed the development of a myriad of new concepts, that will be the driving force for many more exciting studies of cardiovascular development. We will cherish our memories and her legacy dearly.

Figure 4. Prof. Dr. Adriana C. Gittenberger—de Groot. 1945–2020.

Author Contributions: All authors contributed to the manuscript and have approved the submitted version. All authors have read and agreed to the published version of the manuscript.

Funding: This research received no external funding.

Conflicts of Interest: The authors declare no conflict of interest.

References

1. Hierck, B.P.; Witte, B.; Poelmann, R.E.; Gittenberger-de Groot, A.C.; Gittenberger, E. Chirality in snails is determined by highly conserved asymmetry genes. *J. Molluscan. Stud.* **2005**, *71*, 192–195. [CrossRef]
2. Gittenberger-de Groot, A.C.; Bartelings, M.M.; Poelmann, R.E.; Haak, M.C.; Jongbloed, M.R.M. Embryology of the heart and its impact on understanding fetal and neonatal heart disease. *Semin. Fetal. Neonatal. Med.* **2013**, *18*, 237–244. [CrossRef] [PubMed]
3. Grewal, N.; Gittenberger-de Groot, A.C.; Poelmann, R.E.; Klautz, R.J.M.; Lindeman, J.H.N.; Goumans, M.J.; Palmen, M.; Mohamed, S.A.; Sievers, H.H.; Bogers, A.J.; et al. Ascending aorta dilation in association with bicuspid aortic valve: A maturation defect of the aortic wall. *J. Thorac. Cardiovasc. Surg.* **2014**, *148*, 1583–1590. [CrossRef] [PubMed]
4. Gittenberger-de Groot, A.C.; Calkoen, E.E.; Poelmann, R.E.; Bartelings, M.M.; Jongbloed, M.R.M. Morphogenesis and molecular considerations on congenital cardiac septal defects. *Ann. Med.* **2014**, *46*, 640–652. [CrossRef]
5. Sendra, M.; Domínguez, J.N.; Torres, M. Dissecting the Complexity of Early Heart Progenitor Cells. *J. Cardiovasc. Dev. Dis.* **2022**, *9*, 5. [CrossRef]
6. Peterson, J.C.; Kelder, T.P.; Goumans, M.J.T.H.; Jongbloed, M.R.M.; DeRuiter, M.C. The Role of Cell Tracing and Fate Mapping Experiments in Cardiac Outflow Tract Development, New Opportunities through Emerging Technologies. *J. Cardiovasc. Dev. Dis.* **2021**, *8*, 47. [CrossRef]
7. Stefanovic, S.; Etchevers, H.C.; Zaffran, S. Outflow Tract Formation-Embryonic Origins of Conotruncal Congenital Heart Disease. *J. Cardiovasc. Dev. Dis.* **2021**, *8*, 42. [CrossRef]
8. Johnson, A.-L.; Schneider, J.E.; Mohun, T.J.; Williams, T.; Bhattacharya, S.; Henderson, D.J.; Phillips, H.M.; Bamforth, S.D. Early Embryonic Expression of AP-2α Is Critical for Cardiovascular Development. *J. Cardiovasc. Dev. Dis.* **2020**, *7*, 27. [CrossRef]
9. Grunert, M.; Appelt, S.; Grossfeld, P.; Sperling, S.R. The needle in the haystack—Searching for genetic and epigenetic differences in monozygotic twins discordant for tetralogy of fallot. *J. Cardiovasc. Dev. Dis.* **2020**, *7*, 55. [CrossRef]
10. Kirby, M.L.; Gale, T.F.; Stewart, D.E. Neural crest cells contribute to normal aorticopulmonary septation. *Science* **1983**, *220*, 1059–1061. [CrossRef]
11. Poelmann, R.E.; Gittenberger-de Groot, A.C. A subpopulation of apoptosis-prone cardiac neural crest cells targets to the venous pole: Multiple functions in heart development? *Dev. Biol.* **1999**, *207*, 271–286. [CrossRef]

12. Chakrabarti, M.; Al-Sammarraie, N.; Gebere, M.G.; Bhattacharya, A.; Chopra, S.; Johnson, J.; Peña, E.A.; Eberth, J.F.; Poelmann, R.E.; Gittenberger-de Groot, A.C.; et al. Transforming Growth Factor Beta3 is Required for Cardiovascular Development. *J. Cardiovasc. Dev. Dis.* **2020**, *7*, 19. [CrossRef] [PubMed]
13. Leung, C.; Engineer, A.; Kim, M.Y.; Lu, X.; Feng, Q. Myocardium-Specific Deletion of Rac1 Causes Ventricular Noncompaction and Outflow Tract Defects. *J. Cardiovasc. Dev. Dis.* **2021**, *8*, 29. [CrossRef]
14. Wolters, R.; Deepe, R.; Drummond, J.; Harvey, A.B.; Hiriart, E.; Lockhart, M.M.; van den Hoff, M.J.; Norris, R.A.; Wessels, A. Role of the Epicardium in the Development of the Atrioventricular Valves and Its Relevance to the Pathogenesis of Myxomatous Valve Disease. *J. Cardiovasc. Dev. Dis.* **2021**, *8*, 54. [CrossRef] [PubMed]
15. Gittenberger-de Groot, A.C.; Vrancken Peeters, M.P.; Mentink, M.M.; Gourdie, R.G.; Poelmann, R.E. Epicardium-derived cells contribute a novel population to the myocardial wall and the atrioventricular cushions. *Circ. Res.* **1998**, *82*, 1043–1052. [CrossRef] [PubMed]
16. Poelmann, R.E.; Gittenberger-de Groot, A.C.; Goerdajal, C.; Grewal, N.; De Bakker, M.A.G.; Richardson, M.K. Ventricular septation and outflow tract development in crocodilians result in two aortas with bicuspid semilunar valves. *J. Cardiovasc. Dev. Dis.* **2021**, *8*, 132. [CrossRef]
17. Zwanenburg, F.; Deruiter, M.C.; Wisse, L.J.; van Munsteren, C.J.; Bartelings, M.M.; Goumans, M.J.; Ten Harkel, A.D.; Jongbloed, M.R.; Haak, M.C. Deficient myocardial organization and pathological fibrosis in fetal aortic stenosis—Association of prenatal ultrasound with postmortem histology. *J. Cardiovasc. Dev. Dis.* **2021**, *8*, 121. [CrossRef]
18. Kruithof, B.P.T.; van Wijngaarden, A.L.; Mousavi Gourabi, B.; Hjortnaes, J.; Palmen, M.; Ajmone Marsan, N. Superimposed Tissue Formation in Human Aortic Valve Disease: Differences between Regurgitant and Stenotic Valves. *J. Cardiovasc. Dev. Dis.* **2021**, *8*, 79. [CrossRef]
19. Çelik, M.; Mahtab, E.A.F.; Bogers, A.J.J.C. Surgical Aortic Valve Replacement with Concomitant Aortic Surgery in Patients with Purely Bicuspid Aortic Valve and Associated Aortopathy. *J. Cardiovasc. Dev. Dis.* **2021**, *8*, 16. [CrossRef]
20. Grewal, N.; Gittenberger-de Groot, A.C.; von der Thusen, L.J.; Bartelings, M.M.; DeRuiter, M.C.; Klautz, R.J.; Poelmann, R.E. The Development of the Ascending Aortic Wall in Tricuspid and Bicuspid Aortic Valve: A Process from Maturation to Degeneration. *J. Clin. Med.* **2020**, *9*, 908. [CrossRef]
21. Çelik, M.; Milojevic, M.; Durko, A.P.; Oei, F.B.S.; Mahtab, E.A.F.; Bogers, A.J.J.C. Asymptomatic Patients with Severe Aortic Stenosis and the Impact of Intervention. *J. Cardiovasc. Dev. Dis.* **2021**, *8*, 35. [CrossRef] [PubMed]
22. Grewal, N.; Velders, B.J.J.; Gittenberger-de Groot, A.C.; Poelmann, R.; Klautz, R.J.M.; Van Brakel, T.J.; Lindeman, J.H. A Systematic Histopathologic Evaluation of Type-A Aortic Dissections Implies a Uniform Multiple-Hit Causation. *J. Cardiovasc. Dev. Dis.* **2021**, *8*, 12. [CrossRef] [PubMed]
23. Thiene, G.; Basso, C.; Della Barbera, M. Pathology of the Aorta and Aorta as Homograft. *J. Cardiovasc. Dev. Dis.* **2021**, *8*, 76. [CrossRef] [PubMed]
24. Molin, D.G.M.; DeRuiter, M.C.; Wisse, L.J.; Azhar, M.; Doetschman, T.; Poelmann, R.E.; Gittenberger-de Groot, A.C. Altered apoptosis pattern during pharyngeal arch artery remodelling is associated with aortic arch malformations in Tgf-beta2 knock-out mice. *Cardiovasc. Res.* **2002**, *56*, 312–322. [CrossRef]
25. van Rosendael, P.J.; Stöger, J.L.; Kiès, P.; Vliegen, H.W.; Hazekamp, M.G.; Koolbergen, D.R.; Lamb, H.J.; Jongbloed, M.R.; Egorova, A.D. The clinical spectrum of kommerell's diverticulum in adults with a right-sided aortic arch: A case series and literature overview. *J. Cardiovasc. Dev. Dis.* **2021**, *8*, 25. [CrossRef]
26. Bogers, A.J.J.C.; Gittenberger-de Groot, A.C.; Poelmann, R.E.; Peault, B.M.; Huysmans, H.A. Development of the origin of the coronary arteries, a matter of ingrowth or outgrowth? *Anat. Embryol.* **1989**, *180*, 437–441. [CrossRef]
27. Gittenberger-de Groot, A.C.; Koenraadt, W.M.C.; Bartelings, M.M.; Bökenkamp, R.; DeRuiter, M.C.; Hazekamp, M.G.; Bogers, A.J.; Quaegebeur, J.M.; Schalij, M.J.; Vliegen, H.W.; et al. Coding of coronary arterial origin and branching in congenital heart disease: The modified Leiden Convention. *J. Thorac. Cardiovasc. Surg.* **2018**, *156*, 2260–2269. [CrossRef]
28. Hazekamp, M. Coronary Anatomy in Congenital Heart Disease: The Important Contributions of Professor Dr. Adriana Gittenberger-de Groot. *J. Cardiovasc. Dev. Dis.* **2021**, *8*, 27. [CrossRef]
29. Koppel, C.J.; Vliegen, H.W.; Bökenkamp, R.; Ten Harkel, A.D.J.; Kiès, P.; Egorova, A.D.; Jukema, J.W.; Hazekamp, M.G.; Schalij, M.J.; Gittenberger-de Groot, A.C.; et al. The Leiden Convention coronary coding system: Translation from the surgical to the universal view. *Eur. Hear. J. Cardiovasc. Imaging* **2022**, *23*, 412–422. [CrossRef]
30. Katekaru-Tokeshi, D.I.; Jiménez-Santos, M.; Koppel, C.J.; Vliegen, H.W.; Díaz-Zamudio, M.; Castillo-Castellón, F.; Jongbloed, M.R.; Kimura-Hayama, E. Applicability of the Leiden Convention and the Lipton Classification in Patients with a Single Coronary Artery in the Setting of Congenital Heart Disease. *J. Cardiovasc. Dev. Dis.* **2021**, *8*, 93. [CrossRef]
31. Engele, L.J.; Mulder, B.J.M.; Schoones, J.W.; Kiès, P.; Egorova, A.D.; Vliegen, H.W.; Hazekamp, M.G.; Bouma, B.J.; Jongbloed, M.R. The coronary arteries in adults after the arterial switch operation: A systematic review. *J. Cardiovasc. Dev. Dis.* **2021**, *8*, 102. [CrossRef] [PubMed]
32. Gittenberger-de Groot, A.C.; Strengers, J.L. Histopathology of the arterial duct (*ductus arteriosus*) with and without treatment with prostaglandin E1. *Int. J. Cardiol.* **1988**, *19*, 153–166. [CrossRef]
33. Bökenkamp, R.; DeRuiter, M.C.; van Munsteren, C.; Gittenberger-de Groot, A.C. Insights into the pathogenesis and genetic background of patency of the ductus arteriosus. *Neonatology* **2010**, *98*, 6–17. [CrossRef] [PubMed]

34. Gittenberger-de Groot, A.C.; Bokenkamp, R.; Raz, V.; van Munsteren, C.; Poelmann, R.E.; Grewal, N.; DeRuiter, M.C. *Progerin Expression during Normal Closure of the Human Ductus Arteriosus: A Case of Premature Ageing?* Nakanishi, T., Markwald, R.R., Baldwin, H.S., Keller, B.B., Srivastava, D., Yamagishi, H., Eds.; Springer: Tokyo, Japan, 2016; pp. 245–251.
35. Saito, J.; Kojima, T.; Tanifuji, S.; Kato, Y.; Oka, S.; Ichikawa, Y.; Miyagi, E.; Tachibana, T.; Asou, T.; Yokoyama, U. Transcriptome Analysis Reveals Differential Gene Expression between the Closing Ductus Arteriosus and the Patent Ductus Arteriosus in Humans. *J. Cardiovasc. Dev. Dis.* **2021**, *8*, 45. [CrossRef]
36. Gittenberger-de Groot, A.C.; Moulaert, A.J.; Harinck, E.; Becker, A.E. Histopathology of the ductus arteriosus after prostaglandin E1 administration in ductus dependent cardiac anomalies. *Br. Heart J.* **1978**, *40*, 215–320. [CrossRef]
37. Fedrigo, M.; Visentin, S.; Veronese, P.; Barison, I.; Giarraputo, A.; Cosmi, E.; Thiene, G.; Gervasi, M.T.; Basso, C.; Angelini, A. Isolated Dissection of the Ductus Arteriosus Associated with Sudden Unexpected Intrauterine Death. *J. Cardiovasc. Dev. Dis.* **2021**, *8*, 91. [CrossRef]

Journal of
Cardiovascular
Development and Disease

MDPI

Review

Dissecting the Complexity of Early Heart Progenitor Cells

Miquel Sendra [1,*], Jorge N. Domínguez [2], Miguel Torres [1] and Oscar H. Ocaña [1,*]

[1] Developmental Biology Program, Centro Nacional de Investigaciones Cardiovasculares (CNIC), 28029 Madrid, Spain; mtorres@cnic.es
[2] Cardiovascular Development Group, Department of Experimental Biology, University of Jaen, 23071 Jaen, Spain; jorgendm@ujaen.es
* Correspondence: msendra@cnic.es (M.S.); ohocana@cnic.es (O.H.O.)

Abstract: Early heart development depends on the coordinated participation of heterogeneous cell sources. As pioneer work from Adriana C. Gittenberger-de Groot demonstrated, characterizing these distinct cell sources helps us to understand congenital heart defects. Despite decades of research on the segregation of lineages that form the primitive heart tube, we are far from understanding its full complexity. Currently, single-cell approaches are providing an unprecedented level of detail on cellular heterogeneity, offering new opportunities to decipher its functional role. In this review, we will focus on three key aspects of early heart morphogenesis: First, the segregation of myocardial and endocardial lineages, which yields an early lineage diversification in cardiac development; second, the signaling cues driving differentiation in these progenitor cells; and third, the transcriptional heterogeneity of cardiomyocyte progenitors of the primitive heart tube. Finally, we discuss how single-cell transcriptomics and epigenomics, together with live imaging and functional analyses, will likely transform the way we delve into the complexity of cardiac development and its links with congenital defects.

Keywords: cardiac fields; cardiomyocyte; endocardium; progenitor specification; heart tube

Citation: Sendra, M.; Domínguez, J.N.; Torres, M.; Ocaña, O.H. Dissecting the Complexity of Early Heart Progenitor Cells. *J. Cardiovasc. Dev. Dis.* **2022**, *9*, 5. https://doi.org/10.3390/jcdd9010005

Academic Editors: Monique R.M. Jongbloed and Robert Poelmann

Received: 1 December 2021
Accepted: 22 December 2021
Published: 26 December 2021

Publisher's Note: MDPI stays neutral with regard to jurisdictional claims in published maps and institutional affiliations.

1. Introduction

The heart is the first organ to form during embryogenesis. Following the onset of gastrulation, a primitive heart assembles and starts pumping nutrients to the whole embryo, while it continues developing. This remarkable ability to form and function simultaneously has attracted researchers for nearly a century, revealing that heart development involves the interplay between heterogeneous cell sources and complex morphogenetic processes [1]. With at least 0.8% of newborns presenting congenital heart defects [2], understanding heart development is of great interest. Adriana C. Gittenberger-de Groot and colleagues contributed extensively to this end, both characterizing the different cellular sources of the developing heart [3] and applying this knowledge to clinical goals [4].

A key step towards understanding organogenesis is finding how stem cells commit to different cell types. Studying the embryonic origin of the distinct cell populations contributing to an organ helps us to understand developmental defects by identifying within heterogeneous progenitor populations those contributing to specific cellular compartments and functions. In vertebrates, cardiac progenitors in the epiblast are among the earliest to ingress through the primitive streak and differentiate into mesoderm [5–8] (Figure 1). At this point, the transcription factor *Mesp1* is transiently expressed, offering an accurate marker for nascent mesodermal cells including extrambryonic, cardiac and head/neck skeletal muscle progenitors [9]. Once they have migrated to the anterior pole, a subset of cardiac progenitors, known as the First Heart Field (FHF), starts expressing specific differentiation markers. By Early Head Fold (EHF) stage in mouse, embryonic day (E) ~7.5, the pre-myocardium is arranged as a columnar epithelium and the pre-endocardium lays between the pre-myocardium epithelium and the endoderm, revealing the first sign of cellular heterogeneity in the heart [10] (Figure 1, cellular detail of primitive heart tube

progenitors) [11]. Subsequently, the pre-myocardial epithelium separates from the endoderm, creating bilateral hemi-tube structures with endocardial cells in its lumen. This primordium, known as the cardiac crescent in the mouse, undergoes morphogenesis fusing at the midline to form the primitive heart tube, which will contribute to the left ventricle and part of the atria in the mature heart. Continuous with the primitive heart tube, additional cardiac progenitors, known as the Second Heart Field (SHF), remain undifferentiated until recruited later to the right ventricle, outflow tract and the rest of the atria [12,13].

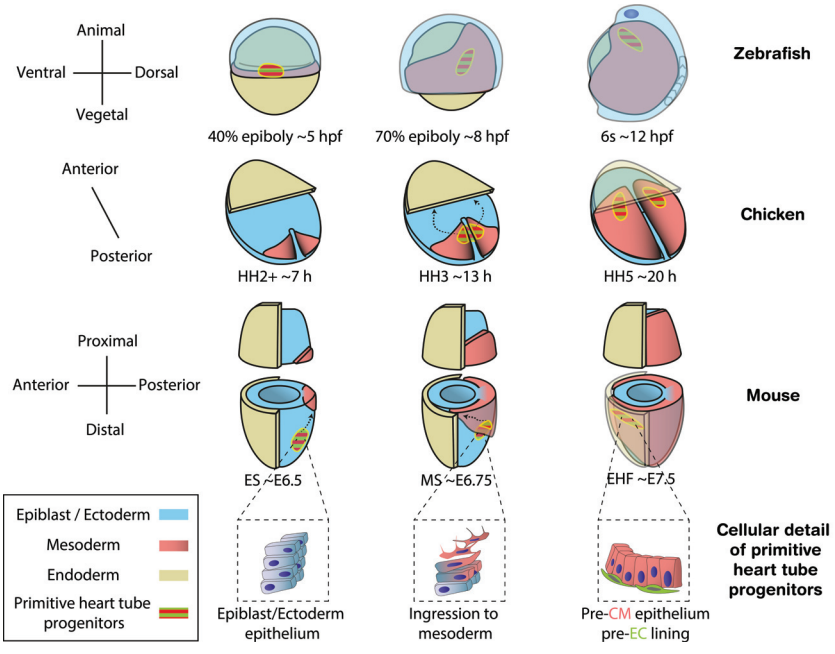

Figure 1. Location of cardiac progenitors in vertebrate models from the onset of gastrulation to the stage preceding primitive heart tube formation. Cardiac progenitors ingress the mesoderm soon after the start of gastrulation, migrating to the opposite side of the embryo to establish the two layers that form the primitive heart tube. The different rows of diagrams show this process in mouse, chicken, zebrafish and a zoom-in for the cellular detail of primitive heart tube progenitors, respectively. Zebrafish diagrams are depicted from dorsal views while those in chick and mouse show ventral views. Morphological staging follows the epiboly rate, Hamburger–Hamilton (HH) and Downs [14] criteria for zebrafish, chicken and mouse, respectively. Approximate time in hours post fertilization (hpf), hours (h) or embryonic day (E) are also provided. CM, cardiomyocytes; EC, endocardium. Dashed arrows depict the migration trajectory of primitive heart tube progenitors during gastrulation.

In this review, we dissect the earliest developmental events that contribute to generate the cellular heterogeneity and complexity of the heart. As other excellent publications review these aspects at later stages in both mammal [1,15,16] and zebrafish models [17], here we will focus on the formation of the primitive heart tube, using the mouse model as a reference. From classic labelling experiments (Table 1) to recent single-cell transcriptomic analysis [18,19], we review studies that have expanded our views on cardiac heterogeneity and the mechanisms that generate it. Finally, we discuss the embryological relevance of such complexity, providing an overview of the public datasets that are available to study it further (Table 2).

Table 1. Clonal analysis studies assessing early cardiac lineage segregation in vertebrate models.

Model	Methodology	Stage	Location	N	Progeny (% from Total)				Reference
					CM	EC	CM + EC	CM + EC + Non Cardiac	
Zebrafish	Single-cell dextran microinjection	Early blastula (∼2.75 hpf)	lateral-marginal zone	29	4	10	21	65	[20]
Zebrafish	Single-cell dextran microinjection	Midblastula (∼3 hpf)	lateral-marginal zone	41	18	7	0	75	[20]
Zebrafish	2–3 cells fluorescein activation	40% epiboly (∼5 hpf)	ventral-marginal zone	69	44	52	4	ND	[21]
Zebrafish	Kaede photoconversion	14-somite (∼18 hpf)	anterior lateral plate mesoderm	39	27	0	2	ND	[22]
Chicken	Replication-defective retrovirus	HH3 (∼14 h)	anterior lateral plate mesoderm	82	95	5	0	ND	[23]
Chicken	Replication-defective retrovirus	HH4 (∼18 h)	rostral portion primitive streak	36	55 *	45 *	0	ND	[23]
Mouse	Doxycyclin induced transgene expression	Early primitive streak (∼E6.5) **	*Mesp1*-expressing cells	13	85	15	0	ND	[24]
Mouse	Doxycyclin induced transgene expression	Late primitive streak (∼E7.0) **	*Mesp1*-expressing cells	6	100	0	0	ND	[24]
Mouse	Doxycyclin induced transgene expression	Late bud (∼E7.5) **	*Mesp1*-expressing cells	17	70	6	24 ***	ND	[24]

ND, Not Determined; hpf, hours post fertilization. * Including labeled clusters that consisted of both CM or EC but either tagged with cytoplasmic β-gal (β-gal) or nuclear directed β-gal (nβ-gal). ** Estimated recombination stage. Mouse retrospective analyses can only offer an approximated stage as the precise mating time and litter variability are unknown. *** A third of the clusters also contain smooth muscle cells.

Table 2. Single-cell sequencing and live imaging data from mouse embryos available in the literature. Links to the raw and processed data and their website interfaces are provided when available (Data).

Resource	Stage	Selection (N Cells)	Method	Depth *	Data	Reference
scRNAseq	ES to LHF ∼E6.5, E7.5, E7.75	∼E6.5 epiblast (501) ∼E7.5 Flk1^{+} (704)	Smart-seq2	∼1 × 10^{6} reads/cell	link list 1	[25]
scRNAseq	∼E6.75, E7.25	Mesp1^{+} ∼E6.75 (83 WT 85 Mesp1$^{-/-}$) ∼E7.25 (173)	Smart-seq2	∼1 × 10^{6} reads/cell **	link list 2	[26]
scRNAseq	∼E8.25	Whole embryo (19,396)	10× genomics	∼2 × 10^{4} UMIs/cell	link list 3	[27]
scRNAseq	ES to 7 s ∼E6.5, E6.75, E7.25, E7.5, E7.75, E8.0, E8.25, E8.5	Whole embryo (116,312) Per stage: supplementary	10× genomics	∼2 × 10^{4} UMIs/cell	link list 4	[28]
scRNAseq	4 s, 8 s, 21 s ∼E7.75, E8.25, E9.25	Dissected cardiac region E7.75 (4326 WT 3535 Hand2$^{-/-}$) E8.25 (5664 WT 4112 Hand2$^{-/-}$) E9.25 (11,376 WT)	10× genomics	∼2 × 10^{4} UMIs/cell	link list 5	[29]

Table 2. *Cont.*

Resource	Stage	Selection (N Cells)	Method	Depth *	Data	Reference
scRNAseq	LHF, 8 s, 13 s, 20 s ~E7.75, E8.25, E8.75, E9.25	Nkx2-5^{+} (690), Isl1^{+} (640) Per stage: supplementary 1	Modified Smart-seq2	~1 × 10^{6} reads/cell	link list 6	[30]
scRNAseq	Pre-Streak stages ~E5.25, E5.5, E6.25, E6.5	Whole embryo E5.25 (331), E5.5 (269) E6.25 (321), E6.5 (803)	Smart-seq2	~1 × 10^{6} reads/cell **	link list 7	[31]
scRNAseq	~E7.5, E8.5, E9.5	Nkx2-5^{+} E7.5 (61), E8.5 (58) E9.5 (81) Isl1^{+} E7.5 (30), E8.5 (167) E9.5 (348 WT 50 Isl1$^{-/-}$)	Smart-seq2	~1 × 10^{6} reads/cell **	link list 8	[32]
scRNAseq	PrS to Presomitic ~E6.5 to E8.25	Whole embryo (33,700 from 153 embryos)	MARS-seq	~4 × 10^{3} UMIs/cell	link list 9	[33]
scRNAseq	LHF to 4 s ~E7.75 to E8.25	dissected cardiac region (3105)	Smart-seq2	~1 × 10^{6} reads/cell **	link list 10	[18]
scRNAseq	0B to somite stage ~E7.25 to E8.25	Mesp1^{+} (9072)	10× genomics	60,450 UMIs/cell	link list 11	[19]
snATACseq	~E8.5, E9.5	Isl1^{+} (695)	[34]	~1.5 × 10^{4} reads/nucleus *	link list 12	[32]
snATACseq	~E8.25	Whole embryo (19,453)	[35]	~2 × 10^{4} reads/nucleus *	link list 13	[28]
scNMTseq	~4.5, E5.5, E6.5, E7.5	Whole embryo (856)	[36]	~1 × 10^{6} reads/cell ***	link list 14	[37]
Live imaging	LB to 4 s ~E7.5 to E8.5	Cardiac region: 4 embryos Tdtomato mosaic Nkx2-5:GFP	Two-photon microscopy	10 min 5 µm	NA	[13]
Live imaging	LS to 2 s ~E7.0 to E8.25	4 Whole embryos, H2B:eGFP	Adaptative light-sheet microscopy	4 min 2 µm	link list 15	[38]
Live imaging	MS to LB ~E6.75 to 7.5	4 Whole embryo: T-cre mT/mG mosaic	Two-photon microscopy	20 min 3 µm	NA	[39]

NA, not available; s, somite pairs. * Median reads or time-frame and z size are shown for scOmics or live imaging experiments, respectively. In scRNAseq, lower depth approaches amplify cDNA before sequencing to increase sensitivity. Before that, captured molecules are labeled with a unique molecular identifier (UMI). For more info read [40]. ** Value not provided, calculated from the counts matrix. *** Corresponding to scRNAseq.

Link list (accessed on 25 December 2021):

1. Raw data https://www.ebi.ac.uk/arrayexpress/experiments/E-MTAB-4026/; Browser http://gastrulation.stemcells.cam.ac.uk/scialdone2016
2. Raw data https://www.ncbi.nlm.nih.gov/geo/query/acc.cgi?acc=GSE100471; Browser http://singlecell.stemcells.cam.ac.uk/mesp1
3. Raw and processed data https://www.ebi.ac.uk/arrayexpress/experiments/E-MTAB-6153/
4. Raw data https://www.ebi.ac.uk/arrayexpress/experiments/E-MTAB-6967/; Processed data https://github.com/MarioniLab/EmbryoTimecourse2018; Browser https://marionilab.cruk.cam.ac.uk/MouseGastrulation2018/
5. Raw data https://www.ncbi.nlm.nih.gov/geo/query/acc.cgi?acc=GSE126128; Browser https://cells.ucsc.edu/?ds=mouse-cardiac
6. Raw data https://www.ncbi.nlm.nih.gov/geo/query/acc.cgi?acc=GSE109071
7. Raw data https://www.ncbi.nlm.nih.gov/geo/query/acc.cgi?acc=GSE108963
8. Raw and processed data https://www.ebi.ac.uk/ena/browser/view/PRJEB23303?show=reads
9. Raw and processed data https://www.ncbi.nlm.nih.gov/geo/query/acc.cgi?acc=GSE169210; Browser https://tanaylab.weizmann.ac.il/embflow/
10. Raw, processed data and Browser https://marionilab.cruk.cam.ac.uk/heartAtlas/;

11. Raw data https://www.ncbi.nlm.nih.gov/geo/query/acc.cgi?acc=GSE176306; Browser https://cells.ucsc.edu/?ds=chi-10x-mouse-cardiomyocytes
12. Raw and processed data https://www.ebi.ac.uk/ena/browser/view/PRJEB23303?show=reads;
13. Raw and processed data https://www.ncbi.nlm.nih.gov/geo/query/acc.cgi?acc=GSE133244; Browser https://gottgens-lab.stemcells.cam.ac.uk/snATACseq_E825/
14. Raw data https://www.ncbi.nlm.nih.gov/geo/query/acc.cgi?acc=GSE121708; Processed data ftp://ftp.ebi.ac.uk/pub/databases/scnmt_gastrulation
15. Raw data https://idr.openmicroscopy.org/webclient/?show=project-502

2. Cell Fate Specification Preceding Primitive Heart Tube Formation

Once the primitive heart tube is assembled, it contains two cell types: cardiomyocytes (CMs), which form the muscular wall and endocardial cells (ECs), which are specialized endothelial cells lining the cardiac lumen [41]. Besides forming a continuum with the embryonic vasculature, ECs are involved in the formation of trabeculae [42–44] and contribute to the formation of the cardiac valves and septa [45,46]. ECs differ from other endothelial cells in their gene expression profile [47–49] and follow specific differentiation programs [42]. In the course of evolution, CMs arose from the transformation of mesenteric coelomic epithelium in early metazoans [50] while endothelial cells appeared later in vertebrates, likely from adherent hemocytes [51]. With these phylogenetic differences, CMs and ECs are found side-by-side at the anterior splanchnic mesoderm at the initiation of heart tube formation (Figure 1). Their ontogeny has been studied across multiple organisms, but it remains unclear if they originate from a homogeneous pool or from two distinct populations, pre-specified to adopt CM or EC fate [11,52].

2.1. Temporal Sequence of Fate Acquisition

Knowing when a fate decision takes place is the first step to understand the mechanisms governing it. In classic embryology, a single cell or a group of cells is considered *specified* when it systematically yields a certain cell type. A tool to address the temporal sequence specification is clonal analysis [53]. By labelling single cells at different developmental stages and examining their progenies, one can infer when cell lineages become restricted—i.e., a progenitor cell that gave rise to both CMs and ECs was not specified to either fate at the time it was labelled. In prospective clonal analysis, researchers know the stage and location of the progenitor cell. This is achieved by direct labelling through manipulation of oviparous or *ex utero* viviparous embryos. In retrospective clonal analysis, cells are genetically labelled *in utero* so the embryonic stage and cell location are only approximated or unknown [54].

Clonal analysis experiments in zebrafish, chicken and mouse models traced the location of cardiovascular progenitors and pointed to an early specification of CMs and ECs, happening around the onset of gastrulation. To ease the interpretation of these valuable data, we summarized the experiments in Table 1. Prospective labelling in zebrafish early blastula (512 cells, 2.75 hpf) defined an area at the lateral marginal zone, enriched for unspecified cardiovascular progenitors [20]. Labelling the same area at 40% epiboly stage (5 hpf) yields few mixed progenies containing both CMs and ECs, indicating they are already specified when gastrulation begins [21]. Fate mapping in both cases shows that CM and EC progenitors are spatially intermingled. In chicken embryos, the rostral half of the primitive streak contains both cardiac progenitors [55,56], which are already specified to form either CM or EC progenies [23,57]. Retrospective clonal analysis in mouse embryos also suggests an early specification. Genetically labelled *Mesp1*-expressing cells around the onset of gastrulation (∼E6.25) give rise to clusters in the left ventricle at E14.5 containing either only CM or only EC [24]. Conversely, a quarter of *Mesp1*-expressing clones labelled at ∼E7.25 gave rise to mixed progenies in the right ventricle [24], indicating that although the primitive heart tube arises from precursors that are already specified at gastrulation, later pools of progenitors from the second heart field can be multipotent [58]. In line with this re-

sult, lineage tracing and in vitro studies have suggested the existence of mouse [58–62] and human [63] multipotent cardiac progenitors. A way to characterize further these progenitors would be to examine recent scRNAseq datasets for a cardiac multipotency signature in gastrulating mouse [18,28,29] and human embryos [64]. Together, these studies show CM and EC specification occurs at the onset of gastrulation or even before across vertebrate species, which is surprisingly long before the start of heart morphogenesis; however, pools of cardiac progenitors established later at the second heart field may remain multipotent.

Regardless of the timing of specification, the lineage relationship between CMs and ECs is controversial. Genetic lineage tracing of cardiac transcription factors and stem cell experiments support both cell types arise from a cardiac-specific common progenitor [11,59–61,65–67]. In contrast, zebrafish mid-blastula clones containing both CMs and ECs also give rise to blood vessels and blood cells [20] (Table 1), suggesting a CM-EC exclusive progenitor does not exist or it does very transiently. An alternative lineage tree proposes that ECs derive from the hematopoietic/vascular progenitors, and then migrate to populate the developing heart tube in zebrafish embryos [68,69]. To assess the lineage relationship among cardiac, hematoendothelial and other mesodermal progenitors, future clonal analysis experiments should examine the presence of labelled cells in all mesodermal tissues and not only in the heart [19]. New approaches such as CRISPR/Cas9-based lineage tracing [70,71] and *in toto* live-cell tracking [38], will also help to answer this long-standing question.

2.2. Molecular Mechanisms of Specification

Understanding the mechanisms underlying cell fate decisions involves characterizing the cellular heterogeneity that precedes lineage specification [72]. A homogeneous niche of progenitors can segregate by various mechanisms to form subpopulations with different fates. Recently, the development of single cell transcriptomics and genomics transformed the way we study cellular heterogeneity in vivo [28,37,73]. The simultaneous characterization of the different cell populations forming an embryo allows one to make predictions about their ontogeny as well as showcasing gene regulatory networks responsible for it [74].

Single-cell RNA sequencing (scRNAseq) of gastrulating *Mesp1*-positive cells displays the transcriptional divergence of cardiac progenitors in vivo, revealing that CM and EC branches first diverge at ∼E7.25 [26]. If pre-specified CM and EC progenitors exist at PS ingression (∼E6.75 in mouse)—see Section 2.1—the transcriptional divergence captured at ∼E7.25 by this approach may account for the earliest signs of differentiation but it remains unknown whether this segregation is a direct effect of their prior specification. Analyzing the trajectory of cardiac cells in emerging scRNAseq datasets (Table 2), especially in those prioritizing sequence depth over cell number, would shed light on whether transcriptional differences account for CM and EC early specification.

As demonstrated in *Drosophila*, single-cell chromatin accessibility mapping also allows identifying molecular processes involved in fate specification [75]. In addition to differences in RNA expression, epigenetic modifications contribute to cellular heterogeneity. As an example, early haematoendothelial clusters defined by scRNAseq in mouse can be further classified by their open chromatin regions corresponding to *Tal1*-bound cell-type specific enhancers [76]. Similarly, chromatin accessibility mapping in mouse ∼E8.5 *Isl1*-expressing cells reveals distinct epigenetic signatures, likely corresponding to differently fated progenitors [32]. This shows how cells within a scRNAseq cluster can differ in terms of accessibility to regulatory loci that account for changes in responsiveness to signaling cues. Thus, epigenetic analyses may distinguish fate specification in transcriptionally homogeneous populations, as these changes can anticipate RNA expression divergence. In fact, analysis of poised enhancers—distinguished from active enhancers by the H3K27me3 mark [77]—predicts developmental competence in human derived endodermal stem cells [78]. This, together with the functional relevance of chromatin remodeling complexes in gastrulation and cardiogenesis [79,80] makes epigenetic heterogeneity a candidate mechanism

to explain CM and EC early segregation in primitive heart tube formation. The increasing availability of single-cell transposase-accessible chromatin (scATACseq) methods [34] will likely motivate researchers to explore epigenetic heterogeneity in the coming years.

3. Differentiation of Primitive Heart Tube Progenitors

3.1. Signaling Cues Driving CM and EC Differentiation

After ingression, CM and EC progenitors migrate to the anterior-proximal side of the embryo proper (see Section 1 and Figure 1), where signaling cues from the subjacent endoderm promote their differentiation [81,82]. Integration of the BMP, FGF and Wnt pathways forges an environment that promotes primitive heart tube morphogenesis among vertebrate species [83]. For example, *Bmp2* and *Fgf8* zebrafish mutant embryos express less *Nkx2-5* and differentiate fewer CMs. Removal of endoderm also causes a downregulation of cardiac markers in chicken, which can be rescued by supplying exogenous FGF8 or BMP2 [84]. In vitro, BMP2 released from anterior visceral endoderm cell lines induces CM generation in embryoid bodies [85]. On the other hand, Wnt/β-catenin signaling prevents premature CM differentiation at the lateral plate mesoderm, but its expression is necessary for CM progenitor proliferation and ingression through the primitive streak [86]. In vitro, the timing of Wnt activation/deactivation cycles is also critical for CM differentiation in human induced pluripotent stem cells [87] and heart organoids [88]. Likewise, *Wnt5a*-mediated Wnt inhibition promotes EC differentiation in mouse early cardiac progenitors, while hindering CM differentiation [89]. Altogether, the signaling environment provided by the endoderm ensures that CM and EC differentiation occurs at the right time and location. In fact, the anterior intestinal portal can induce cardiac identity from non-cardiac mesoderm and pattern the ventricular and atrial domains in chicken, pinpointing the anterior endoderm as a heart organizer in vertebrates [90].

Besides diffusible cues, local signaling also plays a role in CM and EC differentiation. For example, cells with active Notch do not form CM colonies and forced activation of NOTCH1 in embryonic stem (ES) cells inhibits their differentiation to CM, while Notch inactivation promotes it [91,92]. This inhibitory effect also takes place in vivo: in Drosophila, loss and gain of function studies show Notch inhibits CM differentiation [93]; in Xenopus, Notch signaling limits the number of CM through the Serrate ligand [94]; in chicken, retroviral overexpression of Notch intracellular domain (NICD) in the heart tube reduces the expression of CM markers [95]; and in mouse, although NICD overexpression does not alter the number of CM or marker expression, it results in CM maturation defects including disrupted sarcomeric structures [96]. Conversely, *Notch1* is required for the development of the endothelium [97,98] and its expression marks mesodermal progenitors differentiating towards EC [26].

Unlike that of endothelial cells, CM differentiation is tightly coupled to gastrulation. Removal of the transcription factors *Etv2* or *Npas4l* yields embryos that lack endothelial cells but undergo gastrulation normally, forming a heart tube without ECs [99,100]. To date, no genetic manipulation produced embryos that gastrulate but fail to form CMs: all mutants without CMs also fail to gastrulate, lacking all anterior mesoderm tissues [101–106]. In some of these, stuck mesodermal cells express CM differentiation markers [106] or even form bilateral heart tubes [9]. This suggests that once gastrulation is initiated successfully, CM differentiation will occur regardless of the anterior endoderm signaling cues [107]. In fact, gastrulation and early heart tube formation share many common genetic cascades implicating members of the *Mesp* transcription factor, Fgf and Wnt signaling pathways. An interpretation is that differentiation towards CM is determined concomitantly with gastrulation, or even represents the default state of anterior mesoderm, and the signaling environment may only modulate when and where the differentiation takes place. In support of this notion, non-cardiac mesoderm regions need to repress the CM programs to avoid ectopic differentiation [69,108–110].

3.2. Redirection of Cardiac Progenitor Differentiation upon Perturbation

Although primitive heart tube progenitors get specified to CMs and ECs at early stages (see Section 2.1), their definitive differentiation depends on surrounding signaling cues (see Section 3.1) and can be modified upon perturbation. In zebrafish, embryos lacking transcription factors as *Tal1* and *Etv2* have fewer ECs but expand their CM pool [42,108], with some *Etv2* endothelial progenitors differentiating to CMs [108]. Indeed, scRNAseq shows FGF and Wnt signaling detours vascular progenitors towards a muscular fate in the absence of *Etv2* [111]. In line with this, injecting *Tal1* or *Etv2* mRNA at the lateral plate mesoderm expands the endothelial domain while reducing the number of CMs [69]. In mouse, deletion of *Tal1* yields CM-like differentiation in both yolk sac and endocardium through cell-autonomous Wnt antagonism [112]. Likewise, the enforced activation or inhibition of Wnt reduced or increased, respectively, endothelial differentiation in cardiac progenitors [89]. Finally, overexpression of *Sox17*, which is expressed downstream of *Etv2*, causes ectopic expression of PECAM1 endothelial marker in CMs [113].

Overall, these studies show CM and EC progenitors can modulate their fate in vivo upon perturbation of differentiation pathways, redirecting their fate even after specified. In vitro differentiation studies also illustrate the versatility of early mesodermal progenitors. A subset of ES-derived mesodermal cells, which start expressing *Flk1*, can differentiate to either CMs or ECs in a context-dependent manner [59,61]. Notably, a sub-population of the *Flk1*-negative ES-derived mesodermal cells can also be redirected in vitro towards a myocardial cell fate in mouse and human [114–116]. However, these results must be interpreted with caution, as stem cells can take differentiation roads that are not developmentally relevant.

3.3. Plasticity of Cardiac Progenitors

In early cardiac progenitors, cellular plasticity has been reported in vivo after primitive heart tube formation [1,117] and in ES cells models [118]. An example of in vivo cell plasticity is the interchangeability between atrial and ventricular CM progenitors. In chicken, cardiac ventricle progenitors derive from anterior regions of the cardiac mesoderm while atria progenitors arise from more posterior regions [55,119–122]. However, presumptive atrial cells can adopt ventricular properties when placed in the prospective ventricular domain [123] up to HH8 stage—when heart tube assembles. In mouse embryos, deletion of *COUP-TFII* in atrial CMs can switch their identity to ventricular CMs up to stage ~12.5, long after the formation of the cardiac chambers [124].

Together, the experiments cited in these three subsections show the definitive differentiation of cardiac progenitors is not fixed as it can change upon positional cues or intrinsic signaling perturbations. This way, despite the mechanisms normally involved in establishing the identity of cardiac cells, the signaling environment plays a role in their definitive differentiation [125].

4. Molecular Heterogeneity of the Cardiomyocyte Sources within the Primitive Heart Tube

Studying the molecular regulation of the different cell populations composing the primitive heart tube is important to understand their subsequent role in morphogenesis. Molecular signatures give us hints about cell behavior, features and susceptibility to signaling cues. Two recent outstanding papers have characterized the primitive heart tube transcriptional heterogeneity with unprecedented detail, reporting a novel cardiac progenitor pool that contributes to FHF cardiomyocytes and contains the earliest known progenitors of the epicardium [18,19] (Figure 2).

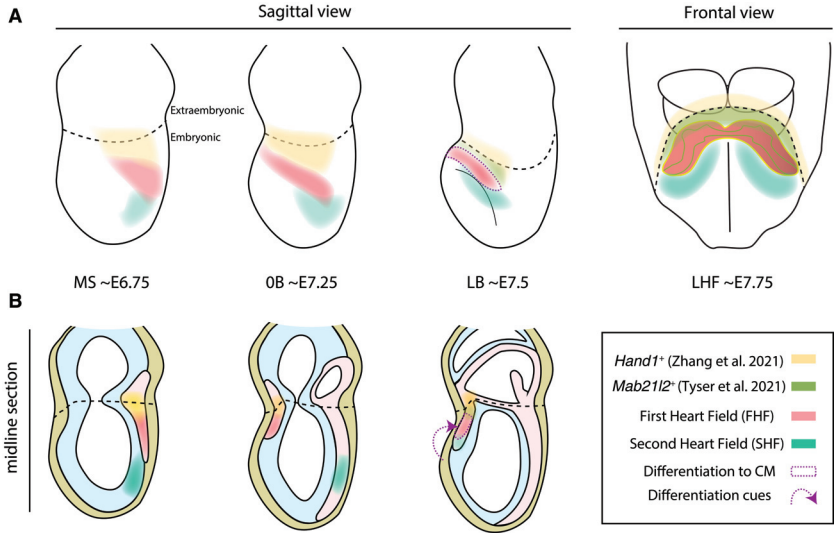

Figure 2. Progenitor domains contributing to heart tube cell populations in the mouse. Diagrams show whole embryos (**A**) and midline sections (**B**). Notice how the First Heart Field (FHF), Second Heart Field (SHF) and the recently characterized *Mab21l2*/*Hand1* population stay in a continuum until differentiation cues recruit the FHF to form the primitive heart tube. In the section diagrams (**B**), endoderm, epiblast and mesoderm are painted in yellow, cyan and light red, following Figure 1 color code. Diagrams were done based on [18,19].

Single-cell RNA sequencing (scRNAseq) of the mouse anterior cardiac region at cardiac crescent to linear heart tube stages (∼E7.75 to ∼E8.25) identified six different cardiac clusters in the anterior-proximal region of the embryo proper [18]. Differential expression analysis linked two of the clusters to the first and second heart field, respectively, while a third cluster represented an intermediate differentiation state between both. Strikingly, one of the clusters did not fit any previously known categorization, as it expressed some FHF markers, like *Hand1* and *Tbx5*, but lacked canonical differentiation markers, such as *Nkx2-5*. RNA fluoresence in situ hybridization of marker *Mab21l2*, a protein coding gene implicated in cardiac and neural development [126,127], mapped this novel cluster at the rostral border of the cardiac crescent, forming a narrow band of splanchnic mesoderm at the confluence of the embryonic and extraembryonic compartments of the embryo (Figure 2).

Analysis of the scRNAseq data revealed two distinct trajectories towards differentiated CMs, parting from the SHF cluster and the *Mab21l2* cluster, respectively; the first connected SHF to differentiated CM via an intermediate state, which likely corresponds to the incorporation of SHF progenitors to the heart tube at the arterial pole [13,128,129]; the second trajectory linked the newly identified *Mab21l2* cluster to differentiated CM via another intermediate state, unveiling a previously undescribed source of CMs. Lineage tracing of cells expressing *Mab21l2* at ∼E6.5–E7.5 yielded left ventricle CMs as well as epicardial cells. However, this cluster does not contribute to CMs of the right ventricle or outflow track. This implies that the *Mab21l2* cluster, dubbed Juxta Cardiac Field (JCF) by the authors, supplies CMs to the FHF and contains the earliest known progenitors of the epicardium.

With a similar strategy, scRNAseq and trajectory analysis of *Mesp1*-expressing cells from ∼E7.25–E8.25 mouse embryos also predicted a cardiac population [19] that partially overlaps the *Mab21l2* cluster [18] but expands beyond the extraembryonic boundary (Figure 2). Lineage tracing of *Hand1*-expressing cells at ∼E5.75–E6.75 yielded a contribution to the heart tube similar to that of the *Mab21l2* cluster [18], reinforcing the idea of the cardiac potential this cell population. In addition, retrospective clonal analysis of *Hand1*-expressing

cells at ∼E6.75–E8.25 revealed that these progenitors are multipotent. While most progenies contributed only to the yolk sac, a fourth contained a mixture of two or three distinct lineages including yolk sack, pericardium, proepicardium and atrioventricular canal or left ventricle CM [19]. As retrospective analyses render only approximate staging, multipotent clones may have resulted either from early inductions at the primitive streak or from later mesodermal cells that cross the embryonic/extraembryonic boundary. The latter would disagree with live imaging data reporting a clear segregation between embryonic and extraembryonic cells following the onset of gastrulation [39]. Estimating the induction time of the clones from their cell counts or prospectively labelling the *Hand1* domain would clarify for how long this novel population remains multipotent.

Altogether, these studies uncover a previously uncharacterized cardiac progenitor population contributing mainly to the left ventricle and epicardium. In both publications, this population lies at the embryonic/extraembryonic boundary and constitutes a spatially and transcriptionally distinct population from *Tbx18*-expressing sinus venosus progenitors, which are recruited from a more caudal splanchnic mesoderm area [130]. While the first study defined this population at cardiac crescent stages (∼E7.75) using *Mab2l12* as a marker [18], the second described a broader and earlier population expressing *Hand1* at ∼E6.25–E7.25 [19], making the *Mab21l2* domain a likely subset among *Hand1*-expressing cells (Figure 2). Whether this population remains multipotent at cardiac crescent stages or only holds this ability at earlier stages is a pending question.

5. Discussion and Future Perspectives

Early heart development is a complex process involving heterogeneous sources of cell progenitors. Such complexity allows the heart to function while it keeps forming but makes the process susceptible to errors, likely responsible for the high incidence of congenital heart defects. Although single-gene mutations are linked to certain rare diseases [131], understanding the wide spectrum of congenital heart defects requires the integration of multiple gene regulatory networks that pattern the heterogeneous set of cellular functions in the heart.

An early lineage diversification in cardiac development emerges around gastrulation, when progenitor cells specify towards myocardial and endocardial fates. Chicken and zebrafish prospective clonal analysis demonstrate CM and EC progenitors are already segregated once they are recruited to the mesoderm, with retrospective experiments in mouse suggesting a similar outcome (see Section 2.1). However, it is still unclear when this fate decision takes place and what are the mechanisms governing it. Classic precepts consider that a common cardiac progenitor bifurcates into either CM or EC, but alternative models suggest ECs derive from a common endothelial lineage, shared with the rest of the vessels in the embryo proper and yolk sac (see Section 2.1). As the endothelium is a relatively recent innovation in evolution, this raises the question of whether early vertebrates recycled the CM program in the mesoderm to form endothelial cells and build complex circulatory systems. A dedicated analysis of single-cell genomics and live imaging data (Table 2) will likely define the ontogeny of CM and EC populations, charting the definitive Waddington landscape [132] of primitive heart tube specification. Interpretation of the big data generated by these approaches requires the use of programming and mathematics [133], but step-by-step tutorials allow researchers from a life sciences background to access these tools [40]. In fact, an increasing number of papers are setting an example by providing user-friendly guidance on the use of their code, easing the reanalysis of their data [28,38].

In a broader view, these high-resolution data are reshaping our perspectives on how embryos develop. In classic embryology textbooks, embryos were classified into two broad categories: regulative and mosaic embryos [134]. In the first type, characteristic of vertebrates, cells organize to form different organs by regulating their fate "on the go" through interactions with their surroundings. Regulative embryos can adapt to perturbations as cell decisions are continuously rechecked according to positional information and the signaling environment. In mosaic embryos, characteristic of the invertebrates, each cell or group

of cells have a restricted fate, which is acquired autonomously through intrinsic factors. A century later, we know that in reality all embryos are both mosaic and regulative to some extent. Ascidian and nematode embryos, examples of stereotyped development with invariant cell lineages, also employ cell-cell contacts and cytokine signaling to orchestrate organ differentiation once they reach a certain cell number [135,136]. Conversely, mouse ES cells cannot contribute to some extraembryonic tissues such as the trophoblast and primitive endoderm, suggesting an intrinsic restriction in cell potency in early vertebrate embryos [137]. Thus, as shown in this review for the primitive heart tube, both intrinsic cell heterogeneity and signaling cues collaborate to progressively define cellular identity during embryo development.

In the discussion between regulative and predetermined conceptions, the division of cardiac progenitors as multiple predefined populations is a topic of debate. While some studies show an early segregation of the first and second heart field as predetermined populations with distinct susceptibility to differentiation [24,26,58], others argue that the earlier differentiation of the FHF is governed by positional cues and not by intrinsic cellular differences [138]. Likewise, the recently characterized *Mab21l2/Hand1* progenitors contributing to cardiomyocytes and epicardium (see Section 4 and Figure 2) could be defined as a separate cardiac field. In favor of this notion, these progenitors show a unique transcriptomic signature and contribute systematically to specific regions of the heart. Nonetheless, it still remains to be tested whether the contributions of these regions are essential for heart development. In the case of FHF and SHF, elimination of the contribution of either population results in fatal cardiac malformations [139], whereas elimination of the contribution of these newly described regions to the cardiomyocyte pool has not been explored. On the other hand, the definition of developmental fields based solely on the recombination pattern of a particular transgene poses some questions, like whether the transgene labels cells before the full specification of the fields. In any case, the description of these novel *Mab21l2/Hand1* progenitors deepens our understanding on the heterogeneous sources of the cells that form the heart tube. A key question that arises is whether these heterogeneous sources confer developmental robustness and functional diversity to the mammalian heart. In that sense, it will be interesting to assess whether the *Mab21l2/Hand1* progenitors are also present in anamniotes [17] or instead constitutes an evolutionary novelty that contributed to increase the complexity of the heart tube. Thus, exploiting single-cell omics and live-imaging data will lead to novel insights in understanding heart development (Table 2). The same way pioneer work by Gittenberger-de Groot and colleagues illuminated the different sources contributing to the arterial pole [140], identifying the states of the interacting components of the heart will continue to shed light on our understanding of congenital heart defects.

Author Contributions: Writing—original draft preparation, M.S., O.H.O.; writing—review and editing, M.S. O.H.O. J.N.D., M.T. All authors have read and agreed to the published version of the manuscript.

Funding: Stated in acknowledgements.

Institutional Review Board Statement: Not applicable.

Informed Consent Statement: Not applicable.

Data Availability Statement: Not applicable.

Acknowledgments: Grant support PGC2018-096486-B-I00 from the Spanish Ministerio de Ciencia eInnovación and Grant H2020-MSCA-ITN-2016-722427 from the EU Horizon 2020 program to MT.MS was supported by a La Caixa Foudation PhD fellowship (LCF/BQ/DE18/11670014) and TheCompany of Biologists travelling fellowship (DEVTF181145). OH.O. is supported by the Ministerio deCiencia e Innovación (grant RTI2018-097617-J-I00). The CNIC is supported by the Spanish Ministeryof Science and the ProCNIC Foundation.

Conflicts of Interest: The authors declare no conflict of interest.

References

1. Meilhac, S.M.; Buckingham, M.E. The deployment of cell lineages that form the mammalian heart. *Nat. Rev. Cardiol.* **2018**, *15*, 705–724. [CrossRef]
2. Zimmerman, M.S.; Smith, A.G.C.; Sable, C.A.; Echko, M.M.; Wilner, L.B.; Olsen, H.E.; Atalay, H.T.; Awasthi, A.; Bhutta, Z.A.; Boucher, J.L.A.; et al. Global, regional, and national burden of congenital heart disease, 1990–2017: A systematic analysis for the Global Burden of Disease Study 2017. *Lancet Child Adolesc. Health* **2020**, *4*, 185–200. [CrossRef]
3. Gittenberger-de Groot, A.C.; Winter, E.M.; Bartelings, M.M.; Jose Goumans, M.; DeRuiter, M.C.; Poelmann, R.E. The arterial and cardiac epicardium in development, disease and repair. *Differentiation* **2012**, *84*, 41–53. [CrossRef] [PubMed]
4. Gittenberger-De Groot, A.C.; Moulaert, A.J.; Harinck, E.; Becker, A.E. Histopathology of the ductus arteriosus after prostaglandin E1 administration in ductus dependent cardiac anomalies. *Br. Heart J.* **1978**, *40*, 215–220. [CrossRef]
5. Lawson, K.A.; Pedersen, R.A. Clonal analysis of cell fate during gastrulation and early neurulation in the mouse. *Ciba Foundation Symp.* **1992**, *165*, 3–21. [CrossRef]
6. Lawson, K.A.; Meneses, J.J.; Pedersen, R.A. Clonal analysis of epiblast fate during germ layer formation in the mouse embryo. *Development* **1991**, *113*, 891–911. [CrossRef] [PubMed]
7. Tam, P.P.; Zhou, S.X. The allocation of epiblast cells to ectodermal and germ-line lineages is influenced by the position of the cells in the gastrulating mouse embryo. *Dev. Biol.* **1996**, *178*, 124–132. [CrossRef] [PubMed]
8. Tam, P.P.; Behringer, R.R. Mouse gastrulation: The formation of a mammalian body plan. *Mech. Dev.* **1997**, *68*, 3–25. [CrossRef]
9. Saga, Y.; Miyagawa-Tomita, S.; Takagi, A.; Kitajima, S.; Miyazaki, J.I.; Inoue, T. MesP1 is expressed in the heart precursor cells and required for the formation of a single heart tube. *Development* **1999**, *126*, 3437–3447. [CrossRef] [PubMed]
10. Street, D. Early differentiation of the heart in mouse embryos. *J. Anat.* **1981**, *133*, 235–246.
11. Harris, I.S.; Black, B.L. Development of the endocardium. *Pediatr. Cardiol.* **2010**, *31*, 391–399. [CrossRef] [PubMed]
12. Buckingham, M.; Meilhac, S.; Zaffran, S. Building the mammalian heart from two sources of myocardial cells. *Nat. Rev. Genet.* **2005**, *6*, 826–835. [CrossRef]
13. Ivanovitch, K.; Temiño, S.; Torres, M. Live imaging of heart tube development in mouse reveals alternating phases of cardiac differentiation and morphogenesis. *eLife* **2017**, *6*, e30668. [CrossRef] [PubMed]
14. Downs, K.M.; Davies, T. Staging of gastrulating mouse embryos by morphological landmarks in the dissecting microscope. *Development (Camb. Engl.)* **1993**, *118*, 1255–1266. [CrossRef]
15. Jensen, B.; Christoffels, V.M.; Moorman, A.F. An appreciation of anatomy in the molecular world. *J. Cardiovasc. Dev. Dis.* **2020**, *7*, 44. [CrossRef]
16. Kelly, R.G.; Buckingham, M.E.; Moorman, A.F. Heart fields and cardiac morphogenesis. *Cold Spring Harb. Perspect. Med.* **2014**, *4*, a015750. [CrossRef]
17. Kemmler, C.L.; Riemslagh, F.W.; Moran, H.R.; Mosimann, C. From stripes to a beating heart: Early cardiac development in zebrafish. *J. Cardiovasc. Dev. Dis.* **2021**, *8*, 1–21. [CrossRef] [PubMed]
18. Tyser, R.C.; Ibarra-Soria, X.; McDole, K.; Jayaram, S.A.; Godwin, J.; Brand, T.A.D.; Miranda, A.M.; Scialdone, A.; Keller, P.J.; Marioni, J.C.; et al. Characterization of a common progenitor pool of the epicardium and myocardium. *Science* **2021**, *371*, eabb2986. [CrossRef]
19. Zhang, Q.; Carlin, D.; Zhu, F.; Cattaneo, P.; Ideker, T.; Evans, S.M.; Bloomekatz, J.; Chi, N.C. Unveiling Complexity and Multipotentiality of Early Heart Fields. *Circ. Res.* **2021**, *129*, 474–487. [CrossRef] [PubMed]
20. Lee, R.K.; Stainier, D.Y.; Weinstein, B.M.; Fishman, M.C. Cardiovascular development in the zebrafish II. Endocardial progenitors are sequestered within the heart field. *Development* **1994**, *120*, 3361–3366. [CrossRef]
21. Keegan, B.R. Organization of cardiac chamber progenitors in the zebrafish blastula. *Development* **2004**, *131*, 3081–3091. [CrossRef]
22. Mao, L.M.; Boyle Anderson, E.A.; Ho, R.K. Anterior lateral plate mesoderm gives rise to multiple tissues and requires tbx5a function in left-right asymmetry, migration dynamics, and cell specification of late-addition cardiac cells. *Dev. Biol.* **2021**, *472*, 52–66. [CrossRef] [PubMed]
23. Wei, Y.; Mikawa, T. Fate diversity of primitive streak cells during heart field formation in ovo. *Dev. Dyn.* **2000**, *219*, 505–513. [CrossRef]
24. Lescroart, F.; Chabab, S.; Lin, X.; Rulands, S.; Paulissen, C.; Rodolosse, A.; Auer, H.; Achouri, Y.; Dubois, C.; Bondue, A.; et al. Early lineage restriction in temporally distinct populations of Mesp1 progenitors during mammalian heart development. *Nat. Cell Biol.* **2014**, *16*, 829–840. [CrossRef]
25. Scialdone, A.; Tanaka, Y.; Jawaid, W.; Moignard, V.; Wilson, N.K.; Macaulay, I.C.; Marioni, J.C.; Göttgens, B. Resolving early mesoderm diversification through single-cell expression profiling. *Nature* **2016**, *535*, 289–293. [CrossRef]
26. Lescroart, F.; Wang, X.; Lin, X.; Swedlund, B.; Gargouri, S.; Sànchez-dànes, A.; Dubois, C.; Paulissen, C.; Kinston, S.; Göttgens, B.; et al. Defining the earliest step of cardiovascular lineage segregation by single-cell RNA-seq. *Science* **2018**, *4174*, 1–9. [CrossRef] [PubMed]
27. Ibarra-Soria, X.; Jawaid, W.; Pijuan-Sala, B.; Ladopoulos, V.; Scialdone, A.; Jörg, D.J.; Tyser, R.C.; Calero-Nieto, F.J.; Mulas, C.; Nichols, J.; et al. Defining murine organogenesis at single-cell resolution reveals a role for the leukotriene pathway in regulating blood progenitor formation. *Nat. Cell Biol.* **2018**, *20*, 127–134. [CrossRef]

28. Pijuan-Sala, B.; Griffiths, J.A.; Guibentif, C.; Hiscock, T.W.; Jawaid, W.; Calero-Nieto, F.J.; Mulas, C.; Ibarra-Soria, X.; Tyser, R.C.; Ho, D.L.L.; et al. A single-cell molecular map of mouse gastrulation and early organogenesis. *Nature* **2019**, *566*, 490–495. [CrossRef]
29. de Soysa, T.Y.; Ranade, S.S.; Okawa, S.; Ravichandran, S.; Huang, Y.; Salunga, H.T.; Schricker, A.; del Sol, A.; Gifford, C.A.; Srivastava, D. Single-cell analysis of cardiogenesis reveals basis for organ-level developmental defects. *Nature* **2019**, *572*, 120–124. [CrossRef]
30. Cheng, S.; Pei, Y.; He, L.; Peng, G.; Reinius, B.; Tam, P.P.; Jing, N.; Deng, Q. Single-Cell RNA-Seq Reveals Cellular Heterogeneity of Pluripotency Transition and X Chromosome Dynamics during Early Mouse Development. *Cell Rep.* **2019**, *26*, 2593–2607. [CrossRef]
31. Xiong, H.; Luo, Y.; Yue, Y.; Zhang, J.; Ai, S.; Li, X.; Wang, X.; Zhang, Y.L.; Wei, Y.; Li, H.H.; et al. Single-Cell Transcriptomics Reveals Chemotaxis-Mediated Intraorgan Crosstalk during Cardiogenesis. *Circ. Res.* **2019**, *125*, 398–410. [CrossRef]
32. Jia, G.; Preussner, J.; Chen, X.; Guenther, S.; Yuan, X.; Yekelchyk, M.; Kuenne, C.; Looso, M.; Zhou, Y.; Teichmann, S.; et al. Single cell RNA-seq and ATAC-seq analysis of cardiac progenitor cell transition states and lineage settlement. *Nat. Commun.* **2018**, *9*, 1–17. [CrossRef]
33. Mittnenzweig, M.; Mayshar, Y.; Cheng, S.; Ben-Yair, R.; Hadas, R.; Rais, Y.; Chomsky, E.; Reines, N.; Uzonyi, A.; Lumerman, L.; et al. A single-embryo, single-cell time-resolved model for mouse gastrulation. *Cell* **2021**, *184*, 2825–2842. [CrossRef]
34. Chen, Q.; Shi, J.; Tao, Y.; Zernicka-Goetz, M. Tracing the origin of heterogeneity and symmetry breaking in the early mammalian embryo. *Nat. Commun.* **2018**, *9*, 1–11. [CrossRef]
35. Preissl, S.; Fang, R.; Huang, H.; Zhao, Y.; Raviram, R.; Gorkin, D.U.; Zhang, Y.; Sos, B.C.; Afzal, V.; Dickel, D.E.; et al. Single-nucleus analysis of accessible chromatin in developing mouse forebrain reveals cell-type-specific transcriptional regulation. *Nat. Neurosci.* **2018**, *21*, 432–439. [CrossRef]
36. Clark, S.J.; Argelaguet, R.; Kapourani, C.A.; Stubbs, T.M.; Lee, H.J.; Alda-Catalinas, C.; Krueger, F.; Sanguinetti, G.; Kelsey, G.; Marioni, J.C.; et al. ScNMT-seq enables joint profiling of chromatin accessibility DNA methylation and transcription in single cells. *Nat. Commun.* **2018**, *9*, 1–9. [CrossRef]
37. Argelaguet, R.; Clark, S.J.; Mohammed, H.; Stapel, L.C.; Krueger, C.; Kapourani, C.A.; Imaz-Rosshandler, I.; Lohoff, T.; Xiang, Y.; Hanna, C.W.; et al. Multi-omics profiling of mouse gastrulation at single-cell resolution. *Nature* **2019**, *576*, 487–491. [CrossRef]
38. McDole, K.; Guignard, L.; Amat, F.; Berger, A.; Malandain, G.; Royer, L.A.; Turaga, S.C.; Branson, K.; Keller, P.J. In Toto Imaging and Reconstruction of Post-Implantation Mouse Development at the Single-Cell Level. *Cell* **2018**, *175*, 859–876. [CrossRef]
39. Saykali, B.; Mathiah, N.; Nahaboo, W.; Racu, M.L.; Hammou, L.; Defrance, M.; Migeotte, I. Distinct mesoderm migration phenotypes in extra-embryonic and embryonic regions of the early mouse embryo. *eLife* **2019**, *8*, e42434. [CrossRef]
40. Luecken, M.D.; Theis, F.J. Current best practices in single-cell RNA-seq analysis: A tutorial. *Mol. Syst. Biol.* **2019**, *15*, e8746. [CrossRef]
41. Rosenquist, G.C. Location and movements of cardiogenic cells in the chick embryo: The heart-forming portion of the primitive streak. *Dev. Biol.* **1970**, *22*, 461–475. [CrossRef]
42. Stainier, D.Y.; Weinstein, B.M.; Detrich, H.W.; Zon, L.I.; Fishman, M.C. Cloche, an early acting zebrafish gene, is required by both the endothelial and hematopoietic lineages. *Development* **1995**, *121*, 3141–3150. [CrossRef]
43. Gassmann, M.; Casagranda, F.; Orloli, D.; Simon, H.; Lai, C.; Kleint, R.; Lemke, G. Aberrant neural and cardiac development in mice lacking the ErbB4 neuregulin receptor. *Nature* **1995**, *378*, 390–394. [CrossRef]
44. Peshkovsky, C.; Totong, R.; Yelon, D. Dependence of cardiac trabeculation on neuregulin signaling and blood flow in zebrafish. *Dev. Dyn.* **2011**, *240*, 446–456. [CrossRef]
45. Nakajima, Y.; Mironov, V.; Yamagishi, T.; Nakamura, H.; Markwald, R.R. Expression of smooth muscle alpha-actin in mesenchymal cells during formation of avian endocardial cushion tissue: A role for transforming growth factor β3. *Dev. Dyn.* **1997**, *209*, 296–309. [CrossRef]
46. Brown, C.B.; Boyer, A.S.; Runyan, R.B.; Barnett, J.V. Antibodies to the type II TGFβ receptor block cell activation and migration during atrioventricular cushion transformation in the heart. *Dev. Biol.* **1996**, *174*, 248–257. [CrossRef]
47. Feng, W.; Chen, L.; Nguyen, P.K.; Wu, S.M.; Li, G. Single Cell Analysis of Endothelial Cells Identified Organ-Specific Molecular Signatures and Heart-Specific Cell Populations and Molecular Features. *Front. Cardiovasc. Med.* **2019**, *6*, 165. [CrossRef]
48. Drake, C.J.; Fleming, P.A. Vasculogenesis in the day 6.5 to 9.5 mouse embryo. *Blood* **2000**, *95*, 1671–1679. [CrossRef]
49. De La Pompa, J.L.; Timmerman, L.A.; Takimoto, H.; Yoshida, H.; Elia, A.J.; Samper, E.; Potter, J.; Wakeham, A.; Marengere, L.; Langille, B.L.; et al. Role of the NF-ATc transcription factor in morphogenesis of cardiac valves and septum. *Nature* **1998**, *392*, 182–186. [CrossRef]
50. Poelmann, R.E.; Gittenberger-de Groot, A.C. Development and evolution of the metazoan heart. *Dev. Dyn.* **2019**, *248*, 634–656. [CrossRef]
51. Muñoz-Chápuli, R.; Carmona, R.; Guadix, J.A.; Macías, D.; Pérez-Pomares, J.M. The origin of the endothelial cells: An evo-devo approach for the invertebrate/vertebrate transition of the circulatory system. *Evol. Dev.* **2005**, *7*, 351–358. [CrossRef] [PubMed]
52. Nakano, A.; Nakano, H.; Smith, K.A.; Palpant, N.J. The developmental origins and lineage contributions of endocardial endothelium. *Biochim. Biophys. Acta (BBA)-Mol. Cell Res.* **2016**, *1863*, 1937–1947. [CrossRef]
53. Conklin, E.G. Mosaic development in ascidian eggs. *J. Exp. Zool.* **1905**, *2*, 145–223. [CrossRef]
54. Petit, A.C.; Legué, E.; Nicolas, J.F. Methods in clonal analysis and applications. *Reprod. Nutr. Dev.* **2005**, *45*, 321–339. [CrossRef]

55. Garcia-Martinez, V.; Schoenwolf, G.C. Primitive-streak origin of the cardiovascular system in avian embryos. *Dev. Biol.* **1993**, *159*, 706–719. [CrossRef]
56. Stalsberg, H.; DeHaan, R.L. The precardiac areas and formation of the tubular heart in the chick embryo. *Dev. Biol.* **1969**, *19*, 128–159. [CrossRef]
57. Mikawa, T.; Borisov, A.; Brown, A.M.; Fischman, D.A. Clonal analysis of cardiac morphogenesis in the chicken embryo using a replication-defective retrovirus: I. Formation of the ventricular myocardium. *Dev. Dyn.* **1992**, *193*, 11–23. [CrossRef]
58. Devine, W.P.; Wythe, J.D.; George, M.; Koshiba-Takeuchi, K.; Bruneau, B.G. Early patterning and specification of cardiac progenitors in gastrulating mesoderm. *eLife* **2014**, *3*, 1–23. [CrossRef] [PubMed]
59. Kattman, S.J.; Huber, T.L.; Keller, G.M. Multipotent Flk-1+ Cardiovascular Progenitor Cells Give Rise to the Cardiomyocyte, Endothelial, and Vascular Smooth Muscle Lineages. *Dev. Cell* **2006**, *11*, 723–732. [CrossRef] [PubMed]
60. Milgrom-Hoffman, M.; Harrelson, Z.; Ferrara, N.; Zelzer, E.; Evans, S.M.; Tzahor, E. The heart endocardium is derived from vascular endothelial progenitors. *Development* **2011**, *138*, 4777–4787. [CrossRef]
61. Misfeldt, A.M.; Boyle, S.C.; Tompkins, K.L.; Bautch, V.L.; Labosky, P.A.; Baldwin, H.S. Endocardial cells are a distinct endothelial lineage derived from Flk1+ multipotent cardiovascular progenitors. *Dev. Biol.* **2009**, *333*, 78–89. [CrossRef]
62. Motoike, T.; Markham, D.W.; Rossant, J.; Sato, T.N. Evidence for novel fate of Flk1+ progenitor: Contribution to muscle lineage. *Genesis* **2003**, *35*, 153–159. [CrossRef]
63. Bu, L.; Jiang, X.; Martin-Puig, S.; Caron, L.; Zhu, S.; Shao, Y.; Roberts, D.J.; Huang, P.L.; Domian, I.J.; Chien, K.R. Human ISL1 heart progenitors generate diverse multipotent cardiovascular cell lineages. *Nature* **2009**, *460*, 113–117. [CrossRef]
64. Tyser, R.C.; Mahammadov, E.; Nakanoh, S.; Vallier, L.; Scialdone, A.; Srinivas, S. Single-cell transcriptomic characterization of a gastrulating human embryo. *Nature* **2021**, *600*, 285–289. [CrossRef]
65. Moretti, A.; Caron, L.; Nakano, A.; Lam, J.T.; Bernshausen, A.; Chen, Y.; Qyang, Y.; Bu, L.; Sasaki, M.; Martin-Puig, S.; et al. Multipotent Embryonic Isl1+Progenitor Cells Lead to Cardiac, Smooth Muscle, and Endothelial Cell Diversification. *Cell* **2006**, *127*, 1151–1165. [CrossRef] [PubMed]
66. Wu, S.M.; Fujiwara, Y.; Cibulsky, S.M.; Clapham, D.E.; ling Lien, C.; Schultheiss, T.M.; Orkin, S.H. Developmental Origin of a Bipotential Myocardial and Smooth Muscle Cell Precursor in the Mammalian Heart. *Cell* **2006**, *127*, 1137–1150. [CrossRef] [PubMed]
67. Stanley, E.G.; Biben, C.; Elefanty, A.; Barnett, L.; Koentgen, F.; Robb, L.; Harvey, R.P. Efficient cre-mediated deletion in cardiac progenitor cells conferred by a 3'UTR-ires-Cre allele of the homeobox gene Nkx2-5. *Int. J. Dev. Biol.* **2002**, *46*, 431–439. [CrossRef] [PubMed]
68. Bussmann, J.; Bakkers, J.; Schulte-Merker, S. Early endocardial morphogenesis requires Scl/Tal1. *PLoS Genet.* **2007**, *3*, 1425–1437. [CrossRef] [PubMed]
69. Schoenebeck, J.J.; Keegan, B.R.; Yelon, D. Vessel and Blood Specification Override Cardiac Potential in Anterior Mesoderm. *Dev. Cell* **2007**, *13*, 254–267. [CrossRef]
70. Chan, M.M.; Smith, Z.D.; Grosswendt, S.; Kretzmer, H.; Norman, T.M.; Adamson, B.; Jost, M.; Quinn, J.J.; Yang, D.; Jones, M.G.; et al. Molecular recording of mammalian embryogenesis. *Nature* **2019**, *570*, 77–82. [CrossRef] [PubMed]
71. McKenna, A.; Findlay, G.M.; Gagnon, J.A.; Horwitz, M.S.; Schier, A.F.; Shendure, J. Whole-organism lineage tracing by combinatorial and cumulative genome editing. *Science* **2016**, *353*, aaf7907. [CrossRef]
72. Elsasser, W.M. Outline of a theory of cellular heterogeneity. *Proc. Natl. Acad. Sci. USA* **1984**, 81, 5126–5129. [CrossRef] [PubMed]
73. Cao, J.; Spielmann, M.; Qiu, X.; Huang, X.; Ibrahim, D.M.; Hill, A.J.; Zhang, F.; Mundlos, S.; Christiansen, L.; Steemers, F.J.; et al. The single-cell transcriptional landscape of mammalian organogenesis. *Nature* **2019**, *566*, 496–502. [CrossRef]
74. Haghverdi, L.; Büttner, M.; Wolf, F.A.; Buettner, F.; Theis, F.J. Diffusion pseudotime robustly reconstructs lineage branching. *Nat. Methods* **2016**, *13*, 845–848. [CrossRef] [PubMed]
75. Cusanovich, D.A.; Reddington, J.P.; Garfield, D.A.; Daza, R.M.; Aghamirzaie, D.; Marco-Ferreres, R.; Pliner, H.A.; Christiansen, L.; Qiu, X.; Steemers, F.J.; et al. The cis-regulatory dynamics of embryonic development at single-cell resolution. *Nature* **2018**, *555*, 538–542. [CrossRef]
76. Pijuan-Sala, B.; Wilson, N.K.; Xia, J.; Hou, X.; Hannah, R.L.; Kinston, S.; Calero-Nieto, F.J.; Poirion, O.; Preissl, S.; Liu, F.; et al. Single-cell chromatin accessibility maps reveal regulatory programs driving early mouse organogenesis. *Nat. Cell Biol.* **2020**, *22*, 487–497. [CrossRef]
77. Crispatzu, G.; Rehimi, R.; Pachano, T.; Bleckwehl, T.; Cruz-Molina, S.; Xiao, C.; Mahabir, E.; Bazzi, H.; Rada-Iglesias, A. The chromatin, topological and regulatory properties of pluripotency-associated poised enhancers are conserved in vivo. *Nat. Commun.* **2021**, *12*, 4344. [CrossRef]
78. Wang, A.; Yue, F.; Li, Y.; Xie, R.; Harper, T.; Patel, N.A.; Muth, K.; Palmer, J.; Qiu, Y.; Wang, J.; et al. Epigenetic priming of enhancers predicts developmental competence of hESC-derived endodermal lineage intermediates. *Cell Stem Cell* **2015**, *16*, 386–399. [CrossRef]
79. Grosswendt, S.; Kretzmer, H.; Smith, Z.D.; Kumar, A.S.; Hetzel, S.; Wittler, L.; Klages, S.; Timmermann, B.; Mukherji, S.; Meissner, A. Epigenetic regulator function through mouse gastrulation. *Nature* **2020**, *584*, 102–108. [CrossRef]
80. Takeuchi, J.K.; Bruneau, B.G. Directed transdifferentiation of mouse mesoderm to heart tissue by defined factors. *Nature* **2009**, *459*, 708–711. [CrossRef]

81. Arai, A.; Yamamoto, K.; Toyama, J. Murine cardiac progenitor cells require visceral embryonic endoderm and primitive streak for terminal differentiation. *Dev. Dyn.* **1997**, *210*, 344–353. [CrossRef]
82. Varner, V.D.; Taber, L.A. Not just inductive: A crucial mechanical role for the endoderm during heart tube assembly. *Development* **2012**, *139*, 1680–1690. [CrossRef] [PubMed]
83. Rowton, M.; Guzzetta, A.; Rydeen, A.B.; Moskowitz, I.P. Control of cardiomyocyte differentiation timing by intercellular signaling pathways. *Semin. Cell Dev. Biol.* **2021**, *118*, 94–106. [CrossRef]
84. Alsan, B.H.; Schultheiss, T.M. Regulation of avian cardiogenesis by Fgf8 signaling. *Development* **2002**. *129*, 1935–43. [CrossRef]
85. Brown, K.; Doss, M.X.; Legros, S.; Artus, J.; Hadjantonakis, A.K.; Foley, A.C. Extraembryonic endoderm (XEN) stem cells producefactors that activate heart formation. *PLoS ONE* **2010**, *5*, e13446. [CrossRef] [PubMed]
86. Tzahor, E. Wnt/β-Catenin Signaling and Cardiogenesis: Timing Does Matter. *Dev. Cell* **2007**, *13*, 10–13. [CrossRef] [PubMed]
87. Zhao, M.; Tang, Y.; Zhou, Y.; Zhang, J. Deciphering Role of Wnt Signalling in Cardiac Mesoderm and Cardiomyocyte Differentiation from Human iPSCs: Four-dimensional control of Wnt pathway for hiPSC-CMs differentiation. *Sci. Rep.* **2019**, *9*, 1–15. [CrossRef]
88. Lewis-Israeli, Y.R.; Wasserman, A.H.; Aguirre, A. Heart organoids and engineered heart tissues: Novel tools for modeling human cardiac biology and disease. *Biomolecules* **2021**, *11*, 1277. [CrossRef] [PubMed]
89. Reichman, D.E.; Park, L.; Man, L.; Redmond, D.; Chao, K.; Harvey, R.P.; Taketo, M.M.; Rosenwaks, Z.; James, D. Wnt inhibition promotes vascular specification of embryonic cardiac progenitors. *Development* **2018**, *145*, dev159905. [CrossRef] [PubMed]
90. Anderson, C.; Khan, M.A.; Wong, F.; Solovieva, T.; Oliveira, N.M.; Baldock, R.A.; Tickle, C.; Burt, D.W.; Stern, C.D. A strategy to discover new organizers identifies a putative heart organizer. *Nat. Commun.* **2016**, *7*, 1–9. [CrossRef]
91. Nemir, M.; Croquelois, A.; Pedrazzini, T.; Radtke, F. Induction of cardiogenesis in embryonic stem cells via downregulation of Notch1 signaling. *Circ. Res.* **2006**, *98*, 1471–1478. [CrossRef] [PubMed]
92. Schroeder, T.; Meier-Stiegen, F.; Schwanbeck, R.; Eilken, H.; Nishikawa, S.; Häsler, R.; Schreiber, S.; Bornkamm, G.W.; Nishikawa, S.I.; Just, U. Activated Notch1 alters differentiation of embryonic stem cells into mesodermal cell lineages at multiple stages of development. *Mech. Dev.* **2006**, *123*, 570–579. [CrossRef]
93. Han, Z.; Bodmer, R. Myogenic cells fates are antagonized by Notch only in asymmetric lineages of the Drosophila heart, with or without cell division. *Development* **2003**, *130*, 3039–3051. [CrossRef] [PubMed]
94. Rones, M.S.; McLaughlin, K.A.; Raffin, M.; Mercola, M. Serrate and Notch specify cell fates in the heart field by suppressing cardiomyogenesis. *Development* **2000**, *127*, 3865–3876. [CrossRef]
95. Chau, M.D.; Tuft, R.; Fogarty, K.; Bao, Z.Z. Notch signaling plays a key role in cardiac cell differentiation. *Mech. Dev.* **2006**. [CrossRef] [PubMed]
96. Watanabe, Y.; Kokubo, H.; Miyagawa-Tomita, S.; Endo, M.; Igarashi, K.; Aisaki, K.I.; Kanno, J.; Saga, Y. Activation of Notch1 signaling in cardiogenic mesoderm induces abnormal heart morphogenesis in mouse. *Development* **2006**, *133*, 1625–1634. [CrossRef]
97. Gale, N.W.; Dominguez, M.G.; Noguera, I.; Pan, L.; Hughes, V.; Valenzuela, D.M.; Murphy, A.J.; Adams, N.C.; Lin, H.C.; Holash, J.; et al. Haploinsufficiency of delta-like 4 ligand results in embryonic lethality due to major defects in arterial and vascular development. *Proc. Natl. Acad. Sci. USA* **2004**, *101*, 15949–15954. [CrossRef]
98. Marcelo, K.L.; Sills, T.M.; Coskun, S.; Vasavada, H.; Sanglikar, S.; Goldie, L.C.; Hirschi, K.K. Hemogenic endothelial cell specification requires c-Kit, notch signaling, and p27-mediated cell-cycle control. *Dev. Cell* **2013**, *27*, 504–515. [CrossRef]
99. Ferdous, A.; Caprioli, A.; Iacovino, M.; Martin, C.M.; Morris, J.; Richardson, J.A.; Latif, S.; Hammer, R.E.; Harvey, R.P.; Olson, E.N.; et al. Nkx2-5 transactivates the Ets-related protein 71 gene and specifies an endothelial/endocardial fate in the developing embryo. *Proc. Natl. Acad. Sci. USA* **2009**, *106*, 814–819. [CrossRef]
100. Reischauer, S.; Stone, O.A.; Villasenor, A.; Chi, N.; Jin, S.W.; Martin, M.; Lee, M.T.; Fukuda, N.; Marass, M.; Witty, A.; et al. Cloche is a bHLH-PAS transcription factor that drives haemato-vascular specification. *Nature* **2016**, *535*, 294–298. [CrossRef]
101. Haraguchi, S.; Kitajima, S.; Takagi, A.; Takeda, H.; Inoue, T.; Saga, Y. Transcriptional regulation of Mesp1 and Mesp2 genes: Differential usage of enhancers during development. *Mech. Dev.* **2001**, *108*, 59–69. [CrossRef]
102. Matsuo, I.; Kuratani, S.; Kimura, C.; Takeda, N.; Aizawa, S. Mouse Otx2 functions in the formation and patterning of rostral head. *Genes Dev.* **1995**, *9*, 2646–2658. [CrossRef]
103. Tellier, A.P.; Archambault, D.; Tremblay, K.D.; Mager, J. The elongation factor Elof1 is required for mammalian gastrulation. *PLoS ONE* **2019**, *14*, e0219410. [CrossRef] [PubMed]
104. Ikeda, W.; Nakanishi, H.; Miyoshi, J.; Mandai, K.; Ishizaki, H.; Tanaka, M.; Togawa, A.; Takahashi, K.; Nishioka, H.; Yoshida, H.; et al. Afadin: A key molecule essential for structural organization of cell- cell junctions of polarized epithelia during embryogenesis. *J. Cell Biol.* **1999**, *146*, 1117–1132. [CrossRef] [PubMed]
105. Sun, X.; Meyers, E.N.; Lewandoski, M.; Martin, G.R. Targeted disruption of Fgf8 causes failure of cell migration in the gastrulating mouse embryo. *Genes Dev.* **1999**, *13*, 1834–1846. [CrossRef]
106. Zhao, R.; Watt, A.J.; Battle, M.A.; Li, J.; Bondow, B.J.; Duncan, S.A. Loss of both GATA4 and GATA6 blocks cardiac myocyte differentiation and results in acardia in mice. *Dev. Biol.* **2008**, *317*, 614–619. [CrossRef]
107. Gannon, M.; Bader, D. Initiation of cardiac differentiation occurs in the absence of anterior endoderm. *Development* **1995**, *121*, 2439–2450. [CrossRef]

108. Palencia-Desai, S.; Kohli, V.; Kang, J.; Chi, N.C.; Black, B.L.; Sumanas, S. Vascular endothelial and endocardial progenitors differentiate as cardiomyocytes in the absence of Etsrp/Etv2 function. *Development* **2011**, *138*, 4721–4732. [CrossRef]
109. Tzahor, E.; Lassar, A.B. Wnt signals from the neural tube block ectopic cardiogenesis. *Genes Dev.* **2001**, *15*, 255–260. [CrossRef]
110. Marvin, M.J.; Di Rocco, G.; Gardiner, A.; Bush, S.M.; Lassar, A.B. Inhibition of Wnt activity induces heart formation from posterior mesoderm. *Genes Dev.* **2001**, *15*, 316–327. [CrossRef]
111. Chestnut, B.; Casie Chetty, S.; Koenig, A.L.; Sumanas, S. Single-cell transcriptomic analysis identifies the conversion of zebrafish Etv2-deficient vascular progenitors into skeletal muscle. *Nat. Commun.* **2020**, *11*, 1–16. [PubMed]
112. Van Handel, B.; Montel-Hagen, A.; Sasidharan, R.; Nakano, H.; Ferrari, R.; Boogerd, C.J.; Schredelseker, J.; Wang, Y.; Hunter, S.; Org, T.; et al. Scl represses cardiomyogenesis in prospective hemogenic endothelium and endocardium. *Cell* **2012**, *150*, 590–605. [CrossRef]
113. Saba, R.; Kitajima, K.; Rainbow, L.; Engert, S.; Uemura, M.; Ishida, H.; Kokkinopoulos, I.; Shintani, Y.; Miyagawa, S.; Kanai, Y.; et al. Endocardium differentiation through Sox17 expression in endocardium precursor cells regulates heart development in mice. *Sci. Rep.* **2019**, *9*, 1–11. [CrossRef]
114. Kouskoff, V.; Lacaud, G.; Schwantz, S.; Fehling, H.J.; Keller, G. Sequential development of hematopoietic and cardiac mesoderm during embryonic stem cell differentiation. *Proc. Natl. Acad. Sci. USA* **2005**, *102*, 13170–13175. [CrossRef] [PubMed]
115. Nostro, M.C.; Cheng, X.; Keller, G.M.; Gadue, P. Wnt, Activin, and BMP Signaling Regulate Distinct Stages in the Developmental Pathway from Embryonic Stem Cells to Blood. *Cell Stem Cell* **2008**, *2*, 60–71. [CrossRef] [PubMed]
116. Yang, L.; Soonpaa, M.H.; Adler, E.D.; Roepke, T.K.; Kattman, S.J.; Kennedy, M.; Henckaerts, E.; Bonham, K.; Abbott, G.W.; Linden, R.M.; et al. Human cardiovascular progenitor cells develop from a KDR+ embryonic-stem-cell-derived population. *Nature* **2008**, *453*, 524–528. [CrossRef]
117. Santini, M.P.; Forte, E.; Harvey, R.P.; Kovacic, J.C. Developmental origin and lineage plasticity of endogenous cardiac stem cells. *Development* **2016**, *143*, 1242–1258. [CrossRef] [PubMed]
118. Van Vliet, P.; Wu, S.M.; Zaffran, S.; Pucéat, M. Early cardiac development: A view from stem cells to embryos. *Cardiovasc. Res.* **2012**, *96*, 352–362. [CrossRef]
119. Rosenquist, G.C.; DeHaan, R.L. *Contributions to Embryology*; Carnegie Institution of Washington: Washington, DC, USA, 1966; Volume 38, pp. 111–121.
120. Cui, C.; Cheuvront, T.J.; Lansford, R.D.; Moreno-Rodriguez, R.A.; Schultheiss, T.M.; Rongish, B.J. Dynamic positional fate map of the primary heart-forming region. *Dev. Biol.* **2009**, *332*, 212–222. [CrossRef]
121. Lopez-Sanchez, C.; Garcia-Masa, N.; Gañan, C.M.; Garcia-Martinez, V. Movement and commitment of primitive streak precardiac cells during cardiogenesis. *Int. J. Dev. Biol.* **2009**, *53*, 1445–1455. [CrossRef]
122. Redkar, A.; Montgomery, M.; Litvin, J. Fate map of early avian cardiac progenitor cells. *Development* **2001**, *128*, 2269–2279. [CrossRef] [PubMed]
123. Satin, J.; Fujii, S.; DeHaan, R.L. Development of cardiac beat rate in early chick embryos is regulated by regional cues. *Dev. Biol.* **1988**, 129, 103–113. [CrossRef]
124. pin Wu, S.; Cheng, C.M.; Lanz, R.B.; Wang, T.; Respress, J.L.; Ather, S.; Chen, W.; Tsai, S.J.; Wehrens, X.H.; Tsai, M.J.; et al. Atrial Identity Is Determined by a COUP-TFII Regulatory Network. *Dev. Cell* **2013**, *25*, 417–426. [CrossRef]
125. Joubin, K.; Stern, C.D. Molecular interactions continuously define the organizer during the cell movements of gastrulation. *Cell* **1999**, *98*, 559–571. [CrossRef]
126. Saito, Y.; Kojima, T.; Takahashi, N. Mab21l2 is essential for embryonic heart and liver development. *PLoS ONE* **2012**, *7*, e32991. [CrossRef] [PubMed]
127. Baldessari, D.; Badaloni, A.; Longhi, R.; Zappavigna, V.; Consalez, G.G. MAB21L2, a vertebrate member of the Male-abnormal 21 family, modulates BMP signaling and interacts with SMAD1. *BMC Cell Biol.* **2004**, 5, 48. [CrossRef]
128. Domínguez, J.N.; Meilhac, S.M.; Bland, Y.S.; Buckingham, M.E.; Brown, N.A. Asymmetric fate of the posterior part of the second heart field results in unexpected left/right contributions to both poles of the heart. *Circ. Res.* **2012**, *111*, 1323–1335. [CrossRef]
129. Zaffran, S.; Kelly, R.G.; Meilhac, S.M.; Buckingham, M.E.; Brown, N.A. Right ventricular myocardium derives from the anterior heart field. *Circ. Res.* **2004**, *95*, 261–268. [CrossRef] [PubMed]
130. Mommersteeg, M.T.; Domínguez, J.N.; Wiese, C.; Norden, J.; De Gier-De Vries, C.; Burch, J.B.; Kispert, A.; Brown, N.A.; Moorman, A.F.; Christoffels, V.M. The sinus venosus progenitors separate and diversify from the first and second heart fields early in development. *Cardiovasc. Res.* **2010**, *87*, 92–101. [CrossRef]
131. Bruneau, B.G.; Nemer, G.; Schmitt, J.P.; Charron, F.; Robitaille, L.; Caron, S.; Conner, D.A.; Gessler, M.; Nemer, M.; Seidman, C.E.; et al. A murine model of Holt-Oram syndrome defines roles of the T-Box transcription factor Tbx5 in cardiogenesis and disease. *Cell* **2001**, *106*, 709–721. [CrossRef]
132. Waddington, C.H. *The Strategy of the Genes. A Discussion of Some Aspects of Theoretical Biology. With an Appendix by H. Kacser*; CAB Direct: London, UK, 1957; pp 152–169.
133. Sáez, M.; Blassberg, R.; Camacho-Aguilar, E.; Siggia, E.D.; Rand, D.A.; Briscoe, J. Statistically derived geometrical landscapes capture principles of decision-making dynamics during cell fate transitions. *Cell Syst.* **2021**, (In Press, Corrected Proof). [CrossRef]
134. Gilbert, S.F. *Developmental Biology*, 8th ed.; Sinauer Associates: Sunderland, MA, USA, 2006; p. 751.

135. Guignard, L.; Fiúza, U.M.; Leggio, B.; Laussu, J.; Faure, E.; Michelin, G.; Biasuz, K.; Hufnagel, L.; Malandain, G.; Godin, C.; et al. Contact area-dependent cell communication and the morphological invariance of ascidian embryogenesis. *Science* **2020**, *369*, eaar5663. [CrossRef]
136. Wiegner, O.; Schierenberg, E. Regulative development in a nematode embryo: A hierarchy of cell fate transformations. *Dev. Biol.* **1999**. [CrossRef] [PubMed]
137. Rossant, J. Stem Cells and Early Lineage Development. *Cell* **2008**, *132*, 527–531. [CrossRef] [PubMed]
138. Moorman, A.F.; Christoffels, V.M.; Anderson, R.H.; Van Den Hoff, M.J. The heart-forming fields: One or multiple? *Philos. Trans. R. Soc. Biol. Sci.* **2007**, *362*, 1257–1265. [CrossRef] [PubMed]
139. Cai, C.L.; Liang, X.; Shi, Y.; Chu, P.H.; Pfaff, S.L.; Chen, J.; Evans, S. Isl1 identifies a cardiac progenitor population that proliferates prior to differentiation and contributes a majority of cells to the heart. *Dev. Cell* **2003**, *5*, 877–889. [CrossRef]
140. Noden, D.M.; Poelmann, R.E.; Gittenberger-de Groot, A.C. Cell origins and tissue boundaries during outflow tract development. *Trends Cardiovasc. Med.* **1995**, *5*, 69–75. [CrossRef]

Journal of
Cardiovascular
Development and Disease

MDPI

Review

The Role of Cell Tracing and Fate Mapping Experiments in Cardiac Outflow Tract Development, New Opportunities through Emerging Technologies

Joshua C. Peterson [1,†], Tim P. Kelder [1,†], Marie José T. H. Goumans [2], Monique R. M. Jongbloed [1,3] and Marco C. DeRuiter [1,*]

[1] Department Anatomy & Embryology, Leiden University Medical Center, 2300RC Leiden, The Netherlands; J.C.Peterson@lumc.nl (J.C.P.); T.P.Kelder@lumc.nl (T.P.K.); M.R.M.Jongbloed@lumc.nl (M.R.M.J.)
[2] Department Cellular and Chemical Biology, Leiden University Medical Center, 2300RC Leiden, The Netherlands; M.J.T.H.Goumans@lumc.nl
[3] Department of Cardiology, Leiden University Medical Center, 2300RC Leiden, The Netherlands
* Correspondence: m.c.deruiter@lumc.nl; Tel.: +31-71-52-69308
† These authors contributed equally to this work.

Abstract: Whilst knowledge regarding the pathophysiology of congenital heart disease (CHDs) has advanced greatly in recent years, the underlying developmental processes affecting the cardiac outflow tract (OFT) such as bicuspid aortic valve, tetralogy of Fallot and transposition of the great arteries remain poorly understood. Common among CHDs affecting the OFT, is a large variation in disease phenotypes. Even though the different cell lineages contributing to OFT development have been studied for many decades, it remains challenging to relate cell lineage dynamics to the morphologic variation observed in OFT pathologies. We postulate that the variation observed in cellular contribution in these congenital heart diseases might be related to underlying cell lineage dynamics of which little is known. We believe this gap in knowledge is mainly the result of technical limitations in experimental methods used for cell lineage analysis. The aim of this review is to provide an overview of historical fate mapping and cell tracing techniques used to study OFT development and introduce emerging technologies which provide new opportunities that will aid our understanding of the cellular dynamics underlying OFT pathology.

Keywords: cardiac development; congenital heart disease; lineage tracing; outflow tract; developmental biology; bicuspid aortic valve; cell identity

Citation: Peterson, J.C.; Kelder, T.P.; Goumans, M.J.T.H.; Jongbloed, M.R.M.; DeRuiter, M.C. The Role of Cell Tracing and Fate Mapping Experiments in Cardiac Outflow Tract Development, New Opportunities through Emerging Technologies. *J. Cardiovasc. Dev. Dis.* **2021**, *8*, 47. https://doi.org/10.3390/jcdd8050047

Academic Editor: Andy Wessels

Received: 29 March 2021
Accepted: 22 April 2021
Published: 26 April 2021

1. General Introduction

The development of the cardiac outflow tract (OFT), a region of the heart connecting the ventricles to the great arteries of the heart, has been studied for more than a century [1]. Cellular lineage tracing experiments laid the foundation for our knowledge regarding congenital heart disease (CHD). Whilst major progress has been made and CHDs as a whole are understood increasingly better, the degree of understanding varies greatly among the individual congenital defects. CHDs affecting the OFT like bicuspid aortic valve, tetralogy of Fallot, transposition of the great arteries, double outlet right ventricle and pulmonary atresia are well known disorders, yet it remains challenging to explain such morphological emergences with our current models of OFT development. Common among many of these congenital diseases is a broad phenotypical variation arising from a singular genetic deficiency. Murine knockout models used to study such aforementioned CHDs, such as *Notch1* [2], *Gata5* [3] and *Nos3* [4] mutant mice, have been known for their incomplete penetration, yet any agreement addressing such phenotypical variation remains elusive. Whilst lineage tracing studies have contributed significantly to our understanding of a particular cell type heritage, it still falls short to explain, how a cell's lineage primes cellular behavior to allow for proper cell adaptation (such as cell maturation) upon environmental

cues. Epigenetic modification of chromatin have been described to affect gene expression and could act to consolidate directional developmental gradients [5,6]. As such a cell's identity may arise not only from a genetic component but from a combination of expressed genes and cell lineage epigenetic signatures [7].

A single genetic mutation could give rise to multiple phenotypical outcomes if the imprinted epigenetics are dissimilar among cell lineages [8]. Currently we are limited in our understanding about the role of cell identity in CHD. However given that a cell's identity is highly plastic [9], understanding the role of the identity of a cell might explain the broad phenotypical variation observed in these congenital heart diseases and could aid with disease risk stratification. Lineage tracing experiments built the foundation of our current understanding and new developments in methods could provide more detailed definitions of cell types and cell lineage dynamics to better explain how aberrant cell behavior contributes to the multivariate phenotypes seen in CHD.

1.1. Basic Cardiac Development and Anatomy of the OFT

The heart is formed from the anterior splanchnic mesoderm of the embryonic plate. During gastrulation, mesodermal cells arise from the primitive streak, and migrate cranially and laterally to the notochord to form the cardiogenic plates expressing Nkx2.5 [10] and GATA4 [11]. The first sign of cardiomyocyte differentiation is seen in this region at Hamburger and Hamilton (HH) stage 8–9 in chick and between embryonic day (E) 6.5–7.5 in mice, when cardiac troponin-I (cTnI) and sarcomeric myosin (MF20) are first detected. Fusion of the bilateral plates of splanchnic mesoderm establishes the primary heart tube (PHT), that shows peristaltic contraction at 3 weeks of development in a human, E8.0–8.5 in mouse and HH stage 10–11 in chick embryos [12–15]. During further development, cells from the splanchnic mesoderm differentiate into cardiomyocytes and are added to the PHT. The splanchnic mesoderm that gives rise to the cardiomyocytes of the cardiac crescent and PHT is called the first heart field (FHF). The FHF will contribute to part of the atria, atrioventricular canal (AVC), inlet of the right ventricle and left ventricle [12]. In the next phase of heart formation, cells are added to specific structures at the venous (atrial septum and smooth myocardial wall of the atrium) and arterial poles (outflow tract and the right ventricle). These cells are considered to be derived from a distinct cardiogenic field, the second heart field (SHF) [12]. How the distinction between FHF and SHF is related to the ultimate phenotype of the left and right ventricular myocardium is an intriguing question but is not the focus of this review. The addition of cells at the arterial and venous poles initiates the process of cardiac looping, the transformation of the linear heart tube into an S-shaped heart tube with primitive ventricular and atrial chambers [16]. These primitive chambers are connected by the AVC. In the AVC and the OFT, the myocardium secretes cardiac jelly, a hydrophilic substance rich in hyaluronic acid, proteoglycans and extracellular matrix. This results in the formation of localised swellings called the endocardial cushions acting as primitive valves, aiding in maintaining unidirectional flow in the heart tube [17,18]. The endocardial cushions of the OFT mature into aortic and pulmonary valves through contribution of cell lineages of neural crest [19,20], endothelial [21,22] and second heart field cells [23–25], but are also crucial to the development of the interventricular septum [18,26]. The separation of the aorta and the pulmonary trunk is the result of OFT septation. During OFT septation, extracardiac neural crest cells migrate into the endocardial cushions forming a central mass of condensed mesenchyme, resulting in an aortopulmonary septum followed by invagination of cardiomyocytes. The rotation and elongation of the aortic and pulmonary orifices is the result of the pulmonary push driven by cells of the second heart field lineage [27]. OFT septation is completed when the aortic orifice connects to the left ventricular outflow tract whilst the pulmonary orifice remains connected above the right ventricle [28]. In addition to cardiac growth, several processes, including the outgrowth and remodelling of the different chambers, coronary artery development and formation of the cardiac conduction system, will establish the

mature electro-mechanically functional 4-chambered heart with separated pulmonary and systemic circulations (reviewed in [29,30]).

1.2. OFT Development

The OFT can first be observed between E8.0–E8.5 in mice and week 3 of development in humans during formation of the PHT where it connects the primitive ventricle with the aortic sac. During cardiac looping the OFT elongates and remodels forming the OFT cushions. Aortopulmonary septation occurs at the level of: (1) the great arteries, (2) the valvular level and (3) of the outflow tract [31].

The aortopulmonary septum is formed by contributions of neural crest cells and second heart field cells [32–34]. The initially unseparated vascular part of the outflow tract is called the aortic sac. For adequate separation of the different levels of the developing outflow tract, development of the aortopulmonary septum and adequate fusion of the outflow cushions are mandatory [35]. Neural crest cells will be positioned at the level of the aortic sac, as well as in the condensed mesenchyme of the septal outflow tract cushion at and below the orifice level [36]. As a result of this process, separation of the aortic sac will extend from the arterial orifice level (i.e., the level of the developing arterial valve) to the myocardial outflow tract.

The aortopulmonary septum will gradually separate the common aortopulmonary trunk into the aorta and pulmonary trunk. At the valvular level, this process will also separate the OFT cushions at the aortic and pulmonary orifices giving rise to the semilunar valves. Later the coronary arteries will grow into the aortic sinuses of Valsalva and the myocardial and smooth muscle components of the OFT will mature.

Historically, the developing OFT has been studied using classical light microscopy, histological staining and electron microscopy [14,37,38]. A comprehensive basis providing insight in OFT development was founded using these techniques. Unfortunately, as cells undergo intrinsic and phenotypical changes during development, analysing the developmental origin of the OFT was not possible using these early methods. To examine cell lineage development, several techniques such as genetic tracing and vital dye labelling of cells have been developed. Extensive lineage tracing experiments examining OFT morphogenesis have revealed an important role for multiple cell types and signaling pathways in OFT development.

2. Cell Tracing Techniques Applied to OFT Development

In the next section, the different techniques used to study OFT development will be described briefly. The main focus of this section will be to review fate mapping experiments that contributed to our current understanding of OFT development.

2.1. Vital Dye and Viral Labelling Experiments

With vital dye it is possible to directly label clusters of cells. This method is widely used in developmental biology in several species and has provided essential information on the developmental origin of the OFT.

2.1.1. Basics of Vital Dye and Viral Labelling Experiments during Heart Development

Labelling of cells is performed with a glass capillary mounted to micromanipulators, and a pneumatic micro-injector to inject small amounts of dye or virus in the region of interest.

Vital dye labelling is performed with lipophilic dyes, such as diI-C18-(3) [39], which can label distinct cell compartments (Figure 1A) [40]. Commercial dyes are available in different colours, which enables simultaneous labelling of different clusters of cells and studying the direction of migration and potential intermingling of different cell clusters.

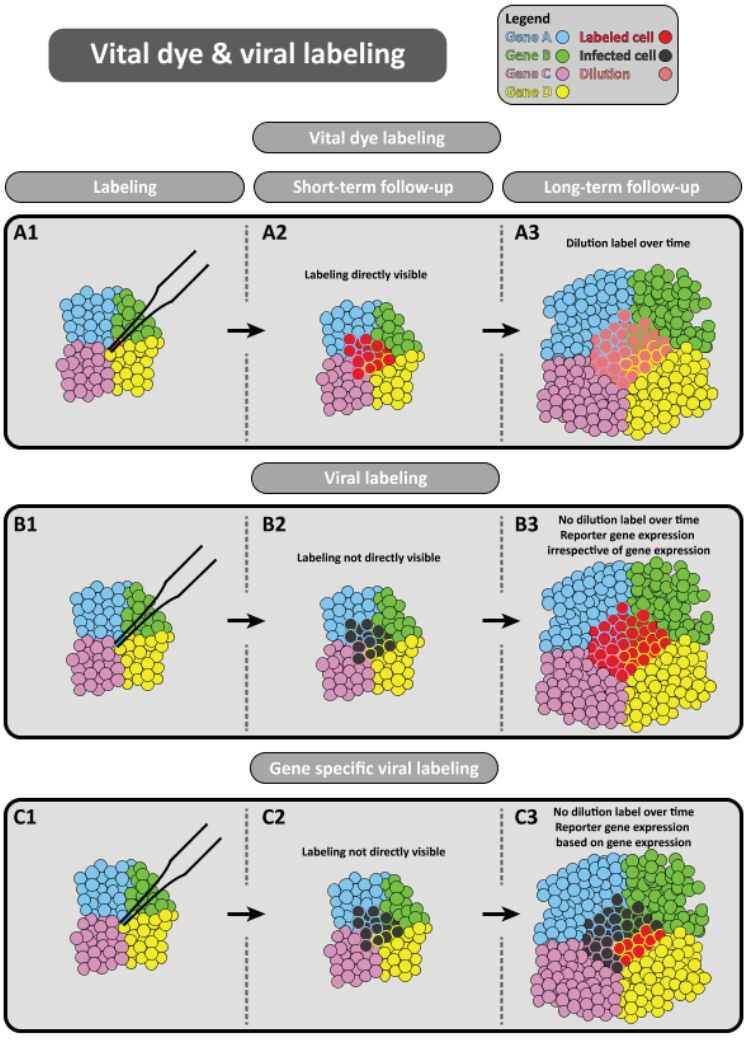

Figure 1. Vital dye and viral labeling techniques. (**A**) Lipophilic dyes are used to visualise and track distinct cell compartments over time. (**B**) Alternatively, retroviral vectors can allow for expression of a reporter gene (such as *LacZ*) to enable cell tracing of infected cells. (**C**) Placing the reporter gene under the transcriptional control of a cell specific promoter allows for increased accuracy in targeting cells through gene specific viral labelling.

Viral labelling experiments are aimed at induction of reporter gene expression in specific regions of the embryo. This technique utilises the ability of retroviruses to infect the cell and to incorporate its genome in the genome of the infected cell [41–43]. Retroviral vectors driving the expression of a reporter gene (such as *LacZ*) enable cell tracing of the infected cells (Figure 1B). More targeted viral tracing can be performed by placing expression of the reporter gene under the transcriptional control of a cell type specific promoter, which enables tracing of cells that express the gene of interest (Figure 1C) [44].

2.1.2. Advantages of Vital Dye Labelling Experiments

With physical labelling of a progenitor pool, it is possible to select that specific group of cells based on location and to time the exact moment of labelling. An important advantage of this technique is the opportunity to select a cluster of cells based without prior knowledge of the cell type. Performing physical labelling experiments is relatively cost efficient and easy, especially in chick, fish and amphibian embryos. Furthermore, labelling can be combined with other microsurgical procedures.

2.1.3. Limitations of Vital Dye and Viral Labelling

To perform microinjection of minute quantities of either vital dye or viral constructs, the embryo needs to be physically accessible to the researcher. For this reason most labelling experiments examining heart development using micro-injections have been performed in oviparous vertebrates, such as zebrafish [45], xenopus [46] and chick embryos [47,48]. For use in mice, it is first necessary to extract the embryo from the uterus, followed by re-incubation in culture medium, for example in rolling bottles [49].

Physical labelling experiments require a progenitor population of interest to study. Knowledge about the location of a possible progenitor pool is required to correctly target these cells. Moreover, when targeting a progenitor population, the lineage trace is limited to cells solely derived from that original cluster. This complicates examining structures derived from multiple progenitor clusters because non-labelled cell contributions could be interpreted as inefficient labelling.

Furthermore, physically labelling cells is relatively invasive, and manipulation of the embryo may induce developmental defects. It is therefore necessary to carefully select embryos that show no macroscopic abnormalities and to include control embryos. Toxicity of the dyes itself appears to be negligible [50,51].

With viral labelling, there is random integration of the viral genome in the host cell's DNA, which could result in damage or abnormal functioning of the infected cell [52]. Leakage of dye or infection of cells in the vicinity of the designated progenitor pool could result in incorrect interpretation regarding the fate of the progenitor cell population. It is therefore essential to evaluate the location of dye directly after administration in great detail [40,53]. Histological evaluation of embryos directly after labelling is crucial, but this also terminates lineage tracing in those embryos. Live-imaging of vital dyes [51,54,55] could help to minimise this limitation. Furthermore, delay in reporter gene expression with viral labelling omits direct evaluation of the location of labelling. In addition, efficiency of reporter gene expression in the desired cells has to be tested prior to ascertain activation of expression in the specific cell type within the animal model (i.e., species differences in expression levels in specific cell types). Rapid cell division in early embryos results in dilution of the vital dyes, which complicates long-term follow-up of the labelled cells [56]. The extent of dilution is dependent on the rate of proliferation and the amount of dye administered, which therefore necessitates titration of the dye with every new experiment. With retroviral labelling, integration of the reporter gene in the host cell's DNA results in stable and high expression of the reporter gene in the daughter cells [57], which overcomes the problem of dilution. Therefore, a disadvantage of vital dye labelling is dilution, whilst the possibility of direct evaluation after labelling is an important advantage. The opposite is true for viral labelling, where direct evaluation is not possible, but dilution of dye does not occur after stable integration of the viral vector. Therefore, a possible solution to overcome these limitations is to combine vital dye labelling with viral labelling. Finally, to perform viral labelling experiments, advanced biosafety laboratories are crucial to safely perform experiments with potentially hazardous viral constructs.

2.1.4. Vital Dye and Viral Labelling Experiments Aimed at Understanding OFT Development

Studies performing dye injected lineage tracing have aided in understanding heart development by carefully fate mapping groups of cardiac precursor cells [58,59]. Prior

to the concept of vital dye lineage tracing descriptive embryological studies in the early 20th century examining human embryos postulated the concept of the primitive cardiac cavities [38]. These primitive cardiac cavities where demarcated by local folds. Using these folds as fixed borders, the outgrowth of cardiac structures such as the development of the atria and ventricles could be described. The introduction of vital dye injected lineage tracing pioneered by de la Cruz refuted the concept of primitive cardiac cavities and showed that structures such as the primordium of the trabeculated portion of the right ventricle could be determined at the straight heart tube stage prior to the formation of primitive cardiac cavities [47].

2.2. Lineage Tracing Using the Quail-Chick Chimeric System

The use of chimeric models is an alternative lineage tracing approach as compared to the previous mentioned vital dye injections. The quail-chick chimeric system proved a vital tool for understanding cell lineage development.

2.2.1. Basics of the Quail-Chick Chimeric System

The quail chick chimera system was devised in 1969 [60–62]. In the quail-chick chimera system a subset of cells derived from quail, i.e., cells of the neural fold, are transplanted in stage-matched chick embryos (or vice versa) (Figure 2). As a result, the quail derived cells develop into functional tissues resulting in viable chimeric quail-chick offspring. The quail-chick marker system relies on the differences in heterochromatic DNA in the nuclei of chick and quail. With the use of a nuclear Feulgen staining or a donor specific antibody [63] distinction could be made between host and donor cells, allowing researchers to study embryonic development at later stages as compared to vital dye labelling. In addition to the quail-chic chimeric system, xenopus hybrids were also used to study early stages of embryonic development [64].

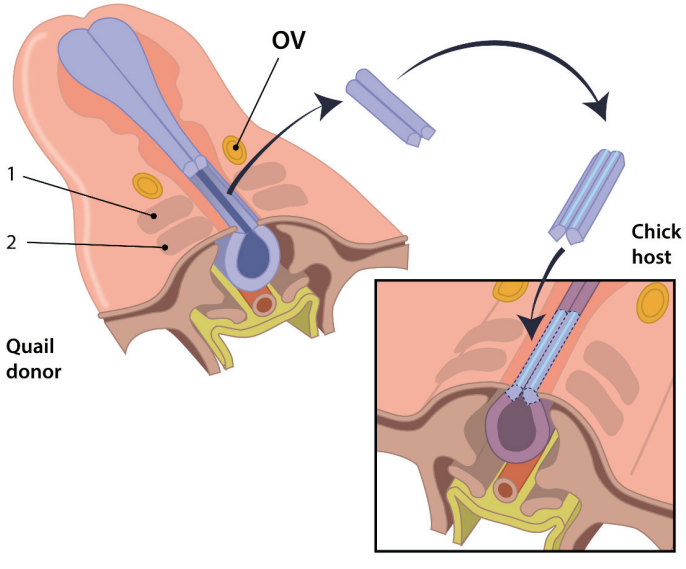

Figure 2. The quail-chick chimeric system. A schematic representation of heterospecific transplantation of the neural crest tissue common to chimeric lineage tracing. The dorsal part of the neural tube of the quail, containing the neural crest cells, is excised and interchanged into a chick host of a comparable embryonic stage at the same locus. 1: somite 1, 2: somite 2, OV: otic vesicle. Image obtained with permission from TP Kelder & R Vincente-Steijn et al. [48].

2.2.2. Advantages of the Quail-Chick Chimeric System

The quail-chick chimera system allows for cell lineage tracing using the genetic footprint of the host cells. As a result, this method of lineage tracing results in a permanent change through which chimeric models overcome the limitation of vital dye dilution mentioned previously. Therefore, chimeric systems allow researchers to examine a specific cell population for longer time periods as compared to injecting cells with vital dyes. Moreover, whilst vital dyes may suffer from dye leakage during injection, chimeric models have no such issues. Another advantage of chimeric models is that it enabled researchers to perform in-vitro cell manipulation prior to transplantation.

2.2.3. Disadvantages of the Quail-Chick Chimeric System

Similar to vital dyes, chimeric models require physical access to an embryo favouring oviparous vertebrates over mammalian embryos. Nevertheless, lineage tracing through cell transplantation has often been applied in mice studies examining multilineage differentiation through bone marrow transplantation in irradiated mice but also to study early mammalian development through injection of cells in the developing morula [65]. Moreover, with the recent developments in stem cell biology the study of heart development using mice-rat chimeric models could lead to new insights [66]. In contrast to vital dye injections, in chimeric models a graft versus host rejection may occur in postnatal studies. Another challenge when making interspecies grafts is the need to perform microsurgery on two stage-matched embryos increasing the experimental complexity. Moreover, chimeric models are generally best used when cells are transplanted superficially, such is the case with cells of the spinal cord or epicardium. Transplantation of difficult to reach mesodermal cells is likely to complicate experimental reproducibility.

2.2.4. The Quail-Chick Chimeric System and Insight into OFT Development

Chimeric models like the chick-quail system were paramount for understanding the role of NCCs in cardiac development. Le Lievre and LeDouarin showed that NCCs formed the tunica media of the great arteries [67]. Kirby and Steward used quail-chick chimeras to observe migration of NCCs into the heart, contributing to the aortopulmonary septum and showed how ablation of the NCC population resulted in persistent truncus arteriosus [34]. Moreover, transplantation studies using chimeric models made the initial observation of cellular pluripotency because quail NCCs could expand into subsets of totipotent and pluripotent progenitors [68]. The quail-chick chimera system was also used to determine that neural crest cells were contributing to the formation of semilunar valves [69] as well as to elastogenesis in the developing cardiovascular system [70]. A role for NCCs in coronary artery formation was demonstrated by Arima et al. which found NCCs contributing to heart development and smooth muscle heterogeneity within a coronary artery using the quail-chick chimeric model [71].

2.3. Genetic Lineage Tracing

A widely used tool in developmental biology is based on site-specific recombination within the genome. Most mouse models developed for genetic lineage tracing utilise the P1 Bacteriophage derived enzyme Cre-recombinase, which recognises a 34-bp sequence called the *loxP* site, and induces recombination between pairs of these sites [72]. The Cre-*loxP* system, combined with the ability to knock-in sequences at specific sites in the genome has been used to study the origin of the developing OFT.

2.3.1. Basics of Genetic Lineage Tracing

To use the Cre-*loxP* system for genetic tracing, several steps are necessary (Figure 3). The basis of the Cre-*loxP* system is crossing a Cre transgenic mouse strain with a mouse in which a reporter gene is flanked by *LoxP* sequences ("floxed"). First, the sequence coding for Cre-recombinase is knocked into the locus of the gene of interest, for example Isl1. The next step is crossing the $Isl1^{Cre}$ mouse line with a reporter line (Figure 3A). The

genetic tracing experiments in this review were mostly performed in reporter lines that utilise the Rosa26 locus (R26R), but different loci (e.g., Gata4 [73]) have also been used in other studies. Important characteristics of a potential reporter locus are ubiquitous expression of the gene and viability and fertility of the mouse strain after homozygous inactivation of the reporter locus by insertion of a reporter gene, such as *LacZ* or a single or multiple fluorescent proteins. To control expression of the reporter gene, a floxed sequence preventing transcriptional read-through (also referred to as a "stop-cassette") is placed before the reporter gene sequence (Figure 3A).

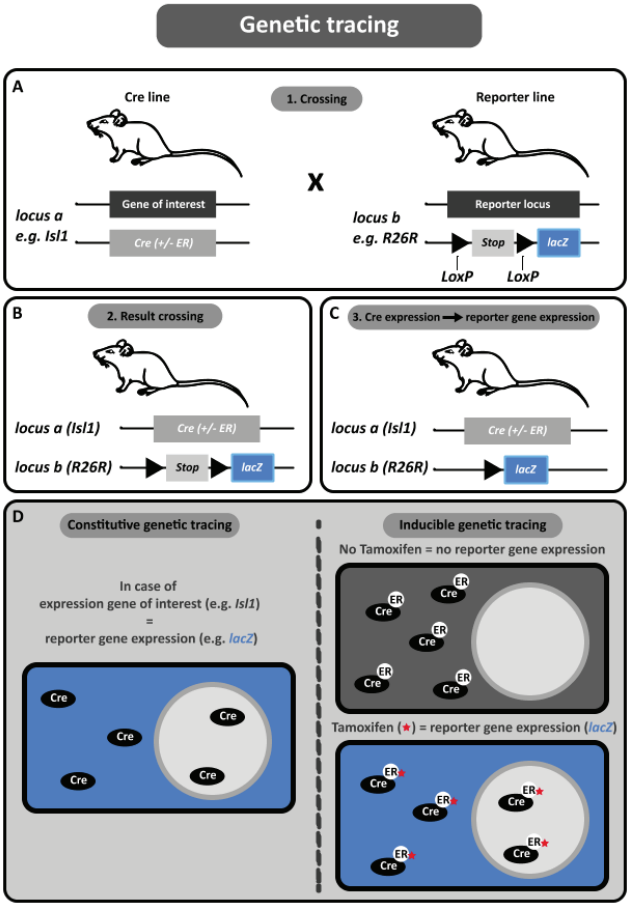

Figure 3. Genetic lineage tracing. (**A**) Genetic lineage tracing can be achieved using the Cre-*LoxP* system. Upon expression, the Cre recombinase specifically targets *LoxP* DNA motives and allows for excision of DNA elements floxed by *LoxP* sites. The reporter line contains a stop-cassette inhibiting expression of the reporter gene in the absence of Cre. (**B**) Crossing the reporter line with the Cre line results in offspring carrying both constructs. (**C**) Cells expressing the gene of interest will express the Cre-recombinase. Cre will then permanently remove the stop-cassette and thus allow expression of the reporter gene, resulting in cell lineage labelling. (**D**) Modified Cre-recombinases can be used to allow for more temporal control in genetic labelling. Cre-ER variants can prevent Cre-recombinase activity by restricting mobility to the cells cytoplasm in absence of Tamoxifen. Upon stimulation of Tamoxifen-Cre activity is restored resulting in an inducible system for genetic lineage tracing.

Crossing the floxed reporter line with the cell type specific Cre line results in offspring carrying both constructs (Figure 3B). Cells expressing the gene of interest will produce Cre-recombinase, which will result in permanent deletion of the stop-cassette and expression of the reporter gene (Figure 3C). Since expression is under control of the ubiquitous Rosa26 promoter, these cells and their progeny will retain reporter gene expression, thereby enabling tracing of these cells over a long period of time. The above-described method is referred to as "constitutive" genetic tracing in this review (Figure 3D).

A variation of genetic tracing, referred to as "*inducible*" genetic tracing, enables temporal control of recombination (Figure 3D). This system is based on fusion of a mutated ligand-binding domain (LBD) of the human estrogen receptor (ER) and Cre-recombinase. The resulting protein is only sensitive to the anti-estrogen Tamoxifen, not to the endogenously present estradiol [74]. The fusion gene is inserted in the locus of the gene of interest, which results in production of the fusion protein upon expression of the gene of interest. The Cre fusion protein is located in the cytoplasm and is unable to enter the nucleus, due to the presence of the mutated LBD. Administration of Tamoxifen results in binding to the LBD, which enables translocation of Cre-recombinase to the nucleus, where it induces gene specific recombination [75]. Thus, recombination can only occur after administration of Tamoxifen, resulting in temporal control of lineage labelling (Figure 3D).

In 2007, multicolour lineage tracing using the Brainbow labelling cassettes was introduced to the genetic lineage tracing toolset [76]. The Brainbow cassettes (Brainbow-1,2 and 3.2) are genetic labelling constructs exploiting the Cre-*loxP* system to allow for stochastic recombination events to obtain single cell resolution lineage labelling. This method is based on combining multiple fluorescent reporter gene sequences in the Brainbow cassettes flanked by a combination of cis- and trans-*loxP* sites. Upon Cre expression, driven by the gene of interest, the fluorescent reporter genes randomly change configuration within the cassette affecting expression of the cell marker. Because multiple copies of fluorescent reporters are embedded within the Brainbow cassettes (i.e., CFP, YFP, RFP) it allows for multiple fluorescent signatures related to the combination of reporters being stochastically expressed after recombination (i.e., Expression of a CFP-CFP-CFP combination would allow for a "Blue" signal, whilst a RFP-RFP-CFP combination would result in a "Magenta" signal). Combining multicolour lineage tracing with tamoxifen induction can result in a multicolour lineage tracing model with temporal control.

2.3.2. Advantages of Genetic Tracing

The most important advantage of genetic tracing is the ability to visualise the complete heritage of a progenitor population driven by a single marker gene of interest. Combination of these results with previous known expression patterns (e.g., based on immunohistochemical staining patterns) allows for the reconstruction a genetic fate map during development of the OFT.

Furthermore, genetic lineage tracing is non-invasive, as long as insertion of the sequence for Cre does not impair normal development of the embryo. This is an important advantage as compared to performing prospective tracing with microinjection of vital dyes or viral constructs (see Section 2.1.3).

Inducible genetic tracing has an important advantage over constitutive genetic tracing, as it allows for temporal control of Cre expression. Constitutive genetic tracing is solely dependent on the natural timing of Cre expression related to the driving promotor. Expression of the gene of interest at any given (and frequently unknown) time point will result in reporter gene expression (if the level of Cre expression is sufficient to induce reporter gene expression, see below). With inducible tracing, reporter gene expression will only occur in the presence of Tamoxifen [74].

2.3.3. Disadvantages of Genetic Tracing

Reporter gene expression in the tissue or structure of interest can result from several scenarios. In the ideal situation, it can show that at time point 0, a certain structure with

known expression of the gene of interest is a progenitor for the structure with reporter gene expression at a later time point. However, a possible pitfall can arise from interference resulting from aspecific lineage markers. In scenarios when a gene of interest gives rise to multiple progenitor populations of different origin, interpretation of developing structures would be troubled, which could lead to an inaccurate conclusion regarding the lineage developmental contribution. This difficulty in interpretation of genetic tracing experiments was demonstrated by constitutive genetic tracing of *Tbx18*. *Tbx18* is commonly used as a marker for the sinus venosus and epicardium. Constitutive genetic tracing was performed with a $Tbx18^{Cre}$ in the $R26R^{LacZ}$ background and reporter gene expression was found in myocardial cells, which led to the conclusion that these cardiomyocytes derived from epicardial cells [77]. However, later experiments showed active expression of *Tbx18* in cardiomyocytes, which was put forward as an explanation for the observed reporter gene expression [78]. Using constitutive genetic tracing, reporter gene expression in cells shows that either these cells have expressed or still actively express the gene of interest.

Even though timing is far more accurately determined using inducible genetic tracing, exact timing of recombination and reporter gene expression remains difficult. It was shown that after intraperitoneal injection of Tamoxifen at E8.5 in pregnant dams, the first signs of *LacZ* activity in the embryos were seen 6 h after injection, with an increase in expression at 12, 24 and 48 h [79]. Analysis of reporter gene expression after Tamoxifen injection therefore is dependent on the duration of Tamoxifen exposure, which complicates exact timing. Furthermore, the dosage of Tamoxifen has also been shown to influence reporter gene expression, with higher doses resulting in reporter gene expression in more cells [79]. Recent findings also revealed that the basal activity of Tamoxifen induced Cre (CreERT2) can be sufficient to induce genetic recombination even in the absence of tamoxifen induction [80]. Depending on the reporter line this may result in aspecific cell labelling [80]. This shows that analysis of reporter gene expression and interpretation of these results can be a challenge and might require further substantiation to guarantee efficacy.

The complete absence of reporter gene expression is also difficult to interpret as this can be caused by absence of expression of the gene of interest, or absence of recombination due to sub-threshold levels of Cre expression, not sufficient to induce reporter gene expression.

Recent studies might raise questions regarding the accuracy of using Cre driven genes as a reliable cell lineage marker. In genetic tracing experiments, interpreting specific gene expression can be problematic, but a far more complex problem arises in case of lack of reporter gene expression. A large number of genetic tracing experiments utilise the *R26R* locus, which is also the most commonly used reporter locus described in the current review. Genetic tracing experiments comparing the *R26R* locus with a *Gata4* based reporter system showed differences in reporter gene expression between the two lines [73]. Constitutive genetic tracing of *Isl1* and *Nkx2-5* (both genes are discussed in more detail below) showed more extensive reporter gene expression in the *Gata4* reporter line, indicating that the *Gata4* locus was more sensitive to recombination then the *R26R* locus [73]. The difference in reporter gene expression shows that different reporter strains have different thresholds for reporter gene expression, resulting in different conclusions based on the reporter used. An example of the importance of this is shown by reassessment of the fate of *Isl1*+ progenitors [73]. This gene is commonly used as marker for the SHF [81,82]. However, the expanded pattern of reporter gene expression in the *Gata4* reporter line showed that nearly all cells (including the LV, which is commonly described as being derived from the FHF) of the heart derive from progenitor cells that did express *Isl1*, albeit perhaps at a low level for a brief period. This suggest that Isl1 is either not specific enough or not reliable as a SHF marker [73]. In this case, mRNA [83] and protein [40] expression of Isl1 in the cardiac crescent, classically considered to be a FHF structure, further support these observations.

Therefore, when performing constitutive or inducible genetic tracing experiments, one should be cautious with interpretation of the results (Figure 4 illustrates this in more detail). In constitutive genetic tracing, reporter gene expression demonstrates that labelled cells have expressed or still actively express the promotor driven Cre. It does not provide

information on the initial source/location of the progenitor cells. With inducible genetic tracing, temporal control of Cre expression is possible. Expression of the reporter gene shows that Cre is present in the labelled cell between the time of Tamoxifen administration and the moment of analysis. Finally, interpretation of negative results in genetic tracing is challenging and results need to be verified by additional tracing techniques and gene/protein expression experiments at sequential stages of development.

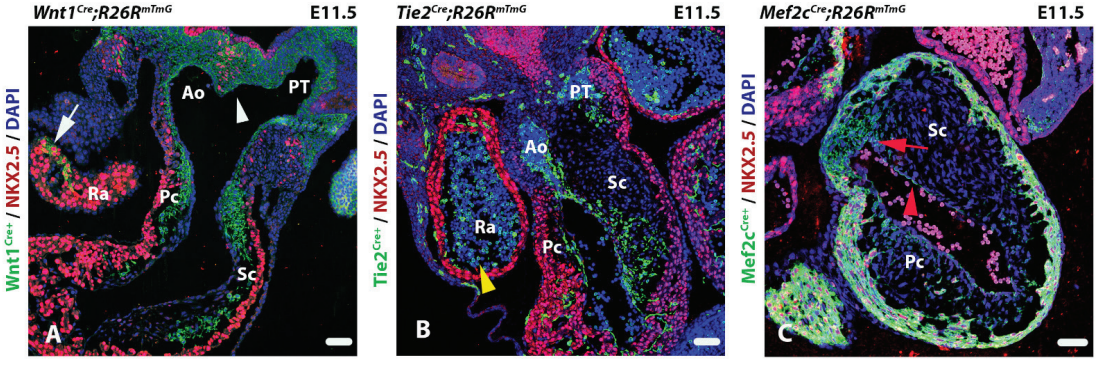

Figure 4. Transversal sections of immunofluorescent outflow tracts show challenges with genetic lineage tracing. (**A**) A *Wnt1*^{Cre}; *R26R*^{mTmG} embryo showing neural crest cell derived cells (green). Interestingly, *Wnt1* derived cells with NKX2.5 stained nuclei can also be observed at the so-called flow divider [84], in front of the primitive foregut which is the central part of the second heart filed contribution (white arrowhead) as well as in the atrial myocardium (white arrow). (**B**) a *Tie2*^{Cre}; *R26R*^{mTmG} embryo showing endothelial derived cells (green). Endothelial cells undergoing epithelial to mesenchymal transition give rise to cells within the septal and parietal cushions. Cells derived from myeloid lineages also express *Tie2* resulting in lineage positive blood cells (yellow arrowhead). (**C**) A *Mef2c*^{Cre}; *R26R*^{mTmG} embryo showing second heart field derived cells (green). Cre positive endothelial cells can also be found lining the heart (red arrowhead). *Mef2c* derived cells also contribute directly to the septal cushion (red arrow). Ra: Right atrium, Ao: Aorta, PT: Pulmonary trunk, Pc: Parietal cushion, Sc: Septal cushion. Scalebar: 50 µm.

2.3.4. Using Genetic Lineage Tracing to Study OFT Development

Genetic lineage tracing has been applied extensively to identify cell lineages contributing to OFT formation. The early observations of neural crest derived cells contributing to the developing heart were further substantiated using the neural crest specific *Wnt*^{Cre} transgenic mouse (Figure 4A) [20]. This model, when crossed with a Cre-specific reporter line, allowed for lineage tracing of NCCs revealing their role in semilunar valve development as well as the cardiac conduction system [85]. The appearance of the OFT cushions and a role for endothelial cells was observed in early studies using electron microscopy [86]. However, the development of the *Tie2*^{Cre} transgenic model was essential for the study of endothelial cell lineages in vivo (Figure 4B) [22]. Other genetic markers have been extensively used to define cell lineages such as the *Isl1*+ SHF [81,82] and the *Mef2c*^{Cre} SHF lineage model (Figure 4C) [87]. Table 1 shows an overview of genetic lineage tracing models that are often used in OFT studies, the morphological structures these lineages contribute to, and the possible conflicts arising from the genetic lineage interpretations.

Recent developments in genetic lineage tracing have introduced a dual genetic tracing system to address the dynamic origins of cardiac valve mesenchyme [88]. Dual genetic tracing allows for the study of multiple cell lineages simultaneously by using multiple site-specific recombinases such as Nigri-*nox* to complement the Cre-*loxP* system [89]. Dual genetic lineage tracing could aid in addressing the specificity concerns of traditional Cre-*loxP* lineage tracing systems.

Table 1. An overview of common genetic lineage tracing models used in OFT studies.

Transgenic Mouse Lines	Commonly Used as Cell Lineage Marker for:	Observed Tissue Expression	Possible Lineage Conflicts
Hcn4$^{Cre\text{-}ert2}$	First heart field [90]	Cardiac conduction system [90] Myocardium [90]	Second heart field
Hoxa1^{Cre}	Cardiac precursors [91]	Aortopulmonary septum [91] Cardiac conduction system [91] Coronary arteries [91] Endothelial lining [91] Myocardium [91] Semilunar valves [91]	Endothelial Neural Crest Second heart field
Isl1^{Cre}	Second heart field [81]	Atrioventricular valves [73] Cardiac conduction System [90] Cushion mesenchyme [73] Endocardium [73] Myocardium [92] Proepicardium [93] Semilunar Valves [73]	Endothelial Epicardial First heart field Neural Crest
Krox20^{Cre}	Neural Crest [94]	Endocardium [94] Semilunar valves [94]	Endothelial
Mef2c^{Cre}	Second heart field [87]	Ascending aorta [95] Coronary arteries [96] Cushion mesenchyme [95] Endocardium [95] Myocardium [87,95] Semilunar valves [95]	Endothelial Epicardial
Nkx2-5^{Cre}	First and Second heart field [97]	Ascending aorta [98] Coronary artery [98] Endocardium [73] Epicardium [93] Myocardium [97], Semilunar valves [98]	Endothelial Epicardial
Pax3^{Cre}	Neural Crest [99]	Aortopulmonary septum [100] Ascending aorta [99] Cushion mesenchyme [100] Semilunar valves [100]	
Tbx18^{Cre}	Proepicardium/epicardium [77]	Cardiac conduction system [90] Epicardium [77] Myocardium [77]	First heart field Second heart field
Tbx2^{Cre}	Proepicardium/epicardium [101]	Cardiac conduction system [102] Coronary arteries [101] Epicardium [101] Myocardium [101,103]	First heart field Second heart field
Tie2^{Cre}	Endothelium [22]	Atrioventricular valves [22,104] Coronary arteries [105] Cushion mesenchyme [22,104] Endocardium [22,104] Hematopoietic cells [106] Semilunar valves [104]	Hematopoietic
Tnnt2^{Cre}	Myocardium [107]	Ascending aorta [25] Myocardium [25,107] Semilunar valves [25]	

Table 1. *Cont.*

Transgenic Mouse Lines	Commonly Used as Cell Lineage Marker for:	Observed Tissue Expression	Possible Lineage Conflicts
Wnt11^{CreER}	Cardiac precursors [108]	Endocardium [108] Epicardium [108] Myocardium [108] Semilunar valves [108]	First heart field Endothelial Epicardial Second heart field
Wnt1^{Cre}	Neural Crest [20]	Aortopulmonary septum [20] Ascending aorta [20] Cardiac conduction system [109] Coronary arteries [71] Cushion mesenchyme [20] Epicardium [110] Myocardium [110,111] Semilunar valves [20]	Epicardial Second heart field
WT1^{Cre}	Proepicardium/epicardium [112]	Coronary arteries [112] Epicardium [93] Myocardium [93]	Endothelial lineage First heart field Second heart field

2.4. Retrospective Clonal Analysis

The aforementioned techniques can all be described as prospective fate mapping techniques. Knowledge on gene and protein expression profile, timing of expression and/or location of progenitors is essential to perform subsequent prospective labelling of this progenitor pool [52]. The following section focuses on retrospective clonal analysis.

2.4.1. Basics of Retrospective Clonal Analysis

Retrospective clonal analysis is based on infrequent and spontaneous recombination of the *nLaacZ* reporter [113]. This reporter gene encodes the *LacZ* gene, with an inactivating duplication inserted in the reading frame, thereby inhibiting transcription of functional β-galactosidase. A spontaneous and rare recombination event can result in removal of the duplication and subsequent production of β-galactosidase (Figure 5A) [113]. Reporter gene expression can be followed in progeny of cells in which spontaneous recombination of the *nLaacZ* construct occurred [113]. Targeting of this construct to an allele which is highly expressed in cardiac muscle, (e.g., α-cardiac-actin) enables retrospective clonal analysis of cardiac cells, irrespective of gene expression [114–116].

Clonal analysis is based on statistical evaluation of the chance that reporter gene expression in different cells is based on separate spontaneous recombination events, or that these different cells are progeny of one recombination event (and thus share a common progenitor during development). A statistical method commonly used is the fluctuation test of Luria and Delbrück [117]. This famous experiment showed that mutations in bacteria occur spontaneously (not induced by selection) and at a constant rate, which was used to formulate a probability distribution [117]. This distribution is used to calculate the probability of one *or* more recombination events, and will therefore determine whether cells showing reporter gene expression are most likely clonally related or are derived from different recombination events (Figure 5B) [113–115,118]. Early recombination (i.e., during early stages of development) will give large clusters of cells with reporter gene expression (Figure 5C), while late spontaneous recombination will give smaller clusters of *LacZ* positive cells (Figure 5D).

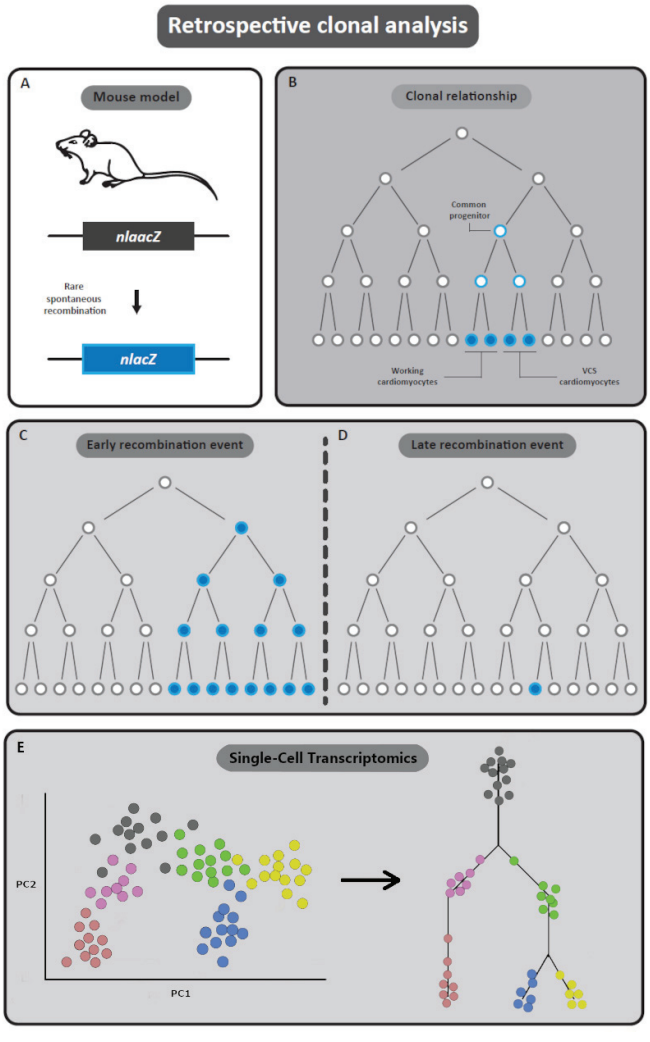

Figure 5. Retrospective lineage tracing. (**A**,**B**) Traditional retrospective lineage tracing exploits spontaneous and rare recombination events. The nlaacZ sequence was designed to be inactive by default but increase the odds of recombination events within the region. Upon spontaneous recombination, β-galactosidase is expressed resulting in a lineage label. (**C**,**D**) Early recombination (i.e., during early stages of development) will give large clusters of cells with reporter gene expression, whilst late spontaneous recombination results in smaller clusters of *LacZ* positive cells. (**E**) Modern retrospective lineage tracing derives lineage hierarchy from single cell transcriptomics data. Principle component analysis (PC) aids in clustering groups of cells based on similarity in gene expression profiles. Follow up algorithms can then produce a phylogenetic lineage tree derived from expressional gradients among cell clusters to reconstruct cell lineage development.

Recent studies performing retrospective clonal analysis have been adopting next-generation sequencing techniques to study lineage tracing. Recent advances in single cell sequencing technologies allow transcriptome profiling of thousands of single cells. This allowed for the collection of large datasets detailing cellular expression profiles with unprecedented resolution. Alongside advances in sequencing technologies, computational

methods designed to examine lineage trajectory reconstruction based on single-cell transcriptomics data have also evolved [119,120]. Single-cell transcriptomics allows for the investigation of the transcriptional state of thousands of individual single cells. As a result, cell-type diversity in heterogeneous samples can be reliably captured. As cells transition between different states during embryologic development, their expression profiles give insight into their lineage fate and cellular identity.

If sufficient amounts of cells in these transition states are captured, differentiation trajectories through which tissues are derived can be reconstructed through hierarchical clustering of cells based on the gradient in expressional similarities (Figure 5E).

2.4.2. Advantages of Retrospective Clonal Analysis

To perform prospective lineage tracing, some basic knowledge on the progenitor population that will be traced is required. This information is not necessary when performing retrospective clonal analysis. Studying whether certain structures or clusters of cells are clonally related is done independent of gene expression or any other preconceived idea of a possible progenitor pool. Retrospective clonal analysis can therefore establish clonal relationships that are less apparent at first sight, such as the clonal relationship between head musculature and cardiomyocytes from the outflow tract and right ventricle [121,122].

Furthermore, as described previously, prospective genetic tracing is hampered by the difficulty to draw conclusions from the absence of reporter gene expression. With the retrospective clonal approach, analysis is based on *LacZ* positive cells. *LacZ* expression in different structures or tissues is mapped and statistical analysis is performed to calculate whether these different tissues or structures are clonally related [113]. Moreover, as with genetic tracing, retrospective clonal analysis is non-invasive.

When performing retrospective lineage tracing using single-cell sequencing, an advantage is the ability to perform lineage tracing using naturally occurring somatic mutations or copy number variations (CNVs). CNVs can be used as genetic markers to link clones of cells to a common progenitor. This approach allows for lineage tracing without manual labelling or genetic modification. Even though CNVs are relatively uncommon in healthy tissue, they are highly abundant in cancerous tissue and have been used to study tumour evolution [123,124]. Alternative to CNVs is lineage tracing using single-nucleotide variations (SNVs) and genomic insertion/deletions (indels). Both SNVs and Indels are often present in non-coding regions of the genome and have been used for the reconstruction of phylogenetic trees of tumours from bulk DNA [125]. This technique, however, is not limited to tumour lineage analysis as lineage tracing using somatic SNVs in mitochondrial DNA can be performed with any eukaryotic cell [126]. Moreover, combining the genetic variation in non-coding regions of DNA with the RNA expression profiles when performing lineage tracing has recently been successfully demonstrated [127].

2.4.3. Limitations of Retrospective Clonal Analysis

The retrospective approach has several drawbacks. Since data is analysed retrospectively, it is not possible to locate the common progenitor, either in time or space. Therefore, it is not possible to perform further experiments with these progenitors (e.g., characterisation or ablation). Retrospective clonal analysis has to be performed in conjunction with other fate mapping techniques to build the complete lineage tree of a structure or organ. In this sense, the most important advantage of this technique is also its most important drawback. Starting with a certain progenitor pool based on timing, location and/or gene/protein expression profile excludes contributions from other (sometimes unexpected) progenitors but does directly pinpoint a possibly important progenitor pool for the structure/tissue of interest. Furthermore, spontaneous recombination of the *nlaacZ* gene is rare and it is therefore necessary to obtain a large library of embryos with *LacZ* positive clones and as a result, large quantities of embryos or adult mice will have to be analysed. A challenge when performing single cell sequencing for lineage tracing lies in the sparse distribution of SNVs and CNVs within the genome. To achieve confident detection of SNVs, large quantities

of reads will have to be generated to achieve adequate sequencing depth. A large portion of the generated data is unsuitable for lineage tracing as these would contain identical sequences. However, enrichment of regions of DNA with greater odds of developing nucleotide variations such as microsatellites could apprehend these challenges.

2.4.4. Retrospective Clonal Analysis Aimed at the Development of the OFT

Many of the cardiac lineages contributing to OFT development have been found using prospective lineage tracing techniques (Table 1). However, a recent study examining cell populations at the aortic root and pulmonary trunk determined a novel SHF derived cell population called arterial mesothelial cells (AMC) populating a local niche at the base of the great arteries [128]. Whilst AMCs have first been observed as a distinctive cell type using chick-quail chimera's [129], the study of Lioux et al. used a clonal analysis strategy based on the ubiquitous, low-frequency random recombination of two independent reporters to distinguish this population from the frequency of colour matching between labelled cells in different clusters or different cell types within single clusters [130].This approach allowed for an unbiased characterisation of the fate of SHF precursors at the base of the great arteries and detailed the contribution of SHF to the coronary lymphatic vasculature [128]. Moreover, another study examining the cardiac outflow tract using single cell RNA sequencing (scRNA-seq) found convergent development of the vascular smooth muscle cell lineage suggesting a method of myocardial-to-VSMC differentiation or mesenchymal-to-VSMC differentiation [131].

3. New Technologies for Lineage Tracing in OFT Development

Lineage tracing has contributed greatly to our understanding of OFT development. Nevertheless, there is still much to be learned regarding multifactorial CHDs. To advance our understanding of phenotypical variation, research efforts should be aimed at understanding the relation between cell lineage and cellular identity. The methods previously described in this review are inadequate to address such issues, as this would require detailed description of the variation among single cells within a lineage population. The introduction of novel analysis methods which combine lineage tracing and single cell analysis could provide new opportunities to examine cell lineage plasticity and phenotypical variation in CHD. These methods will be discussed in the following section.

3.1. Spatially Resolved Transcriptomics

Current lineage tracing techniques, such as genetic lineage tracing, rely primarily on spatial information to reconstruct OFT development over multiple embryonic stages. The tracking of cell lineage movements can give insight into the environment in which these cells function. However, evaluating the internal cellular state of these cells within such environments can be challenging. Single cell RNA sequencing (scRNA-seq) is a technique which can be used to examine a cell's innerworkings because it allows for quantification of all the RNA molecules within a single cell. This cellular transcriptome can be used to examine gene expression patterns and to make cell type specific expression profiles. By collecting expression profiles of multiple cells of the same cell type, it is possible to examine the cellular variation in gene expression within a specific cell population. This allows researchers to evaluate the variation in cell states within a particular cell lineage, and reconstruct subclusters structural to a cell lineage population. Whilst scRNA-seq can be used to obtain genome-wide expression data of cells allowing for unprecedented cell type identification, it does not provide any spatial resolution to determine where these cells were located within the embryo. As a result, experiments using scRNA-seq to identify new cell types and cell states still require the use of visualisation techniques such as in-situ hybridisation using the genetic markers found during sequencing. However, in-situ hybridisation can only provide spatial information regarding a few genes at any given moment. Tomo-seq is a technique which combines genome-wide expression data with spatial information [132,133]. This is achieved by performing RNA-seq on individual cryosections

of an embryo or tissue allowing the generation of genome-wide spatial expression maps in 3D. By sequencing sequential tissue sections, spatial information regarding the head to tail axis can be maintained. As a result, gene expression data can be projected with respect to the head to tail axis. Performing this approach using multiple axis (dorsal-ventral, right-left) allows for the reconstruction of gene expression patterns in 3D in the developing embryo [133]. Although Tomo-seq allows for 3D expression pattern analysis, one limitation is that it is unable to provide single cell resolution in 3D. An alternative method called transcriptome in vivo analysis (TIVA) does allow for single cell sequencing whilst maintaining single cell spatial resolution. TIVA is a noninvasive tool enabling capture of mRNA from single spatially defined cells in living and intact tissue for transcriptome analysis [134]. This is achieved by addition of a cell permeable TIVA tag to the tissue sample which upon photo activation is able to capture cellular mRNA. This technique is an excellent advance over more traditional laser capture techniques or pipette cell isolation adapted for scRNA-seq due to the non-invasive design. The limited throughput, however, might restrict explorative research to specific cases in which the number of cells of interest might be relatively low. A practical example in which TIVA might prove very valuable for OFT studies, is to examine the properties of valvular interstitial cells (VICs) contributing to the aortic and pulmonary valves. VICs may derive from multiple cell lineages such as SHF, NCC or endothelial lineages and VIC dysfunction has been suggested to underly valvular diseases such as calcification [135]. TIVA could enable researchers to examine how cell lineage background influence VIC formation and how cell lineage deficiencies could relate to valvular disease by assigning a spatial criterium to scRNA-seq.

3.2. Lineage Tracing through DNA Barcoding

DNA-barcoding technologies are another potential tool for lineage tracing. Lineage tracing using DNA barcoding is a technique that combines aspects of both prospective and retrospective lineage tracing. Similar to genetic lineage tracing using fluorescent reporters, DNA-barcoding technologies introduce genetic modifications into progenitor cells to study cell lineage development. However, whilst lineage tracing using fluorescent reporters is limited to only a number of reporter genes, DNA barcodes allow for more complex labelling methods. Techniques such as scGESTALT [136], ScarTrace [137] and LINNAEUS [138] have demonstrated how the CRISPR-Cas9 system could be used to generate genetic barcodes to perform whole-organism lineage tracing in zebrafish embryos. The CRISPR-Cas9 system allows genomic editing on a specific DNA locus determined by the supplied guide RNA. In the absence of a template for homologous repair, Cas9 may introduce short DNA insertions or deletions at the targeted site [139]. These genetic aberrations, which vary in size and position, can then be used as a genetic barcoded label to evaluate a cell's offspring. If the guide RNA was designed specific to a region within a constitutive expressed gene, then scRNA-seq can capture the barcode within the transcriptome of a cell. Since the process of barcoding is randomly determined, a cell's lineage can only be evaluated after single cell sequencing. This can be achieved through computational reconstruction of full lineage trees from the single cell level. Even though these methods still rely on microinjection of Cas9 and guide RNAs in an early stage zebrafish embryos, DNA-barcoding has also been achieved using retroviral integration [140] or polylox recombination [141] in mice. For an in dept comparison of barcoding techniques, the reader is referred to a recent review of Wagner and Klein [142]. Lineage tracing using barcodes could be an excellent method to examine cell lineage commitment because it allows to retrospectively evaluate cell lineage branching events. The differences in lineage trajectories among FHF and SHF lineages would be an interesting topic to be evaluated using such methods. Moreover, if barcoding events are temporally restricted and multiple stages of embryonic development are analysed, then it could enable reconstruction of all cell lineage trajectories contributing to heart development simultaneously. Genetic mutations or epigenetic influences affecting cellular identity could also be examined as these would influence the relative distributions

among (sub)populations of cell lineages. As such, these methods could aim to elucidate the relationship between phenotypical variation and cell lineage variation.

3.3. Multi-Omics Lineage Tracing

Whilst barcoding techniques for lineage tracing require aspects of a prospective approach to lineage tracing, recent technological developments using a multi-omics sequencing approach for lineage tracing could allow for complete retrospective lineage tracing. RETrace is an example of a recent lineage tracing technique which captures both DNA microsatellite loci and methylation-informative cytosines from a single cell in order to simultaneously characterise both lineage and cell type [143]. The utilisation of microsatellite regions as markers for retrospective lineage tracing was successfully demonstrated at single cell level [144]. However, enabling DNA methylation profiling of the same cell allows for better cell characterisation than either method alone. Even though still in early development, a multi-omics approach to lineage tracing would ideally combine the cell lineage identification capability using natural occurring CNV and SNVs captured using whole genome sequencing whilst allowing for accurate cell type identification through gene expression analysis using scRNA-seq and also include epigenetic profiling techniques such as methylome analysis [145] or include histone signatures [146] to investigate cellular identity and cell lineage dynamics. Multi-omics lineage tracing would enable researchers to investigate the relations between cellular variation, epigenetic modification and disease susceptibility related to CHD. This knowledge could potentially translate to novel methods of treatment and therapy aimed at influencing the epigenome of patients.

3.4. Reference Maps for Lineage Tracing

The large amounts of data derived from lineage tracing using transcriptomics are likely to extent the depth at which sub-lineages and cell states will be defined. To facilitate accurate definitions of such sub lineages and intermediate cell states, large quantities of single cell data could be combined. A project called the Human Cell Atlas (HCA) aims to characterise all human cell types using scRNA-seq and single cell transposase accessible chromatin sequencing (scATAC-seq), and combine it with data regarding cell lineage, location and cell states [147]. The scope extents to unify single cell sequencing data towards common reference models similar to the efforts of the Human Genome Project [148]. Having the infrastructure to navigate cell lineage development will greatly contribute to the understanding of human health and treatment of disease. (For more information regarding the HCA project, the reader is referred to the HCA white paper [149]). Initiatives such as these could allow for the comparison of many cell lineage populations among the various types of CHD to determine key processes critical to human cardiovascular development.

4. Future Perspectives, Combining Old Strengths with New Technologies

With the advances in lineage tracing, new insights regarding cell fate came forth and the role of prospective lineage tracing paved the way for modern developmental biology. In this review we describe the use of lineage tracing techniques and their limitations with respect to OFT development. The recent technological methods described in the final section of this review have the potential to allow more fateful reconstruction of lineage dynamics than previous methods.

The development of next-generation sequencing technology has enabled new and exciting research opportunities for lineage tracing experiments. From our perspective we expect that results obtained from retrospective lineage tracing using naturally occurring mutations and single cell transcriptomics will challenge our current definitions of cell lineages and advance our understanding of cellular dynamics and lineage plasticity. Assuming technological improvements will continue to be developed in the coming years, we can expect an integration of (epi)genetics signatures with single cell sequencing to aid with tracing cellular heritage. Continued development and a multi-omics approach will allow

future research to expand the scope of cellular identity and resolve the mechanisms explaining congenital variation in more detail and with better accuracy than current available methods. As a result, a multi-omics approach will help to elucidate the mechanisms for normal OFT development and aid in understanding the pathophysiological pathways leading to the multivariate phenotypes common to OFT diseases. As sequencing techniques become more and more accessible, multi-omics sequencing approaches combined with single cell resolution will become the new frontier for future lineage tracing studies.

Author Contributions: J.C.P. and T.P.K. drafted the manuscript and designed the figures. M.C.D., M.R.M.J. and M.J.T.H.G. were involved in planning, supervision and critical review of the manuscript. All authors were involved in the assessment of relevant literature and substantially contributed to the conception and design of the manuscript. All authors have read and agreed to the published version of the manuscript.

Funding: Funding and salary support were provided by The Dutch Heart foundation (Project code: 31190BAV).

Acknowledgments: We are very grateful for all the support provided by Adriana C. Gittenberger-de Groot. Her work fueled our passions for cardiac development and congenital heart disease. The rigorous scientific discussions carry warm memories and helped pave the road to academic excellence. We thank her for all her support throughout the years and the care she took for all her colleagues and collaborators.

Conflicts of Interest: The authors declare no conflict of interest.

Abbreviations

AMC	arterial mesothelial cells
SHF	second heart field
AVC	atrioventricular canal
SNV	single nucleotide variation
CHD	congenital heart disease
TIVA	transcriptome in vivo analysis
CNV	copy number variations
VIC	valvular interstitial cell
E	embryonic day
ER	estrogen receptor
FHF	first heart field
GFP	green fluorescent protein
HH	Hamburger and Hamilton
HCA	Human Cell Atlas
LBD	ligand-binding domain
mT/mG	membrane-bound Tomato/membrane-bound GFP
NCCs	neural crest cells
OFT	outflow tract
PHT	primary heart tube
R26R	Rosa26 reporter
scRNA-seq	single cell RNA sequencing

References

1. Thompson, P. Description of a Human Embryo of Twenty-Three Paired Somites. *J. Anat. Physiol.* **1907**, *41*, 159–171. [PubMed]
2. Garg, V.; Muth, A.N.; Ransom, J.F.; Schluterman, M.K.; Barnes, R.; King, I.N.; Grossfeld, P.D.; Srivastava, D. Mutations in NOTCH1 cause aortic valve disease. *Nature* **2005**, *437*, 270–274. [CrossRef]
3. Laforest, B.; Andelfinger, G.; Nemer, M. Loss of Gata5 in mice leads to bicuspid aortic valve. *J. Clin. Investig.* **2011**, *121*, 2876–2887. [CrossRef] [PubMed]
4. Peterson, J.C.; Chughtai, M.; Wisse, L.J.; Gittenberger-de Groot, A.C.; Feng, Q.; Goumans, M.-J.T.H.; VanMunsteren, J.C.; Jongbloed, M.R.M.; DeRuiter, M.C. Bicuspid aortic valve formation: Nos3 mutation leads to abnormal lineage patterning of neural crest cells and the second heart field. *Dis. Model. Mech.* **2018**, *11*, 655–658. [CrossRef]

5. Klemm, S.L.; Shipony, Z.; Greenleaf, W.J. Chromatin accessibility and the regulatory epigenome. *Nat. Rev. Genet.* **2019**, *20*, 207–220. [CrossRef] [PubMed]
6. Perino, M.; Veenstra, G.J.C. Chromatin Control of Developmental Dynamics and Plasticity. *Dev. Cell* **2016**, *38*, 610–620. [CrossRef] [PubMed]
7. Fisher, A.G. Cellular identity and lineage choice. *Nat. Rev. Immunol.* **2002**, *2*, 977–982. [CrossRef]
8. Peaston, A.E.; Whitelaw, E. Epigenetics and phenotypic variation in mammals. *Mamm. Genome* **2006**, *17*, 365–374. [CrossRef]
9. Merrell, A.J.; Stanger, B.Z. Adult cell plasticity in vivo: De-differentiation and transdifferentiation are back in style. *Nat. Rev. Mol. Cell Biol.* **2016**, *17*, 413–425. [CrossRef]
10. Olson, E.N.; Srivastava, D. Molecular pathways controlling heart development. *Science* **1996**, *272*, 671–676. [CrossRef]
11. Laverriere, A.C.; MacNeill, C.; Mueller, C.; Poelmann, R.E.; Burch, J.B.E.; Evans, T. GATA-4/5/6, a subfamily of three transcription factors transcribed in developing heart and gut. *J. Biol. Chem.* **1994**, *269*, 23177–23184. [CrossRef]
12. Buckingham, M.; Meilhac, S.; Zaffran, S. Building the mammalian heart from two sources of myocardial cells. *Nat. Rev. Genet.* **2005**, *6*, 826–835. [CrossRef]
13. Abu-Issa, R.; Kirby, M.L. Heart field: From mesoderm to heart tube. *Annu. Rev. Cell Dev. Biol.* **2007**, *23*, 45–68. [CrossRef] [PubMed]
14. DeRuiter, M.C.; Poelmann, R.E.; VanderPlas-de Vries, I.; Mentink, M.M.T.; Gittenberger-de Groot, A.C. The development of the myocardium and endocardium in mouse embryos—Fusion of two heart tubes? *Anat. Embryol.* **1992**, *185*, 461–473. [CrossRef] [PubMed]
15. Tyser, R.C.V.; Srinivas, S. The first heartbeat—Origin of cardiac contractile activity. *Cold Spring Harb. Perspect. Biol.* **2020**, *12*, 1–12. [CrossRef] [PubMed]
16. Moorman, A.F.M.; Christoffels, V.M. Cardiac chamber formation: Development, genes, and evolution. *Physiol. Rev.* **2003**. [CrossRef]
17. Combs, M.D.; Yutzey, K.E. Heart valve development: Regulatory networks in development and disease. *Circ. Res.* **2009**, *105*, 408–421. [CrossRef]
18. Kirby, M.L. *Cardiac Development*; Oxford University Press: Oxford, UK, 2007.
19. Waldo, K.; Miyagawa-Tomita, S.; Kumiski, D.; Kirby, M.L. Cardiac neural crest cells provide new insight into septation of the cardiac outflow tract: Aortic sac to ventricular septal closure. *Dev. Biol.* **1998**, *196*, 129–144. [CrossRef]
20. Jiang, X.; Rowitch, D.H.; Soriano, P.; McMahon, A.P.; Sucov, H.M. Fate of the mammalian cardiac neural crest. *Development* **2000**, *127*, 1607–1616. [CrossRef]
21. Eisenberg, L.M.; Markwald, R.R. Molecular regulation of atrioventricular valvuloseptal morphogenesis. *Circ. Res.* **1995**, *77*, 1–6. [CrossRef]
22. Kisanuki, Y.Y.; Hammer, R.E.; Miyazaki, J.; Williams, S.C.; Richardson, J.A.; Yanagisawa, M. Tie2-Cre transgenic mice: A new model for endothelial cell-lineage analysis in vivo. *Dev. Biol.* **2001**, *230*, 230–242. [CrossRef] [PubMed]
23. Zaffran, S.; Kelly, R.G. New developments in the second heart field. *Differentiation* **2012**, *84*, 17–24. [CrossRef]
24. Eley, L.; Alqahtani, A.M.S.; Macgrogan, D.; Richardson, R.V.; Murphy, L.; Salguero-jimenez, A.; Sintes, M.; San, R.; Tiurma, S.; Mccutcheon, L.; et al. A novel source of arterial valve cells linked to bicuspid aortic valve without raphe in mice. *eLife* **2018**, *7*, 1–27. [CrossRef]
25. Mifflin, J.J.; Dupuis, L.E.; Alcala, N.E.; Russell, L.G.; Kern, C.B. Intercalated cushion cells within the cardiac outflow tract are derived from the myocardial troponin T type 2 (Tnnt2) Cre lineage. *Dev. Dyn.* **2018**, *247*, 1005–1017. [CrossRef] [PubMed]
26. Miquerol, L.; Kelly, R.G. Organogenesis of the vertebrate heart. *Wiley Interdiscip. Rev. Dev. Biol.* **2013**. [CrossRef]
27. Scherptong, R.W.; Jongbloed, M.R.; Wisse, L.J.; Vicente-Steijn, R.; Bartelings, M.M.; Poelmann, R.E.; Schalij, M.J.; Gittenberger-De Groot, A.C. Morphogenesis of outflow tract rotation during cardiac development: The pulmonary push concept. *Dev. Dyn* **2012**, *241*, 1413–1422. [CrossRef]
28. Gittenberger-De Groot, A.C.; Bartelings, M.M.; Deruiter, M.C.; Poelmann, R.E. Basics of cardiac development for the understanding of congenital heart malformations. *Pediatric Res.* **2005**, *57*, 169–176. [CrossRef]
29. Gittenberger-de Groot, A.C.; Bartelings, M.M.; Poelmann, R.E.; Haak, M.C.; Jongbloed, M.R.M. Embryology of the heart and its impact on understanding fetal and neonatal heart disease. *Semin. Fetal Neonatal Med.* **2013**, *18*, 237–244. [CrossRef]
30. Gittenberger-de Groot, A.C.; Calkoen, E.E.; Poelmann, R.E.; Bartelings, M.M.; Jongbloed, M.R.M. Morphogenesis and molecular considerations on congenital cardiac septal defects. *Ann. Med.* **2014**, *46*, 640–652. [CrossRef] [PubMed]
31. Bartelings, M.M.; Gittenberger-de Groot, A.C. Morphogenetic considerations on congenital malformations of the outflow tract. Part 1: Common arterial trunk and tetralogy of Fallot. *Int. J. Cardiol.* **1991**, *32*, 213–230. [CrossRef]
32. Poelmann, R.E.; Gittenberger-de Groot, A.C.; Biermans, M.W.M.; Dolfing, A.I.; Jagessar, A.; van Hattum, S.; Hoogenboom, A.; Wisse, L.J.; Vicente-Steijn, R.; de Bakker, M.A.G.; et al. Outflow tract septation and the aortic arch system in reptiles: Lessons for understanding the mammalian heart. *Evodevo* **2017**, *8*, 9. [CrossRef]
33. Poelmann, R.E.; Mikawa, T.; Gittenberger-De Groot, A.C. Neural crest cells in outflow tract septation of the embryonic chicken heart: Differentiation and apoptosis. *Dev. Dyn.* **1998**, *212*, 373–384. [CrossRef]
34. Kirby, M.L.; Gale, T.F.; Stewart, D.E. Neural crest cells contribute to normal aorticopulmonary septation. *Science* **1983**, *220*, 1059–1061. [CrossRef]

35. Anderson, R.; Mohun, T.; Spicer, D.; Bamforth, S.; Brown, N.; Chaudhry, B.; Henderson, D. Myths and Realities Relating to Development of the Arterial Valves. *J. Cardiovasc. Dev. Dis.* **2014**, *1*, 177–200. [CrossRef]
36. Gittenberger-de Groot, A.C.; Bartelings, M.M.; Bogers, A.J.J.C.; Boot, M.J.; Poelmann, R.E. The embryology of the common arterial trunk. *Prog. Pediatric Cardiol.* **2002**, *15*, 1–8. [CrossRef]
37. DeHaan, R.L. Migration patterns of the precardiac mesoderm in the early chick embryo. *Exp. Cell Res.* **1963**, *29*, 544–560. [CrossRef]
38. Davis, C. Development of the human heart from its first appearance to the stage found in embryos of twenty paired somites. *Carnegie Inst. Contr. Embryol.* **1927**, *19*, 245–284.
39. Axelrod, D. Carbocyanine dye orientation in red cell membrane studied by microscopic fluorescence polarization. *Biophys. J.* **1979**, *26*, 557–573. [CrossRef]
40. Kelder, T.P.; Vicente-Steijn, R.; Harryvan, T.J.T.; Kosmidis, G.; Gittenberger-de Groot, A.C.; Poelmann, R.R.E.; Schalij, M.M.J.; DeRuiter, M.M.C.; Jongbloed, M.R.M. The sinus venosus myocardium contributes to the atrioventricular canal: Potential role during atrioventricular node development? *J. Cell. Mol. Med.* **2015**, *19*, 1375–1389. [CrossRef] [PubMed]
41. Sanes, J.R. Analysing cell lineage with a recombinant retrovirus. *Trends Neurosci.* **1989**, *12*, 21–28. [CrossRef]
42. Sanes, J.R.; Rubenstein, J.L.; Nicolas, J.F. Use of a recombinant retrovirus to study post-implantation cell lineage in mouse embryos. *EMBO J.* **1986**, *5*, 3133–3142. [CrossRef]
43. Price, J.; Turner, D.; Cepko, C. Lineage analysis in the vertebrate nervous system by retrovirus-mediated gene transfer. *Proc. Natl. Acad. Sci. USA* **1987**, *84*, 156–160. [CrossRef]
44. Pacak, C.A.; Byrne, B.J. AAV vectors for cardiac gene transfer: Experimental tools and clinical opportunities. *Mol. Ther.* **2011**, *19*, 1582–1590. [CrossRef]
45. Stainier, D.Y.R.; Lee, R.K.; Fishman, M.C. Cardiovascular development in the zebrafish: I. Myocardial fate map and heart tube formation. *Development* **1993**, *119*, 31–40. [CrossRef]
46. Krotoski, D.M.; Fraser, S.E.; Bronner-Fraser, M. Mapping of neural crest pathways in Xenopus laevis using inter- and intra-specific cell markers. *Dev. Biol.* **1988**, *127*, 119–132. [CrossRef]
47. De la Cruz, M.V.; Sánchez Gómez, C.; Arteaga, M.M.; Argüello, C. Experimental study of the development of the truncus and the conus in the chick embryo. *J. Anat.* **1977**, *123*, 661–686.
48. Kelder, T.P.; Vicente-Steijn, R.; Poelmann, R.E.; Mummery, C.L.; DeRuiter, M.C.; Jongbloed, M.R.M. The avian embryo to study development of the cardiac conduction system. *Differentiation* **2016**, *91*, 90–103. [CrossRef]
49. Domínguez, J.N.; Meilhac, S.M.; Bland, Y.S.; Buckingham, M.E.; Brown, N.A. Asymmetric fate of the posterior part of the second heart field results in unexpected left/right contributions to both poles of the heart. *Circ. Res.* **2012**, *111*, 1323–1335. [CrossRef]
50. Honig, M.G.; Hume, R.I. Fluorescent carbocyanine dyes allow living neurons of identified origin to be studied in long-term cultures. *J. Cell Biol.* **1986**, *103*, 171–187. [CrossRef] [PubMed]
51. Progatzky, F.; Dallman, M.J.; Lo Celso, C. From seeing to believing: Labelling strategies for in vivo cell-tracking experiments. *Interface Focus* **2013**, *3*, 20130001. [CrossRef] [PubMed]
52. Buckingham, M.E.; Meilhac, S.M. Tracing cells for tracking cell lineage and clonal behavior. *Dev. Cell* **2011**, *21*, 394–409. [CrossRef] [PubMed]
53. Bressan, M.; Liu, G.; Mikawa, T. Early mesodermal cues assign avian cardiac pacemaker fate potential in a tertiary heart field. *Science* **2013**, *340*, 744–748. [CrossRef] [PubMed]
54. Lo Celso, C.; Fleming, H.E.; Wu, J.W.; Zhao, C.X.; Miake-Lye, S.; Fujisaki, J.; Côté, D.; Rowe, D.W.; Lin, C.P.; Scadden, D.T. Live-animal tracking of individual haematopoietic stem/progenitor cells in their niche. *Nature* **2009**, *457*, 92–96. [CrossRef]
55. Sipkins, D.A.; Wei, X.; Wu, J.W.; Runnels, J.M.; Côté, D.; Means, T.K.; Luster, A.D.; Scadden, D.T.; Lin, C.P. In vivo imaging of specialized bone marrow endothelial microdomains for tumour engraftment. *Nature* **2005**, *435*, 969–973. [CrossRef]
56. Honig, M.G.; Hume, R.I. Dil and diO: Versatile fluorescent dyes for neuronal labelling and pathway tracing. *Trends Neurosci.* **1989**, *12*, 333–335, 340–341. [CrossRef]
57. Mikawa, T.; Hyer, J.; Itoh, N.; Wei, Y. Retroviral vectors to study cardiovascular development. *Trends Cardiovasc. Med.* **1996**, *6*, 79–86. [CrossRef]
58. Barbosky, L.; Lawrence, D.K.; Karunamuni, G.; Wikenheiser, J.C.; Doughman, Y.-Q.; Visconti, R.P.; Burch, J.B.E.; Watanabe, M. Apoptosis in the developing mouse heart. *Dev. Dyn.* **2006**, *235*, 2592–2602. [CrossRef]
59. Schaefer, K.S.; Doughman, Y.Q.; Fisher, S.A.; Watanabe, M. Dynamic patterns of apoptosis in the developing chicken heart. *Dev. Dyn.* **2004**, *229*, 489–499. [CrossRef]
60. Le Douarin, N. Particularites du noyau interphasique chez la caille Japonaise (Coturnix coturnix japonica). *Bull. Biol. Fr. Belg.* **1969**, *103*, 435–452.
61. Le Douarin, N. A biological cell labeling technique and its use in experimental embryology. *Dev. Biol.* **1973**, *30*, 217–222. [CrossRef]
62. Le Douarin, N.M. The avian embryo as a model to study the development of the neural crest: A long and still ongoing story. *Mech. Dev.* **2004**, *121*, 1089–1102. [CrossRef]
63. Selleck, M.A.; Bronner-Fraser, M. Origins of the avian neural crest: The role of neural plate-epidermal interactions. *Development* **1995**, *121*, 525–538. [CrossRef]

64. Koga, M.; Kageura, H.; Yamana, K. Use of Hybrids between Xenopus laevis and Xenopus borealis in Chimera Formation: Dorsalization of Ventral Cells: (cell lineage/chimera/hybrid/Xenopus/dorsalization). *Dev. Growth Differ.* **1986**, *28*, 177–183. [CrossRef]
65. Tam, P.P.L.; Rossant, J. Mouse embryonic chimeras: Tools for studying mammalian development. *Development* **2003**, *130*, 6155–6163. [CrossRef] [PubMed]
66. Sereti, K.I.; Nguyen, N.B.; Kamran, P.; Zhao, P.; Ranjbarvaziri, S.; Park, S.; Sabri, S.; Engel, J.L.; Sung, K.; Kulkarni, R.P.; et al. Analysis of cardiomyocyte clonal expansion during mouse heart development and injury. *Nat. Commun.* **2018**, *9*, 1–13. [CrossRef] [PubMed]
67. Le Lievre, C.S.; Le Douarin, N.M. Mesenchymal derivatives of the neural crest: Analysis of chimaeric quail and chick embryos. *J. Embryol. Exp. Morphol.* **1975**, *34*, 125–154. [PubMed]
68. Baroffio, A.; Dupin, E.; Le Douarin, N.M. Common precursors for neural and mesectodermal derivatives in the cephalic neural crest. *Development* **1991**, *112*, 301–305. [CrossRef] [PubMed]
69. Takamura, K.; Okishima, T.; Ohdo, S.; Hayakawa, K. Association of cephalic neural crest cells with cardiovascular development, particularly that of the semilunar valves. *Anat. Embryol.* **1990**, *182*, 263–272. [CrossRef] [PubMed]
70. Rosenquist, T.H.; McCoy, J.R.; Waldo, K.L.; Kirby, M.L. Origin and propagation of elastogenesis in the developing cardiovascular system. *Anat. Rec.* **1988**, *221*, 860–871. [CrossRef] [PubMed]
71. Arima, Y.; Miyagawa-Tomita, S.; Maeda, K.; Asai, R.; Seya, D.; Minoux, M.; Rijli, F.M.; Nishiyama, K.; Kim, K.S.; Uchijima, Y.; et al. Preotic neural crest cells contribute to coronary artery smooth muscle involving endothelin signalling. *Nat. Commun.* **2012**, *3*, 1–11. [CrossRef]
72. Sauer, B. Inducible gene targeting in mice using the Cre/lox system. *Methods* **1998**, *14*, 381–392. [CrossRef] [PubMed]
73. Ma, Q.; Zhou, B.; Pu, W.T. Reassessment of Isl1 and Nkx2-5 cardiac fate maps using a Gata4-based reporter of Cre activity. *Dev. Biol.* **2008**, *323*, 98–104. [CrossRef] [PubMed]
74. Feil, R.; Brocard, J.; Mascrez, B.; LeMeur, M.; Metzger, D.; Chambon, P. Ligand-activated site-specific recombination in mice. *Proc. Natl. Acad. Sci. USA* **1996**, *93*, 10887–10890. [CrossRef] [PubMed]
75. Indra, A.K.; Warot, X.; Brocard, J.; Bornert, J.M.; Xiao, J.H.; Chambon, P.; Metzger, D. Temporally-controlled site-specific mutagenesis in the basal layer of the epidermis: Comparison of the recombinase activity of the tamoxifen-inducible Cre-ER(T) and Cre-ER(T2) recombinases. *Nucleic Acids Res.* **1999**, *27*, 4324–4327. [CrossRef] [PubMed]
76. Livet, J.; Weissman, T.A.; Kang, H.; Draft, R.W.; Lu, J.; Bennis, R.A.; Sanes, J.R.; Lichtman, J.W. Transgenic strategies for combinatorial expression of fluorescent proteins in the nervous system. *Nature* **2007**, *450*, 56–62. [CrossRef]
77. Cai, C.-L.; Martin, J.C.; Sun, Y.; Cui, L.; Wang, L.; Ouyang, K.; Yang, L.; Bu, L.; Liang, X.; Zhang, X.; et al. A myocardial lineage derives from Tbx18 epicardial cells. *Nature* **2008**, *454*, 104–108. [CrossRef]
78. Christoffels, V.M.; Grieskamp, T.; Norden, J.; Mommersteeg, M.T.M.; Rudat, C.; Kispert, A. Tbx18 and the fate of epicardial progenitors. *Nature* **2009**, *458*, E8–E9. [CrossRef]
79. Hayashi, S.; McMahon, A.P. Efficient recombination in diverse tissues by a tamoxifen-inducible form of Cre: A tool for temporally regulated gene activation/inactivation in the mouse. *Dev. Biol.* **2002**, *244*, 305–318. [CrossRef]
80. Álvarez-Aznar, A.; Martínez-Corral, I.; Daubel, N.; Betsholtz, C.; Mäkinen, T.; Gaengel, K. Tamoxifen-independent recombination of reporter genes limits lineage tracing and mosaic analysis using CreERT2 lines. *Transgenic Res.* **2020**, *29*, 53–68. [CrossRef]
81. Cai, C.-L.; Liang, X.; Shi, Y.; Chu, P.-H.; Pfaff, S.L.; Chen, J.; Evans, S. Isl1 identifies a cardiac progenitor population that proliferates prior to differentiation and contributes a majority of cells to the heart. *Dev. Cell* **2003**, *5*, 877–889. [CrossRef]
82. Sun, Y.; Liang, X.; Najafi, N.; Cass, M.; Lin, L.; Cai, C.-L.; Chen, J.; Evans, S.M. Islet 1 is expressed in distinct cardiovascular lineages, including pacemaker and coronary vascular cells. *Dev. Biol.* **2007**, *304*, 286–296. [CrossRef]
83. Yuan, S.; Schoenwolf, G.C. Islet-1 marks the early heart rudiments and is asymmetrically expressed during early rotation of the foregut in the chick embryo. *Anat. Rec.* **2000**, *260*, 204–207. [CrossRef]
84. Baardman, M.E.; Zwier, M.V.; Wisse, L.J.; Gittenberger-De Groot, A.C.; Kerstjens-Frederikse, W.S.; Hofstra, R.M.W.; Jurdzinski, A.; Hierck, B.P.; Jongbloed, M.R.M.; Berger, R.M.F.; et al. Common arterial trunk and ventricular non-compaction in Lrp2 knockout mice indicate a crucial role of LRP2 in cardiac development. *DMM Dis. Model. Mech.* **2016**, *9*, 413–425. [CrossRef] [PubMed]
85. Nakamura, T.; Colbert, M.C.; Robbins, J. Neural crest cells retain multipotential characteristics in the developing valves and label the cardiac conduction system. *Circ. Res.* **2006**, *98*, 1547–1554. [CrossRef]
86. Bolender, D.L.; Markwald, R.R. Epithelial-mesenchymal transformation in chick atrioventricular cushion morphogenesis. *Scan. Electron. Microsc.* **1979**, *3*, 313–321.
87. Verzi, M.P.; McCulley, D.J.; De Val, S.; Dodou, E.; Black, B.L. The right ventricle, outflow tract, and ventricular septum comprise a restricted expression domain within the secondary/anterior heart field. *Dev. Biol.* **2005**, *287*, 134–145. [CrossRef] [PubMed]
88. Liu, K.; Yu, W.; Tang, M.; Tang, J.; Liu, X.; Liu, Q.; Li, Y.; He, L.; Zhang, L.; Evans, S.M.; et al. A dual genetic tracing system identifies diverse and dynamic origins of cardiac valve mesenchyme. *Development* **2018**, *145*. [CrossRef]
89. Liu, K.; Jin, H.; Zhou, B. Genetic lineage tracing with multiple DNA recombinases: A user's guide for conducting more precise cell fate mapping studies. *J. Biol. Chem.* **2020**, *295*, 6413–6424. [CrossRef] [PubMed]
90. Liang, X.; Wang, G.; Lin, L.; Lowe, J.; Zhang, Q.; Bu, L.; Chen, Y.; Chen, J.; Sun, Y.; Evans, S.M. HCN4 dynamically marks the first heart field and conduction system precursors. *Circ. Res.* **2013**, *113*, 399–407. [CrossRef]

91. Makki, N.; Capecchi, M.R. Hoxa1 lineage tracing indicates a direct role for Hoxa1 in the development of the inner ear, the heart, and the third rhombomere. *Dev. Biol.* **2010**, *341*, 499–509. [CrossRef]
92. Yang, L.; Cai, C.L.; Lin, L.; Qyang, Y.; Chung, C.; Monteiro, R.M.; Mummery, C.L.; Fishman, G.I.; Cogen, A.; Evans, S. Isl1 Cre reveals a common Bmp pathway in heart and limb development. *Development* **2006**, *133*, 1575–1585. [CrossRef]
93. Zhou, B.; Ma, Q.; Rajagopal, S.; Wu, S.M.; Domian, I.; Rivera-Feliciano, J.; Jiang, D.; von Gise, A.; Ikeda, S.; Chien, K.R.; et al. Epicardial progenitors contribute to the cardiomyocyte lineage in the developing heart. *Nature* **2008**, *454*, 109–113. [CrossRef]
94. Odelin, G.; Faure, E.; Coulpier, F.; Di Bonito, M.; Bajolle, F.; Studer, M.; Avierinos, J.-F.; Charnay, P.; Topilko, P.; Zaffran, S. Krox20 defines a subpopulation of cardiac neural crest cells contributing to arterial valves and bicuspid aortic valve. *Development* **2017**, *145*, dev151944. [CrossRef]
95. Crucean, A.; Alqahtani, A.; Barron, D.J.; Brawn, W.J.; Richardson, R.V.; O'Sullivan, J.; Anderson, R.H.; Henderson, D.J.; Chaudhry, B. Re-evaluation of hypoplastic left heart syndrome from a developmental and morphological perspective. *Orphanet J. Rare Dis.* **2017**, *12*, 1–10. [CrossRef]
96. Tian, X.; Hu, T.; Zhang, H.; He, L.; Huang, X.; Liu, Q.; Yu, W.; He, L.; Yang, Z.; Zhang, Z.; et al. Subepicardial endothelial cells invade the embryonic ventricle wall to form coronary arteries. *Cell Res.* **2013**, *23*, 1075–1090. [CrossRef]
97. Moses, K.A.; DeMayo, F.; Braun, R.M.; Reecy, J.L.; Schwartz, R.J. Embryonic expression of an Nkx2-5/Cre gene using ROSA26 reporter mice. *Genesis* **2001**, *31*, 176–180. [CrossRef] [PubMed]
98. Harmon, A.W.; Nakano, A. Nkx2-5 lineage tracing visualizes the distribution of second heart field-derived aortic smooth muscle. *Genesis* **2013**, *51*, 862–869. [CrossRef]
99. Epstein, J.A.; Li, J.; Lang, D.; Chen, F.; Brown, C.B.; Jin, F.; Lu, M.M.; Thomas, M.; Liu, E.; Wessels, A.; et al. Migration of cardiac neural crest cells in Splotch embryos. *Development* **2000**, *127*, 1869–1878. [CrossRef]
100. Epstein, J.; Buck, C.A. Transcriptional regulation of cardiac development: Implications for congenital heart disease and DiGeorge syndrome. *Pediatric Res.* **2000**, *48*, 717–724. [CrossRef] [PubMed]
101. Greulich, F.; Rudat, C.; Farin, H.F.; Christoffels, V.M.; Kispert, A. Lack of Genetic Interaction between Tbx18 and Tbx2/Tbx20 in Mouse Epicardial Development. *PLoS ONE* **2016**, *11*, e0156787. [CrossRef] [PubMed]
102. Aanhaanen, W.T.J.; Brons, J.F.; Domínguez, J.N.; Rana, M.S.; Norden, J.; Airik, R.; Wakker, V.; De Gier-De Vries, C.; Brown, N.A.; Kispert, A.; et al. The Tbx2+ primary myocardium of the atrioventricular canal forms the atrioventricular node and the base of the left ventricle. *Circ. Res.* **2009**, *104*, 1267–1274. [CrossRef] [PubMed]
103. Singh, R.; Hoogaars, W.M.; Barnett, P.; Grieskamp, T.; Rana, M.S.; Buermans, H.; Farin, H.F.; Petry, M.; Heallen, T.; Martin, J.F.; et al. Tbx2 and Tbx3 induce atrioventricular myocardial development and endocardial cushion formation. *Cell. Mol. Life Sci.* **2012**, *69*, 1377–1389. [CrossRef]
104. De Lange, F.J.; Moorman, A.F.M.; Anderson, R.H.; Männer, J.; Soufan, A.T.; De Gier-De Vries, C.; Schneider, M.D.; Webb, S.; van den Hoff, M.J.B.; Christoffels, V.M.; et al. Lineage and morphogenetic analysis of the cardiac valves. *Circ. Res.* **2004**, *95*, 645–654. [CrossRef]
105. Payne, S.; De Val, S.; Neal, A. Endothelial-specific cre mouse models is your cre CREdibile? *Arterioscler. Thromb. Vasc. Biol.* **2018**, *38*, 2550–2561. [CrossRef]
106. Tang, Y.; Harrington, A.; Yang, X.; Friesel, R.E.; Liaw, L. The contribution of the Tie2+ lineage to primitive and definitive hematopoietic cells. *Genesis* **2010**, *48*, 563–567. [CrossRef]
107. Jiao, K.; Kulessa, H.; Tompkins, K.; Zhou, Y.; Batts, L.; Baldwin, H.S.; Hogan, B.L.M. An essential role of Bmp4 in the atrioventricular septation of the mouse heart. *Genes Dev.* **2003**, *17*, 2362–2367. [CrossRef]
108. Sinha, T.; Lin, L.; Li, D.; Davis, J.; Evans, S.; Wynshaw-Boris, A.; Wang, J. Mapping the dynamic expression of Wnt11 and the lineage contribution of Wnt11-expressing cells during early mouse development. *Dev. Biol.* **2015**, *398*, 177–192. [CrossRef]
109. Poelmann, R.E.; Jongbloed, M.R.M.; Molin, D.G.M.; Fekkes, M.L.; Wang, Z.; Fishman, G.I.; Doetschman, T.; Azhar, M.; Gittenberger-De Groot, A.C. The neural crest is contiguous with the cardiac conduction system in the mouse embryo: A role in induction? *Anat. Embryol.* **2004**, *208*, 389–393. [CrossRef] [PubMed]
110. Stottmann, R.W.; Choi, M.; Mishina, Y.; Meyers, E.N.; Klingensmith, J. BMP receptor IA is required in mammalian neural crest cells for development of the cardiac outflow tract and ventricular myocardium. *Development* **2004**, *131*, 2205–2218. [CrossRef] [PubMed]
111. Hatzistergos, K.E.; Durante, M.A.; Valasaki, K.; Wanschel, A.C.B.A.; William Harbour, J.; Hare, J.M. A novel cardiomyogenic role for Isl1+ neural crest cells in the inflow tract. *Sci. Adv.* **2020**, *6*, eaba9950. [CrossRef]
112. Zhou, B.; Pu, W.T. Genetic Cre-loxP assessment of epicardial cell fate using Wt1-Driven cre alleles. *Circ. Res.* **2012**, *111*, e276. [CrossRef]
113. Bonnerot, C.; Nicolas, J.F. Clonal analysis in the intact mouse embryo by intragenic homologous recombination. *Comptes Rendus Acad. Sci. III* **1993**, *316*, 1207–1217.
114. Meilhac, S.M.; Kelly, R.G.; Rocancourt, D.; Eloy-Trinquet, S.; Nicolas, J.-F.; Buckingham, M.E. A retrospective clonal analysis of the myocardium reveals two phases of clonal growth in the developing mouse heart. *Development* **2003**, *130*, 3877–3889. [CrossRef]
115. Miquerol, L.; Moreno-Rascon, N.; Beyer, S.; Dupays, L.; Meilhac, S.M.; Buckingham, M.E.; Franco, D.; Kelly, R.G. Biphasic development of the mammalian ventricular conduction system. *Circ. Res.* **2010**, *107*, 153–161. [CrossRef]

116. Miquerol, L.; Bellon, A.; Moreno, N.; Beyer, S.; Meilhac, S.M.; Buckingham, M.; Franco, D.; Kelly, R.G. Resolving cell lineage contributions to the ventricular conduction system with a Cx40-GFP allele: A dual contribution of the first and second heart fields. *Dev. Dyn.* **2013**, *242*, 665–677. [CrossRef]
117. Luria, S.E.; Delbrück, M. Mutations of Bacteria from Virus Sensitivity to Virus Resistance. *Genetics* **1943**, *28*, 491–511. [CrossRef] [PubMed]
118. Lescroart, F.; Mohun, T.; Meilhac, S.M.; Bennett, M.; Buckingham, M. Lineage tree for the venous pole of the heart: Clonal analysis clarifies controversial genealogy based on genetic tracing. *Circ. Res.* **2012**, *111*, 1313–1322. [CrossRef]
119. Cannoodt, R.; Saelens, W.; Saeys, Y. Computational methods for trajectory inference from single-cell transcriptomics. *Eur. J. Immunol.* **2016**, *46*, 2496–2506. [CrossRef] [PubMed]
120. Todorov, H.; Cannoodt, R.; Saelens, W.; Saeys, Y. Network Inference from Single-Cell Transcriptomic Data. In *Methods in Molecular Biology*; Humana Press: New York, NY, USA, 2019; Volume 1883, pp. 235–249.
121. Lescroart, F.; Kelly, R.G.; Le Garrec, J.-F.; Nicolas, J.-F.; Meilhac, S.M.; Buckingham, M. Clonal analysis reveals common lineage relationships between head muscles and second heart field derivatives in the mouse embryo. *Development* **2010**, *137*, 3269–3279. [CrossRef] [PubMed]
122. Bredman, J.J.; Weijs, W.A.; Korfage, H.A.; Brugman, P.; Moorman, A.F. Myosin heavy chain expression in rabbit masseter muscle during postnatal development. *J. Anat.* **1992**, *180 Pt 2*, 263–274.
123. Navin, N.; Kendall, J.; Troge, J.; Andrews, P.; Rodgers, L.; McIndoo, J.; Cook, K.; Stepansky, A.; Levy, D.; Esposito, D.; et al. Tumour evolution inferred by single-cell sequencing. *Nature* **2011**, *472*, 90–94. [CrossRef]
124. Wang, Y.; Waters, J.; Leung, M.L.; Unruh, A.; Roh, W.; Shi, X.; Chen, K.; Scheet, P.; Vattathil, S.; Liang, H.; et al. Clonal evolution in breast cancer revealed by single nucleus genome sequencing. *Nature* **2014**, *512*, 155–160. [CrossRef] [PubMed]
125. Abbosh, C.; Birkbak, N.J.; Wilson, G.A.; Jamal-Hanjani, M.; Constantin, T.; Salari, R.; Le Quesne, J.; Moore, D.A.; Veeriah, S.; Rosenthal, R.; et al. Phylogenetic ctDNA analysis depicts early-stage lung cancer evolution. *Nature* **2017**, *545*, 446–451. [CrossRef] [PubMed]
126. Xu, J.; Nuno, K.; Litzenburger, U.M.; Qi, Y.; Corces, M.R.; Majeti, R.; Chang, H.Y. Single-cell lineage tracing by endogenous mutations enriched in transposase accessible mitochondrial DNA. *eLife* **2019**, *8*, e45105. [CrossRef] [PubMed]
127. Ding, J.; Lin, C.; Bar-Joseph, Z. Cell lineage inference from SNP and scRNA-Seq data. *Nucleic Acids Res.* **2019**, *47*, e56. [CrossRef]
128. Lioux, G.; Liu, X.; Temiño, S.; Oxendine, M.; Ayala, E.; Ortega, S.; Kelly, R.G.; Oliver, G.; Torres, M. A Second Heart Field-Derived Vasculogenic Niche Contributes to Cardiac Lymphatics. *Dev. Cell* **2020**, *52*, 350–363. [CrossRef] [PubMed]
129. Gittenberger-De Groot, A.C.; Vrancken Peeters, M.P.F.M.; Bergwerff, M.; Mentink, M.M.T.; Poelmann, R.E. Epicardial outgrowth inhibition leads to compensatory mesothelial outflow tract collar and abnormal cardiac septation and coronary formation. *Circ. Res.* **2000**, *87*, 969–971. [CrossRef] [PubMed]
130. Arques, C.G.; Doohan, R.; Sharpe, J.; Torres, M. Cell tracing reveals a dorsoventral lineage restriction plane in the mouse limb bud mesenchyme. *Development* **2007**, *134*, 3713–3722. [CrossRef]
131. Liu, X.; Chen, W.; Li, W.; Li, Y.; Priest, J.R.; Zhou, B.; Wang, J.; Zhou, Z. Single-Cell RNA-Seq of the Developing Cardiac Outflow Tract Reveals Convergent Development of the Vascular Smooth Muscle Cells. *Cell Rep.* **2019**, *28*, 1346–1361. [CrossRef]
132. Kruse, F.; Junker, J.P.; van Oudenaarden, A.; Bakkers, J. Tomo-seq: A method to obtain genome-wide expression data with spatial resolution. *Methods Cell Biol.* **2016**, *135*, 299–307. [CrossRef]
133. Junker, J.P.; Noel, E.S.; Guryev, V.; Peterson, K.A.; Shah, G.; Huisken, J.; McMahon, A.P.; Berezikov, E.; Bakkers, J.; Van Oudenaarden, A.; et al. Genome-wide RNA Tomography in the Zebrafish Embryo. *Cell* **2014**, *159*, 662–675. [CrossRef] [PubMed]
134. Lovatt, D.; Ruble, B.K.; Lee, J.; Dueck, H.; Kim, T.K.; Fisher, S.; Francis, C.; Spaethling, J.M.; Wolf, J.A.; Grady, M.S.; et al. Transcriptome in vivo analysis (TIVA) of spatially defined single cells in live tissue. *Nat. Methods* **2014**, *11*, 190–196. [CrossRef]
135. Rutkovskiy, A.; Malashicheva, A.; Sullivan, G.; Bogdanova, M.; Kostareva, A.; Stensløkken, K.O.; Fiane, A.; Vaage, J. Valve interstitial cells: The key to understanding the pathophysiology of heart valve calcification. *J. Am. Heart Assoc.* **2017**, *6*. [CrossRef] [PubMed]
136. Raj, B.; Wagner, D.E.; McKenna, A.; Pandey, S.; Klein, A.M.; Shendure, J.; Gagnon, J.A.; Schier, A.F. Simultaneous single-cell profiling of lineages and cell types in the vertebrate brain. *Nat. Biotechnol.* **2018**, *36*, 442–450. [CrossRef] [PubMed]
137. Alemany, A.; Florescu, M.; Baron, C.S.; Peterson-Maduro, J.; Van Oudenaarden, A. Whole-organism clone tracing using single-cell sequencing. *Nature* **2018**, *556*, 108–112. [CrossRef]
138. Spanjaard, B.; Hu, B.; Mitic, N.; Olivares-Chauvet, P.; Janjuha, S.; Ninov, N.; Junker, J.P. Simultaneous lineage tracing and cell-type identification using CrIsPr-Cas9-induced genetic scars. *Nat. Biotechnol.* **2018**, *36*, 469–473. [CrossRef] [PubMed]
139. Junker, J.P.; Spanjaard, B.; Peterson-Maduro, J.; Alemany, A.; Hu, B.; Florescu, M.; van Oudenaarden, A. Massively parallel clonal analysis using CRISPR/Cas9 induced genetic scars. *bioRxiv* **2016**, 56499. [CrossRef]
140. Weinreb, C.; Rodriguez-Fraticelli, A.; Camargo, F.D.; Klein, A.M. Lineage tracing on transcriptional landscapes links state to fate during differentiation. *Science* **2020**, *367*, eaaw3381. [CrossRef]
141. Pei, W.; Feyerabend, T.B.; Rössler, J.; Wang, X.; Postrach, D.; Busch, K.; Rode, I.; Klapproth, K.; Dietlein, N.; Quedenau, C.; et al. Polylox barcoding reveals haematopoietic stem cell fates realized in vivo. *Nature* **2017**, *548*, 456–460. [CrossRef]
142. Wagner, D.E.; Klein, A.M. Lineage tracing meets single-cell omics: Opportunities and challenges. *Nat. Rev. Genet.* **2020**, *21*, 410–427. [CrossRef]

143. Wei, C.J.Y.; Zhang, K. Retrace: Simultaneous retrospective lineage tracing and methylation profiling of single cells. *Genome Res.* **2020**, *30*, 602–610. [CrossRef]
144. Biezuner, T.; Spiro, A.; Raz, O.; Amir, S.; Milo, L.; Adar, R.; Chapal-Ilani, N.; Berman, V.; Fried, Y.; Ainbinder, E.; et al. A generic, cost-effective, and scalable cell lineage analysis platform. *Genome Res.* **2016**, *26*, 1588–1599. [CrossRef] [PubMed]
145. Liu, Y.; Siejka-Zielińska, P.; Velikova, G.; Bi, Y.; Yuan, F.; Tomkova, M.; Bai, C.; Chen, L.; Schuster-Böckler, B.; Song, C.X. Bisulfite-free direct detection of 5-methylcytosine and 5-hydroxymethylcytosine at base resolution. *Nat. Biotechnol.* **2019**, *37*, 424–429. [CrossRef] [PubMed]
146. Ku, W.L.; Nakamura, K.; Gao, W.; Cui, K.; Hu, G.; Tang, Q.; Ni, B.; Zhao, K. Single-cell chromatin immunocleavage sequencing (scChIC-seq) to profile histone modification. *Nat. Methods* **2019**, *16*, 323–325. [CrossRef] [PubMed]
147. Regev, A.; Teichmann, S.A.; Lander, E.S.; Amit, I.; Benoist, C.; Birney, E.; Bodenmiller, B.; Campbell, P.; Carninci, P.; Clatworthy, M.; et al. Science forum: The human cell atlas. *eLife* **2017**, *6*, e27041. [CrossRef] [PubMed]
148. Pullen, L.C. Human Cell Atlas Poised to Transform Our Understanding of Organs. *Am. J. Transplant.* **2018**. [CrossRef]
149. Regev, A.; Teichmann, S.; Rozenblatt-Rosen, O.; Stubbington, M.; Ardlie, K.; Amit, I.; Arlotta, P.; Bader, G.; Benoist, C.; Biton, M.; et al. The Human Cell Atlas White Paper. *arXiv* **2018**, arXiv:1810.05192.

Journal of
Cardiovascular
Development and Disease

MDPI

Review

Outflow Tract Formation—Embryonic Origins of Conotruncal Congenital Heart Disease

Sonia Stefanovic *, Heather C. Etchevers and Stéphane Zaffran *

Aix-Marseille Université, INSERM, MMG, U1251, 27 boulevard Jean Moulin, 13005 Marseille, France; heather.etchevers@inserm.fr

* Correspondence: sonia.stefanovic@inserm.fr (S.S.); stephane.zaffran@inserm.fr (S.Z.)

Abstract: Anomalies in the cardiac outflow tract (OFT) are among the most frequent congenital heart defects (CHDs). During embryogenesis, the cardiac OFT is a dynamic structure at the arterial pole of the heart. Heart tube elongation occurs by addition of cells from pharyngeal, splanchnic mesoderm to both ends. These progenitor cells, termed the second heart field (SHF), were first identified twenty years ago as essential to the growth of the forming heart tube and major contributors to the OFT. Perturbation of SHF development results in common forms of CHDs, including anomalies of the great arteries. OFT development also depends on paracrine interactions between multiple cell types, including myocardial, endocardial and neural crest lineages. In this publication, dedicated to Professor Andriana Gittenberger-De Groot and her contributions to the field of cardiac development and CHDs, we review some of her pioneering studies of OFT development with particular interest in the diverse origins of the many cell types that contribute to the OFT. We also discuss the clinical implications of selected key findings for our understanding of the etiology of CHDs and particularly OFT malformations.

Keywords: congenital heart defects; cardiac progenitor cells; outflow tract; second heart field; neural crest; endocardium; cushion; valve

Citation: Stefanovic, S.; Etchevers, H.C.; Zaffran, S. Outflow Tract Formation—Embryonic Origins of Conotruncal Congenital Heart Disease. *J. Cardiovasc. Dev. Dis.* **2021**, *8*, 42. https://doi.org/10.3390/jcdd8040042

Received: 11 March 2021
Accepted: 3 April 2021
Published: 9 April 2021

Publisher's Note: MDPI stays neutral with regard to jurisdictional claims in published maps and institutional affiliations.

1. Introduction

Congenital heart defects (CHDs) are the most common form of birth defect, affecting up to 1 in every 100 live births. Anomalies in cardiac outflow tract (OFT) are among the most frequent CHDs, with a prevalence of 30%, likely reflecting the complex morphogenetic events underlying heart development [1,2]. The cardiac OFT, comprised of the *conus* or *bulbus cordis* and the *truncus arteriosus* (together called the conotruncal region), is a rapidly remodeling structure during embryogenesis at the arterial pole of the heart, as it connects the embryonic ventricles to the aortic sac [3]. The OFT forms during heart looping from progenitor cells in splanchnic pharyngeal mesoderm. At its maximal extension, the OFT is a torsioned myocardial cylinder lined with endocardial cells. Septation of the OFT, to give rise to the base (trunk) of the aorta and pulmonary arteries, involves interactions between multiple cell types, including myocardial, endocardial and neural crest cells. During this process, the myocardial wall of the OFT rotates prior to and during the septation of this region [4]. Two opposing endocardial cushions swell into the extracellular matrix (ECM) composing the cardiac jelly between the myocardial sleeve and the endocardial lining. These will form the major septal OFT cushions, designated as inferior or superior, at the origin of the semilunar (aortic and pulmonary) valves and the transition from heart to great arteries. OFT remodeling is associated with formation of an outlet septum, semilunar valve morphogenesis, coronary arteriogenesis and maturation of the myocardial and smooth muscle components at the base of the great arteries.

The septation of the OFT is established first by the fusion of the superior and inferior cushions at their distal end and proceeds proximally in the direction of the ventricles. Absence of OFT septation leads to persistent truncus arteriosus (PTA), while an unbalanced

septation of the OFT can induce double outlet right ventricle (DORV), overriding aorta (OA), ventricular septal defect (VSD), or other anomalies such as tetralogy of Fallot (ToF). In addition, anomalies may be associated with abnormal rotation of the OFT, leading to a lack of alignment of the aorta or pulmonary artery with their respective ventricles [4]. These CHDs are frequently diagnosed in newborns with cyanosis. Here, we will discuss the embryological mechanisms of CHDs associated with OFT defects.

2. Embryonic Origins of the OFT

2.1. Myocardial Progenitors

Distinct sets of cardiac progenitors differentiate in a coordinated manner to form the different parts of the heart. Embryonic heart development starts from the earliest stages of gastrulation, around embryonic day (E) 6.5 in the mouse or within a few hours' incubation of the chicken egg, with the specification of an initial pool of cardiac progenitors expressing the transcription factor Mesp1 [5,6]. These cells ingress and migrate from the primitive streak to the anterior part of the embryo, where within a few (chick) to 24 h (mouse), they form a "first heart field" (FHF) known as the cardiac crescent in mouse or a bilateral pair of primary heart fields in chick [7]. By E7.5–8.0, during folding of the mouse embryo and formation of the foregut, the two sides of the cardiac crescent are brought together to form the linear heart tube.

The embryonic myocardium of this initial tube is characterized by lower proliferation, a poorly developed contractile apparatus and slow conduction relative to later stages [8]. Rapid growth of the heart is driven by progressive addition of progenitor cells from adjacent pharyngeal mesoderm to its arterial and venous poles. These cells, collectively known as the second heart field (SHF), were first identified in the mouse and chick models [9,10] but appear to be present in all vertebrate embryos examined to date. SHF progenitors, located in a dorsomedial position relative to the linear heart tube, are kept in an undifferentiated and rapidly proliferating state. The SHF gives rise to right ventricular and OFT myocardium at the arterial pole, and to atrial myocardium including the dorsal mesenchymal protrusion (DMP) at the venous pole [10]. Perturbation of the SHF during elongation of the forming heart results in a spectrum of OFT defects associated with early embryonic lethality [11–13]. Lineage tracing analysis in mice has revealed that the SHF is sub-divided into distinct anterior and posterior regions (aSHF and pSHF) [14,15] (Figure 1). Indeed, aSHF progenitors engender the right ventricular and proximal OFT myocardium, while progenitor cells located in the pSHF contribute to the formation of the atrial and atrioventricular septation through development of the dorsal mesenchymal protrusion (DMP) that forms the muscular base of the primary atrial septum [16]. In addition, a subset of SHF cells form the myocardium at the base of the pulmonary artery [14]. Specific regions in the embryonic heart tube acquire a chamber-specific gene program, and from E8.5 on, differentiate and expand or "balloon" by rapid proliferation to form the ventricular and atrial chamber myocardium. In contrast, the regions between these differentiating chambers, such as the *sinus venosus*, the atrioventricular canal (AVC) and the OFT, either do not differentiate or expand during this temporal window, and consequently form constrictions. The inflow tract cells of the heart tube then develop into atrial cells, pulmonary myocardial cells and myocardial cells of the proximal superior caval veins.

The relevance of the SHF to congenital malformations has stimulated research into the mechanisms regulating the process of cardiac tube elongation. A complex network of signaling inputs and transcriptional regulators controls the elevated proliferation and differentiation delay relative to FHF cells. Identification of SHF-restricted regulatory elements has provided evidence that different transcriptional programs operate in distinct SHF sub-populations, giving rise to specific subregions of the definitive heart. Cells expressing *Cre* recombinase under the control of a SHF-restricted regulatory element from the *Mef2c* transcription factor gene contribute widely to the OFT and right ventricle, as well as to a population of cells at the venous pole of the heart giving rise to the primary atrial septum and the DMP [17–20]. Expression of the LIM homeodomain transcription factor

Islet-1 (*Isl1*) in SHF cells showed that these progenitors contribute to the venous, as well as the arterial pole of the heart [13]. The secreted fibroblast growth factor 10, encoded by *Fgf10*, is also a marker of the murine aSHF and subsequent arterial pole myocardium [21]. The cardiac *ISL1* expression domain is conserved during human embryonic development; in early heart tissue, ISL1 binds a *FGF10* enhancer element [22]. Retinoic acid (RA) has been shown to pattern the SHF [23,24]. Genetic lineage analysis in the mouse has shown that combinatorial expression of anterior Homeobox (Hox) genes *Hoxa1*, *Hoxa3* and *Hoxb1* defines distinct sub-domains within the posterior domain of the SHF that contribute to most of the atrial and sub-pulmonary myocardium [14,25]. Thus, animal models are relevant to studying conserved molecular circuitry in regions prone to human CHDs.

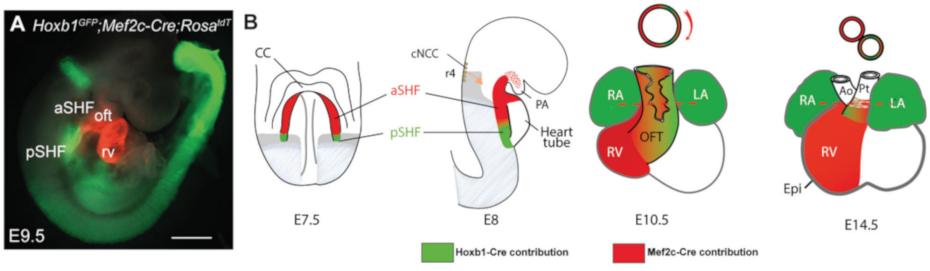

Figure 1. Subdomains within the SHF. (**A**) Whole-mount fluorescence microscopy of triple transgenic *Mef2c-Cre*;*Hoxb1-GFP*;*Rosa*^{tdT} embryos at stage E9.5. (**B**) Diagram showing stages of heart development and contribution of the anterior second heart field (red) and the posterior second heart field (green) to the heart. Frontal view is shown for embryonic day 7.5 (E7.5), E10.5, E14.5 and lateral view for E8. Genetic lineage analysis of *Hoxb1*-expressing cells using the *Hoxb1*-IRES-*Cre* mouse line showed that *Hoxb1*+ progenitors contribute to both atria, the DMP and the myocardium at the base of the pulmonary trunk. Genetic lineage analysis of *Mef2c-Cre*-labelled cells using the *Mef2c-Cre*;*Rosa*^{tdT} mouse line showed that Tomato-positive (Tomato+) cells are detected in the DMP, the great arteries (aorta and pulmonary trunk) and the right ventricle. The left ventricle is derived exclusively from the first heart field, which also contributes to atria formation. SHF, second heart field; Ao, aorta; CC, cardiac crescent; cNCC, cardiac neural crest cells; Epi, epicardium; LA, left atrium; LV, left ventricle; PA, pharyngeal arch; Pt, pulmonary trunk; RA, right atrium; RV, right ventricle; a/pSHF, anterior/posterior second heart field. Scale bar: 500 μm.

Recently, we have used chromatin accessibility analysis with ATAC-seq (Assay of Transposase Accessible Chromatin sequencing) to define accessible sites for transcriptional regulation in SHF subpopulations [26]. The ATAC-seq method utilizes a transposase, which preferentially integrates sequencing adapters in regions of open chromatin such as active promoter regions, enhancers, and insulators, and can be performed on relatively small amounts of cells. Such datasets are important to understand the tightly regulated genetic networks governing heart development and to determine how these networks become deregulated in CHD. Integration with transcriptomes of sorted cardiac progenitor cells led to the discovery of novel pSHF markers (*Aldh1a2*, *Bmp4*, *Gata4*, *Nr2f2*, etc.) that contribute to the formation of the OFT and venous pole of the heart, illustrating how these datasets provide multiple new avenues of investigation for the future [26].

2.2. Endocardial Cushions

The heart tube is formed by both future ventricular and atrial myocardium and a non-chamber myocardial phenotype in the AVC, OFT and inner curvature [27]. This myocardium signals to underlying AVC and OFT endocardium to activate an endocardial-to-mesenchymal transition (EndMT), in which a subset of endocardial cells migrates into the underlying ECM to give rise to the mesenchyme of the valves and the septa [28]. Reciprocal signals between the endocardium and the myocardium have been shown to induce EndMT, mediated by the transforming growth factor β, bone morphogenetic protein (BMP) and Notch signaling pathways, among others [29,30]. Primary myocardium

of the AVC and OFT is normally characterized by *Bmp2* and *Bmp4* expression [31,32], while *Bmp2*-deficient hearts lack AVC and OFT cushions [32–34]. Studies in mice have revealed that the AVC T-box transcription factors, Tbx2 and Tbx3, repress chamber-specific gene expression [32,33] and that Bmp2 directly regulates *Tbx2* expression in the cushion regions [35]. Notch signaling is crucial to patterning the forming heart and presumptive chamber and valve tissues by restricting *Bmp2* and *Tbx2* expression to the cushions [29]. Notch is activated throughout the endocardium of the AVC and OFT regions. Ectopic activation of *Notch2*, or the Notch target genes *Hey1* and *Hey2* in the chicken heart, results in downregulation of Bmp2 in the AVC [36], suggesting that the Notch pathway suppresses *Bmp2* expression in chamber myocardium. However, Bmp and Notch signals cooperate to induce EndMT in the AVC and OFT regions in mouse embryos [37]. Alterations of AVC and OFT cushion architecture result from ligation-induced changes in blood flow in the chicken embryo model, highlighting additional interactions with shear stress-responsive signaling pathways during the EndMT process [30].

EndMT in the AVC and OFT regions is essential for generating a pool of mesenchymal cells that subsequently become valvular interstitial cells during cardiac valve maturation. However, other cell lineages contribute to endocardial cushions. In the AVC, lineage analysis using *Tie2-Cre;Rosa26R* mice has shown that the majority of mesenchymal cells are derived from endocardial cells following EndMT [38]. In contrast, lineage tracing studies of the OFT using quail-chick chimeras and, later, *Wnt1-Cre*-expressing mice, have demonstrated that cardiac neural crest cells (CNCC) contribute significantly to both arterial valves and the aorticopulmonary septum [38–40] (Figure 2). These respond directly to Bmp signaling. *Cre*-mediated *Bmpr1a* deletion in the CNCC lineage alone leads to hypoplasia of the early OFT cushions and retrograde, often lethal, diastolic arterial flow at E10.5–11.5. By E12.5, surviving mouse embryos also develop a persistent truncus arteriosus (PTA) [41]. Two recent studies have reported that the intercalated leaflets of the semilunar valves arise directly from aSHF progenitors of the outflow wall rather than indirectly after EndMT or from CNCC [42,43]. Thus, the mesenchymal cell populations forming the cushions come from multiple sources and coordinately direct blood outflow from the heart into the aorta and pulmonary trunk.

Recently, single-cell transcriptomic analysis generated a reference of cell transcriptomic states in OFT development [44]. This study identified convergent development of the vascular smooth muscle cell (vSMC) lineage, where intermediate cell populations were found to be involved in either myocardial-to-vSMC trans-differentiation or a mesenchymal-to-vSMC transition. The OFT myocardium derives from the SHF [45], so the vSMC derived from myocardial trans-differentiation are actually a small portion of SHF-derived vSMC, whereas most are derived from either SHF or CNCC-mesenchyme (see below). Transitions between cell lineages during OFT development are thus more complicated than previously appreciated.

2.3. Cardiac Neural Crest

The CNCC is a subpopulation of neural crest cells that contributes most cells of the perivascular walls of the posterior pharyngeal (aortic) arteries [46,47] and is also indispensable for septation of the more proximal OFT, as described briefly above. CNCC originate from dorsal neural folds corresponding to the prospective posterior hindbrain and first vertebral segments of spinal cord, at the boundary with non-neural ectoderm and at the head–neck interface. A broader term that includes the CNCC is the "vagal" neural crest, since these also provide glial and perineural support cells accompanying the vagal nerve to all its targets, many neurons of the corresponding cranial ganglia, and the autonomic enteric nervous system innervating the fore- and mid-gut (reviewed in Reference [48]).

CNCC migrate circumpharyngeally around the endoderm [49] in a dorsal-to-ventral manner, reflecting their temporal order of arrival rather than inherent differences in competence [50]. They also mix to a lesser extent along the rostro-caudal axis to adjacent

pharyngeal arches [51,52] and do the same at the level of adjacent rostral somitic segments corresponding to the first vertebrae [53]. These dynamic scenarios were deduced from fate maps of painstaking quail-chick chimeras using microsurgery and experimental embryology, stemming from the first demonstrations fifty years ago that neural crest gives rise to mesenchyme ("mesectoderm") responsible for a broad array of diverse cephalic, pharyngeal and cardiac connective tissues and organs in amniotes [54]. The predominant contributions of CNCC to pericytes and smooth muscle of the aortic sac, pharyngeal arteries, aorticopulmonary septum and OFT valves, as well as to the anterior cardinal veins and venous pole, were determined by these means [51,55] (Figure 2B,C). Cardiac parasympathetic ganglia are likewise derived from vagal CNCC [56,57]. Quail-chick chimeras allowed the more recent demonstration that vSMC of the coronary arteries and of the smaller vessels of the upper interventricular septum are derived from pre-otic hindbrain neural crest, although some of these also originate from the proepicardium [58].

Additional appreciation for these migratory pathways and the molecularly controlled extent of cellular admixture came from the contributions of tools in mouse genetics to lineage-trace NCC subsets. *Wnt1-Cre*-driven conditional recombination of a floxed cassette that lifted the transgenic brake for transcription of beta-galactosidase, or later of fluorescent protein transgenes, validated the participation of CNCC derivatives to the composition of the cardiac OFT, tricuspid valves, the vascular smooth muscle of proximal coronary arteries and their septal branches and many surrounding tissues [38,39,58–61] (Figure 2A, D–F). Tracing lineage analysis using *Krox20-Cre* mice has revealed that a subset of CNCC migrated from rhombomere 5–6 region contributes to semilunar valve development [40]. Furthermore, it became possible to examine how the cells were organized in genetic backgrounds that induce OFT malformations, such as the "rescued" *Raldh2*$^{-/-}$ mutant, where judiciously administered maternal RA can prolong fetal life into mid-gestation as a model of PTA or vitamin A deficiency syndrome [62]. In this example, CNCC are present and viable, but more haphazardly oriented and in an inappropriate location within mutant OFT cushions; subsequently, endocardial contact alone is not enough to ensure fusion and septation but requires close proximity of functionally organized CNCC derivatives (Figure 2B).

Like the pSHF, it is less recognized that a subpopulation of CNCC simultaneously invests the venous pole of the heart when shaping the OFT. This was demonstrated by Poelmann and Gittenberger-de Groot [55] in chicken embryos using a replication-incompetent retrovirus expressing *LacZ* to infect pre-migratory CNCC and trace their cellular progeny to the dorsal mesocardium, the inter-atrial septum, and the presumptive cardiac conduction system and semilunar valves. Lineage tracing in mice confirmed that multipotent CNCC also contribute directly to some proximal conduction system elements of the posterior inter-nodal tract, His bundle and bundle branches [61]. Subsequent studies by independent authors using lineage tracing or single-cell transcriptomics have validated the differentiation of CNCC into some cells of the conduction system or even proximal IVS and OFT myocardial cells [63–65].

That CNCC can differentiate into some cardiomyocytes in the mammalian heart is less surprising in light of its substantial contributions to this lineage in the zebrafish OFT but also in its atrium, AV junction and ventricle [66,67]. Only pre-somitic neural crest differentiates into myocardium in this animal that lacks a divided systemic and pulmonary circulation [67]. By contrast, in the amphibian *Xenopus laevis*, the SHF provides OFT cells and presumably also its incomplete septum; CNCC, as defined by the experimental techniques used, seemed to not be required for septal cushion formation [68]. However, after CNCC ablation or labeling, the residual Xenopus OFT septum expresses the Sox8 transcription factor in common with facial neural crest-derived mesenchyme, and recently, Sox8 has been shown in the chick to be a specific core member of the gene regulatory network (GRN) of CNCC [69]. It therefore is possible that the authors examining this question in the amphibian model missed a distinct CNCC contribution to its proximal heart, or that the GRN was co-opted by mesenchyme of SHF origin to accomplish an

analogous purpose. CNCC are present in all vertebrate models that have been examined to date, but their precise roles and contributions are organism-specific, reflecting their remarkable plasticity. An interesting example is the crocodile, one of the few reptiles examined with a nearly complete separation of the systemic from the pulmonary circulation. A large septal cushion provides valvular leaflets to each of the three arterial trunks—the right aorta is systemic and has a bicuspid valve, while the left aorta, which irrigates the viscera, and the pulmonary artery have tricuspid valves. Leaflets also serve to block a foramen between the two aortae during systole, reducing pulmonary pressure and favoring blood flow to the brain, even under prolonged diving conditions, Remarkably, the interventricular septum between the left and right OFT remains incomplete until at least birth and shows chondrification within the condensed mesenchyme closest to the OFT, considered by the authors to be most likely of CNCC origin [70]. Enabling new capacities for tissue differentiation and patterning has conferred an obvious evolutionary advantage for adaptation of the head, heart and lungs to a wide range of aqueous or terrestrial environments, from benthic pressures to high-altitude hypoxia. It is important to keep such species-specific adaptations in mind when extrapolating the findings from experimentally tractable models like chick and mouse to human cardiac development.

Orofacial, ear and neck and cardiac OFT anomalies are all heavily reliant on cephalic and vagal neural crest cell influx and remodeling and can be phenocopied in animal models [46], and they are often associated with birth defects in humans. Characteristic signs of genetic conditions such as chromosome 21 trisomy or 22q11.2 microdeletion, they are also frequently induced by the environment during pregnancy (for example, fetal alcohol spectrum disorders and vitamin A or folic acid deficiencies). Both thymic and cardiac OFT malformations such as PTA in the 22q11 microdeletion syndromic spectrum can be reproduced by the ablation of the posterior hindbrain neural folds that would have given rise to CNCC [71], the first major demonstration that paracrine signaling to or from this mesenchymal lineage is critical for the development of organs not themselves primarily constructed from NCC (reviewed in Reference [46]). Severe craniofacial and cardiac malformations are also associated in mice with ectopic expression of *Hoxb1* in *Wnt1-Cre*-recombined CNCC, leading to combinations of hypoplastic posterior pharyngeal arches, interrupted aortic arch (IAA) type B, DORV or OA in addition to cleft palate. CNCC rostrocaudal identity, as determined in part by *Hox* gene expression combinations, impacts its competence to pattern the distal branches of the aortic arches and to influence the rotation of the OFT during its septation [72,73].

As CNCC migrate through the ventral mesenchyme of the posterior pharyngeal arches and the mesoderm of the SHF in order to partition, shape and align the great arteries of the OFT, they interact with all three germ layers through both direct cell contact and through paracrine signaling. One such factor needed to maintain CNCC in this area (and elsewhere in the head) is Fgf8, of both ectodermal and endodermal origin. Like *Tbx1* and *Raldh2* mutants, hypomorphic murine *Fgf8* mutants also phenocopy multiple symptoms of human 22q11.2 microdeletion, including PTA, IAA type B, VSD and patent ductus arteriosus (see below). Insufficient Fgf8 leads to massive circumpharyngeal CNCC apoptosis, as shown by co-labeling neural crest by TUNEL to detect apoptotic cells and anti-AP-2α as they migrate from the post-otic hindbrain into the lateral developing fourth and sixth arches [74].

Failure of normal rotation of OFT myocardium may underlie major forms of CHDs. Rotation of the myocardial wall of the OFT is intimately linked to the influx of CNCC. Mammalian embryos undergo a counterclockwise rotation of the OFT [4,75]. The continued addition of right-sided myocardium during normal development results in movement without spiralization of the OFT, in which the pulmonary trunk orifice is pushed in a rightward and anterior direction, a mechanism referred to as "pulmonary push" [76]. In *Lrp2* knockout embryos, the bulk of the SHF population remains in a mid-sagittal position after insufficient pulmonary push [77]. *Lrp2* encodes megalin, a multiligand endocytic co-receptor that is necessary to transduce retinol, Shh and Fgf8, among other environmental signals. Its full knockout leads to PTA in mice, and occasionally in humans, by

exhausting the pool of OFT myocardial progenitors through premature differentiation [78]. However, compound heterozygous *LRP2* missense variants have also been associated with hypoplastic left heart syndrome in humans [79], implying that other factors also mediate lateralized SHF contributions to the myocardial base of the truncal arteries.

3. Retinoic Acid Signaling

3.1. RA Is Required for the Differentiation of Heart Progenitors into the Myocardium of the OFT

Several conotruncal heart defects have been reported in fetal vitamin A deficiency syndrome. Either an excess or lack of retinoic acid (RA), the most active derivative of Vitamin A, causes conotruncal heart defects, indicating that properly controlled RA dosage and signaling is required for normal OFT development [80,81]. This is corroborated by the frequent OFT and aortic arch malformations associated with the complex Matthew-Wood syndrome (also termed Microphthalmia, syndrome 9, Online Catalog of Human Genes and Genetic Disorders (OMIM) 601186), due to inactivating mutations of the *STRA6* gene, which encodes a transmembrane receptor allowing vitamin A cellular uptake [82–85]. Many heart phenotypes that occur in either fetal vitamin A deficiency syndrome or in excessive maternal exposure to vitamin A or its analog, isotretinoin, are recapitulated in animal models that are mutant for RA nuclear receptors [86]. Conotruncal defects are observed in retinoid acid receptors RARα/RARβ and RARα/RARγ double-mutant hearts and also in hearts with double null alleles in one RXR (α, β, or γ) and one RAR [87–91]. In RA receptor mutant mice (RARα1/RARβ double mutant), the OFT is shortened and misaligned [91]. PTA occurs with high incidence in RARα1/RARβ double mutant mice. In these mutants, truncated OFT and abnormal conotruncal cushion ridges are observed. In RXRα-deficient hearts, OFT septation defects are observed, but there are no apparent defects in RXRβ or RXRγ single mutants [87–90,92,93]. Therefore, RXRα is the major RXR regulating OFT development.

RA mediates SHF patterning in part through the generation and maintenance of heart progenitors in the aSHF [23,24]. The SHF deficiency in RA receptor-null embryos results in a shortened OFT and thereby in alignment defects. As a related consequence, the tissue of the shortened OFT is mis-specified when septation is initiated [91]. Raldh2, a critical enzyme for the synthesis of endogenous RA in the early embryo, is expressed in caudal pharyngeal mesoderm. Analysis of aSHF marker gene expression, including *Fgf8* and *Tbx1*, in *Raldh2*-mutant embryos shows that RA signaling defines both the posterior boundary of the aSHF [94,95] and its anteromedial boundary with the FHF in the zebrafish [96]. Consistent with these observations, an excess of RA, cardioteratogenic in humans, results in downregulation of *Tbx1* expression in avian embryos [97]. Expression of *Raldh2* and one or more of the *Cyp26* genes, encoding a RA degradation enzyme, is often complementary within a tissue. This establishes a RA gradient between adjacent high and low RA-expressing regions [98–100].

3.2. Cell-Autonomous RA Signaling Is Dispensable for the Migration and Fate Differentiation of CNCC

Experimental ablation of sources of CNCC induces many of the cardiac and extracardiac malformations found in vitamin A deficiency [69,96]. However, neural crest-targeted deletion of Rxrα/Rarα1 leads to normal cardiovascular morphology, indicating that cell-autonomous RA signaling through this specific combination is dispensable for CNCC migration and differentiation [101]. Excess RA signaling, on the other hand, blocks both CNCC migration and proliferation by preventing c-Jun N-terminal kinase (JNK) phosphorylation in response to such growth factors as Platelet Derived Growth Factor-AA (PDGF-AA) and antagonizing subsequent activation of the transcriptional regulator c-Jun in the AP-1 transcriptional complex [102]. Knockout mice for c-jun invariably develop PTA and abnormal aortic arch remodeling [103]. This AP-1 component is also necessary in all other *Isl1*-expressing OFT cell lineages to prevent less penetrant aortic or pulmonary valve defects, VSD or DORV [104].

3.3. RA Signaling Defects Are Associated with DiGeorge Syndrome

TBX1 is within the most candidate gene-relevant interval in human 22q11.2 deletion syndrome (DiGeorge/velocardiofacial syndrome), and *Tbx1*-mutant mice show similar phenotypes to those of human 22q11.2, in particular TOF [105]. Studies have shown the importance of the Tbx1-Fgf8-Isl1 network in the regulation of OFT development [106]. Conditional deletion of *Fgf8*-in the Nkx2.5-Cre lineage results in truncated OFT, suggesting that Fgf8 plays a role in the proliferation and differentiation of heart progenitors [106]. Mutant mice with a hypomorphic allele of *Raldh2* die perinatally because of cardiovascular defects, similar to those observed in human 22q11.2 deletion syndrome. In this RA-deficient model, anterior pharyngeal arches develop normally, whereas the absence of hypoplastic posterior pharyngeal arches leads to impaired development of the distal OFT and thereby to TOF, DORV and PTA. CNCC migrate toward the posterior pharyngeal arches but fail to invest them [95,107]. In the *Raldh2* mutant, the expression of *Tbx1* is not altered, but the expression levels of its targets *Fgf8*, *Isl1*, *Hoxa1* and *Hoxb1* are downregulated in the posterior pharyngeal endoderm/ectoderm, showing RA's central role in coordinating aSHF development [95,107]. *Raldh2* SHF expression is expanded anteriorly (cranially) in *Tbx1* mutant embryos, whereas the expression of the three *Cyp26s* is downregulated; consequently, RA signaling is increased and expanded in the anterior SHF [108]. In a compound mutant (*Raldh2*$^{+/-}$; *Tbx1*$^{+/-}$), in which RA synthesis is decreased in the Tbx1$^{+/-}$ state, conotruncal heart defects/aortic arch anomalies are partially rescued. Therefore, when RA signaling is upregulated in the SHF of patients with 22q11.2 syndrome or of *Tbx1*-deletion mutant mice, it can exacerbate the phenotype. Likewise, decreased levels of embryonic RA synthesis accelerate recovery from arterial growth delay in a mouse model of DiGeorge syndrome [109]. Differences in perceived levels of embryonic RA may contribute to the variability of great artery anomalies observed in DGS/VCFS patients [109].

4. Hox Transcription Factors

Homeobox-containing *Hox* genes are known RA signaling targets that play critical roles in patterning all bilaterian embryos [110]. *Raldh2*-null mice showed that RA regulates not only the expression pattern of *Hox* genes but also thereby the fate differentiation of *Hox*-expressing domains [14]. Anterior *Hox* genes *Hoxa1, Hoxa3* and *Hoxb1* expression define distinct sub-domains within the pSHF that contribute to a large part of the atrial and sub-pulmonary myocardium [14,25]. This indicates that *Hox*-expressing progenitor cells of the pSHF contribute to both poles of the heart tube. Fate mapping and clonal analysis experiments have confirmed that pSHF cells contribute to the OFT, and that sub-pulmonary and inflow tract myocardial cells are clonally related [111,112]. *Hoxa1*, *Hoxa3* and *Hoxb1* are expressed in overlapping sub-populations of cardiac progenitor cells in the pSHF and downregulated prior to differentiation [14]. *Hoxb1*- and *Hoxa1*-expressing progenitor cells located in the pSHF segregate to both cardiac poles, contributing to the inflow tract and the inferior wall of the OFT [14]. Furthermore, a RA-responsive *Hoxa3* enhancer has recently been shown to be expressed in progenitor cells of a subset of OFT myocardium [25]. Interestingly, a *Mesp1*+ subpopulation co-expresses the anterior *Hox* genes *Hoxa1*, *Hoxa2*, *Hoxb1* and *Hoxb2*. This *Hox*-positive subpopulation of cardiovascular progenitors is located at E7.25, close to the primitive streak, suggesting that it corresponds to the last cardiovascular progenitor population to emerge from it [113].

Hoxb1 plays a key role in patterning those cardiac progenitor cells that contribute to both cardiac poles [15]. Progenitor cells expressing *Hoxb1* alone or concomitantly with *Hoxa1* contribute to the proximal dorsal OFT or distal OFT, respectively (Figure 1). In contrast, cardiac progenitors that contribute to the superior wall of the OFT and right ventricle do not transcribe *Hox* genes. Genetic tracing of *Hoxb1*+ lineages in *Tbx1*-deficient embryos showed that the deployment of Hoxb1-positive cells during OFT formation is regulated by Tbx1 [114]. A double deletion mutant of *Hoxa1* and *Hoxb1* shows conotruncal heart defects as well as aortic arch anomalies due to both impaired SHF development and CNCC defects [73,115]. A spatially patterned pharyngeal region is necessary for CNCC to

complete their migration and differentiation, borne out by many other studies documenting the upstream signals and early impact of pharyngeal mesoderm and endoderm on neural crest fate [116,117].

Spatial mis-expression of *Hoxb1* in the anterior SHF results in hypoplastic right ventricle. Activation of *Hoxb1* in embryonic stem cells arrests cardiac differentiation in vitro, whereas *Hoxb1*-deficient embryos display premature cardiac differentiation [15]. Moreover, ectopic differentiation in the pSHF of embryos lacking both *Hoxb1* and its paralog *Hoxa1* induces atrioventricular septal defects [15]. *Hoxb1* is thus required for normal deployment of SHF cells during OFT development [115].

A RA-responsive enhancer of *Hoxa3* induces reporter (*LacZ*) expression in the murine pharyngeal endoderm as well as a subpopulation of CNCC [25]. Indeed, *Hoxa3*-knockout mice show a constellation of symptoms overlapping that induced by experimental CNCC ablation: missing aortic arteries and thymus, hypoplastic thyroid glands, aortic stenosis, hypoplastic right ventricle, bicuspid pulmonary valve and persistent patent ductus arteriosus (PDA) with atrial dilation [118]. Like SHF progenitors, the rostrocaudal identity and competence of CNCC is largely determined before EMT, as experimental substitution of pre-migratory neural crest expressing additional (trunk) or no (cephalic) *Hox* genes in place of avian CNCC can induce PTA, DORV and VSD, although their competence to differentiate into cardiac ganglionic cells is less origin-restricted [119]. It is possible to confer CNCC and mesectodermal competence on trunk-level neural crest by the ectopic expression of the *Sox8*, *Tgif1* and *Ets1* transcription factors from the newly identified CNCC-specific GRN [69]. Single-cell transcriptomic studies have found that the post-otic CNCC in mouse embryos is uniquely characterized by *Hoxd3*, *Pax3* and *Nkx1-2* expression, while both *Hoxb1*+ and *Hoxd3*+ CNCC subpopulations co-express *Hoxb2*, *Hoxb3* and *Meis1* [64]. TALE-superclass transcription factors (three-amino acid length extension) such as Pbx1/2/3 or Meis1/2, which are co-factors of anterior Hox proteins, are also expressed in cardiac progenitors, implying a wider role for HOX/TALE complexes during SHF development [120–122].

5. Other Signaling Pathways

The Fgf, Bmp, Shh, Wnt, Pdgf, endothelin, nitric oxide, planar cell polarity and other signaling cascades have been implicated in the direct or indirect maintenance of CNCC and their subsequent influence on the other cell lineages of the OFT, but a complete discussion of their roles is beyond the scope of this review. However, a general theme appears to be that the molecular signals we identify as important in the specification and function of any given lineage in the cardiac OFT usually have a direct role to play in derivatives of the other lineages as well.

6. Future Direction and Clinical Implications

How environmental influences impact the molecular mediators of cardiac OFT development has immediate clinical repercussions. Diabetes mellitus during pregnancy, a frequent condition, increases the risk for congenital heart disease in the offspring, primarily affecting OFT and pharyngeal arch arteries. Cardiac anomalies are often observed in fetuses of diabetic animal models, including rightward displacement of the aorta, DORV and PTA combined with VSD due to a misaligned outlet septum [123]. These defects are strikingly like the DiGeorge syndrome in humans, which has indeed occurred in children of diabetic mothers together with overrepresentation of PTA and DORV. Multiple malformations associated with defective CNCC development in the offspring of diabetic animal models show morphological similarities to those seen in humans [123]. In chicken embryos, exposure of CNCC to elevated D-glucose before their emigration reproducibly induces congenital heart malformations in the OFT and pharyngeal arch arteries, mediated in part by oxidative stress [124]. Mammalian maternal diabetes results in transient and localized alterations in glycation products, VEGF expression and Smad2 phosphorylation, overlapping with those regions of the developing heart that are most sensitive to diabetes-induced CHD [125].

Interaction between genetic and non-genetic factors in epigenetic modifications including DNA methylation and histone modification are likely involved.

Single-cell RNA sequencing has been applied to study the cellular diversity of heart progenitors [126,127] or embryonic or adult hearts at the whole-organ level [128–131], allowing efficient examination of developmental lineage trajectories [44]. For example, this type of analysis has identified the transcription factor *Hand2* as a specifier of OFT cells, where examining *Hand2*-null embryos at multiple time points demonstrated failure of OFT myocardial cell specification. Loss of *Hand2* in mouse embryos also leads to dysregulation of RA signaling and disruption of cardiac progenitor patterning [126]. To date, there are few examples of such population analyses of cell states and regulatory networks in diseases with OFT malformations. The near future will certainly supply multi-omics studies to complement the experimental embryology work of the last few decades, to not only know the many lineages and molecular influences needed to shape the vulnerable conotruncal region of the human heart but to enable promising perspectives in prevention, early diagnosis and increasingly effective surgical reconstructions.

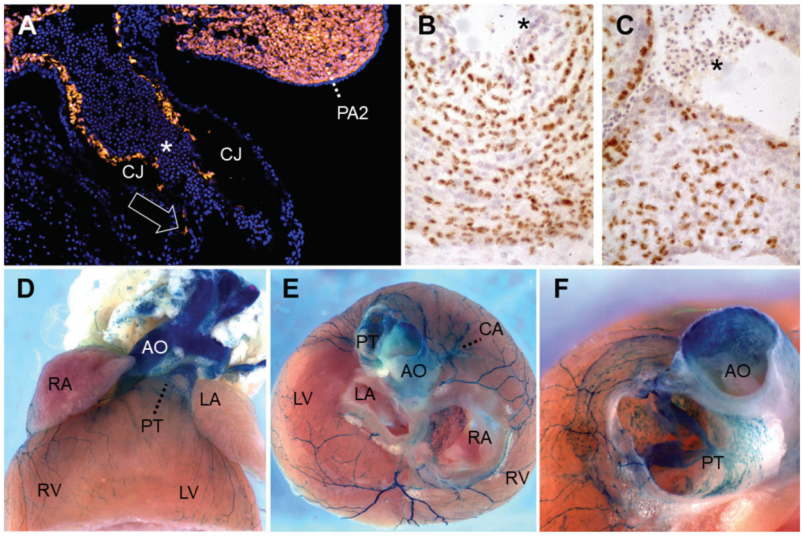

Figure 2. Lineage-tracing of neural crest cells in the cardiac outflow tract. (**A**) *Wnt1-Cre*-mediated recombination induces Tomato red fluorescent protein expression in neural crest-derived cells (NCC) of PA2 as well as in those (arrow) migrating caudally into the outflow tract, along the endothelial abluminal surface on embryonic day (E)10 in mouse. Blue, DAPI-stained nuclei. (**B**,**C**) Quail-chick chimeras with a unilateral isotopic and isochronic substitution of a rhombomere 8 neural fold at the level of somites 1–3 at the 5-somite stage. By embryonic day 8.5 (Hamburger-Hamilton stage 33), these demonstrate permanent immunoreactivity for the QCPN antibody, brown, in many of the NCC within the (**B**) proximal pulmonary trunk and (**C**) aortic valve leaflets. Hematoxylin counterstain. (**D**–**F**) *Wnt1-Cre*-mediated recombination induces b-galactosidase activity in the presence of Xgal substrate in NCC of the adult murine heart on postnatal day 50. (**D**) Ventral view. (**E**) After removing the atria, one observes labeled great artery smooth muscle as well as at the base of the coronary arteries, the large branches of autonomic nerves and numerous melanocytes lining the right interatrial septum around the *foramen ovale*, all of NCC origin. Melanocytes are also frequently seen along valve leaflets, *chordae tendinae*, on and within the interventricular septum and within the proximal great arteries [132–136]. Anterior view, ventral to top. (**F**) A slightly more ventral view of the same heart shows labeled cells within the *tunica media* of the murine ascending aorta and pulmonary trunk base, as well as in leaflets and mesenchyme of the pulmonary valve. All photos courtesy of the authors. (**B**) and (**C**) have been previously published as Figure 5K,L in Reference [52]. Asterisks: nucleated primitive erythroblasts. Abbreviations: AO, ascending aorta; CA, coronary artery; CJ, cardiac jelly; LA, left atrium; LV, left ventricle; PA2, pharyngeal arch 2; PT, pulmonary (arterial) trunk; RA, right atrium; RV, right ventricle; Xgal, 5-bromo-4-chloro-3-indolyl-β-D-galactopyranoside.

Author Contributions: All authors contributed substantially to discussions of the article content, writing the manuscript, and review or editing of the manuscript before submission. All authors have read and agreed to the published version of the manuscript.

Funding: Funded by ERA-CVD-2019 and ANR-JCJC 2020 to S.S., ANR-Heartbox-2018 to S.Z., and AFM-PS3-MoThARD to H.C.E. and S.Z.

Institutional Review Board Statement: Not applicable.

Informed Consent Statement: Not applicable.

Data Availability Statement: Not applicable.

Conflicts of Interest: The authors declare no conflict of interest.

References

1. Hoffman, J. The global burden of congenital heart disease. *Cardiovasc. J. Afr.* **2013**, *24*, 141–145. [CrossRef]
2. Hoffman, J.I.; Kaplan, S. The incidence of congenital heart disease. *J. Am. Coll. Cardiol.* **2002**, *39*, 1890–1900. [CrossRef]
3. Anderson, R.H.; Tretter, J.T.; Spicer, D.E.; Mori, S. The Fate of the Outflow Tract Septal Complex in Relation to the Classification of Ventricular Septal Defects. *J. Cardiovasc. Dev. Dis.* **2019**, *6*, 9. [CrossRef]
4. Bajolle, F.; Zaffran, S.; Kelly, R.G.; Hadchouel, J.; Bonnet, D.; Brown, N.A.; Buckingham, M.E. Rotation of the myocardial wall of the outflow tract is implicated in the normal positioning of the great arteries. *Circ. Res.* **2006**, *98*, 421–428. [CrossRef]
5. Saga, Y.; Miyagawa-Tomita, S.; Takagi, A.; Kitajima, S.; Miyazaki, J.; Inoue, T. MesP1 is expressed in the heart precursor cells and required for the formation of a single heart tube. *Development* **1999**, *126*, 3437–3447. [PubMed]
6. Hatada, Y.; Stern, C.D. A fate map of the epiblast of the early chick embryo. *Development* **1994**, *120*, 2879–2889. [PubMed]
7. Stalsberg, H.; DeHaan, R.L. The precardiac areas and formation of the tubular heart in the chick embryo. *Dev. Biol.* **1969**, *19*, 128–159. [CrossRef]
8. Christoffels, V.; Jensen, B. Cardiac Morphogenesis: Specification of the Four-Chambered Heart. *Cold Spring Harb. Perspect. Biol.* **2020**, *12*, a037143. [CrossRef]
9. Kelly, G.R.; Buckingham, M.E.; Moorman, A.F. Heart fields and cardiac morphogenesis. *Cold Spring Harb. Perspect. Med.* **2014**, *4*, a015750. [CrossRef] [PubMed]
10. Zaffran, S.; Kelly, R.G. New developments in the second heart field. *Differentiation* **2012**, *84*, 17–24. [CrossRef]
11. Prall, O.W.; Menon, M.K.; Solloway, M.J.; Watanabe, Y.; Zaffran, S.; Bajolle, F.; Biben, C.; McBride, J.J.; Robertson, B.R.; Chaulet, H.; et al. An Nkx2-5/Bmp2/Smad1 negative feedback loop controls heart progenitor specification and proliferation. *Cell* **2007**, *128*, 947–959. [CrossRef]
12. Zhang, L.; Nomura-Kitabayashi, A.; Sultana, N.; Cai, W.; Cai, X.; Moon, A.M.; Cai, C.L. Mesodermal Nkx2.5 is necessary and sufficient for early second heart field development. *Dev. Biol.* **2014**, *390*, 68–79. [CrossRef]
13. Cai, C.L.; Liang, X.; Shi, Y.; Chu, P.H.; Pfaff, S.L.; Chen, J.; Evans, S. Isl1 identifies a cardiac progenitor population that proliferates prior to differentiation and contributes a majority of cells to the heart. *Dev. Cell* **2003**, *5*, 877–889. [CrossRef]
14. Bertrand, N.; Roux, M.; Ryckebüsch, L.; Niederreither, K.; Dollé, P.; Moon, A.; Capecchi, M.; Zaffran, S. Hox genes define distinct progenitor sub-domains within the second heart field. *Dev. Biol.* **2011**, *353*, 266–274. [CrossRef] [PubMed]
15. Stefanovic, S.; Laforest, B.; Desvignes, J.P.; Lescroart, F.; Argiro, L.; Maurel-Zaffran, C.; Salgado, D.; Plaindoux, E.; De Bono, C.; Pazur, K.; et al. Hox-dependent coordination of mouse cardiac progenitor cell patterning and differentiation. *Elife* **2020**, *9*, e55124. [CrossRef] [PubMed]
16. Briggs, L.E.; Kakarla, J.; Wessels, A. The pathogenesis of atrial and atrioventricular septal defects with special emphasis on the role of the dorsal mesenchymal protrusion. *Differentiation* **2012**, *84*, 117–130. [CrossRef] [PubMed]
17. De Bono, C.; Thellier, C.; Bertrand, N.; Sturny, R.; Jullian, E.; Cortes, C.; Stefanovic, S.; Zaffran, S.; Théveniau-Ruissy, M.; Kelly, R.G. T-box genes and retinoic acid signaling regulate the segregation of arterial and venous pole progenitor cells in the murine second heart field. *Hum. Mol. Genet.* **2018**, *27*, 3747–3760. [CrossRef] [PubMed]
18. Verzi, M.P.; McCulley, D.J.; De Val, S.; Dodou, E.; Black, B.L. The right ventricle, outflow tract, and ventricular septum comprise a restricted expression domain within the secondary/anterior heart field. *Dev. Biol.* **2005**, *287*, 134–145. [CrossRef]
19. Dodou, E.; Verzi, M.P.; Anderson, J.P.; Xu, S.M.; Black, B.L. Mef2c is a direct transcriptional target of ISL1 and GATA factors in the anterior heart field during mouse embryonic development. *Development* **2004**, *131*, 3931–3942. [CrossRef]
20. Goddeeris, M.M.; Schwartz, R.; Klingensmith, J.; Meyers, E.N. Independent requirements for Hedgehog signaling by both the anterior heart field and neural crest cells for outflow tract development. *Development* **2007**, *134*, 1593–1604. [CrossRef]
21. Kelly, G.R.; Brown, N.A.; Buckingham, M.E. The arterial pole of the mouse heart forms from Fgf10-expressing cells in pharyngeal mesoderm. *Dev. Cell* **2001**, *1*, 435–440. [CrossRef]
22. Golzio, C.; Havis, E.; Daubas, P.; Nuel, G.; Babarit, C.; Munnich, A.; Vekemans, M.; Zaffran, S.; Lyonnet, S.; Etchevers, H.C. ISL1 directly regulates FGF10 transcription during human cardiac outflow formation. *PLoS ONE* **2012**, *7*, e30677. [CrossRef]
23. Stefanovic, S.; Zaffran, S. Mechanisms of retinoic acid signaling during cardiogenesis. *Mech. Dev.* **2017**, *143*, 9–19. [CrossRef]

24. Hochgreb, T.; Linhares, V.L.; Menezes, D.C.; Sampaio, A.C.; Yan, C.Y.; Cardoso, W.V.; Rosenthal, N.; Xavier-Neto, J. A caudorostral wave of RALDH2 conveys anteroposterior information to the cardiac field. *Development* **2003**, *130*, 5363–5374. [CrossRef] [PubMed]
25. Diman, N.Y.; Remacle, S.; Bertrand, N.; Picard, J.J.; Zaffran, S.; Rezsohazy, R. A retinoic acid responsive Hoxa3 transgene expressed in embryonic pharyngeal endoderm, cardiac neural crest and a subdomain of the second heart field. *PLoS ONE* **2011**, *6*, e27624. [CrossRef] [PubMed]
26. Buenrostro, J.D.; Wu, B.; Litzenburger, U.M.; Ruff, D.; Gonzales, M.L.; Snyder, M.P.; Chang, H.Y.; Greenleaf, W.J. Single-cell chromatin accessibility reveals principles of regulatory variation. *Nature* **2015**, *523*, 486–490. [CrossRef] [PubMed]
27. Moorman, F.A.; Christoffels, V.M. Cardiac chamber formation: Development, genes, and evolution. *Physiol. Rev.* **2003**, *83*, 1223–1267. [CrossRef]
28. Eisenberg, M.L.; Markwald, R.R. Molecular regulation of atrioventricular valvuloseptal morphogenesis. *Circ. Res.* **1995**, *77*, 1–6. [CrossRef]
29. MacGrogan, D.; Luxán, G.; Driessen-Mol, A.; Bouten, C.; Baaijens, F.; de la Pompa, J.L. How to make a heart valve: From embryonic development to bioengineering of living valve substitutes. *Cold Spring Harb. Perspect Med.* **2014**, *4*, a013912. [CrossRef]
30. Poelmann, R.E.; Gittenberger-de Groot, A.C. Hemodynamics in Cardiac Development. *J. Cardiovasc. Dev. Dis.* **2018**, *5*, 54. [CrossRef]
31. McCulley, D.J.; Kang, J.O.; Martin, J.F.; Black, B.L. BMP4 is required in the anterior heart field and its derivatives for endocardial cushion remodeling, outflow tract septation, and semilunar valve development. *Dev. Dyn.* **2008**, *237*, 3200–3209. [CrossRef] [PubMed]
32. Ma, L.; Lu, M.F.; Schwartz, R.J.; Martin, J.F. Bmp2 is essential for cardiac cushion epithelial-mesenchymal transition and myocardial patterning. *Development* **2005**, *132*, 5601–5611. [CrossRef] [PubMed]
33. Habets, P.E.; Moorman, A.F.; Clout, D.E.; van Roon, M.A.; Lingbeek, M.; van Lohuizen, M.; Campione, M.; Christoffels, V.M. Cooperative action of Tbx2 and Nkx2.5 inhibits ANF expression in the atrioventricular canal: Implications for cardiac chamber formation. *Genes Dev.* **2002**, *16*, 1234–1246. [CrossRef]
34. Hoogaars, W.M.; Tessari, A.; Moorman, A.F.; de Boer, P.A.; Hagoort, J.; Soufan, A.T.; Campione, M.; Christof-fels, V.M. The transcriptional repressor Tbx3 delineates the developing central conduction system of the heart. *Cardiovasc. Res.* **2004**, *62*, 489–499. [CrossRef]
35. Yamada, M.; Revelli, J.P.; Eichele, G.; Barron, M.; Schwartz, R.J. Expression of chick Tbx-2, Tbx-3, and Tbx-5 genes during early heart development: Evidence for BMP2 induction of Tbx2. *Dev. Biol.* **2000**, *228*, 95–105. [CrossRef]
36. Rutenberg, J.B.; Fischer, A.; Jia, H.; Gessler, M.; Zhong, T.P.; Mercola, M. Developmental patterning of the cardiac atrioventricular canal by Notch and Hairy-related transcription factors. *Development* **2006**, *133*, 4381–4390. [CrossRef]
37. Papoutsi, T.; Luna-Zurita, L.; Prados, B.; Zaffran, S.; de la Pompa, J.L. Bmp2 and Notch cooperate to pattern the embryonic endocardium. *Development* **2018**, *145*. [CrossRef]
38. De Lange, F.J.; Moorman, A.F.; Anderson, R.H.; Männer, J.; Soufan, A.T.; de Gier-de Vries, C.; Schneider, M.D.; Webb, S.; van den Hoff, M.J.; Christoffels, V.M. Lineage and morphogenetic analysis of the cardiac valves. *Circ. Res.* **2004**, *95*, 645–654. [CrossRef] [PubMed]
39. Jiang, X.; Rowitch, D.H.; Soriano, P.; McMahon, A.P.; Sucov, H.M. Fate of the mammalian cardiac neural crest. *Development* **2000**, *127*, 1607–1616.
40. Odelin, G.; Faure, E.; Coulpier, F.; Di Bonito, M.; Bajolle, F.; Studer, M.; Avierinos, J.F.; Charnay, P.; Topilko, P.; Zaf-fran, S. Krox20 defines a subpopulation of cardiac neural crest cells contributing to arterial valves and bicuspid aortic valve. *Development* **2018**, *145*. [CrossRef] [PubMed]
41. Nomura-Kitabayashi, A.; Phoon, C.K.; Kishigami, S.; Rosenthal, J.; Yamauchi, Y.; Abe, K.; Yamamura, K.; Samtani, R.; Lo, C.W.; Mishina, Y. Outflow tract cushions perform a critical valve-like function in the early embryonic heart requiring BMPRIA-mediated signaling in cardiac neural crest. *Am. J. Physiol. Heart Circ. Physiol.* **2009**, *297*, H1617–H1628. [CrossRef]
42. Eley, L.; Alqahtani, A.M.; MacGrogan, D.; Richardson, R.V.; Murphy, L.; Salguero-Jimenez, A.; Sintes Rodriguez San Pedro, M.; Tiurma, S.; McCutcheon, L.; Gilmore, A.; et al. A novel source of arterial valve cells linked to bicuspid aortic valve without raphe in mice. *Elife* **2018**, *7*, e34110. [CrossRef] [PubMed]
43. Mifflin, J.J.; Dupuis, L.; Alcala, N.E.; Russell, L.G.; Kern, C.B. Intercalated cushion cells within the cardiac outflow tract are derived from the myocardial troponin T type 2 (Tnnt2) Cre lineage. *Dev. Dyn.* **2018**, *247*, 1005–1017. [CrossRef] [PubMed]
44. Liu, X.; Chen, W.; Li, W.; Li, Y.; Priest, J.R.; Zhou, B.; Wang, J.; Zhou, Z. Single-Cell RNA-Seq of the Developing Cardiac Outflow Tract Reveals Convergent Development of the Vascular Smooth Muscle Cells. *Cell Rep.* **2019**, *28*, 1346–1361. [CrossRef] [PubMed]
45. Waldo, K.L.; Hutson, M.R.; Ward, C.C.; Zdanowicz, M.; Stadt, H.A.; Kumiski, D.; Abu-Issa, R.; Kirby, M.L. Secondary heart field contributes myocardium and smooth muscle to the arterial pole of the developing heart. *Dev. Biol.* **2005**, *281*, 78–90. [CrossRef] [PubMed]
46. Etchevers, C.H.; Dupin, E.; le Douarin, N.M. The diverse neural crest: From embryology to human pathology. *Development* **2019**, *146*. [CrossRef] [PubMed]
47. Le Lièvre, C.; Le Douarin, N. Role of mesectoderm in the genesis of aortic arches of the bird embryo. *Comptes Rendus Acad. Hebd. Seances Acad. Sci. D* **1973**, *276*, 383–386.

48. Hutchins, E.J.; Kunttas, E.; Piacentino, M.L.; Howard, A.G.A.t.; Bronner, M.E.; Uribe, R.A. Migration and diversification of the vagal neural crest. *Dev. Biol.* **2018**, *444* (Suppl. S1), S98–S109. [CrossRef] [PubMed]
49. Kuratani, C.S.; Kirby, M.L. Initial migration and distribution of the cardiac neural crest in the avian embryo: An introduction to the concept of the circumpharyngeal crest. *Am. J. Anat.* **1991**, *191*, 215–227. [CrossRef]
50. Boot, M.J.; Gittenberger-De Groot, A.C.; Van Iperen, L.; Hierck, B.P.; Poelmann, R.E. Spatiotemporally separated cardiac neural crest subpopulations that target the outflow tract septum and pharyngeal arch arteries. *Anat. Rec. A Discov. Mol. Cell Evol. Biol.* **2003**, *275*, 1009–1018. [CrossRef] [PubMed]
51. Bergwerff, M.; Verberne, M.E.; DeRuiter, M.C.; Poelmann, R.E.; Gittenberger-de Groot, A.C. Neural crest cell contribution to the developing circulatory system: Implications for vascular morphology? *Circ. Res.* **1998**, *82*, 221–231. [CrossRef]
52. Etchevers, H.C.; Vincent, C.; Le Douarin, N.M.; Couly, G.F. The cephalic neural crest provides pericytes and smooth muscle cells to all blood vessels of the face and forebrain. *Development* **2001**, *128*, 1059–1068.
53. Teillet, A.M.; Kalcheim, C.; le Douarin, N.M. Formation of the dorsal root ganglia in the avian embryo: Segmental origin and migratory behavior of neural crest progenitor cells. *Dev. Biol.* **1987**, *120*, 329–347. [CrossRef]
54. Le Lièvre, C.S.; Le Douarin, N.M. Mesenchymal derivatives of the neural crest: Analysis of chimaeric quail and chick embryos. *J. Embryol. Exp. Morphol.* **1975**, *34*, 125–154. [PubMed]
55. Poelmann, R.E.; Gittenberger-de Groot, A.C. A subpopulation of apoptosis-prone cardiac neural crest cells targets to the venous pole: Multiple functions in heart development? *Dev. Biol.* **1999**, *207*, 271–286. [CrossRef]
56. Kirby, M.L.; Stewart, D.E. Neural crest origin of cardiac ganglion cells in the chick embryo: Identification and extirpation. *Dev. Biol.* **1983**, *97*, 433–443. [CrossRef]
57. Verberne, M.E.; Gittenberger-de Groot, A.C.; Poelmann, R.E. Lineage and development of the parasympathetic nervous system of the embryonic chick heart. *Anat. Embryol.* **1998**, *198*, 171–184. [CrossRef]
58. Arima, Y.; Miyagawa-Tomita, S.; Maeda, K.; Asai, R.; Seya, D.; Minoux, M.; Rijli, F.M.; Nishiyama, K.; Kim, K.S.; Uchijima, Y.; et al. Preotic neural crest cells contribute to coronary artery smooth muscle involving endothelin signalling. *Nat. Commun.* **2012**, *3*, 1267. [CrossRef]
59. Jain, R.; Engleka, K.A.; Rentschler, S.L.; Manderfield, L.J.; Li, L.; Yuan, L.; Epstein, J.A. Cardiac neural crest orchestrates remodeling and functional maturation of mouse semilunar valves. *J. Clin. Invest.* **2011**, *121*, 422–430. [CrossRef]
60. Phillips, H.M.; Mahendran, P.; Singh, E.; Anderson, R.H.; Chaudhry, B.; Henderson, D.J. Neural crest cells are required for correct positioning of the developing outflow cushions and pattern the arterial valve leaflets. *Cardiovasc. Res.* **2013**, *99*, 452–460. [CrossRef]
61. Nakamura, T.; Colbert, M.C.; Robbins, J. Neural crest cells retain multipotential characteristics in the developing valves and label the cardiac conduction system. *Circ. Res.* **2006**, *98*, 1547–1554. [CrossRef]
62. El Robrini, N.; Etchevers, H.C.; Ryckebüsch, L.; Faure, E.; Eudes, N.; Niederreither, K.; Zaffran, S.; Bertrand, N. Cardiac outflow morphogenesis depends on effects of retinoic acid signaling on multiple cell lineages. *Dev. Dyn.* **2016**, *245*, 388–401. [CrossRef] [PubMed]
63. Hatzistergos, K.E.; Takeuchi, L.M.; Saur, D.; Seidler, B.; Dymecki, S.M.; Mai, J.J.; White, I.A.; Balkan, W.; Kanashiro-Takeuchi, R.M.; Schally, A.V.; et al. cKit+ cardiac progenitors of neural crest origin. *Proc. Natl. Acad. Sci. USA* **2015**, *112*, 13051–13056. [CrossRef] [PubMed]
64. Soldatov, R.; Kaucka, M.; Kastriti, M.E.; Petersen, J.; Chontorotzea, T.; Englmaier, L.; Akkuratova, N.; Yang, Y.; Häring, M.; Dyachuk, V.; et al. Spatiotemporal structure of cell fate decisions in murine neural crest. *Science* **2019**, *364*. [CrossRef]
65. Tang, W.; Martik, M.L.; Li, Y.; Bronner, M.E. Cardiac neural crest contributes to cardiomyocytes in amniotes and heart regeneration in zebrafish. *Elife* **2019**, *8*, e47929. [CrossRef] [PubMed]
66. Sato, M.; Yost, H.J. Cardiac neural crest contributes to cardiomyogenesis in zebrafish. *Dev. Biol.* **2003**, *257*, 127–139. [CrossRef]
67. Li, Y.X.; Zdanowicz, M.; Young, L.; Kumiski, D.; Leatherbury, L.; Kirby, M.L. Cardiac neural crest in zebrafish embryos contributes to myocardial cell lineage and early heart function. *Dev. Dyn.* **2003**, *226*, 540–550. [CrossRef]
68. Lee, Y.H.; Saint-Jeannet, J.P. Cardiac neural crest is dispensable for outflow tract septation in Xenopus. *Development* **2011**, *138*, 2025–2034. [CrossRef]
69. Gandhi, S.; Ezin, M.; Bronner, M.E. Reprogramming Axial Level Identity to Rescue Neural-Crest-Related Congenital Heart Defects. *Dev. Cell.* **2020**, *53*, 300–315. [CrossRef]
70. Poelmann, R.E.; Gittenberger-de Groot, A.C.; Biermans, M.W.M.; Dolfing, A.I.; Jagessar, A.; van Hattum, S.; Hoogenboom, A.; Wisse, L.J.; Vicente-Steijn, R.; de Bakker, M.A.G.; et al. Outflow tract septation and the aortic arch system in reptiles: Lessons for understanding the mammalian heart. *Evodevo* **2017**, *8*, 9. [CrossRef]
71. Bockman, D.E.; Kirby, M.L. Dependence of thymus development on derivatives of the neural crest. *Science* **1984**, *223*, 498–500. [CrossRef]
72. Zaffran, S.; Odelin, G.; Stefanovic, S.; Lescroart, F.; Etchevers, H.C. Ectopic expression of Hoxb1 induces cardiac and craniofacial malformations. *Genesis* **2018**, *56*, e23221. [CrossRef]
73. Roux, M.; Laforest, B.; Eudes, N.; Bertrand, N.; Stefanovic, S.; Zaffran, S. Hoxa1 and Hoxb1 are required for pharyngeal arch artery development. *Mech. Dev.* **2017**, *143*, 1–8. [CrossRef]
74. Frank, D.U.; Fotheringham, L.K.; Brewer, J.A.; Muglia, L.J.; Tristani-Firouzi, M.; Capecchi, M.R.; Moon, A.M. An Fgf8 mouse mutant phenocopies human 22q11 deletion syndrome. *Development* **2002**, *129*, 4591–4603. [PubMed]

75. Bajolle, F.; Zaffran, S.; Meilhac, S.M.; Dandonneau, M.; Chang, T.; Kelly, R.G.; Buckingham, M.E. Myocardium at the base of the aorta and pulmonary trunk is prefigured in the outflow tract of the heart and in subdomains of the second heart field. *Dev. Biol.* **2008**, *313*, 25–34. [CrossRef]
76. Scherptong, R.W.; Jongbloed, M.R.; Wisse, L.J.; Vicente-Steijn, R.; Bartelings, M.M.; Poelmann, R.E.; Schalij, M.J.; Gittenberger-De Groot, A.C. Morphogenesis of outflow tract rotation during cardiac development: The pulmonary push concept. *Dev. Dyn.* **2012**, *241*, 1413–1422. [CrossRef] [PubMed]
77. Baardman, M.E.; Zwier, M.V.; Wisse, L.J.; Gittenberger-de Groot, A.C.; Kerstjens-Frederikse, W.S.; Hofstra, R.M.; Jurdzinski, A.; Hierck, B.P.; Jongbloed, M.R.; Berger, R.M.; et al. Common arterial trunk and ventricular non-compaction in Lrp2 knockout mice indicate a crucial role of LRP2 in cardiac development. *Dis. Models Mech.* **2016**, *9*, 413–425. [CrossRef] [PubMed]
78. Christ, A.; Marczenke, M.; Willnow, T.E. LRP2 controls sonic hedgehog-dependent differentiation of cardiac progenitor cells during outflow tract formation. *Hum. Mol. Genet.* **2020**, *29*, 3183–3196. [CrossRef] [PubMed]
79. Theis, J.L.; Vogler, G.; Missinato, M.A.; Li, X.; Nielsen, T.; Zeng, X.I.; Martinez-Fernandez, A.; Walls, S.M.; Kervadec, A.; Kezos, J.N.; et al. Patient-specific genomics and cross-species functional analysis implicate LRP2 in hypoplastic left heart syndrome. *Elife* **2020**, *9*, e59554. [CrossRef]
80. Sakabe, M.; Kokubo, H.; Nakajima, Y.; Saga, Y. Ectopic retinoic acid signaling affects outflow tract cushion development through suppression of the myocardial Tbx2-Tgfβ2 pathway. *Development* **2012**, *139*, 385–395. [CrossRef]
81. Yasui, H.; Nakazawa, M.; Morishima, M.; Miyagawa-Tomita, S.; Momma, K. Morphological observations on the pathogenetic process of transposition of the great arteries induced by retinoic acid in mice. *Circulation* **1995**, *91*, 2478–2486. [CrossRef]
82. Golzio, C.; Martinovic-Bouriel, J.; Thomas, S.; Mougou-Zrelli, S.; Grattagliano-Bessieres, B.; Bonniere, M.; Delahaye, S.; Munnich, A.; Encha-Razavi, F.; Lyonnet, S.; et al. Matthew-Wood syndrome is caused by truncating mutations in the retinol-binding protein receptor gene STRA6. *Am. J. Hum. Genet.* **2007**, *80*, 1179–1187. [CrossRef]
83. Pasutto, F.; Sticht, H.; Hammersen, G.; Gillessen-Kaesbach, G.; Fitzpatrick, D.R.; Nürnberg, G.; Brasch, F.; Schirmer-Zimmermann, H.; Tolmie, J.L.; Chitayat, D.; et al. Mutations in STRA6 cause a broad spectrum of malformations including anophthalmia, congenital heart defects, diaphragmatic hernia, alveolar capillary dysplasia, lung hypoplasia, and mental retardation. *Am. J. Hum. Genet.* **2007**, *80*, 550–560. [CrossRef]
84. Chassaing, N.; Golzio, C.; Odent, S.; Lequeux, L.; Vigouroux, A.; Martinovic-Bouriel, J.; Tiziano, F.D.; Masini, L.; Piro, F.; Maragliano, G.; et al. Phenotypic spectrum of STRA6 mutations: From Matthew-Wood syndrome to non-lethal anophthalmia. *Hum. Mutat.* **2009**, *30*, E673–E681. [CrossRef]
85. Kawaguchi, R.; Yu, J.; Honda, J.; Hu, J.; Whitelegge, J.; Ping, P.; Wiita, P.; Bok, D.; Sun, H. A membrane receptor for retinol binding protein mediates cellular uptake of vitamin A. *Science* **2007**, *315*, 820–825. [CrossRef] [PubMed]
86. Lammer, E.J.; Chen, D.T.; Hoar, R.M.; Agnish, N.D.; Benke, P.J.; Braun, J.T.; Curry, C.J.; Fernhoff, P.M.; Grix, A.W., Jr.; Lott, I.T.; et al. Retinoic acid embryopathy. *N. Engl. J. Med.* **1985**, *313*, 837–841. [CrossRef] [PubMed]
87. Kastner, P.; Grondona, J.M.; Mark, M.; Gansmuller, A.; LeMeur, M.; Decimo, D.; Vonesch, J.L.; Dollé, P.; Chambon, P. Genetic analysis of RXR alpha developmental function: Convergence of RXR and RAR signaling pathways in heart and eye morphogenesis. *Cell* **1994**, *78*, 987–1003. [CrossRef]
88. Kastner, P.; Mark, M.; Ghyselinck, N.; Krezel, W.; Dupé, V.; Grondona, J.M.; Chambon, P. Genetic evidence that the retinoid signal is transduced by heterodimeric RXR/RAR functional units during mouse development. *Development* **1997**, *124*, 313–326. [PubMed]
89. Lee, R.Y.; Luo, J.; Evans, R.M.; Giguere, V.; Sucov, H.M. Compartment-selective sensitivity of cardiovascular morphogenesis to combinations of retinoic acid receptor gene mutations. *Circ. Res.* **1997**, *80*, 757–764. [CrossRef] [PubMed]
90. Mendelsohn, C.; Lohnes, D.; Décimo, D.; Lufkin, T.; LeMeur, M.; Chambon, P.; Mark, M. Function of the retinoic acid receptors (RARs) during development (II). Multiple abnormalities at various stages of organogenesis in RAR double mutants. *Development* **1994**, *120*, 2749–2771. [PubMed]
91. Li, P.; Pashmforoush, M.; Sucov, H.M. Retinoic acid regulates differentiation of the secondary heart field and TGFbeta-mediated outflow tract septation. *Dev. Cell* **2010**, *18*, 480–485. [CrossRef]
92. Pan, J.; Baker, K.M. Retinoic acid and the heart. *Vitam. Horm.* **2007**, *75*, 257–283.
93. Rhinn, M.; Dollé, P. Retinoic acid signalling during development. *Development* **2012**, *139*, 843–858. [CrossRef]
94. Ryckebusch, L.; Wang, Z.; Bertrand, N.; Lin, S.-C.; Chi, X.; Schwartz, R.; Zaffran, S.; Niederreither, K. Retinoic acid deficiency alters second heart field formation. *Proc. Natl. Acad. Sci. USA* **2008**, *105*, 2913–2918. [CrossRef]
95. Sirbu, O.I.; Zhao, X.; Duester, G. Retinoic acid controls heart anteroposterior patterning by down-regulating Isl1 through the Fgf8 pathway. *Dev. Dyn.* **2008**, *237*, 1627–1635. [CrossRef]
96. Duong, T.B.; Holowiecki, A.; Waxman, J.S. Retinoic acid signaling restricts the size of the first heart field within the anterior lateral plate mesoderm. *Dev. Biol.* **2021**, *473*, 119–129. [CrossRef] [PubMed]
97. Roberts, C.; Ivins, S.M.; James, C.T.; Scambler, P.J. Retinoic acid down-regulates Tbx1 expression in vivo and in vitro. *Dev. Dyn.* **2005**, *232*, 928–938. [CrossRef] [PubMed]
98. Blentic, A.; Gale, E.; Maden, M. Retinoic acid signalling centres in the avian embryo identified by sites of expression of synthesising and catabolising enzymes. *Dev. Dyn.* **2003**, *227*, 114–127. [CrossRef]
99. Guris, D.L.; Duester, G.; Papaioannou, V.E.; Imamoto, A. Dose-dependent interaction of Tbx1 and Crkl and locally aberrant RA signaling in a model of del22q11 syndrome. *Dev. Cell.* **2006**, *10*, 81–92. [CrossRef]

100. Reijntjes, S.; Gale, E.; Maden, M. Generating gradients of retinoic acid in the chick embryo: Cyp26C1 expression and a comparative analysis of the Cyp26 enzymes. *Dev. Dyn.* **2004**, *230*, 509–517. [CrossRef] [PubMed]
101. Jiang, X.; Choudhary, B.; Merki, E.; Chien, K.R.; Maxson, R.E.; Sucov, H.M. Normal fate and altered function of the cardiac neural crest cell lineage in retinoic acid receptor mutant embryos. *Mech. Dev.* **2002**, *117*, 115–122. [CrossRef]
102. Li, J.; Molkentin, J.D.; Colbert, M.C. Retinoic acid inhibits cardiac neural crest migration by blocking c-Jun N-terminal kinase activation. *Dev. Biol.* **2001**, *232*, 351–361. [CrossRef] [PubMed]
103. Eferl, R.; Sibilia, M.; Hilberg, F.; Fuchsbichler, A.; Kufferath, I.; Guertl, B.; Zenz, R.; Wagner, E.F.; Zatloukal, K. Functions of c-Jun in liver and heart development. *J. Cell Biol.* **1999**, *145*, 1049–1061. [CrossRef]
104. Zhang, T.; Liu, J.; Zhang, J.; Thekkethottiyil, E.B.; Macatee, T.L.; Ismat, F.A.; Wang, F.; Stoller, J.Z. Jun is required in Isl1-expressing progenitor cells for cardiovascular development. *PLoS ONE* **2013**, *8*, e57032. [CrossRef]
105. Jerome, L.A.; Papaioannou, V.E. DiGeorge syndrome phenotype in mice mutant for the T-box gene, Tbx1. *Nat. Genet.* **2001**, *27*, 286–291. [CrossRef] [PubMed]
106. Ilagan, R.; Abu-Issa, R.; Brown, D.; Yang, Y.P.; Jiao, K.; Schwartz, R.J.; Klingensmith, J.; Meyers, E.N. Fgf8 is required for anterior heart field development. *Development* **2006**, *133*, 2435–2445. [CrossRef]
107. Vermot, J.; Niederreither, K.; Garnier, J.M.; Chambon, P.; Dollé, P. Decreased embryonic retinoic acid synthesis results in a DiGeorge syndrome phenotype in newborn mice. *Proc. Natl. Acad. Sci. USA* **2003**, *100*, 1763–1768. [CrossRef]
108. Roberts, C.; Ivins, S.; Cook, A.C.; Baldini, A.; Scambler, P.J. Cyp26 genes a1, b1 and c1 are down-regulated in Tbx1 null mice and inhibition of Cyp26 enzyme function produces a phenocopy of DiGeorge Syndrome in the chick. *Hum. Mol. Genet.* **2006**, *15*, 3394–3410. [CrossRef]
109. Ryckebüsch, L.; Bertrand, N.; Mesbah, K.; Bajolle, F.; Niederreither, K.; Kelly, R.G.; Zaffran, S. Decreased levels of embryonic retinoic acid synthesis accelerate recovery from arterial growth delay in a mouse model of DiGeorge syndrome. *Circ. Res.* **2010**, *106*, 686–694. [CrossRef]
110. Deschamps, J.; van Nes, J. Developmental regulation of the Hox genes during axial morphogenesis in the mouse. *Development* **2005**, *132*, 2931–2942. [CrossRef]
111. Domínguez, J.N.; Meilhac, S.M.; Bland, Y.S.; Buckingham, M.E.; Brown, N.A. Asymmetric fate of the posterior part of the second heart field results in unexpected left/right contributions to both poles of the heart. *Circ. Res.* **2012**, *111*, 1323–1335. [CrossRef]
112. Lescroart, F.; Mohun, T.; Meilhac, S.M.; Bennett, M.; Buckingham, M. Lineage tree for the venous pole of the heart: Clonal analysis clarifies controversial genealogy based on genetic tracing. *Circ. Res.* **2012**, *111*, 1313–1322. [CrossRef] [PubMed]
113. Lescroart, F.; Wang, X.; Lin, X.; Swedlund, B.; Gargouri, S.; Sànchez-Dànes, A.; Moignard, V.; Dubois, C.; Paulissen, C.; Kinston, S.; et al. Defining the earliest step of cardiovascular lineage segregation by single-cell RNA-seq. *Science* **2018**, *359*, 1177–1181. [CrossRef] [PubMed]
114. Rana, M.S.; Théveniau-Ruissy, M.; De Bono, C.; Mesbah, K.; Francou, A.; Rammah, M.; Domínguez, J.N.; Roux, M.; Laforest, B.; Anderson, R.H.; et al. Tbx1 coordinates addition of posterior second heart field progenitor cells to the arterial and venous poles of the heart. *Circ. Res.* **2014**, *115*, 790–799. [CrossRef] [PubMed]
115. Roux, M.; Laforest, B.; Capecchi, M.; Bertrand, N.; Zaffran, S. Hoxb1 regulates proliferation and differentiation of second heart field progenitors in pharyngeal mesoderm and genetically interacts with Hoxa1 during cardiac outflow tract development. *Dev. Biol.* **2015**, *406*, 247–258. [CrossRef]
116. Wendling, O.; Dennefeld, C.; Chambon, P.; Mark, M. Retinoid signaling is essential for patterning the endoderm of the third and fourth pharyngeal arches. *Development* **2000**, *127*, 1553–1562.
117. Couly, G.; Creuzet, S.; Bennaceur, S.; Vincent, C.; Le Douarin, N.M. Interactions between Hox-negative cephalic neural crest cells and the foregut endoderm in patterning the facial skeleton in the vertebrate head. *Development* **2002**, *129*, 1061–1073.
118. Chisaka, O.; Capecchi, M.R. Regionally restricted developmental defects resulting from targeted disruption of the mouse homeobox gene hox-1.5. *Nature* **1991**, *350*, 473–479. [CrossRef]
119. Kirby, M.L. Plasticity and predetermination of mesencephalic and trunk neural crest transplanted into the region of the cardiac neural crest. *Dev. Biol.* **1989**, *134*, 402–412. [CrossRef]
120. Wamstad, J.A.; Alexander, J.M.; Truty, R.M.; Shrikumar, A.; Li, F.; Eilertson, K.E.; Ding, H.; Wylie, J.N.; Pico, A.R.; Capra, J.A.; et al. Dynamic and coordinated epigenetic regulation of developmental transitions in the cardiac lineage. *Cell* **2012**, *151*, 206–220. [CrossRef]
121. Paige, S.L.; Thomas, S.; Stoick-Cooper, C.L.; Wang, H.; Maves, L.; Sandstrom, R.; Pabon, L.; Reinecke, H.; Pratt, G.; Keller, G.; et al. A temporal chromatin signature in human embryonic stem cells identifies regulators of cardiac development. *Cell* **2012**, *151*, 221–232. [CrossRef]
122. Stankunas, K.; Shang, C.; Twu, K.Y.; Kao, S.C.; Jenkins, N.A.; Copeland, N.G.; Sanyal, M.; Selleri, L.; Cleary, M.L.; Chang, C.P. Pbx/Meis deficiencies demonstrate multigenetic origins of congenital heart disease. *Circ. Res.* **2008**, *103*, 702–709. [CrossRef] [PubMed]
123. Simán, C.M.; Gittenberger-De Groot, A.C.; Wisse, B.; Eriksson, U.J. Malformations in offspring of diabetic rats: Morphometric analysis of neural crest-derived organs and effects of maternal vitamin E treatment. *Teratology* **2000**, *61*, 355–367. [CrossRef]
124. Roest, P.A.; van Iperen, L.; Vis, S.; Wisse, L.J.; Poelmann, R.E.; Steegers-Theunissen, R.P.; Molin, D.G.; Eriksson, U.J.; Gittenberger-De Groot, A.C. Exposure of neural crest cells to elevated glucose leads to congenital heart defects, an effect that can be prevented by N-acetylcysteine. *Birth Defects Res. A Clin. Mol. Teratol.* **2007**, *79*, 231–235. [CrossRef] [PubMed]

125. Roest, P.A.; Molin, D.G.; Schalkwijk, C.G.; van Iperen, L.; Wentzel, P.; Eriksson, U.J.; Gittenberger-de Groot, A.C. Specific local cardiovascular changes of Nepsilon-(carboxymethyl)lysine, vascular endothelial growth factor, and Smad2 in the developing embryos coincide with maternal diabetes-induced congenital heart defects. *Diabetes* **2009**, *58*, 1222–1228. [CrossRef] [PubMed]
126. De Soysa, T.Y.; Ranade, S.S.; Okawa, S.; Ravichandran, S.; Huang, Y.; Salunga, H.T.; Schricker, A.; Del Sol, A.; Gifford, C.A.; Srivastava, D. Single-cell analysis of cardiogenesis reveals basis for organ-level developmental defects. *Nature* **2019**, *572*, 120–124. [CrossRef] [PubMed]
127. Pijuan-Sala, B.; Griffiths, J.A.; Guibentif, C.; Hiscock, T.W.; Jawaid, W.; Calero-Nieto, F.J.; Mulas, C.; Ibarra-Soria, X.; Tyser, R.C.V.; Ho, D.L.L.; et al. A single-cell molecular map of mouse gastrulation and early organogenesis. *Nature* **2019**, *566*, 490–495. [CrossRef]
128. DeLaughter, D.M.; Bick, A.G.; Wakimoto, H.; McKean, D.; Gorham, J.M.; Kathiriya, I.S.; Hinson, J.T.; Homsy, J.; Gray, J.; Pu, W.; et al. Single-Cell Resolution of Temporal Gene Expression during Heart Development. *Dev. Cell* **2016**, *39*, 480–490. [CrossRef]
129. Pinto, A.R.; Ilinykh, A.; Ivey, M.J.; Kuwabara, J.T.; D'Antoni, M.L.; Debuque, R.; Chandran, A.; Wang, L.; Arora, K.; Rosenthal, N.A.; et al. Revisiting Cardiac Cellular Composition. *Circ. Res.* **2016**, *118*, 400–409. [CrossRef]
130. Li, G.; Xu, A.; Sim, S.; Priest, J.R.; Tian, X.; Khan, T.; Quertermous, T.; Zhou, B.; Tsao, P.S.; Quake, S.R.; et al. Transcriptomic Profiling Maps Anatomically Patterned Subpopulations among Single Embryonic Cardiac Cells. *Dev. Cell* **2016**, *39*, 491–507. [CrossRef]
131. Skelly, D.A.; Squiers, G.T.; McLellan, M.A.; Bolisetty, M.T.; Robson, P.; Rosenthal, N.A.; Pinto, A.R. Single-Cell Transcriptional Profiling Reveals Cellular Diversity and Intercommunication in the Mouse Heart. *Cell Rep.* **2018**, *22*, 600–610. [CrossRef]
132. Poelmann, R.E.; Jongbloed, M.R.; Molin, D.G.; Fekkes, M.L.; Wang, Z.; Fishman, G.I.; Doetschman, T.; Azhar, M.; Gittenberger-de Groot, A.C. The neural crest is contiguous with the cardiac conduction system in the mouse embryo: A role in induction? *Anat. Embryol.* **2004**, *208*, 389–393. [CrossRef]
133. Mjaatvedt, C.H.; Kern, C.B.; Norris, R.A.; Fairey, S.; Cave, C.L. Normal distribution of melanocytes in the mouse heart. *Anat. Rec. A Discov. Mol. Cell Evol. Biol.* **2005**, *285*, 748–757. [CrossRef] [PubMed]
134. Balani, K.; Brito, F.C.; Kos, L.; Agarwal, A. Melanocyte pigmentation stiffens murine cardiac tricuspid valve leaflet. *J. R. Soc. Interface* **2009**, *6*, 1097–1102. [CrossRef] [PubMed]
135. Yajima, I.; Colombo, S.; Puig, I.; Champeval, D.; Kumasaka, M.; Belloir, E.; Bonaventure, J.; Mark, M.; Yamamoto, H.; Taketo, M.M.; et al. A subpopulation of smooth muscle cells, derived from melanocyte-competent precursors, prevents patent ductus arteriosus. *PLoS ONE* **2013**, *8*, e53183. [CrossRef] [PubMed]
136. Hulin, A.; Hortells, L.; Gomez-Stallons, M.V.; O'Donnell, A.; Chetal, K.; Adam, M.; Lancellotti, P.; Oury, C.; Potter, S.S.; Salomonis, N.; et al. Maturation of heart valve cell populations during postnatal remodeling. *Development* **2019**, *146*. [CrossRef] [PubMed]

Journal of
Cardiovascular
Development and Disease

MDPI

Article

Early Embryonic Expression of *AP-2α* Is Critical for Cardiovascular Development

Amy-Leigh Johnson [1], Jürgen E. Schneider [2], Timothy J. Mohun [3], Trevor Williams [4], Shoumo Bhattacharya [5], Deborah J. Henderson [1], Helen M. Phillips [1] and Simon D. Bamforth [1,*]

1 Newcastle University Biosciences Institute, Centre for Life, Newcastle NE1 3BZ, UK; bs06alj@gmail.com (A.-L.J.); deborah.henderson@newcastle.ac.uk (D.J.H.); helen.phillips@newcastle.ac.uk (H.M.P.)
2 Biomedical Imaging, University of Leeds, Leeds LS2 9JT, UK; J.E.Schneider@leeds.ac.uk
3 The Francis Crick Institute, London NW1 1AT, UK; tim.mohun@gmail.com
4 Department of Craniofacial Biology, University of Colorado Anshutz Medical Campus, Aurora, CO 80045, USA; trevor.williams@cuanschutz.edu
5 Department of Cardiovascular Medicine, University of Oxford, Wellcome Trust Centre for Human Genetics, Oxford OX3 7BN, UK; sbhattac@well.ox.ac.uk
* Correspondence: simon.bamforth@newcastle.ac.uk; Tel.: +44-191-241-8764

Received: 22 June 2020; Accepted: 22 July 2020; Published: 23 July 2020

Abstract: Congenital cardiovascular malformation is a common birth defect incorporating abnormalities of the outflow tract and aortic arch arteries, and mice deficient in the transcription factor *AP-2α* (*Tcfap2a*) present with complex defects affecting these structures. AP-2α is expressed in the pharyngeal surface ectoderm and neural crest at mid-embryogenesis in the mouse, but the precise tissue compartment in which *AP-2α* is required for cardiovascular development has not been identified. In this study we describe the fully penetrant *AP-2α* deficient cardiovascular phenotype on a C57Bl/6J genetic background and show that this is associated with increased apoptosis in the pharyngeal ectoderm. Neural crest cell migration into the pharyngeal arches was not affected. Cre-expressing transgenic mice were used in conjunction with an *AP-2α* conditional allele to examine the effect of deleting *AP-2α* from the pharyngeal surface ectoderm and the neural crest, either individually or in combination, as well as the second heart field. This, surprisingly, was unable to fully recapitulate the global *AP-2α* deficient cardiovascular phenotype. The outflow tract and arch artery phenotype was, however, recapitulated through early embryonic Cre-mediated recombination. These findings indicate that *AP-2α* has a complex influence on cardiovascular development either being required very early in embryogenesis and/or having a redundant function in many tissue layers.

Keywords: transcription factor AP-2α; cardiovascular development; outflow tract; pharyngeal arch artery; neural crest cell; pharyngeal ectoderm

1. Introduction

Congenital cardiovascular malformation is a major cause of morbidity and death in childhood, with an incidence of 1% in live-born infants [1,2]. A significant proportion of these malformations affect the outflow tract (OFT) and aortic arch arteries, resulting in the mixing of oxygenated and deoxygenated blood and the inefficient systemic delivery of blood to the body. The mammalian OFT develops to separate the common trunk exiting the heart into the aorta and pulmonary trunk, and this process begins at embryonic day (E) 10.5 in the mouse. Cardiac jelly in the OFT is invaded by neural crest cells (NCC), forming the two major OFT cushions which spiral around each other with one positioned septally and caudally, and the other parietally and cranially [3]. By E11.5 the aortopulmonary septum, which is comprised of second heart field (SHF) cells and NCC [4], protrudes

into the OFT cavity and separates the future aorta and pulmonary trunk vessels by fusing with the distal ends of the OFT cushions. The proximal intra-pericardial components of the aorta and the pulmonary trunk are separated from the ventricular outflow tracts by the aortopulmonary septal complex, comprising of neural crest-derived mesenchyme. After E12.5 the major and intercalated OFT cushions remodel to form the tricuspid arterial valves and subsequently the aortic root is transferred to the left ventricle, with the pulmonary trunk remaining as the sole outlet from the right ventricle [3].

The great arteries of the mammalian heart are derived from the pharyngeal arch arteries (PAAs) which form within the pharyngeal arches. These are temporary embryological structures that develop as a series of repeated protuberances on either side of the developing pharynx [5]. The pharyngeal arches consist of paraxial mesoderm- and NCC-derived mesenchyme, enclosed by two epithelial layers—the pharyngeal ectoderm and endoderm. The PAAs form symmetrically and sequentially during early embryogenesis in a cranial to caudal sequence and are rapidly remodelled to form the asymmetric aortic arch arteries seen in the adult [6,7]. The first two pairs of PAAs degenerate early and contribute to the vascular plexus within the forming jaw, and the third PAAs, on both the right and the left, form the common carotid arteries. The fourth PAA persists on the right as the proximal region of the subclavian artery, whilst on the left it contributes to the section of the mature aortic arch between the origins of the left common carotid artery and the left subclavian artery. The right sixth PAA regresses, while the left sixth PAA forms the arterial duct. The development of the PAAs appears to be particularly sensitive to insult during embryonic life, and a variety of teratogens, (e.g., retinoic acid [8,9]), blood flow perturbations [10,11] and gene mutations in mouse models [12] result in defects of the cardiovascular system. Additionally, neural crest ablation in the mouse gives rise to a wide spectrum of OFT and aortic arch patterning defects [13,14]. Moreover, gene interactions within the pharyngeal epithelia are crucial for PAA development [15–17].

Mice lacking the non-DNA binding transcription factor, *Cited2*, die in utero with complex cardiovascular and neural tube malformations [18–21] and CITED2 has been shown to physically interact with, and co-activate, AP-2α (*TFAP2A* in humans) [20]. *AP-2α*, similar to *Cited2*, is necessary for cardiovascular and neural tube development [22–24]. Mutations in *TFAP2A* have been identified in patients with Peters' anomaly [25], which frequently has comorbidities with congenital heart defects [26,27], and cause branchio-oculo-facial syndrome, a disease characterised by a branchial (or cutaneous) defect, abnormalities of the eyes and a distinct facial phenotype [28]. These patients may also present with cardiovascular defects, such as atrial septal defect and Tetralogy of Fallot [29,30]. Additionally, *TFAP2A* has been associated with the negative regulation of the T-box gene, *TBX20*, the expression of which is increased in atrial and ventricular biopsies of patients with Tetralogy of Fallot [31]. Other AP-2 family members have been implicated in congenital heart defects, with mutations in *TFAP2B*, causing Char syndrome, where patients present with persistent arterial duct [32], and decreased TFAP2C levels have been identified in cardiac biopsies of Tetralogy of Fallot patients [31].

In the mouse, AP-2α is expressed in the surface ectoderm and lateral edge of the neural plate at the 3-somite stage (~E8.0) [33], and in the neural crest cells migrating from the hindbrain region at the 5-somite stage [34]. By E9.5, AP-2α is expressed in the neural crest derived mesenchyme of the pharyngeal arches, and the pharyngeal ectoderm, and this expression extends into the mesenchyme and ectoderm of pharyngeal arches four and six by E10.5 [24]. The cardiovascular defects observed in *AP-2α*-null mice affect the OFT (e.g., common arterial trunk) and the aortic arch arteries (e.g., interrupted aortic arch) but these present differently depending on the genetic background used [22–24]. Although the OFT and arch artery defects are characteristic of a NCC phenotype [35], published genetic evidence using *Cre*-lox techniques suggests that NCC deletion of *AP-2α* does not result in cardiovascular malformations although there is perinatal lethality associated with neural tube defects and cleft palate [36]. This raises important questions as to how cardiovascular defects arise that appear to be NCC-related, but which have been shown not to be caused by a cell-autonomous NCC phenotype.

In this study we describe the fully penetrant *AP-2α*-null cardiovascular phenotype on an enriched C57Bl/6J genetic background. We also sought to identify the tissue-specific requirement of *AP-2α*

in cardiovascular development using null and conditional alleles of *AP-2α* and *Cre* recombinase expressing transgenic mice. We demonstrate that an early embryonic deletion of *AP-2α* is required to recapitulate the cardiovascular defects seen in the constitutive knockout.

2. Materials and Methods

2.1. Mice

All mice used in this study have been described elsewhere: *Tcfap2a*$^{lacZ\text{-}KI}$ (referred to as *AP-2α*$^{+/-}$) [24], a floxed allele of *Tcfap2a* (referred to as *AP-2α*^{flox}) [36]; *Foxg1Cre* [37]; *Nkx2-5Cre* [38]; *Wnt1Cre* [39]; *Isl1Cre* [40]; *PGKCre* [41]; *R26R*^{lacZ} [42]; *R26R*^{eyfp} [43]. All mice used in this study were backcrossed using a traditional congenic breeding strategy [44] for sufficient generations onto C57Bl/6J to give an average contribution of >90% C57Bl/6J genomic DNA, and were genotyped by standard PCR using allele-specific primers (sequences available on request). All studies involving animals were performed in accordance with the UK Home Office Animals (Scientific Procedures) Act 1986.

2.2. Breeding

Stud male mice were produced by crossing *AP-2α*$^{+/-}$ with each *Cre* strain. The *AP-2α*^{flox} mice were crossed with *R26R*^{eyfp} to produce double homozygous females. Male and female mice were mated and the detection of a vaginal plug the next morning was considered to be embryonic day (E) 0.5. Pregnant females were culled on the required day and embryos collected. Embryos at E9.5–E11.5 were staged by somite counting.

2.3. Imaging

The magnetic resonance imaging (MRI) of E15.5 embryos was performed on a 9.4T MR system and analysed and segmented as described [45]. Following MRI, selected embryos were processed for standard histology and haematoxylin and eosin staining. Mid-gestation embryos (E10.5 and E11.5) were analysed by High Resolution Episcopic Microscopy (HREM) as described [46,47]. To create the 3-dimensional (3D) reconstructions of the heart and arch arteries, MRI and HREM images were converted into volume datasets and segmented using Amira software (Thermo Fisher Scientific, Waltham, MA, USA). Structures were manually outlined using the label field function of Amira and surface rendered to produce the 3D images [45]. X-Gal staining to reveal *lacZ* activity was performed using standard procedures. To visualise the patency of pharyngeal arch arteries at E10.5, embryos were injected with India ink via the left ventricle with pulled Pasteur pipettes.

2.4. Immunohistochemistry

Embryos were embedded in paraffin wax and sectioned. Slides were dewaxed, rehydrated and immunostained with the following primary antibodies: mouse anti-AP-2α (3B5, Santa Cruz Biotechnology, Dallas, TX, USA; Catalogue number: sc-12726); rat anti-mouse CD-31 (BD Biosciences, San Jose, CA, USA; Catalogue number: 550274); chicken anti-GFP (Abcam, Cambridge, UK; Catalogue number: ab13970); anti-cleaved caspase3 (Cell Signalling Technology, Danvers, MA, USA; Catalogue number: 9661); anti-phospho-histone H3 (Millipore, Watford, UK; Catalogue number: 06-570). For cell fate analysis, three embryos for each genotype ($n \geq 3$ sections per embryo) were assessed and the number of positively stained cells divided by the total number of cells to give an apoptotic or proliferative index. NCC were labelled genetically with eYFP using the *Wnt1Cre* allele, and sections immunostained with the anti-GFP antibody, and the NCC counted ($n = 3$ embryos per genotype; $n \geq 3$ sections per embryo). Cell counting was performed using ImageJ software (National Institutes of Health, Bethesda, MD, USA) using the cell counter feature.

2.5. RT-PCR

Embryos were collected at E9.5 and the pharyngeal arch region dissected free in ice-cold PBS. Total RNA was extracted using TRIzol and a PureLink™ RNA mini spin column kit, and cDNA synthesis was carried out using the High Capacity cDNA reverse transcription kit (all from ThermoFisher Scientific, Waltham, MA, USA). Oligonucleotides were designed to identify the *AP-2α* wild-type (5′-TTAAGAAAGGCCCCGTGTCCCTG and 5′-CGTTGGGGTTTACCACGCCAC), floxed and recombined alleles (5′-TTAAGAAAGGCCCCGTGTCCCTG and 5′-TAACCGCTGCACACACCGCC), and *Gapdh* (5′-TGTGCAGTGCCAGCCTCGTC and 5′-TGACCAGGCGCCCAATACGG).

2.6. Western Blotting

Embryos were collected at E10.5, dissected in ice-cold PBS and lysed in 300 μL Laemmli buffer. Lysates were electrophoresed through a 10% polyacrylamide gel and subsequently transferred to PVDF membrane. The membrane was blocked in 5% milk solution and incubated with AP-2α antibody, diluted 1:1000. Secondary antibody was a polyclonal goat anti-mouse HRP (Agilent, Santa Clara, CA, USA) diluted 1:10,000.

2.7. Statistical Analysis

Cell counts were analysed using a two-tailed unpaired *t*-test (Prism 8.01 software, GraphPad, San Diego, CA USA). Fisher's exact test was used to compare defect frequencies between different genotypes (SPSS). Groups were considered significantly different when $p < 0.05$.

3. Results

3.1. Cardiovascular Phenotype in C57Bl/6J AP-2α$^{-/-}$ Embryos

In this study we wanted to identify the tissue in which AP-2α is required to control normal cardiovascular development. Firstly, however, we analysed the developing cardiovascular system in embryos deficient for *AP-2α* (*AP-2α*$^{-/-}$) on an enriched C57Bl/6J genetic background using histology, magnetic resonance imaging (MRI) and high-resolution episcopic microscopy (HREM). *AP-2α*$^{+/-}$ mice, which have an IRES-*lacZ* sequence inserted to disrupt the dimerization and DNA binding domains of the AP-2α protein [24], were intercrossed and embryos collected at E15.5 for analysis. This revealed that all *AP-2α*$^{-/-}$ embryos ($n = 10$) analysed had a ventricular septal defect (VSD) or an interventricular communication with an OFT defect (10/10), as shown in Figure 1 and Table 1, with six embryos showing a double outlet right ventricle, as shown in Figure 1D,E,I,J, two showing an over-riding aorta, as shown in Figure 1C,H, and two exhibiting transposition of the great arteries (TGA). One embryo with TGA also had an aberrant right subclavian artery (A-RSA), a right-sided aortic arch and an isolated left subclavian artery, as shown in Figure 1B,G. Although TGA is a hallmark of heterotaxy [48,49], we did not observe any other left–right patterning defects in *AP-2α*$^{-/-}$ embryos. Other aortic arch artery defects were also observed, including interrupted aortic arch ($n = 3/10$), as shown in Figure 1H, cervical origin of the aortic arch ($n = 2/10$), as shown in Figure 1I, and A-RSA ($n = 3/10$ retro-oesophageal and $n = 6/10$ with a cervical origin), as shown in Figure 1H–J. All *AP-2α*$^{-/-}$ embryos, except one, also presented with the previously reported craniofacial and ventral body wall defects [22,23]. One embryo, with a closed ventral body wall, had less severe craniofacial abnormalities, presenting only with a cleft palate and abnormal eyes. This embryo displayed a VSD, TGA and A-RSA, as shown in Figure 1O,P,Q. This suggests that the cardiovascular defects seen in *AP-2α*$^{-/-}$ embryos are not secondary to the craniofacial and ventral body wall abnormalities. In comparison to the published data [22,24], the mice used in this study presented with a significantly increased prevalence of aortic arch artery defects, as shown in Figure 1R,S. This, therefore, demonstrates that *AP-2α*$^{-/-}$ embryos on an enriched C57Bl/6J genetic background have fully penetrant cardiovascular defects affecting the aortic arch arteries, as well as the OFT.

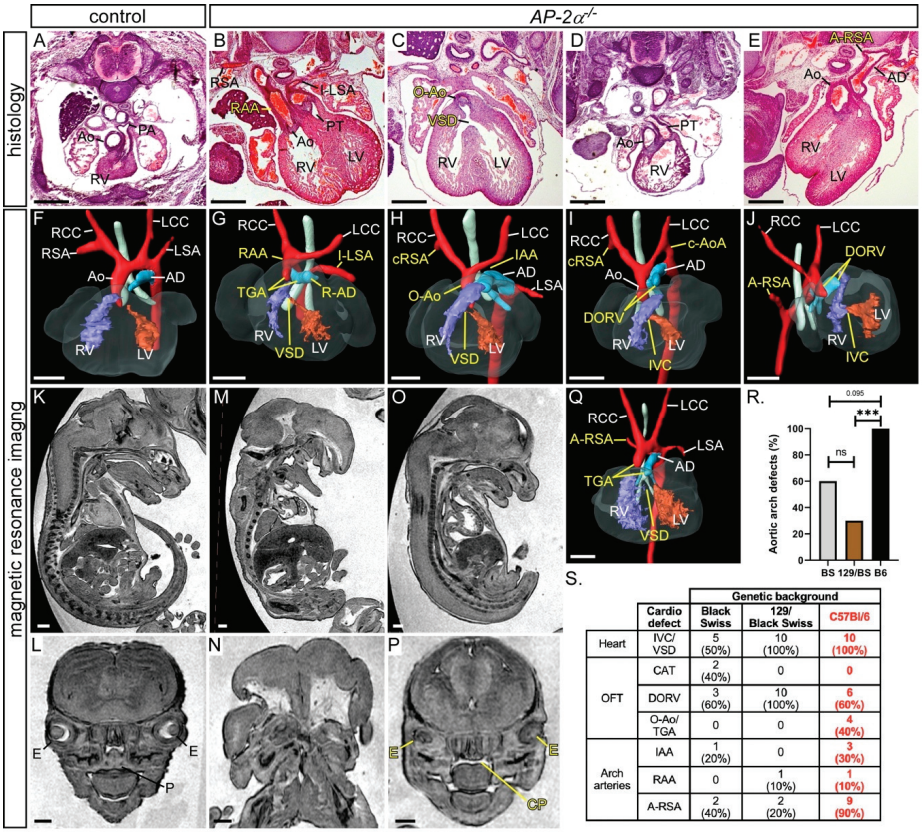

	Cardio defect	Genetic background: Black Swiss	129/ Black Swiss	C57Bl/6
Heart	IVC/ VSD	5 (50%)	10 (100%)	10 (100%)
OFT	CAT	2 (40%)	0	0
	DORV	3 (60%)	10 (100%)	6 (60%)
	O-Ao/ TGA	0	0	4 (40%)
Arch arteries	IAA	1 (20%)	0	3 (30%)
	RAA	0	1 (10%)	1 (10%)
	A-RSA	2 (40%)	2 (20%)	9 (90%)

Figure 1. Defects in *AP-2α*$^{-/-}$ embryos. Images were created from haematoxylin and eosin stained transverse sections (**A**–**E**) and MRI datasets (**F**–**P**) from E15.5 embryos. Control *AP-2α*$^{+/+}$ embryos had normal cardiovascular structures (**A**,**F**), bodies (**K**) and palates (**L**). *AP-2α*$^{-/-}$ embryos show a range of defects including transposition of the great arteries (TGA; **B**,**G**,**Q**), right-sided aortic arch (RAA) and arterial duct (R-AD), with an isolated left subclavian artery (l-LSA; **B**,**G**), interruption of the aortic arch (IAA; **H**), over-riding aorta (O-Ao; **C**,**H**), and cervical origin of the right subclavian artery (cRSA; **H**,**I**), cervical origin of the aortic arch (c-AoA; **I**) and double-outlet right ventricle (DORV; **D**,**E**,**I**,**J**), and retro-oesophageal right subclavian artery (A-RSA; **E**,**J**,**Q**). All outflow tract defects were associated with a ventricular septal defect (VSD) or an interventricular communication (IVC; **C**,**G**–**J**,**Q**). *AP-2α*$^{-/-}$ embryos usually also present with severe ventral body wall (**M**) and craniofacial defects (**M**,**N**). One *AP-2α*$^{-/-}$ embryo presented with a mild external phenotype (**O**) and minor craniofacial defects consisting of abnormal eyes (E) and cleft palate (CP; **P**), although this was accompanied by a severe cardiovascular abnormality (**Q**). (**R**,**S**) Effect of genetic background on the *AP-2α*-null cardiovascular phenotype. Data for Black Swiss (BS) and 129/Black Swiss (129/BS) genetic backgrounds reproduced from [24]; C57Bl/6J (B6) data from this study (red font). There is a significant increase in the number of *AP-2α*$^{-/-}$ aortic arch artery defects on the B6 background. *** $p < 0.005$, Fisher's exact test (**R**). Abbreviations: AD, arterial duct; Ao, aorta; LCC, left common carotid; LSA, left subclavian artery; LV, left ventricle; OFT, outflow tract; P, palate; PT, pulmonary trunk; RCC, right common carotid; RSA, right subclavian artery; RV, right ventricle. Scale, 500 μm.

Table 1. Cardiovascular defects observed in *AP-2α* mutant embryos.

Genotype	*n*	Abnormal	VSD	DORV	O-Ao	TGA	IAA +/− A-RSA	cAoA +/− A-RSA	RAA +/− A-SA	A-RSA
AP-2α$^{-/-}$	10	10 (100%)	4	6	2	2 [a]	3	2	1	4
AP-2α$^{-/f}$*;Foxg1Cre*	9	0	-	-	-	-	-	-	-	-
AP-2α$^{-/f}$*;Nkx2-5Cre*	14	2 (14%)	0	0	0	0	0	1	1	0
AP-2α$^{-/f}$*;Wnt1Cre*	25 [b]	3 (12%)	1	0	0	0	0	0	1	1
AP-2α$^{-/f}$*; Foxg1Cre;Wnt1Cre*	6	0	-	-	-	-	-	-	-	-
AP-2α$^{-/f}$*; Nkx2-5Cre;Wnt1Cre*	9	1 (11%)	1	0	0	0	0	0	0	1
AP-2α$^{-/f}$*;Isl1Cre*	11	4 (36%) [c]	2	1	0	0	2	0	0	1
AP-2α$^{-/f}$*;PGKCre*	10	10 (100%)	1	7 [d]	0	0	1	4	1	4

[a] One *AP-2α*$^{-/-}$ embryo with TGA also had a right-sided arterial duct. [b] *AP-2α*$^{-/f}$*;Wnt1Cre* embryos from *AP-2α* and *Wnt1Cre* breeding (n = 19) and complex *Foxg1Cre;Wnt1Cre* breeding (n = 6). [c] One *AP-2α*$^{-/f}$*;Isl1Cre* embryo also had a hypoplastic aorta. All OFT defects (i.e., DORV, O-Ao and TGA) were associated with a VSD or an interventricular communication. [d] The number of OFT defects in *AP-2α*$^{-/f}$*;PGKCre* embryos (7/10) is not significantly different to *AP-2α*$^{-/-}$ embryos (10/10; p = 0.211, Fisher's exact test). Abbreviations: A-RSA, anomalous right subclavian artery (i.e., retro-esophageal, cervical or isolated); A-SA; aberrant right or left subclavian (as A-RSA but also includes isolated left subclavian artery); cAoA, cervical aortic arch; DORV, double outlet right ventricle; IAA, interrupted aortic arch; O-Ao, overriding aorta; OFT, outflow tract; RAA, right-sided aortic arch; TGA, transposition of the great arteries; VSD, ventricular septal defect.

As the aortic arch arteries were found to be 100% affected in *AP-2α*$^{-/-}$ embryos on a C57Bl/6J genetic background we next examined whether the PAAs forming during E10.5-E11.5 developed abnormally using HREM (E10.5 to E11.5; 35–47 somites; n = 9) and intracardial ink injection (E10.5; 34–39 somites; n = 10). By HREM, four *AP-2α*$^{-/-}$ embryos examined at E10.5-E11.0 (35–43 somites), prior to remodelling of the third and fourth PAAs and the OFT, the fourth pharyngeal arch was observed to be smaller than in wild-type embryos, as shown in Figure 2B,C. The second PAA was abnormally persistent in two embryos, the fourth PAAs bilaterally absent or hypoplastic in all four embryos, and the sixth PAAs not yet formed in two embryos, as shown in Figure 2E,F and Table 2. By ink injection at E10.5, control embryos (34–42 somites; n = 7) had a symmetrical third, fourth and sixth PAAs that were patent to ink, and the first and second PAAs had regressed, as shown in Figure 2G. In *AP-2α*$^{-/-}$ embryos, 8/10 had a fourth PAA defect where this vessel was either unilaterally (n = 3/10) or bilaterally (n = 5/10) not patent to ink or hypoplastic in appearance, as shown in Figure 2H,I and Table 2. Moreover, 4/10 embryos also presented with a unilateral abnormally persisting second PAA patent to ink, and delayed formation of the sixth PAAs, as shown in Figure 2H,I and Table 2. At the E11.5 stage in wild-type embryos, the OFT was septated and the right sixth PAA had begun to regress, although the third and fourth PAAs remained symmetrical, as shown in Figure 2J. Of the five E11.5 *AP-2α*$^{-/-}$ embryos examined (45–47 somites), the second PAA was unilaterally persistent in four embryos and the fourth PAAs were either absent or hypoplastic in four embryos, as shown in Figure 2K,L and Table 2. The majority of the unilateral second PAA defects in *AP-2α*$^{-/-}$ embryos at E10.5-E11.5 affected the right second PAA (in 8/9 cases) whereas the fourth PAAs were affected bilaterally in 10/19 cases, with the right fourth PAA affected unilaterally in 4/19, and the left in 2/19 cases. In all *AP-2α*$^{-/-}$ embryos examined by HREM at E11.5 the OFT remained unseptated and the sixth PAAs were bilaterally present, as shown in Figure 2K,L.

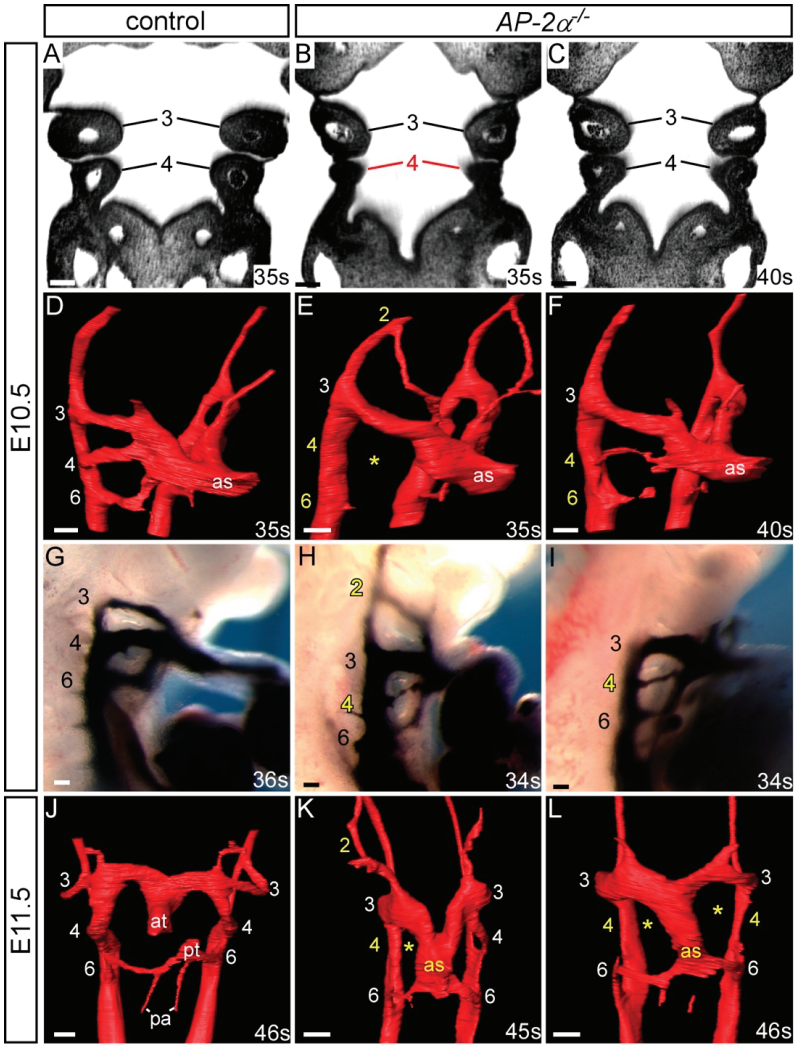

Figure 2. Pharyngeal arch artery patterning defects in *AP-2α*$^{-/-}$ embryos. Images were created from 3-D reconstructions of HREM datasets (**A**–**F**, **J**–**L**) and from ink injections (**G**–**I**). (**A**,**D**) Control *AP-2α*$^{+/+}$ embryos display normal development of the pharyngeal arches (**A**) and PAA (**D**) at E10.5. In *AP-2α*$^{-/-}$, the embryos, the caudal pharyngeal arch can appear hypoplastic (**B**) or normal (**C**), and the PAAs are frequently abnormal showing persistence of the second and absence of the fourth (**E**) or a hypoplastic fourth PAA (**F**). The sixth PAA formation was observed to be delayed in some embryos (**E**,**F**). (**G**–**I**) Ink injection shows that the third, fourth and sixth PAAs are symmetrical and patent to ink in control embryos (**G**). In *AP-2α*$^{-/-}$ embryos the second PAA was patent (**H**) and the fourth hypoplastic (**H**,**I**) or absent (not shown). (**J**–**L**) By E11.5 the outflow tract is septated in control embryos (**J**). In *AP-2α*$^{-/-}$ embryos, the septation of the outflow tract is delayed, and the second PAA is persistent and the fourth PAA is unilaterally (**K**) or bilaterally (**L**) absent. Pharyngeal arches (**A**–**C**) and PAAs (**D**–**L**) are numbered. Somite numbers (s) are given. Abbreviations: at, aortic trunk; as, aortic sac; pa, pulmonary artery; pt, pulmonary trunk. Scale, 100 μm.

Table 2. Pharyngeal arch artery defects in *AP-2α*$^{-/-}$ embryos.

Genotype	*n*	PAA	Abnormal	Unilateral Defect	Bilateral Defect	Present	Hypo/Int/Absent	Absent
AP-2α$^{-/-}$	19	2	11 (58%)	10	1	1	0	0
		4	16 (84%)	6	10	-	8	2
		6	11 (58%)	5	6	-	4	2

Embryos were collected and assessed for PAA defects. *AP-2α*$^{-/-}$ mutants were either injected intracardially with ink (E10.5; *n* = 10) or imaged using HREM (E10.5-E11.5; *n* = 9) to visualise the PAA. Data are combined. For each embryo, left and right PAA 1–6 was scored as having a unilateral or bilateral defect, and the bilateral defects categorised as either present, a combination of hypoplastic, interrupted and/or absent (Hypo/Int/Abs), and bilaterally absent. The first and third PAA were unaffected in all embryos examined. All control *AP-2α*$^{+/-}$ embryos (*n* = 9) were normal.

To investigate the endothelial cells lining the developing fourth PAA, we immunostained embryo sections with anti-PECAM-1 antibody to label endothelial cells. Embryos were collected at the stages when the fourth PAAa are beginning to form (late E9.5) and have formed (mid E10.5), and five embryos for each genotype (somite range 26–34) were examined. During E9.5, the fourth pharyngeal arch becomes apparent, with PECAM-1 stained endothelial cells of the forming fourth PAA visible close to the dorsal aorta in control (*AP-2α*$^{+/-}$) and *AP-2α*$^{-/-}$ embryos, as shown in Figure 3A–D. In control embryos with 30 to 34 somites, the fourth pharyngeal arch is well defined with the fourth PAA displaying a similar diameter to the third PAAs, surrounded by positively stained PECAM-1 endothelium, as shown in Figure 3E,F. However, in *AP-2α*$^{-/-}$ embryos of an equivalent stage, PECAM-1 positive cells were either clustered and disorganised or had formed a vessel of small diameter, as shown in Figure 3G,H. It therefore appears that the fourth PAA in the *AP-2α*$^{-/-}$ embryos are failing to form correctly.

AP-2α$^{-/-}$ embryos at E15.5 displayed OFT defects, such as double outlet right ventricle, over-riding aorta and TGA, as shown in Figure 1. We therefore examined the HREM datasets of *AP-2α*$^{-/-}$ embryos at E11.5 to see if malrotation of the OFT cushions could explain these phenotypes. During mid-E11.5, the major septal and parietal cushions are positioned side-by-side, as shown in Figure 4A–C. In *AP-2α*$^{-/-}$ embryos, however, the OFT cushions were mal-positioned with the parietal cushion more anterior to the septal cushion, as shown in Figure 4D–F, reminiscent of the orientation of the cushions at the early E11.5 stage [16].

These results demonstrate that the cardiovascular phenotype of *AP-2α*$^{-/-}$ embryos on an enriched C57Bl/6J genetic background, as assessed by histology, imaging, ink injections and immunostaining, is caused primarily by the fourth PAA not forming correctly, and aberrant OFT alignment with the ventricles.

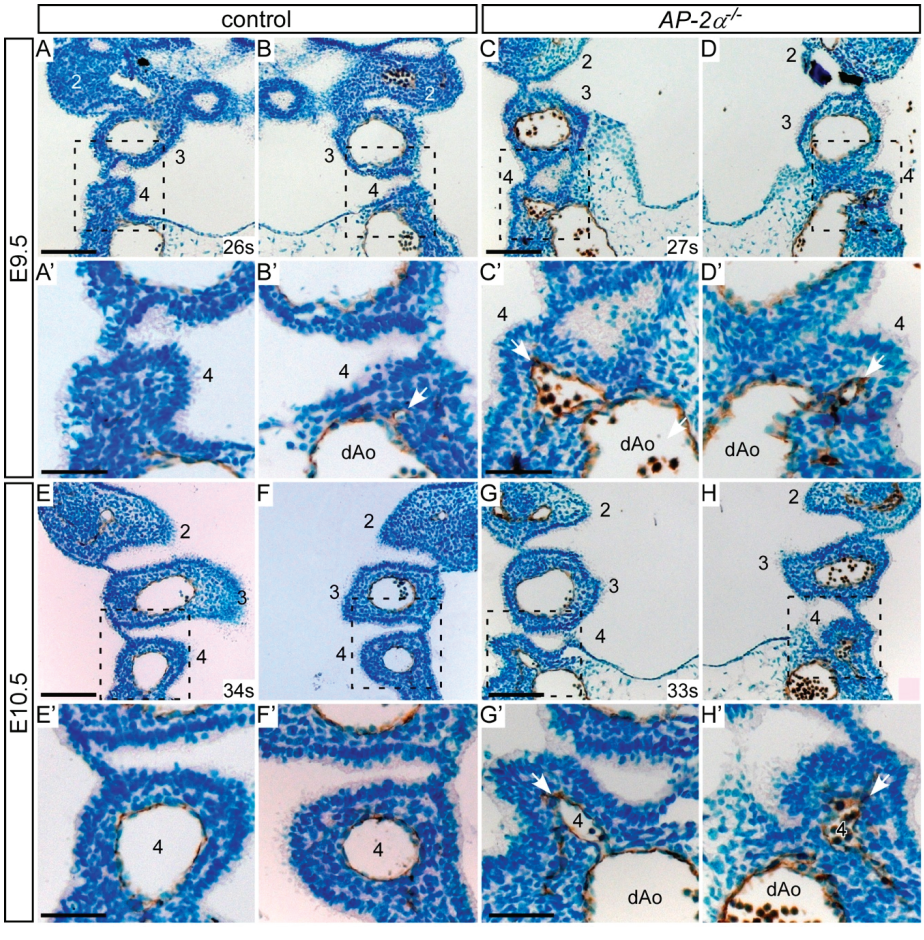

Figure 3. Pharyngeal arch artery development in *AP-2α*$^{-/-}$ embryos. Coronal sections were immunostained with anti-PECAM1 antibody to label endothelial cells of the PAA. (**A**–**D**) During the E9.5 stage the fourth pharyngeal arch is forming but the fourth PAA itself is only beginning to appear in the control and *AP-2α*$^{-/-}$ embryos. PECAM1 positive endothelial cells can be seen budding from the dorsal aorta (dAo; *arrows*). (**E**,**F**) In control embryos at E10.5 the fourth PAAs have formed, have a diameter similar to the third PAAs, and are lined with PECAM1 positive endothelial cells. (**G**,**H**) In *AP-2α*$^{-/-}$ embryos at E10.5 the third PAAs have formed normally but the fourth PAAs are much smaller and appear more irregular in shape (*arrows*). Each PAA is numbered, and somite numbers (s) are given. Scales: (**A**–**G**), 100 μm; (**A'**–**G'**), 50 μm.

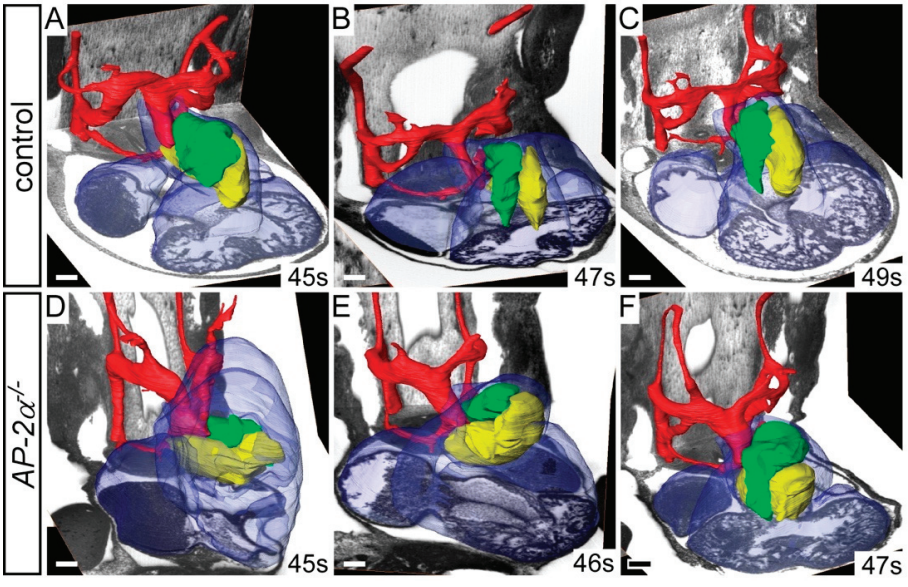

Figure 4. *AP-2α*$^{-/-}$ embryos display aberrant rotation of the outflow tract. Image datasets were acquired by high-resolution episcopic microscopy. (**A**–**F**) Outflow tract rotation during E11.5 (45–49 s). (**A**–**C**) In control embryos, the major outflow tract cushions (parietal in green; septal in yellow) have rotated in an anti-clockwise direction, resulting in the cushions being aligned side by side. (**D**–**F**) In *AP-2α*$^{-/-}$ embryos, the cushions have not rotated correctly resulting in the parietal cushion lying anterior to the septal cushion. Somite (s) counts indicated. Scale bars: 100 μm.

3.2. Cell Fates in *AP-2α*$^{-/-}$ Embryos

NCC are important for PAA remodelling [35]. We therefore investigated whether the NCC migrating into the pharyngeal arches were affected in *AP-2α*$^{-/-}$ embryos compared to the controls using *Wnt1Cre* and *eYFP* transgenic mice to lineage trace the NCC and maintain a high percentage of C57Bl/6J genetic background. Immunostaining was performed for NCC using an anti-GFP antibody, and cellular apoptosis and proliferation assessed. Embryos were collected at early E10.5 (somite range 32–34), a stage when the fourth PAAs have formed (n = 3 of each genotype). Firstly, apoptosis was assessed in all the cells within the fourth pharyngeal arch by immunostaining for cleaved caspase-3 activity and a significant two-fold increase in the number of apoptotic cells was identified throughout the fourth pharyngeal arch in *AP-2α*$^{-/-}$ embryos compared with control (p = 0.023), as shown in Figure 5A–C. When NCC, endoderm and ectoderm pharyngeal arch tissue were analysed separately, we identified a significant 7.7-fold increase in the number of apoptotic cells in the pharyngeal ectoderm compared to control ectoderm (p = 0.021), as shown in Figure 5C. The levels of apoptosis in the endoderm and NCC were unchanged compared to the controls. For proliferation, the sections were immunostained for phosphohistone H3 activity. The levels of proliferation within the fourth pharyngeal arches of the control and *AP-2α*$^{-/-}$ embryos were not significantly different, either in total or when each pharyngeal arch tissue was analysed separately, as shown in Figure 5D–F.

As cell death and proliferation within NCC was unaffected we next investigated whether the number and density of NCC present in the pharyngeal arches was altered in *AP-2α*$^{-/-}$ embryos using lineage traced NCC (n = 3 of each genotype at E10.5). We found no statistically significant difference in the number or density of NCC within the fourth pharyngeal arches between control and *AP-2α*$^{-/-}$ embryos, as shown in Figure 5G,H.

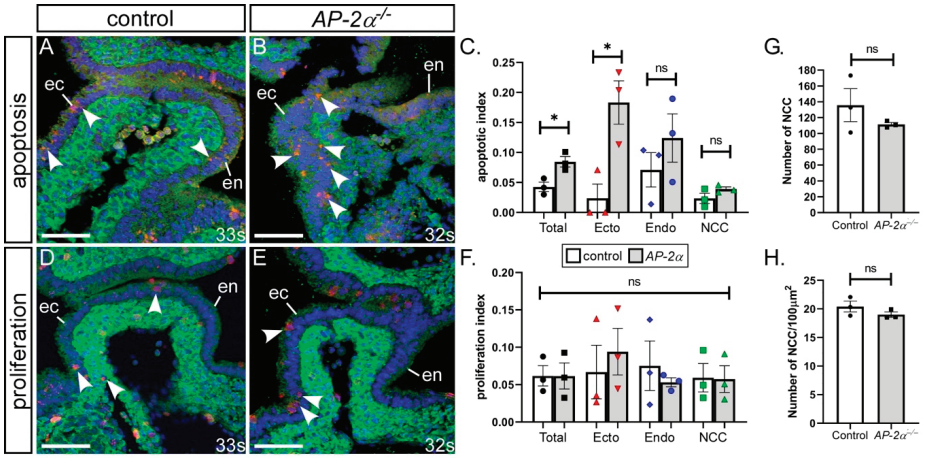

Figure 5. Increased apoptosis in the pharyngeal ectoderm of *AP-2α*$^{-/-}$ embryos. Sections from E10.5 control (*AP-2α*$^{+/-}$; **A**,**D**) and *AP-2α*$^{-/-}$ (**B**,**E**) embryos were immunostained with cleaved anti-caspase3 (*red*; **A**,**B**), anti-phosphohistone H3 (*red*; **D**,**E**) and anti-GFP (*green*; **A**,**B**,**D**,**E**) antibodies to detect apoptosis and proliferating cells within the fourth pharyngeal arch. The number of apoptotic (**C**) and proliferating (**F**) cells were counted and expressed as an index. (**G**,**H**), Neural crest cells (NCC) within the fourth pharyngeal arches of control and *AP-2α*$^{-/-}$ embryos were counted and expressed as the total number (**G**) and the number per 100μm^2 (**H**). Abbreviations: ec/ecto, ectoderm; en/endo, endoderm. * $p < 0.05$ (two-tailed unpaired *t*-test). Somite (s) counts indicated. Scale, 20 μm.

NCC number and density within the pharyngeal arches were, therefore, not affected in *AP-2α*$^{-/-}$ embryos, nor was cellular proliferation. Increased levels of apoptosis, however, were observed in the pharyngeal ectoderm of *AP-2α*$^{-/-}$ embryos at a critical time of fourth PAA development. This indicates that the cardiovascular defects observed may be derived from increased apoptosis within the pharyngeal ectoderm that consequently affects normal development.

3.3. Conditional Deletion of AP-2α from the Pharyngeal Surface Ectoderm

Previous work has demonstrated that, although *AP-2α* is expressed in NCC, conditional deletion using neural crest-specific *Cre* recombinase transgenic mice, *Wnt1Cre* and *P0-Cre*, in conjunction with the *AP-2α*^{flox} allele, does not result in cardiovascular defects [36]. As apoptosis was significantly increased in the pharyngeal ectoderm, we next explored the possibility that *AP-2α* expression in this tissue may be critical for cardiovascular development, as this is the only other domain in which AP-2α is expressed during PAA formation, as shown in Figure S1A,B,K. All control embryos analysed with an *AP-2α*$^{flox/+}$;*Cre* genotype were normal, as shown in Figure 6A–D.

Foxg1Cre is expressed in the pharyngeal ectoderm, endoderm and mesoderm from E8.5, but not in NCC, as shown in Figure S1C,D [37,50]. Mutant E15.5 embryos conditionally lacking *AP-2α* from the pharyngeal ectoderm (*AP-2α*$^{flox/-}$;*Foxg1Cre*) presented with a clefting of the face, and compared to control embryos, the thymus was not observed in its normal position above the heart, or only one lobe was seen in this position (n = 7/9), as shown in Figure S2 and Table 3. No cardiovascular defects, however, were observed, as shown in Table 1. This therefore suggests that conditionally deleting *AP-2α* from the pharyngeal surface ectoderm, in combination with endoderm and mesoderm, at least with *Foxg1Cre*, does not give rise to cardiovascular defects. Due to the complex expression pattern of *Foxg1Cre* in the head [37], and to maintain our focus on the cardiovascular system, we did not assess the impact on craniofacial defects further. As this result was unexpected, we employed a second *Cre* transgenic line, *Nkx2-5Cre*, that has been described to be active in the pharyngeal surface

ectoderm (and pharyngeal mesoderm and endoderm) from E8.0, but is also not expressed in NCC, as shown in Figure S1E,F [38,50]. Mutant *AP-2α*$^{flox/-}$;*Nkx2-5Cre* embryos at E15.5 (n = 14) presented with a craniofacial defect consisting of a midline cleft of the mandible, as shown in Figure 6E,F and Table 3. The thymus was affected in 5/14 embryos, being either bilaterally or unilaterally absent from the normal position or reduced in size and split asymmetrically, as shown in Figure 6G and Table 3. One *AP-2α*$^{flox/-}$;*Nkx2-5Cre* embryo presented with a right-sided aortic arch forming a vascular ring that looped around the back of the trachea and joined the descending aorta (therefore interrupted on the left), as shown in Figure 6H and Table 1, and one embryo showed cervical origin of the aortic arch.

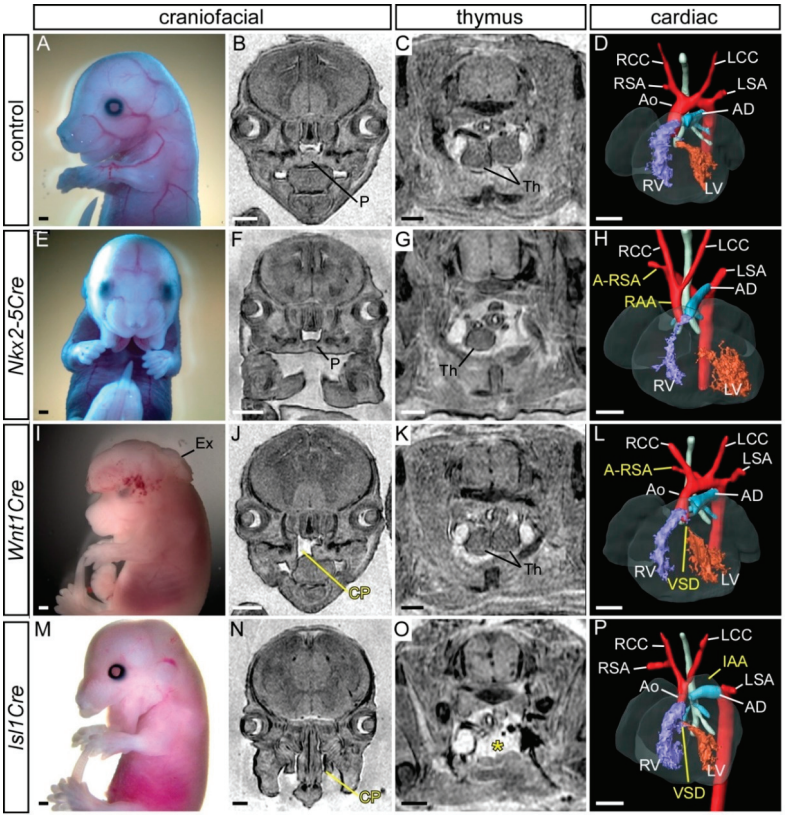

Figure 6. Defects following conditional deletion of *AP-2α*. (**A**–**D**) Control (*AP-2α*$^{+/flox}$) embryo with normal craniofacial appearance (**A**,**B**), thymus (**C**), heart and aortic arch arteries (**D**). (**E**–**H**) Mutant embryo with *AP-2α* conditionally deleted using *Nkx2-5Cre* showing craniofacial (**E**,**F**), thymus (**G**) and a right-sided aortic arch (RAA) and an aberrant right subclavian artery (A-RSA; **H**). (**I**–**L**) Mutant embryo with *AP-2α* conditionally deleted using *Wnt1Cre* showing exencephaly (**I**), cleft palate (CP; **J**), normal thymus (**K**), A-RSA and a ventricular septal defect (VSD; **L**). (**M**–**P**) Mutant embryo with *AP-2α* conditionally deleted using *Isl1Cre* showing craniofacial (**M**,**N**), thymus absent from its normal position (asterisk; **O**), an interrupted aortic arch (IAA) and VSD (**P**). Abbreviations: AD, arterial duct; Ao, aorta; LCC, left common carotid; LSA, left subclavian artery; LV, left ventricle; P, palate; RCC, right common carotid; RSA, right subclavian artery; RV, right ventricle. Scale, 500 μm.

Table 3. Extra-cardiovascular defects in conditionally deleted *AP-2α* embryos.

Genotype	Thymus	Craniofacial
AP-2α$^{-/f}$;Foxg1Cre	Bilaterally or unilaterally absent from normal position, reduced in size and/or split (7/9)	Upper facial cleft (7/9)
AP-2α$^{-/f}$;Nkx2-5Cre	Bilaterally or unilaterally absent from normal position, reduced in size and/or split (5/14)	Midline cleft mandible (14/14)
AP-2α$^{-/f}$;Wnt1Cre	Not affected	Cleft palate (5/19); exencephaly (1/19)
AP-2α$^{-/f}$; Foxg1Cre;Wnt1Cre	Bilaterally or unilaterally absent from normal position (6/6)	Upper facial cleft (6/6); exencephaly (2/6)
AP-2α$^{-/f}$; Nkx2-5Cre;Wnt1Cre	Small, split (1/9)	Midline cleft mandible (9/9)
AP-2α$^{-/f}$;Isl1Cre	Absent from normal position (9/11)	Midline cleft mandible and upper facial cleft (8/11); cleft palate (6/11); exencephaly (1/11)

The selective deletion of *AP-2α* from the pharyngeal ectoderm using either *Foxg1Cre* or *Nkx2-5Cre* transgenic mice did not, therefore, recapitulate the cardiovascular malformations seen in the global *AP-2α*-null embryos.

3.4. Conditional Deletion of AP-2α from the Neural Crest

The possibility that genetic background may have influenced the penetrance of a cardiovascular phenotype in the previously published work raised the question that perhaps the role of *AP-2α* in the neural crest should be re-examined on the inbred C57Bl/6J background. To do this, mice carrying the *Wnt1Cre* transgene were used to conditionally delete *AP-2α* from all NCC [39]. *AP-2α$^{flox/-}$;Wnt1Cre* embryos were examined for cardiovascular defects at E15.5 (n = 19). One embryo presented with exencephaly, as shown in Figure 6I, five had a cleft palate, as shown in Figure 6J, and the thymus was unaffected, as shown in Figure 6K and Table 3. Two embryos had cardiovascular defects: one had a perimembranous VSD with A-RSA, as shown in Figure 6L and Table 1, and one had a vascular ring, as described above. We therefore identified a very low incidence (10%) of cardiovascular abnormalities in embryos with a neural crest cell-specific deletion of *AP-2α* on an enriched C57Bl/6J genetic background.

3.5. Simultaneous Deletion of AP-2α from the Surface Ectoderm and the Neural Crest

AP-2α is expressed in both NCCs and the pharyngeal surface ectoderm, as shown in Figure S1A,B,K. As deletion from either tissue individually did not recapitulate the level of cardiovascular defects seen in the global mutants, we next investigated the possibility that *AP-2α* is required in both tissues simultaneously for correct cardiovascular development. We therefore created mutant mice that would delete *AP-2α* from the pharyngeal ectoderm and NCC simultaneously. Male mice heterozygous for *AP-2α* and transgenic for both *Wnt1Cre* and *Foxg1Cre* were crossed to *AP-2α$^{flox/flox}$* females, and embryos collected at E15.5 for analysis. A craniofacial defect was observed in all embryos of the genotype *AP-2α$^{flox/-}$; Wnt1Cre;Foxg1Cre* (n = 6) similar to that seen in Figure S2. In addition, exencephaly was observed (2/6) as well as thymus defects, as shown in Table 3. By histology, no cardiovascular defects were observed, although an A-RSA was identified in one *AP-2α$^{flox/-}$;Wnt1Cre* embryo from this cohort, as shown in Table 1. From these data, it appears that the simultaneous deletion of *AP-2α* from the NCC and surface ectoderm using *Wnt1Cre* and *Foxg1Cre* is unable to cause cardiovascular defects in mutant embryos. We therefore employed *Nkx2-5Cre* in conjunction with *Wnt1Cre* to delete *AP-2α* from the surface ectoderm and NCC together. All *AP-2α$^{flox/-}$;Wnt1Cre;Nkx2-5Cre* mutant embryos (n = 9)

showed a facial cleft similar to that shown in Figure 6E,F, and one had a thymus defect, as shown in Table 3. One *AP-2α*$^{flox/-}$*;Wnt1Cre;Nkx2-5Cre* mutant embryo had a perimembranous VSD and cervical origin of the right subclavian artery, as shown in Table 1.

In an attempt to delete *AP-2α* from the pharyngeal ectoderm at a slightly earlier time than with *Nkx2-5Cre* and *Foxg1Cre*, we used *Isl1Cre* mice [40]. Isl1 is expressed in the SHF as early as E7.0 [51] and throughout the developing pharyngeal arches in the pharyngeal endoderm, ectoderm and mesoderm, and in NCC, as shown in Figure S1I,J [43,52,53]. The *Isl1Cre* transgenic line will therefore delete *AP-2α* from the surface ectoderm and NCC component of its expression domain. Mutant *AP-2α*$^{flox/-}$*;Isl1Cre* embryos (n = 11) at E15.5 were analysed and showed craniofacial and thymus defects, as shown in Figure 6M–O and Table 3, and four mutants presented with a cardiovascular defect, displaying perimembranous VSD with either interrupted aortic arch or A-RSA, and a hypoplastic aorta, as shown in Figure 6P and Table 1.

Taken together, the conditional, and simultaneous deletion, of *AP-2α* from the pharyngeal ectoderm and/or NCC, somewhat unexpectedly, did not fully recapitulate the cardiovascular defects seen in the global *AP-2α* null embryos. These results indicate that the simultaneous conditional deletion of *AP-2α* from the NCC and the surface ectoderm does not result in highly penetrant cardiovascular malformations, at least not with the *Cre* lines employed here.

3.6. Early Embryonic Recombination of the *AP-2α*^{flox} Allele

Because of the unexpected lack of a penetrant cardiovascular phenotype with any of the *Cre* lines used in this study, we decided to closely analyse the cardiovascular phenotype produced by a global deletion of the *AP-2α*^{flox} allele and compare this to the phenotype seen in the constitutive *AP-2α* deficient embryos.

To achieve the recombination of the *AP-2α*^{flox} allele at an early embryonic stage, we used *PGKCre* transgenic mice, which have been reported to express Cre recombinase in all tissues from E3.5 [41]. To confirm that the *AP-2α*^{flox} allele, as shown in Figure 7A, was being fully recombined we performed RT-PCR on cDNA made from E10.5 embryo RNA. This demonstrated that the *AP-2α*^{flox} allele was correctly recombined in the presence of *PGKCre*, as shown in Figure 7B. We also showed that no truncated AP-2α protein was made by Western blotting, as shown in Figure 7C. These data demonstrated that the *AP-2α*^{flox} allele was completely recombined and created a null allele. To investigate the cardiovascular system, stud males of the genotype *AP-2α*$^{+/-}$*;PGKCre* were created, and crossed to *AP-2α*$^{flox/flox}$ females to generate mutant (*AP-2α*$^{flox/-}$*;PGKCre*) and control (*AP-2α*$^{flox/+}$*;PGKCre*) embryos at E15.5 for analysis. The external phenotype clearly recapitulated the *AP-2α*$^{-/-}$ external phenotype, as shown in Figure 7G [22–24]. All *AP-2α*$^{flox/-}$*;PGKCre* mutant embryos presented with an aortic arch artery defect and 70% with an OFT defect, which was not significantly different from the fully penetrant OFT defects seen in the global *AP-2α* deficient embryos, as shown in Figure 7H, I and Table 1.

These data indicate that cardiovascular defects equalling the prevalence seen in *AP-2α*$^{-/-}$ embryos can only be recapitulated conditionally with an early recombination of the *AP-2α*^{flox} allele throughout the embryo in conjunction with the *AP-2α* null allele.

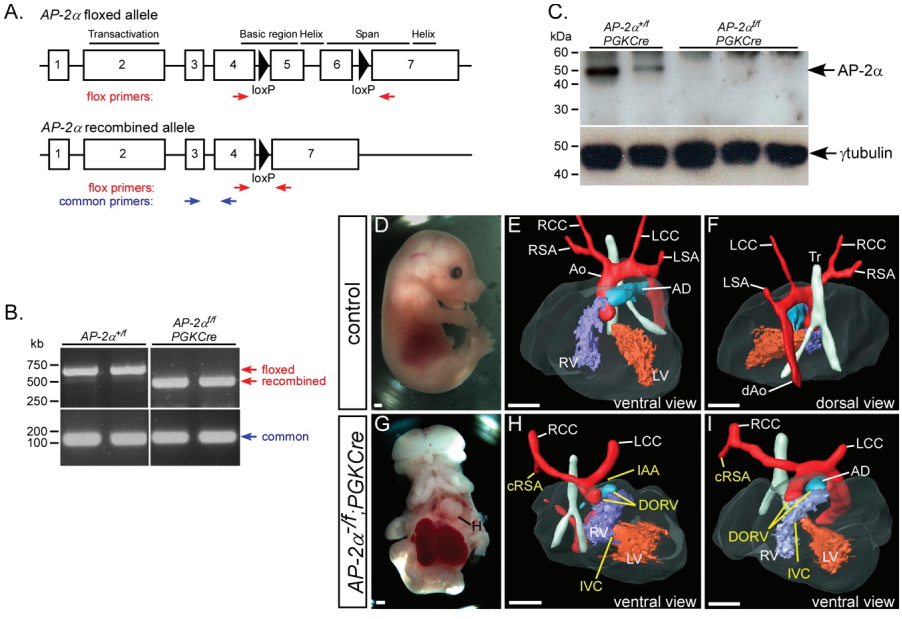

Figure 7. Defects following global conditional deletion of *AP-2α*. (**A**) Cartoon of the *AP-2α*^{flox} allele [36] with the functional domains, *loxP* sites (black triangles) and genotyping primers indicated. (**B**) RT-PCR analysis demonstrates that the *AP-2α*^{flox} allele is fully recombined with *PGKCre*. (**C**) No AP-2α protein is produced following the PGKCre-mediated recombination of the *AP-2α*^{flox} allele. γ-tubulin antibody was used as a loading control. (**D**–**F**) Control (*AP-2α*$^{+/flox}$;*PGKCre*) embryos were externally normal (**D**) and had a normal heart, outflow tract and aortic arch arteries (**E**,**F**). (**G**–**I**) Conditional deletion of *AP-2α* using *PGKCre* (*AP-2α*$^{-/flox}$;*PGKCre*) produced embryos with the typical *AP-2α*-null external phenotype (**G**) and cardiovascular defects, including interruption of the aortic arch (IAA), cervical origin of the right subclavian artery (cRSA) and double-outlet right ventricle (DORV) with interventricular communication (IVC; **H**,**I**). Abbreviations: AD, arterial duct; Ao, aorta; dAo, dorsal aorta; LCC, left common carotid; LSA, left subclavian artery; LV, left ventricle; H, heart; RCC, right common carotid; RSA, right subclavian artery; RV, right ventricle; Tr, trachea. Scale, 500 μm.

4. Discussion

In this study we have defined the cardiovascular phenotype in mice lacking *AP-2α* on a C57Bl/6J genetic background, although we were unable to fully recapitulate the cardiovascular phenotype seen in *AP-2α* deficient embryos using a conditional deletion strategy from the neural crest and/or pharyngeal surface ectoderm. The complete *AP-2α* deficient phenotype, was, however, achieved through very early embryonic recombination of the *AP-2α* conditional allele.

AP-2α is expressed in the NCC and the pharyngeal ectoderm of the pharyngeal arches that house the PAAs that will form and remodel to create the aortic arch arteries that take blood away from the heart [24,33,34]. Conditional deletion of *AP-2α* from the NCC and/or the pharyngeal surface ectoderm, failed to recapitulate the *AP-2α*-null cardiovascular phenotype, although a small percentage displayed an arch artery defect. The conditional deletion of *AP-2α* using *Isl1Cre* did produce the highest number of embryos with a cardiovascular malformation (36%) of all the Cre combinations used. *Isl1Cre* is expressed throughout the SHF including the pharyngeal epithelia [43,52], but it has also been reported to be active in the cardiac neural crest [53]. It could therefore be speculated that the earlier onset of *Isl1Cre* expression [51], combined with activity in the pharyngeal surface ectoderm and NCC, could have sufficiently recombined the *AP-2α*^{flox} allele to produce a limited cardiovascular

phenotype. The overall timing of the expression of the Cre transgenes used in this study, however, may therefore be too late to successfully fully recombine the *AP-2α*^{flox} allele. By employing *PGKCre* mutant mice to conditionally delete *AP-2α* before gastrulation, the full *AP-2α*-deficient phenotype was successfully recapitulated. This is analogous to the *Cited2* knockout mouse, where the full heterogenous cardiovascular and laterality phenotype could only be realized conditionally through deletion at gastrulation [54]. Each Cre line used in this study, however, was able to produce mutant embryos with craniofacial defects, demonstrating that these lines functioned correctly and were able to recombine the *AP-2α*^{flox} allele and impact the formation of these structures later in development. *Foxg1Cre*, for example, has a complex expression pattern in the head itself [37], but we have not assessed how this pattern might cause the observed craniofacial defects, nor with the other Cre strains used in this study. Nevertheless, the high incidence of craniofacial and thymus defects in the conditional mutants reflects the efficacy of *AP-2α* deletion resulting from the Cre transgenes and supports our conclusions concerning the lack of defects caused by loss of *AP-2α* in relation to the cardiovascular system. A recent study has demonstrated that biallelic deletion of *AP-2α* and *AP-2β* from NCC results in more severe craniofacial defects than seen in single NCC mutants [55], indicating that functional redundancy occurs between these two genes. It is possible, therefore, that cardiovascular development may also be affected more severely in these mutants, providing an alternative explanation as to why so few *AP-2α*$^{flox/-}$*;Wnt1Cre* mutant embryos presented with cardiovascular defects here, or not at all in the earlier report [36]. Recently it has been recognized that the *Wnt1Cre* line has ectopic overexpression of Wnt1 in the midbrain, which increases Wnt/ß-catenin signalling, and a new allele has been developed, *Wnt1Cre2*, to overcome this issue [56]. This line, however, has been reported to alter NCC-related phenotypes compared to *Wnt1Cre* [57]. Although we do not predict that ectopic midbrain Wnt1 overexpression using the *Wnt1Cre* allele would affect the cardiovascular system in our study, it is feasible that we may have achieved a different result using the *Wnt1Cre2* allele.

Previous studies have described the cardiovascular defects in *AP-2α*-null embryos and demonstrated a cardiovascular phenotype consisting of a fully penetrant OFT malformation and a partially penetrant arch artery phenotype [24]. Here, using mice on an enriched C57Bl/6J genetic background, we have described the fully penetrant OFT and arch artery defects in *AP-2α*-null embryos, demonstrating that *AP-2α* is critical for the correct development of the cardiovascular system. We did not, however, find any embryos with a common arterial trunk, as previously reported [24], but did identify other OFT defects of over-riding aorta and TGA, with the latter not previously described in *AP-2α*$^{-/-}$ mutant embryos. This difference in the penetrance of arch artery defects, and the range in OFT abnormalities observed, may be attributed to the different genetic backgrounds of the mice used in the various published studies. In our study, all the mice used were calculated to be >90% C57Bl/6J for each line used, whereas the mice in the previous work were on a Black Swiss [22] or a mixed genetic background [24]. The *AP-2α*-null alleles were constructed differently, with the former using a neomycin cassette to replace exon 6, and the latter having an IRES-lacZ cassette inserted into exon 7 of the *AP-2α* gene (also used in this study). Although the presence of a neomycin cassette may influence neighbouring gene expression that could impact any observed phenotype [58], it is more likely that the increased penetrance of arch artery defects observed in our study are due to changes in genetic background that are influencing the presentation of specific phenotypes, as previously shown for *Cited2* and *Gbx2*, among other genes involved in cardiovascular development [15,21].

The PAA defects observed between E10.5 and E11.5 in *AP-2α*-null embryos were predominantly affecting the fourth PAAs, either unilaterally or bilaterally, with the development of this artery appearing to be arrested between E9.5 and E10.5, as shown by PECAM1 staining. Failure of the left fourth PAA to form will result in the interruption of the aortic arch and cervical origin of the aorta, and failure of the right fourth PAA will lead to A-RSA, either retro-oesophageal or with a cervical origin [59]. The destiny of the persistent second PAA is more difficult to ascertain; it may regress at a later time in development or may even contribute to the mature aortic arch topology as a replacement vessel for an absent or aberrantly remodelled one, as is seen in *Pax9*-null embryos [16].

Interestingly, the right fourth PAA appeared to be more susceptible to the deletion of *AP-2α* with 100% of the constitutive and the conditional mutants by the foetal stage displaying a defect affecting the right fourth PAA derived vessel (e.g., retro-oesophageal and cervical origin of the right subclavian artery). Moreover, almost half of the embryos at E10.5–E11.5 had an abnormal right second PAA. Mouse embryos, heterozygous for *Tbx1,* present more frequently with A-RSA than interruption of the aortic arch [16,60], indicating that a right-sided bias does occur in other mouse models of cardiovascular malformation. Although it has been described that the $Tbx1^{+/-}$ fourth PAA phenotype does partially recover during development [16,17,61], this does not seem to be the case in *AP-2α*-deficient mice, as the incidence of right fourth PAA derived defects is fully penetrant.

AP-2α-null embryos display severe neural tube and ventral body wall closure defects (primary thoracoabdominoschisis) [22,23] that may occasionally affect the pericardium [24]. Neural tube defects, such as spina bifida, and foetal thoracoabdominal anomalies, such as gastroschisis and omphalocele, occur concomitantly with CHD [62–64]. It is therefore possible that the *AP-2α*-null cardiovascular phenotype occurs concomitantly, or even secondarily, to the body wall closure defects. This is, however, unlikely, as we identified one *AP-2α*-null embryo with an intact ventral body wall and only a mild craniofacial defect that presented with complex OFT and arch artery defects. Although all *AP-2α*-null embryos present with cardiovascular defects incompatible with post-natal life, they are sufficient to support a circulation in the foetus. Following birth, the closure of the duct would result in the rapid demise of the neonate and death within 48 h. However, given the severity of the other defects, it is highly likely that these would independently result in a more immediate post-natal death. For example, the severe craniofacial, body wall, cranial nerve and skeletal defects would prevent feeding and breathing [22,23]. By E10.5, *AP-2α* is no longer expressed in NCCs, but continues to be expressed within the pharyngeal ectoderm [24]. NCC migration is unaffected in *AP-2α*-null embryos [23] and we did not see any defects in NCC apoptosis, proliferation, number or density within the pharyngeal arches, but did observe a significant increase in the number of apoptotic cells in the fourth pharyngeal arch ectoderm of *AP-2α*-null embryos. Increased apoptosis has also been observed in the third and fourth pharyngeal arch ectoderm of *Eya*-null embryos [65], and these mice also display complex cardiovascular defects, such as interruption of the aortic arch and A-RSA that are seen in $AP\text{-}2\alpha^{-/-}$ embryos [66]. Interestingly, a role for apoptosis in other tissue compartments has been described in animal models of cardiovascular developmental defects. Within the pharyngeal mesenchyme of *Tgfb2*-null mouse embryos at E11.5, apoptotic cells have been observed surrounding the PAAs just before they begin to regress [67]. At later stages, aberrant apoptotic cells were located in the fourth PAAs leading to arch artery defects, such as interrupted aortic arch. Aberrant apoptosis within the tunica media of the arteries has also been implicated in the development of arch artery defects in diabetic rats [68]. To see if a second wave of apoptosis is contributing to the *AP-2α*-null cardiovascular phenotype, the examination of embryos at later stages when the PAA are remodelling (i.e., E11.5–E13.5) would need to be undertaken. At the stage of development analysed in our study, it is not possible to identify the apoptotic ectodermal cells beyond that of a monolayer of columnar, polarised epithelial cells, joined by tight and adherens junctions. The pharyngeal surface ectoderm, however, has been implicated as an important signalling centre for PAA morphogenesis [17,69], so it is possible that AP-2α expression in the ectoderm plays a critical role in mammalian PAA development, akin to the role of ectodermal *tfap2a* in controlling zebrafish skeletogenesis and the promotion of pharyngeal ectoderm survival [70]. Moreover, for the process of ventral body wall closure during development, AP-2α is required for signalling from the surface ectoderm to the underlying mesoderm [71]. As NCC are sensitive to external signals as they migrate [72] we speculate that aberrant signals from the affected pharyngeal ectoderm may alter their behaviour and ability to properly orchestrate the process of OFT septation and ventriculo-arterial connections in $AP\text{-}2\alpha^{-/-}$ embryos, leading to delayed OFT septation, aberrant endocardial cushion rotation and subsequently giving rise to the observed OFT defects. Septation does finally occur in the *AP-2α*-null embryos as no case of common arterial trunk was observed in our mutants. The OFT cushions in the *AP-2α*-null embryos were aberrantly positioned with the parietal

cushion more caudal to the septal cushion, an organisation seen at an earlier stage in development in control embryos [16]. The OFT phenotypes observed, therefore, could be attributed to an alteration in the aortic to pulmonary valve axis angle, following an arrest in normal OFT rotation [73,74]. It should be noted, however, that the aberrant positioning of the OFT cushions in *AP-2α*-null embryos may not represent how the observed defects occur. An alternative mechanism for the correct positioning of the aorta and pulmonary trunk over the correct ventricles is through an asymmetrical lengthening of the right ventricular OFT, which causes the pulmonary trunk to be pushed towards its definitive position in front of the aorta by an asymmetric population of SHF cells [75]. In *Lrp2*-null mice, for example, the abnormal migration of this SHF population, along with defective NCC migration, results in common arterial trunk [76]. Further studies will be required to see if the SHF pulmonary push population has been affected in *AP-2α*-null embryos.

5. Conclusions

In this study we have shown that the complex cardiovascular defects in embryos deficient in *AP-2α* are fully penetrant on a C57Bl/6J genetic background. Conditional deletion experiments suggest that *AP-2α* has a complex influence on cardiovascular development by being required very early in embryogenesis, having a redundant function in multiple tissue layers, or a combination of both factors.

Supplementary Materials: The following are available online at http://www.mdpi.com/2308-3425/7/3/27/s1. Figure S1. E9.5 mouse embryos stained to show expression of lacZ from the *AP-2a*^{lacZ} allele. Figure S2. Non-cardiac defects following conditional deletion of *AP-2α* using *Foxg1Cre*.

Author Contributions: Conceptualization, S.B., T.W. and S.D.B.; resources, S.B. and T.W.; methodology, J.E.S. and T.J.M.; formal analysis, A.-L.J. and S.D.B.; investigation, A.-L.J. and S.D.B.; writing—original draft preparation, S.D.B.; writing—review and editing, D.J.H. and H.M.P.; visualization, A.-L.J. and S.D.B.; supervision, D.J.H., H.M.P. and S.D.B.; project administration, S.D.B.; funding acquisition, S.D.B. All authors have read and agreed to the published version of the manuscript.

Funding: This research was funded by a British Heart Foundation Intermediate Basic Science Fellowship (FS/08/016/24741; to S.D.B.), a British Heart Foundation PhD Studentship (FS/09/015/26934; to S.D.B.), and by NIH grant 2R01 DE12728 (to T.W.). J.E.S. would like to acknowledge infrastructure funding from the British Heart Foundation, UK (SI/14/1/30718).

Acknowledgments: We thank Divya Venkatesh, Kathleen Allinson and Lauren Phillips for technical assistance, and Robert H. Anderson for discussions about cardiac developmental anatomy.

Conflicts of Interest: The authors declare no conflict of interest.

References

1. Hoffman, J.I.E. Incidence, mortality and natural history. In *Paediatric Cardiology*; Anderson, R.H., Baker, E.J., Macartney, F.J., Rigby, M.L., Shinebourne, E.A., Tynan, M., Eds.; Churchill Livingstone: Edinburgh, London, UK, 2002; pp. 111–139.
2. Burn, J.; Goodship, J. Congenital heart disease. In *Principles and Practice of Medical Genetics*; Rimoin, D.L., Connor, J.M., Pyeritz, R.E., Korf, B.R., Eds.; Churchill Livingstone: Edinburgh, London, UK, 2002.
3. Anderson, R.H.; Brown, N.A.; Bamforth, S.D.; Chaudhry, B.; Henderson, D.J.; Mohun, T.J. *Development of the Outflow Tract*; Oxford University Press (OUP): Oxford, UK, 2018; pp. 226–239.
4. Anderson, R.H.; Chaudhry, B.; Mohun, T.J.; Bamforth, S.D.; Hoyland, D.; Phillips, H.M.; Webb, S.; Moorman, A.F.; Brown, N.A.; Henderson, D.J. Normal and abnormal development of the intrapericardial arterial trunks in humans and mice. *Cardiovasc. Res.* **2012**, *95*, 108–115. [CrossRef] [PubMed]
5. Graham, A. Development of the pharyngeal arches. *Am. J. Med Genet.* **2003**, *119*, 251–256. [CrossRef] [PubMed]
6. Hiruma, T.; Nakajima, Y.; Nakamura, H. Development of pharyngeal arch arteries in early mouse embryo. *J. Anat.* **2002**, *201*, 15–29. [CrossRef]
7. Bamforth, S.D.; Chaudhry, B.; Bennett, M.; Wilson, R.; Mohun, T.J.; Van Mierop, L.H.; Henderson, D.J.; Anderson, R.H. Clarification of the identity of the mammalian fifth pharyngeal arch artery. *Clin. Anat.* **2012**, *26*, 173–182. [CrossRef] [PubMed]

8. Lammer, E.J.; Chen, D.T.; Hoar, R.M.; Agnish, N.D.; Benke, P.J.; Braun, J.T.; Curry, C.J.; Fernhoff, P.M.; Grix, A.W.; Lott, I.T.; et al. Retinoic Acid Embryopathy. *N. Engl. J. Med.* **1985**, *313*, 837–841. [CrossRef]
9. Diez-Pardo, J.A.; Tovar, J.A.; Yu, J.; Gonzalez, S.; Martinez, L. Effects of retinoic acid on the neural crest-controlled organs of fetal rats. *Pediatr. Surg. Int.* **2003**, *19*, 355–358. [CrossRef]
10. Hogers, B.; DeRuiter, M.C.; Groot, A.G.-D.; E Poelmann, R. Extraembryonic venous obstructions lead to cardiovascular malformations and can be embryolethal. *Cardiovasc. Res.* **1999**, *41*, 87–99. [CrossRef]
11. Yashiro, K.; Shiratori, H.; Hamada, H. Haemodynamics determined by a genetic programme govern asymmetric development of the aortic arch. *Nature* **2007**, *450*, 285–288. [CrossRef]
12. Bentham, J.; Bhattacharya, S. Genetic Mechanisms Controlling Cardiovascular Development. *Ann. N. Y. Acad. Sci.* **2008**, *1123*, 10–19. [CrossRef]
13. Porras, D.; Brown, C.B. Temporal–spatial ablation of neural crest in the mouse results in cardiovascular defects. *Dev. Dyn.* **2007**, *237*, 153–162. [CrossRef]
14. Olaopa, M.; Zhou, H.-M.; Snider, P.; Wang, J.; Schwartz, R.J.; Moon, A.M.; Conway, S.J. Pax3 is essential for normal cardiac neural crest morphogenesis but is not required during migration nor outflow tract septation. *Dev. Boil.* **2011**, *356*, 308–322. [CrossRef] [PubMed]
15. Stothard, C.A.; Mazzotta, S.; Vyas, A.; Schneider, J.E.; Mohun, T.J.; Henderson, D.J.; Phillips, H.M.; Bamforth, S.D. Pax9 and Gbx2 Interact in the Pharyngeal Endoderm to Control Cardiovascular Development. *J. Cardiovasc. Dev. Dis.* **2020**, *7*, 20. [CrossRef] [PubMed]
16. Phillips, H.M.; Stothard, C.A.; Qureshi, W.M.S.; Kousa, A.I.; Briones-Leon, J.A.; Khasawneh, R.R.; O'Loughlin, C.; Sanders, R.; Mazzotta, S.; Dodds, R.; et al. Pax9 is required for cardiovascular development and interacts with Tbx1 in the pharyngeal endoderm to control 4th pharyngeal arch artery morphogenesis. *Development* **2019**, *146*, dev177618. [CrossRef]
17. Calmont, A.; Ivins, S.; Van Bueren, K.L.; Papangeli, I.; Kyriakopoulou, V.; Andrews, W.D.; Martin, J.F.; Moon, A.M.; Illingworth, E.A.; Basson, M.A.; et al. Tbx1 controls cardiac neural crest cell migration during arch artery development by regulating Gbx2 expression in the pharyngeal ectoderm. *Development* **2009**, *136*, 3173–3183. [CrossRef]
18. Yin, Z.; Haynie, J.; Yang, X.; Han, B.; Kiatchoosakun, S.; Restivo, J.; Yuan, S.; Prabhakar, N.R.; Herrup, K.; Conlon, R.A.; et al. The essential role of Cited2, a negative regulator for HIF-1, in heart development and neurulation. *Proc. Natl. Acad. Sci. USA* **2002**, *99*, 10488–10493. [CrossRef]
19. Martinez-Barbera, J.P.; Rodríguez, T.A.; Greene, N.D.; Weninger, W.J.; Simeone, A.; Copp, A.J.; Beddington, R.S.P.; Dunwoodie, S.L. Folic acid prevents exencephaly in Cited2 deficient mice. *Hum. Mol. Genet.* **2002**, *11*, 283–293. [CrossRef] [PubMed]
20. Bamforth, S.D.; Bragança, J.; Eloranta, J.J.; Murdoch, J.N.; Marques, F.I.; Kranc, K.R.; Farza, H.; Henderson, D.J.; Hurst, H.C.; Bhattacharya, S. Cardiac malformations, adrenal agenesis, neural crest defects and exencephaly in mice lacking Cited2, a new Tfap2 co-activator. *Nat. Genet.* **2001**, *29*, 469–474. [CrossRef] [PubMed]
21. Bamforth, S.D.; Bragança, J.; Farthing, C.R.; Schneider, J.E.; Broadbent, C.; Michell, A.C.; Clarke, K.; Neubauer, S.; Norris, D.; A Brown, N.; et al. Cited2 controls left-right patterning and heart development through a Nodal-Pitx2c pathway. *Nat. Genet.* **2004**, *36*, 1189–1196. [CrossRef]
22. Zhang, J.; Hagopian-Donaldson, S.; Serbedzija, G.; Elsemore, J.; Plehn-Dujowich, D.; McMahon, A.P.; Flavell, R.A.; Williams, T. Neural tube, skeletal and body wall defects in mice lacking transcription factor AP-2. *Nature* **1996**, *381*, 238–241. [CrossRef]
23. Schorle, H.; Meier, P.; Buchert, M.; Jaenisch, R.; Mitchell, P.J. Transcription factor AP-2 essential for cranial closure and craniofacial development. *Nature* **1996**, *381*, 235–238. [CrossRef]
24. Brewer, S.; Jiang, X.; Donaldson, S.; Williams, T.; Sucov, H.M. Requirement for AP-2α in cardiac outflow tract morphogenesis. *Mech. Dev.* **2002**, *110*, 139–149. [CrossRef]
25. Weh, E.; Reis, L.M.; Happ, H.C.; Levin, A.V.; Wheeler, P.G.; David, K.L.; Carney, E.; Angle, B.; Hauser, N.; Semina, E.V. Whole exome sequence analysis of Peters anomaly. *Qual. Life Res.* **2014**, *133*, 1497–1511. [CrossRef] [PubMed]
26. Midha, N.; Sidhu, T.; Chaturvedi, N.; Sinha, R.; Shende, D.R.; Dada, T.; Gupta, V.; Sihota, R. Systemic Associations of Childhood Glaucoma: A Review. *J. Pediatr. Ophthalmol. Strabismus* **2018**, *55*, 397–402. [CrossRef] [PubMed]
27. Traboulsi, E.I.; Maumenee, I.H. Peters' Anomaly and Associated Congenital Malformations. *Arch. Ophthalmol.* **1992**, *110*, 1739–1742. [CrossRef]

28. Milunsky, J.M.; Maher, T.M.; Zhao, G.; Wang, Z.; Mulliken, J.B.; Chitayat, D.; Clemens, M.; Stalker, H.J.; Bauer, M.; Burch, M.; et al. Genotype-phenotype analysis of the branchio-oculo-facial syndrome. *Am. J. Med Genet. Part A* **2010**, *155*, 22–32. [CrossRef]
29. Reiber, J.; Sznajer, Y.; Posteguillo, E.G.; Müller, D.; Lyonnet, S.; Baumann, C.; Just, W. Additional clinical and molecular analyses ofTFAP2Ain patients with the branchio-oculo-facial syndrome. *Am. J. Med Genet. Part A* **2010**, *152*, 994–999. [CrossRef]
30. Gestri, G.; Osborne, R.J.; Wyatt, A.W.; Gerrelli, D.; Gribble, S.; Stewart, H.; Fryer, A.; Bunyan, D.J.; Prescott, K.; Collin, J.R.O.; et al. Reduced TFAP2A function causes variable optic fissure closure and retinal defects and sensitizes eye development to mutations in other morphogenetic regulators. *Qual. Life Res.* **2009**, *126*, 791–803. [CrossRef]
31. Hammer, S.; Toenjes, M.; Lange, M.; Fischer, J.J.; Dunkel, I.; Mebus, S.; Grimm, C.; Hetzer, R.; Berger, F.; Sperling, S. Characterization of TBX20 in human hearts and its regulation by TFAP2. *J. Cell. Biochem.* **2008**, *104*, 1022–1033. [CrossRef]
32. Satoda, M.; Zhao, F.; Diaz, G.A.; Burn, J.; Goodship, J.; Davidson, H.R.; Pierpont, M.E.M.; Gelb, B.D. Mutations in TFAP2B cause Char syndrome, a familial form of patent ductus arteriosus. *Nat. Genet.* **2000**, *25*, 42–46. [CrossRef]
33. Arkell, R.; Beddington, R.S. BMP-7 influences pattern and growth of the developing hindbrain of mouse embryos. *Developement* **1997**, *124*, 1–12.
34. Mitchell, P.J.; Timmons, P.M.; Hebert, J.M.; Rigby, P.W.; Tjian, R. Transcription factor AP-2 is expressed in neural crest cell lineages during mouse embryogenesis. *Genes Dev.* **1991**, *5*, 105–119. [CrossRef] [PubMed]
35. Hutson, M.R.; Kirby, M.L. Neural crest and cardiovascular development: A 20-year perspective. *Birth Defects Res. Part C: Embryo Today: Rev.* **2003**, *69*, 2–13. [CrossRef]
36. Brewer, S.; Feng, W.; Huang, J.; Sullivan, S.; Williams, T. Wnt1-Cre-mediated deletion of AP-2α causes multiple neural crest-related defects. *Dev. Boil.* **2004**, *267*, 135–152. [CrossRef]
37. Hébert, J.M.; McConnell, S.K. Targeting of cre to the Foxg1 (BF-1) Locus Mediates loxP Recombination in the Telencephalon and Other Developing Head Structures. *Dev. Boil.* **2000**, *222*, 296–306. [CrossRef] [PubMed]
38. Moses, K.A.; DeMayo, F.J.; Braun, R.M.; Reecy, J.M.; Schwartz, R.J. Embryonic expression of an Nkx2-5/Cre gene using ROSA26 reporter mice. *Genes* **2001**, *31*, 176–180. [CrossRef] [PubMed]
39. Danielian, P.; Muccino, D.; Rowitch, D.H.; Michael, S.K.; McMahon, A.P. Modification of gene activity in mouse embryos in utero by a tamoxifen-inducible form of Cre recombinase. *Curr. Boil.* **1998**, *8*, 1323–S2. [CrossRef]
40. Yang, L.; Cai, C.-L.; Lin, L.; Qyang, Y.; Chung, C.; Monteiro, R.; Mummery, C.L.; Fishman, G.I.; Cogen, A.; Evans, S.M. Isl1Cre reveals a common Bmp pathway in heart and limb development. *Development* **2006**, *133*, 1575–1585. [CrossRef]
41. Lallemand, Y.; Luria, V.; Haffner-Krausz, R.; Lonai, P. Maternally expressed PGK-Cre transgene as a tool for early and uniform activation of the Cre site-specific recombinase. *Transgenic Res.* **1998**, *7*, 105–112. [CrossRef]
42. Soriano, P. Generalized lacZ expression with the ROSA26 Cre reporter strain. *Nat. Genet.* **1999**, *21*, 70–71. [CrossRef]
43. Srinivas, S.; Watanabe, T.; Lin, C.-S.; William, C.M.; Tanabe, Y.; Jessell, T.M.; Costantini, F. Cre reporter strains produced by targeted insertion of EYFP and ECFP into the ROSA26 locus. *BMC Dev. Boil.* **2001**, *1*, 4. [CrossRef]
44. Markel, P.; Shu, P.; Ebeling, C.; Carlson, G.A.; Nagle, D.L.; Smutko, J.S.; Moore, K.J. Theoretical and empirical issues for marker-assisted breeding of congenic mouse strains. *Nat. Genet.* **1997**, *17*, 280–284. [CrossRef] [PubMed]
45. Bamforth, S.D.; Schneider, J.E.; Bhattacharya, S. High-Throughput Analysis of Mouse Embryos by Magnetic Resonance Imaging. *Cold Spring Harb. Protoc.* **2012**, *2012*, 93–101. [CrossRef] [PubMed]
46. Geyer, S.; Mohun, T.J.; Weninger, W.J. Visualizing Vertebrate Embryos with Episcopic 3D Imaging Techniques. *Sci. World J.* **2009**, *9*, 1423–1437. [CrossRef] [PubMed]
47. Weninger, W.J.; Mohun, T.J. Three-dimensional analysis of molecular signals with episcopic imaging techniques. *Methods Mol. Biol.* **2007**, *411*, 35–46. [PubMed]
48. Johnson, A.-L.; Bamforth, S.D. Molecular Pathways and Animal Models of d-Transposition of the Great Arteries. In *Congenital Heart Diseases: The Broken Heart*; Rickert-Sperling, S., Kelly, R.G., Driscoll, D.J., Eds.; Springer Vienna: Vienna, Austria, 2016; pp. 449–458. [CrossRef]

49. Unolt, M.; Putotto, C.; Silvestri, L.M.; Marino, D.; Scarabotti, A.; Massaccesi, V.; Caiaro, A.; Versacci, P.; Marino, B. Transposition of great arteries: New insights into the pathogenesis. *Front. Pediatr.* **2013**, *1*, 1–11. [CrossRef]
50. Zhang, Z.; Cerrato, F.; Xu, H.; Vitelli, F.; Morishima, M.; Vincentz, J.; Furuta, Y.; Ma, L.; Martin, J.F.; Baldini, A.; et al. Tbx1 expression in pharyngeal epithelia is necessary for pharyngeal arch artery development. *Development* **2005**, *132*, 5307–5315. [CrossRef]
51. Cai, C.-L.; Liang, X.; Shi, Y.; Chu, P.-H.; Pfaff, S.L.; Chen, J.; Evans, S. Isl1 Identifies a Cardiac Progenitor Population that Proliferates Prior to Differentiation and Contributes a Majority of Cells to the Heart. *Dev. Cell* **2003**, *5*, 877–889. [CrossRef]
52. Park, E.J.; Ogden, L.A.; Talbot, A.; Evans, S.; Cai, C.-L.; Black, B.L.; Frank, D.U.; Moon, A.M. Required, tissue-specific roles for Fgf8 in outflow tract formation and remodeling. *Development* **2006**, *133*, 2419–2433. [CrossRef]
53. Engleka, K.A.; Manderfield, L.J.; Brust, R.; Li, L.; Cohen, A.; Dymecki, S.M.; Epstein, J.A. Islet1 derivatives in the heart are of both neural crest and second heart field origin. *Circ. Res.* **2012**, *110*, 922–926. [CrossRef] [PubMed]
54. Macdonald, S.T.; Bamforth, S.D.; Chen, C.-M.; Farthing, C.R.; Franklyn, A.; Broadbent, C.; Schneider, J.E.; Saga, Y.; Lewandoski, M.; Bhattacharya, S. Epiblastic Cited2 deficiency results in cardiac phenotypic heterogeneity and provides a mechanism for haploinsufficiency. *Cardiovasc. Res.* **2008**, *79*, 448–457. [CrossRef]
55. Van Otterloo, E.; Li, H.; Jones, K.L.; Williams, T. AP-2α and AP-2β cooperatively orchestrate homeobox gene expression during branchial arch patterning. *Development* **2018**, *145*, dev157438. [CrossRef] [PubMed]
56. Lewis, A.E.; Vasudevan, H.N.; O'Neill, A.K.; Soriano, P.; Bush, J.O. The widely used Wnt1-Cre transgene causes developmental phenotypes by ectopic activation of Wnt signaling. *Dev. Boil.* **2013**, *379*, 229–234. [CrossRef] [PubMed]
57. Wang, X.; Astrof, S. Neural crest cell-autonomous roles of fibronectin in cardiovascular development. *Development* **2015**, *143*, 88–100. [CrossRef] [PubMed]
58. Olson, E.; Arnold, H.-H.; Rigby, P.; Wold, B. Know Your Neighbors: Three Phenotypes in Null Mutants of the Myogenic bHLH Gene MRF4. *Cell* **1996**, *85*, 1–4. [CrossRef]
59. Bergwerff, M.; DeRuiter, M.C.; Hall, S.; E Poelmann, R.; Groot, A.G.-D. Unique vascular morphology of the fourth aortic arches: Possible implications for pathogenesis of type-B aortic arch interruption and anomalous right subclavian artery. *Cardiovasc. Res.* **1999**, *44*, 185–196. [CrossRef]
60. Lindsay, E.A.; Vitelli, F.; Su, H.; Morishima, M.; Huynh, T.; Pramparo, T.; Jurecic, V.; Ogunrinu, G.; Sutherland, H.F.; Scambler, P.; et al. Tbx1 haploinsufficiency in the DiGeorge syndrome region causes aortic arch defects in mice. *Nature* **2001**, *410*, 97–101. [CrossRef]
61. Randall, V.; McCue, K.; Roberts, C.; Kyriakopoulou, V.; Beddow, S.; Barrett, A.; Vitelli, F.; Prescott, K.; Shaw-Smith, C.; Devriendt, K.; et al. Great vessel development requires biallelic expression of Chd7 and Tbx1 in pharyngeal ectoderm in mice. *J. Clin. Investig.* **2009**, *119*, 3301–3310. [CrossRef]
62. Kunz, L.H.; Gilbert, W.M.; Towner, D. Increased incidence of cardiac anomalies in pregnancies complicated by gastroschisis. *Am. J. Obstet. Gynecol.* **2005**, *193*, 1248–1252. [CrossRef]
63. Gibbin, C.; Touch, S.; Broth, R.E.; Berghella, V. Abdominal wall defects and congenital heart disease. *Ultrasound Obstet. Gynecol.* **2003**, *21*, 334–337. [CrossRef]
64. Koçak, G.; Önal, Ç.; Koçak, A.; Karakurt, C.; Ateş, Ö.; Çayli, S.R.; Yoloğlu, S. Prevalence and Outcome of Congenital Heart Disease in Patients with Neural Tube Defect. *J. Child Neurol.* **2008**, *23*, 526–530. [CrossRef]
65. Xu, P.-X.; Zheng, W.; Laclef, C.; Maire, P.; Maas, R.L.; Peters, H.; Xu, X. Eya1 is required for the morphogenesis of mammalian thymus, parathyroid and thyroid. *Development* **2002**, *129*, 3033–3044.
66. Guo, C.; Sun, Y.; Zhou, B.; Adam, R.M.; Li, X.; Pu, W.T.; Morrow, B.E.; Moon, A.; Li, X. A Tbx1-Six1/Eya1-Fgf8 genetic pathway controls mammalian cardiovascular and craniofacial morphogenesis. *J. Clin. Investig.* **2011**, *121*, 1585–1595. [CrossRef] [PubMed]
67. Molin, D.G.; DeRuiter, M.C.; Wisse, L.J.; Azhar, M.; Doetschman, T.; Poelmann, R.; Groot, A.C.G.-D. Altered apoptosis pattern during pharyngeal arch artery remodelling is associated with aortic arch malformations in Tgfβ2 knock-out mice. *Cardiovasc. Res.* **2002**, *56*, 312–322. [CrossRef]
68. Roest, P.A.; Nordstrand, H.; Wisse, L.J.; Poelmann, R.; Eriksson, U.; Groot, A.C.G.-D. Disturbed morphogenesis of cardiac outflow tract and increased rate of aortic arch anomalies in the offspring of diabetic rats. *Birth Defects Res. Part A: Clin. Mol. Teratol.* **2004**, *70*, 927–938. [CrossRef]

69. Macatee, T.L.; Hammond, B.P.; Arenkiel, B.R.; Francis, L.; Frank, D.U.; Moon, A.M. Ablation of specific expression domains reveals discrete functions of ectoderm- and endoderm-derived FGF8 during cardiovascular and pharyngeal development. *Development* **2003**, *130*, 6361–6374. [CrossRef] [PubMed]
70. Knight, R.; Javidan, Y.; Zhang, T.; Nelson, S.; Schilling, T.F. AP2-dependent signals from the ectoderm regulate craniofacial development in the zebrafish embryo. *Development* **2005**, *132*, 3127–3138. [CrossRef]
71. Brewer, S.; Williams, T. Loss of AP-2α impacts multiple aspects of ventral body wall development and closure. *Dev. Boil.* **2004**, *267*, 399–417. [CrossRef]
72. Trainor, P. Specification of neural crest cell formation and migration in mouse embryos. *Semin. Cell Dev. Boil.* **2005**, *16*, 683–693. [CrossRef] [PubMed]
73. Bostrom, M.P.; Hutchins, G.M. Arrested rotation of the outflow tract may explain double-outlet right ventricle. *Circ.* **1988**, *77*, 1258–1265. [CrossRef]
74. LoMonico, M.P.; Bostrom, M.P.G.; Moore, G.W.; Hutchins, G.M. Arrested Rotation of the Outflow Tract May Explain Tetralogy of Fallot and Transposition of the Great Arteries. *Pediatr. Pathol.* **1988**, *8*, 267–281. [CrossRef]
75. Scherptong, R.W.; Jongbloed, M.R.; Wisse, L.J.; Bartelings, M.M.; Poelmann, R.; Schalij, M.J.; Groot, A.C.G.-D.; Vicente-Steijn, R. Morphogenesis of outflow tract rotation during cardiac development: The pulmonary push concept. *Dev. Dyn.* **2012**, *241*, 1413–1422. [CrossRef] [PubMed]
76. Baardman, M.E.; Zwier, M.V.; Wisse, L.J.; De Groot, A.C.G.; Kerstjens-Frederikse, W.S.; Hofstra, R.M.W.; Jurdzinski, A.; Hierck, B.P.; Jongbloed, M.R.M.; Berger, R.M.F.; et al. Common arterial trunk and ventricular non-compaction in Lrp2 knockout mice indicate a crucial role of LRP2 in cardiac development. *Dis. Model. Mech.* **2016**, *9*, 413–425. [CrossRef] [PubMed]

Journal of
Cardiovascular
Development and Disease

MDPI

Article

The Needle in the Haystack—Searching for Genetic and Epigenetic Differences in Monozygotic Twins Discordant for Tetralogy of Fallot

Marcel Grunert [1,2,3], Sandra Appelt [1,2,3], Paul Grossfeld [4] and Silke R. Sperling [1,2,3,5,*]

1 Cardiovascular Genetics, Charité—Universitätsmedizin Berlin, 13125 Berlin, Germany; marcel.grunert@charite.de (M.G.); sandra.appelt@charite.de (S.A.)
2 Berlin Institute of Health (BIH), 10178 Berlin, Germany
3 DZHK (German Centre for Cardiovascular Research), Partner Site Berlin, 10178 Berlin, Germany
4 Division of Cardiology, University of California San Diego, Rady's Hospital MC 5004, San Diego, CA 92123, USA; pgrossfeld@health.ucsd.edu
5 Department of Biology, Chemistry, and Pharmacy, Freie Universität Berlin, 14195 Berlin, Germany
* Correspondence: silke.sperling@charite.de; Tel.: +49-30450540123

Received: 3 November 2020; Accepted: 30 November 2020; Published: 2 December 2020

Abstract: Congenital heart defects (CHDs) are the most common birth defect in human with an incidence of almost 1% of all live births. Most cases have a multifactorial origin with both genetics and the environment playing a role in its development and progression. Adding an epigenetic component to this aspect is exemplified by monozygotic twins which share the same genetic background but have a different disease status. As a result, the interplay between the genetic, epigenetic and the environmental conditions might contribute to the etiology and phenotype. To date, the underlying causes of the majority of CHDs remain poorly understood. In this study, we performed genome-wide high-throughput sequencing to examine the genetic, structural genomic and epigenetic differences of two identical twin pairs discordant for Tetralogy of Fallot (TOF), representing the most common cyanotic form of CHDs. Our results show the almost identical genetic and structural genomic identity of the twins. In contrast, several epigenetic alterations could be observed given by DNA methylation changes in regulatory regions of known cardiac-relevant genes. Overall, this study provides first insights into the impact of genetic and especially epigenetic factors underlying monozygotic twins discordant for CHD like TOF.

Keywords: congenital heart disease; Tetralogy of Fallot; monozygotic twins; discordant phenotype; genetics; variations; epigenetics; DNA methylation; candidate genes

1. Introduction

The heart is the first functional organ during embryogenesis, and congenital heart disease (CHD) represents the most common birth defect in humans, affecting about 1% of all newborns [1]. Despite improvements in recognition and therapeutic opportunities based on anatomical, physiological and surgical considerations, CHD remains a leading cause of infant and child mortality. The majority of CHDs are most likely caused be the interplay of multiple subtle genetic, structural genomic or epigenetic alterations [2,3]. In addition, most of them are modulated by gen–environment interactions [2], of which epigenetic alterations are proposed to represent an important transmitter. The symptoms of CHD may vary from none to severe, which attests to its complex nature. This spread is well illustrated in Tetralogy of Fallot (TOF), the most common cyanotic form of CHDs. TOF is characterized by a ventricular septal defect (VSD) with an overriding aorta as well as an obstruction of the right ventricular outflow tract (pulmonary stenosis) and right ventricular hypertrophy. These four anatomical features can all exhibit variable levels of severity.

Over recent decades and in particular with the advent of high-throughput DNA sequencing, several CHD-associated sequence variations have been identified by genetic studies of affected individuals and families [3–8]. Using a homogeneous TOF cohort with well-defined features, we recently identified a multigenic background of rare deleterious mutations in several genes, which discriminate TOF cases from controls and which are essential for apoptosis and cell growth, the assembly of the sarcomere as well as for the neural crest and secondary heart field [9]. One central mechanism of epigenetic control is DNA methylation. Thus, we also performed a genome-wide DNA methylation study on myocardial biopsies of TOF and VSD patients [10]. We found clear methylation differences between patients and controls and moreover, between patient groups. However, the underlying specific causes for the majority of CHDs including complex forms such as TOF remain poorly understood.

Monozygotic twins are also known as identical twins because they share nearly 100% of their genetic information stored in DNA. However, they are often discordant for complex diseases such as diabetes, neurodevelopmental disorders, cancer as well as CHD [11–14]. Considering that monozygotic twins are genetically identical, epigenetic mechanisms like DNA methylation might be modulators of the phenotypic discordance by mediating between the environment and phenotypic expression [13]. For CHD for example, Lyu et al. showed, in the case of an identical twin pair discordant for double outlet right ventricle, a high correlation between hypermethylated promoters based on reduced representation bisulfite sequencing and down-regulated gene expression levels in the patient compared to the healthy twin [14]. In this study, we will investigate for the first-time genome-wide genetic and epigenetic differences between two monozygotic twin pairs discordant for TOF, providing a deeper understanding of the interplay between genetic, structural genomic and epigenetic alterations involved in the etiology of this complex disease.

2. Materials and Methods

2.1. Study Participants and Ethics Statement

To obtain genomic DNA (gDNA) for whole genome sequencing (WGS) and whole genome bisulfite sequencing (WGBS), blood samples were taken from four individuals (two identical twins discordant for TOF, i.e., one affected case each (i.e., Twin1_TOF and Twin2_TOF) and one healthy monozygotic sibling each (i.e., Twin1_H and Twin2_H)). The first pair of twins are male individuals (i.e., Twin1) and the second pair are female individuals (i.e., Twin2) (Figure 1). Since a healthy co-twin in a discordant twin pair serves as a well-matched control with the same genetic background, no further controls were included in this study. The local institutional review board of University of California San Diego approved the study (UCSD IRB protocol #111523) and informed consent was obtained from all participants or guardians. The study protocol conforms to the ethical guidelines of the 1975 Declaration of Helsinki.

2.2. Whole Genome Sequencing (WGS)

Genomic DNA from blood of TOF patients and healthy siblings was extracted using Puregene DNA purification kit (Gentra). DNA degradation and contamination were monitored on 1% agarose gels. Moreover, DNA concentration was measured using Qubit DNA Assay Kit in Qubit 2.0 Flurometer (Life Technologies, Carlsbad, CA, USA). Library preparation and sequencing (2×150 bp paired-end Illumina sequencing; NextSeq PE150 with Q30 $\geq$ 80%) was performed by Novogene. Briefly, a total amount of 1 μg DNA per sample was used as input material for the DNA sample preparations. Sequencing libraries were generated using NEBNext DNA Library Prep Kit following manufacturer's recommendations and indices were added to each sample. The genomic DNA was randomly fragmented to a size of 350 bp by shearing, then DNA fragments were end polished, A-tailed, and ligated with the NEBNext adapter for Illumina sequencing, and further PCR enriched by P5 and indexed P7 oligos. The PCR products were purified (AMPure XP system) and resulting libraries were analyzed for size distribution by Agilent 2100 Bioanalyzer and quantified using real-time PCR.

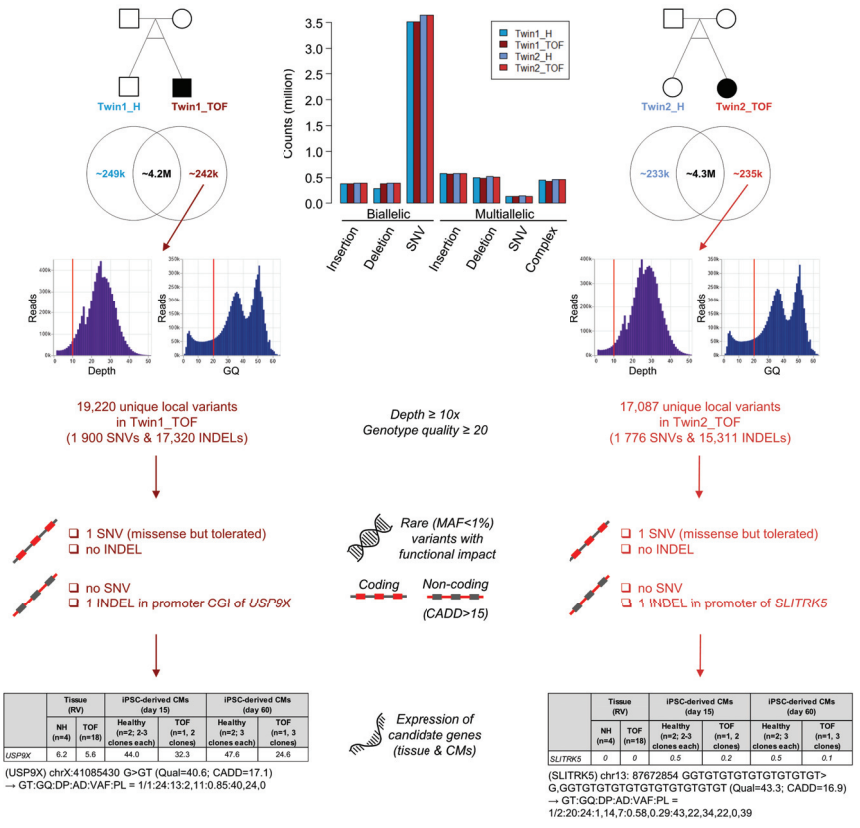

	Tissue (RV)		iPSC-derived CMs (day 15)		iPSC-derived CMs (day 60)	
	NH (n=4)	TOF (n=18)	Healthy (n=2; 2-3 clones each)	TOF (n=1, 2 clones)	Healthy (n=2; 3 clones each)	TOF (n=1, 3 clones)
USP9X	6.2	5.6	44.0	32.3	47.6	24.6

	Tissue (RV)		iPSC-derived CMs (day 15)		iPSC-derived CMs (day 60)	
	NH (n=4)	TOF (n=18)	Healthy (n=2; 2-3 clones each)	TOF (n=1, 2 clones)	Healthy (n=2; 3 clones each)	TOF (n=1, 3 clones)
SLITRK5	0	0	0.5	0.2	0.5	0.1

Figure 1. Filtering of local variations and candidate genes identified in affected Tetralogy of Fallot (TOF) twins using whole genome sequencing. Variant positions are based human reference genome (GRCh38.p13/hg38). AD, allelic depth; CADD, combined annotation dependent depletion; CMs, cardiomyocytes; DP, read depth; GT, genotype; GQ, genotype quality; H, healthy; INDEL, insertion and deletion; MAF, minor allele frequency; NH, normal heart; PL = Phred-scaled genotype likelihoods; Qual, base quality (Phred score); RV, right ventricle; SNV, single nucleotide variations; TOF, Tetralogy of Fallot; VAF, variant allele frequency.

Each sample was sequenced on four sequencing lanes (Table S1). On average, sequencing resulted in approximately 332 million read pairs per sample (Table S1). The quality of the sequencing samples was checked using FASTQC v1.7 [15] and Qualimap v2.2.1 [16]. All samples passed sequence quality. On average, a duplication rate of 10.4%, a GC content of 40.4% and mean base quality of 37.9 (Phred score) were observed over all samples (Table S1 and Figure S1A). After initial quality check, the reads were mapped to the human reference genome (GRCh38.p13/hg38) using Bowtie2 v2.4.1 with the "very-sensitive" parameter setting, which is more sensitive and more accurate [17]. On average, 98.8% of the reads per sample could be mapped. The average sequencing read depth over the human reference genome is 30.1× with a coverage of 99.5% (Table S2 and Figure S1B). Duplicate reads were marked using Picard tools v1.140 (http://broadinstitute.github.io/picard, v1.140).

Calling of local variations (single nucleotide variations (SNVs) as well as insertions and deletions; INDELs) was performed using DeepVariant v0.10.0 with default parameters [18]. Variants that passed DeepVariant default quality filters and with a genotype quality greater than or equal to 20 and a read depth greater than or equal to 10 were annotated using Ensembl Variant Effect Predictor (VEP;

release 100) [19]. Local variations with a minor allele frequency greater or equal than 0.01 (1%) in the 1000 Genomes or Genome Aggregation Database (gnomAD) global populations [20] as well as variations with low functional impact based on Ensembl calculated variant consequences were filtered out [19]. Non-synonymous variants must be predicted to be damaging by either PolyPhen-2 [21], SIFT [22] or MutationTaster2 [23]. Moreover, variants in the non-coding region were filtered for those with a CADD (Combined Annotation Dependent Depletion) score greater than 15 (Phred-scaled) [24], a cutoff on deleteriousness. Structural variations (SVs) were called using Manta v1.6.0 with default parameters [25]. Moreover, common SVs based on gnomAD-SV were filtered out [20]. Copy number variations (CNVs) were called using Control-FREEC v11.5 with default parameters [26]. Both SVs and CNVs were further overlapped with genomic features obtained from VEP.

2.3. Whole Genome Bisulfite Sequencing (WGBS)

For WGBS, gDNA obtained from blood of the two twin pairs (in total four individuals) was extracted using Puregene DNA purification kit (Gentra) and further used to create bisulfite-treated DNA libraries. Library preparation and sequencing was performed by Novogene using EZ DNA Methylation Gold Kit from Zymo Research and 150 bp paired-end Illumina-Kit. Briefly, unmethylated cl857 Sam7 Lambda DNA (48,502 bp, Promega D1521) was combined with gDNA to act as an internal control to monitor the bisulfite conversion rate. Afterwards, DNA was sheared into 200–400 bp fragments, sequence ends were repaired and 3′ ends were adenylated. Next, methylation sequencing adapters were added and DNA was treated with bisulfite. Treatment of DNA with sodium bisulfite deaminates unmethylated cytosines to uracil while methylated cytosines are resistant to this conversion, allowing therefore for the discrimination between methylated and unmethylated CpG sites. Finally, bisulfite treated library was subjected to PCR amplification followed by standard DNA paired-end Illumina sequencing (HiSeq PE150 with Q30 ≥ 80%). In general, sodium bisulfite pre-treatment of DNA coupled with high-throughput sequencing allows us to study DNA methylation quantitatively and genome-wide at single cytosine site resolution.

Each sample was sequenced on six sequencing lanes (Table S3). On average, sequencing resulted in approximately 344 million read pairs per sample (Table S3). The quality of the sequencing samples was checked using FASTQC v1.7 and Qualimap v2.2.1. All samples passed sequence quality. On average, a duplication rate of 10%, a GC content of 21.1% and mean base quality of 36.95 (Phred score) were observed over all samples (Table S3 and Figure S2). The bisulfite conversation was efficient based on the base composition (<1–2% of C in the forward strand and G in the reverse strand) (Figure S3A) and based on the bisulfite conversion rate (>99.7%) (Figure S3B). The bisulfite conversion efficiency was calculated for each sample based on unmethylated control sequences (spike-ins) added to the library prior to fragmentation (i.e., 100—percentage of C methylated in CpG context when mapping against the control genome *Enterobacteria phage lambda*). After initial quality assessment, adapter trimming was performed by Trim Galore v0.4.4 [27]. Afterwards, sequencing reads were mapped to the human reference genome (GRCh38.p3) using Bismark v0.18.2 [28]. On average, 75% of the ~344 million reads per sample could be mapped (Table S4). After mapping, reads of all sequencing lanes were merged for each sample using SAMtools v1.2 [29] and subjected to deduplication using Bismark. Out of ~258 million mapped reads per sample, ~229 million left after deduplication (Tables S4 and S5). All mapped reads have a high mean base quality of ~35.7 (Phred score) with a GC content of ~21.3% (Figure S4A and Table S5). The average sequencing depth is 21.1× per base (Figure S4B and Table S5). To correct for methylation bias at 3′ and 5′ end of each read, MethylDackel v0.3.0 was used [30]. For forward reads, no cutoffs were suggested; however, there are clear drops in the methylation level at the beginning (15–18 bp) and end (149 bp) of the reads for which cutoffs were suggested by MethylDackel (Figure S5A) and incorporated during methylation level extraction using Bismark. As expected, the samples have, on average, a CpG methylation rate of 82.5%. CHG and CHH methylation rates are very low at under 1% each (Figure S5B and Table S5). Differential methylation analyses of CpG sites between two samples are performed using methylSig v0.4.4 [31]. As methylSig only allows comparisons with at least two

samples per group, each sample was duplicated. Furthermore, CpGs were filtered by coverage with a minimum coverage of 10 and a maximum of 500 (default values). Differential methylation is defined by a methylation difference of at least 25%. Differential methylated CpGs are further overlapped (at least 1 bp) or associated (i.e., nearest gene approach) with hg38 annotated genomic features as described in detail elsewhere [10]. Briefly, the overlap includes 50,497 promoters of UCSC RefSeq genes (−500 bp/+2 kb to TSS); 30,477 CpG islands (CGIs) based on UCSC track "cpgIslandsExt"; promoter CGIs (i.e., overlap of promoter and CGIs with at least 1 bp), CGI shores (i.e., regions outside CpG islands but within 2 kb of any CpG island), transcription factor binding sites (TFBS) predicted by the Transfac Matrix Database and conserved in the multiple alignment of human, mouse and rat, including cardiac transcription factors (TFs); and cardiac enhancers (p300 ChIP-seq data of human adult and fetal hearts [32]).

2.4. Filtering for Disease-Relevant Genetic and Epigenetic Alterations

Candidate genes with genetic, structural genomic or epigenetic alterations were overlapped with various datasets to filter for known or possible disease-relevant genes. This includes heart- and muscle relevant genes (865 genes based on several resources) [9]; cardiovascular-associated genes (list of 4275 genes created by the Cardiovascular Gene Annotation Initiative in collaboration with EMBL-EBI); genes which are differentially expressed in CHD patients (in particular TOF, VSD, atrial septal defect (ASD), hypoplastic left heart syndrome (HLHS), transposition of the great arteries combined with pulmonary artery (TGA-PS)) [9,33–37]; genes which are differentially methylated in the promoter, gene body or related enhancer of CHD patients (in particular TOF, VSD, LS-CHD) [10,38–41]; genes which overlap CNVs associated with CHD (including TOF, LS-CHD, HLHS and conotruncal defects) [42–56]; known human CHD genes [3,6,54]; and genes which are differentially expressed and targeted by differentially expressed microRNAs in CHD patients (TOF and HLHS) [57–59]. Moreover, candidate genes must be expressed (RPKM (reads per kilo base per million mapped reads) or TPM (transcript per million) value > 1) in the right ventricular tissue of normal or TOF hearts [9], or during cardiac differentiation (i.e., in cardiomyocytes of day 15 and/or day 60 derived from induced pluripotent stem cells of healthy, unaffected individuals and TOF patients) [60].

2.5. Statistics

General bioinformatics and statistical analyses were conducted using R (including Bioconductor packages) and Perl.

3. Results

3.1. Genomic Variations in Affected Twins

Whole genome sequencing of monozygotic twins resulted in approximately 4.4–4.6 million local variations (i.e., SNVs and INDELs) for each twin, with SNVs constituting the largest class of called genomic variations. Out of these raw variants, up to 6% are unique for either twin. Considering that monozygotic twins are genetically identical, this number seems very high; however, there are differences in terms of sequencing depth and quality, which may result in different calling results. Using a minimum sequencing depth of 10× and a genotype quality of at least 20, the number of local variants drops in Twin1_TOF from 4,167,698 to 19,220 (0.46%) and in Twin2_TOF from 4,331,595 to 17,087 (0.39%) unique ones compared to the respective unaffected twin (Figure 1). To identify possible disease-associated alterations, these unique variants were further annotated and filtered for rare variants (MAF < 1%) with functional impact on the coding or non-coding genomic sequence. For the coding part, this resulted in no single INDEL and only one missense SNV for each affected twin, which are further predicted to be tolerated (Figure 1). For the non-coding sequence of Twin1_TOF, there is a homozygous INDEL (i.e., insertion) in the promoter region of *Ubiquitin Specific Peptidase 9 X-Linked* (*USP9X*). The promoter also represents a CpG island (CGI). In Twin2_TOF, we also identified no SNV but one INDEL in

the promoter of *SLIT and NTRK Like Family Member 5* (*SLITRK5)*. Both non-coding variants are potentially pathogenic with a CADD score greater than 15. The related genes were further checked for being expressed in the human heart. Moreover, considering that TOF is a developmental disorder, these genes should be expressed during development. Thus, we examined their expression in the right ventricular tissue of normal and TOF hearts [9] as well as during cardiac differentiation using cardiomyocytes derived from induced pluripotent stem cells of healthy, unaffected individuals and TOF patients [60]. Out of these two genes, *SLITRK5* is not expressed in the heart or during cardiomyocyte differentiation (Figure 1). We further overlapped the two genes with known cardiovascular-associated genes and several CHD-related datasets, but without any overlap for both genes. In addition to unique variants in the two affected TOF twins (i.e., variants that do not occur in the healthy sibling), we also searched for variations with zygosity differences between the healthy and affected siblings. However, after filtering there is no SNV or INDEL in the coding and non-coding sequence of both twin pairs, which can explain the phenotype differences (Figure S6).

3.2. Structural Genomic Variations in Affected Twins

Besides local variations, we are interested in copy number variations as well as structural variations, which are unique for the affected TOF twins. For Twin1_TOF, we identified 11 CNVs, which are associated with 9 genes (Table S6). The majority of these CNVs are copy number gains (i.e., 9 out of 11) and only two represent a copy number loss. For Twin2_TOF, we found four CNVs (two gains and two losses), of which only one copy number gain affects a genomic feature, namely the rRNA *RNA5SP19*. The very few genomic features affected by CNVs in Twin1_TOF are either protein-coding or T cell receptors, where the latter represent an adaptive immune response (Table S6). The protein-coding genes were checked for cardiac expression and further overlapped with a list of cardiovascular-associated genes and other CHD-related datasets. The latter revealed only for *UDP Glucuronosyltransferase Family 2 Member B17* (*UGT2B17)* an overlap with cardiovascular-associated genes and known CNVs in CHD patients; however, the gene is not expressed in the normal or TOF heart or during cardiomyocyte differentiation. The only expressed gene associated with a CNV in twin1_TOF is *Fc Fragment of IgA Receptor* (*FCAR)*, but without any overlap to other cardiac-related annotations or datasets. In summary, there is no real candidate gene with a CNV in both affected twins.

To find possible disease-relevant SVs, we filtered for unique ones in the affected twins, which are rare and have a high or modifier functional impact. In total, we found 30 rare SVs in Twin1_TOF and 20 rare SVs in Twin2_TOF with modifier impact only, affecting 20 and 13 genes, respectively (Tables S7 and S8 and Figure S7). Both affected twins share five SVs. Overall, 83% of the genes associated with SVs are expressed in the normal or TOF heart or during cardiac differentiation. Moreover, the majority of these expressed genes overlap with several cardiac related genes or datasets. For example, *ANTXR Cell Adhesion Molecule 1 (ANTXR1)* and *L3MBTL Histone Methyl-Lysine Binding Protein 4* (*L3MBTL4)* with SVs in Twin1_TOF are also differentially expressed (significantly up-regulated) in right ventricle of TOF patients compared to normal hearts [9]. Moreover, both are differentially methylated in VSD patients compared to normal hearts (i.e., significantly hypermethylated cardiac enhancer near *ANTXR1* and hypermethylated gene body of *L3MBTL4*) [10]. The genes with SVs in Twin2_TOF, encoding for *Bardet-Biedl Syndrome 2* (*BBS2*) and *Teneurin Transmembrane Protein 4* (*TENM4*), are also associated with differential DNA methylation in VSD cases versus normal hearts (i.e., significantly hypermethylated gene body of *BBS2* and hypermethylated promoter of *TENM4*) [10].

3.3. DNA Methylation Differences between Discordant Twins

To investigate the impact of DNA methylation changes between discordant twins, we performed WGBS and studied the methylation level of approximately 28 million CpG sites in the human genome. In general, the global CpG methylation shows no obvious differences between each affected and healthy twin (Figures S8 and S9A), with a somewhat higher coverage in Twin1_TOF compared to Twin1_H

and a similar one for Twin2_TOF and Twin2_H (Figure S9B). Moreover, genomic features associated to genes have a higher methylation level (Figure 2A).

Next, we searched for differentially methylated CpG sites (DMCs) with at least 25% differences between the discordant twins. We found 299,643 DMCs in Twin1 and ~150,000 more DMCs (in total 457,108) in Twin2 (Table 1). For Twin1, there are more hypomethylated CpGs, while Twin2 is more balanced regarding hypo- and hyper-methylation (Figure 2B,C, left each). However, the overlap of DMCs with genomic features is similar for both twin pairs, with the majority of DMCs in non-coding regions (intergenic and intronic; Figure 2B,C, right each). Nevertheless, there are DMCs in coding and even more interestingly in regulatory regions such as promoters, CGIs, promoter CGIs, CGI shores, TFBS (cardiac and/or located in promoters) and cardiac enhancers (Table 1).

Table 1. Differentially methylated CpG sites with ≥25% methylation difference between the healthy and affected twin and their overlap (≥1 bp) or association (i.e., nearest gene approach) with different genomic features. CGIs, CpG islands; DMCs, differentially methylated CpGs; H, healthy; TFBS, transcription factor binding site; TOF, Tetralogy of Fallot.

	Twin1_TOF vs. Twin1_H	**Twin2_TOF vs. Twin2_H**
Differentially methylated CpGs (DMCs) with ≥25% methylation difference	*299,643*	*457,108*
DMCs in promoters	18,052	22,537
DMCs in CpG islands (CGIs)	397	713
DMCs in promoter CGIs	131	429
DMCs in CGI shores	17,337	21,455
DMCs at TFBS	23,716	31,789
DMCs at cardiac TFBS	2066	2751
DMCs at TFBS in promoters	2125	2929
DMCs at cardiac TFBS in promoters	215	264
DMCs in cardiac enhancers (p300)	2042	2518

Of particular interest is the methylation pattern of dense regions of CpGs, the CGIs. For Twin1, we found 397 DMCs in CGIs and 131 of these are located in promoters. For Twin2, there are 713 DMCs in CGIs and the majority (in total 429) overlap promoter regions. Next, we overlapped (promoter) CGI-associated genes with cardiovascular-associated genes including known CHD genes and found several cardiac-related genes (Figure 3A,B). In total, there are 4 and 20 genes with DMCs in promoter CGIs for Twin1 and Twin2, respectively. Interestingly, 3 out 4 genes in Twin1 also harbors DMCs in Twin2. These genes are *BARX Homeobox 2* (*BARX2*), *Kinesin Family Member C3* (*KIFC3*) and *Nuclear Factor of Activated T Cells 1* (*NFATC1*). The latter is a transcription factor required for valve formation [61] and thus, a known CHD gene. In addition to *NFACT1*, there is another transcription factor and well-known CHD gene in Twin2 with DMCs in its promoter CGI, namely *T-Box Transcription Factor 20* (*TBX20*) [62,63].

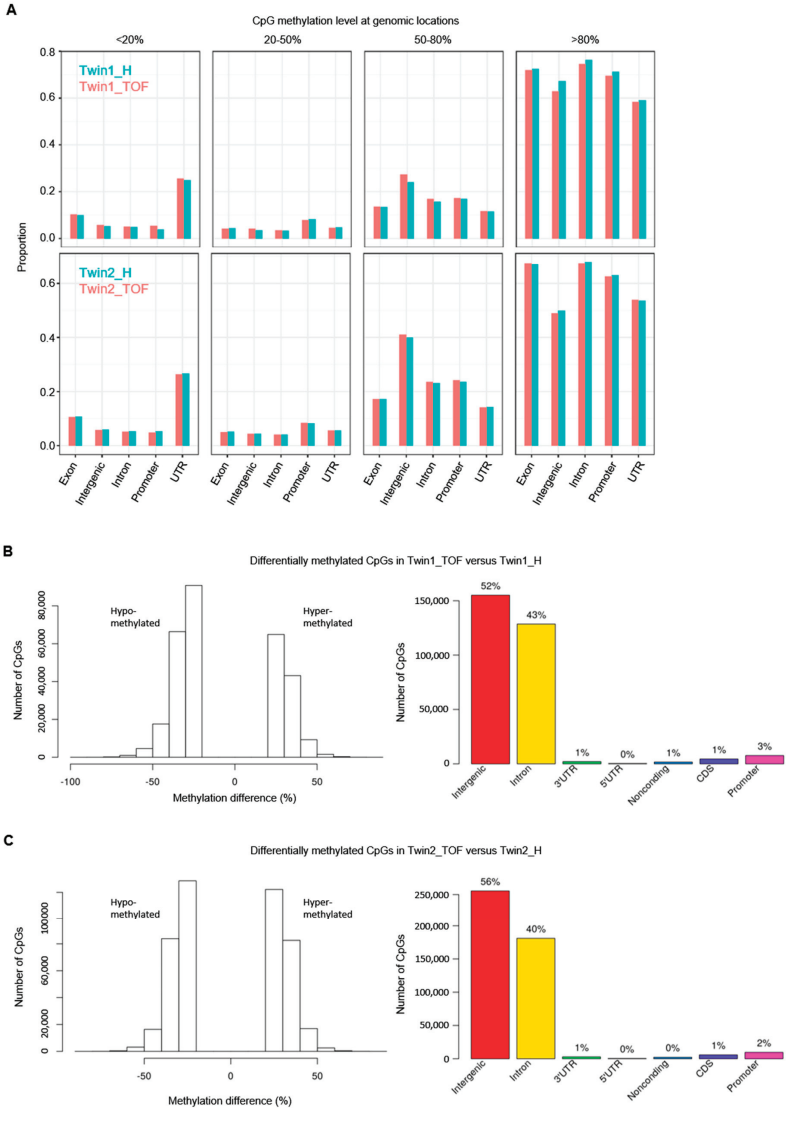

Figure 2. DNA methylation levels and differences of CpG sites in twins and their genomic locations. (**A**) Overview of methylation levels of CpGs at genomic locations. Proportions of CpG are given over the total count for each feature (no pairwise comparison of single CpG sites). (**B**) Differentially methylated (hypo- and hyper-methylated) CpG sites in Twin1_TOF compared to Twin1_H and their genomic locations. (**C**) Differentially methylated (hypo- and hyper-methylated) CpG sites in Twin2_TOF compared to Twin2_H and their genomic locations. Differentially methylated CpGs with at least 25% methylation difference between affected (*_TOF) and healthy (*_H) twin.

Besides the regulatory impact of CpG Islands, we also examined genes that have DMCs at TBFS in their promoter. In total, 27 and 45 genes in Twin1 and Twin2, respectively, harbor such DMCs and overlap with cardiovascular-associated genes (Figure 3C,D). Four of these genes were found between both twin pairs (i.e., *CPNE1, NEDD4L, PPFIA2, RBM12*). Moreover, there are four different known

CHD genes with DMCs at TBFS in their promoter in Twin1 (i.e., *DNAH5, FOXP1, LAMA4, NIPBL*) and Twin2 (i.e., *CACNA1D, CBL, DMD, NSD1*).

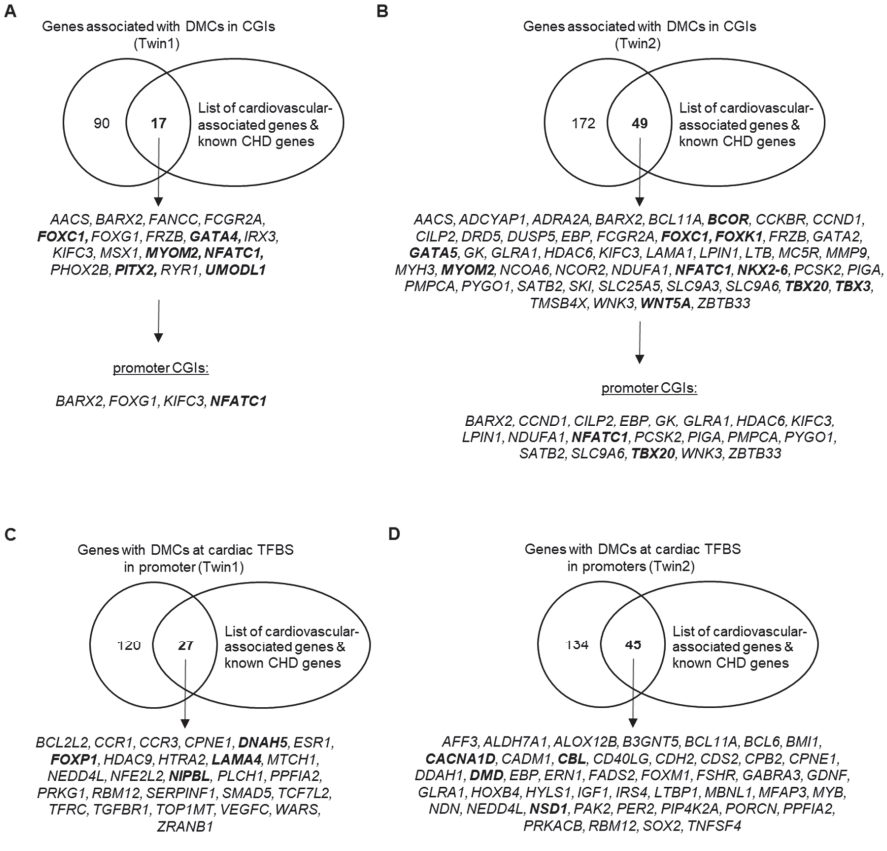

Figure 3. Overlap of protein-coding genes associated with differentially methylated CpGs in CGIs and promoter CGIs or at cardiac TFBS in promoters with cardiovascular-associated genes and known CHD genes. Known CHD genes are marked in bold. (**A**) Genes associated with DMCs of Twin1_TOF versus Twin1_H (i.e., Twin1) in CGIs or promoter CGIs. (**B**) Genes associated with DMCs of Twin2_TOF versus Twin2_H (i.e., Twin2) in CGIs or promoter CGIs. (**C**) Genes with DMCs of Twin1 at cardiac TFBS in their promoter. (**D**) Genes with DMCs of Twin2 at cardiac TFBS in their promoter. CGIs; CpG islands; CHD, congenital heart disease; DMCs, differentially methylated CpG sites; TFBS, transcription factor binding sites.

Figure 4 shows the difference in the methylation level of both twins at the promoter of four selected known CHD genes, including TFBS in these regions. In addition, the mean methylation level obtained from methyl-CpG binding domain (MBD) protein-enriched genome sequencing (MBD-seq) of tissues from normal hearts as well as from a homogenous group of TOF and VSD patients is provided [10]. Figure 4 above shows the methylation level at the promoter CGI of *NFATC1* and *TBX20*. The methylation level at the promoter of two essential cardiac transcription factors, *NKX2-5* and *GATA4*, which both harbor single DMCs in their promoter region with more than 25% methylation difference between healthy and affected twin, is shown in the bottom of Figure 4. In general, the observations in WGBS partially differ with the methylation pattern observed in MBD-seq, which may be due to the resolution (1 bp in WGBS vs. ~150 bp in MDB-seq) and coverage (i.e., single CpGs in WGBS ≥ 5×)

or simply based on the homogeneity of the affected twin compared to other TOF and VSD patients. However, for both WGBS and MBD-seq one can observe methylation alterations in the promoter of these selected genes.

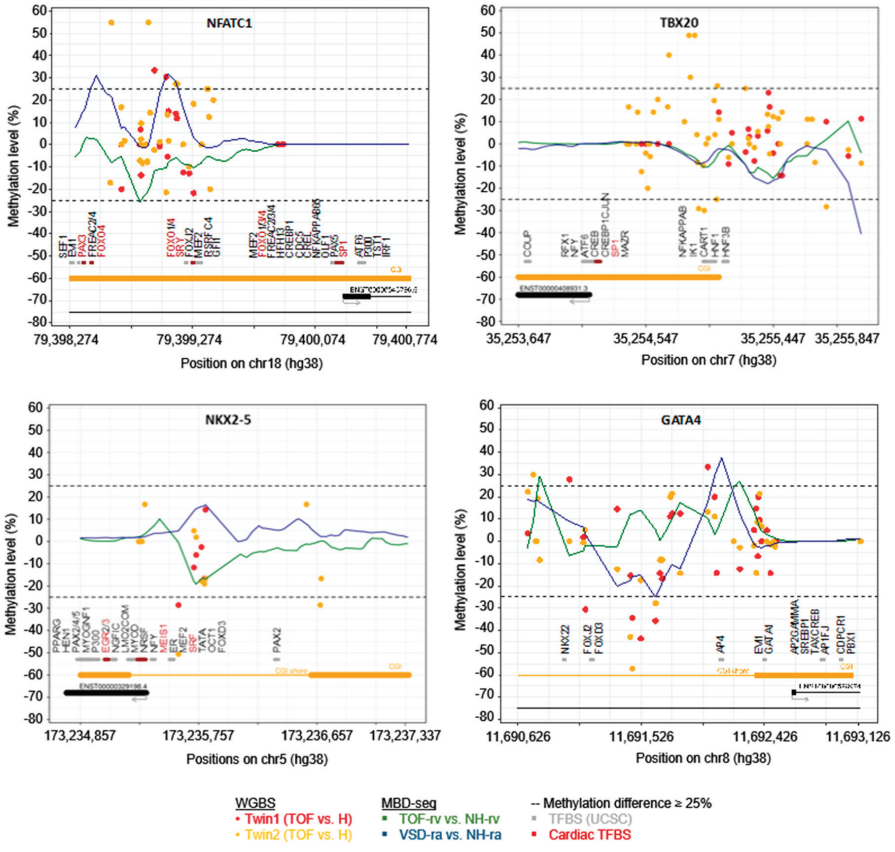

Figure 4. DNA methylation level at promoter regions of *NFATC1*, *TBX20*, *NKX2-5* and *GATA4* in healthy and affected twins obtained by WGBS (n = 1 each; coverage at CpGs ≥ 5×) as well as in right ventricular or atrial tissue of normal hearts and patients with TOF or VSD obtained by methyl-CpG binding domain protein-enriched genome sequencing (MBD-seq) (n = 7 for TOF-rv; n = 8 for VSD-ra; n = 3 for NH-rv; n = 4 for NH-ra). Promoters are defined as −2 kb/+500 bp of transcriptional start site. CGIs and CGI shores are indicated by orange line at the bottom. Moreover, binding sites of transcription factors (obtained from UCSC) are provided in gray or for cardiac factors in red. For WGBS, methylation at single CpG is provided. CGIs, CpG islands; NH, normal heart; H, healthy; RA, right atrium; RV, right ventricle; TFBS, transcription factor binding site; TOF, Tetralogy of Fallot; VSD, ventricular septal defect; WGBS, whole genome bisulfite sequencing.

4. Discussion

Out of millions of unique local variations (i.e., SNVs and INDELs) for each affected twin obtained from WGS, we identified no single candidate gene in one of the two monozygotic discordant twin pairs, which might explain the difference regarding TOF (Figure 1). Searching for candidate genes affected by structural genomic variations, we observed in both TOF twins several SV candidates but no relevant CNVs. For SVs, there are several candidates in both affected twins who are also expressed in the adult heart and during cardiac differentiation (Table S9). Moreover, most of these expressed genes

also overlap with cardiovascular-associated genes and CHD-related datasets. Most interestingly for Twin1_TOF, the affected genes *ANTXR* and *L3MBTL* are also found to be differentially expressed in right ventricle of TOF versus normal hearts [9] and in addition, differentially methylated in right atrium of VSD versus normal hearts [10]. *L3MBTL* is involved in transcriptional repression [64]. Its MBT domain binds to methylated histone residues, which is linked to the formation and maintenance of heterochromatin [65]. For Twin2_TOF, the affected genes *BBS2* and *TENM4* are also differentially methylated in VSD versus normal hearts [10]. However, none of the affected genes is known to be involved in TOF or CHD in general so far. Moreover, since we do not have any tissue available from the twins (only blood samples), we unfortunately cannot make any statement regarding the regulatory impact of these SVs on the expression of related genes. Due to ethical restrictions, it is further practically impossible to obtain such tissue from the healthy, unaffected twin; however, follow-up studies based on induced pluripotent stem cells and derived cardiomyocytes might be an option to verify the evidence for their causative impact.

As mentioned above, some of the genes with SVs in the TOF twins are already known to be associated with differential DNA methylation in cardiac tissue of patients with TOF and in its sub-feature, VSD [10]. To study the epigenetic differences based on DNA methylation between the monozygotic discordant twin pairs, we used blood sample for WGBS as for WES analysis of genetic and structural genomic alteration. CpG methylation can persist in steady-state from early embryonic development throughout a lifetime, and only a fraction of 22% of autosomal CpGs shows dynamic methylation in the normal developmental context [66,67]. With respect to the study of altered DNA methylation pattern, this enables the analysis of up to 80% of CpG methylations in cells independent from the affected cell type. Overall, we observed no differences based on the global CpG methylation between each of the two twin pairs. However, we found numerous single CpGs differentially methylated with more than 25% difference between the twins (Table 1). Most interesting are those DMCs in promoters that also overlap with CGIs or TFBS (Figure 3). Usually, CGIs are largely unmethylated [68] and frequently located in promoters [69]. Multiple methylated CpGs in promoter CGIs cause stable silencing of genes and thus, hypermethylated promoter CGIs are often known to be disease-related [70]. For both affected twins, we found DMCs in the promoter CGI of a gene encoding for the TF NFATC1 (top left of Figure 4), which is required for normal valve formation [61]. Moreover, genetic and structural genomic alterations in *NFATC1* have already been identified in patients with CHD such as VSD or tricuspid atresia [71,72]. For Twin2_TOF, we identified several DMCs in the promoter CGI of *TBX20* (top right of Figure 4), a cardiac TF [63]. Mutations in *TBX20* have been identified in different types of cardiac defects regarding septation, chamber growth, and valvulogenesis [62]. Tbx20 interacts with the TF Gata4 to active both Mef2c and *Nkx2-5* enhancers [73], which all are core cardiac TFs [63]. These factors regulate each other's expression, partly with combinatorial impact of downstream targets. Disturbances of their associated cardiac regulatory network have been associated with various congenital heart malformations [63]. For both cardiac TFs GATA4 and *NKX2-5*, we found DMCs in the promoter region of both affected twins, who further represent CGI shores (bottom of Figure 4). These regions are within 2 kb of a CGI and they are known to occur most of the tissue-specific methylation [74].

There are many other candidate genes associated or overlapping DMCs with different regulatory features (Table 1); however, it clearly shows that the difference between the two monozygotic discordant twin pairs is rather observed in epigenetic alterations than on the genetic or structural genomic level. Nevertheless, the impact of these epigenetic variations on candidate gene expression and thus, their causality for the phenotypic discordance needs to be verified by further studies, in functional respect but also in terms of cases and comparisons (i.e., this study comprises just two cases with each one affected vs. one healthy twin comparison). However, our study confirms other studies on identical twins that discordances in a disease such as CHD cannot be explained by genetic or structural genomic differences [14,75–79]. Moreover, blood-derived DNA might be chimeric between the identical twins and as shared blood circulations have been found during embryogenesis in most monozygotic

twin pregnancies [80], hematopoietic stem cells can be transferred between twins. Such a created hematopoietic system might mask the underlying genetic, structural genomic and also epigenetic differences between the monozygotic twin discordant for a disease like TOF [75].

Recent large-scale studies with up to thousands of CHD cases and of controls only show possible genetic or structural genomic causes for a minority of cases [4,7,44,53,81]. The reasons for this might be found in the multifactoriality paired with complex inheritance patterns and low prevalence [82]. Moreover, the majority of cases occur sporadic, possibly triggered by stochastic or environmental events during maternal pregnancy [83,84]. The latter is accompanied by epigenetic changes such as those related to histone modifications and DNA methylation, important modulators of gene–environment interactions. Moreover, deregulated microRNA abundance levels also seem to play a role in the development of CHD in twins [85]. Stochastic events such as an unequal division of the inner mass cells during twinning or an unequal allocation of developmental markers and precursor cells might be responsible for a discordance in monozygotic twins [86], which might be of interest with respect to a possible premature stop of cellular growth in TOF. Moreover, this may result, for example, in altered sub-populations of ventricular and atrial cardiomyocytes [87], which in turn might be disease-causing. In general, monozygotic twins are up to seven times more likely to develop a congenital heart malformation, which further usually occurs in just one of the twins [86,88]. Reasons for this increased risk include the twin–twin competition for maternal resources resulting in, for example, unequal placental sharing, unequal sharing of the vascular system or other placental mechanisms like diffusion and endocrine function, which increases the probability of a skewed in utero environment affecting the twins [86,89–91]. Interestingly, a study based on the Danish Twin Registry showed (unlike several other studies) that there is no higher risk of CHD in monozygotic twins compared to dizygotic ones [92]. This indicates that the intrauterine environment of twin gestation is predisposed to the development of CHD in a certain way. Moreover, it is suggested that twin gestation changes maternal nutrition to the fetus and nutritional deficiencies might increase the sensitivity of the fetus to other teratogenic factors such as prenatal exposure or poor maternal health [92].

The search for the underlying mechanisms of CHD in twins is like searching for the needle in the haystack. The four pieces of the TOF pathology can all exhibit variable levels of severity and as a result, no two TOF cases are the same. However, studying the genetic and epigenetic mechanisms in identical discordant twins can provide important insights into complex diseases such as congenital heart malformations. Therefore, we studied here the genetic, structural genomic and epigenetic differences of two identical twin pairs discordant for TOF. The two cases show common and unique patterns of epigenetic modifications, which might also be related to a common and unique level of pathological features. Understanding the mechanisms that trigger the molecular plasticity, namely the underlying genetic composition, the epigenetic make-up and environmental insults, is quite challenging but will enhance our current knowledge of CHD.

Supplementary Materials: The following are available online at http://www.mdpi.com/2308-3425/7/4/55/s1, Figure S1: Statistics of reads obtained from whole genome sequencing. Figure S2: Statistics of input reads obtained from whole genome bisulfite sequencing. Figure S3: Bisulfite conversion efficiency. Figure S4: Quality measurements of deduplicated mapped reads obtained from whole genome bisulfite sequencing. Figure S5: Methylation bias and rates. Figure S6: Filtering of possible disease-relevant local variations identified in affected TOF twins based on zygosity differences between healthy and affected sibling. Figure S7: Filtering of possible disease-relevant structural variations (SVs) identified in affected TOF twins using whole genome sequencing. Figure S8: Global DNA methylation levels of twins. Line plots show the DNA methylation along the chromosomal length (GRCh38.p13/hg38). Figure S9: DNA methylation rate and coverage of CpGs. Table S1: Overview of sequencing reads obtained from whole genome sequencing. Table S2: Statistics of read mapping, coverage and read depth in each sample obtained from whole genome sequencing. Table S3: Overview of sequencing reads obtained from whole genome bisulfite sequencing. Table S4: Mapping result of reads obtained from whole genome bisulfite sequencing. Table S5: Read statistics after mapping and deduplication as well as methylation rates over CpGs, CHGs and CHHs in each sample obtained from whole genome bisulfite sequencing. Table S6: Copy number variations identified in Twin1_TOF and Twin2_TOF based on whole genome sequencing data. Table S7: Structural variations uniquely identified in Twin1_TOF based on whole genome sequencing data. Table S8: Structural variations uniquely identified in Twin2_TOF based on whole genome sequencing data. Table S9: Candidate genes with structural variations in Twin1_TOF and/or Twin2_TOF.

Author Contributions: Conceptualization, M.G. and S.R.S.; resources, P.G.; formal analysis, M.G. and S.A.; data curation, M.G. and S.A.; writing—original draft preparation, M.G.; writing—review and editing, M.G., S.R.S. and P.G.; visualization, M.G. and S.A.; supervision, S.R.S. and P.G.; funding acquisition, S.R.S. All authors have read and agreed to the published version of the manuscript.

Funding: This work was supported by the Berlin Institute of Health [BIH-CRG2-ConDi] (S.R.S.).

Acknowledgments: We are deeply grateful to the patients and families for their cooperation. We thank Andreas Perrot for review and discussion of the manuscript.

Conflicts of Interest: The authors declare no conflict of interest.

References

1. van der Linde, D.; Konings, E.E.M.; Slager, M.A.; Witsenburg, M.; Helbing, W.A.; Takkenberg, J.J.M.; Roos-Hesselink, J.W. Birth prevalence of congenital heart disease worldwide: A systematic review and meta-analysis. *J. Am. Coll. Cardiol.* **2011**, *58*, 2241–2247. [CrossRef]
2. Nora, J.J. Multifactorial inheritance hypothesis for the etiology of congenital heart diseases. The genetic-environmental interaction. *Circulation* **1968**, *38*, 604–617. [CrossRef] [PubMed]
3. Rickert-Sperling, S.; Kelly, R.G.; Driscoll, D.J. (Eds.) *Congenital Heart Diseases: The Broken Heart; Clinical Features, Human Genetics and Molecular Pathways*; Springer: Wien, Austria, 2016; ISBN 978-3-7091-1883-2.
4. Page, D.J.; Miossec, M.J.; Williams, S.G.; Monaghan, R.M.; Fotiou, E.; Cordell, H.J.; Sutcliffe, L.; Topf, A.; Bourgey, M.; Bourque, G.; et al. Whole Exome Sequencing Reveals the Major Genetic Contributors to Nonsyndromic Tetralogy of Fallot. *Circ. Res.* **2019**, *124*, 553–563. [CrossRef] [PubMed]
5. Fahed, A.C.; Gelb, B.D.; Seidman, J.G.; Seidman, C.E. Genetics of congenital heart disease: The glass half empty. *Circ. Res.* **2013**, *112*, 707–720. [CrossRef] [PubMed]
6. Andersen, T.A.; Troelsen, K.d.L.L.; Larsen, L.A. Of mice and men: Molecular genetics of congenital heart disease. *Cell. Mol. Life Sci.* **2014**, *71*, 1327–1352. [CrossRef] [PubMed]
7. Sifrim, A.; Hitz, M.-P.; Wilsdon, A.; Breckpot, J.; Turki, S.H.A.; Thienpont, B.; McRae, J.; Fitzgerald, T.W.; Singh, T.; Swaminathan, G.J.; et al. Distinct genetic architectures for syndromic and nonsyndromic congenital heart defects identified by exome sequencing. *Nat. Genet.* **2016**, *48*, 1060–1065. [CrossRef] [PubMed]
8. Jin, S.C.; Homsy, J.; Zaidi, S.; Lu, Q.; Morton, S.; DePalma, S.R.; Zeng, X.; Qi, H.; Chang, W.; Sierant, M.C.; et al. Contribution of rare inherited and de novo variants in 2871 congenital heart disease probands. *Nat. Genet.* **2017**, *49*, 1593–1601. [CrossRef]
9. Grunert, M.; Dorn, C.; Schueler, M.; Dunkel, I.; Schlesinger, J.; Mebus, S.; Alexi-Meskishvili, V.; Perrot, A.; Wassilew, K.; Timmermann, B.; et al. Rare and private variations in neural crest, apoptosis and sarcomere genes define the polygenic background of isolated Tetralogy of Fallot. *Hum. Mol. Genet.* **2014**, *23*, 3115–3128. [CrossRef]
10. Grunert, M.; Dorn, C.; Cui, H.; Dunkel, I.; Schulz, K.; Schoenhals, S.; Sun, W.; Berger, F.; Chen, W.; Sperling, S.R. Comparative DNA methylation and gene expression analysis identifies novel genes for structural congenital heart diseases. *Cardiovasc. Res.* **2016**, *112*, 464–477. [CrossRef]
11. Yuan, W.; Xia, Y.; Bell, C.G.; Yet, I.; Ferreira, T.; Ward, K.J.; Gao, F.; Loomis, A.K.; Hyde, C.L.; Wu, H.; et al. An integrated epigenomic analysis for type 2 diabetes susceptibility loci in monozygotic twins. *Nat. Commun.* **2014**, *5*, 5719. [CrossRef]
12. Arora, M.; Reichenberg, A.; Willfors, C.; Austin, C.; Gennings, C.; Berggren, S.; Lichtenstein, P.; Anckarsäter, H.; Tammimies, K.; Bölte, S. Fetal and postnatal metal dysregulation in autism. *Nat. Commun.* **2017**, *8*, 15493. [CrossRef]
13. Castillo-Fernandez, J.E.; Spector, T.D.; Bell, J.T. Epigenetics of discordant monozygotic twins: Implications for disease. *Genome Med.* **2014**, *6*, 60. [CrossRef]
14. Lyu, G.; Zhang, C.; Ling, T.; Liu, R.; Zong, L.; Guan, Y.; Huang, X.; Sun, L.; Zhang, L.; Li, C.; et al. Genome and epigenome analysis of monozygotic twins discordant for congenital heart disease. *BMC Genom.* **2018**, *19*, 428. [CrossRef]
15. Andrews, S.R. FastQC. Available online: https://github.com/s-andrews/FastQC (accessed on 1 August 2020).
16. Okonechnikov, K.; Conesa, A.; García-Alcalde, F. Qualimap 2: Advanced multi-sample quality control for high-throughput sequencing data. *Bioinformatics* **2016**, *32*, 292–294. [CrossRef]
17. Langmead, B.; Salzberg, S.L. Fast gapped-read alignment with Bowtie 2. *Nat. Methods* **2012**, *9*, 357–359. [CrossRef]

18. Poplin, R.; Chang, P.-C.; Alexander, D.; Schwartz, S.; Colthurst, T.; Ku, A.; Newburger, D.; Dijamco, J.; Nguyen, N.; Afshar, P.T.; et al. A universal SNP and small-indel variant caller using deep neural networks. *Nat. Biotechnol.* **2018**, *36*, 983–987. [CrossRef]
19. McLaren, W.; Gil, L.; Hunt, S.E.; Riat, H.S.; Ritchie, G.R.S.; Thormann, A.; Flicek, P.; Cunningham, F. The Ensembl Variant Effect Predictor. *Genome Biol.* **2016**, *17*, 122. [CrossRef]
20. Karczewski, K.J.; Francioli, L.C.; Tiao, G.; Cummings, B.B.; Alföldi, J.; Wang, Q.; Collins, R.L.; Laricchia, K.M.; Ganna, A.; Birnbaum, D.P.; et al. The mutational constraint spectrum quantified from variation in 141,456 humans. *Nature* **2020**, *581*, 434–443. [CrossRef]
21. Adzhubei, I.; Jordan, D.M.; Sunyaev, S.R. Predicting functional effect of human missense mutations using PolyPhen-2. *Curr. Protoc. Hum. Genet.* **2013**, *7*, 7–20. [CrossRef]
22. Kumar, P.; Henikoff, S.; Ng, P.C. Predicting the effects of coding non-synonymous variants on protein function using the SIFT algorithm. *Nat. Protoc.* **2009**, *4*, 1073–1081. [CrossRef]
23. Schwarz, J.M.; Cooper, D.N.; Schuelke, M.; Seelow, D. MutationTaster2: Mutation prediction for the deep-sequencing age. *Nat. Methods* **2014**, *11*, 361–362. [CrossRef]
24. Kircher, M.; Witten, D.M.; Jain, P.; O'Roak, B.J.; Cooper, G.M.; Shendure, J. A general framework for estimating the relative pathogenicity of human genetic variants. *Nat. Genet.* **2014**, *46*, 310–315. [CrossRef]
25. Chen, X.; Schulz-Trieglaff, O.; Shaw, R.; Barnes, B.; Schlesinger, F.; Källberg, M.; Cox, A.J.; Kruglyak, S.; Saunders, C.T. Manta: Rapid detection of structural variants and indels for germline and cancer sequencing applications. *Bioinformatics* **2016**, *32*, 1220–1222. [CrossRef]
26. Boeva, V.; Popova, T.; Bleakley, K.; Chiche, P.; Cappo, J.; Schleiermacher, G.; Janoueix-Lerosey, I.; Delattre, O.; Barillot, E. Control-FREEC: A tool for assessing copy number and allelic content using next-generation sequencing data. *Bioinformatics* **2012**, *28*, 423–425. [CrossRef]
27. Krueger, F. Trim Galore. Available online: https://github.com/FelixKrueger/TrimGalore (accessed on 1 August 2020).
28. Krueger, F.; Andrews, S.R. Bismark: A flexible aligner and methylation caller for Bisulfite-Seq applications. *Bioinformatics* **2011**, *27*, 1571–1572. [CrossRef]
29. Li, H.; Handsaker, B.; Wysoker, A.; Fennell, T.; Ruan, J.; Homer, N.; Marth, G.; Abecasis, G.; Durbin, R. 1000 Genome Project Data Processing Subgroup the Sequence Alignment/Map format and SAMtools. *Bioinformatics* **2009**, *25*, 2078–2079. [CrossRef]
30. Devon, Ryan MethylDackel. Available online: https://github.com/dpryan79/MethylDackel (accessed on 1 August 2020).
31. Park, Y.; Figueroa, M.E.; Rozek, L.S.; Sartor, M.A. MethylSig: A whole genome DNA methylation analysis pipeline. *Bioinformatics* **2014**, *30*, 2414–2422. [CrossRef]
32. May, D.; Blow, M.J.; Kaplan, T.; McCulley, D.J.; Jensen, B.C.; Akiyama, J.A.; Holt, A.; Plajzer-Frick, I.; Shoukry, M.; Wright, C.; et al. Large-scale discovery of enhancers from human heart tissue. *Nat. Genet.* **2011**, *44*, 89–93. [CrossRef]
33. Kaynak, B.; von Heydebreck, A.; Mebus, S.; Seelow, D.; Hennig, S.; Vogel, J.; Sperling, H.-P.; Pregla, R.; Alexi-Meskishvili, V.; Hetzer, R.; et al. Genome-wide array analysis of normal and malformed human hearts. *Circulation* **2003**, *107*, 2467–2474. [CrossRef]
34. Toenjes, M.; Schueler, M.; Hammer, S.; Pape, U.J.; Fischer, J.J.; Berger, F.; Vingron, M.; Sperling, S. Prediction of cardiac transcription networks based on molecular data and complex clinical phenotypes. *Mol. Biosyst.* **2008**, *4*, 589–598. [CrossRef]
35. Ricci, M.; Xu, Y.; Hammond, H.L.; Willoughby, D.A.; Nathanson, L.; Rodriguez, M.M.; Vatta, M.; Lipshultz, S.E.; Lincoln, J. Myocardial alternative RNA splicing and gene expression profiling in early stage hypoplastic left heart syndrome. *PLoS ONE* **2012**, *7*, e29784. [CrossRef] [PubMed]
36. Schlesinger, J.; Tönjes, M.; Schueler, M.; Zhang, Q.; Dunkel, I.; Sperling, S.R. Evaluation of the LightCycler 1536 Instrument for high-throughput quantitative real-time PCR. *Methods* **2010**, *50*, S19–S22. [CrossRef]
37. Rodemoyer, A.; Kibiryeva, N.; Bair, A.; Marshall, J.; O'Brien, J.E.; Bittel, D.C. A tissue-specific gene expression template portrays heart development and pathology. *Hum. Genom.* **2014**, *8*, 6. [CrossRef]
38. Sheng, W.; Wang, H.; Ma, X.; Qian, Y.; Zhang, P.; Wu, Y.; Zheng, F.; Chen, L.; Huang, G.; Ma, D. LINE-1 methylation status and its association with tetralogy of fallot in infants. *BMC Med. Genom.* **2012**, *5*, 20. [CrossRef]

39. Sheng, W.; Qian, Y.; Zhang, P.; Wu, Y.; Wang, H.; Ma, X.; Chen, L.; Ma, D.; Huang, G. Association of promoter methylation statuses of congenital heart defect candidate genes with Tetralogy of Fallot. *J. Transl. Med.* **2014**, *12*, 31. [CrossRef]
40. Chowdhury, S.; Erickson, S.W.; MacLeod, S.L.; Cleves, M.A.; Hu, P.; Karim, M.A.; Hobbs, C.A. Maternal genome-wide DNA methylation patterns and congenital heart defects. *PLoS ONE* **2011**, *6*, e16506. [CrossRef]
41. Sheng, W.; Qian, Y.; Wang, H.; Ma, X.; Zhang, P.; Diao, L.; An, Q.; Chen, L.; Ma, D.; Huang, G. DNA methylation status of NKX2-5, GATA4 and HAND1 in patients with tetralogy of fallot. *BMC Med. Genom.* **2013**, *6*, 46. [CrossRef]
42. Bansal, V.; Dorn, C.; Grunert, M.; Klaassen, S.; Hetzer, R.; Berger, F.; Sperling, S.R. Outlier-based identification of copy number variations using targeted resequencing in a small cohort of patients with Tetralogy of Fallot. *PLoS ONE* **2014**, *9*, e85375. [CrossRef]
43. Warburton, D.; Ronemus, M.; Kline, J.; Jobanputra, V.; Williams, I.; Anyane-Yeboa, K.; Chung, W.; Yu, L.; Wong, N.; Awad, D.; et al. The contribution of de novo and rare inherited copy number changes to congenital heart disease in an unselected sample of children with conotruncal defects or hypoplastic left heart disease. *Hum. Genet.* **2014**, *133*, 11–27. [CrossRef]
44. Greenway, S.C.; Pereira, A.C.; Lin, J.C.; DePalma, S.R.; Israel, S.J.; Mesquita, S.M.; Ergul, E.; Conta, J.H.; Korn, J.M.; McCarroll, S.A.; et al. De novo copy number variants identify new genes and loci in isolated sporadic tetralogy of Fallot. *Nat. Genet.* **2009**, *41*, 931–935. [CrossRef]
45. Tomita-Mitchell, A.; Mahnke, D.K.; Struble, C.A.; Tuffnell, M.E.; Stamm, K.D.; Hidestrand, M.; Harris, S.E.; Goetsch, M.A.; Simpson, P.M.; Bick, D.P.; et al. Human gene copy number spectra analysis in congenital heart malformations. *Physiol. Genom.* **2012**, *44*, 518–541. [CrossRef] [PubMed]
46. Payne, A.R.; Chang, S.-W.; Koenig, S.N.; Zinn, A.R.; Garg, V. Submicroscopic chromosomal copy number variations identified in children with hypoplastic left heart syndrome. *Pediatr. Cardiol.* **2012**, *33*, 757–763. [CrossRef]
47. de Souza, K.R.; Mergener, R.; Huber, J.; Campos Pellanda, L.; Riegel, M. Cytogenomic Evaluation of Subjects with Syndromic and Nonsyndromic Conotruncal Heart Defects. *Biomed. Res. Int.* **2015**, *2015*, 401941. [CrossRef]
48. Geng, J.; Picker, J.; Zheng, Z.; Zhang, X.; Wang, J.; Hisama, F.; Brown, D.W.; Mullen, M.P.; Harris, D.; Stoler, J.; et al. Chromosome microarray testing for patients with congenital heart defects reveals novel disease causing loci and high diagnostic yield. *BMC Genom.* **2014**, *15*, 1127. [CrossRef] [PubMed]
49. Bittel, D.C.; Zhou, X.-G.; Kibiryeva, N.; Fiedler, S.; O'Brien, J.E.; Marshall, J.; Yu, S.; Liu, H.-Y. Ultra high-resolution gene centric genomic structural analysis of a non-syndromic congenital heart defect, Tetralogy of Fallot. *PLoS ONE* **2014**, *9*, e87472. [CrossRef] [PubMed]
50. Aguayo-Gómez, A.; Arteaga-Vázquez, J.; Svyryd, Y.; Calderón-Colmenero, J.; Zamora-González, C.; Vargas-Alarcón, G.; Mutchinick, O.M. Identification of Copy Number Variations in Isolated Tetralogy of Fallot. *Pediatr. Cardiol.* **2015**, *36*, 1642–1646. [CrossRef]
51. Hitz, M.-P.; Lemieux-Perreault, L.-P.; Marshall, C.; Feroz-Zada, Y.; Davies, R.; Yang, S.W.; Lionel, A.C.; D'Amours, G.; Lemyre, E.; Cullum, R.; et al. Rare copy number variants contribute to congenital left-sided heart disease. *PLoS Genet.* **2012**, *8*, e1002903. [CrossRef] [PubMed]
52. Erdogan, F.; Larsen, L.A.; Zhang, L.; Tümer, Z.; Tommerup, N.; Chen, W.; Jacobsen, J.R.; Schubert, M.; Jurkatis, J.; Tzschach, A.; et al. High frequency of submicroscopic genomic aberrations detected by tiling path array comparative genome hybridisation in patients with isolated congenital heart disease. *J. Med. Genet.* **2008**, *45*, 704–709. [CrossRef]
53. Soemedi, R.; Wilson, I.J.; Bentham, J.; Darlay, R.; Töpf, A.; Zelenika, D.; Cosgrove, C.; Setchfield, K.; Thornborough, C.; Granados-Riveron, J.; et al. Contribution of global rare copy-number variants to the risk of sporadic congenital heart disease. *Am. J. Hum. Genet.* **2012**, *91*, 489–501. [CrossRef]
54. Wilson, K.D.; Shen, P.; Fung, E.; Karakikes, I.; Zhang, A.; InanlooRahatloo, K.; Odegaard, J.; Sallam, K.; Davis, R.W.; Lui, G.K.; et al. A rapid, high-quality, cost-effective, comprehensive and expandable targeted next-generation sequencing assay for inherited heart diseases. *Circ. Res.* **2015**, *117*, 603–611. [CrossRef]
55. Silversides, C.K.; Lionel, A.C.; Costain, G.; Merico, D.; Migita, O.; Liu, B.; Yuen, T.; Rickaby, J.; Thiruvahindrapuram, B.; Marshall, C.R.; et al. Rare copy number variations in adults with tetralogy of Fallot implicate novel risk gene pathways. *PLoS Genet.* **2012**, *8*, e1002843. [CrossRef]
56. Richards, A.A.; Santos, L.J.; Nichols, H.A.; Crider, B.P.; Elder, F.F.; Hauser, N.S.; Zinn, A.R.; Garg, V. Cryptic chromosomal abnormalities identified in children with congenital heart disease. *Pediatr. Res.* **2008**, *64*, 358–363. [CrossRef]

57. O'Brien, J.E.; Kibiryeva, N.; Zhou, X.-G.; Marshall, J.A.; Lofland, G.K.; Artman, M.; Chen, J.; Bittel, D.C. Noncoding RNA expression in myocardium from infants with tetralogy of Fallot. *Circ. Cardiovasc. Genet.* **2012**, *5*, 279–286. [CrossRef]
58. Sucharov, C.C.; Sucharov, J.; Karimpour-Fard, A.; Nunley, K.; Stauffer, B.L.; Miyamoto, S.D. Micro-RNA expression in hypoplastic left heart syndrome. *J. Card. Fail.* **2015**, *21*, 83–88. [CrossRef]
59. Grunert, M.; Appelt, S.; Dunkel, I.; Berger, F.; Sperling, S.R. Altered microRNA and target gene expression related to Tetralogy of Fallot. *Sci. Rep.* **2019**, *9*, 19063. [CrossRef]
60. Grunert, M.; Appelt, S.; Schönhals, S.; Mika, K.; Cui, H.; Cooper, A.; Cyganek, L.; Guan, K.; Sperling, S.R. Induced pluripotent stem cells of patients with Tetralogy of Fallot reveal transcriptional alterations in cardiomyocyte differentiation. *Sci. Rep.* **2020**, *10*, 10921. [CrossRef]
61. Wu, B.; Baldwin, H.S.; Zhou, B. Nfatc1 directs the endocardial progenitor cells to make heart valve primordium. *Trends Cardiovasc. Med.* **2013**, *23*, 294–300. [CrossRef]
62. Kirk, E.P.; Sunde, M.; Costa, M.W.; Rankin, S.A.; Wolstein, O.; Castro, M.L.; Butler, T.L.; Hyun, C.; Guo, G.; Otway, R.; et al. Mutations in cardiac T-box factor gene TBX20 are associated with diverse cardiac pathologies, including defects of septation and valvulogenesis and cardiomyopathy. *Am. J. Hum. Genet.* **2007**, *81*, 280–291. [CrossRef]
63. Grunert, M.; Dorn, C.; Rickert-Sperling, S. Cardiac Transcription Factors and Regulatory Networks. In *Congenital Heart Diseases: The Broken Heart*; Rickert-Sperling, S., Kelly, R.G., Driscoll, D.J., Eds.; Springer: Vienna, Austria, 2016; pp. 139–152. ISBN 978-3-7091-1882-5.
64. Boccuni, P.; MacGrogan, D.; Scandura, J.M.; Nimer, S.D. The human L(3)MBT polycomb group protein is a transcriptional repressor and interacts physically and functionally with TEL (ETV6). *J. Biol. Chem.* **2003**, *278*, 15412–15420. [CrossRef]
65. Trojer, P.; Li, G.; Sims, R.J.; Vaquero, A.; Kalakonda, N.; Boccuni, P.; Lee, D.; Erdjument-Bromage, H.; Tempst, P.; Nimer, S.D.; et al. L3MBTL1, a histone-methylation-dependent chromatin lock. *Cell* **2007**, *129*, 915–928. [CrossRef]
66. Ziller, M.J.; Gu, H.; Müller, F.; Donaghey, J.; Tsai, L.T.-Y.; Kohlbacher, O.; De Jager, P.L.; Rosen, E.D.; Bennett, D.A.; Bernstein, B.E.; et al. Charting a dynamic DNA methylation landscape of the human genome. *Nature* **2013**, *500*, 477–481. [CrossRef]
67. Chen, P.-Y.; Feng, S.; Joo, J.W.J.; Jacobsen, S.E.; Pellegrini, M. A comparative analysis of DNA methylation across human embryonic stem cell lines. *Genome Biol.* **2011**, *12*, R62. [CrossRef]
68. Gardiner-Garden, M.; Frommer, M. CpG islands in vertebrate genomes. *J. Mol. Biol.* **1987**, *196*, 261–282. [CrossRef]
69. Deaton, A.M.; Bird, A. CpG islands and the regulation of transcription. *Genes Dev.* **2011**, *25*, 1010–1022. [CrossRef]
70. Jones, P.A. Functions of DNA methylation: Islands, start sites, gene bodies and beyond. *Nat. Rev. Genet.* **2012**, *13*, 484–492. [CrossRef]
71. Yehya, A.; Souki, R.; Bitar, F.; Nemer, G. Differential duplication of an intronic region in the NFATC1 gene in patients with congenital heart disease. *Genome* **2006**, *49*, 1092–1098. [CrossRef]
72. Abdul-Sater, Z.; Yehya, A.; Beresian, J.; Salem, E.; Kamar, A.; Baydoun, S.; Shibbani, K.; Soubra, A.; Bitar, F.; Nemer, G. Two heterozygous mutations in NFATC1 in a patient with Tricuspid Atresia. *PLoS ONE* **2012**, *7*, e49532. [CrossRef]
73. Takeuchi, J.K.; Mileikovskaia, M.; Koshiba-Takeuchi, K.; Heidt, A.B.; Mori, A.D.; Arruda, E.P.; Gertsenstein, M.; Georges, R.; Davidson, L.; Mo, R.; et al. Tbx20 dose-dependently regulates transcription factor networks required for mouse heart and motoneuron development. *Development* **2005**, *132*, 2463–2474. [CrossRef]
74. Irizarry, R.A.; Ladd-Acosta, C.; Wen, B.; Wu, Z.; Montano, C.; Onyango, P.; Cui, H.; Gabo, K.; Rongione, M.; Webster, M.; et al. The human colon cancer methylome shows similar hypo- and hypermethylation at conserved tissue-specific CpG island shores. *Nat. Genet.* **2009**, *41*, 178–186. [CrossRef]
75. Xu, Y.; Li, T.; Pu, T.; Cao, R.; Long, F.; Chen, S.; Sun, K.; Xu, R. Copy Number Variants and Exome Sequencing Analysis in Six Pairs of Chinese Monozygotic Twins Discordant for Congenital Heart Disease. *Twin Res. Hum. Genet.* **2017**, *20*, 521–532. [CrossRef]
76. Breckpot, J.; Thienpont, B.; Gewillig, M.; Allegaert, K.; Vermeesch, J.R.; Devriendt, K. Differences in Copy Number Variation between Discordant Monozygotic Twins as a Model for Exploring Chromosomal Mosaicism in Congenital Heart Defects. *Mol. Syndromol.* **2012**, *2*, 81–87. [CrossRef]

77. Chaiyasap, P.; Kulawonganunchai, S.; Srichomthong, C.; Tongsima, S.; Suphapeetiporn, K.; Shotelersuk, V. Whole genome and exome sequencing of monozygotic twins with trisomy 21, discordant for a congenital heart defect and epilepsy. *PLoS ONE* **2014**, *9*, e100191. [CrossRef]
78. Hui, D.S.; Bonow, R.O.; Stolker, J.M.; Braddock, S.R.; Lee, R. Discordant Aortic Valve Morphology in Monozygotic Twins: A Clinical Case Series. *JAMA Cardiol.* **2016**, *1*, 1043–1047. [CrossRef]
79. Zhang, R.; Thiele, H.; Bartmann, P.; Hilger, A.C.; Berg, C.; Herberg, U.; Klingmüller, D.; Nürnberg, P.; Ludwig, M.; Reutter, H. Whole-Exome Sequencing in Nine Monozygotic Discordant Twins. *Twin Res. Hum. Genet.* **2016**, *19*, 60–65. [CrossRef]
80. Erlich, Y. Blood ties: Chimerism can mask twin discordance in high-throughput sequencing. *Twin Res. Hum. Genet.* **2011**, *14*, 137–143. [CrossRef]
81. Zaidi, S.; Choi, M.; Wakimoto, H.; Ma, L.; Jiang, J.; Overton, J.D.; Romano-Adesman, A.; Bjornson, R.D.; Breitbart, R.E.; Brown, K.K.; et al. De novo mutations in histone-modifying genes in congenital heart disease. *Nature* **2013**, *498*, 220–223. [CrossRef]
82. Lindinger, A.; Schwedler, G.; Hense, H.-W. Prevalence of congenital heart defects in newborns in Germany: Results of the first registration year of the PAN Study (July 2006 to June 2007). *Klin. Padiatr.* **2010**, *222*, 321–326. [CrossRef]
83. Cosselman, K.E.; Navas-Acien, A.; Kaufman, J.D. Environmental factors in cardiovascular disease. *Nat. Rev. Cardiol.* **2015**, *12*, 627–642. [CrossRef]
84. Porter, G.A. Environmental Signals. In *Congenital Heart Diseases: The Broken Heart*; Rickert-Sperling, S., Kelly, R.G., Driscoll, D.J., Eds.; Springer: Vienna, Austria, 2016; pp. 223–235. ISBN 978-3-7091-1882-5.
85. Abu-Halima, M.; Weidinger, J.; Poryo, M.; Henn, D.; Keller, A.; Meese, E.; Abdul-Khaliq, H. Micro-RNA signatures in monozygotic twins discordant for congenital heart defects. *PLoS ONE* **2019**, *14*, e0226164. [CrossRef]
86. Czyz, W.; Morahan, J.M.; Ebers, G.C.; Ramagopalan, S.V. Genetic, environmental and stochastic factors in monozygotic twin discordance with a focus on epigenetic differences. *BMC Med.* **2012**, *10*, 93. [CrossRef]
87. Litviňuková, M.; Talavera-López, C.; Maatz, H.; Reichart, D.; Worth, C.L.; Lindberg, E.L.; Kanda, M.; Polanski, K.; Heinig, M.; Lee, M.; et al. Cells of the adult human heart. *Nature* **2020**. [CrossRef]
88. Karatza, A.A.; Wolfenden, J.L.; Taylor, M.J.O.; Wee, L.; Fisk, N.M.; Gardiner, H.M. Influence of twin-twin transfusion syndrome on fetal cardiovascular structure and function: Prospective case-control study of 136 monochorionic twin pregnancies. *Heart* **2002**, *88*, 271–277. [CrossRef]
89. Marceau, K.; McMaster, M.T.B.; Smith, T.F.; Daams, J.G.; van Beijsterveldt, C.E.M.; Boomsma, D.I.; Knopik, V.S. The Prenatal Environment in Twin Studies: A Review on Chorionicity. *Behav. Genet.* **2016**, *46*, 286–303. [CrossRef]
90. Wong, H.S.; Kidd, A.; Zuccollo, J.; Parker, S.; Richardson, V.; Tait, J.; Pringle, K.C. A case of amyoplasia in a monochorionic twin pregnancy: A sequela from twin-twin transfusion syndrome? *Fetal Diagn. Ther.* **2009**, *25*, 31–35. [CrossRef] [PubMed]
91. Norris, A.W.; Wang, C.; Yao, J.; Walsh, S.A.; Sawatzke, A.B.; Hu, S.; Sunderland, J.J.; Segar, J.L.; Ponto, L.L.B. Effect of insulin and dexamethasone on fetal assimilation of maternal glucose. *Endocrinology* **2011**, *152*, 255–262. [CrossRef]
92. Mahle, W.T. What we can learn from twins: Congenital heart disease in the danish twin registry. *Circulation* **2013**, *128*, 1173–1174. [CrossRef]

Journal of
Cardiovascular
Development and Disease

MDPI

Article

Transforming Growth Factor Beta3 is Required for Cardiovascular Development

Mrinmay Chakrabarti [1], Nadia Al-Sammarraie [1], Mengistu G. Gebere [1], Aniket Bhattacharya [1], Sunita Chopra [1], John Johnson [1], Edsel A. Peña [2], John F. Eberth [1], Robert E. Poelmann [3], Adriana C. Gittenberger-de Groot [3] and Mohamad Azhar [1,4,*]

1 Department of Cell Biology and Anatomy, University of South Carolina School of Medicine, Columbia, SC 29209, USA; Mrinmay.Chakrabarti@uscmed.sc.edu (M.C.); Nadia.Al-Sammarraie@uscmed.sc.edu (N.A.-S.); Mengistu.Gebere@uscmed.sc.edu (M.G.G.); Aniket.Bhattacharya@uscmed.sc.edu (A.B.); sunita.chopra42@gmail.com (S.C.); John.Johnson@uscmed.sc.edu (J.J.); John.Eberth@uscmed.sc.edu (J.F.E.)
2 Department of Statistics, University of South Carolina, Columbia, SC 290208, USA; pena@stat.sc.edu
3 Department of Cardiology, Leiden University Medical Center, 2333 ZC Leiden, The Netherlands; R.E.Poelmann@lumc.nl (R.E.P.); A.C.Gittenberger-de_Groot@lumc.nl (A.C.G.-d.G.)
4 William Jennings Bryan Dorn VA Medical Center, Columbia, SC 29209, USA
* Correspondence: Mohamad.Azhar@uscmed.sc.edu

Received: 23 April 2020; Accepted: 20 May 2020; Published: 24 May 2020

Abstract: Transforming growth factor beta3 (*TGFB3*) gene mutations in patients of arrhythmogenic right ventricular dysplasia/cardiomyopathy (ARVD1) and Loeys-Dietz syndrome-5 (LDS5)/Rienhoff syndrome are associated with cardiomyopathy, cardiac arrhythmia, cardiac fibrosis, cleft palate, aortic aneurysms, and valvular heart disease. Although the developing heart of embryos express *Tgfb3*, its overarching role remains unclear in cardiovascular development and disease. We used histological, immunohistochemical, and molecular analyses of *Tgfb3*$^{-/-}$ fetuses and compared them to wildtype littermate controls. The cardiovascular phenotypes were diverse with approximately two thirds of the *Tgfb3*$^{-/-}$ fetuses having one or more cardiovascular malformations, including abnormal ventricular myocardium (particularly of the right ventricle), outflow tract septal and alignment defects, abnormal aortic and pulmonary trunk walls, and thickening of semilunar and/or atrioventricular valves. Ventricular septal defects (VSD) including the perimembranous VSDs were observed in *Tgfb3*$^{-/-}$ fetuses with myocardial defects often accompanied by the muscular type VSD. In vitro studies using TGFβ3-deficient fibroblasts in 3-D collagen lattice formation assays indicated that TGFβ3 was required for collagen matrix reorganization. Biochemical studies indicated the 'paradoxically' increased activation of canonical (SMAD-dependent) and noncanonical (MAP kinase-dependent) pathways. TGFβ3 is required for cardiovascular development to maintain a balance of canonical and noncanonical TGFβ signaling pathways.

Keywords: transforming growth factor beta-3; cardiac development; loeys dietz syndrome-5; arrhythmogenic right ventricular dysplasia; rienhoff syndrome; cleft palate; congenital heart disease; outflow tract septation; signaling networks

1. Introduction

Transforming growth factor beta3 (TGFβ3) is a multifunctional growth factor and cytokine well-known for its involvement in craniofacial development [1–5]. In humans, the TGFB3 gene is involved in arrhythmogenic right ventricular dysplasia (ARVD) familial 1 (ARVD1) (OMIM#107970) [6, 7], now being referred to as arrhythmogenic right ventricular cardiomyopathy (ARVC). ARVC involves progressive fibrofatty replacement of the myocardium, resulting in ventricular tachycardia and sudden

death in young athletes and patients. The ARVC primarily affects the right ventricle (RV) but emerging evidence suggests that it may also affect the left too (LV) [6,8]. Overall, presentation of the disease is highly variable among affected individuals. Furthermore, *TGFB3* mutations in Loeys-Dietz Syndrome 5 (LDS5)/Rienhoff syndrome (RNHF) (OMIM#615582) are associated with connective tissue disorders and Marfan syndrome (MFS)-like features, including congenital heart defects (CHD), aortic aneurysms, and valvular disease [9–11]. For instance, aorta from LDS5 patients exhibit paradoxically increased TGFβ signaling, which is thought to be involved in the diverse aortopathies [9]. Other features of these patients overlap clinically with Shprintzen–Goldberg syndrome (SGS) (OMIM#182212) and Marfan syndrome (MFS) (OMIM#154700), including cleft palate. De novo *TGFB3* mutations also cause congenital syndromes characterized by a combination of clinical features of Beals-Hecht syndrome (CCA) (OMIM#121050), RNHF, MFS, and Loeys-Dietz syndrome (LDS) [12–14].

TGFβ3 has been implicated in several cellular processes in a context-dependent and tissue-specific fashion, including epithelial-mesenchymal transition (EMT), cell growth, apoptosis, differentiation, extracellular matrix (ECM) production and remodelling, all of which are critical processes involved in both the development and homeostasis of cardiovascular tissues [15–19]. TGFβ3 interacts with the heteromeric TGFβR2 and TGFβR1 receptor complex, which results in the phosphorylation and activation of SMAD2 and SMAD3 [20]. In association with SMAD4, the phosphorylated SMAD2/3 molecules migrate to the nucleus [21]. TGFβ ligands can induce SMAD1/5/9, so-called BMP-driven SMADs, via involvement of BMP Type I receptors in endothelial cells and/or fibroblasts, thereby bringing about crosstalk between TGFβ and BMP signaling pathways [22]. In addition, TGFβ ligands can signal through non-SMAD mechanisms, including MAP kinase pathways [23]. Thus, given the non-overlapping, dozens of phenotypes among the TGFβ3 ligand knockout mice [24], as well as the multiple TGFβ signaling pathways that have been identified [25], there are several potential mechanisms through which TGFβ3 can affect the complex differentiation and morphogenetic processes required to develop the essential components of the heart.

The expression of *TGFB3* has been detected in the developing mouse heart and adult human heart [26,27]. TGFβ signaling is a critical contributor to collagen accumulation and defective collagen reorganization during fibrofatty lesion formation in ARVD1 and myocardial fibrosis in the infarcted failing hearts [28]. To address the role of TGFβ3 in vivo, two different laboratories independently generated *Tgfb3* knockout (*Tgfb3*$^{-/-}$) mice [1,2]. Unfortunately, *Tgfb3*$^{-/-}$ newborn mice have a cleft palate and die within 24 h of birth. Although cardiovascular disease was not the focus of the two studies, none of the studies reported any congenital heart defects in the *Tgfb3*$^{-/-}$ fetuses. Consequently, the exact role of TGFβ3 in cardiovascular development remains unknown. Given the recent reports of genetic involvement of TGFB3 mutations in the cardiovascular disease in humans [6,7,9,12], our paradigm-shifting findings demonstrate that the majority of *Tgfb3*$^{-/-}$ fetuses develop both cardiac outflow tract (OFT) and atrioventricular (AV) canal defects and that the loss of *Tgfb3* leads to major myocardial defects, particularly affecting the right ventricular myocardium. Our data also identify downstream mechanisms and specific components of the SMAD- and MAP kinase (MAPK)-dependent signaling pathways that are involved in cardiovascular malformations in TGFβ3-deficient mice.

2. Materials and Methods

2.1. Ethics Statement

All animal procedures were performed according to the Guidelines for the Care and Use of Laboratory Animals published by the National Institutes of Health and were approved by the Institutional Animal Care and Use Committee of the University of South Carolina (Animal use proposal reference #: 2451-101423-042519, protocol approval date: 25 April 2019, protocol expiration date: 25 April 2022) Mice were euthanized by an overdose of isoflurane in a sealed container as approved by the IACUC.

2.2. Mouse Strains

Mice were housed at the University of South Carolina Animal Research Facility at the School of Medicine. The Institutional Animal Care and Use Committee (University of South Carolina) approved all mouse breeding and experimental procedures. *Tgfb3*$^{+/-}$ mice [1] were backcrossed on to a C57BL/6 background for more than 12 generations, and maintained on the C57BL/6 genetic background. *Tgfb3*$^{-/-}$ embryos were generated and genotyped as described [1]. Timed mating was performed, and the noontime of the positive vaginal plugs was considered as embryonic day (E) 0.5. The DNA sequence of the *Tgfb3* specific primers that were used for genotyping includes: TGGGAGTCATGGCTGTAACT (IMF-10, forward primer), CACTCACACTGGCAAGTAGT (IMR-10, reverse primer). PCR genotyping was done as described [1]. PCR genotyping of embryonic tissues genomic DNA identified wildtype, *Tgfb3*$^{+/-}$, and *Tgfb3*$^{-/-}$ fetuses for experiments.

2.3. Histology and Immunohistochemistry

Wildtype, *Tgfb3*$^{+/-}$, and *Tgfb3*$^{-/-}$ embryos/fetuses were collected between E13.5 and E18.5 and processed for histological and immunohistochemical, morphometric, and molecular analyses. Hematoxylin and eosin (H&E) staining was performed on 7 μm thick serial sections of the heart for routine histological examination. Immunohistochemistry (IHC) was done on 4% paraformaldehyde fixed 7 μm thick paraffin sections by using immunostaining kits (LSAB2 kit, Universal, HRP Rabbit/Mouse (Cat #: K0675), according to the protocol of the manufacturer (Agilent Dako, USA), and as previously published [29]. Antigen retrieval was performed in Target Retrieval Solution pH 6.0 (catalog no. S1700; Agilent Dako, USA) for 15–20 min at 95°C. Anti-muscle actin (Clone: HHF35, catalog no. M0635; Agilent Dako; 1:50 dilution) immunostained sections were counterstained with hematoxylin nuclear stain. All sections were visualized and photographed under brightfield optics on a Nikon Optiphot-2 (equipped with AxioCam MRc Camera) and EVOS TM FL Auto Imaging System (ThermoFisher, Inc., Grand Island, NY, USA). For photographing elastin autofluorescence in hematoxylin and eosin stained sections, 470/22 excitation and 510/42 emission filters were used on a Zeiss Axiovert 200 (Thornwood, NY, USA) (equipped with Axiocam 503 color camera and ZEN 2.3 SP1 Imaging software).

2.4. TUNEL Staining

The TUNEL assay was used to detect apoptosis in outflow tract cushions. Paraffin sections from E13.5-14.5 OFT cushions from wildtype and *Tgfb3*$^{-/-}$ embryos were subjected to the TUNEL assay using FragEL™ DNA Fragmentation Detection Kit, Colorimetric - TdT Enzyme (Sigma-Aldrich, Cat#QIA33, St. Louis, MO, USA). All nuclei were also stained with methyl green (Vector Laboratories). Stained samples were observed with a Nikon E400 light microscope and photographs (10 × Obj) were used for quantitative analysis (Image Pro Plus software, Media Cybernetics, Rockville, MD, USA) by analyzing up to 500 cells/sample from 4–5 sections of the OFT septum spaced 24 μm apart for 3 samples each of *Tgfb3*$^{-/-}$ and control embryos. The percent (%) average apoptosis from each sample was plotted using a scatter plot.

2.5. Cell Proliferation

Cell proliferation was monitored by immunohistochemistry. Paraffin sections of E13.5-14.5 outflow tract septal cushions from *Tgfb3*$^{-/-}$ and wildtype embryos were subjected to immunohistochemistry with a phospho-histone H3 (Ser10) antibody (Cell Signaling Inc, #9701, Danvers, MA, USA). Stained samples were observed with a Nikon E400 light microscope and photographs (×Obj) were used for quantitative analysis (Image Pro Plus software) by analyzing the number of pHH3-positive cells per sample collected from the region around fibrous OFT septum in 4–5 sections spaced 24 μm apart for 3 samples each of *Tgfb3*$^{-/-}$ and control embryos.

2.6. AMIRA Three-Dimensional (3-D) Reconstruction and Volumetric Analysis

Seven-micrometer paraffin serial sections were obtained on a microtome and stained with hematoxylin and eosin (H&E). TIFF images of the complete aortic valves from wildtype and *Tgfb3*$^{-/-}$ embryos (E4.5-15.5) were captured using the 4× objective on a Nikon Optiphot-2 light microscope and loaded into the AMIRA software package (FEI Visualization Science Group, Burlington, MA, USA) [30]. All sections were aligned, and the aortic valve (left and right coronary and non-coronary leaflets) was segmented. A 3D model of the aortic valves was then generated from which the volume of the aortic valve cushion was determined for both wildtype and *Tgfb3*$^{-/-}$ fetuses. Results were compared using a Student's *t*-test.

2.7. RNAscope In Situ Hybridization

In situ hybridization was carried out using a *Tgfb3* RNA probe synthesized by Advanced Cell Diagnostics (Newark, CA, USA) (ACD, #406211) [31]. Detection was done using the RNAscope 2.5 HD Duplex Reagent Mouse Kit (Cat. No 322430) according to the manufacturer's protocol (ACD). After the signal had developed, sections dehydrated in a series of ethanol and xylene were mounted using permount (Vector Lab, Burlingame, CA, USA).

2.8. Collagen Gel Contraction Assays

Three independent mouse embryonic fibroblast lines were generated for each wildtype and *Tgfb3* knock out E14.5 embryos as described [32]. Mouse fibroblasts were maintained in DMEM (Invitrogen) supplemented with 10% bovine serum, 5% fetal calf serum and 1% penicillin/streptomycin (Sigma-Aldrich, St. Louis, MO, USA) at 37 °C/5% CO2. In addition to reorganization, collagen contraction assays are indicative of the capacity for embedded cells to generate mechanical loads [33]. The capability of mouse fibroblasts to form lattices in collagen gels was assessed by plating 105 cells in 2mg/mL collagen type-I (in 18mM acetic acid) prepared in complete media and supplemented with 0.1 M NaOH, as detailed [34]. Free-floating collagen gels were incubated at 37 °C for 5 days, with or without recombinant TGFβ1 (0.1 ng/mL or 1 ng/mL, Sigma-Aldrich, St. Louis, MO). Images were acquired and best-fit shapes (circle or free form) were used to calculate the surface area of the gels using image processing utilities in Zeiss (ZEN) Imaging Software. The initial area of the collagen gel on day 1 was used to normalize across experiments. The percent (%) decrease in gel surface area after 5 days denotes the degree of collagen contraction, with higher values indicate greater contraction [35]. The results are presented as scatter dot-plots with the box denoting the mean ± SEM and dots representing individual data points.

2.9. Western Blot Analysis

Western blotting was performed with the samples of individual heart with the great vessels of the arterial pole, which were collected from wild type and *Tgfb3* knockout (E18.5) fetuses. Since there was not enough protein available for Western blot analyses from individual heart at mid-gestation (E14.5), we used pooled samples (three fetal hearts and aortas/sample) from wildtype, *Tgfb3*$^{+/-}$ and *Tgfb3*$^{-/-}$ fetuses at E14.5. The fetal hearts were cut into small pieces and homogenized using Wheaton tapered tissue grinders (Thermo Scientific, Rockford, IL) in M-PER mammalian protein extraction reagent (Thermo Scientific, Rockford, IL) with complete mini protease inhibitor cocktail (Sigma-Aldrich, states. Louis, MO, USA) and Halt protease and phosphatase inhibitor single-use cocktail (Thermo Scientific, Rockford, IL, USA) as per the manufacturer's protocol. Homogenized tissue lysates were subjected to brief sonication for 20 s on ice and kept at room temperature for 20 min. Then, centrifugation was performed at 15,000 rpm for 20 min at 4 °C and the supernatants were collected. Total protein concentration in the supernatant was determined using Pierce BCA protein assay kit (Thermo Scientific, Rockford, IL, USA) and the samples were stored at −80 °C until further use. For pooled samples, we collected and pooled three hearts and ascending aortas per sample after

genotyping from wildtype, *Tgfb3*$^{+/-}$ and *Tgfb3*$^{-/-}$ fetuses (E14.5). Western blotting was performed with equal amounts of protein samples and the primary IgG antibodies against phospho-SMAD2 (Cell Signaling Technology, cat #3108), SMAD2 (Cell Signaling, cat #5339), phospho-SMAD3 (Cell Signaling, cat #9520), SMAD3 (Cell Signaling, cat #9523), phospho-SMAD1/5 (Cell Signaling, cat #9516), SMAD1/5 (Cell Signaling, cat #9743), phospho-p38 (Cell Signaling, cat #4511), p38 (Cell Signaling, cat #8690), phospho-ERK1/2(Cell Signaling, cat #4370), ERK1/2 (Cell Signaling, cat #4695) at a dilution of 1:1000. Primary IgG antibodies against all these proteins were purchased from Cell Signaling Technology, Inc. (Danvers, MA, USA). The horseradish peroxidase-conjugated anti-mouse or anti-rabbit secondary IgG antibody (Cell Signaling, cat#7074) was used at 1:5000 dilution to detect a primary IgG antibody. In a separate Western blot, the levels of β-actin in all wildtype and *Tgfb3*$^{-/-}$ tissue samples were determined. Western blots were incubated with Clarity Western ECL detection reagents (Bio-Rad Laboratories, USA) and exposed to X-OMAT AR films (Eastman Kodak, Rochester, NY, USA) for autoradiography. The autoradiograms were scanned on an EPSON scanner using Photoshop software (Adobe Systems, Seattle, WA, USA). β-actin, clone AC-15 monoclonal primary antibody (Sigma-Aldrich, St. Louis, MO, USA) was used as an internal housekeeping control to compare equal loading in the SDS-PAGE. Since the β-actin values were not different between the wildtype and *Tgfb3*$^{-/-}$ tissue samples, the data from all blots were normalized to β-actin values obtained from an independent blot. The ratio of both phosphorylated protein/β-actin and phosphorylated protein/total protein were plotted as scatter dot-plots with the box denoting the mean ± SEM and dots representing individual data points.

Microsoft Excel was used for recording and managing the raw data. Data were presented as mean ± SEM. Continuous data were presented as bar/scatter/dot plots, showing the individual data points together with the average/error bars. All data points regardless whether they were included or excluded from statistical analysis presented on scatter plots. Statistical significance was calculated using either the Student's *t* test or the Mann–Whitney (nonparametric test) (two-tailed, for two-group comparison) using the GraphPad Prism 8 statistical program (GraphPad, San Diego, CA, USA). Exact *p*-values were calculated, and the probability values <0.05 were considered as significant.

3. Results

3.1. Systemic Tgfb3 Deletion Disrupts Cardiac Development

Analysis of hematoxylin and eosin (H&E)-stained serial sections as well as muscle actin immunohistochemistry (via an anti-HHF-35 clone) of selected sections from embryonic day 13.5 to 18.5 was used to determine the cardiac pathomorphology in *Tgfb3*$^{-/-}$ fetuses. Cardiovascular morphology was compared between wildtype (n = 14) and *Tgfb3*$^{-/-}$ (n = 19) and the cardiovascular malformations in the *Tgfb3*$^{-/-}$ were determined and cataloged. Approximately two thirds cases of the *Tgfb3*$^{-/-}$ fetuses developed malformations of the outflow tract and AV canal (Table 1 and Table S1). Importantly, the data revealed an abnormally smaller right ventricle than the left ventricle and that right ventricular myocardial development was impaired in about 21% cases of the *Tgfb3*$^{-/-}$ fetuses (Figure 1A–C and Figure S1A–C). Approximately 26% of the *Tgfb3*$^{-/-}$ fetuses showed the myocardial defects affecting both right and left ventricles, affecting both the compact and the trabeculated myocardium (Figure 1 and Figure S1). The myocardium of the interventricular septum and apex region was very spongy and poorly formed (Figure 1 A,C and Figure S1A,C). Severely impaired myocardium of the interventricular septum was associated with the muscular type of the ventricular septal defect (VSD) in the *Tgfb3*$^{-/-}$ fetuses (Figure 1A,C and Figure S1D,E). Histological analysis also revealed slightly impaired ventricular myocardium in 1/3 cases of *Tgfb3*$^{+/-}$ fetuses (E14.5) (Figure S1F,G). In situ hybridization analysis of wildtype hearts (E12.5) detected higher expression of *Tgfb3* in the compact and trabecular myocardium of the right ventricle and to a lesser degree in the left ventricle (Figure 1D,E). Overall, these results indicate that TGFβ3 is required for ventricular myocardial development and that it plays a more important role in the formation of the right ventricle.

Table 1. Summary of cases with or without cardiovascular defects in *Tgfb3* knockout mice (Embryonic Day 13.5 to 18.5; $n = 19$).

ID#	Genotype	Age	DORV	AV Thickening	PV Thickening	Vascular walls Abnormalities	VSD	AVSD	Thin Myocardium	RV Hyperplasia	MV Thickening	TV Thickening
KO1	*Tgfb3*$^{-/-}$	e16.5-17.5	No	No	No	No	No	No	No	No	No	No
KO2	*Tgfb3*$^{-/-}$	e13.5	No	Yes	Yes	No	Perimembranous	No	Yes	No	Yes	Yes
KO3	*Tgfb3*$^{-/-}$	e14.5-15.5	No	No	No	No	No	No	No	No	Yes	Yes
KO4	*Tgfb3*$^{-/-}$	e14.5-15.5	No	Yes	Yes	No	Muscular	No	No	No	Yes	Yes
KO5	*Tgfb3*$^{-/-}$	e14.5-15.5	No	Yes	Yes	No	Muscular	No	Yes	No	No	No
KO6	*Tgfb3*$^{-/-}$	e14.5-15.5	No	No	No	No	No	No	No	No	No	No
KO7	*Tgfb3*$^{-/-}$	e14.5-15.5	No	No	No	No	No	No	No	No	No	No
KO8	*Tgfb3*$^{-/-}$	e16.5-17.5	No	No	No	No	No	No	No	No	No	No
KO9	*Tgfb3*$^{-/-}$	e13.5	No	Yes	Yes	No	Perimembranous	No	No	Yes	Yes	Yes
KO10	*Tgfb3*$^{-/-}$	e16.5-17.5	No	Yes	Yes	No	No	No	No	No	No	No
KO11	*Tgfb3*$^{-/-}$	e14.5-15.5	No	Yes	Yes	ND	No	No	No	Yes	Yes	Yes
KO12	*Tgfb3*$^{-/-}$	e18.5	No	Yes	Yes	Yes	No	No	Yes	No	No	No
KO13	*Tgfb3*$^{-/-}$	e18.5	No	Yes	Yes	Yes	Perimembranous	No	No	Yes	No	No
KO14	*Tgfb3*$^{-/-}$	e15.5-16.5	No	Yes	Yes	No	No	No	Yes	No	No	No
KO15	*Tgfb3*$^{-/-}$	e15.5-16.5	Subaortic	Yes	Yes	Yes	Perimembranous	No	No	Yes	Yes	Yes
KO16	*Tgfb3*$^{-/-}$	E18.5	No	No	No	No	No	No	No	No	No	No
KO17	*Tgfb3*$^{-/-}$	e13.5	No	Yes	Yes	No	No	No	No	No	Yes	Yes
KO18	*Tgfb3*$^{-/-}$	e14.5	No	No	No	No	No	No	No	No	No	No
KO19	*Tgfb3*$^{-/-}$	e13.5	No	Yes	Yes	No	Muscular	No	Yes	No	Yes	Yes
	Number of cases (%)		1 (5.2%)	12 (63.15%)	12 (63.15%)	3 (15.7%)	P: 4 (21%); M: 3 (15.7%)	0 (0%)	6 (31.5%)	4 (21%)	8 (42.1%)	8 (42.1%)
Total cases	*Tgfb3*$^{-/-}$	19										
Total cases	Wildtype (*Tgfb3*$^{+/+}$)	14										

Abbreviations: DORV, double outlet right ventricle; AV, atrioventricular valve; PV, pulmonary valve; VSD, ventricular septal defect; AVSD, atrioventricular septal defect; RV, right ventricule; MV, mitral valve; TV, tricuspid valve.

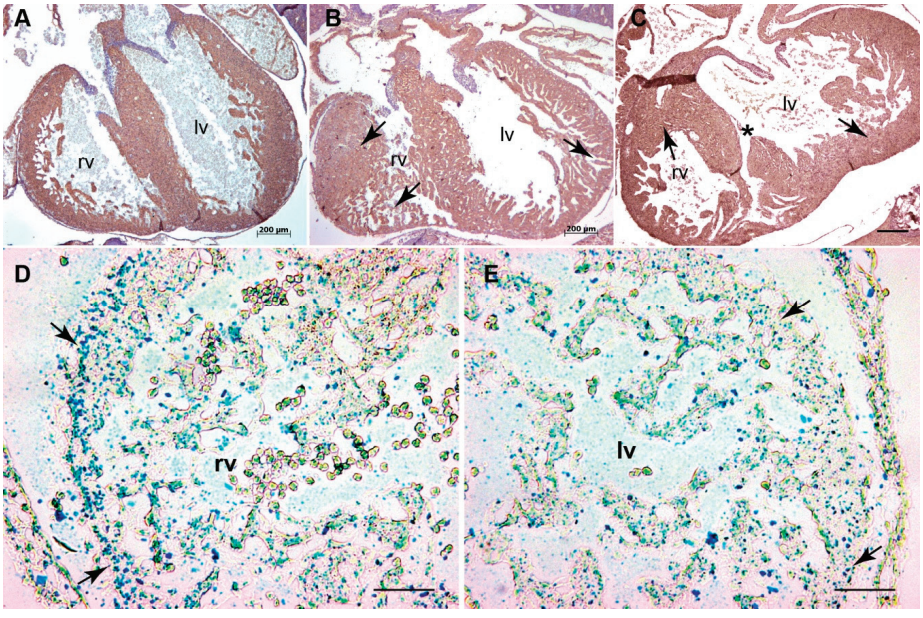

Figure 1. *Tgfb3* deletion leads to an impaired myocardium in mouse embryos. (**A**–**C**), Cross- sections of E15.5-16.5 fetuses showing cardiac muscle actin (clone HHF35) immunohistochemistry for wildtype (**A**) and two different TGFβ3-deficient fetuses (**B**,**C**). TGFβ3-deficient fetuses developed non-uniform right ventricular myocardium with heterogeneous regions of thicker (**B**, left arrow) and thinner (**B**, bottom arrow) myocardium and spongy (**B**, right arrow) and thicker (**C**, right arrow) left ventricular myocardium compared to the wildtype littermate fetus (**A**), Other mutant fetus had a muscular ventricular septal defect (VSD) (**C**, asterisk) (n = 6). (**D**,**E**), Representative images revealed *Tgfb3* expression (green-blue punctate dots, arrows) in the compact and trabecular myocardium of the right (**D**) and left ventricles (**E**) from wildtype E12.5 embryo. Scale bars = 200 µm for (**A**–**C**), 50 µm for (**D**,**E**). Abbreviations: rv, right ventricle; lv, left ventricle.

3.2. *Tgfb3* Deletion Leads to Outflow Tract Cushion Remodeling and Septal Defects

Histological examination of the H&E stained serial sections from wildtype and *Tgfb3*$^{-/-}$ fetuses at E13.5-18.5 revealed that about two thirds of the cases of the homozygous mutant fetuses developed various cardiac outflow tract malformations with variable penetrance (Table 1 and Table S1). Cardiac muscle immunohistochemistry (via anti-cardiac muscle actin) was performed to confirm the OFT malformations. Major cardiac OFT malformations included double-outlet right ventricle (DORV) and a large OFT ventricular septal defect (VSD) with extension into inflow (about 5% cases) (Figure 2A–D), thickening of the pulmonary and aortic valve (about two thirds of cases) (Figure 3A–E and Figure S2A–D), abnormal ascending aortic and pulmonary trunk walls (about 16% cases) (Figure 3A,B and Figure S3). The DORV was mainly subaortic in nature and exhibited defective fusion and remodeling of the RV OFT septum (Figure 2A,B and Figure 3C–E). The walls of the aorta and pulmonary trunk appeared morphologically immature and the vascular smooth muscle cells distributed randomly in the vascular walls of *Tgfb3*$^{-/-}$ fetuses compared to their control littermates (Figure 3A,B and Figure S3). In addition, histological analysis also revealed hypoplastic vascular walls of aorta and/or pulmonary trunk and mildly thickened aortic and/or pulmonary valves in one third of cases of *Tgfb3*$^{+/-}$ fetuses (E14.5) (Figure S2A,B,D,E). There These OFT defects were consistent with the significant expression of *Tgfb3* in OFT cushion mesenchyme and walls of aorta and pulmonary trunk (Figure 3F). Morphometric comparison and volume measurements via AMIRA 3D reconstruction of serial sections

confirmed the hyperplastic nature of the OFT cushions in *Tgfb3*$^{-/-}$ fetuses compared to the wildtype littermate fetuses (Figure S4). Since the OFT septum was abnormal in *Tgfb3*$^{-/-}$ embryos, TUNEL assay was used to quantify the apoptosis. The OFT septum consists of two cell populations—cardiac neural crest (NCC) and second heart field (SHF)-derived cells. Apoptosis is a phenomenon of NCC [36]. RNAscope in situ hybridization confirmed that *Tgfb3* is significantly expressed in the OFT septum. Apoptosis centrally in the OFT septum (Figure 3G–I) could activate TGFβ3 in the circle of SHF-derived cells around it for their proper differentiation and proliferation (Figure 3J–L). To get the measurements of the difference in apoptosis between wildtype and *Tgfb3*$^{-/-}$ embryos the number of cells (as indicated in Figure 3I) were counted within the central NCC bound area. TUNEL analysis showed that the apoptosis of cushion mesenchymal cells at the OFT septum was significantly decreased in the affected *Tgfb3*$^{-/-}$ fetuses compared to wildtype littermates (Figure 3G–I). Immunohistochemical analysis via anti-phospho-histone H3 (Ser10) revealed an increase in the myocardial cell proliferation surrounding the central fibrous OFT septum and in the right ventricular myocardium (Figure 3J–L). This indicates that TGFβ3 is required for cardiac apoptosis and proliferation, which are important to cushion mesenchymal differentiation and maturation. Collectively, the data indicate that the loss of *Tgfb3* affects cardiac outflow tract cushion remodeling and septal and alignment processes.

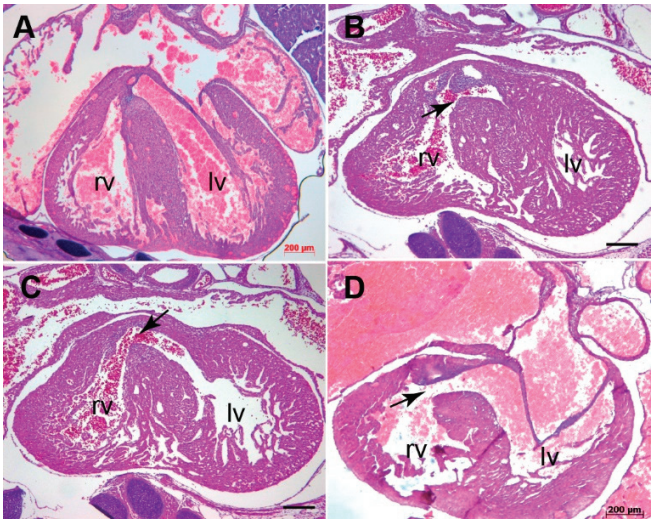

Figure 2. *Tgfb3* knockout mouse fetuses exhibit outflow tract septal and alignment defects. (**A**–**D**), Hematoxylin and eosin staining of hearts for E15.5-16.5 wildtype (**A**) and two different *Tgfb3*$^{-/-}$ fetuses (**B**–**D**). *Tgfb3*$^{-/-}$ fetuses develop both double-outlet right ventricle (**B**, arrow) and perimembranous ventricular septal defect (**C**,**D**; arrows). Scale bars = 200 µm for (**A**–**D**). Abbreviations: rv, right ventricle; lv, left ventricle.

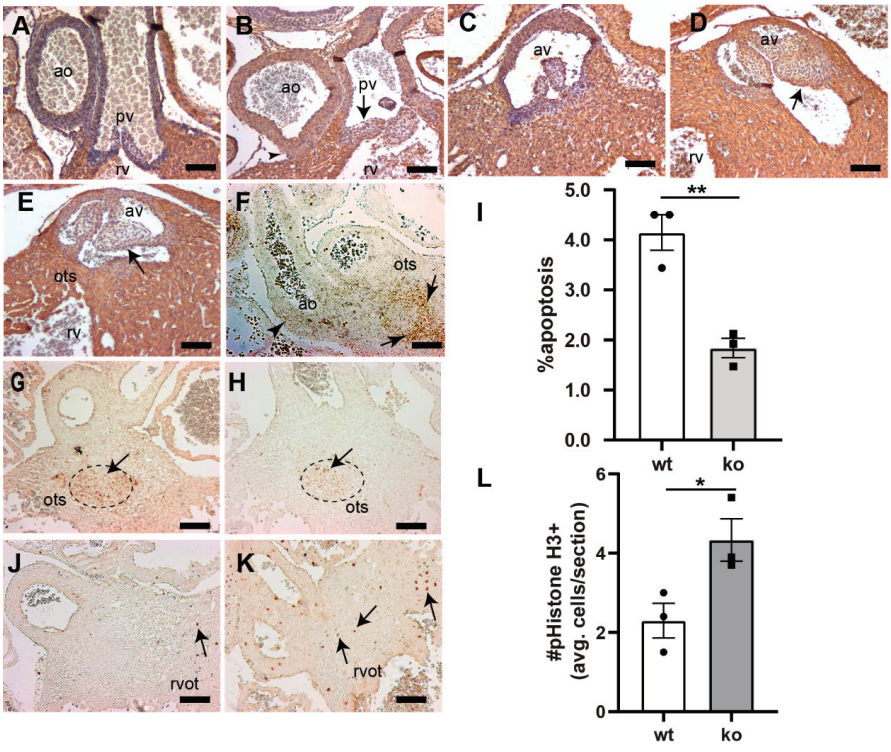

Figure 3. Loss of *Tgfb3* in mice results in the outflow tract cushion and vascular wall defects. (**A**–**E**), Cross-sections of E15.5–16.5 fetuses showing cardiac muscle actin (clone HHF35) immunohistochemistry for wildtype controls (**A**,**C**) and TGFβ3-deficient fetuses (**B**,**D**,**E**). *Tgfb3*$^{-/-}$ fetuses develop dysmorphic pulmonary (**B**) and aortic valve (**D**,**E**), and abnormal ascending aortic and pulmonary trunk walls (**B**) morphology. *Tgfb3*$^{-/-}$ fetuses also demonstrating hypoplastic outlet septum (**E**). (**F**) Representative image of a wildtype embryo (E11.5) using RNAscope in situ hybridization reveals *Tgfb3* expression (brown punctate dots) in the vascular wall (arrowhead) and outflow tract septum (arrow). (**G**,**H**), Apoptosis (E13.5) using TUNEL staining (brown colored nuclei) in outflow tract septum mesenchyme. Compared to wildtype controls (**G**), *Tgfb3*$^{-/-}$ OFT septum have a reduced number of apoptotic cells (**H**). (**I**) Quantification of fraction of cells undergoing apoptosis. Mean ± SEM of % average apoptosis from at least 4 sections for each sample was used for comparison. Quantification was predominantly done in the area of outflow tract septum marked by a dotted circle. Reduced apoptosis in *Tgfb3*$^{-/-}$ hearts was noted as compared to wildtype embryos (** $p = 0.004$, Student's t test; $p = 0.07$, Nonparametric (Mann Whitney test)). (**J**–**L**), Cell proliferation (E13.5) using phospho-histone H3 (Ser10) immunohistochemistry. Mean ± SEM of average pHistoneH3+ cells/section from at least 4 sections for each sample was used for comparison. Quantification was mainly restricted to the region around the fibrous outflow tract septum (**L**). Increased cell proliferation in *Tgfb3*$^{-/-}$ hearts (K, arrows) was observed as compared to wildtype (**J**) embryos (* $p = 0.04$, Student's t test; $p > 0.05$, Nonparametric (Mann Whitney test)). Scale bars = 100 μm for (**A**–**E**,**F**–**H**,**J**,**K**). Abbreviations: rv, right ventricle; av, aortic valve; pv, pulmonary valve; ao, ascending aorta; ots, outlet septum, rvot, right ventricular OFT.

3.3. Tgfb3 Deletion Leads to AV Cushion Remodeling Defects

Analysis of H&E stained serial sections revealed that approximately 42% cases of *Tgfb3*$^{-/-}$ fetuses developed malformations of the AV valves (Table 1 and Table S1). Mitral and/or tricuspid valve thickening was observed in all affected cases of the overall mutants analyzed (Figure 4A–D). Importantly, a significant proportion of the *Tgfb3*$^{-/-}$ fetuses developed VSD, which included perimembranous VSD (about 21% cases) (Figure 2A,C,D). The perimembranous VSD is normally linked to OFT VSD with an extension into the inlet septum and that it not obligatory related to abnormal AV valves. Thus, the perimembranous VSD is due to abnormal OFT cushion remodeling and is not related to AV cushion remodeling defects. Histological analysis did not reveal the presence of any AV septal defect (AVSD) in *Tgfb3*$^{-/-}$ embryos. These data indicate a requirement of TGFβ3 in the AV cushion remodeling and but not in AV septal formation during heart development.

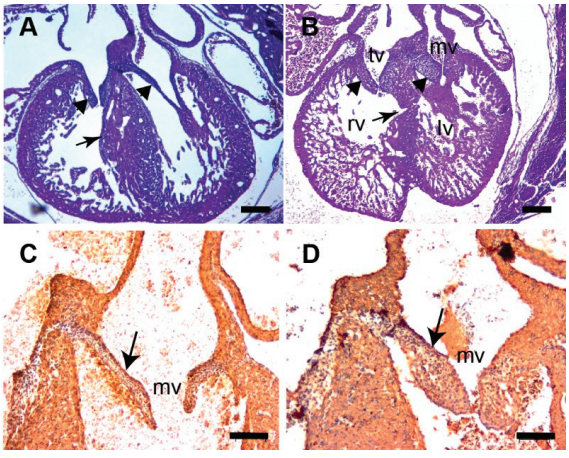

Figure 4. *Tgfb3* knockout fetuses exhibit atrioventricular valve thickening. (**A**,**B**) H&E stained sections of wildtype (**A**) and Tgfb3$^{-/-}$ fetus (E14.5-15.5) showing mitral valve and tricuspid valve thickening (**B**, arrowheads). Note that the ventricular myocardium is thin and abnormal with muscular ventricular septal defect in *Tgfb3*$^{-/-}$ (**B**, arrow). (**C**,**D**), Cardiac muscle actin (clone HHF35) immunohistochemistry of cross-sections of E15.5-16.5 wildtype (**C**) and *Tgfb3*$^{-/-}$ (**D**) fetuses. *Tgfb3*$^{-/-}$ fetus develop thickened mitral valves (**D**, arrow). Scale bars = 200 μm for (**A**,**B**), 50 μm for (**C**,**D**). Abbreviations: rv, right ventricle; lv, left ventricle; tv, tricuspid valve; mv, mitral valve.

3.4. TGFβ3 Is Required for Extracellular Matrix Reorganization

Given the involvement of TGFB3 in the development of fibrofatty lesions in the ARVD1, TGFβ3-deficient whole mouse embryonic fibroblasts were generated and tested for their ability to reorganize collagen in vitro in a three-dimensional collagen lattice formation assay. TGFβ3-deficient and wildtype fibroblasts were seeded in collagen gels and cultured for five days with or without 0.1 ng/mL and 1 ng/mL TGFβ1. The degree of collagen contraction (i.e., decrease in the surface area of the collagen gel) over time was determined. The wild type fibroblasts contracted in response to exogenously added TGFβ1, as expected, in a dose-dependent fashion. TGFβ3-deficient fibroblasts exhibited a reduced contraction compared to the wild type. Nonetheless, they remained responsive to TGFβ1 induction (Figure 5A–E). The difference in the degree of contraction between TGFβ3-deficient and wildtype whole mouse embryonic fibroblasts was rescued by exogenously added TGFβ1, indicating that the excess TGFβ1 is able to rescue the impaired ability of TGFβ3-deficient whole mouse embryonic fibroblasts to reorganize collagen lattices.

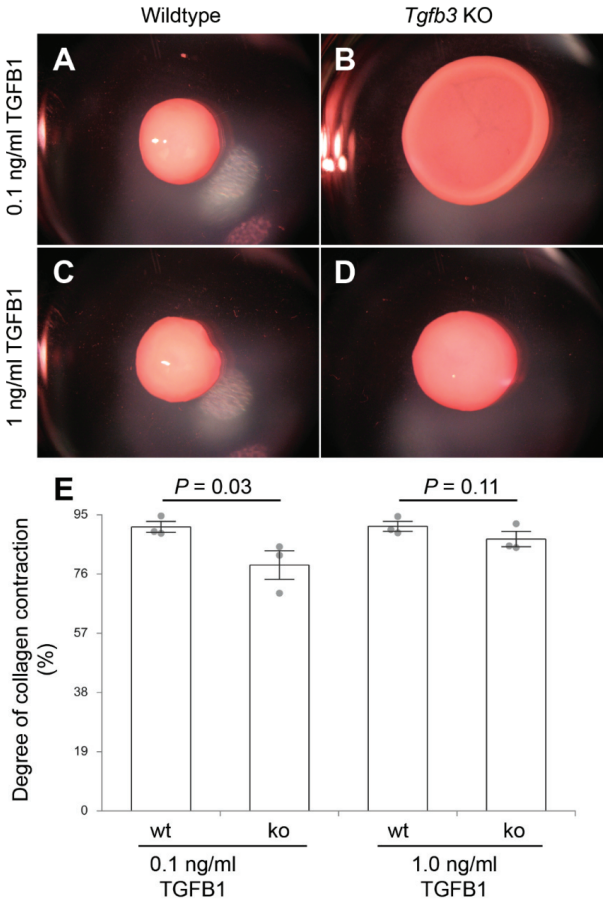

Figure 5. Collagen lattice formation assay. (**A**–**D**), dissecting microscope images of fibroblast-laden collagen gels after 5-days using three independent fibroblast cell lines ($n = 3$) from wildtype (**A**,**C**) or *Tgfb3*$^{-/-}$ embryos (**B**,**D**) in the presence of low (0.1 ng/mL) (**A**,**B**) and high (1 ng/mL) (**C**,**D**) doses of exogenous recombinant TGFB1. TGFβ3-deficient whole mouse embryonic fibroblasts treated with the low dose of exogenous TGFB1 have decreased contractility compared to the wildtype fibroblasts while higher doses rescue contractility and lattice formation (**E**). *p*-Values are indicated in the histogram. Numerical data are presented as scatter dot-plots with the box denoting the mean; error bars identify the SEM.

3.5. Tgfb3 Deletion Leads to Hyper-Activated SMAD2/3 and SMAD1/5 Signaling Pathways

To determine the role of TGFβ3 in the regulation of downstream SMADs, the activation of important downstream TGFβ-dependent SMADs in isolated whole hearts with attached ascending aorta from the wildtype ($n = 6$) and *Tgfb3*$^{-/-}$ ($n = 6$) fetuses (E18.5) was determined by Western blot analysis. The changes in the TGFβ receptor-dependent phosphorylation of serine/threonine residues of SMADs (i.e., pSMAD2), SMAD3 (i.e., pSMAD3), and SMAD1/5 (i.e., pSMAD1/5) were quantified via densitometric analysis from the Western blots. There was no significant change in the total amount of the SMAD2, SMAD3, SMAD1/5, and β-actin proteins in the *Tgfb3*$^{-/-}$ hearts compared to wildtype hearts (Figure 6A–C). Importantly, these biochemical data showed that the levels of pSMAD2, pSMAD3, and pSMAD1/5 were significantly increased in the hearts of the *Tgfb3*$^{-/-}$ fetuses compared to the wildtype fetuses (Figure 6A–C). We found that 2/3 cases of mutants fall within a high SMAD-dependent

TGFβ signaling cluster, whereas the levels of activated SMADs were not significantly altered in one third of cases of *Tgfb3*$^{-/-}$ fetuses compared to wildtype fetuses. Biochemical analysis of 'pooled' tissue samples (three hearts with ascending aortas/sample) confirmed elevated pSMAD2 in *Tgfb3*$^{-/-}$ fetuses and also revealed increased pSMAD2 in *Tgfb3*$^{+/-}$ fetuses compared to wildtype fetuses at E14.5 (Figure 6E). Importantly, pSMAD2 levels were higher in *Tgfb3*$^{-/-}$ fetuses than the *Tgfb3*$^{+/-}$ fetuses, suggesting that loss of *Tgfb3* in a dose-dependent fashion triggers SMAD2 activation. Taken together, heterozygous or homozygous loss-of-function of *Tgfb3* results in paradoxically increased levels of activated SMAD2, SMAD3, and SMAD1/5 in the fetal cardiovascular tissues.

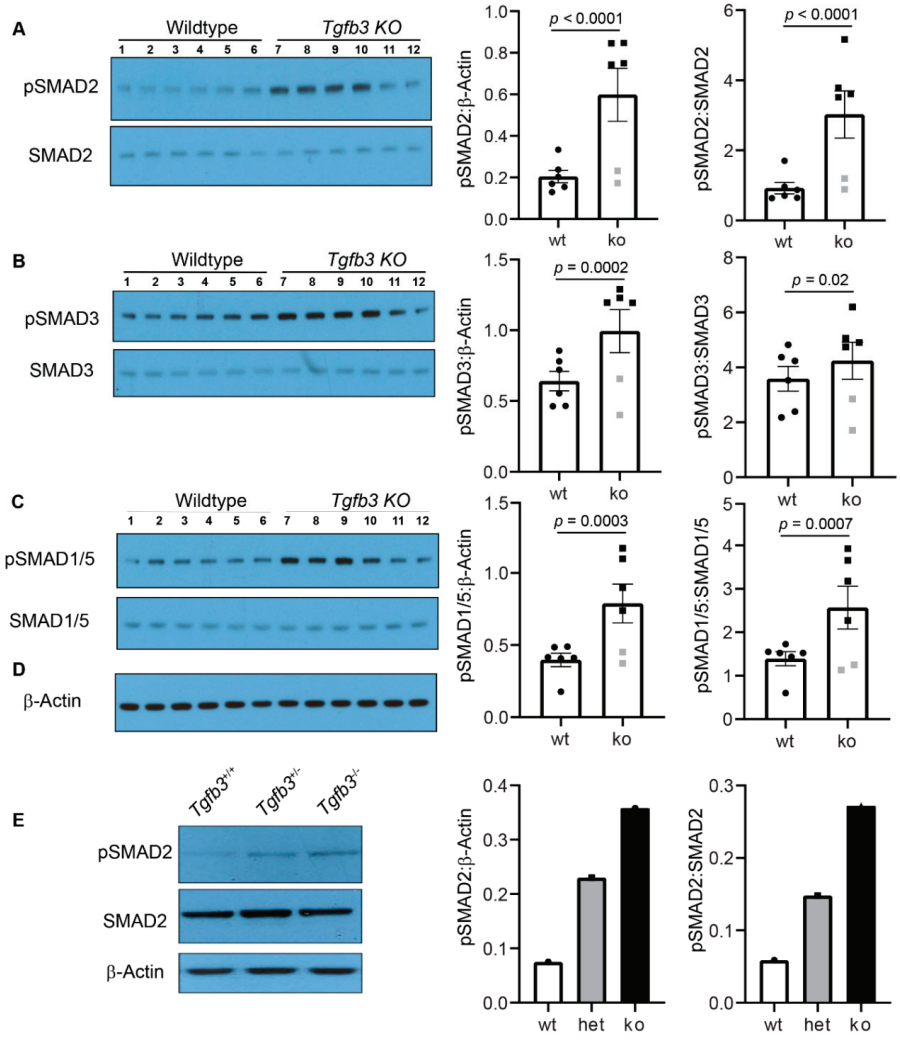

Figure 6. TGFβ3 is required for TGFβ-SMAD cardiovascular pathway activation. (**A**–**C**), Western blot analysis of fetal hearts and the accompanied ascending aorta (E18.5) shows protein levels of the phosphorylated SMADs (pSMAD2, pSMAD3, pSMAD1/5) and total SMADs (SMAD2, SMAD3, SMAD1/5).

SMAD1/5). (**D**) A common and independent β-actin blot (**C**, bottom) was used for normalizing data from pSMAD2, pSMAD3, and pSMAD1/5 blots. There was no difference in the β-actin levels between any cardiovascular tissues taken from wildtype and Tgfb3$^{-/-}$ mice. Densitometric quantification of phosphorylated proteins after normalization to β-actin and total non-phosphorylated proteins is shown on the right (**A**–**C**). E, Representative western blots of pooled samples (3 hearts and aortas/sample) from wildtype, *Tgfb3*$^{+/-}$, and *Tgfb3*$^{-/-}$ fetuses (E14.5) for pSMAD2, SMAD2, and β-actin. Each western blot was repeated three times with similar results. Western blots and densitometric quantification show the levels of pSMAD2 (60 kDa) and SMAD2 (60 kDa) (**A**,**D**), pSMAD3 (52 kDa) and SMAD3 (52 kDa) (**B**), pSMAD1/5 (60 kDa) and SMAD1/5 (60 kDa) (**C**), and β-actin (42 kDa) (**A**–**D**). Note that levels of pSMAD2, pSMAD3, and pSMAD1/5 are increased in individual samples taken from TGFβ3-deficient mice (**A**–**C**). The levels of pSMAD2 were also higher in pooled samples of both *Tgfb3*$^{+/-}$ and *Tgfb3*$^{-/-}$ fetuses compared to pooled sample from wildtype fetuses. *Tgfb3*$^{-/-}$ had slightly higher levels of pSMAD2 than the *Tgfb3*$^{+/-}$ fetuses. Data points excluded from statistical analysis (Student's *t* test) are indicated by grey symbols (**A**–**C**). Individual densitometric values from each pooled samples were plotted (**E**). All western blots (**A**–**C**) with individual samples were done in triplicate. Thus, all data points represent an average values of three independent blots (**A**–**C**). *p*-values are shown in the figure. Numerical data from multiple individual samples are presented as scatter dot-plots with boxes denoting the mean; error bars indicate the SEM.

3.6. TGFβ3-Deficiency Triggers Activation of Non-Canonical MAPK-Mediated TGFβ Signaling Pathways

TGFβ signaling under pathophysiological conditions can occur via non-SMAD pathways, including p38 MAPK and ERK1/2 MAPK [23]. Consequently, Western blot analysis was done on wildtype (n = 6) and *Tgfb3*$^{-/-}$ (n = 6) whole individual hearts with ascending aorta to determine the changes in the downstream components of the non-canonical TGFβ pathway. The densitometric analysis found no change in the levels of β-actin and total p38 protein (Figure 7A). Importantly, the data revealed significantly increased activation of p38 MAPK (i.e., pp38 MAPK) in the *Tgfb3*$^{-/-}$ hearts and aorta compared to the wildtype (Figure 7A). Moreover, the data showed that levels of activated ERK1/2 MAPK (i.e., pERK1/2), when normalized to total ERK1/2, were also higher in the cardiovascular tissues of the *Tgfb3*$^{-/-}$ fetuses than the wildtype (Figure 7B). Finally, Western blot analysis of pooled cardiovascular tissue samples (three hearts and aortas/sample) not only confirmed the elevated levels of pp38 and pERK1/2 in *Tgfb3*$^{-/-}$ fetuses but they also revealed increased levels of pp38 and pERK1/2 in Tgfb3$^{+/-}$ fetuses compared to wildtype fetuses (Figure 7C). Additionally, pp38 and pERK1/2 levels were higher in *Tgfb3*$^{-/-}$ fetuses than the *Tgfb3*$^{+/-}$ fetuses, suggesting that loss of *Tgfb3* in a dose-dependent fashion triggers the activation of both pp38 and pERK1/2 MAPKs. Collectively, these findings indicate that heterozygous or homozygous loss of *Tgfb3* in vivo leads to hyper-activation of SMAD-independent non-canonical TGFβ signaling through p38 MAPK and ERK1/2 MAPK pathways.

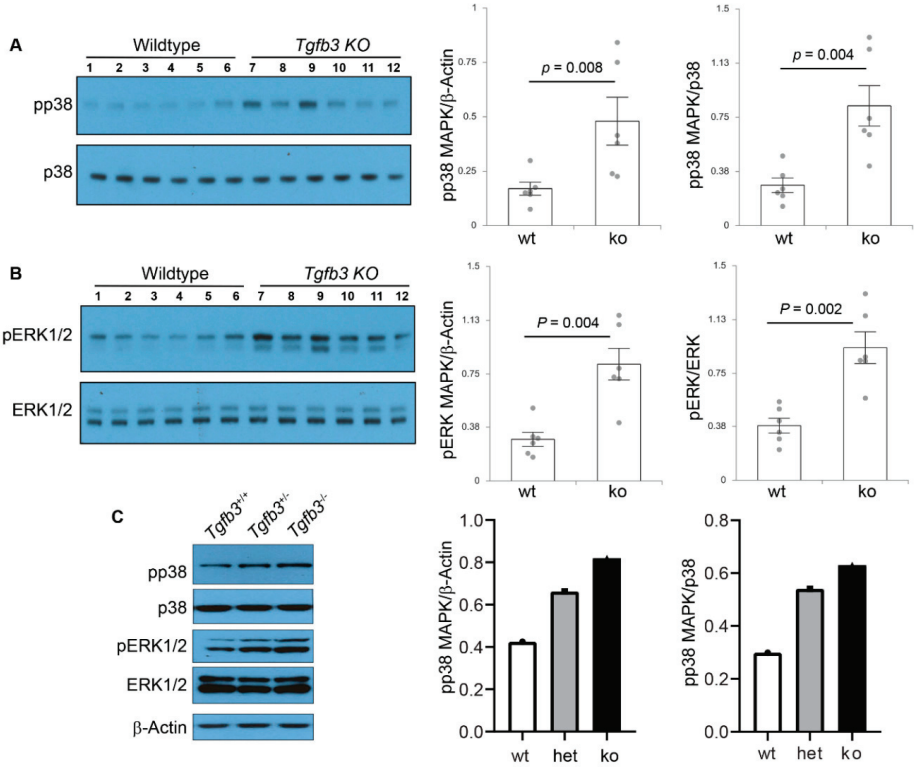

Figure 7. TGFβ3 is required for SMAD-independent non-canonical TGFβ cardiovascular pathway activation. (**A**,**B**) Western blot analysis of fetal hearts and accompanying ascending aortas (E18.5) show protein levels of phosphorylated p38 MAPK (pp38), total p38 MAPK (p38), phosphorylated ERK1/2 MAPK (pERK1/2), and total ERK1/2 MAPK (ERK1/2). Densitometric quantification of phosphorylated proteins after normalization to β-actin (via a common β-actin blot used in Figure 6D) and total non-phosphorylated proteins is shown on the right (**A**,**B**). Western blots and densitometric quantification show levels of pp38 (43 kDa) and p38 (40 kDa) (**A**), pERK1/2 (44/42 kDa) and ERK1/2 (44/42 kDa) (**A**,**B**). Note that similar results are obtained with normalization to either β-actin or the respective total p38 and ERK1/2 proteins. Note also that levels of pp38 MAPK and pERK1/2 MAPK are significantly increased in TGFβ3-deficient cardiovascular tissues. No data points were excluded from statistical analysis. Nonparametric test (Mann Whitney test) was used for analysis. *p*-values are shown in the figure. Numerical data are presented as scatter dot-plots with boxes denoting the mean; error bars indicate the SEM. (**C**) Representative western blots of pooled samples (3 hearts and aortas/sample for each genotype) showing elevated levels of pp38 and pERK1/2 in $Tgfb3^{+/-}$ and $Tgfb3^{-/-}$ fetuses (E14.5). Each western blot was repeated three times with similar results. Individual values for each samples were plotted. Notably, there is a trend of higher levels of both pp38 and pERK1/2 in $Tgfb3^{-/-}$ fetal hearts compared to $Tgfb3^{+/-}$ fetuses.

4. Discussion

This study has established that a significant fraction of the $Tgfb3^{-/-}$ mice develop a variety of cardiovascular malformations including DORV, ventricular septal defects (OFT, perimembranous, muscular), abnormal vascular walls, aortic valve and AV valve thickening, and impaired ventricular myocardium; especially that of the RV. Approximately two thirds of cases of the $Tgfb3^{-/-}$ mice develop one or more cardiovascular malformations and these phenotypic differences are not due to the

genetic background of these mice since all mice used in this study are on the C57BL/6 background produced via non-sibs mating. In addition, *Tgfb3*$^{+/-}$ fetuses develop mild cardiovascular malformations, including hypoplastic arterial walls, OFT cushion thickening, and impaired ventricular myocardium. These findings are consistent with the gene expression studies reported here and previous studies showing strong *Tgfb3* expression in the developing heart [26]. Two studies, in particular, established that systemic deletion of *Tgfb3* in mice leads to a cleft palate and perinatal lethality [1,2]. *Tgfb3*$^{-/-}$ mice (one third of cases), which do not have any obvious cardiovascular structural defects, still die perinatally and have a cleft palate. *Tgfb3* heterozygous mice survive normally. Many mutations in mice that cause a cleft palate also lead to heart defects [37]. *TGFB3* mutations in the LDS5 (also known as RNHF syndrome) typically cause cleft palate and is also characterized by several cardiovascular malformations, including thoracic and/or abdominal aneurysms, persistent foramen ovale, atrial or ventricular septal defects, atrioventricular block, aortic and mitral valve disease, and familial arrhythmogenic right ventricular dysplasia (ARVD1/C) involving replacement of the ventricular myocardium with fatty and fibrous elements, preferentially in the free wall of the right ventricle [9,12,13,38]. It is interesting that *Tgfb3*$^{-/-}$ fetuses have no atrial septal defects (ASD) and inflow tract abnormalities such as atrioventricular septal defects (AVSD), double inlet left ventricle (DILV), and common AV canal. This would indicate that abnormal OFT remodeling such as related to NCC and anterior SHF may be involved in OFT-related defects of *Tgfb3*$^{-/-}$ embryos. Overall, the data presented in this study is consistent with clinical genetic findings and indicate that TGFβ3 is required for multiple important aspects of cardiovascular development.

Tgfb3 is expressed in post-EMT cushion mesenchyme during cushion remodeling and differentiation, which is consistent with the OFT and AV cushion remodeling and OFT septation defects in *Tgfb3*$^{-/-}$ embryos. This is a contrast with the *Tgfb2*$^{-/-}$ embryos which develop both OFT and AV septation defects [39]. The data is also in line with previous studies indicating that TGFβ3 is not expressed in the mouse heart during EMT and that the cardiac EMT is not affected in *Tgfb3*$^{-/-}$ embryos [40,41]. TGFβs are known to induce apoptosis [42–44]. As a consequence, the effect of absence of TGFβ3 might result in down-regulated apoptosis, as shown here. Therefore, it is unlikely that down-regulated TGFβ3 represses apoptosis. Furthermore, latent TGFβ3, as demonstrated in the SHF [45] needs to be activated and apoptotic neural crest cells, by changing the micro-environment, might just activate TGFβs. Definitive proof that this chain of events is reversed involves experiments inhibiting apoptosis by deleting, e.g., apoptosis-specific genes as performed by Watanabe and Fisher [46] in the chicken embryo, which included outflow tract malformations even though the focus was not on TGFβ signaling. In addition, cell lineage tracing superimposed on systemic or conditional *Tgfb3* null embryos will be another approach to reveal the effect of *Tgfb3* on cellular apoptosis in the OFT septum. Collectively, the OFT cushion remodeling defects are consistent with the presence of both aortic and pulmonary valve thickening in the *Tgfb3*$^{-/-}$ fetuses. OFT septal malformations such as the DORV, are mainly subaortic in nature and exhibit defective fusion and remodeling of the outlet septum in *Tgfb3*$^{-/-}$ embryos. In some of the *Tgfb3*$^{-/-}$ fetuses, the aorta was positioned directly over a VSD due to an OFT alignment defect, which might be the result of abnormal inner curvature remodeling. On the other hand, the AV cushion remodeling defects are involved in the thickening of mitral and/or tricuspid valves in *Tgfb3*$^{-/-}$ fetuses. Notably, both outflow tract cushion and AV cushion defects are not present in all *Tgfb3*$^{-/-}$ fetuses. The overall cardiovascular tissue expression of *Tgfb3* is quite distinct but can slightly overlap to that of *Tgfb2* during cardiovascular development [26,47]. It is possible that TGFβ2 could slightly compensate for the loss of TGFβ3 during development. These suggestions are consistent with the clinical findings indicating the presence of aortic and mitral valve diseases and aortic aneurysm in the LDS patients with genetic mutations in *TGFB2* (LDS4) or TGFB3 (LDS5) [9,38,48]. Such a prediction is also supported by the observation that *Tgfb3* deletion worsens embryonic developmental phenotypes of *Tgfb2* knockout embryos [49]. Importantly, *Tgfb3* expression increases in comparison to *Tgfb2* during heart development [47]. This raises a possibility whether TGFβ3 could represent the predominant

TGFβ isoform during later stages of cardiac remodeling, a suggestion consistent with the mutations in TGFB3 in adult cardiac disease patients [7,50].

TGFB3 mutations result in dysregulated collagen matrix reorganization and fibrotic lesions associated with the ventricular fibrosis and aortic or mitral valve disease [6]. Several studies have indicated that TGFβ signaling is required for collagen production, remodeling, and organization [35,51,52]. Collagen organization is critical for heart development, and structure and function in the adult myocardium and heart valves [28]. A direct role of TGFβ3 on collagen reorganization has determined for the first time in this study. The data reveals that TGFβ3-deficient whole mouse fibroblasts are defective in their ability to reorganize the collagen matrix and that exogenous addition of higher doses of TGFβ1 can compensate for the loss of TGFβ3. This supports the hypothesis that loss of *Tgfb3* results in a compensatory TGFβ ECM response. This failure of reorganization is indicative of altered contractile machinery and/or adhesion molecules [33]. *TGFB3* mutations have also been reported in patients with mitral and aortic valve disease and that hyper-activated TGFβ signaling has been implicated in mammalian valve disease [9,53]. Thus, the results presented in this study, establishing a unique and important requirement of TGFβ3 in collagen fiber organization, are novel and represent a significant step which will increase our understanding of the role of TGFβ3 signaling in heart development and cardiac pathophysiology.

One of the observations and potential limitations of our study is the variable phenotypic penetrance of cardiovascular anomalies in *Tgfb3*$^{-/-}$ mice, which hinders the morphometric comparison and the investigation of the underlying cellular, developmental, molecular and biochemical mechanisms. Given that pSMAD2/3 levels are not significantly increased in one third of cases of the mutant hearts, it is difficult to conclude from the results whether the increased pSMAD2/3 levels cause the cardiovascular malformations in the *Tgfb3*$^{-/-}$ fetuses. It is possible that increased TGFβ signaling instead represents a compensatory mechanism and that a failure to fully compensate for the loss of TGFβ3 signaling results in phenotypically variable cardiovascular anomalies in the *Tgfb3*$^{-/-}$ fetuses. Such a prediction is consistent with more severe developmental phenotype and mid-gestational lethality reported in *Tgfb3* and *Tgfb2* double knockout embryos compared to the cardiovascular phenotypes reported in the *Tgfb3*$^{-/-}$ embryos in our study [49].

Another very significant finding in this study is that genetic disruption of *Tgfb3* leads to impaired ventricular myocardium. Regulatory mutations in the *TGFB3* associated with the increased TGFβ signaling have been identified in patients showing a typical ARVD1/C phenotype [7]. Notably, fibro-fatty replacement of the right ventricular myocardium in these ARVD1/C patients involves both fibrosis and myocardial apoptosis [6]. Our data suggest that TGFβ3-deficient hearts exhibit increased activation of SMAD-dependent (SMAD2/3 and SMAD1/5) and non-SMAD (p38 MAPK and ERK1/2 MAPK) pathways. TGFβ signaling via the SMAD2/3 pathways can induce the expression of extracellular matrix genes and the phenotypic transformation of fibroblasts into myofibroblasts, and stimulate pro-collagen and collagen synthesis [54]. Moreover, increased TGFβ signaling via the TRAF6-TAK1-p38 MAPK pathway can lead to apoptosis. In a remarkable study, Li et al. (2011) have shown that the loss of Jup1 (i.e., plakoglobin), which leads to impaired cell differentiation, increased myocardial apoptosis and fibrosis, and elevated TGFβ signaling causes ARVD1/C in mice [8]. Mutations in genes encoding desmosomal proteins including plakoglobin (JUP1) have also been reported in about half of the ARVC patients. Thus, it is possible that increased TGFβ signaling is a major and common underlying mechanism of ARVC pathogenesis. We provided histological and biochemical evidence showing that mild cardiovascular malformations (such as hypoplastic arterial walls, myocardial defects, OFT cushion defects) in Tgfb3$^{+/-}$ embryos are also associated with hyper-activated canonical and noncanonical TGFβ signaling. This observation is quite similar to the increased SMAD2 activation seen in aortic tissue and fibroblasts of LDS5 and ARVD1/C patients harboring *TGFB3* heterozygous mutations. Together, this suggests that increased TGFβ signaling may be a compensatory response to the loss of TGFβ3 and that the extent of TGFβ overactivation beyond a certain threshold (i.e., wildtype < *Tgfb3* heterozygous < *Tgfb3* homozygous) could result in range of cardiovascular pathomorphologies. Since this increased TGFβ signaling seems compatible with the survival of *Tgfb3*$^{+/-}$ mice, it is possible that adult *Tgfb3*$^{+/-}$

mice will develop progressive cardiovascular disease such as aortic aneurysm, valvular heart disease, and cardiomyopathy. We are currently analyzing adult *Tgfb3*$^{+/-}$ mice at different ages in longitudinal studies to establish a correlation between TGFβ hyperactivation and development and progression of cardiovascular pathophysiology and disease (i.e., cardiac dysfunction, heart valve disease, aortic aneurysm via echocardiography).

In this study, we describe the abnormal vascular walls (aorta and pulmonary trunk) phenotype in both *Tgfb3* heterozygous and *Tgfb3* knockout fetuses, which nicely links this phenotype to LDS5 (human *TGFB3* mutations). Our data also show the expression of *Tgfb3* in the great vessels as well as in the condensed mesenchyme of the OFT septum, which is consistent with earlier findings [26]. That is a rare combination. Since, in the OFT (vascular and septation), the NCC interact with SHF [55–57], the total phenotypic outcomes in *Tgfb3* mutants may be the effect of a lack of TGFβ3 on both cell types. Since adventitial fibroblasts receive arterial epicardial derived cells [58], it is possible that the epicardial cells in the abnormal vascular walls in *Tgfb3*$^{-/-}$ embryos could be defective. The myocardial defects described in this study may be based on a defective contribution of epicardium derived fibroblasts with a higher involvement (but not selective) of the RV. The atrioventricular valves, both mitral and tricuspid receive epicardial cells [58–60], and therefore TGFβ3 might play an important role in epicardial morphogenesis. *Tgfb3* expression data support the idea that the role of epicardium is a crucial link to ventricular myocardial problems and the AV cushions [26,60]. Both ventricular myocardium and AV cushions receive epicardial cells that mainly differentiate into fibroblasts [58–60]. There is a difference in homing and timing of epicardium to RV and LV [61], which could explain why, in *Tgfb3*$^{-/-}$ embryos, the RV is more involved, although surely the LV is also affected as well. There are several models in which epicardium is defective, either after mechanical removing the epicardium in the quail or in mouse mutant models (PDGFRα, Podoplanin, RxR) [58,62]. All of these animal models present with very thin myocardium and a spongy ventricular septum with often muscular VSD. Recently, *Tgfb3* conditional knockout mice have been generated [63] and will be useful in future investigation to determine the cell-specific role of TGFβ3 in cardiovascular development and adult cardiovascular disease. In conclusion, TGFβ3 is required for cardiovascular development in mice by maintaining a proper balance of downstream SMAD-dependent and MAPK-dependent TGFβ signaling mechanisms.

Supplementary Materials: The following are available online at http://www.mdpi.com/2308-3425/7/2/19/s1. Table S1. Cardiovascular defects in *Tgfb3* knockout mice (Embryonic Day 13.5 to 18.5 (n = 19). Figure S1. Systemic *Tgfb3* deletion disrupts ventricular myocardial development and leads to muscular VSD. A–C, H&E stained sections of wildtype and different *Tgfb3*$^{-/-}$ fetuses (E15.5-16.5) showing abnormal size, shape, and myocardium of the right ventricle in *Tgfb3*$^{-/-}$ (B,C, left arrow) and mitral valve thickening (B,C, arrowheads). The left ventricular myocardium in *Tgfb3*$^{-/-}$ fetuses (B,C, right arrow) was also not normal. D,E, Cardiac muscle actin (clone HHF35) immunohistochemistry of cross sections of E14.5-15.5 fetuses showing myocardium of both right and left ventricles was affected in some *Tgfb3*$^{-/-}$ resulting in muscular VSD (E, arrow). F,G, H&E stained sections of wildtype and *Tgfb3*$^{+/-}$ fetuses (E14.5-15.5) showing mild thinning of the right ventricular myocardium (G, left arrowhead) and moderately thickened left ventricular myocardium (G, right arrowhead) in *Tgfb3*$^{+/-}$ fetuses compared to wildtype heart (F). Scale bars: 200 μm for A–G. Abbreviations: rv, right ventricle; lv, left ventricle; tv, tricuspid valve; mv, mitral valve. Figure S2. *Tgfb3* deletion leads to pulmonary and aortic valve defects. A–D, Hematoxylin and eosin staining for E15.5 wildtype (A,D), *Tgfb3*$^{+/-}$ (B,D), and *Tgfb3*$^{-/-}$ (C,F) fetuses. *Tgfb3*$^{+/-}$ fetus displays thinning of vascular walls of aorta and pulmonary trunk (B, arrowheads), mild thickening of both pulmonary (B, arrow) and aortic (E, arrow) valves compared to wildtype fetus (A,B). Notably, *Tgfb3*$^{-/-}$ fetuses develop severe forms of these cardiovascular defects (C,F). Scale bars: 200 μm for A-F. Figure S3. Abnormal ascending aortic walls in *Tgfb3* knockout fetuses. A–D, Elastin autofluorescence (C,D) of hematoxylin and eosin-stained (A,B) sections. Compared to wildtype littermate (C), *Tgfb3*$^{-/-}$ fetus shows poorly formed elastic lamellae and disorganized vascular smooth muscle cells in the aortic wall (arrows, D). Fluorescence images (C,D) were taken from region of aorta indicated by boxes (A,B). Arrows indicate elastic fibers (C,D) and the white dotted lines demarcates the aortic wall from vaso vasorum (D). Scale bars = 100 μm for A,B; 25 μm for C,D. Figure S4. Measurement of aortic valve volume in *Tgfb3* knockout fetuses. A–G, Morphometric comparison and volume measurements using AMIRA 3D segmentation of aortic valves from wildtype (A,C,E) and *Tgfb3*$^{-/-}$ (B,D,F) embryos (E15.5) showing non-coronary leaflets in red, left coronary leaflets in green, and the right coronary leaflets in yellow. The hyperplastic nature of the outflow tract cushions in *Tgfb3*$^{-/-}$ embryos compared to the wildtype littermate embryos (G). Student's *t* test was used.

p-Values are indicated in the histogram. Numerical data are presented as scatter dot-plots with boxes, with the box denoting the mean; error bars identify the S.E.M (n = 3 per genotype).

Author Contributions: Conceptualization, M.A. Methodology, M.C., N.A.-S., M.G.G., E.A.P., A.B., S.C., and J.J. Writing—Original draft preparation, M.A., M.C., and A.B. Writing—Review & Editing, J.F.E., R.E.P., and A.C.G.-d.G. Supervision, M.A. Funding, M.A. All authors have read and agreed to the published version of the manuscript.

Funding: This work was supported by, in parts, funds from the University of South Carolina, the National Institutes of Health grants R01HL126705, R01HL145064, R01CA218578-1A1 and the American Heart Association grant 17GRNT33650018 (M.A), American Heart Association-Predoctoral Fellowship 18PRE34080051 (N.A.), and University of South Carolina-ASPIRE I Postdoctoral Award (M.C.).

Acknowledgments: We thank Lorain Junor, Shalom Hre, Qingbo Lou, Taylor Dunphy, Ipsita Pradhan, Kacey Booth, Zeeshan Ayub, Waqas Hussain, Pragya Jaiswal, and Kim McRae for their assistance in image processing and morphometric measurements, mouse genotyping, tissue processing and sectioning, and histology. We also thank the Instrumentation Resource Facility at the University of South Carolina School of Medicine and the Dorn VA Medical Center for the instrumentation support.

Conflicts of Interest: The authors declare no conflict of interest.

References

1. Proetzel, G.; Pawlowski, S.A.; Wiles, M.V.; Yin, M.; Boivin, G.P.; Howles, P.N.; Ding, J.; Ferguson, M.W.J.; Doetschman, T. Transforming growth factor-beta 3 is required for secondary palate fusion. *Nat. Genet.* **1995**, *11*, 409–414. [CrossRef]
2. Kaartinen, V.; Voncken, J.W.; Shuler, C.; Warburton, D.; Bu, D.; Heisterkamp, N.; Groffen, J. Abnormal lung development and cleft palate in mice lacking TGF–β3 indicates defects of epithelial–mesenchymal interaction. *Nat. Genet.* **1995**, *11*, 415–421. [CrossRef]
3. Hu, L.; Liu, J.; Li, Z.; Ozturk, F.; Gurumurthy, C.; Romano, R.-A.; Sinha, S.; Nawshad, A. TGFβ3 Regulates Periderm Removal Through ΔNp63 in the Developing Palate. *J. Cell. Physiol.* **2015**, *230*, 1212–1225. [CrossRef]
4. Chopra, S.; Al-Sammarraie, N.; Lai, Y.; Azhar, M. Increased canonical WNT/β-catenin signalling and myxomatous valve disease. *Cardiovasc. Res.* **2017**, *113*, 6–9. [CrossRef]
5. Azhar, M.; Ware, S.M. Genetic and Developmental Basis of Cardiovascular Malformations. *Clin. Perinatol.* **2016**, *43*, 39–53. [CrossRef]
6. Tamargo, J. TGFβ3 mutations cause arrhythmogenic right ventricular dysplasia type 1 and open the door to understanding the biological role of TGFβ3 (where there's a will, there's a way). *Cardiovasc. Res.* **2012**, *96*, 188–190. [CrossRef]
7. Beffagna, G.; Occhi, G.; Nava, A.; Vitiello, L.; Ditadi, A.; Basso, C.; Bauce, B.; Carraro, G.; Thiene, G.; Towbin, J.A.; et al. Regulatory mutations in transforming growth factor-beta3 gene cause arrhythmogenic right ventricular cardiomyopathy type 1. *Cardiovasc. Res.* **2005**, *65*, 366–373. [CrossRef] [PubMed]
8. Li, D.; Liu, Y.; Maruyama, M.; Zhu, W.; Chen, H.; Zhang, W.; Reuter, S.; Lin, S.-F.; Haneline, L.S.; Field, L.J.; et al. Restrictive loss of plakoglobin in cardiomyocytes leads to arrhythmogenic cardiomyopathy. *Hum. Mol. Genet.* **2011**, *20*, 4582–4596. [CrossRef] [PubMed]
9. Bertoli-Avella, A.M.; Gillis, E.; Morisaki, H.; Verhagen, J.M.; De Graaf, B.M.; Van De Beek, G.; Gallo, E.; Kruithof, B.P.; Venselaar, H.; Myers, L.A.; et al. Mutations in a TGF-β ligand, TGFB3, cause syndromic aortic aneurysms and dissections. *J. Am. Coll. Cardiol.* **2015**, *65*, 1324–1336. [CrossRef] [PubMed]
10. Schepers, D.; Tortora, G.; Morisaki, H.; MacCarrick, G.; Lindsay, M.; Liang, D.; Mehta, S.G.; Hague, J.; Verhagen, J.M.; Van De Laar, I.M.; et al. A mutation update on the LDS-associated genes TGFB2/3 and SMAD2/3. *Hum. Mutat.* **2018**, *39*, 621–634. [CrossRef]
11. Mégarbané, A.; Deepthi, A.; Obeid, M.; Al-Ali, M.T.; Gambarini, A.; El-Hayek, S. Homozygous deletion of exons 2–7 within TGFB3 gene in a child with severe Loeys-Dietz syndrome and Marfan-like features. *Am. J. Med. Genet. Part A* **2020**, *182*, 1230–1235. [CrossRef]
12. Matyas, G.; Naef, P.; Tollens, M.; Oexle, K. De novo mutation of the latency-associated peptide domain of TGFB3 in a patient with overgrowth and Loeys-Dietz syndrome features. *Am. J. Med. Genet. Part A* **2014**, *164*, 2141–2143. [CrossRef] [PubMed]

13. Rienhoff, H.Y.; Yeo, C.-Y.; Morissette, R.; Khrebtukova, I.; Melnick, J.; Luo, S.; Leng, N.; Kim, Y.-J.; Schroth, G.; Westwick, J.; et al. A mutation in TGFB3 associated with a syndrome of low muscle mass, growth retardation, distal arthrogryposis and clinical features overlapping with marfan and loeys–dietz syndrome. *Am. J. Med. Genet. Part A* **2013**, *161*, 2040–2046. [CrossRef] [PubMed]
14. Rienhoff, H.Y. Response to "De novo mutation of the TGFB3 latency-associated peptide domain in a patient with overgrowth and Loeys-Dietz syndrome features". *Am. J. Med. Genet. Part A* **2014**, *164*, 2144–2145. [CrossRef]
15. Akhurst, R.J. The paradoxical TGF-beta vasculopathies. *Nat. Genet.* **2012**, *44*, 838–839. [CrossRef] [PubMed]
16. Doetschman, T.; Barnett, J.V.; Runyan, R.; Camenisch, T.D.; Heimark, R.L.; Granzier, H.L.; Conway, S.J.; Azhar, M. Transforming growth factor beta signaling in adult cardiovascular diseases and repair. *Cell Tissue Res.* **2011**, *347*, 203–223. [CrossRef] [PubMed]
17. Dobaczewski, M.; Chen, W.; Frangogiannis, N.G. Transforming growth factor (TGF)-beta signaling in cardiac remodeling. *J. Mol. Cell Cardiol.* **2011**, *51*, 600–606. [CrossRef]
18. Morikawa, M.; Derynck, R.; Miyazono, K. TGF-β and the TGF-β Family: Context-Dependent Roles in Cell and Tissue Physiology. *Cold Spring Harb. Perspect. Boil.* **2016**, *8*, a021873. [CrossRef]
19. Markwald, R.R.; Norris, R.A.; Moreno-Rodriguez, R.; Levine, R.A. Developmental basis of adult cardiovascular diseases: Valvular heart diseases. *Ann. N. Y. Acad. Sci.* **2010**, *1188*, 177–183. [CrossRef]
20. Goumans, M.J.; Dijke, P.T. TGF-β Signaling in Control of Cardiovascular Function. *Cold Spring Harb. Perspect. Boil.* **2018**, *10*, a022210. [CrossRef]
21. Hill, C.S. Transcriptional Control by the SMADs. *Cold Spring Harb. Perspect. Boil.* **2016**. [CrossRef]
22. Ramachandran, A.; Vizan, P.; Das, D.; Chakravarty, P.; Vogt, J.; Rogers, K.; Müller, P.; Hinck, A.P.; Sapkota, G.P.; Hill, C.S. TGF-β uses a novel mode of receptor activation to phosphorylate SMAD1/5 and induce epithelial-to-mesenchymal transition. *eLife* **2018**, *7*. [CrossRef] [PubMed]
23. Mu, Y.; Gudey, S.; Landström, M. Non-Smad signaling pathways. *Cell Tissue Res.* **2011**, *347*, 11–20. [CrossRef]
24. Doetschman, T. Interpretation of phenotype in genetically engineered mice. *Lab. Anim. Sci.* **1999**, *49*, 137–143. [PubMed]
25. Heldin, C.-H.; Moustakas, A. Signaling Receptors for TGF-β Family Members. *Cold Spring Harb. Perspect. Boil.* **2016**, 8. [CrossRef]
26. Molin, D.G.; Bartram, U.; Van der Heiden, K.; Van Iperen, L.; Speer, C.P.; Hierck, B.P.; Poelmann, R.E.; Gittenberger-de-Groot, A.C. Expression patterns of Tgfbeta1-3 associate with myocardialisation of the outflow tract and the development of the epicardium and the fibrous heart skeleton. *Dev. Dyn.* **2003**, *227*, 431–444. [CrossRef]
27. Rampazzo, A.; Beffagna, G.; Nava, A.; Occhi, G.; Bauce, B.; Noiato, M.; Basso, C.; Frigo, G.; Thiene, G.; Towbin, J.; et al. Arrhythmogenic right ventricular cardiomyopathy type 1 (ARVD1): Confirmation of locus assignment and mutation screening of four candidate genes. *Eur. J. Hum. Genet.* **2003**, *11*, 69–76. [CrossRef] [PubMed]
28. Frangogiannis, N.G. Fibroblasts and the extracellular matrix in right ventricular disease. *Cardiovasc. Res.* **2017**, *113*, 1453–1464. [CrossRef]
29. Azhar, M.; Brown, K.; Gard, C.; Chen, H.; Rajan, S.; Elliott, D.A.; Stevens, M.V.; Camenisch, T.D.; Conway, S.J.; Doetschman, T. Transforming growth factor Beta2 is required for valve remodeling during heart development. *Dev. Dyn.* **2011**, *240*, 2127–2141. [CrossRef]
30. Menon, V.; Eberth, J.F.; Goodwin, R.L.; Potts, J.D. Altered Hemodynamics in the Embryonic Heart Affects Outflow Valve Development. *J. Cardiovasc. Dev. Dis.* **2015**, *2*, 108–124. [CrossRef]
31. Wang, F.; Flanagan, J.; Su, N.; Wang, L.-C.; Bui, S.; Nielson, A.; Wu, X.; Vo, H.-T.; Ma, X.-J.; Luo, Y. RNAscope: A novel in situ RNA analysis platform for formalin-fixed, paraffin-embedded tissues. *J. Mol. Diagn.* **2012**, *14*, 22–29. [CrossRef] [PubMed]
32. Todaro, G.J.; Green, H. Quantitative studies of the growth of mouse embryo cells in culture and their development into established lines. *J. Cell Boil.* **1963**, *17*, 299–313. [CrossRef] [PubMed]
33. Lane, B.A.; Harmon, K.A.; Goodwin, R.L.; Yost, M.J.; Shazly, T.; Eberth, J.F. Constitutive modeling of compressible type-I collagen hydrogels. *Med. Eng. Phys.* **2018**, *53*, 39–48. [CrossRef] [PubMed]
34. Haskett, D.; Doyle, J.J.; Gard, C.; Chen, H.; Ball, C.; Estabrook, M.A.; Encinas, A.C.; Dietz, H.C.; Utzinger, U.; Geest, J.P.V.; et al. Altered tissue behavior of a non-aneurysmal descending thoracic aorta in the mouse model of Marfan syndrome. *Cell Tissue Res.* **2011**, *347*, 267–277. [CrossRef] [PubMed]

35. Snider, P.; Hinton, R.B.; Moreno-Rodriguez, R.A.; Wang, J.; Rogers, R.; Lindsley, A.; Li, F.; Ingram, D.A.; Menick, D.; Field, L.; et al. Periostin is required for maturation and extracellular matrix stabilization of noncardiomyocyte lineages of the heart. *Circ. Res.* **2008**, *102*, 752–760. [CrossRef]
36. Poelmann, R.E.; Groot, A.C.G.-D. Apoptosis as an instrument in cardiovascular development. *Birth Defects Res. C* **2005**, *75*, 305–313. [CrossRef]
37. Ferguson, M.W.J. Craniofacial malformations: Towards a molecular understanding. *Nat. Genet.* **1994**, *6*, 329–330. [CrossRef]
38. Loeys, B.L.; Dietz, H.C. Loeys-Dietz Syndrome. In *Gene Reviews [Internet]*; Adam, M.P., Ardinger, H.H., et al., Eds.; University of Washington: Seattle, WA, USA, 2018; pp. 1993–2020. Available online: https://www.ncbi.nlm.nih.gov/books/NBK1133/ (accessed on 23 April 2020).
39. Bartram, U.; Molin, D.G.; Wisse, L.J.; Mohamad, A.; Sanford, L.P.; Doetschman, T.; Speer, C.P.; Poelmann, R.E.; Gittenberger-de Groot, A.C. Double-outlet right ventricle and overriding tricuspid valve reflect disturbances of looping, myocardialization, endocardial cushion differentiation, and apoptosis in Tgfb2 knockout mice. *Circulation* **2001**, *103*, 2745–2752. [CrossRef]
40. Mercado-Pimentel, M.E.; Runyan, R. Multiple Transforming Growth Factor-β Isoforms and Receptors Function during Epithelial-Mesenchymal Cell Transformation in the Embryonic Heart. *Cells Tissues Organs* **2007**, *185*, 146–156. [CrossRef]
41. Azhar, M.; Runyan, R.; Gard, C.; Sanford, L.P.; Miller, M.L.; Andringa, A.; Pawlowski, S.; Rajan, S.; Doetschman, T.; Doetschman, T. Ligand-specific function of transforming growth factor beta in epithelial-mesenchymal transition in heart development. *Dev. Dyn.* **2009**, *238*, 431–442. [CrossRef]
42. Hoover, L.L.; Burton, E.G.; O'Neill, M.L.; Brooks, B.A.; Sreedharan, S.; Dawson, N.A.; Kubalak, S.W. Retinoids regulate TGFβ signaling at the level of Smad2 phosphorylation and nuclear accumulation. *Biochim. et Biophys. Acta (BBA)-Bioenerg.* **2008**, *1783*, 2279–2286. [CrossRef] [PubMed]
43. Kubalak, S.W.; Hutson, D.R.; Scott, K.K.; Shannon, R.A. Elevated transforming growth factor beta2 enhances apoptosis and contributes to abnormal outflow tract and aortic sac development in retinoic X receptor alpha knockout embryos. *Development* **2002**, *129*, 733–746. [PubMed]
44. Walker, D.L.; Vacha, S.J.; Kirby, M.L.; Lo, C. Connexin43 deficiency causes dysregulation of coronary vasculogenesis. *Dev. Boil.* **2005**, *284*, 479–498. [CrossRef] [PubMed]
45. Guner-Ataman, B.; Paffett-Lugassy, N.; Adams, M.S.; Nevis, K.R.; Jahangiri, L.; Obregon, P.; Kikuchi, K.; Poss, K.D.; Burns, C.E.; Burns, C.G. Zebrafish second heart field development relies on progenitor specification in anterior lateral plate mesoderm and nkx2.5 function. *Development* **2013**, *140*, 1353–1363. [CrossRef]
46. Watanabe, M.; Jafri, A.; Fisher, S.A. Apoptosis Is Required for the Proper Formation of the Ventriculo-Arterial Connections. *Dev. Boil.* **2001**, *240*, 274–288. [CrossRef]
47. Vrljicak, P.; Chang, A.C.Y.; Morozova, O.; Wederell, E.D.; Niessen, K.; Marra, M.A.; Karsan, A.; Hoodless, P. Genomic analysis distinguishes phases of early development of the mouse atrio-ventricular canal. *Physiol. Genom.* **2009**, *40*, 150–157. [CrossRef]
48. Lindsay, M.E.; Schepers, D.; Bolar, N.A.; Doyle, J.J.; Gallo, E.; Fert-Bober, J.; Kempers, M.J.; Fishman, E.K.; Chen, Y.; Myers, L.; et al. Loss-of-function mutations in TGFB2 cause a syndromic presentation of thoracic aortic aneurysm. *Nat. Genet.* **2012**, *44*, 922–927. [CrossRef]
49. Dunker, N.; Krieglstein, K. Tgfbeta2$^{-/-}$ Tgfbeta3$^{-/-}$ double knockout mice display severe midline fusion defects and early embryonic lethality. *Anat. Embryol.* **2002**, *206*, 73–83.
50. Hu, B.C.; Li, L.; Sun, R.; Gao, P.; Zhu, D.; Wang, J.-G.; Chu, S.-L. The association between transforming growth factor β3 polymorphisms and left ventricular structure in hypertensive subjects. *Clin. Chim. Acta* **2010**, *411*, 558–562. [CrossRef]
51. Khalil, H.; Kanisicak, O.; Prasad, V.; Correll, R.N.; Fu, X.; Schips, T.G.; Vagnozzi, R.J.; Liu, R.; Huynh, T.; Lee, S.-J.; et al. Fibroblast-specific TGF-β-Smad2/3 signaling underlies cardiac fibrosis. *J. Clin. Investig.* **2017**, *127*, 3770–3783. [CrossRef]
52. Fix, C.; Carver-Molina, A.; Chakrabarti, M.; Azhar, M.; Carver, W. Effects of the isothiocyanate sulforaphane on TGF-β1-induced rat cardiac fibroblast activation and extracellular matrix interactions. *J. Cell. Physiol.* **2019**, *234*, 13931–13941. [CrossRef]
53. Ng, C.M.; Cheng, A.; Myers, L.A.; Martínez-Murillo, F.; Jie, C.; Bedja, D.; Gabrielson, K.L.; Hausladen, J.M.; Mecham, R.P.; Judge, D.P.; et al. TGF-β–dependent pathogenesis of mitral valve prolapse in a mouse model of Marfan syndrome. *J. Clin. Investig.* **2004**, *114*, 1586–1592. [CrossRef]

54. Murata, H.; Zhou, L.; Ochoa, S.; Hasan, A.; Badiavas, E.; Falanga, V. TGF-β3 Stimulates and Regulates Collagen Synthesis Through TGF-β1-Dependent and Independent Mechanisms. *J. Investig. Dermatol.* **1997**, *108*, 258–262. [CrossRef]
55. Groot, A.C.G.-D.; Calkoen, E.E.; Poelmann, R.E.; Bartelings, M.M.; Jongbloed, M.R.M. Morphogenesis and molecular considerations on congenital cardiac septal defects. *Ann. Med.* **2014**, *46*, 640–652. [CrossRef]
56. Conway, S.J.; Kaartinen, V. TGFbeta superfamily signaling in the neural crest lineage. *Cell Adh. Migr.* **2011**, *5*, 232–236. [CrossRef]
57. Neeb, Z.; Lajiness, J.D.; Bolanis, E.; Conway, S.J. Cardiac outflow tract anomalies. *Wiley Interdiscip. Rev. Dev. Boil.* **2013**, *2*, 499–530. [CrossRef]
58. Groot, A.C.G.-D.; Winter, E.M.; Bartelings, M.M.; Goumans, M.J.; DeRuiter, M.C.; Poelmann, R.E. The arterial and cardiac epicardium in development, disease and repair. *Differentiation* **2012**, *84*, 41–53. [CrossRef]
59. Lockhart, M.M.; Hoff, M.V.D.; Wessels, A. The Role of the Epicardium in the Formation of the Cardiac Valves in the Mouse. In *Etiology and Morphogenesis of Congenital Heart Disease*; Springer Science and Business Media LLC: Berlin, Germany, 2016; pp. 161–167.
60. Wessels, A.; Pérez-Pomares, J.M. The epicardium and epicardially derived cells (EPDCs) as cardiac stem cells. *Anat. Rec. Part A Discov. Mol. Cell. Evol. Boil.* **2003**, *276*, 43–57. [CrossRef]
61. Vicente-Steijn, R.; Scherptong, R.W.C.; Kruithof, B.P.T.; Duim, S.N.; Goumans, M.J.T.H.; Wisse, L.J.; Zhou, B.; Pu, W.T.; Poelmann, R.E.; Schalij, M.J.; et al. Regional differences in WT-1 and Tcf21 expression during ventricular development: Implications for myocardial compaction. *PLoS ONE* **2015**, *10*. [CrossRef]
62. Poelmann, R.E.; Groot, A.C.G.-D.; Vicente-Steijn, R.; Wisse, L.J.; Bartelings, M.M.; Everts, S.; Hoppenbrouwers, T.; Kruithof, B.P.T.; Jensen, B.; De Bruin, P.W.; et al. Evolution and Development of Ventricular Septation in the Amniote Heart. *PLoS ONE* **2014**, *9*. [CrossRef]
63. Doetschman, T.; Georgieva, T.; Li, H.; Reed, T.D.; Grisham, C.; Friel, J.; Estabrook, M.A.; Gard, C.; Sanford, L.; Azhar, M. Generation of mice with a conditional allele for the transforming growth factor beta3 gene. *Genes* **2012**, *50*, 59–66. [CrossRef] [PubMed]

Sample availability: not available.

Journal of
Cardiovascular
Development and Disease

MDPI

Article

Myocardium-Specific Deletion of Rac1 Causes Ventricular Noncompaction and Outflow Tract Defects

Carmen Leung [1], Anish Engineer [1], Mella Y. Kim [1], Xiangru Lu [1] and Qingping Feng [1,2,*]

[1] Department of Physiology and Pharmacology, Schulich School of Medicine and Dentistry, Western University, London, ON N6A 5C1, Canada; carmen.leung73@gmail.com (C.L.); aengine@uwo.ca (A.E.); ykim655@uwo.ca (M.Y.K.); slu48@uwo.ca (X.L.)
[2] Department of Medicine, Schulich School of Medicine and Dentistry, Western University, London, ON N6A 5C1, Canada
* Correspondence: qfeng@uwo.ca; Tel.: +1-519-850-2989

Abstract: Background: Left ventricular noncompaction (LVNC) is a cardiomyopathy that can lead to arrhythmias, embolic events and heart failure. Despite our current knowledge of cardiac development, the mechanisms underlying noncompaction of the ventricular myocardium are still poorly understood. The small GTPase *Rac1* acts as a crucial regulator of numerous developmental events. The present study aimed to investigate the cardiomyocyte specific role of *Rac1* in embryonic heart development. Methods and Results: The *Nkx2.5-Cre* transgenic mice were crossed with $Rac1^{f/f}$ mice to generate mice with a cardiomyocyte specific deletion of *Rac1* ($Rac1^{Nkx2.5}$) during heart development. Embryonic $Rac1^{Nkx2.5}$ hearts at E12.5–E18.5 were collected for histological analysis. Overall, $Rac1^{Nkx2.5}$ hearts displayed a bifid apex, along with hypertrabeculation and a thin compact myocardium. $Rac1^{Nkx2.5}$ hearts also exhibited ventricular septal defects (VSDs) and double outlet right ventricle (DORV) or overriding aorta. Cardiomyocytes had a rounded morphology and were highly disorganized, and the myocardial expression of Scrib, a planar cell polarity protein, was reduced in $Rac1^{Nkx2.5}$ hearts. In addition, cell proliferation rate was significantly decreased in the $Rac1^{Nkx2.5}$ ventricular myocardium at E9.5. Conclusions: *Rac1* deficiency in the myocardium impairs cardiomyocyte elongation and organization, and proliferative growth of the heart. A spectrum of CHDs arises in $Rac1^{Nkx2.5}$ hearts, implicating *Rac1* signaling in the ventricular myocardium as a crucial regulator of OFT alignment, along with compact myocardium growth and development.

Keywords: *Rac1*; proliferation; cell polarity; congenital heart defects; compact myocardium; trabeculation

Citation: Leung, C.; Engineer, A.; Kim, M.Y.; Lu, X.; Feng, Q. Myocardium-Specific Deletion of Rac1 Causes Ventricular Noncompaction and Outflow Tract Defects. *J. Cardiovasc. Dev. Dis.* **2021**, *8*, 29. https://doi.org/10.3390/jcdd8030029

Academic Editor: Monique R.M. Jongbloed

Received: 10 February 2021
Accepted: 12 March 2021
Published: 15 March 2021

1. Introduction

Congenital heart defects (CHDs) are the most common human birth defects, affecting up to 5% of live births [1,2]. The severity of these types of defects ranges from simple defects with no symptoms at birth, such as a small atrial septal defect (ASD), to complicated defects that are life-threatening and require intervention, such as Tetralogy of Fallot (TOF) [3,4]. One particular defect known as left ventricular noncompaction (LVNC) or "spongy myocardium" has no treatment at present, with the major therapy being heart failure and anticoagulation medications [5]. LVNC is classified as a rare genetic cardiomyopathy, occurring in 0.01% to 0.27% of the population, characterized by arrest of normal myocardium development, leading to a thin compact myocardial layer and an extensive non-compacted trabecular network [6,7]. Noncompaction of the ventricular myocardium can increase the risk of cardiac embolism, atrial fibrillation, ventricular arrhythmia and heart failure [5,7]. Although this defect occurs mostly in the LV, right ventricular (RV) noncompaction has also been reported in less than one-half of LVNC patients [8,9].

The ventricles grow and mature through a process of proliferation and differentiation to form trabeculation and compact myocardium [10]. In the mouse, trabecular formation

begins at approximately E9.5 where cardiomyocytes grow to form protrusions of muscular ridges [11]. The trabeculae then undergo a process of remodeling/compaction where the bases of the trabeculation thicken and collapse into the myocardial wall. Proliferation of the compact myocardium is concomitant with remodeling. By E14.5, mature trabeculation is formed, along with a thick, compact myocardium [12,13]. Numerous signaling pathways have been implicated in development of the ventricular chambers including Notch, BMP, FGF, retinoic acid and planar cell polarity (PCP) signaling [10,14]. In addition, various mouse models of ventricular noncompaction defect have been generated but the ventricular defects between the mouse models are not consistent, reflecting the complex process of ventricular myocardium development. To date, the complete signaling mechanisms underlying ventricular myocardium development are still not completely understood [15,16].

The small GTPase, *Rac1*, acts as a crucial regulator of numerous developmental events including proliferation, cell cycle progression, cell survival, differentiation and regulation of cell shape, morphology and polarity [17]. Specifically, the importance of *Rac1* signaling in embryonic heart development has emerged in recent studies [18,19]. Our previous work has demonstrated a critical role of *Rac1* signaling in the anterior SHF and anterior-SHF derived structures including the RV, interventricular septum and the OFT. *Rac1* regulates cardiomyocyte polarization in the RV and formation of the cardiac apex [18]. In order to study the cardiomyocyte specific role of *Rac1* in heart development, the *Rac1* gene is deleted in the myocardium using the *Nkx2.5-Cre* transgenic mouse, which drives Cre recombinase activity in both the RV and LV [20]. We show that *Rac1* signaling is crucial for ventricular myocardium development and cardiomyocyte specific deficiency of *Rac1* leads to a spectrum of CHDs including a thin compact myocardium and hypertrabeculation, similar to clinical features of LVNC. *Rac1* deficient hearts also had a bifid cardiac apex and OFT alignment defects. Furthermore, we showed that a *Rac1* deficiency in the myocardium disrupts proliferation along with the organization and polarization of cardiomyocytes.

2. Methods

2.1. Mice

The *Rac1*$^{f/f}$ mouse line (Stock #5550) and *mT/mG* mouse line (Stock #7676) were purchased from Jackson Laboratory, Bar Harbor, ME, USA [21,22]. The *Nkx2.5-Cre* transgenic mouse was provided by Dr. Chi-Chung Hui at The Hospital for Sick Children, University of Toronto, originally generated by McFadden and colleagues [20]. The *mT/mG* mouse is a global double-fluorescent Cre reporter mouse. This reporter mouse expresses membrane-targeted Tomato (mT) before Cre-excision and membrane-targeted GFP (mG) after excision of mT [22]. A breeding program to generate *Nkx2.5-Cre;Rac1*$^{f/f}$ (*Rac1*$^{Nkx2.5}$) and *Nkx2.5-Cre;mT/mG* mice was carried out and genotyping was performed as described previously [18]. Genotyping primer sequences are listed in Table 1. Mouse experiments and procedures were approved by the Animal Care Committee at Western University in accordance with the guidelines of the Canadian Council of Animal Care.

Table 1. PCR primer sequences for genotyping genetically modified mice.

Mice	Forward (5′-3′)	Reverse (5′-3′)
Nkx2.5-Cre	TGCCACGACCAAGTGACAGC	CCAGGTTACGGATATAGTTCATG
Rac1$^{f/f}$	TCCAATCTGTGCTGCCCATC	GATGCTTCTAGGGGTGAGCC
mTmG	CTCTGCTGCCTCCTGGCTTCT	CGAGGCGGATCACAAGCAATA Mutant reverse: TCAATGGGCGGGGGTCGTT

2.2. Histological Analysis

Embryonic samples (thoracic cavity) were fixed overnight in 4% paraformaldehyde at 4 °C, dehydrated and paraffin embedded. Samples were serially sectioned at 5 µm from the top of the aortic arch to the apex of the heart with a Leica RM2255 microtome. Sections were

mounted onto positively charged albumin/glycerin coated microslides. Slides were stained with hematoxylin and eosin (H/E) for histological analysis and images were captured using a light microscope (Observer D1, Zeiss, Oberkochen, Germany).

2.3. Immunohistochemistry

Immunohistochemical staining was performed on paraffin heart sections. Antigen retrieval was carried out in sodium citrate buffer (pH 6.0) at 92 °C using a BP-111 laboratory microwave (Microwave Research & Applications, Carol Stream, IL, USA). Immunostaining was performed with primary antibodies for GFP (Abcam, Cambridge, MA, USA) and Scrib (Santa Cruz, Santa Cruz, CA, USA) followed by incubation with biotinylated secondary antibody and avidin and biotinylated HRP (Santa Cruz). 3-3′ diaminobenzidine tetrahydrochloride (DAB, Dallas, TX, USA) substrate solution was used to visualize the substrate and slides were counterstained with hematoxylin. Images were captured with Zeiss Observer D1 microscope using AxioVision Rel 4.7 software. For proliferation and apoptosis analysis, E9.5 heart samples were fixed in 4% paraformaldehyde for one hour, cryoprotected in 30% sucrose and embedded in FSC22 frozen section media (Leica, Wetzlar, Germany). Samples were sectioned in a sagittal orientation with a Leica cryostat at 10 µm thick onto glass slides. Slides were incubated with anti-phosphohistone-H3 (phospho S10) (Abcam), anti-cleaved caspase-3 (Cell Signaling) primary antibody, Alexa Fluor 647 wheat germ agglutinin (Invitrogen, Waltham, MA, USA), Alexa Fluor 488 phalloidin (Life Technologies, Carlsbad, CA, USA) and counterstained with Hoechst 33342 (Invitrogen). Confocal images were obtained at the Biotron Research Centre, Western University with a Zeiss LSM 510 Duo microscope. Cardiomyocyte cell size was assessed by measuring the cross-sectional diameter at the nuclear level in ~50 cardiomyocytes per section and 5 sections per heart in the LV free wall using AxioVision software (Zeiss, Oberkochen, Germany) [23].

2.4. Quantitative Real Time RT-PCR

Total RNA was isolated from E12.5 ventricular myocardium using the RNeasy Mini Kit (QIAGEN). Reverse transcription reaction was performed, as described previously [18]. Briefly, M-MLV Reverse Transcriptase (Invitrogen) and EvaGreen qPCR Mastermix (Abm, Vancouver, BC, Canada) were used for real time thermal cycling. 28S rRNA was used as an internal control. Samples were amplified for 35 cycles using the Eppendorf Mastercycler Realplex Real-Time PCR machine (Hamburg, Germany). Real time RT-PCR primer sequences are listed in Table 2. The mRNA level of *Rac1* in relation to 28S rRNA was determined using a comparative C_T method [24,25].

Table 2. Primer sequences for real time RT-PCR analysis.

Gene	Forward (5′-3′)	Primer Sequence (5′-3′)
Rac1	TTGTCCAGCTGTGTCCCATA	AACCTGCCTGCTCATCAGTT
Gata4	GCCTGCGATGTCTGAGTGAC	CACTATGGGCACAGCAGCTC
Nkx2.5	GACAGCGGCAGGACCAGACT	CGTTGTAGCCATAGGCATTG
Tbx5	AGGAGCACAGTGAGGCACAA	GGGCCAGAGACACCATTCTC
Tbx20	CACCTATGGGGAAGAGGATGTTC	GTCGCTATGGATGCTGTACTGGT
Mef2c	TACCCCGGTGGTTTCCGTAG	CCCAACTGACTGAGGGCAGA
Scrib	AGGAGGAGAACAGGGATGAGGAG	CCTTTGTAGGGGGTAGAGCCTTT
Bmp10	CCACTCGGATCAGGAGGAAC	CACACAGCAGGCTTTGGAAG
Hand1	TGGCTACCAGTTACATCGCCTAC	GTGCGCCCTTTAATCCTCTTCT
Hand2	GCTACATCGCCTACCTCATGGAT	TCTTGTCGTTGCTGCTCACTGT
28S	ACATTGTTCCAACATGCCAG	TTGAAAATCCGGGGGAGAG

2.5. Western Blot Analysis

Rac1 protein expression from E12.5 ventricular myocardium was measured by western blot analysis. Briefly, 25 μg of protein from isolated ventricular tissue was separated by 12% SDS-Page gel and transferred to nitrocellulose membranes. Blots were probed with antibodies against *Rac1* (1:500, Santa Cruz) and α-actinin (1:5000, Sigma, St. Louis, MO, USA). Blots were then washed and probed with horseradish peroxidase conjugated secondary antibodies (1:2500, Bio-Rad, Hercules, CA, USA) and detected using an ECL detection method. Densitometry was then performed to quantify the signal.

2.6. Statistical Analysis

Data are presented as means ± SEM. An unpaired Student's *t* test was employed to determine statistical significance between the two groups. Differences were considered significant at $p < 0.05$.

3. Results

3.1. Generation of a Cardiomyocyte Specific Rac1 Knockout Mouse

The Cre recombinase in the *Nkx2.5-Cre* mouse line is activated after E8.5 and initial specification of cardiac progenitors [20]. *Nkx2.5-Cre* transgenic mice and $Rac1^{f/f}$ mice were crossed to generate *Nkx2.5-Cre;*$Rac1^{f/f}$ ($Rac1^{Nkx2.5}$) offspring (Figure 1A,B). To confirm a knockdown in *Rac1* mRNA expression, a real-time RT-PCR analysis was performed in RNAs isolated from E12.5 ventricles. The *Rac1* mRNA expression was significantly decreased by approximately 35% in $Rac1^{Nkx2.5}$ ventricular myocardium compared to littermate $Rac1^{f/f}$ controls (Figure 1C). *Rac1* protein levels in the ventricular myocardium were analyzed using western blotting. The ratio of *Rac1* to α-actinin protein levels was reduced by 49% in E12.5 $Rac1^{Nkx2.5}$ ventricular myocardium compared to littermate $Rac1^{f/f}$ controls (Figure 1D). These results confirm that *Nkx2.5-Cre*-mediated recombination sufficiently downregulates *Rac1* mRNA and protein expression in the ventricular myocardium of the developing heart.

3.2. Lineage Tracing of Nkx2.5-Cre Transgenic Mouse

To trace where the Cre recombinase is active in *Nkx2.5-Cre* transgenic hearts, *Nkx2.5-Cre* mice were crossed to *mT/mG* reporter mice, which marks all tissues possessing Cre recombinase activity with GFP. McFadden et al., the group who first created the *Nkx2.5-Cre* transgenic mouse, used a lacZ reporter to show that the Cre recombinase is active throughout the ventricular myocardium with minimal recombination in the OFT and atria [20]. Using the *Nkx2.5-Cre;mT/mG* mouse, we showed that the Cre recombinase was active throughout the ventricular myocardium and a large portion of the atria at E12.5 (Figure 2A). In addition, a majority of the pulmonary artery myocardium and part of the aorta were GFP^+ in *Nkx2.5-Cre;mT/mG* hearts (Figure 2B). Closer analysis of the aortic valves showed that some of the cells in the early aortic valves were also GFP^+ in *Nkx2.5-Cre;mT/mG* hearts (Figure 2C), indicating the contribution of *Nkx2.5* expressing cells to the development of the OFT and atria. Furthermore, closer examination of the epicardium and endocardial cells at E18.5 showed that these cells remained RFP^+, indicating no Cre recombinase activity in these cell types (Figure 2D–F). Thus, the *Nkx2.5-Cre* mouse drives recombination in the ventricular myocardium, atria and part of the OFT.

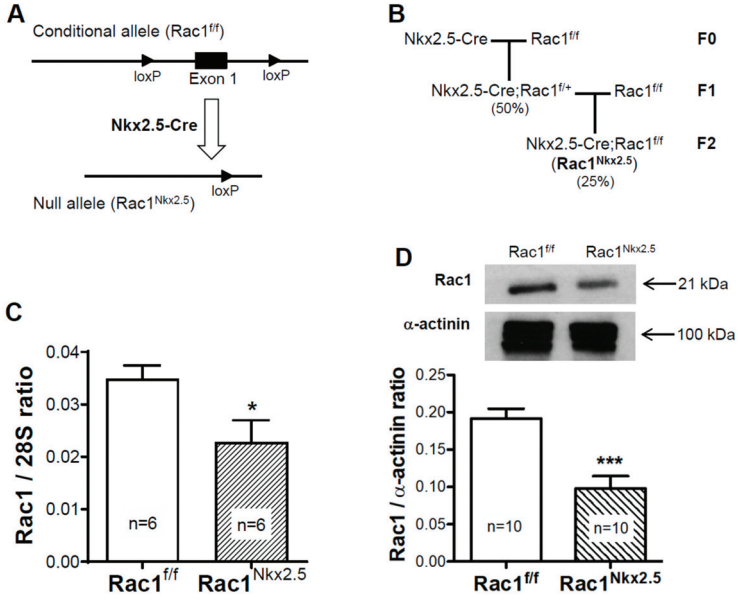

Figure 1. Generation of mouse line with a myocardium specific deletion of *Rac1* (*Rac1*$^{Nkx2.5}$). A schema of the floxed *Rac1* allele and *Nkx2.5-Cre* mediated generation of the *Rac1* null allele (**A**). *Rac1*$^{Nkx2.5}$ mice were generated by crossing *Nkx2.5-Cre* transgenic mice with *Rac1*$^{f/f}$ mice for 2 generations with the expected genotype frequencies indicated in brackets (**B**). *Rac1* mRNA expression was significantly reduced in E12.5 *Rac1*$^{Nkx2.5}$ ventricular myocardium compared to *Rac1*$^{f/f}$ littermates (**C**). Western blot analysis of E12.5 ventricular myocardium showed a significant decrease in *Rac1* protein levels in *Rac1*$^{Nkx2.5}$ hearts compared to controls (**D**). * $p < 0.05$, *** $p < 0.001$ by unpaired Student's *t*-test.

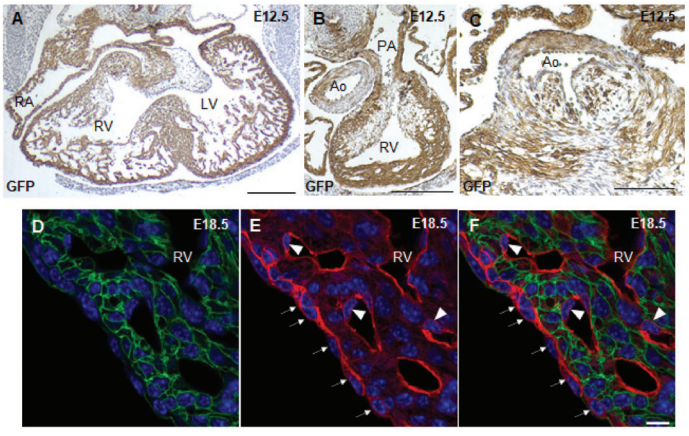

Figure 2. Lineage tracing with *Nkx2.5-Cre;mT/mG* mice. GFP immunostaining of E12.5 *Nkx2.5-Cre;mT/mG* paraffin heart sections showed Cre recombinase activity in the atrial and ventricular myocardium (**A**), OFT (**B**) and aortic valve leaflets (**C**). Fluorescence imaging of cryosections of E18.5 *Nkx2.5-Cre;mT/mG* hearts showed that the epicardium (arrows) and endothelial cells (arrowhead) remain RFP^{+} in *Nkx2.5-Cre;mT/mG* hearts (**D**–**F**). RV, right ventricle; LV, left ventricle; PA, pulmonary artery; Ao, aorta; epi, epicardium. Scale bars: 250 μm (**A**–**C**), 10 μm (**D**–**F**).

3.3. Congenital Heart Defects in $Rac1^{Nkx2.5}$ Mice

$Rac1^{Nkx2.5}$ embryos were alive from E11.5–18.5, but all neonates were found dead at P0 (n = 5). Gross morphological analysis of these P0 $Rac1^{Nkx2.5}$ hearts revealed a bifid cardiac apex, similar to what was observed and reported in our previous study with a *Mef2c-Cre* anterior second heart field-specific deletion of *Rac1* [18]. Examination of all $Rac1^{Nkx2.5}$ hearts at earlier embryonic time points showed evidence of a bifid cardiac apex as well (Figure 3A). In addition, $Rac1^{Nkx2.5}$ hearts had incomplete development of the interventricular septum, resulting in a ventricular septal defect (VSD) (Figure 3B,C, Table 3). Alignment of the outflow tract (OFT) to the ventricles was also defective in $Rac1^{Nkx2.5}$ hearts compared to littermate $Rac1^{f/f}$ controls. A double outlet right ventricle (DORV) was observed in 11 of the 17 $Rac1^{Nkx2.5}$ hearts (Figure 3D–G, Table 3) and 6 of the 17 $Rac1^{Nkx2.5}$ hearts exhibited an overriding aorta (Table 3). In addition, both the left ventricle (LV) and right ventricle (RV) of $Rac1^{Nkx2.5}$ hearts show a thin compact myocardium and hypertrabeculation (Figure 4A–D). The compact myocardium of both $Rac1^{Nkx2.5}$ ventricles at E15.5 was poorly formed and significantly thinner while the trabecular to compact myocardium ratio increased by more than 2.5-fold compared to littermate $Rac1^{f/f}$ controls (Figure 4E,F). These findings suggest a critical role for *Rac1* in interventricular septum formation, OFT alignment and development of the trabecular and compact ventricular myocardium.

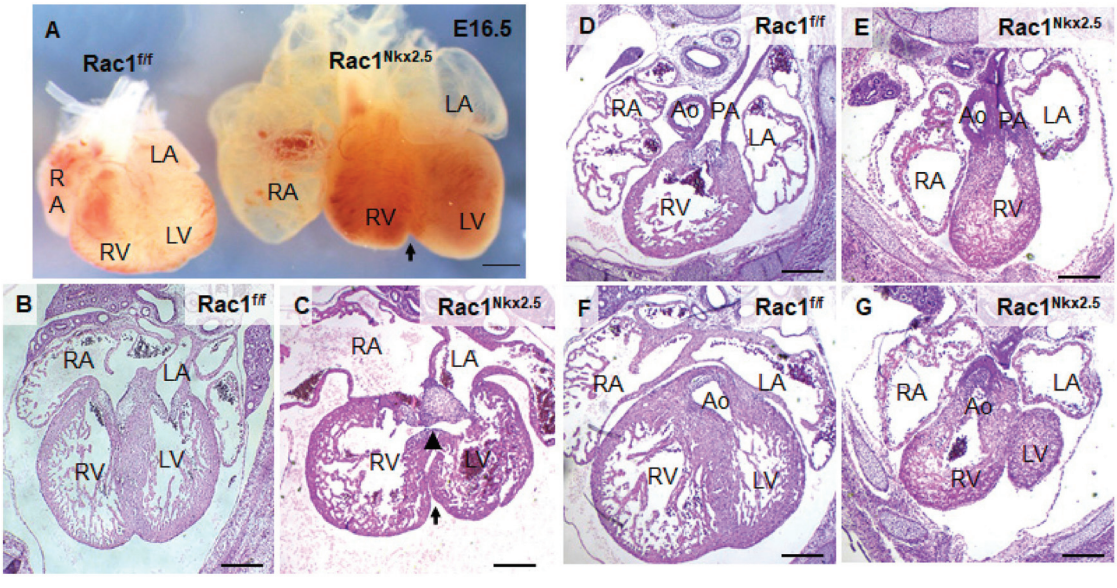

Figure 3. Congenital heart defects in $Rac1^{Nkx2.5}$. (**A**) Bifid cardiac apex in an E16.5 $Rac1^{Nkx2.5}$ heart. Arrow indicates bifurcation between the RV and LV. (**B**,**C**) Ventricular septal defect (arrowhead) was found in E15.5 $Rac1^{Nkx2.5}$ hearts with an arrow indicating the bifid cardiac apex. (**D**–**G**) Double outlet right ventricle (DORV) was found in E15.5 $Rac1^{Nkx2.5}$ hearts. The pulmonary artery and aorta were connected to the RV and LV, respectively in $Rac1^{f/f}$ control hearts (**D**,**F**). However, both pulmonary artery and aorta were connected to the RV in $Rac1^{Nkx2.5}$ hearts (**E**,**G**). RA, right atrium; LA, left atrium. Scale bars: 500 μm.

Table 3. Congenital heart defects in *Rac1*$^{Nkx2.5}$ mice (E14.5—P0).

	Bifid Apex	VSD	DORV	Overriding Aorta	Thin Compact Myocardium
N = 17	17	17	11	6	17
%	100	100	64.7	35.3	100

VSD, ventricular septal defect; DORV, double outlet right ventricle. All 17 *Rac1*^{SHF} hearts had more than one type of CHD. No CHDs defects were found in littermate E14.5-P0 *Rac1*$^{f/f}$ hearts (n = 11).

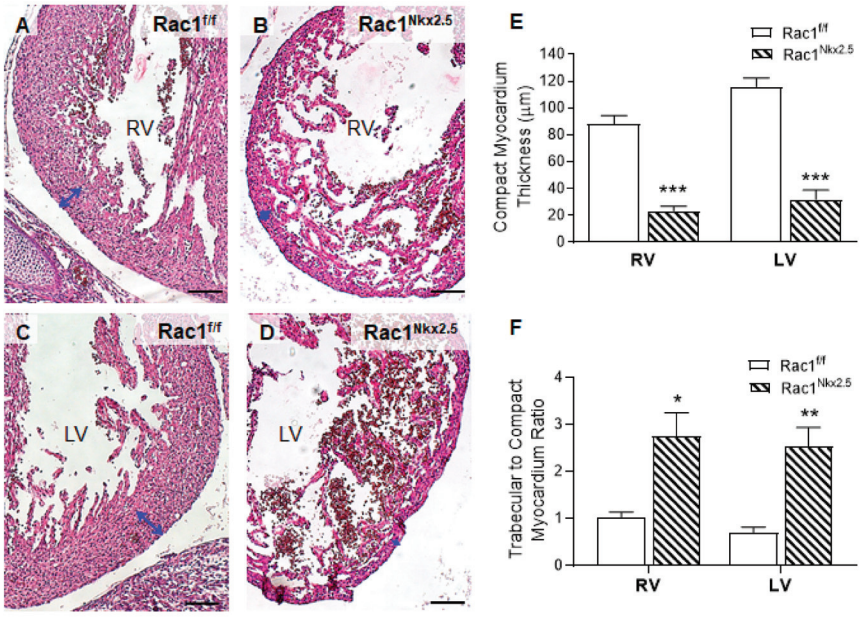

Figure 4. Ventricular myocardium abnormalities in *Rac1*$^{Nkx2.5}$ hearts at E15.5. In comparison to *Rac1*$^{f/f}$ controls (**A**,**C**), the *Rac1*$^{Nkx2.5}$ mice (**B**,**D**) show thin compact myocardium and hypertrabeculation in the RV and LV wall. The thickness of the compact myocardium in *Rac1*$^{Nkx2.5}$ hearts (n = 5) was decreased while trabecular to compact myocardium ratio was increased as compared to littermate controls (n = 6) (**E**,**F**). Double-headed arrows in (**A**–**D**) indicate measurements of compact myocardium thickness. * $p < 0.05$, ** $p < 0.01$, *** $p < 0.001$ vs. *Rac1*$^{f/f}$ by Student's t-test. Scale bars: 100 μm.

3.4. Loss of F-Actin Filament Organization and Cardiomyocyte Polarity in Rac1$^{Nkx2.5}$ *Hearts*

To analyze F-actin filament organization and cardiomyocyte polarity in the ventricular myocardium, E18.5 *Rac1*$^{Nkx2.5}$ heart sections were double stained with phalloidin and wheat germ agglutinin (WGA) to mark F-actin filaments and cell borders, respectively. Our data show that *Rac1*$^{Nkx2.5}$ hearts had severely disrupted F-actin filament organization compared to controls, which had long, parallel running F-actin filaments throughout the myocardium (Figure 5A,B). Additionally, WGA staining revealed rounded, spherically shaped cardiomyocytes in *Rac1*$^{Nkx2.5}$ hearts, in both the RV and LV (Figure 5D). In comparison, littermate ventricular myocardium had cardiomyocytes that underwent polarization with an elongated shape and were well organized/aligned in both the RV and LV (Figure 5C). Furthermore, quantitative analysis revealed that the cardiomyocyte cell size was significantly larger in *Rac1*$^{Nkx2.5}$ compared to the littermate controls (Figure 5E). This data suggests a crucial role for *Rac1* in F-actin filament organization, polarization and elongation of cardiomyocytes during embryonic heart development.

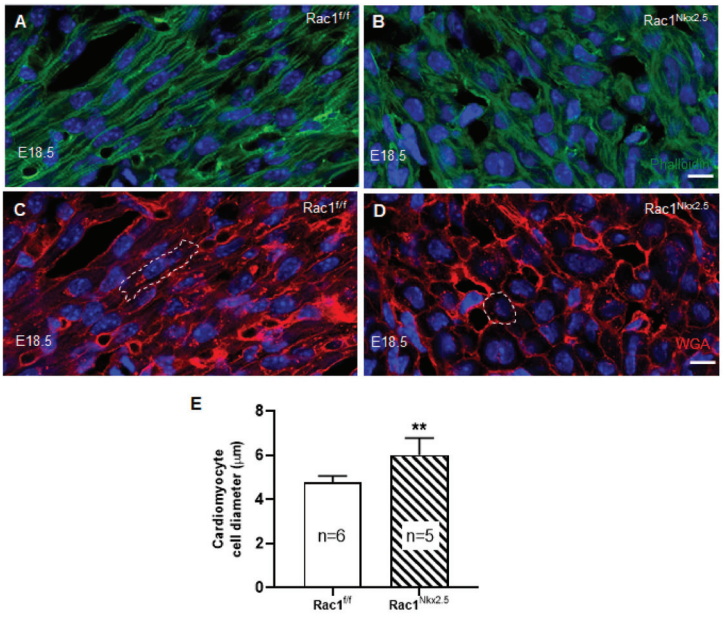

Figure 5. Disruption of F-actin organization and cardiomyocyte polarity in *Rac1*$^{Nkx2.5}$ hearts. E18.5 cryosections of the heart were double stained for phalloidin and wheat germ agglutinin (WGA) to assess F-actin organization and cardiomyocyte cell polarity, respectively. The images were taken from the corresponding areas of LV myocardium free wall in *Rac1*$^{f/f}$ and *Rac1*$^{Nkx2.5}$ mice. F-actin filament organization was disrupted in *Rac1*$^{Nkx2.5}$ myocardium (**B**) compared to littermate controls (**A**). WGA staining shows rounded cardiomyocytes in *Rac1*$^{Nkx2.5}$ ventricular myocardium (**D**) compared to the elongated cardiomyocytes in littermate controls (**C**). The cell borders of a cardiomyocyte in (**C**,**D**) are outlined. The short axis of cardiomyocyte diameter was significantly larger in *Rac1*$^{Nkx2.5}$ compared to littermates (**E**). ** $p < 0.01$ by unpaired Student's *t*-test. Scale bars: 10 μm.

3.5. Decreased Scrib Protein Expression in Rac1$^{Nkx2.5}$ *Hearts*

Scrib plays an important role in cell polarity through interacting with *Rac1* in the developing myocardium. Loss of either *Scrib* or *Rac1* leads to a reduction in membrane association of the other [19]. To analyze the expression of Scrib, immunostaining was performed on E15.5 *Rac1*$^{Nkx2.5}$ hearts. Scrib was highly expressed in the myocardium surrounding the opening of the aorta in control E15.5 hearts (Figure 6A). In comparison, the expression of Scrib in this area was reduced in E15.5 *Rac1*$^{Nkx2.5}$ heart sections (Figure 6B). Similar to what was described in our previous study [18], Scrib protein expression was abundant in the interventricular junction in control hearts at E15.5. However, expression of Scrib was reduced in E15.5 *Rac1*$^{Nkx2.5}$ the myocardium of interventricular junction compared to littermate controls (Figure 6C–F). Overall, Scrib protein expression was significantly decreased in E15.5 *Rac1*$^{Nkx2.5}$ hearts compared to littermate controls (Figure 6G). The loss of Scrib expression in *Rac1*$^{Nkx2.5}$ hearts suggests a disruption in cell polarity and the PCP pathway, further supporting a failure of cardiomyocytes to undergo polarization.

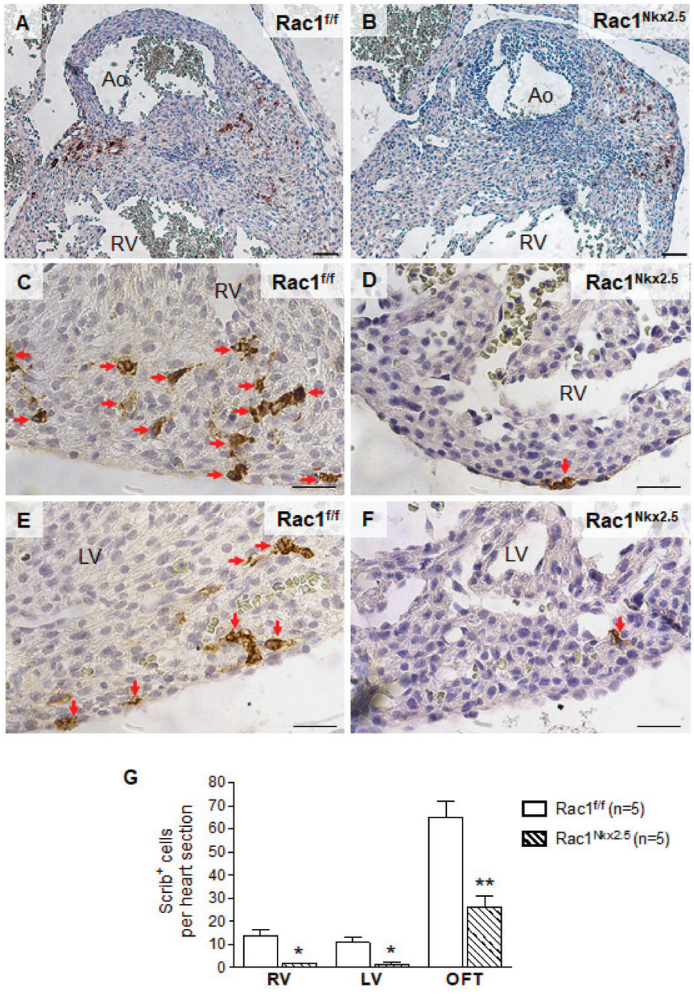

Figure 6. Loss of Scrib expression in *Rac1*$^{Nkx2.5}$ hearts. Scrib immunostaining was performed on E15.5 *Rac1*$^{Nkx2.5}$ and *Rac1*$^{f/f}$ heart sections. The areas analyzed included the myocardium surrounding the aorta (**A**,**B**), RV (**C**,**D**) and the LV (**E**,**F**). Five sections per heart were used. The number of Scrib-expressing positive cells was significantly decreased in the myocardium surrounding the aorta (OFT), RV and LV of *Rac1*$^{Nkx2.5}$ hearts (**G**). * $p < 0.05$, ** $p < 0.01$ by Student's *t*-test. Scale bars: 50 µm.

3.6. Decreased Cell Proliferation in Rac1$^{Nkx2.5}$ *Hearts*

The observed defects in *Rac1*$^{Nkx2.5}$ ventricular myocardium development could also be attributed to a decrease in cell proliferation and/or aberrant apoptosis. Cell proliferation has been shown to be highest at E9.5 in the developing mouse heart [26]. Thus, proliferation of E9.5 *Rac1*$^{Nkx2.5}$ hearts was analyzed by immunostaining for phospho-histone H3 (pHH3) and cyclin D1, which are a marker of the mitotic phase of cell division and a cell cycle regulator, respectively. The cell proliferation rate assessed by pHH3$^+$ and cyclin D1$^+$ cells in the ventricular myocardium was significantly reduced in E9.5 *Rac1*$^{Nkx2.5}$ hearts compared to littermate *Rac1*$^{f/f}$ controls (Figure 7A–F). Immunostaining for cleaved caspase-3 (CC3), a marker of activated apoptosis, showed little to no apoptosis in both control E9.5 and *Rac1*$^{Nkx2.5}$ ventricular myocardium (Figure 7G,H). However, apoptosis was detected in

tissues outside the heart (Figure 7I,J). The decreased proliferation rate in *Rac1*$^{Nkx2.5}$ hearts suggests a critical role for *Rac1* in regulating cardiomyocyte proliferation in the ventricular myocardium, after initial specification of cardiac progenitors.

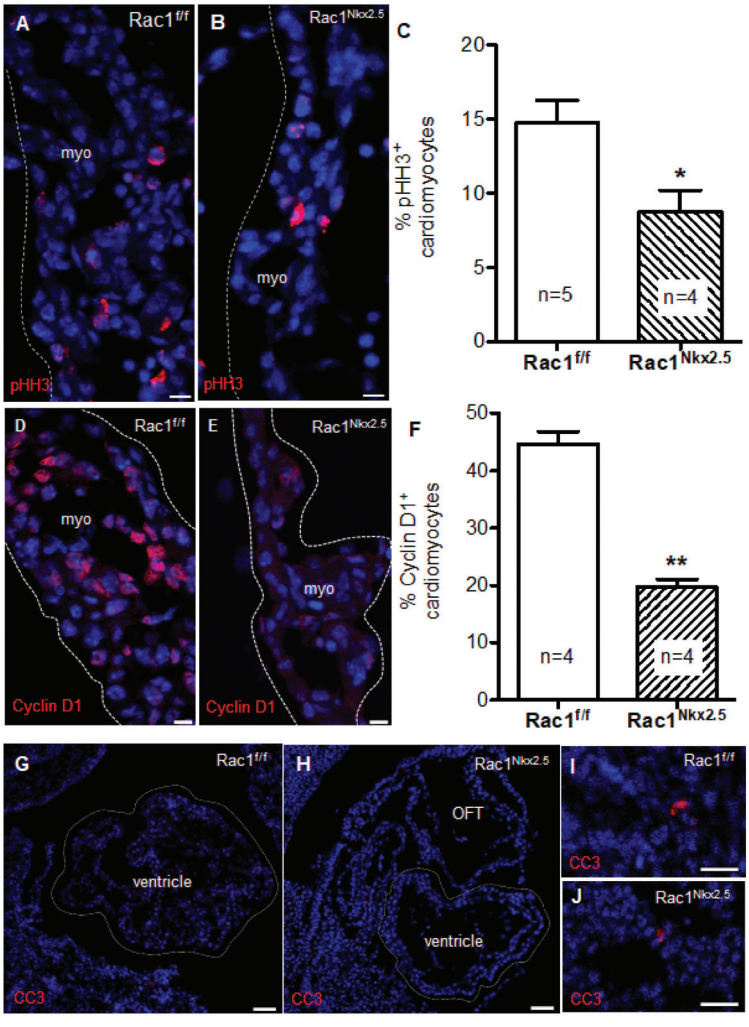

Figure 7. Decreased proliferation rate in *Rac1*$^{Nkx2.5}$ hearts. Phospho-histone H3 (pHH3) immunostaining to mark proliferating cells undergoing mitosis in ventricular myocardium (myo) of E9.5 *Rac1*$^{Nkx2.5}$ and *Rac1*$^{f/f}$ hearts (**A**,**B**). Proliferation rate was significantly decreased in E9.5 *Rac1*$^{Nkx2.5}$ ventricular myocardium compared to littermate controls (**C**). Cyclin D1 immunostaining in E9.5 *Rac1*$^{f/f}$ and *Rac1*$^{Nkx2.5}$ ventricular myocardium marked cell progression through G1 (**D**,**E**). Cyclin D1 expression was significantly decreased in E9.5 *Rac1*$^{Nkx2.5}$ ventricular myocardium compared to littermate controls (**F**). Cleaved caspase-3 (CC3) immunostaining to mark apoptotic cells in ventricular myocardium of E9.5 *Rac1*$^{Nkx2.5}$ and *Rac1*$^{f/f}$ hearts. No apoptosis was detected in E9.5 *Rac1*$^{Nkx2.5}$ and *Rac1*$^{f/f}$ ventricular myocardium (**G**,**H**). Apoptotic cells were detected in tissues outside of the heart in *Rac1*$^{f/f}$ and *Rac1*$^{Nkx2.5}$ embryos (**I**,**J**). * $p < 0.05$, ** $p < 0.01$ by unpaired Student's *t*-test. Scale bars: 10 μm (**A**,**B**), 50 μm (**D**–**G**).

3.7. Decreased Scrib and Cardiac Transcription Factor Expression in $Rac1^{Nkx2.5}$ Hearts

To assess the genetic pathways regulated by *Rac1* signaling, we analyzed the mRNA expression of factors critical to embryonic heart development in E12.5 hearts. Since Scrib-*Rac1* interaction is crucial for normal heart development, *Scrib* mRNA levels were assessed. Consistent with its protein expression (Figure 6), *Scrib* mRNA levels were significantly reduced in E12.5 $Rac1^{Nkx2.5}$ compared to $Rac1^{f/f}$ hearts (Figure 8A). Additionally, cardiac transcription and growth factors including *Nkx2.5*, *Gata4*, *Tbx5*, *Tbx20*, *Hand1*, *Hand2* and *Bmp10*, except *Mef2c*, were all significantly decreased in E12.5 $Rac1^{Nkx2.5}$ compared to $Rac1^{f/f}$ hearts (Figure 8B–I). These results indicate that transcriptional regulation of heart development was severely disrupted in the $Rac1^{Nkx2.5}$ hearts.

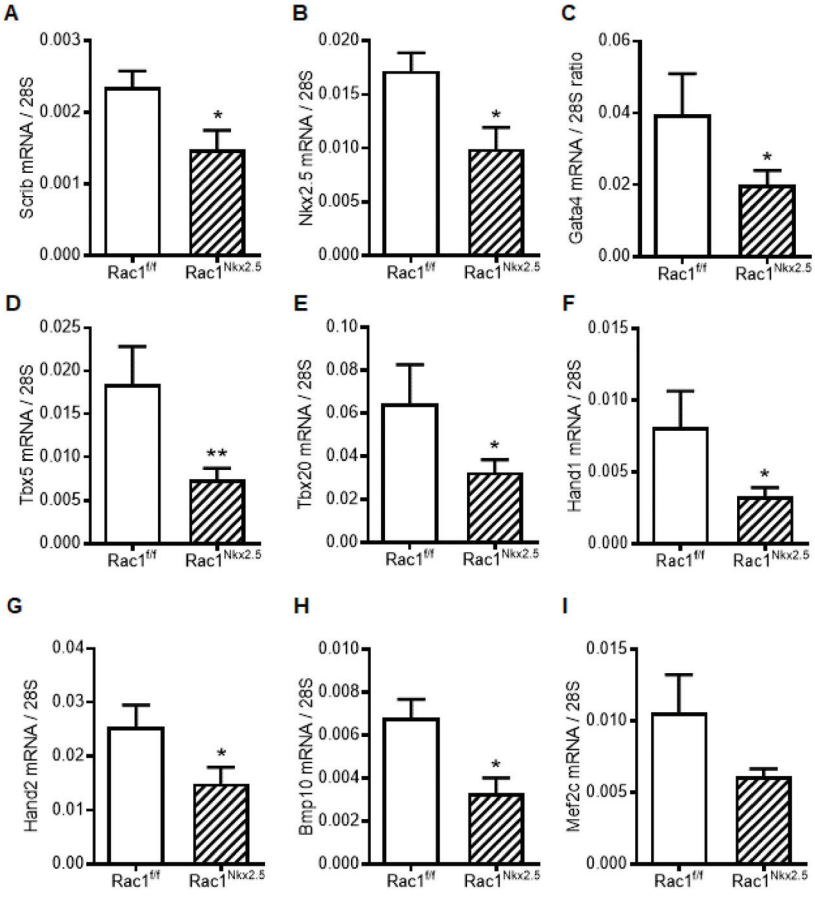

Figure 8. Myocardial mRNA expression of transcription and growth factors in E12.5 $Rac1^{f/f}$ and $Rac1^{Nkx2.5}$ hearts. (**A**) *Scrib*. (**B**) *Nkx2.5*. (**C**) *Gata4*. (**D**) *Tbx5*. (**E**) *Tbx20*. (**F**) *Hand1*. (**G**) *Hand2*. (**H**) *Bmp10*. (**I**) *Mef2c*. Data are expressed as mRNA to 28S ratios. n = 5–6 per group. * $p < 0.05$, ** $p < 0.01$ by unpaired Student's t test.

4. Discussion

Recent studies have implicated PCP signaling and cell polarity as critical regulators of compact myocardium development. *Vangl2*, *Scrib* and *Dishevelled* mouse mutants have cardiomyocytes that are not polarized and the ventricular myocardium is thinned, resembling LVNC [27–29]. *Rac1* is a known downstream effector of PCP signaling; however, the

cardiomyocyte specific role of *Rac1* in heart development is unclear [30]. In the present study, we demonstrated that downregulation of *Rac1* signaling in the ventricular myocardium disrupted formation of a trabecular network and development of the compact myocardium. In addition, $Rac1^{Nkx2.5}$ mice had a bifid cardiac apex, defects in ventricular septum formation and OFT alignment. The F-actin filament organization and polarization of cardiomyocytes in the *Rac1* deficient ventricular myocardium was also abnormal. Overall, cell proliferation was decreased in $Rac1^{Nkx2.5}$ hearts, along with expression of the PCP protein, Scrib. Our study demonstrates a critical role for *Rac1* signaling in outflow tract and compact myocardium development (Figure 9).

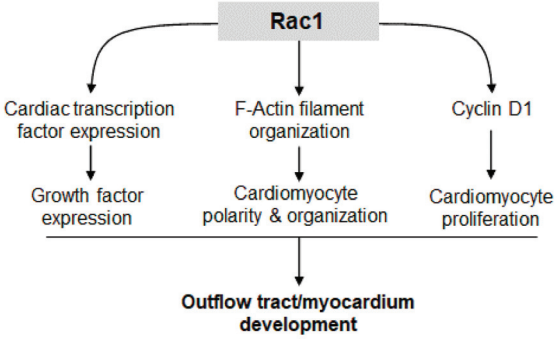

Figure 9. *Rac1* signaling promotes cardiac transcription/growth factor expression, cardiomyocyte polarity and proliferation, leading to normal development of the outflow tract and compact myocardium.

Cell proliferation is a regulated spatially and temporally during heart development. The rate of cell proliferation in the ventricular myocardium peaks at E9.5 and gradually decreases during development [26]. Studies have shown that cardiomyocyte proliferation is the major determinant of overall cardiac size during heart development. The mass of the heart must increase to match the increasing circulatory demands of the growing embryo [31]. *Rac1* has been shown to regulate cell proliferation through various pathways. Our data showed that a *Rac1* deficiency in the ventricular myocardium decreased the expression of factors critical to cardiogenesis, cardiomyocyte differentiation and proliferation including *Nkx2.5*, *Gata4*, *Tbx5*, *Tbx20*, *Hand 1*, *Hand2* and *Bmp10*. Additionally, Cyclin D1 protein levels and cell proliferation were reduced in E9.5 $Rac1^{Nkx2.5}$ hearts. These results suggest that *Rac1* promotes cardiac transcription and growth factor expression, leading to cell cycle progression and cardiomyocyte proliferation in the developing heart (Figure 9).

An earlier report by Boczonadi et al. also used a $Nkx2.5\text{-}Cre;Rac1^{f/f}$ mouse line in their studies [19]. However, the *Nkx2.5-Cre* mouse used by Boczonadi et al. was an *Nkx2.5* heterozygous mouse since the Cre recombinase gene was knocked into the *Nkx2.5* genetic locus [32]. In contrast, the *Nkx2.5-Cre* mouse used in the present study is a transgenic mouse and retains two intact alleles of *Nkx2.5* [20]. The $Nkx2.5\text{-}Cre;Rac1^{f/f}$ mice used in Boczonadi et al. were embryonically lethal due to their interaction with E13.5, which precluded analysis of ventricular septation and OFT alignment with the developing ventricles [19]. However, at E12.5 these mice did show underdeveloped ventricles with a thin ventricular wall. The earlier lethality of the $Nkx2.5\text{-}Cre;Rac1^{f/f}$ mouse line compared to the $Rac1^{Nkx2.5}$ used in the current study is likely due to the heterozygous expression of *Nkx2.5* compounded with decreased *Rac1* signaling in the ventricular myocardium. Furthermore, whether the underdeveloped heart reported in the study by Boczonadi et al. [19] is exclusively due to deficient *Rac1* signaling or also due to downregulation of *Nkx2.5* is unclear. Our data implicates *Rac1* signaling specifically and we were able to demonstrate that $Rac1^{Nkx2.5}$ hearts exhibit VSDs and OFT alignment defects.

Molecular players in the planar cell polarity (PCP) pathway are not only critical for normal myocardial development but also govern OFT development. For example, mutation in *Vangl2*, a member of the highly conserved non-canonical Wnt signaling cascade, results in cardiac malalignment and DORV [28]. In addition, *Dishevelled 2* knockout mice show transposition of the great arteries, persistent truncus arteriosus and DORV, with the latter being the most common cardiac defect [33]. Notably, anterior SHF specific deletion of *Rac1* results in a spectrum of OFT alignment defects including DORV via a disruption of migration of neural crest cells and cardiomyocytes into the OFT [34]. In the present study, *Nkx2.5-Cre-driven* GFP expression is seen in pulmonary and aortic walls, and in aortic valve leaflets, suggesting cardiomyocyte migration to the OFT. The OFT myocardium produces axon guidance molecules such as Sema3c, a chemoattractant that navigates neural crest cells to the OFT [34]. Reductions in cardiomyocyte proliferation and migration to the OFT may diminish cardiomyocyte contribution to the OFT and impede neural crest cell migration, leading to OFT alignment defects.

Our previous work reported a bifid cardiac apex when *Rac1* was specifically deleted in the anterior SHF and all anterior SHF-derived cells [18]. We had postulated that loss of *Rac1* signaling in the RV led to an inability of the nonpolarized and disorganized cardiomyocytes to bridge the interventricular junction to unify the two developing ventricles and form a distinct cardiac apex. However, in the present study using the $Rac1^{Nkx2.5}$ hearts, we show that development of normal cardiac apex is also dependent on polarity and organization of the cardiomyocytes in the LV myocardium. Interestingly, other reports where PCP signaling was disrupted did not report observations of a bifid cardiac apex, despite similar reports of cardiomyocyte disorganization [27,28]. *Rac1* is a known downstream effector of PCP signaling, regulating actin cytoskeleton dynamics and cell polarity [35,36]. Our findings suggest that development of a bifid cardiac apex involves a pathway specific to a disruption of *Rac1* signaling. In addition, since *Rac1* is a pleiotropic effector of numerous cellular events, the concomitant disruption of several cellular mechanisms is likely responsible for bifid cardiac apex, along with the other observed CHDs in $Rac1^{Nkx2.5}$ hearts.

Our lineage tracing analysis with the *mT/mG* global double florescence mouse showed similar GFP^+ expression in domains of the heart that were reported by McFadden et al, who used a lacZ reporter. However, we also showed Cre recombinase activity in the OFT and atria, which were reported to be minimal by McFadden et al [20]. This discrepancy in Cre recombinase activity may be due to the additional β-galactosidase enzymatic reaction step that is required to visualize the blue color of lacZ staining, making it a less efficient reporter compared to a GFP reporter. These results suggest that future lineage tracing analysis should use a florescence reporter as a more reliable readout of expression compared to a lacZ reporter.

Rac1 is involved in reactive oxygen species (ROS) generation through activation of NADPH oxidase [37]. ROS mediates numerous cellular functions including proliferation, cell survival, differentiation and migration [37,38]. The levels of ROS are finely tuned in a cell to regulate these diverse functions. For example, excess ROS induces apoptosis while basal levels of ROS regulate gene expression and proliferation [37,39]. Work in our lab has shown that ROS levels must be tightly regulated to facilitate normal cardiac development. Excess ROS induced by pregestational maternal diabetes and decreased levels of ROS in the NADPH oxidase *Nox2* knockout mouse both have a detrimental effect on heart development, leading to a spectrum of CHDs [40–42]. Whether the CHDs observed in the $Rac1^{Nkx2.5}$ hearts can also be attributed to decreased ROS levels should be determined in future studies.

5. Conclusions

A *Rac1* deficiency in the myocardium disrupts cardiomyocyte organization and proliferation, leading to bifid cardiac apex, VSDs and OFT alignment and ventricular myocardial compaction defects. Our study suggests a critical role for *Rac1* regulation of cardiomyocyte proliferation, organization and polarization in development of the outflow tract and ven-

tricular myocardium. Whether perturbed *Rac1* signaling in the ventricular myocardium underlies human cases of LVNC warrants further investigation.

Author Contributions: C.L. and Q.F. conceived the experiments. C.L., A.E., X.L. and Q.F. designed the experiments. C.L., A.E., M.Y.K. and X.L. performed the experiments and data analyses. C.L. drafted the manuscript. C.L., A.E., X.L. and Q.F. revised the manuscript. All authors contributed to the interpretation of results and proofreading of the manuscript. All authors have read and agreed to the published version of the manuscript.

Funding: This work was supported by operating grants to Q.F. from Natural Sciences and Engineering Research Council of Canada (NSERC) and Canadian Institutes of Health Research (CIHR). C.L. was supported by an NSERC Scholarship. Q.F. is a Richard and Jean Ivy Chair in Molecular Toxicology at Western University.

Institutional Review Board Statement: Animal use was approved by the Animal Care Committee at Western University (protocol #2007-011, date of approval: 12 March 2014) in accordance with the guidelines of the Canadian Council of Animal Care.

Informed Consent Statement: Not applicable.

Data Availability Statement: The data that support the findings of this study are available from the corresponding author upon reasonable request.

Conflicts of Interest: The authors declare no conflict of interest. The funders had no role in the design of the study; in the collection, analyses, or interpretation of data; in the writing of the manuscript, or in the decision to publish the results.

References

1. Pierpont, M.E.; Basson, C.T.; Benson, D.W.; Gelb, B.D.; Giglia, T.M.; Goldmuntz, E.; McGee, G.; Sable, C.A.; Srivastava, D.; Webb, C.L. Genetic Basis for Congenital Heart Defects: Current Knowledge: A Scientific Statement from the American Heart Association Congenital Cardiac Defects Committee, Council on Cardiovascular Disease in the Young: Endorsed by the American Academy of Pediatrics. *Circulation* **2007**, *115*, 3015–3038. [CrossRef]
2. Hoffman, J.I.; Kaplan, S.; Liberthson, R.R. Prevalence of Congenital Heart Disease. *Am. Heart J.* **2004**, *147*, 425–439. [CrossRef]
3. Sun, R.; Liu, M.; Lu, L.; Zheng, Y.; Zhang, P. Congenital Heart Disease: Causes, Diagnosis, Symptoms, and Treatments. *Cell Biochem. Biophys.* **2015**, *72*, 857–860. [CrossRef]
4. Warnes, C.A. The Adult with Congenital Heart Disease: Born to Be Bad? *J. Am. Coll. Cardiol.* **2005**, *46*, 1–8. [CrossRef]
5. Guha, K.; Treibel, T.A.; Roussin, I.; Prasad, S.K.; Duncan, A.M.; Brookes, C.; McDonagh, T.A.; Sharma, R. Treatment of Left Ventricular Non-Compaction with Cardiac Resynchronization Therapy. *QJM* **2013**, *106*, 575–579. [CrossRef]
6. Chin, T.K.; Perloff, J.K.; Williams, R.G.; Jue, K.; Mohrmann, R. Isolated Noncompaction of Left Ventricular Myocardium. A Study of Eight Cases. *Circulation* **1990**, *82*, 507–513. [CrossRef]
7. Finsterer, J. Left Ventricular Non-Compaction and Its Cardiac and Neurologic Implications. *Heart Fail. Rev.* **2010**, *15*, 589–603. [CrossRef] [PubMed]
8. Zambrano, E.; Marshalko, S.J.; Jaffe, C.C.; Hui, P. Isolated Noncompaction of the Ventricular Myocardium: Clinical and Molecular Aspects of a Rare Cardiomyopathy. *Lab. Investig.* **2002**, *82*, 117–122. [CrossRef] [PubMed]
9. Ritter, M.; Oechslin, E.; Sutsch, G.; Attenhofer, C.; Schneider, J.; Jenni, R. Isolated Noncompaction of the Myocardium in Adults. *Mayo Clin. Proc.* **1997**, *72*, 26–31. [CrossRef] [PubMed]
10. Samsa, L.A.; Yang, B.; Liu, J. Embryonic Cardiac Chamber Maturation: Trabeculation, Conduction, and Cardiomyocyte Proliferation. *Am. J. Med. Genet. C Semin. Med. Genet.* **2013**, *163C*, 157–168. [CrossRef] [PubMed]
11. Sedmera, D.; Pexieder, T.; Vuillemin, M.; Thompson, R.P.; Anderson, R.H. Developmental Patterning of the Myocardium. *Anat. Rec.* **2000**, *258*, 319–337. [CrossRef]
12. Risebro, C.A.; Riley, P.R. Formation of the Ventricles. *Sci. World J.* **2006**, *6*, 1862–1880. [CrossRef]
13. Pasumarthi, K.B.; Field, L.J. Cardiomyocyte Cell Cycle Regulation. *Circ. Res.* **2002**, *90*, 1044–1054. [CrossRef] [PubMed]
14. Zhang, W.; Chen, H.; Qu, X.; Chang, C.P.; Shou, W. Molecular Mechanism of Ventricular Trabeculation/Compaction and the Pathogenesis of the Left Ventricular Noncompaction Cardiomyopathy (LVNC). *Am. J. Med. Genet. C Semin. Med. Genet.* **2013**, *163C*, 144–156. [CrossRef] [PubMed]
15. Oechslin, E.; Jenni, R. Left Ventricular Non-Compaction Revisited: A Distinct Phenotype with Genetic Heterogeneity? *Eur. Heart J.* **2011**, *32*, 1446–1456. [CrossRef] [PubMed]
16. Luedde, M.; Ehlermann, P.; Weichenhan, D.; Will, R.; Zeller, R.; Rupp, S.; Muller, A.; Steen, H.; Ivandic, B.T.; Ulmer, H.E.; et al. Severe Familial Left Ventricular Non-Compaction Cardiomyopathy Due to a Novel Troponin T (TNNT2) Mutation. *Cardiovasc. Res.* **2010**, *86*, 452–460. [CrossRef] [PubMed]
17. Duquette, P.M.; Lamarche-Vane, N. Rho GTPases in Embryonic Development. *Small GTPases* **2014**, *5*, 8. [CrossRef] [PubMed]

18. Leung, C.; Lu, X.; Liu, M.; Feng, Q. Rac1 Signaling Is Critical to Cardiomyocyte Polarity and Embryonic Heart Development. *J. Am. Heart Assoc.* **2014**, *3*, e001271. [CrossRef] [PubMed]
19. Boczonadi, V.; Gillespie, R.; Keenan, I.; Ramsbottom, S.A.; Donald-Wilson, C.; Al Nazer, M.; Humbert, P.; Schwarz, R.J.; Chaudhry, B.; Henderson, D.J. Scrib: Rac1 Interactions Are Required for the Morphogenesis of the Ventricular Myocardium. *Cardiovasc. Res.* **2014**, *104*, 103–115. [CrossRef]
20. McFadden, D.G.; Barbosa, A.C.; Richardson, J.A.; Schneider, M.D.; Srivastava, D.; Olson, E.N. The Hand1 and Hand2 Transcription Factors Regulate Expansion of the Embryonic Cardiac Ventricles in a Gene Dosage-Dependent Manner. *Development* **2005**, *132*, 189–201. [CrossRef]
21. Glogauer, M.; Marchal, C.C.; Zhu, F.; Worku, A.; Clausen, B.E.; Foerster, I.; Marks, P.; Downey, G.P.; Dinauer, M.; Kwiatkowski, D.J. Rac1 Deletion in Mouse Neutrophils Has Selective Effects on Neutrophil Functions. *J. Immunol.* **2003**, *170*, 5652–5657. [CrossRef]
22. Muzumdar, M.D.; Tasic, B.; Miyamichi, K.; Li, L.; Luo, L. A Global Double-Fluorescent Cre Reporter Mouse. *Genesis* **2007**, *45*, 593–605. [CrossRef] [PubMed]
23. Xiang, F.L.; Lu, X.; Hammoud, L.; Zhu, P.; Chidiac, P.; Robbins, J.; Feng, Q. Cardiomyocyte-Specific Overexpression of Human Stem Cell Factor Improves Cardiac Function and Survival Post Myocardial Infarction in Mice. *Circulation* **2009**, *120*, 1065–1074. [CrossRef]
24. Liu, Y.; Lu, X.; Xiang, F.L.; Poelmann, R.E.; Gittenberger-de Groot, A.C.; Robbins, J.; Feng, Q. Nitric Oxide Synthase-3 Deficiency Results in Hypoplastic Coronary Arteries and Postnatal Myocardial Infarction. *Eur. Heart J.* **2014**, *35*, 920–931. [CrossRef]
25. Engineer, A.; Saiyin, T.; Lu, X.; Kucey, A.S.; Urquhart, B.L.; Drysdale, T.A.; Norozi, K.; Feng, Q. Sapropterin Treatment Prevents Congenital Heart Defects Induced by Pregestational Diabetes Mellitus in Mice. *J. Am. Heart Assoc.* **2018**, *7*, e009624. [CrossRef] [PubMed]
26. De Boer, B.A.; van den Berg, G.; de Boer, P.A.; Moorman, A.F.; Ruijter, J.M. Growth of the Developing Mouse Heart: An Interactive Qualitative and Quantitative 3D Atlas. *Dev. Biol.* **2012**, *368*, 203–213. [CrossRef]
27. Phillips, H.M.; Hildreth, V.; Peat, J.D.; Murdoch, J.N.; Kobayashi, K.; Chaudhry, B.; Henderson, D.J. Non-Cell-Autonomous Roles for the Planar Cell Polarity Gene Vangl2 in Development of the Coronary Circulation. *Circ. Res.* **2008**, *102*, 615–623. [CrossRef] [PubMed]
28. Phillips, H.M.; Rhee, H.J.; Murdoch, J.N.; Hildreth, V.; Peat, J.D.; Anderson, R.H.; Copp, A.J.; Chaudhry, B.; Henderson, D.J. Disruption of Planar Cell Polarity Signaling Results in Congenital Heart Defects and Cardiomyopathy Attributable to Early Cardiomyocyte Disorganization. *Circ. Res.* **2007**, *101*, 137–145. [CrossRef]
29. Sinha, T.; Wang, B.; Evans, S.; Wynshaw-Boris, A.; Wang, J. Disheveled Mediated Planar Cell Polarity Signaling Is Required in the Second Heart Field Lineage for Outflow Tract Morphogenesis. *Dev. Biol.* **2012**, *370*, 135–144. [CrossRef]
30. Simons, M.; Mlodzik, M. Planar Cell Polarity Signaling: From Fly Development to Human Disease. *Annu. Rev. Genet.* **2008**, *42*, 517–540. [CrossRef]
31. Sedmera, D.; Hu, N.; Weiss, K.M.; Keller, B.B.; Denslow, S.; Thompson, R.P. Cellular Changes in Experimental Left Heart Hypoplasia. *Anat. Rec.* **2002**, *267*, 137–145. [CrossRef]
32. Moses, K.A.; DeMayo, F.; Braun, R.M.; Reecy, J.L.; Schwartz, R.J. Embryonic Expression of an Nkx2-5/Cre Gene Using ROSA26 Reporter Mice. *Genesis* **2001**, *31*, 176–180. [CrossRef] [PubMed]
33. Hamblet, N.S.; Lijam, N.; Ruiz-Lozano, P.; Wang, J.; Yang, Y.; Luo, Z.; Mei, L.; Chien, K.R.; Sussman, D.J.; Wynshaw-Boris, A. Dishevelled 2 Is Essential for Cardiac Outflow Tract Development, Somite Segmentation and Neural Tube Closure. *Development* **2002**, *129*, 5827–5838. [CrossRef] [PubMed]
34. Leung, C.; Liu, Y.; Lu, X.; Kim, M.; Drysdale, T.A.; Feng, Q. Rac1 Signaling Is Required for Anterior Second Heart Field Cellular Organization and Cardiac Outflow Tract Development. *J. Am. Heart Assoc.* **2016**, *5*, e002508. [CrossRef] [PubMed]
35. Schlessinger, K.; Hall, A.; Tolwinski, N. Wnt Signaling Pathways Meet Rho GTPases. *Genes Dev.* **2009**, *23*, 265–277. [CrossRef] [PubMed]
36. Niehrs, C. The Complex World of WNT Receptor Signalling. *Nat. Rev. Mol. Cell Biol.* **2012**, *13*, 767–779. [CrossRef]
37. Engineer, A.; Saiyin, T.; Greco, E.R.; Feng, Q. Say NO to ROS: Their Roles in Embryonic Heart Development and Pathogenesis of Congenital Heart Defects in Maternal Diabetes. *Antioxidants* **2019**, *8*, 436. [CrossRef]
38. Covarrubias, L.; Hernandez-Garcia, D.; Schnabel, D.; Salas-Vidal, E.; Castro-Obregon, S. Function of Reactive Oxygen Species during Animal Development: Passive or Active? *Dev. Biol.* **2008**, *320*, 1–11. [CrossRef]
39. Chowdhury, A.R.; Ghosh, I.; Datta, K. Excessive Reactive Oxygen Species Induces Apoptosis in Fibroblasts: Role of Mitochondrially Accumulated Hyaluronic Acid Binding Protein 1 (HABP1/P32/GC1qR). *Exp. Cell Res.* **2008**, *314*, 651–667. [CrossRef]
40. Moazzen, H.; Lu, X.; Liu, M.; Feng, Q. Pregestational Diabetes Induces Fetal Coronary Artery Malformation via Reactive Oxygen Species Signaling. *Diabetes* **2015**, *64*, 1431–1443. [CrossRef]
41. Moazzen, H.; Lu, X.; Ma, N.L.; Velenosi, T.J.; Urquhart, B.L.; Wisse, L.J.; Groot, A.C.; Feng, Q. N-Acetylcysteine Prevents Congenital Heart Defects Induced by Pregestational Diabetes. *Cardiovasc. Diabetol.* **2014**, *13*, 46. [CrossRef] [PubMed]
42. Moazzen, H.; Wu, Y.; Engineer, A.; Lu, X.; Aulakh, S.; Feng, Q. NOX2 Is Critical to Endocardial to Mesenchymal Transition and Heart Development. *Oxid. Med. Cell Longev.* **2020**, *2020*, 1679045. [CrossRef] [PubMed]

Journal of
Cardiovascular
Development and Disease

MDPI

Review

Role of the Epicardium in the Development of the Atrioventricular Valves and Its Relevance to the Pathogenesis of Myxomatous Valve Disease

Renélyn Wolters [1,†], Ray Deepe [1,†], Jenna Drummond [1,†], Andrew B. Harvey [1], Emilye Hiriart [1], Marie M. Lockhart [1], Maurice J. B. van den Hoff [2], Russell A. Norris [1] and Andy Wessels [1,*]

[1] Department of Regenerative Medicine and Cell Biology, Medical University of South Carolina, 173 Ashley Avenue, Charleston, SC 29425, USA; woltersr@musc.edu (R.W.); deepe@musc.edu (R.D.); drummonj@musc.edu (J.D.); harveyan@musc.edu (A.B.H.); hiriart.emilie@gmail.com (E.H.); marie.lockhart@gmail.com (M.M.L.); norrisra@musc.edu (R.A.N.)
[2] Department of Medical Biology, Amsterdam UMC, Academic Medical Center, Meibergdreef 15, 1105 AZ Amsterdam, The Netherlands; m.j.vandenhoff@amsterdamumc.nl
* Correspondence: wesselsa@musc.edu; Tel.: +1-843-792-8183
† These authors contributed equally to this work.

Abstract: This paper is dedicated to the memory of Dr. Adriana "Adri" Gittenberger-de Groot and in appreciation of her work in the field of developmental cardiovascular biology and the legacy that she has left behind. During her impressive career, Dr. Gittenberger-de Groot studied many aspects of heart development, including aspects of cardiac valve formation and disease and the role of the epicardium in the formation of the heart. In this contribution, we review some of the work on the role of epicardially-derived cells (EPDCs) in the development of the atrioventricular valves and their potential involvement in the pathogenesis of myxomatous valve disease (MVD). We provide an overview of critical events in the development of the atrioventricular junction, discuss the role of the epicardium in these events, and illustrate how interfering with molecular mechanisms that are involved in the epicardial-dependent formation of the atrioventricular junction leads to a number of abnormalities. These abnormalities include defects of the AV valves that resemble those observed in humans that suffer from MVD. The studies demonstrate the importance of the epicardium for the proper formation and maturation of the AV valves and show that the possibility of epicardial-associated developmental defects should be taken into consideration when determining the genetic origin and pathogenesis of MVD.

Keywords: atrioventricular valve; epicardium; lateral cushion; major cushion; myxomatous degeneration

Citation: Wolters, R.; Deepe, R.; Drummond, J.; Harvey, A.B.; Hiriart, E.; Lockhart, M.M.; van den Hoff, M.J.B.; Norris, R.A.; Wessels, A. Role of the Epicardium in the Development of the Atrioventricular Valves and Its Relevance to the Pathogenesis of Myxomatous Valve Disease. *J. Cardiovasc. Dev. Dis.* **2021**, *8*, 54. https://doi.org/10.3390/jcdd8050054

Received: 26 April 2021
Accepted: 8 May 2021
Published: 12 May 2021

1. Introduction

Myxomatous degeneration involving the leaflets of the left atrioventricular valve (mitral valve) leads to myxomatous valve disease (MVD), a common cause of Mitral Valve Prolapse (MVP). MVP affects nearly 1 in 40 individuals [1–6] and is a serious condition characterized by abnormal systolic "bulging" or "billowing" of leaflets of the mitral valve into the left atrium, a situation typically accompanied by mitral regurgitation [7]. There are no therapies known to improve or reverse the valve abnormality, and surgical and catheter-based approaches to improve valve function are invasive and expensive. MVP can be found in a variety of conditions, including rare syndromic diseases, such as Marfan syndrome (MFS), Loeys–Dietz syndrome (LDS), Aneurysm-osteoarthritis syndrome (AOS), Williams–Beuren syndrome (WBS), and Ehlers–Danlos syndrome (EDS) [6]. Non-syndromic MVP is, however, more common. Insight into the genetic etiology of familial non-syndromic MVP has been obtained from studying pedigrees of families in which multiple individuals have MVD. This approach has thus far led to the identification of a small number of causal genes, including FILAMIN-A (FLNA) [1,2,4] and Dachsous (DCHS1) [3]. Despite these

advancements, relatively little is known about the molecular and cellular mechanisms involved in MVP pathogenesis. It is interesting to note that while MVP is the most serious and widespread AV valve abnormality, tricuspid valve prolapse is observed in up to 50% of patients with primary or non-syndromic MVP [8,9]. In this contribution, we will review the developmental events that underlie the formation of the respective leaflets of the atrioventricular (AV) valves, specifically focusing on the role of the epicardium in this specific event. We will show that epicardium/epicardially-derived cells (EPDCs) [10] are not only playing a crucially important role for the development of the AV junction and AV valves, but also that molecular mechanisms that govern the regulation of epicardial development in this part of the heart may need more attention in efforts to elucidate the underlying mechanisms leading to MVD/MVP at later stages of life.

2. The Atrioventricular Cushions

Shortly after the formation of the primary heart tube, an extracellular matrix (ECM)-rich substance, often referred to as the cardiac jelly, can be found between the myocardium and endocardium (Figure 1). As the heart tube starts to loop, further accumulation of the cardiac jelly in the region that will become the AV junction is the first indication of AV cushion formation. The superior and inferior cushion, together known as the major AV cushions, are the first to form. They are found, respectively, on the ventral and dorsal wall (Figure 1B,D). In the mouse, this process starts around embryonic day (ED) 9.5. In these early stages, very few cells can be found in these cushions. Soon after, cell–cell interactions weaken in a subset of endocardial cells that line the cushions. This is followed by delamination and migration of these cells into the cushions where these endocardially-derived cells (ENDCs) then assume a mesenchymal phenotype. This process is referred to as endocardial-to-mesenchymal transition/transformation (endMT) [11,12].

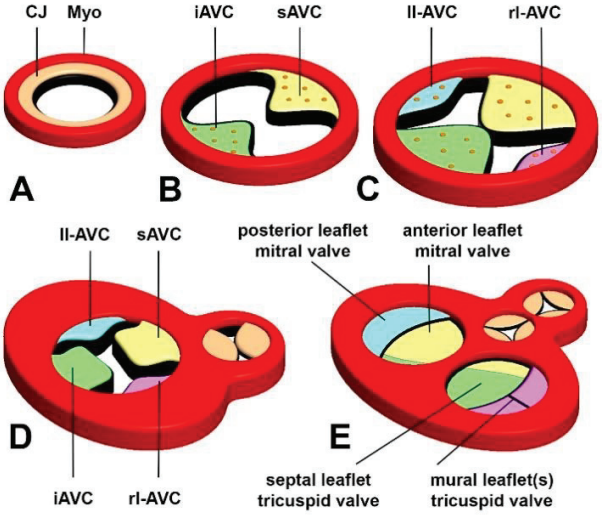

Figure 1. Origin and Fate of the AV cushions. This illustration reflects the respective stages of AV cushion formation. (**A**) Cardiac jelly accumulates between myocardium and endocardium in the tubular heart, (**B**) formation of the major AV cushions, (**C**) fusion of the major cushions and formation of the lateral cushions. (**D**,**E**) illustrate how the respective cushion contribute to the leaflets of the formed heart. CJ, cardiac jelly; Myo, myocardium; iAVC, inferior AV cushion; sAVC, superior AV cushion; ll-AVC, left lateral AV cushion; rlAVC, right lateral AV cushion, muMiV, mural leaflet of the mitral valve.

A significant body of work has been conducted over the last few decennia that has led to the understanding that regulation of endMT is critically dependent on the unique molecular signature of the AV junctional myocardium as well as specific molecular characteristics of the AV endocardium [13–15]. The process of endMT is regulated by an intricate network of regulatory pathways and transcription factors and involves ligands and receptors of the TGFbeta superfamily of growth factors (e.g., TGFbeta2, BMP2 and BMPR1A), transcription factors (e.g., SOX9), and ligands and intermediates of the Notch, Hippo, and Wnt/beta-catenin signaling pathways [16–24]. Eventually, the ENDCs in the cushions become fibroblasts and are recognized in the maturing valves as (endocardially-derived) valve interstitial cells (endVICs). The fusion of the two major cushions in the midline of the common AV canal divides the canal into a separate left and right AV orifice [25].

The formation of the major AV cushions is followed by the formation of two lateral AV cushions. The lateral cushions, which are considerably smaller than the major cushions, develop on the lateral (or parietal) walls of the left and right myocardial AV junctions [25,26]. It is interesting to note that most of the experimental in vitro studies conducted to unravel the mechanism controlling endMT of the AV cushions have historically been performed using AV explants at stages in which the major AV cushions are developing, but before the onset of development of the lateral AV cushions. While, to the best of our knowledge, there are no data available to indicate that endMT in the lateral cushions is regulated by different mechanisms, the spatiotemporal difference in where and when they emerge remains to be resolved. Although not directly related to the development of the AV cushions and valves, it is worth noting that endMT is also responsible for the generation of mesenchymal cells that are found in the mesenchymal cap situated on the leading edge of the primary atrial septum [27–31]. Not much is known, however, regarding the mechanisms that control endMT in this structure [31].

3. Contribution of the AV Cushions to the AV Valves

For many years, it has been recognized that all four AV cushions are critical components for the development of the AV valves. In his work "Anatomie Menschlicher Embryonen III—Das Herz" (1885), Wilhelm His writes: "*An der Bildung der Atrioventricularklappen betheiligen sich einestheils die Muskelwand des Ohrkanales und des anstossenden Ventrikelgebietes, anderntheils die Bindesubstanzmasse der vier Atrioventricularlippen*" (freely translated: "*the tissues that contribute to the formation of the atrioventricular valves include the muscular wall of the (left and right) atrioventricular canals and the adjacent ventricular tissues, as well as the extracellular matrix of the four atrioventricular cushions*"). Our current understanding of cushion development is the result of more detailed descriptive and experimental studies and imaging techniques developed over the last 50 years or so. These new insights are the result of significant technological advances, development of experimental embryology, sophisticated in vivo and in vitro techniques, and breakthroughs in biochemistry, molecular biology, and, last but not least, transgenic mouse technology.

In the human heart, we distinguish two AV valves. The left AV valve (or mitral valve) will develop in the left AV junction, whereas, in the right AV junction, the right AV valve (or the tricuspid valve) will appear. The (fused) major AV cushions mainly contribute to the AV valve leaflets that are associated with the ventricular septum (Figure 1). The lateral AV cushions (Figures 1 and 2A–C) contribute to the leaflets that are attached to the left and right atrioventricular junction. Histological analysis indicates that the superior AV cushion forms the "anlage" of the anterior (or aortic) leaflet of the mitral valve. The posterior (or mural) leaflet of the mitral valve, however, derives from the left lateral AV cushion. At the right side of the heart, the inferior AV cushion provides the bulk of the septal leaflet of the tricuspid valve (Figure 1D,E and Figure 2C,D). With subsequent development, the valve leaflets further mature and become organized in three layers: the atrialis, spongiosa, and fibrosa [32]. Each layer comprises a specific extracellular matrix composition and valve interstitial cells, which are essential for proper function of the leaflets. Given the fact that a significant amount of research on the development of the AV valves and investigations on

the molecular pathways and pathogenic events that underlie the diseases of these valves are conducted in mice, it is important to recognize that, whereas the general mechanisms that lead to the formation of the valves are quite similar between mice and humans, the ultrastructure of the developed leaflets differs significantly. For instance, the valves in the human heart are, at their distal ends, contiguous with the papillary muscles via long and numerous tendinous chords (known as the chordae tendineae), while, in the mouse, these tendinous chords are not as prominent [25]. Furthermore, the right AV valve in the mouse does not have the typical three leaflet configuration as observed in the human, but rather consists of only two leaflets [33].

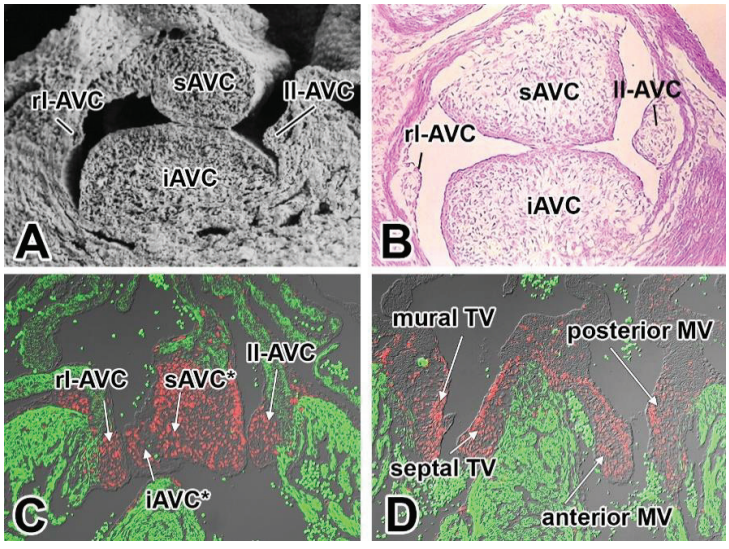

Figure 2. The AV cushions and their derivatives. A scanning electron microscopical (**A**) image and (**B**) a histological section show the major and lateral AV cushions at 13 ED. Immunofluorescently-stained sections of a 13.5 ED (**C**) and a 15 ED (**D**) heart show how the respective cushions contribute to the AV valve leaflets as the heart develops. The sections were stained for myosin heavy chain (green) and SOX9 (red). The asterisks in (**C**) are added to indicate that after the major cushions have fused, it is no longer possible to say with certainty whether a particular cell is derived from the iAVC or sAVC. Abbreviations: iAVC, inferior AV cushion; sAVC, superior AV cushion; ll-AVC, left lateral AV cushion; rl-AVC, right lateral AV cushion, MV, mitral valve; TV, tricuspid valve.

4. The Epicardium and Epicardially-Derived Cells (EPDCs)

The epicardium is a mesothelium-derived epithelium covering the myocardial surface of the heart. The development of the epicardium starts with the formation of the proepicardium, a morphological entity resembling a "cluster of grapes" located at the interface of the liver and sinus venosus at the cardiac venous pole [34–38]. The proepicardium is derived from a cardiac mesodermal progenitor pool by the cooperative interaction between BMP and FGF signaling [39,40]. After the proepicardium has formed, cells detach from the proepicardium and adhere to the "naked" myocardial surface of the looping heart, where they spread as an epithelium over the developing cardiac compartments [38,41]. Subsequently, an ECM-rich space develops between the myocardium and epicardium. This space is known as the subepicardium. In a process similar to what we see in the AV cushions, an epicardial-to-mesenchymal transformation (epiMT) results in the generation of epicardially-derived cells (EPDCs) [10]. Whereas historically, the epicardium was first and foremost seen as a protective layer and allowing for smooth movement in the peri-

cardial environment during the cardiac cycle, a series of studies published over the last 20 years has convincingly demonstrated that the epicardium plays a far more important role in the development and function of the heart than previously thought. This insight developed as a result of early cell fate studies using quail-chick chimeras [10,35,42] as well as other labeling approaches using experimental embryology with molecular marking techniques [43]. These studies demonstrated that EPDCs can cross the boundary between the subepicardial space and the adjacent myocardium and can subsequently migrate into the myocardial walls. Moreover, these and other studies have shown that, after populating the myocardial walls, the EPDCs can differentiate into interstitial fibroblasts, pericytes, coronary smooth muscle cells, and coronary endothelium [10,42–46]. In a number of these cell-fate tracing studies, it was suggested that EPDCs contributed to the developing AV valves [10,35,42]. In the context of this contribution, we will concentrate on the role that EPDCs play in the development of the tissues at the AV junction, and, in particular, the AV valves.

5. The Formation of EPDCs at the AV Junction (AV-EPDCs)

Whereas tracking the fate of EPDCs with various avian model systems did reveal significant new insights in the potential role of the epicardium in heart development [10,35,42,43], the complex experimental nature of the microsurgical manipulations, as well as concerns about the biological relevance of some of the approaches (e.g., would cells from an explanted proepicardium isolated from a quail and transferred to a chick embryo truly recapitulate the behavior of endogenous chick epicardial cells, etc), prompted the development of different approaches allowing the study of EPDCs in the developing mammalian heart. The emergence of the cre-lox mouse technology [47] opened new avenues to explore the role of the epicardium in the mouse. Based on the epicardial-specific expression of several transcription factors (e.g., TBX18 and WT1), a number of "epicardial-specific" cre-mouse models were developed that allowed the labeling of the epicardium and fate tracing of EPDCs during development. In our published and ongoing studies, we use the mWt1/IRES/GFP-Cre mouse (referred to as $mWt1^{Cre}$) in combination with the B6.129(Cg)-Gt(ROSA)26$Sor^{tm4(ACTB-tdTomato,-EGFP)Luo}$/J (referred to as $R26^{mT/mG}$) reporter mouse [46]. Using this model (in this paper, referred to as the $Wt1^{Cre}$;$R26^{mT/mG}$ model), we have conducted cell fate studies and are continuing to investigate the importance of AV-EPDCs in the development of the AV junction by targeting molecular pathways that we consider to be important for epicardial cell biology [48,49].

While the generation of EPDCs through epiMT takes place in all regions of the epicardium covering the chamber myocardium, it is more prevalent in the epicardium lining the ventricles than the epicardium on the atria. EpiMT is particularly prominent in the epicardium found at the AV junction. Here, the accumulation of extracellular matrix (ECM) and AV-EPDCs (as we will call this specific population of EPDCs in the AV junction in the rest of this contribution to differentiate them from the EPDCs in other parts of the heart) leads to the formation of the AV sulcus (Figure 3). As mentioned, the molecular regulation responsible for the formation of AV-ENDCs in the AV cushions has been studied in detail. The formation of AV-EPDCs in the AV sulcus has, however, not been studied to the same extent. As described above, the myocardial AV junction plays a crucial role in the regulation of endMT in the AV cushions. While there are many regulatory mechanisms involved in this process, TGFbeta2 [50,51] and BMP2 [18,52], in particular, are of particular importance as both are expressed at a relatively high level in the AV myocardium. In one of the following sections, we will come back to the role of growth factor signaling and epicardial development.

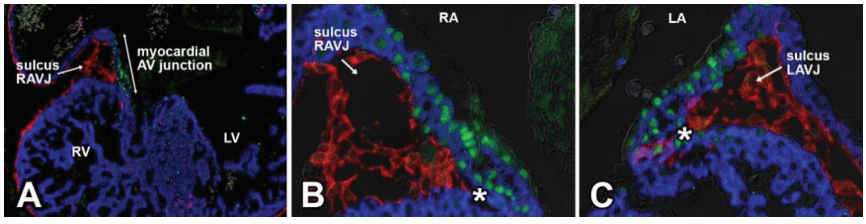

Figure 3. Epicardially-derived cells in the AV sulcus at ED12. EGFP-labeled AV-EPDCs (pseudo-colored in red) are providing the mesenchyme of the AV sulcus. Staining for the transcription factor TBX3 (green) delineates the AV-junctional myocardium (**A**–**C**). As demonstrated in (**A**–**C**), the AV-EPDCs penetrate the myocardial wall (blue) at the lower boundary of the AV-junctional myocardium. (**B**) is a higher magnification of (**A**).

6. Contribution of AV-EPDCs to the Developing AV Valves

In 2012, we published an epicardial cell-fate study using the $Wt1^{Cre}$;$R26^{mT/mG}$ model. Part of the study was focused on the role of AV-EPDCs in the developmental events at the AV junction during valvuloseptal development [46]. We described how, after the onset of formation of the AV sulcus, the AV-EPDCs that have been generated through epiMT migrate toward the myocardial AV junction and then penetrate the junction at the lower boundary of the AV myocardium. As a result, the embryonic AV myocardium becomes incorporated into the lower margin of the atrial chambers (Figure 3). Importantly, it also leads to the formation of the annulus fibrosus, which, in the adult heart, is a ring of connective tissue that physically and electrically insulates the working myocardium of the atria from that of the ventricles, thus preventing ventricular pre-excitation during atrial activation [46,53]. Subsequent to the formation of the annulus fibrosus, a cohort of AV-EPDCs migrates into the lateral AV cushions, i.e., the cushions that participate in the formation of the parietal AV valve leaflets [46,54]. This process starts around ED12. As the lateral cushions further develop into the parietal leaflets of the left and right AV valves, the number of AV-EPDCs in these leaflets gradually increases and large numbers of AV-EPDCs are found in the parietal leaflets even after birth. These observations challenged the long-held belief that (virtually) all cells in the developed AV valves derive from the endocardial cell lineage [55].

A specific feature associated with the contribution of AV-EPDCs into the cushions is that they position themselves right underneath the layer of valve endocardial cells that lines the atrial side of the developing leaflet. This part of the leaflet is, specifically in the human, typically referred to as the atrialis [32] (Figure 4).

The contribution of AV-EPDCs to the developing tissues at the AV junction is schematically depicted in Figure 5.

At this point, we have not yet elucidated the mechanisms that control the directional migration of the AV-EPDCs into the parietal leaflets. It is, however, in the context of this special review, of interest to note that unpublished/preliminary results have identified a few candidate mechanisms that we are currently pursuing.

MMP2 and Type IV Collagen: As has been published previously, migrating EPDCs in the AV junction express Matrix-specific Metalloproteinase 2 (MMP2) [53]. Our preliminary data show that MMP2, which is also known as type IV collagenase, becomes upregulated in the AV-EPDCs as they move from the epicardial surface toward the AV myocardium before they invade the AV junction (Figure 6). This suggests a role for MMP2 in the migration of AV-EPDCs into the junctional myocardium and into the AV valves. As one of the major known functions of MMP2 is to cleave type IV collagen, we decided to investigate whether type IV collagen could potentially be a target for MMP2 in the developing heart valves. Immunostaining for type IV collagen of hearts at stages of active AV-EPDC migration showed that this collagen isoform is expressed in the region under the endocardial lining at the atrial aspect of the leaflets, i.e., the area through which the AV-EPDCs migrate as they

start to populate the parietal leaflets. This observation suggests that the valve endocardial cells produce type IV collagen and makes it plausible that the collagenase activity of MMP2 in the AV-EPDCs facilitates the migration of these cells by degradation of type IV collagen.

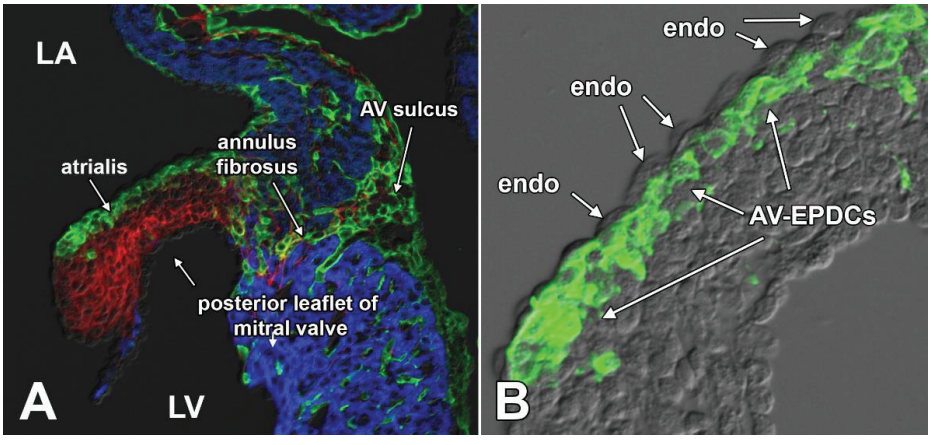

Figure 4. AV-EPDCs migrate into and occupy the subendocardial space at the atrial side of the left parietal leaflet (posterior leaflet of mitral valve). This figure shows the left AV junction of a ~16 ED $Wt1^{cre}$;$R26^{mG}$ heart. The section shown in (**A**) was stained for myosin heavy chain (MF20, blue), EGFP expression to delineate EPDCs (green), and periostin (red). Panel (**B**) shows a detail of the leaflet, only showing the EGFP expression, demonstrating that the EGFP-positive AV-EPDCs are located immediately below the endocardial lining of the leaflet. LA, left atrium; LV, left ventricle; endo, endocardium.

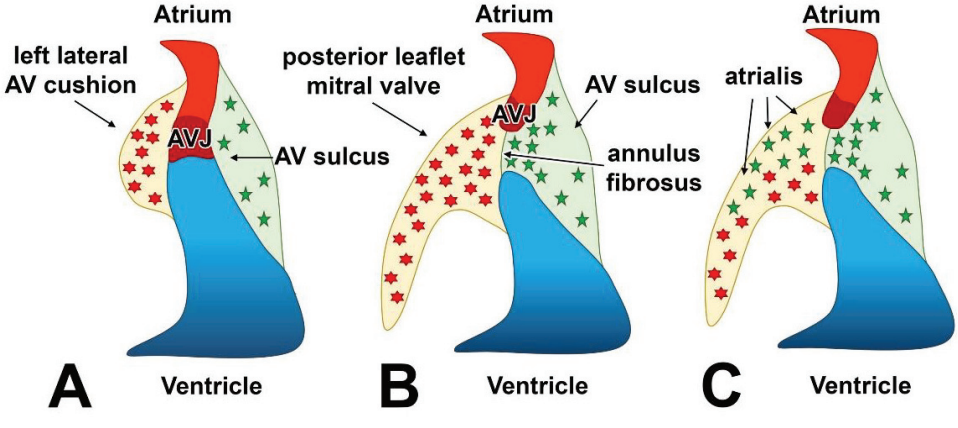

Figure 5. Schematic depiction of the epicardial contribution during the development of the left AV junction. Panel (**A**) shows that at early stages of development, the atrial and ventricular myocardium are contiguous through the AV-junctional myocardium. End-MT generates ENDCs (red cells) in the left lateral AV cushion, while epiMT is responsible for the formation of AV-EPDCs (green cells). Panel (**B**) depicts the situation in which AV-EPDCs have formed the annulus fibrosus. In panel (**C**), it is demonstrated that the AV-EPDCs start to populate the lateral AV valve leaflet (i.e., the posterior leaflet of the mitral valve).

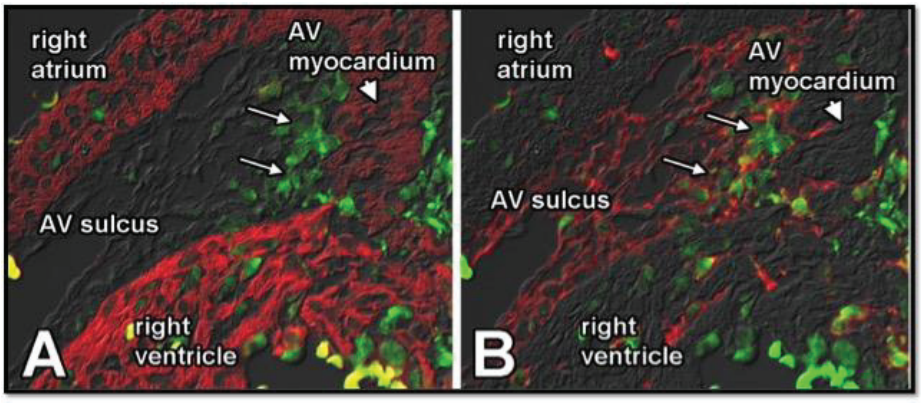

Figure 6. MMP2 expression in AV-EPDC in the AV sulcus. Sister sections of a $Wt1^{cre}$;$R26^{mG}$ heart were stained for MMP2 (green in (**A**,**B**)), myosin (red in (**A**)), and EGFP (to delineate EPDCs, red in (**B**). The figure shows that MMP2 is upregulated in the AV-EPDC as they are migrating toward the AV myocardium.

VCAM-1 and α4 Integrin: Migration is an integrated process requiring temporary interactions between environmental substrates and receptors on the migrating cells. The cell surface receptor α4 integrin mediates cell–extracellular matrix (ECM) and cell–cell adhesion by interacting with vascular cell adhesion molecule 1 (Vcam-1) [56,57]. Migration of epicardial cells over the surface of the myocardium is known to be critically dependent on the expression of the α4 integrin on the epicardial cell surface and expression of Vcam-1 in the myocardium. Mice that lack either α4 integrin or Vcam-1 fail to develop an epicardium and die in early embryonic stages [57,58]. To determine whether α4 integrin and Vcam-1 could also be involved in migration of AV-EPDCs in the valves, we conducted expression studies on ED13.5 and ED14.5 mouse embryos. The immunolabeling confirmed α4 integrin expression on a subset of epicardial cells, the expression being strongest in the epicardial cells plastered against the atrial myocardium (Figure 7A). We saw little α4 integrin expression in epicardially-derived cells, including AV-EPDCs, suggesting that EPDCs lose their α4 integrin expression after undergoing epiMT. Surprisingly, expression of α4 integrin was found in the endocardial lining of the AV valve leaflets (Figure 7C). Immunolabeling for Vcam-1 showed, as expected, expression in atrial and ventricular myocardium (Figure 7B). Vcam-1 expression was also observed in valve mesenchyme, specifically in cells in close spatial association with the endocardium (Figure 7D). While these observations merely demonstrate a spatial relationship between the expression of α4 integrin and Vcam-1 and the location where AV-EPDCs eventually become localized, we believe it merits further investigation on the role of these factors in the migration of AV-EPDCs into the AV junctional tissues and the parietal leaflets of the AV valves.

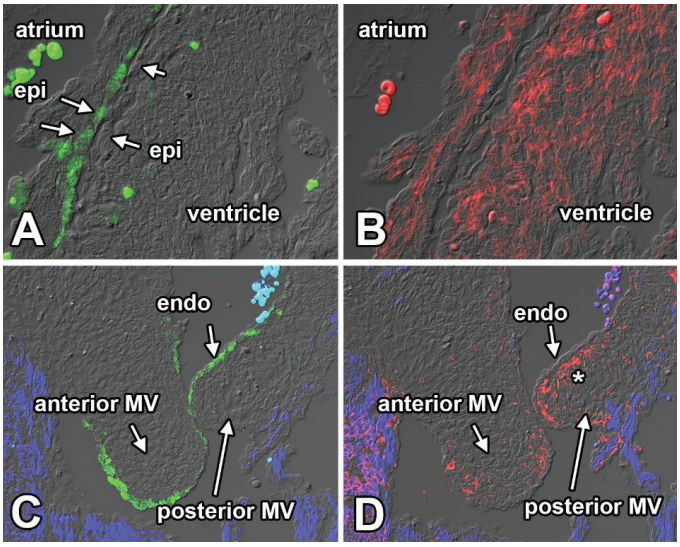

Figure 7. α4 Integrin and VCAM-1 expression. Immunostained sections of a 13.5 ED heart labeled for α4 Integrin (green in (**A**,**C**)) and VCAM-1 (red in (**B**,**D**)) and myosin heavy chain (blue in (**C**,**D**)). The figure shows expression of α4 Integrin in the atrial epicardium (**A**) and valve endocardium (**C**) and expression of VCAM-1 in atrial and ventricular myocardium (**B**) and valve mesenchyme (asterisk in (**D**). endo, endocardium; epi, epicardium.

7. Molecular Control of Epicardial Development at the AV Junction

Insight into the molecular regulation of epiMT in general has, over the years, largely been obtained from in vitro studies using chick and mouse epicardial explants and from studies using primary epicardial cell cultures and immortalized epicardial cell lines [59–65]. Combined, these studies have identified several factors implicated in the process, including the transcription factors WT1 [66], SNAIL and SLUG, growth factors such as BMP2 [61], TGFβ1 [67] and TGFβ2 [68], and cell surface receptors, including PDGFRα [65], PDGFRβ [65], TGFβR1/Alk5 [68], TGFβR3 [60,61], and BMPR /ALK3 [48,61]. Molecular analysis of isolated EPDCs from the AV regions of 14.5 ED hearts showed that some genes identified in the aforementioned studies were expressed in/by the AV-EPDC, including SMAD1, SNAIL and SLUG, factors involved in EMT (epiMT in this case), genes that are typically associated with fibroblast differentiation, such as periostin, procollagen I, fibronectin I, vimentin, discoidin domain receptor 2 (DDR2), and tenascin C, as well as matrix metalloproteinase 2 (MMP2), an enzyme that is important in the regulation of cell migration [53]. In a more recent paper, the significance of the PRMT1-p53 pathway in epiMT, the migration of EPDC into the ventricular myocardial walls and the formation of coronary vessels has been reported [69]. The specific role of this pathway at the AV junction, however, remains to be determined.

When focusing on AV-epiMT, it is important to note that, of the growth factors mentioned, only BMP2 and TGFβ2 are expressed at high levels within the AV myocardium [18,48,70–72]. The expression of these two secreted growth factors has been proven to be of critical importance for the induction and regulation of endMT in the AV cushions which are located at the luminal side (or inside) of the myocardial AV junction. Based on these considerations, we decided a few years ago to investigate the role of BMP signaling in the AV epicardium [48]. To determine the importance of BMP signaling for epicardial-dependent development of the AV junction, we created the $WT1^{cre}$;$ALK3^{fl/fl}$ mouse, which allowed us to specifically delete ALK3 from the epicardial lineage [48,49]. When crossed

with the ROSA26$^{mT/mG}$ mouse [73] (WT1^{cre};ALK3$^{fl/fl}$;R26^{mG}), it enabled us to follow the fate of the EPDCs in the absence of ALK3. In this current review, we will highlight the results as they relate to the development and maturation of the AV valve leaflets and discuss the significance of the observations in the context of the pathogenesis of myxomatous valve disease (MVD).

The transcription factor SOX9 has been implicated in the regulation of endMT, in controlling proliferation of ENDCs [74–76], and plays an essential role in the development of the endocardial cushions [77–80]. Its expression is regulated by BMP2. Just like BMP2, SOX9 is also involved in the transcriptional regulation of the expression of ECM components in developing cardiac structures, such as Cartilage Link Protein (Crtl1) and Tenascin [74–76]. In the epicardium, SOX9 is expressed at a relatively low level. The importance for SOX9 in the ventricular epicardium was demonstrated in studies that showed that reduced SOX9 expression in an epicardial-specific PDGFR knockout mice led to the loss of epicardial cell migration and reduced epiMT [65]. As described in our earlier studies [46], co-labeling for EGFP and SOX9 in WT1^{cre};R26$^{mT/mG}$ specimens shows prominent expression of SOX9 in the EGFP-positive AV-EPDCs within the AV-sulcus (Figure 8). As SOX9 is a known target for BMP2, this strongly suggests that the elevated expression levels of BMP2 in the AV myocardium is responsible for the upregulation of SOX9 in the AV-EPDCs. SOX9 expression is also observed in the AV-EPDCs that form the annulus fibrosus and in the AV-EPDCs that populate the AV valve leaflets that derive from the lateral AV cushions.

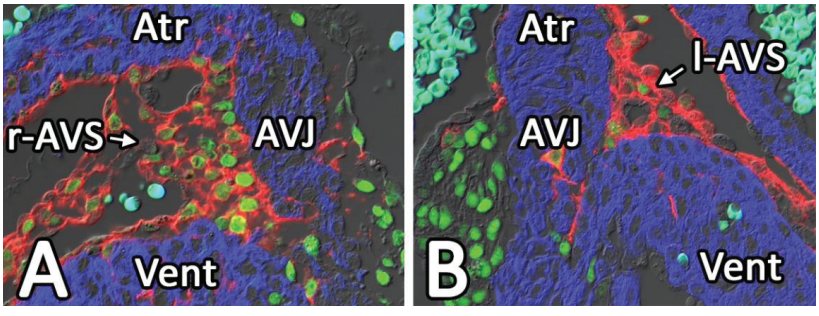

Figure 8. SOX9 is upregulated in AV-EPDCs as they migrate from the epicardium toward the right (**A**) and left (**B**) AV junction. A section of a 13 ED WT1^{cre};R26$^{mT/mG}$ heart was stained for SOX9 (green), EGFP (immunolocalized and visualized in the red channel) to localize EPDCs, and the myocardium (myosin heavy chain) in blue. Atr, atrium; AVJ, (myocardial) AV junction; l-AVS, left AV sulcus; r-AVS, right AV sulcus; Vent, ventricle.

8. Significance of Epicardial ALK3 and SOX9 Expression in AV Valve Development

As shown in our earlier study [46], AV-EPDCs are responsible, in part, for the formation of the AV sulcus and annulus fibrosus and contribute significantly to the cellular content of the parietal AV valve leaflets in late fetal and neonatal hearts. Deletion of ALK3 from the epicardial cell lineage using the WT1^{cre};ALK3$^{fl/fl}$ model resulted in failure of the AV sulcus and annulus fibrosus to properly develop and led to a significant reduction in the number of AV-EPDCs in the parietal leaflets. In control hearts between ED15 and day one after birth (P1), AV-EPDCs occupy up to 50% of the total cell population in the left and right parietal AV valve leaflets, whereas, in the WT1^{cre};ALK3$^{fl/fl}$;R26^{mG} mice, that number fell to less than 20% (Figure 9). An interesting, and unexpected, finding was that the overall number of cells within the leaflets did not significantly change, an observation from which we concluded that the number of cells with a non-epicardial origin was increased. Although this still formally needs to be proven, we believe that these non-epicardially derived cells are mostly AV-ENDCs. When the studies that led to this publication on the WT1^{cre};ALK3$^{fl/fl}$ model were conducted, there were no tools available to confirm that this was the case. New developments in the generation of mouse models that facilitate

the tracing of multiple cell populations within one specimen (see, for instance, [54]) will allow us to test this hypothesis. Interestingly, we did not observe a significant increase in the level of proliferation of the non-EPDCs. As we believe that the non-EPDCs cells are endocardially-derived, the increase in their number could point at a higher rate of endMT in the absence of the AV-EPDCs. In this context, it is important to reiterate that as they migrate into the lateral cushions/developing parietal valve leaflets, the AV-EPDCs position themselves right under the endocardium on the leading edge of the cushions (see Figure 4). Our current working hypothesis is that, by positioning themselves between the AV myocardium and the endocardium, AV-EPD Cs play a role in controlling endMT. In the absence/reduced presence of AV-EPDCs, this control may be lifted, resulting in an increase in endMT. Studies to test this hypothesis are ongoing.

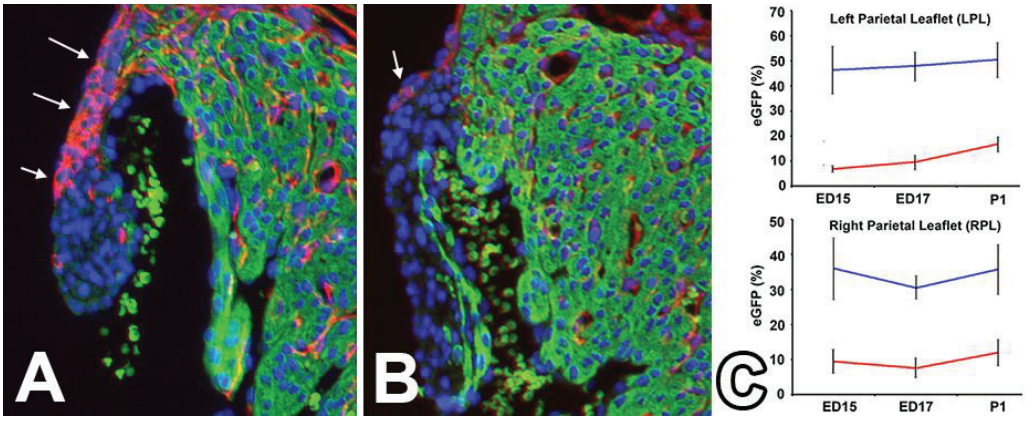

Figure 9. Contribution of EPDCs to the posterior leaflet of the mitral valve of control (**A**) and $WT1^{cre}$;$ALK3^{fl/fl}$;$R26^{mG}$ (**B**) hearts at ED17. The sections in panels (**A**,**B**) were stained for EGFP (immunolocalized and visualized in the red channel) to localize EPDCs, the myocardium (myosin heavy chain in green), and DAPI to visualize all nuclei. Panel (**C**) shows a graph with the percentage of EGFP-positive cells (determined using AMIRA 3D software), in the left and right parietal leaflets of ED15, ED17, and postnatal day 1 (P1) hearts. The blue line represents percentage of EGFP-positive cells in control hearts, the red line represents this percentage in the heart of $WT1^{cre}$;$ALK3^{fl/fl}$;$R26^{mG}$ specimens (adapted from Lockhart et al., 2014).

To determine the role of SOX9 in the epicardial-dependent development of the AV junction, we generated the $WT1^{cre}$;$SOX9^{fl/fl}$ model. Our preliminary and unpublished results from this ongoing study indicate that removing SOX9 from the epicardial lineage has a moderate effect on the development of the AV sulcus when compared to what was observed in the $WT1^{cre}$;$ALK3^{fl/fl}$ mouse. This may indicate that epiMT is not affected to the same degree as observed in the $WT1^{cre}$;$ALK3^{fl/fl}$ mouse but this will remain to be established. The impact on the migration of AV-EPDCs into the parietal leaflets of the AV valves, including the posterior leaflet of the mitral valve as demonstrated in Figure 10, however, is pronounced. This suggests that SOX9 is involved in migration of AV-EPDCs in post-epiMT stages. In an earlier study, in which the importance for SOX9 in the ventricular epicardium was investigated, it was shown that reduced SOX9 expression in epicardial-specific PDGFR knockout mice not only resulted in a reduction in epiMT, but also a loss of epicardial cell migration [65]. Our findings on the behavior of the EPDCs at the AV junction in the $WT1^{cre}$;$SOX9^{fl/fl}$ mouse are, therefore, compatible with the reported role of SOX9 in EPDCs in other parts of the heart.

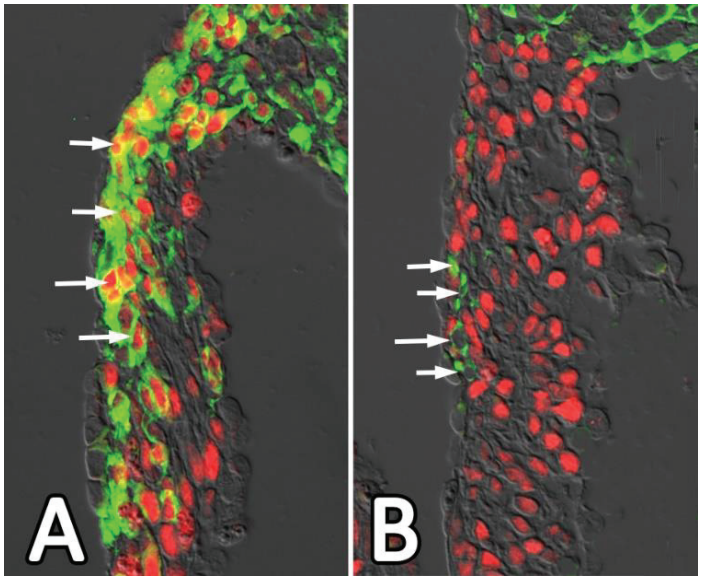

Figure 10. AV-EPDCs (green) in posterior leaflet of the mitral valve in control (**A**) and $WT1^{cre}$;$SOX9^{fl/fl}$; $R26^{mG}$ (**B**) specimens at 17.5 ED. The sections are stained for the presence of EGFP (in green), indicating the presence of EPDCs and SOX9 (red). Note the abundance of SOX9-positive AV-EPDCs in the leaflet of control heart (arrows in (**A**)) and virtual absence of AV-EPDCs in the posterior leaflet of the knockout heart (**B**). The few AV-EPDCs that are found in this leaflet do not express SOX9 (arrows in (**B**)). Note also that EGFP-positive EPDCs in the top right corner of (**B**) do not express SOX9.

9. Consequence of Reduced Presence of AV-EPDCs in the Valve Leaflets—A Link to Myxomatous Valve Disease

In our study on the $WT1^{cre}$;$ALK3^{fl/fl}$ mouse [48], we found that even though the overall cellular composition of the leaflets significantly changed as a result of the deletion of ALK3 from the epicardial cell lineage, the morphology of the parietal leaflets remained remarkably normal throughout fetal development. Histological analysis of post-natal mitral valve morphology of $WT1^{cre}$;$ALK3^{fl/f}$ and control littermates up to 20 weeks after birth showed, however, that the valve leaflets, and, in particular, the posterior leaflet of the mitral valve, were significantly enlarged. Anatomically, these leaflets resembled AV valve leaflets as seen in human patients with MVD/MVP [81] (Figure 11). Myxomatous degeneration of AV valves in humans and mouse models for MVD is typically associated with increased expression of proteoglycans and glycosaminoglycans (GAGs) [3,82,83]. To determine the level of expression of GAGs and proteoglycans in the postnatal $WT1^{cre}$;$ALK3^{fl/fl}$;$R26^{mG}$ heart, we conducted immunolabeling for versican-β and hyaluronan. In control hearts, versican-β and hyaluronan were found in the distal tip of the parietal leaflets, while, in the enlarged leaflets of $WT1^{cre}$;$ALK3^{fl/fl}$;$R26^{mG}$ specimens, large amounts of hyaluronan and versican-β were detected throughout the leaflets, consistent with a myxomatous phenotype as seen in humans [48].

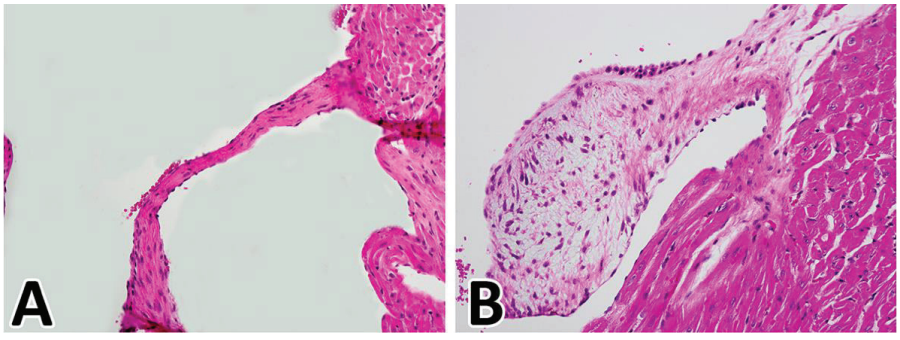

Figure 11. Myxomatous Valve Degeneration in the $WT1^{cre}$;$ALK3^{fl/fl}$ mouse. Panel (**A**) shows H/E staining of the posterior leaflet of the mitral valve of a control heart, panel (**B**) shows the H/E staining of the myxomatous leaflet in a $WT1^{cre}$;$ALK3^{fl/fl}$ littermate collected 10 days after birth.

Given the fact that the reduction in contribution of the AV-EPDCs to the developing valves of the $WT1^{cre}$;$SOX9^{fl/fl}$;$R26^{mG}$ mouse resembled what we have seen in the $WT1^{cre}$;$ALK3^{fl/fl}$;$R26^{mG}$ mouse, we sought to determine whether the reduction in AV-EPDCs in the valve leaflets would also lead to valve abnormalities later in life. Neonatal $WT1^{cre}$;$SOX9^{fl/fl}$;$R26^{mG}$ specimens and mice at one and two months of age were collected and analyzed. Like the $WT1^{cre}$;$ALK3^{fl/fl}$;$R26^{mG}$, the $WT1^{cre}$;$SOX9^{fl/fl}$;$R26^{mG}$ were also found to develop MVD (Figure 12).

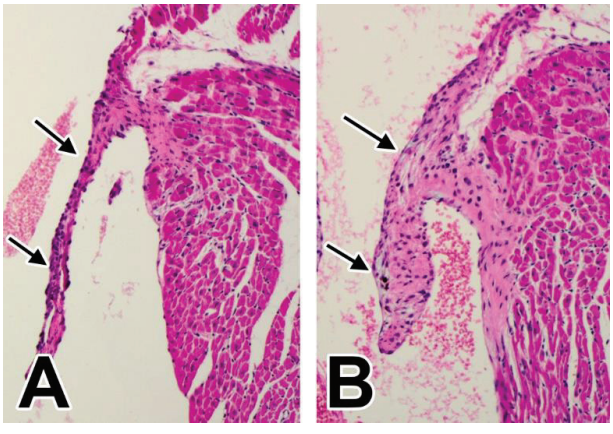

Figure 12. Myxomatous posterior leaflet in a $WT1^{cre}$;$SOX9^{fl/fl}$ specimen at one month after birth. Panel (**A**) shows an H/E staining demonstrating the posterior leaflet of a control heart, panel (**B**) shows the myxomatoyus phenotype of the posterior mitral valve leaflet, in a $WT1^{cre}$;$SOX9^{fl/fl}$ specimen.

Given all of the above, we believe that the pathological features of the valves are, in all likelihood, the direct consequence of the reduced presence of the AV-EPDCs in these valves. How this reduction in the number of AV-EPDCs exactly affects the cell biology and behavior of the non-EPDCs that contribute to valve development and function remains to be determined. The main question generated by these studies is whether "developmental" defects that interfere with the normal epicardial contribution to the leaflets of the AV valves should be considered when investigating the pathogenesis of MVD in the human population.

10. Discussion and Reflection

Dr. Adriana Gittenberger-de Groot ("Adri" for friends and colleagues) was one of the major driving forces in the field of cardiovascular developmental biology. Her first publication dates from 1971 [84] and, for nearly 50 years, she contributed to our current understanding of the development of the heart and the pathogenesis of congenital heart defects. In 1998, she was the lead author on a paper titled *"Epicardium-derived cells contribute a novel population to the myocardial wall and the atrioventricular cushions"* [10], a publication that, together with a few other articles that appeared around the same time [42,43,45], revolutionized our insight into the role of the epicardium in heart development. These studies truly formed the foundation for all the subsequent studies in which the contribution of EPDCs to the developing mouse heart has been studied (mainly using the cre-lox system) and the studies in which the molecular regulation of epicardial development is investigated. Together with her colleagues at Leiden University, Adri has also significantly contributed to many other aspects of heart development, including to our growing understanding of atrioventricular valve development [85,86] and the pathogenesis of congenital heart disease at times when words like PCR, cre-lox mouse models, and confocal microscopy, were not yet part of the developmental biologist's vocabulary. In this review, we have presented some of our published and ongoing work on aspects of heart development and pathogenesis that, directly and indirectly, can be associated with the scientific legacy that Adri has left behind. The possibility that our work shows that there might be a developmental origin for (some forms of) MVD is intriguing. Even without a link to valve pathogenesis, the "how" and "why" of the directional migration of AV-EPDCs into the parietal AV valve leaflets, and the role that these cells might play in valve development and function, are topics that need significant attention in the years to come and that will further our insight into the complexity of valve formation.

Author Contributions: A.W. designed the experiments. R.W., R.D., J.D., A.B.H. E.H. and M.M.L. conducted the majority of the experiments and/or are involved in ongoing projects, A.W. was responsible for the creation of the manuscript, and M.J.B.v.d.H. and R.A.N. provided critical feedback. All authors have read and agreed to the published version of the manuscript.

Funding: This research was partly funded by the following grants of the National Institutes of Health (NIH): R01 HL122906 (AW, RD, RAN), HL131546 (RAN, AW), GM103444 (RAN), HL149696 (RAN) and RR018823; grants from the American Heart Association: 10SRG35540029 (RAN), 19TPA34850095 (RAN) and 19TPA34900016 (RAN); a Research Grant from the CHARGE Syndrome Foundation (AW); and by the Netherlands Heart Foundation through the Molecular Cardiology Program on Heart Failure (MvdH). The contents are solely the responsibility of the authors.

Institutional Review Board Statement: Animal studies described in this article were conducted following protocols approved by the Institutional Animal Care & Use Committee (IACUC) at the Medical University of South Carolina (IACUC-2020-01140).

Conflicts of Interest: The authors declare no conflict of interest.

References

1. Kyndt, F.; Gueffet, J.P.; Probst, V.; Jaafar, P.; Legendre, A.; Le Bouffant, F.; Toquet, C.; Roy, E.; McGregor, L.; Lynch, S.A.; et al. Mutations in the gene encoding filamin a as a cause for familial cardiac valvular dystrophy. *Circulation* **2007**, *115*, 40–49. [CrossRef]
2. Lardeux, A.; Kyndt, F.; Lecointe, S.; Marec, H.L.; Merot, J.; Schott, J.J.; Le Tourneau, T.; Probst, V. Filamin-a-related myxomatous mitral valve dystrophy: Genetic, echocardiographic and functional aspects. *J. Cardiovasc. Transl. Res.* **2011**, *4*, 748–756. [CrossRef] [PubMed]
3. Durst, R.; Sauls, K.; Peal, D.S.; deVlaming, A.; Toomer, K.; Leyne, M.; Salani, M.; Talkowski, M.E.; Brand, H.; Perrocheau, M.; et al. Mutations in dchs1 cause mitral valve prolapse. *Nature* **2015**, *525*, 109–113. [CrossRef]
4. Sauls, K.; de Vlaming, A.; Harris, B.S.; Williams, K.; Wessels, A.; Levine, R.A.; Slaugenhaupt, S.A.; Goodwin, R.L.; Pavone, L.; Merot, J.; et al. Developmental basis for filamin-a associated myxomatous mitral valve disease. *Cardiovasc. Res.* **2012**, *96*, 109–119. [CrossRef] [PubMed]
5. Sauls, K.; Toomer, K.; Williams, K.; Johnson, A.J.; Markwald, R.R.; Hajdu, Z.; Norris, R.A. Increased infiltration of extra-cardiac cells in myxomatous valve disease. *J. Cardiovasc. Dev. Dis* **2015**, *2*, 200–213. [CrossRef]

6. Le Tourneau, T.; Merot, J.; Rimbert, A.; Le Scouarnec, S.; Probst, V.; Le Marec, H.; Levine, R.A.; Schott, J.J. Genetics of syndromic and non-syndromic mitral valve prolapse. *Heart* **2018**, *104*, 978–984. [CrossRef] [PubMed]
7. Levine, R.A.; Hagege, A.A.; Judge, D.P.; Padala, M.; Dal-Bianco, J.P.; Aikawa, E.; Beaudoin, J.; Bischoff, J.; Bouatia-Naji, N.; Bruneval, P.; et al. Mitral valve disease–morphology and mechanisms. *Nat. Rev. Cardiol.* **2015**, *12*, 689–710. [CrossRef]
8. Delling, F.N.; Vasan, R.S. Epidemiology and pathophysiology of mitral valve prolapse: New insights into disease progression, genetics, and molecular basis. *Circulation* **2014**, *129*, 2158–2170. [CrossRef]
9. Ogawa, S.; Hayashi, J.; Sasaki, H.; Tani, M.; Akaishi, M.; Mitamura, H.; Sano, M.; Hoshino, T.; Handa, S.; Nakamura, Y. Evaluation of combined valvular prolapse syndrome by two-dimensional echocardiography. *Circulation* **1982**, *65*, 174–180. [CrossRef] [PubMed]
10. Gittenberger-de Groot, A.C.; Vrancken Peeters, M.P.; Mentink, M.M.; Gourdie, R.G.; Poelmann, R.E. Epicardium-derived cells contribute a novel population to the myocardial wall and the atrioventricular cushions. *Circ. Res.* **1998**, *82*, 1043–1052. [CrossRef]
11. Bolender, D.L.; Markwald, R.R. Epithelial-mesenchymal transformation in chick atrioventricular cushion morphogenesis. *Scan. Electron. Microsc.* **1979**, *3*, 313–321.
12. Markwald, R.; Eisenberg, C.; Eisenberg, L.; Trusk, T.; Sugi, Y. Epithelial-mesenchymal transformations in early avian heart development. *Acta Anat.* **1996**, *156*, 173–186. [CrossRef] [PubMed]
13. Aanhaanen, W.T.; Brons, J.F.; Dominguez, J.N.; Rana, M.S.; Norden, J.; Airik, R.; Wakker, V.; de Gier-de Vries, C.; Brown, N.A.; Kispert, A.; et al. The tbx2+ primary myocardium of the atrioventricular canal forms the atrioventricular node and the base of the left ventricle. *Circ. Res.* **2009**, *104*, 1267–1274. [CrossRef] [PubMed]
14. Cai, X.; Nomura-Kitabayashi, A.; Cai, W.; Yan, J.; Christoffels, V.M.; Cai, C.L. Myocardial tbx20 regulates early atrioventricular canal formation and endocardial epithelial-mesenchymal transition via bmp2. *Dev. Biol.* **2011**, *360*, 381–390. [CrossRef]
15. Singh, R.; Hoogaars, W.M.; Barnett, P.; Grieskamp, T.; Rana, M.S.; Buermans, H.; Farin, H.F.; Petry, M.; Heallen, T.; Martin, J.F.; et al. Tbx2 and tbx3 induce atrioventricular myocardial development and endocardial cushion formation. *Cell. Mol. Life Sci.* **2012**, *69*, 1377–1389. [CrossRef] [PubMed]
16. Zhang, H.; von Gise, A.; Liu, Q.; Hu, T.; Tian, X.; He, L.; Pu, W.; Huang, X.; He, L.; Cai, C.L.; et al. Yap1 is required for endothelial to mesenchymal transition of the atrioventricular cushion. *J. Biol. Chem.* **2014**, *289*, 18681–18692. [CrossRef]
17. Brown, C.B.; Boyer, A.S.; Runyan, R.B.; Barnett, J.V. Requirement of type iii tgf-beta receptor for endocardial cell transformation in the heart. *Science* **1999**, *283*, 2080–2082. [CrossRef]
18. Sugi, Y.; Yamamura, H.; Okagawa, H.; Markwald, R.R. Bone morphogenetic protein-2 can mediate myocardial regulation of atrioventricular cushion mesenchymal cell formation in mice. *Dev. Biol.* **2004**, *269*, 505–518. [CrossRef]
19. Timmerman, L.A.; Grego-Bessa, J.; Raya, A.; Bertran, E.; Perez-Pomares, J.M.; Diez, J.; Aranda, S.; Palomo, S.; McCormick, F.; Izpisua-Belmonte, J.C.; et al. Notch promotes epithelial-mesenchymal transition during cardiac development and oncogenic transformation. *Genes Dev.* **2004**, *18*, 99–115. [CrossRef]
20. Luna-Zurita, L.; Prados, B.; Grego-Bessa, J.; Luxan, G.; del Monte, G.; Benguria, A.; Adams, R.H.; Perez-Pomares, J.M.; de la Pompa, J.L. Integration of a notch-dependent mesenchymal gene program and bmp2-driven cell invasiveness regulates murine cardiac valve formation. *J. Clin. Investig.* **2010**, *120*, 3493–3507. [CrossRef]
21. Liebner, S.; Cattelino, A.; Gallini, R.; Rudini, N.; Iurlaro, M.; Piccolo, S.; Dejana, E. Beta-catenin is required for endothelial-mesenchymal transformation during heart cushion development in the mouse. *J. Cell Biol.* **2004**, *166*, 359–367. [CrossRef]
22. Combs, M.D.; Yutzey, K.E. Heart valve development: Regulatory networks in development and disease. *Circ. Res.* **2009**, *105*, 408–421. [CrossRef]
23. Chen, D.; Zhu, X.; Kofler, N.; Wang, Y.; Zhou, B.; Simons, M. Frs2alpha-dependent cell fate transition during endocardial cushion morphogenesis. *Dev. Biol.* **2020**, *458*, 88–97. [CrossRef] [PubMed]
24. Kovacic, J.C.; Dimmeler, S.; Harvey, R.P.; Finkel, T.; Aikawa, E.; Krenning, G.; Baker, A.H. Endothelial to mesenchymal transition in cardiovascular disease: Jacc state-of-the-art review. *J. Am. Coll. Cardiol.* **2019**, *73*, 190–209. [CrossRef] [PubMed]
25. Wessels, A.; Sedmera, D. Developmental anatomy of the heart: A tale of mice and man. *Physiol. Genom.* **2003**, *15*, 165–176. [CrossRef] [PubMed]
26. Wessels, A.; Markman, M.W.; Vermeulen, J.L.; Anderson, R.H.; Moorman, A.F.; Lamers, W.H. The development of the atrioventricular junction in the human heart. *Circ. Res.* **1996**, *78*, 110–117. [CrossRef]
27. Wessels, A.; Anderson, R.H.; Markwald, R.R.; Webb, S.; Brown, N.A.; Viragh, S.; Moorman, A.F.; Lamers, W.H. Atrial development in the human heart: An immunohistochemical study with emphasis on the role of mesenchymal tissues. *Anat. Rec.* **2000**, *259*, 288–300. [CrossRef]
28. Anderson, R.H.; Brown, N.A.; Webb, S. Development and structure of the atrial septum. *Heart* **2002**, *88*, 104–110. [CrossRef]
29. Snarr, B.S.; Kern, C.B.; Wessels, A. Origin and fate of cardiac mesenchyme. *Dev. Dyn.* **2008**, *237*, 2804–2819. [CrossRef]
30. Jensen, B.; Wang, T.; Moorman, A.F.M. Evolution and development of the atrial septum. *Anat. Rec.* **2018**, *302*, 32–48. [CrossRef] [PubMed]
31. Deepe, R.; Fitzgerald, E.; Wolters, R.; Drummond, J.; Guzman, K.; Hoff, M.; Wessels, A. The mesenchymal cap of the atrial septum and atrial and atrioventricular septation. *J. Cardiovasc. Dev. Dis.* **2020**, *7*, 50. [CrossRef] [PubMed]
32. Hinton, R.B.; Yutzey, K.E. Heart valve structure and function in development and disease. *Annu. Rev. Physiol.* **2011**, *73*, 29–46. [CrossRef]

33. Icardo, J.M.; Arrechedera, H.; Colvee, E. The atrioventricular valves of the mouse. I. A scanning electron microscope study. *J. Anat.* **1993**, *182*, 87–94.
34. Hiriart, E.; Deepe, R.; Wessels, A. Mesothelium and malignant mesothelioma. *J. Dev. Biol.* **2019**, *7*, 7. [CrossRef]
35. Perez-Pomares, J.M.; Phelps, A.; Sedmerova, M.; Carmona, R.; Gonzalez-Iriarte, M.; Munoz-Chapuli, R.; Wessels, A. Experimental studies on the spatiotemporal expression of wt1 and raldh2 in the embryonic avian heart: A model for the regulation of myocardial and valvuloseptal development by epicardially derived cells (epdcs). *Dev. Biol.* **2002**, *247*, 307–326. [CrossRef]
36. Wessels, A.; Perez-Pomares, J.M. The epicardium and epicardially derived cells (epdcs) as cardiac stem cells. *Anat. Rec. A Discov. Mol. Cell. Evol. Biol.* **2004**, *276*, 43–57. [CrossRef] [PubMed]
37. Viragh, S.; Challice, C.E. The origin of the epicardium and the embryonic myocardial circulation in the mouse. *Anat. Rec.* **1981**, *201*, 157–168. [CrossRef]
38. Vrancken Peeters, M.P.; Mentink, M.M.; Poelmann, R.E.; Gittenberger-de Groot, A.C. Cytokeratins as a marker for epicardial formation in the quail embryo. *Anat. Embryol.* **1995**, *191*, 503–508.
39. Kruithof, B.P.; van Wijk, B.; Somi, S.; Kruithof-de Julio, M.; Perez Pomares, J.M.; Weesie, F.; Wessels, A.; Moorman, A.F.; van den Hoff, M.J. Bmp and fgf regulate the differentiation of multipotential pericardial mesoderm into the myocardial or epicardial lineage. *Dev. Biol.* **2006**, *295*, 507–522. [CrossRef]
40. van Wijk, B.; van den Berg, G.; Abu-Issa, R.; Barnett, P.; van der Velden, S.; Schmidt, M.; Ruijter, J.M.; Kirby, M.L.; Moorman, A.F.; van den Hoff, M.J. Epicardium and myocardium separate from a common precursor pool by crosstalk between bone morphogenetic protein- and fibroblast growth factor-signaling pathways. *Circ. Res.* **2009**, *105*, 431–441. [CrossRef]
41. Nahirney, P.C.; Mikawa, T.; Fischman, D.A. Evidence for an extracellular matrix bridge guiding proepicardial cell migration to the myocardium of chick embryos. *Dev. Dyn.* **2003**, *227*, 511–523. [CrossRef]
42. Manner, J. Does the subepicardial mesenchyme contribute myocardioblasts to the myocardium of the chick embryo heart? A quail-chick chimera study tracing the fate of the epicardial primordium. *Anat. Rec.* **1999**, *255*, 212–226. [CrossRef]
43. Dettman, R.W.; Denetclaw, W., Jr.; Ordahl, C.P.; Bristow, J. Common epicardial origin of coronary vascular smooth muscle, perivascular fibroblasts, and intermyocardial fibroblasts in the avian heart. *Dev. Biol.* **1998**, *193*, 169–181. [CrossRef] [PubMed]
44. Perez-Pomares, J.M.; Macias, D.; Garcia-Garrido, L.; Munoz-Chapuli, R. Contribution of the primitive epicardium to the subepicardial mesenchyme in hamster and chick embryos. *Dev. Dyn.* **1997**, *210*, 96–105. [CrossRef]
45. Perez-Pomares, J.M.; Macias, D.; Garcia-Garrido, L.; Munoz-Chapuli, R. The origin of the subepicardial mesenchyme in the avian embryo: An immunohistochemical and quail-chick chimera study. *Dev. Biol.* **1998**, *200*, 57–68. [CrossRef] [PubMed]
46. Wessels, A.; van den Hoff, M.J.; Adamo, R.F.; Phelps, A.L.; Lockhart, M.M.; Sauls, K.; Briggs, L.E.; Norris, R.A.; van Wijk, B.; Perez-Pomares, J.M.; et al. Epicardially derived fibroblasts preferentially contribute to the parietal leaflets of the atrioventricular valves in the murine heart. *Dev. Biol.* **2012**, *366*, 111–124. [CrossRef]
47. Capecchi, M.R. Gene targeting in mice: Functional analysis of the mammalian genome for the twenty-first century. *Nat. Rev. Genet.* **2005**, *6*, 507–512. [CrossRef]
48. Lockhart, M.M.; Boukens, B.J.; Phelps, A.; Brown, C.-L.M.; Toomer, K.A.; Burns, T.A.; Mukherjee, R.D.; Norris, R.A.; Trusk, T.C.; van den Hoff, M.J.B.; et al. Alk3 mediated bmp signaling controls the contribution of epicardially derived cells to the tissues of the atrioventricular junction. *Dev. Biol.* **2014**, *396*, 8–18. [CrossRef]
49. Lockhart, M.M.; Phelps, A.L.; van den Hoff, M.J.; Wessels, A. The epicardium and the development of the atrioventricular junction in the murine heart. *J. Dev. Biol.* **2014**, *2*, 1–17. [CrossRef]
50. Dickson, M.C.; Slager, H.G.; Duffie, E.; Mummery, C.L.; Akhurst, R.J. RNA and protein localisations of tgf beta 2 in the early mouse embryo suggest an involvement in cardiac development. *Development* **1993**, *117*, 625–639. [CrossRef]
51. Boyer, A.S.; Ayerinskas, I.I.; Vincent, E.B.; McKinney, L.A.; Weeks, D.L.; Runyan, R.B. Tgfbeta2 and tgfbeta3 have separate and sequential activities during epithelial-mesenchymal cell transformation in the embryonic heart. *Dev. Biol.* **1999**, *208*, 530–545. [CrossRef]
52. Zhang, H.; Bradley, A. Mice deficient for bmp2 are nonviable and have defects in amnion/chorion and cardiac development. *Development* **1996**, *122*, 2977–2986. [CrossRef]
53. Zhou, B.; von Gise, A.; Ma, Q.; Hu, Y.; Pu, W. Genetic fate mapping demonstrates contribution of epicardium-derived cells to the annulus fibrosis of the mammalian heart. *Dev. Biol.* **2010**, *338*, 251–261. [CrossRef] [PubMed]
54. Liu, K.; Yu, W.; Tang, M.; Tang, J.; Liu, X.; Liu, Q.; Li, Y.; He, L.; Zhang, L.; Evans, S.M.; et al. A dual genetic tracing system identifies diverse and dynamic origins of cardiac valve mesenchyme. *Development* **2018**, *145*, dev167775. [CrossRef]
55. de Lange, F.; Moorman, A.; Anderson, R.; Männer, J.; Soufan, A.; de Gier-de Vries, C.; Schneider, M.; Webb, S.; van den Hoff, M.; Christoffels, V. Lineage and morphogenetic analysis of the cardiac valves. *Circ. Res.* **2004**, *95*, 645–654. [CrossRef] [PubMed]
56. Foster, C.A. Vcam-1/alpha 4-integrin adhesion pathway: Therapeutic target for allergic inflammatory disorders. *J. Allergy Clin. Immunol.* **1996**, *98*, S270–S277. [CrossRef]
57. Yang, J.T.; Rayburn, H.; Hynes, R.O. Cell adhesion events mediated by alpha 4 integrins are essential in placental and cardiac development. *Development* **1995**, *121*, 549–560. [CrossRef]
58. Kwee, L.; Baldwin, H.S.; Shen, H.M.; Stewart, C.L.; Buck, C.; Buck, C.A.; Labow, M.A. Defective development of the embryonic and extraembryonic circulatory systems in vascular cell adhesion molecule (vcam-1) deficient mice. *Development* **1995**, *121*, 489–503. [CrossRef] [PubMed]

59. Craig, E.A.; Austin, A.F.; Vaillancourt, R.R.; Barnett, J.V.; Camenisch, T.D. Tgfbeta2-mediated production of hyaluronan is important for the induction of epicardial cell differentiation and invasion. *Exp. Cell Res.* **2010**, *316*, 3397–3405. [CrossRef]
60. DeLaughter, D.M.; Clark, C.R.; Christodoulou, D.C.; Seidman, C.E.; Baldwin, H.S.; Seidman, J.G.; Barnett, J.V. Transcriptional profiling of cultured, embryonic epicardial cells identifies novel genes and signaling pathways regulated by tgfbetar3 in vitro. *PLoS ONE* **2016**, *11*, e0159710. [CrossRef]
61. Hill, C.R.; Sanchez, N.S.; Love, J.D.; Arrieta, J.A.; Hong, C.C.; Brown, C.B.; Austin, A.F.; Barnett, J.V. Bmp2 signals loss of epithelial character in epicardial cells but requires the type iii tgfbeta receptor to promote invasion. *Cell. Signal.* **2012**, *24*, 1012–1022. [CrossRef]
62. Sanchez, N.S.; Barnett, J.V. Tgfbeta and bmp-2 regulate epicardial cell invasion via tgfbetar3 activation of the par6/smurf1/rhoa pathway. *Cell. Signal.* **2012**, *24*, 539–548. [CrossRef]
63. Sanchez, N.S.; Hill, C.R.; Love, J.D.; Soslow, J.H.; Craig, E.; Austin, A.F.; Brown, C.B.; Czirok, A.; Camenisch, T.D.; Barnett, J.V. The cytoplasmic domain of tgfbetar3 through its interaction with the scaffolding protein, gipc, directs epicardial cell behavior. *Dev. Biol.* **2011**, *358*, 331–343. [CrossRef] [PubMed]
64. Mellgren, A.M.; Smith, C.L.; Olsen, G.S.; Eskiocak, B.; Zhou, B.; Kazi, M.N.; Ruiz, F.R.; Pu, W.T.; Tallquist, M.D. Platelet-derived growth factor receptor beta signaling is required for efficient epicardial cell migration and development of two distinct coronary vascular smooth muscle cell populations. *Circ. Res.* **2008**, *103*, 1393–1401. [CrossRef]
65. Smith, C.L.; Baek, S.T.; Sung, C.Y.; Tallquist, M.D. Epicardial-derived cell epithelial-to-mesenchymal transition and fate specification require pdgf receptor signaling. *Circ. Res.* **2011**, *108*, e15–e26. [CrossRef]
66. von Gise, A.; Zhou, B.; Honor, L.; Ma, Q.; Petryk, A.; Pu, W. Wt1 regulates epicardial epithelial to mesenchymal transition through β-catenin and retinoic acid signaling pathways. *Dev. Biol.* **2011**, *356*, 421–431. [CrossRef] [PubMed]
67. Morabito, C.J.; Dettman, R.W.; Kattan, J.; Collier, J.M.; Bristow, J. Positive and negative regulation of epicardial-mesenchymal transformation during avian heart development. *Dev. Biol.* **2001**, *234*, 204–215. [CrossRef] [PubMed]
68. Compton, L.A.; Potash, D.A.; Mundell, N.A.; Barnett, J.V. Transforming growth factor-beta induces loss of epithelial character and smooth muscle cell differentiation in epicardial cells. *Dev. Dyn.* **2006**, *235*, 82–93. [CrossRef]
69. Jackson-Weaver, O.; Ungvijanpunya, N.; Yuan, Y.; Qian, J.; Gou, Y.; Wu, J.; Shen, H.; Chen, Y.; Li, M.; Richard, S.; et al. Prmt1-p53 pathway controls epicardial emt and invasion. *Cell Rep.* **2020**, *31*, 107739. [CrossRef]
70. Lyons, K.M.; Pelton, R.W.; Hogan, B.L. Organogenesis and pattern formation in the mouse: Rna distribution patterns suggest a role for bone morphogenetic protein-2a (bmp-2a). *Development* **1990**, *109*, 833–844. [CrossRef] [PubMed]
71. Molin, D.G.; Bartram, U.; Van der Heiden, K.; Van Iperen, L.; Speer, C.P.; Hierck, B.P.; Poelmann, R.E.; Gittenberger-de-Groot, A.C. Expression patterns of tgfbeta1-3 associate with myocardialisation of the outflow tract and the development of the epicardium and the fibrous heart skeleton. *Dev. Dyn.* **2003**, *227*, 431–444. [CrossRef] [PubMed]
72. Briggs, L.E.; Phelps, A.L.; Brown, E.; Kakarla, J.; Anderson, R.H.; van den Hoff, M.J.; Wessels, A. Expression of the bmp receptor alk3 in the second heart field is essential for development of the dorsal mesenchymal protrusion and atrioventricular septation. *Circ. Res.* **2013**, *112*, 1420–1432. [CrossRef] [PubMed]
73. Muzumdar, M.D.; Tasic, B.; Miyamichi, K.; Li, L.; Luo, L. A global double-fluorescent cre reporter mouse. *Genesis* **2007**, *45*, 593–605. [CrossRef]
74. Garside, V.C.; Cullum, R.; Alder, O.; Lu, D.Y.; Vander Werff, R.; Bilenky, M.; Zhao, Y.; Jones, S.J.; Marra, M.A.; Underhill, T.M.; et al. Sox9 modulates the expression of key transcription factors required for heart valve development. *Development* **2015**, *142*, 4340–4350. [CrossRef]
75. Lincoln, J.; Kist, R.; Scherer, G.; Yutzey, K. Sox9 is required for precursor cell expansion and extracellular matrix organization during mouse heart valve development. *Dev. Biol.* **2007**, *305*, 120–132. [CrossRef]
76. Akiyama, H.; Chaboissier, M.C.; Behringer, R.R.; Rowitch, D.H.; Schedl, A.; Epstein, J.A.; de Crombrugghe, B. Essential role of sox9 in the pathway that controls formation of cardiac valves and septa. *Proc. Natl. Acad. Sci. USA* **2004**, *101*, 6502–6507. [CrossRef]
77. Pan, Q.; Yu, Y.; Chen, Q.; Li, C.; Wu, H.; Wan, Y.; Ma, J.; Sun, F. Sox9, a key transcription factor of bone morphogenetic protein-2-induced chondrogenesis, is activated through bmp pathway and a ccaat box in the proximal promoter. *J. Cell. Physiol* **2008**, *217*, 228–241. [CrossRef]
78. Zehentner, B.K.; Dony, C.; Burtscher, H. The transcription factor sox9 is involved in bmp-2 signaling. *J. Bone Miner. Res.* **1999**, *14*, 1734–1741. [CrossRef]
79. Theodosiou, N.A.; Tabin, C.J. Sox9 and nkx2.5 determine the pyloric sphincter epithelium under the control of bmp signaling. *Dev. Biol.* **2005**, *279*, 481–490. [CrossRef]
80. Lincoln, J.; Alfieri, C.M.; Yutzey, K.E. Bmp and fgf regulatory pathways control cell lineage diversification of heart valve precursor cells. *Dev. Biol.* **2006**, *292*, 292–302. [CrossRef] [PubMed]
81. Hayek, E.; Gring, C.N.; Griffin, B.P. Mitral valve prolapse. *Lancet* **2005**, *365*, 507–518. [CrossRef]
82. Gupta, V.; Barzilla, J.; Mendez, J.; Stephens, E.; Lee, E.; Collard, C.; Laucirica, R.; Weigel, P.; Grande-Allen, K. Abundance and location of proteoglycans and hyaluronan within normal and myxomatous mitral valves. *Cardiovasc. Pathol. Off. J. Soc. Cardiovasc. Pathol.* **2009**, *18*, 191–197. [CrossRef]

83. Prakash, S.; Borreguero, L.J.J.; Sylva, M.; Flores Ruiz, L.; Rezai, F.; Gunst, Q.D.; de la Pompa, J.L.; Ruijter, J.M.; van den Hoff, M.J.B. Deletion of fstl1 (follistatin-like 1) from the endocardial/endothelial lineage causes mitral valve disease. *Arter. Thromb. Vasc. Biol.* **2017**, *37*, e116–e130. [CrossRef]
84. Oppenheimer-Dekker, A.; Gittenberger-De Groot, A.C. Double-outlet right ventricle without ventricular septal defect. A challenge to the embryologist? Microscopic investigation. *Z. Anat. Entwickl.* **1971**, *134*, 243–254. [CrossRef] [PubMed]
85. Wenink, A.C.; Gittenberger-de Groot, A.C. Embryology of the mitral valve. *Int. J. Cardiol.* **1986**, *11*, 75–84. [CrossRef]
86. Wenink, A.C.; Gittenberger-de Groot, A.C.; Brom, A.G. Developmental considerations of mitral valve anomalies. *Int. J. Cardiol.* **1986**, *11*, 85–101. [CrossRef]

Journal of
Cardiovascular
Development and Disease

MDPI

Article

Ventricular Septation and Outflow Tract Development in Crocodilians Result in Two Aortas with Bicuspid Semilunar Valves

Robert E. Poelmann [1,2,*], Adriana C. Gittenberger-de Groot [2,†], Charissa Goerdajal [1], Nimrat Grewal [3], Merijn A. G. De Bakker [1] and Michael K. Richardson [1]

[1] Sylvius Laboratory, Department of Animal Sciences and Health, Institute of Biology, University of Leiden, Sylvi-usweg 72, 2333BE Leiden, The Netherlands; charissa_go@hotmail.com (C.G.); M.A.G.de.Bakker@biology.leidenuniv.nl (M.A.G.D.B.); m.k.richardson@biology.leidenuniv.nl (M.K.R.)
[2] Department of Cardiology, Leiden University Medical Center, Albinusdreef 2, P.O. Box 9600, 2300RC Leiden, The Netherlands; a.c.gittenberger-degroot@lumc.nl
[3] Department of Cardiothoracic Surgery, Leiden University Medical Center, Albinusdreef 2, P.O. Box 9600, 2300RC Leiden, The Netherlands; N.Grewal@lumc.nl
* Correspondence: R.E.Poelmann@lumc.nl; Tel.: +31-652695875
† Dedicated to the memory of Adriana C. Gittenberger-de Groot whose ideas were instrumental in this research project.

Abstract: Background: The outflow tract of crocodilians resembles that of birds and mammals as ventricular septation is complete. The arterial anatomy, however, presents with a pulmonary trunk originating from the right ventricular cavum, and two aortas originating from either the right or left ventricular cavity. Mixing of blood in crocodilians cannot occur at the ventricular level as in other reptiles but instead takes place at the aortic root level by a shunt, the foramen of Panizza, the opening of which is guarded by two facing semilunar leaflets of both bicuspid aortic valves. **Methods**: Developmental stages of Alligator mississipiensis, Crocodilus niloticus and Caiman latirostris were studied histologically. **Results and Conclusions**: The outflow tract septation complex can be divided into two components. The aorto-pulmonary septum divides the pulmonary trunk from both aortas, whereas the interaortic septum divides the systemic from the visceral aorta. Neural crest cells are most likely involved in the formation of both components. Remodeling of the endocardial cushions and both septa results in the formation of bicuspid valves in all three arterial trunks. The foramen of Panizza originates intracardially as a channel in the septal endocardial cushion.

Keywords: endocardial cushions; semilunar valves; outflow tract; cartilage; foramen of Panizza; left aorta; right aorta; pulmonary trunk; pharyngeal arch arteries; coronary arteries

Citation: Poelmann, R.E.; Gittenberger-de Groot, A.C.; Goerdajal, C.; Grewal, N.; De Bakker, M.A.G.; Richardson, M.K. Ventricular Septation and Outflow Tract Development in Crocodilians Result in Two Aortas with Bicuspid Semilunar Valves. *J. Cardiovasc. Dev. Dis.* **2021**, *8*, 132. https://doi.org/10.3390/jcdd8100132

Academic Editor: Andy Wessels

Received: 29 July 2021
Accepted: 27 September 2021
Published: 15 October 2021

1. Introduction

The bicuspid aortic valve (BAV) is the most common congenital cardiac malformation in humans with a frequency of 0.5–2% [1]. Furthermore, the malformation is associated with aortic aneurysm in 60–80% of the BAV population later in life [2] and is, therefore, of clinical importance [3]. Much is known about the embryonic origin of abnormal leaflet numbers associated with genetic mutations in the human population [4], but also in genetic models of mice such as GATA5 [5], Krox20 [6], Notch [7], aggrecan [8], periostin [9] and nitric oxide synthase [10], in hamsters [11] and also in bird hemodynamics [9,12]. It is evident that several cell populations act in concert during the formation of the semilunar valves. These include the endocardial cushions, neural crest cells and second heart field. Less is known about the development of the arterial valves in reptiles where bicuspidy is the rule [13,14]. Our restricted level of knowledge is comprehensible as a lack of marker experiments is hampering cell lineage research in the reptilian setting, while genetic mutants specifically affecting outflow tract development have not been published to our knowledge. This

does not mean that tools are unavailable. In an evolutionary context, the comparison of development may elucidate the characteristics of bicuspidy in different taxa. Here, we report the development of the arterial valves in three species of crocodilians (*Crocodylus niloticus, Alligator mississipiensis* and *Caiman latirostris*) to be discussed against mammalian and avian backgrounds. The remodeling of the endocardial cushions will be investigated during outflow tract septation, leading to the separation of three main arteries. These are the pulmonary trunk and left-sided aorta both emerging from the right ventricle, and the right-sided aorta emerging from the left ventricle. All three arteries contain bicuspid valve leaflets. Finally, the septal outflow tract cushion (in crocodilians only) is further specialized. Here, we find the origin of two septal components involved in the separation of the three main arterial stems and, furthermore, the intracardiac origin of a channel between the left- and right-sided circulations, i.e., both aortas. After separation and remodeling of the outflow tract, this shunt, known as the foramen of Panizza (first described by the Italian anatomist Bartolomeo Panizza, 1785–1867 [15,16]) connects the roots of the left and right aortas that, in specific circumstances, may convey blood from the right ventricle to the main circulation [17–19] and sometimes vice versa.

1.1. General Description

In crocodilians, the presence of three interconnected ventricular cava, as it is common in reptiles, is apparent in the early stages. However, during the development described here, this distinction becomes lost because interventricular septation takes place, and the resulting division is conveniently described as the left and the right ventricle. This comes with a consequence as, in crocodilians, two aortas persist (as in other reptiles), each deriving from one of those ventricles. To avoid complications related to left/right-sidedness in the body and right/left origin of the respective aortas, we have chosen to use the term "systemic aorta" (sAo) for the morphologically right-sided aorta that derives from the left ventricle, while "visceral aorta" (vAo) denominates the left-sided aorta that branches from the right ventricle (similar to Poelmann [20]. Note: Cook et al. [21] countered the sidedness problem differently by employing the terms "left-ventricular aorta" and "right-ventricular aorta", respectively). Our choice is further substantiated by the observation that the right ventricle perfuses both the abdominal and thoracic viscera as the left-sided aorta (-> vAo) will perfuse the intestines or viscera [22] and the right-sided pulmonary blood will perfuse the lungs (note that viscera and lungs are both "endoderm-derived" organ systems), whereas the left ventricle and right-sided aortic blood (-> sAo) will mostly perfuse the combination of the body wall, extremities and head/neck region (Supplemental Figure S1, adapted from [9])

1.2. Description of Stages

The descriptions are illustrated from caiman embryos (Figures 1–7); only Figure 8 is from an alligator. We chose to start our study with stage 17, although several elements (endocardial cushions, parts of the muscular interventricular septum) already appear earlier. In St 17, the elements start to make up a comprehensible combination leading to complete septation.

Ferguson stage 17. The right and left ventricles are dorsally intersected by the inlet septum (Figure 1a), but otherwise not separated, as the interventricular communication presents itself clearly (Figure 1b). The ventricular inlet septum is fused with the large central AV cushion complex, while the folding septum [20] can hardly be discerned (Figure 1a–c). We have defined the folding septum [20] as a part of the muscular interventricular septum particularly located between the right and left ventricular outflow tracts. Slightly more downstream, the septal outflow tract cushion (sc) becomes apparent, together with the flanking aortic and pulmonary parietal outflow tract cushions (Apc and Ppc) (Figure 1d–f). In the septal cushion, two streaks of condensed mesenchymal cells are evident, one on the pulmonary side (red curve in Figure 1g–i), and the other on the aortic side (blue curve). At their tips (* and + in Figure 1h,i), both contain a histologically very dense cluster of cells. In

a recent study [20], we showed the presence of neural crest cells in this dense cluster by the expression of AP2alpha, a known marker of NC. The pulmonary streak or aorto-pulmonary (AP) septum might contain left-sided NC-derived cells, while the aortic streak or interaortic (IA) septum probably contains right-sided NC cells, as it will be discussed later. The curved lumen of the outflow tract (Figure 1h,i) can be divided into the pulmonary outflow tract (from the right ventricle), the visceral aorta (vAo, also from the right ventricle) and the systemic aorta (sAo, left ventricle). Separation of the outflow tracts (Figure 1j) takes place by 1. the AP septum including a histologically distinguishable ventral myocardial spur (# in Figure 1j–n) located between the pulmonary trunk and the aortas, and 2. the IA septum between sAo and vAo. In the thorax, no further branches will be found emanating from the vAo. The sAo, however, branches further in both carotid arteries (not depicted here).

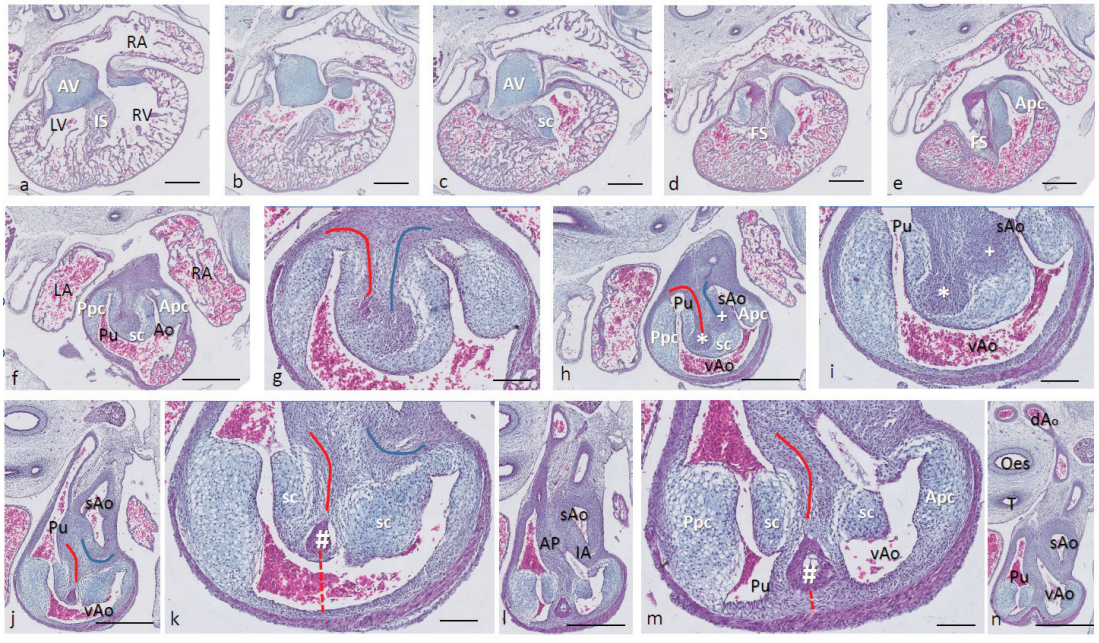

Figure 1. Ferguson stage 17. HE Alcian blue-stained serially sectioned embryo. Figure (**a**–**n**) from AV canal to pharyngeal arch arteries. Generally, the endocardial cushions stand out because of the Alcian blue staining. Figure (**a**), myocardium is spongious with a thin compact outer layer. The inlet septum is the most conspicuous part of the interventricular septum located between the left- and right-sided parts of the undivided common ventricle. Figure (**b**,**c**), the outflow tract septal cushion becomes visible. Figure (**d**,**e**), the folding septum only becomes clear more distally. Figure (**f**), pulmonary and aortic parietal OFT cushions become apparent, flanking the pulmonary channel and the yet common aortic channel. Figure (**g**), magnified Figure (**f**, in the large centrally located septal cushion, two streams of condensed mesenchyme, on the pulmonary side (in red) and the aortic side (in blue). The septal cushion becomes subdivided over the main arterial channels. Figure (**h**,**i**), both streams end separately in a bulbous structure as the basis for the AP septum (*) and IA septum (+). Figure (**j**), magnified in Figure (**k**), the AP stream meets the ventral myocardial spur (#). Figure (**l**), magnified in (**m**), the myocardial spur is part of the ventral myocardium indicated by the red dotted line. At this level, the AP septum is completed. Figure (**n**), pharyngeal arch arteries are separated, and the connection to the dorsal aorta is present. Key to the symbols **#** ventral myocardium, part of AP septum; ***** (presumably) left-sided neural crest cells, part of AP septum; **+** (presumably) right-sided neural crest, part of IA septum; **Δ** dorsal myocardium, part of AP septum. Magnification Figure (**a**–**e**,**f**,**h**,**j**,**l**,**n**), bar 500 μm; (**g**,**i**,**k**,**m**), 200 μm.

Ferguson stage 19. The interventricular situation (Figure 2a,b) has not advanced very much compared to stage 17 as the interventricular communication is still open and the

folding septum (FS) remains inconspicuous (Figure 2c). The septal outflow tract cushion (sc) acquires a dense core (Figure 2c) preceding the differentiation of cartilage in the next stage. The interconnected lumina of the LVOT and RVOT are easily recognized (Figure 2d,e), interrupted by the large septal cushion (sc). The root of the Pu seems to be hconnected sideways (Figure 2d–f) to the ventricular segment as a result of folding of this part of the interventricular septum. The septal cushion is located at the top of the folding septum (Figure 2c,d) that becomes more clear in the next stage. In the as yet common outflow tract, the three arteries become separated by the AP septum and the IA septum. In the AP septum, the region of the originally dense cluster of cells (see Figure 2h *) surrounds a dorsal spur of the myocardium (Δ in Figure 2g,h), being the cranial tip of the folding septum. This dorsal myocardial spur has not yet fused with the ventral myocardial spur (# Figure 2j–m and dashed red line (Figure l) to show the continuation with the ventral wall) as there is a "window", free from the myocardium in between (* in Figure 2h–j). AP separation and IA separation are seemingly spatially independent of each other (Figure 2i,j). The septal cushion is distally completely bisected by the AP septum (Figure 2k). The right-sided IA septum deviates between both aortas with a dense cell cluster at its tip (+ in Figure 2h,i).

The transition of the cardiac tube to the arterial vascular wall deserves special attention. It is evident that the arterial wall extends inside the cardiac tube over a considerable distance estimated to be about 200 μm on the pulmonary side and even about 400 μm on the aortic side (white dashed line in Figure 2k). Downstream, this appearance is even more substantiated (Figure 2m), where nearly the complete ventral wall of the vAo seems to consist of a double layer of the vessel wall and myocardium (white dashed line) with hardly a thin endocardial cushion tissue. This continues to an estimated depth of 350–400 μm into the myocardial tube. As a consequence, we are dealing with two concentric tubes, a myocardial circumference surrounding an arterial wall.

Ferguson stage 20. The interventricular communication between the LVOT and RV is almost closed (Figure 3a). The dense core in the septal and in the aortic parietal cushions starts to differentiate into cartilage, as shown by intense Alcian blue staining (Figure 3a–c), although more downstream, this differentiation is not apparent yet (Figure 3d,e). Here, the IA septum consists of densely packed right-sided neural crest cells, as described in the earlier stages (+ in Figure 3d). The AP septum now contains a clear core of the myocardium (Δ in Figure 3d–f) as part of the incurving dorsal wall of the myocardial tube. Where the septal cushion has connected with the ventral wall, the ventral myocardial spur (# in Figure 3f–h) is also present. The two spurs do not contact each other (* depicts the mesenchymal "window" between the myocardial spurs indicated by Δ and # in Figure 3g). The AP and IA septa deviate (Figure 3h,i) to continue outside the heart as the mesenchymal vessel walls of the respective arteries (Figure 3j–l). The common stem of the carotid arteries (ca) branches from the systemic aorta (Figure 3l). Two sinuses of Valsalva (white arrow) are present in the OFT cushions of the systemic aorta and the pulmonary trunk (Figure 3h,i) as the first sign of the forming semilunar valve leaflets. The situation in the visceral aorta is slightly different as in the parietal cushion, a sinus of Valsalva is still lacking, but in the septal cushion, a very narrow slit is seen, representing the sinus of Valsalva that is connected to the main lumen of the vAo, probably being the first sign of the origin of the foramen of Panizza (see description in the next stage, stage 21).

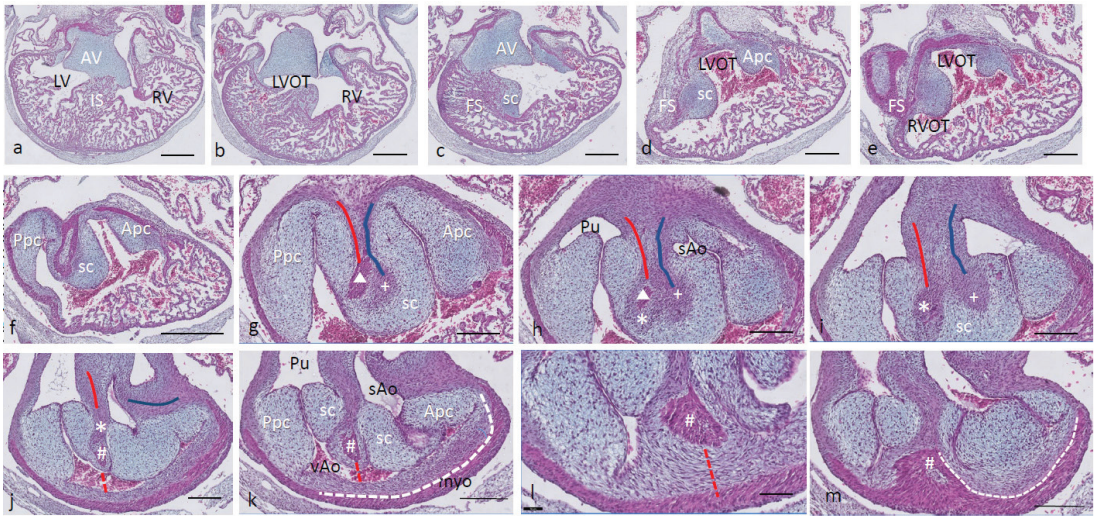

Figure 2. Ferguson stage 19. HE Alcian blue-stained serially sectioned embryo. Figure (**a**–**m**) from AV canal to OFT. Figure (**a**), ventricular myocardial inlet septum attached to the central AV cushions between the left and right ventricles. The myocardium is spongy but for the thin outer compact layer. Figure (**b**), more ventrally, the interventricular communication is visible, while the left ventricular outflow tract becomes apparent. Figure (**c**), muscular folding septum appears as continuation of the inlet septum. The septal OFT cushion is located at the tip of the folding septum. Figure (**d**), septal cushion with Alcian blue-stained condensed mesenchyme. The aortic parietal cushion appears on the other side of the LVOT. Figure (**e**), the septal cushion is located between both outflow tracts, while the folding septum has shifted to the right side. Figure (**f**), in the RVOT the pulmonary parietal cushion is present, and the folding septum including the septal cushion takes up a dorsal position. Figure (**g**), the most cranial remnant of the muscular folding septum is indicated (Δ). The adjacent condensed mesenchyme (+) belonging to the interaortic septum has appeared in the septal cushion. Figure (**h**), a second element of condensed mesenchyme (*) appears ventral to the disappearing myocardium (Δ). Figure (**i**), two streams of condensed mesenchyme as part of the aorto-pulmonary septum (*) and the interaortic septum (+) separate the septal cushion into three subcushions. Figure (**j**), more distally, only the AP septum continues and receives the myocardium (#) from the ventral wall indicated by the red dotted line. Figure (**k**), the condensed mesenchyme of the AP septum is not present anymore, but the myocardial component has enlarged (#). The pulmonary trunk, the visceral aorta and the systemic aorta are indicated, as are the endocardial cushion components. Only the visceral aorta is still encased in the myocardium, but note that the arterial wall of the visceral aorta continues within the myocardial tube (dashed line). Figure (**l**), the visceral and systemic aortas are separated at this level by the AP septum (red line). Figure (**m**), here, the AP septum is myocardialized (#). Key to the symbols **#** ventral myocardium, part of AP septum; * (presumably) left-sided neural crest cells, part of AP septum; + (presumably) right-sided neural crest, part of IA septum; Δ dorsal myocardium, part of AP septum. Magnification Figure (**a**–**f**), bar 500 μm; (**g**–**m**), bar 200 μm; (**g**–**m**), 200 μm; (**l**), 100 μm.

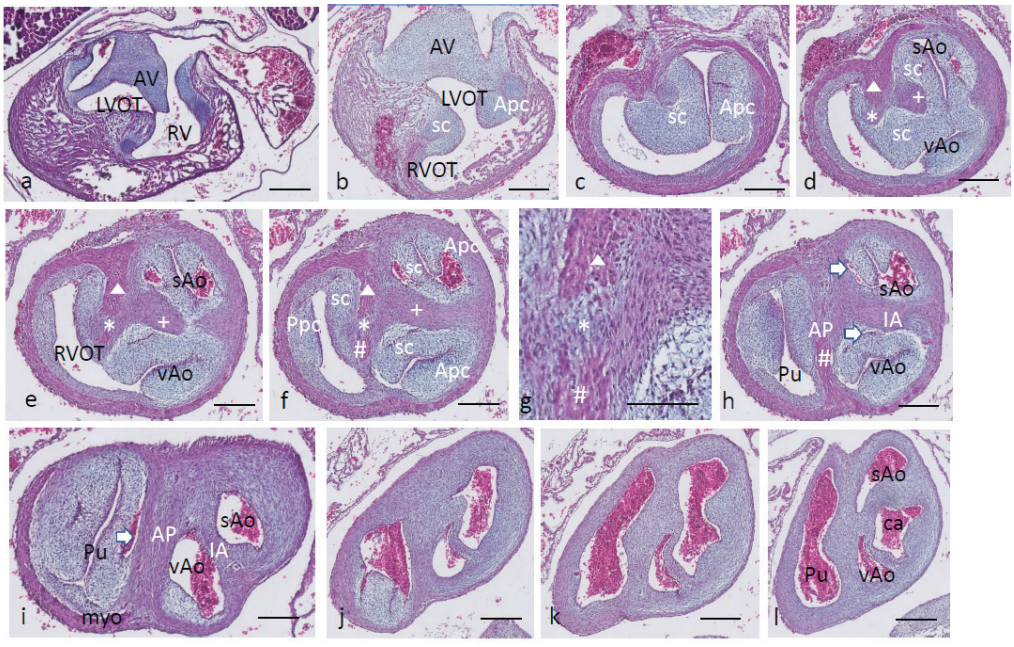

Figure 3. Ferguson stage 20, Figure (**a**–**l**) from AV canal to OFT. Figure (**a**), both in the septal and aortic parietal cushions, cartilage is forming (dark blue) which is less evident more distally (Figure (**b**)). Figure (**c**), the septal cushion containing condensed mesenchyme has a central position. Figure (**d**,**e**), the septal cushion becomes subdivided by both prongs of condensed mesenchyme, belonging to the IA septum (+) and AP septum (*), where the remnant of the folding septum is indicated (Δ). Figure (**f**), the condensed mesenchyme of the IA septum bridges the gap to the aortic parietal cushion whereby the systemic and visceral aortas become separated at this level. The AP septum now contains 3 elements. Enlargement in Figure (**g**), condensed mesenchyme (*), flanked by the myocardium of the folding septum (Δ) and the ventral myocardium (#). Figure (**h**), both IA and AP septa are fully developed at this level. The arrows indicate the sinus of Valsalva in the systemic and visceral aortas. Figure (**i**), the arrow indicates a sinus of Valsalva in the pulmonary trunk. Figure (**j**–**l**) illustrate the branching of the arterial tree, including the pulmonary arteries, and the carotid arteries from the systemic aorta. The visceral aorta does not branch further. Key to the symbols **#** ventral myocardium, part of AP septum; * (presumably) left-sided neural crest cells, part of AP septum; **+** (presumably) right-sided neural crest, part of IA septum; Δ dorsal myocardium, part of AP septum. Magnification Figure (**a**–**f**,**h**–**l**), 500 μm; (**g**), 100 μm.

Ferguson stage 21. The ventricular inflow septum (IS) is seen as the continuation of the folding septum (Figure 4a,b), beyond the topping cartilage of the septal cushion (Figure 4b–e). Another smaller piece of cartilage is found in the aortic parietal cushion (Figure 4c,d). In the outflow tract, the pulmonary side becomes separated from the aortic side by the large septal cushion, containing the elements of the AP septum (* and Δ in Figure 4e–h) as well as the IA septum (+ in Figure 4f–h). Here, an interesting feature becomes apparent, known as the foramen of Panizza (FOP, black arrows in Figure 4f,g), connecting the two septal sinuses of Valsalva of the sAo (white arrow) and vAo. Actually, the FOP in this stadium is a very narrow channel, about 100 μm high in the cranio-caudal direction and about 200 μm between both sinuses. The channel surrounds the advancing tip of the IA (+ in Figure 4f,g) that, at this level, is completed in the arterial direction only (Figure 4h,i). Further downstream, the myocardial tube is replaced by the arterial vessel walls in the concentric manner described above. The stem of the carotid arteries branches from the sAo (Figure 4j,k).

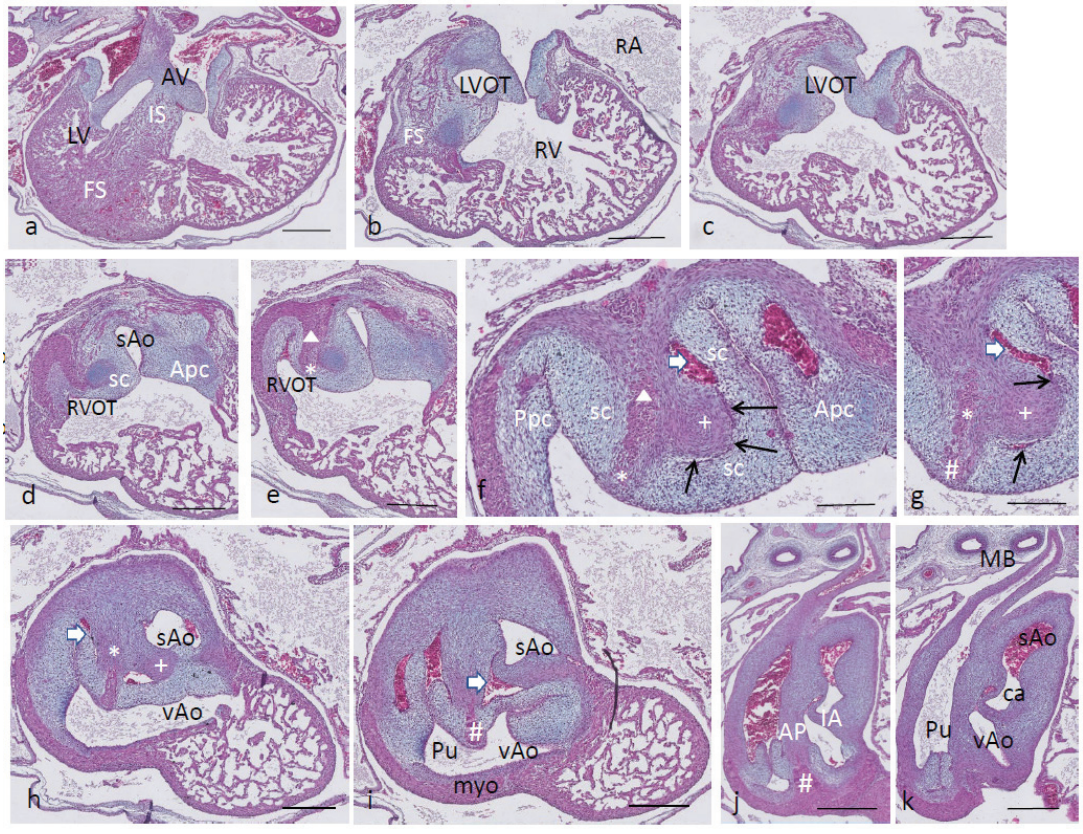

Figure 4. Ferguson stage 21, from AV canal to the arterial tree. Figure (**a**), the ventricular septum shows its two parts: the inlet septum attached to the central AV cushions and the more ventro-distally located folding septum. Figure (**b**,**c**), the septal cushion already showing cartilage differentiation (dark blue) located on the tip of the folding septum. Figure (**d**,**e**), the right ventricular outflow tract rotates to the right, displacing the folding septum (Δ) to the dorsal wall. Figure (**f**,**g**), the AP (*) and IA (+) streams of condensed mesenchyme are visible. The sinus of Valsalva (white arrow) and the tunnel of the foramen of Panizza (black arrows) are indicated. Figure (**h**–**j**), more distally, the AP and IA septa become completed by fusion of the septal cushion with the parietal cushion. Figure (**k**), branching of the arterial tree. Key to the symbols **#** ventral myocardium, part of AP septum; * (presumably) left-sided neural crest cells, part of AP septum; **+** (presumably) right-sided neural crest, part of IA septum; Δ dorsal myocardium, part of AP septum. Magnification Figure (**a**–**e**,**h**–**k**), bar 500 μm; (**f**,**g**), bar 200 μm.

Ferguson stage 22. Most of the features described for stage 21 apply to this stage. The folding septum is more advanced (Figure 5a). The condensed mesenchyme in the septal cushion is further differentiated into cartilage (Figure 5b–d), even reaching the level of the FOP (Figure 5d,e, black arrows). The FOP is seen as a very narrow channel rounding the cartilaginous tip at the base of the IA (Figure 5d,e). The condensed mesenchyme in the aortic parietal cushion is advanced and now contains two cartilaginous centers (Figure 5c), one in the continuation of the aortic vessel wall, and the second one in the cushion mesenchyme. The ventral and dorsal myocardial spurs (# and Δ in Figure 5e) have joined with no mesenchymal window in between anymore, implying that a small myocardial bridge has been established in the AP septum. The IA septum does not acquire a myocardial component in contrast to the AP septum (Figure 5e–g). The branching of the main arterial stems is demonstrated in Figure 5h–i. The pulmonary trunk is divided into

the sixth left and right pulmonary arch arteries (PAA6, Figure 5h), and the vAo, being the left fourth PAA, does not branch further, whereas the stem of the carotid arch arteries splits from the right fourth PAA, being the sAo (Figure 5h–i).

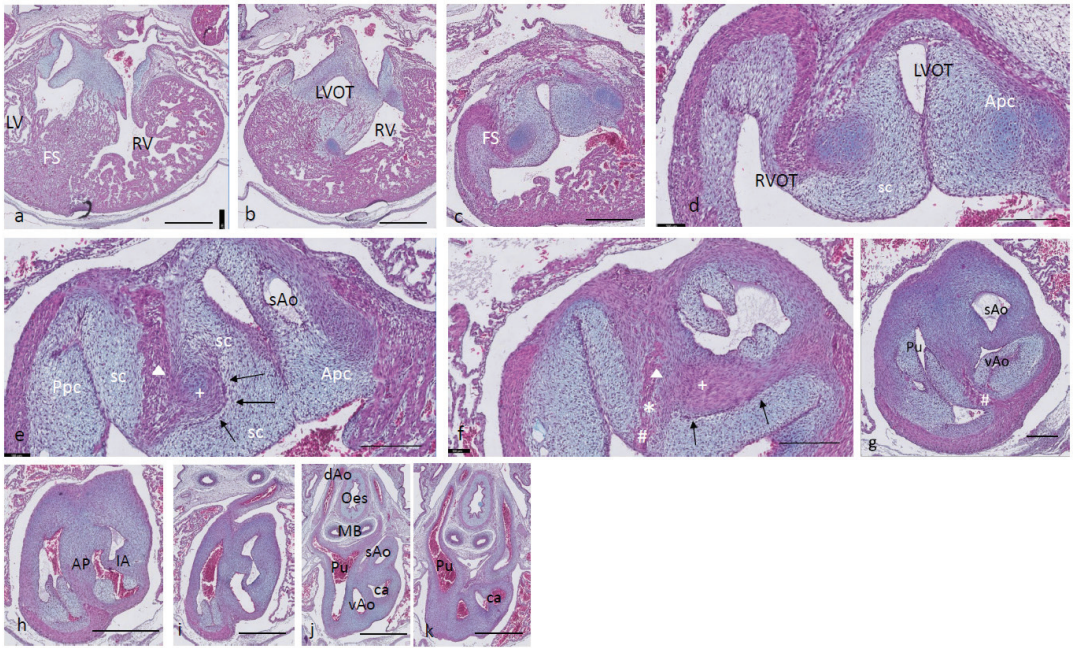

Figure 5. Ferguson stage 22, Figure (**a**–**i**), from AV canals to the arterial tree. Figure (**a**,**b**), septal cushion with cartilage between left and right ventricles. Figure (**c**), cartilage differentiation in both the septal and aortic parietal cushions. Figure (**d**), enlargement of Figure c, the septal cartilage related to the IA septum is located on the left aortic side of the folding septum. Figure (**e**,**f**), the AP (*), (Δ), (#) and the IA (+) septa are completely visible, containing their various elements. The tunnel of the foramen of Panizza is present (black arrows). Figure (**g**–**k**) demonstrate the branching pattern of the arterial tree. Key to the symbols # ventral myocardium, part of AP septum; * (presumably) left-sided neural crest cells, part of AP septum; + (presumably) right-sided neural crest, part of IA septum; Δ dorsal myocardium, part of AP septum. Magnification Figure (**a**–**c**,**h**–**k**), bar 500 μm; (**d**–**g**), 200 μm.

Ferguson stage 24. The folding and inlet septa meet each other at an angle with the septal outflow tract cushion as a hinge (Figure 6a,b). The inlet septum continues between the LVOT and the right ventricle (Figure 6b,c), while the septal and aortic parietal cushions have fused over a short distance (Figure 6d) to reopen again further downstream. A mesenchymal interventricular septum is not apparent yet, in contrast to stage 25. The IA septum is likewise not fully developed, leaving a lumen contact between the sAo and vAo (Figure 6e,f). Both imply that left–right separation has not been established yet. The cartilage prongs are well differentiated both in the septal cushion and aortic parietal cushion, and in the latter, two cartilage elements are present (Figure 6e,f), as in earlier stages. The FOP in the septal cushion is wide open, connecting both the vAo's and sAo's sinus of Valsalva (Figure 6f–i). Further downstream, the septal cartilage partly penetrates the interaortic septum (Figure 6j). In the root of the sAo, the double orifice of the coronary artery is present (orange arrow in Figure 6k,l), splitting immediately in a descendent and a circumflex branch (Figure 6l).

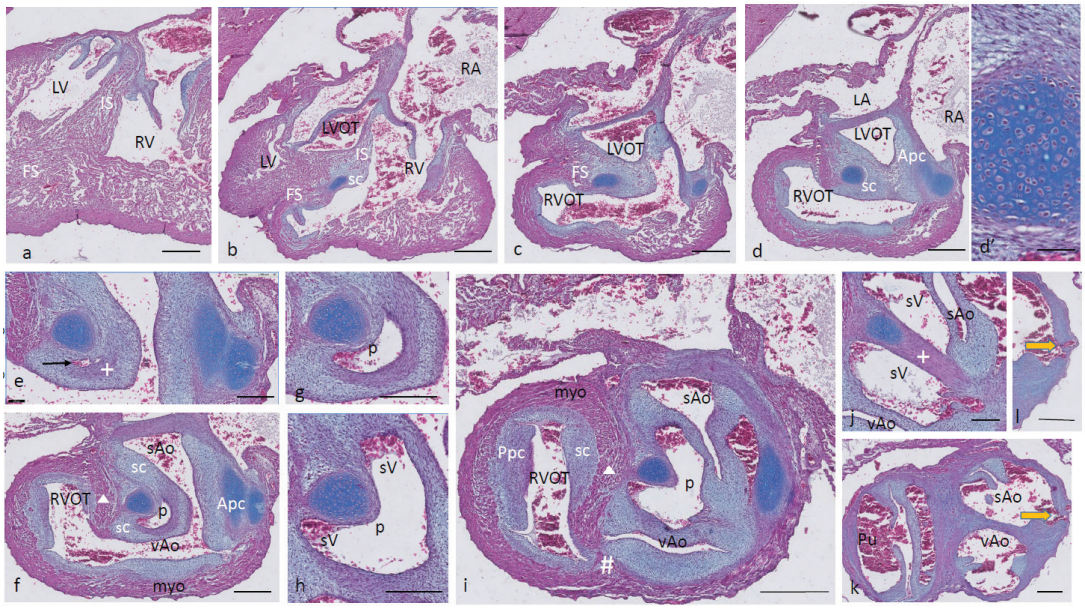

Figure 6. Ferguson stage 24, Figure (**a**–**l**), from AV valves to semilunar valve level. Figure (**a**,**b**), the AV cushions have elongated to form free-edged valve leaflets. Figure (**c**,**d**), folding septum including septal cushion is centrally located between left and right ventricular compartments. Cartilage-rich prongs in both OFT cushions. Note that the parietal cushion now contains two cartilaginous centers. Figure (**d'**) shows a higher magnification of the hypertrophic chondrocytes. Figure (**e**–**h**), the tunnel of the foramen of Panizza (p) is shown rounding the septal cartilage and joining the sinus of Valsalva (sV) of both aortas. Note that the cartilage is surrounded by a fibrous capsule. Figure **i**, the AP septum is completed. Figure (**j**), the IA septum is completed. Figure (**k**,**l**), coronary ostia (yellow arrows) are found in the parietal wall of the systemic aorta, but not the visceral aorta. Key to the symbols **#** ventral myocardium, part of AP septum; (presumably) left-sided neural crest cells, part of AP septum; **+** (presumably) right-sided neural crest, part of IA septum; Δ dorsal myocardium, part of AP septum. Magnification Figure (**a**), bar 1mm; (**b**–**d**,**i**), bar 500 μm; (**e**–**h**,**j**–**l**), bar 200 μm; (**d'**), bar 50 μm.

Ferguson stage 25. The spongious myocardia of the left and right ventricles have increased considerably in mass (Figure 7a,b). The cartilage of the septal outflow tract cushion is embedded deep apically between the left and right ventricles squeezed between the inlet and folding segments (Figure 7a). The presence of the mesenchymal septum (even more visible in the next stage) between the left and right ventricles shows that complete septation has taken place. Even in this stage, the complete separation of the sAo and vAo by the interaortic septum has not been established as there is a narrow lumen contact seen between the LVOT and RVOT (Figure 7b–h) and, as a consequence, also between the (left ventricular) sAo and (right ventricular) vAo. This implies a complete interventricular septation from now on, but for the narrow connection between the sAo and vAo provided by the FOP (black arrows in Figure 7e–g) and the narrow lumen contact between both aortas. Functionally, in this embryo, the FOP is closed as no red blood cells are found trapped in its lumen. The vAo appears very compressed in this particular embryo (Figure 7i).

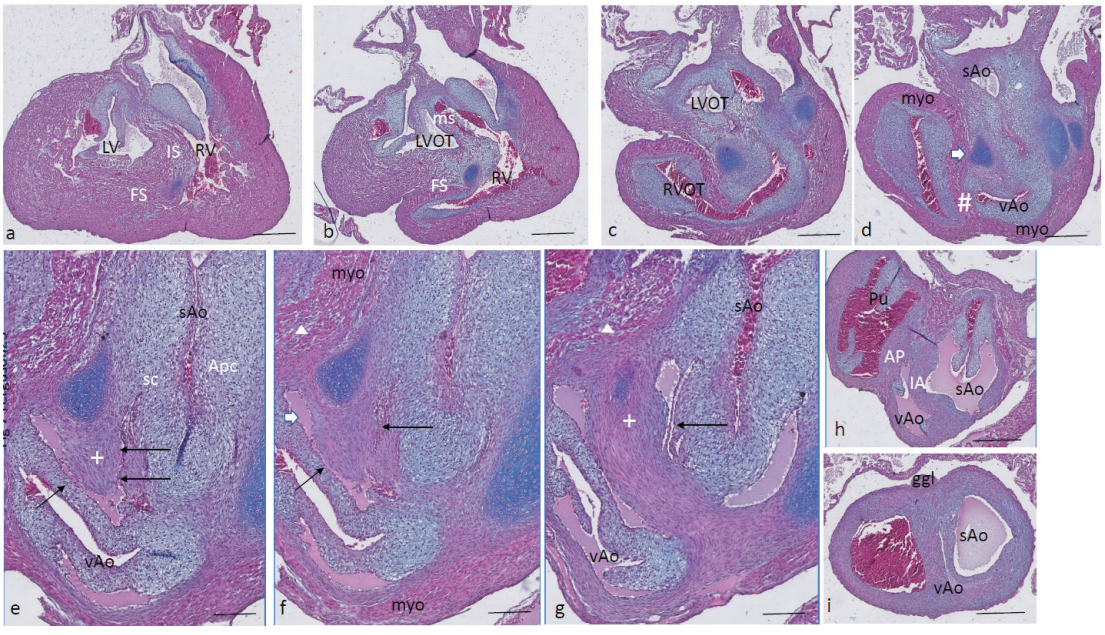

Figure 7. Ferguson stage 25, Figure (**a**–**i**), from AV to semilunar valve leaflets. The myocardium of this specimen is more compact compared to the earlier stages described here. Figure (**a**,**b**), the left and right ventricular compartments are completely septated by the combination of the folding septum, inlet septum and mesenchymal septum. Figure (**c**,**d**), the left and right ventricular outflow tracts and the ensuing arterial trunks are separated by the AP septum and the IA septum. The aortic parietal cushion contains two cartilaginous elements. Figure (**e**,**f**) show the narrow tunnel of the foramen of Panizza (arrows) through the IA septum (+). Figure (**g**), the IA septum at this level is uninterrupted, with the flanking sinus of Valsalva of the visceral and systemic aortas. Figure (**h**,**i**), both AP and IA septa are obvious, and the lumen of the visceral aorta is very narrow in this specimen. Key to the symbols **#** ventral myocardium, part of AP septum; (presumably) left-sided neural crest cells, part of AP septum; **+** (presumably) right-sided neural crest, part of IA septum; **Δ** dorsal myocardium, part of AP septum. Magnification Figure (**a**–**d**,**h**,**i**), bar 500 μm; (**e**–**g**), bar 200 μm.

Beyond Ferguson stage 25 (alligator). In this HE-stained series, the LV and RV are completely septated, and the hallmark of this process is the mesenchymal septum extending over a considerable distance (Figure 8a–d), reaching as far as the IA septum (Figure 8d,e). In the outflow tract, the septal cushion is penetrated by the FOP (black arrow), connecting both septal sinuses of Valsalva of the sAo and the vAo (Figure 8e,f) at the level where the arterial wall is inserted into the myocardium. Slightly more downstream, the IA septum separates the two aortas, whereas the AP septum completely separates the pulmonary trunk from the vAo (Figure 8g,h). Note that Figure 8h is Alcian blue stained to demonstrate the myocardium versus the mesenchymal wall of the arteries.

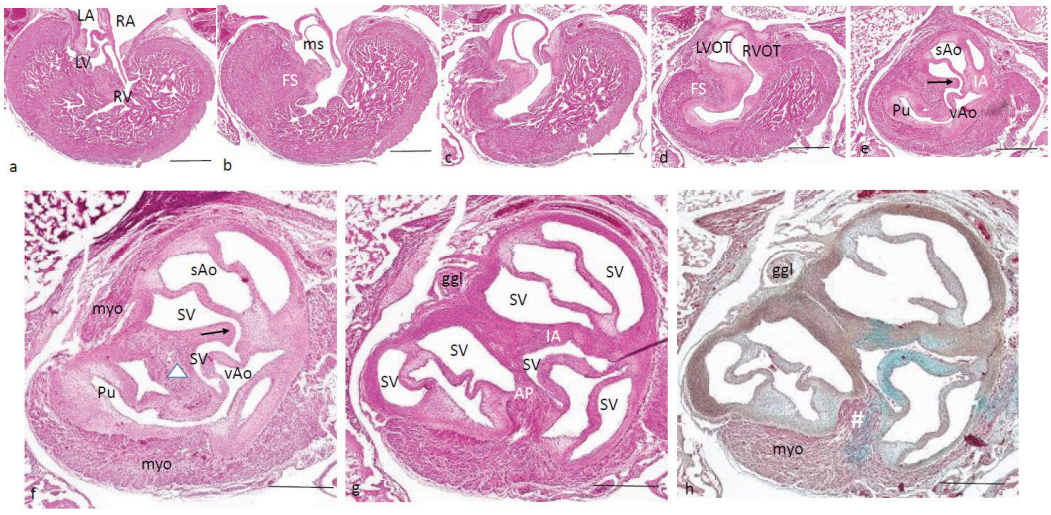

Figure 8. Alligator embryo older > than F stage 25. HE-stained Figure (**h**) is, in addition, Alcian blue stained. Figure (**a**–**h**) from AV valves to semilunar valves. Figure (**a**–**d**), the mesenchymal septum is inserted between the right and left ventricular compartments separating both ventricles. It reaches from the tip of the folding septum near the septal cushion (in Figure (**a**)) towards the IA septum (in Figure (**d**,**e**)). The communication between visceral and systemic aortas is still patent (Figure (**d**)). Figure (**e**,**f**), here, the IA septum is interrupted by the tunnel of the foramen of Panizza (arrow). Figure (**g**,**h**), both the AP septum and the IA septum are complete at this level. Key to the symbols **#** ventral myocardium, part of AP septum; (presumably) left-sided neural crest cells, part of AP septum; **+** (presumably) right-sided neural crest, part of IA septum; **Δ** dorsal myocardium, part of AP septum. Magnification Figure (**a**–**e**), bar 200 μm; (**f**–**h**), bar 500 μm.

2. Material and Methods

The *Caiman latirostris* eggs were donated by René Hedegaard, Krokodille Zoo, Denmark. These were incubated until the desired stage, fixed in formalin at 4 °C overnight, dehydrated through a graded methanol series and stored in 100% methanol at −20 °C. The *Alligator mississipiensis* embryos were obtained through a project by Mark Ferguson, deposited in the Manchester Museum, from the University of Manchester (United Kingdom) and were allowed to be used for scientific purposes. These were fixed and stored in formalin. Additional *Crocodilus niloticus* eggs were obtained from La Ferme au Crocodile, Pierrelatte (France), incubated until the desired stage and treated the same as the caiman embryos above. The total numbers of embryos studied were 8 caiman embryos, 3 crocodile embryos and 10 alligator embryos (Table 1), but in addition, many younger crocodiles were available to us.

Only the caiman material provided a continuous series of stages, while the series of crocodile and alligator material showed gaps, allowing a useful but limited comparison of the species. This holds particularly for the immunostainings for AP2alpha (neural crest) and troponin (myocardium) published before [20].

Staging of the embryos of these species followed the criteria of M. Ferguson [21]. Note that the comparison with chick (Hamburger/Hamilton stage) and mouse (Theiler stage) is very coarse as the differing characteristics are mainly based on unalike external features, such as legs/wings, eye lids, feather buds or whiskers.

The thorax containing the heart and arterial trunks was excised and routinely dehydrated through ethanol. The tissue was embedded standardly in paraffin, sectioned in 7 μm serial sections, collected on objective slides and stained with hematoxylin-eosin and Alcian blue as published [20]. Finally, they were coverslipped using Eukit.

Table 1. Number of embryos and stages used. Fer Ferguson stage (crocodilians), compared with HH Hamburger and Hamilton stage (chicken), and Th Teiler stage (mouse).

Caiman	Crocodile	Alligator	Fer Stage	HH Stage	Th Stage
1	1	5	17	31	21
1	1	1	19	32	22
2		1	20	35	23
2			21/2	36	25
1			24	40	
1	1		25	40+	
		1	26		
		2	27		
			28 hatched	45 hatched	27 born

Stained sections were scanned at 40 × and made electronically available with the Philips IMS system through the Dept of Pathology, LUMC Leiden, maintained by Dr. J Oosting and B. van den Akker.

3. Discussion

3.1. The Endocardial Cushions

More than a century ago, Hochstetter [13] provided a description of crocodilian heart development. He numbered four outflow tract endocardial cushions, Hochstetter's #1 being the septal cushion as described here. Cushion # 2, 3 and 4 appeared as separate cushions in each of the three main arteries, which we took together as the parietal cushion, as early in development, these combine as one cushion. Only during separation does this cushion become divided over the sAo, the vAo and the pulmonary trunk. Furthermore, Hochstetter already discerned the "septum aortico pulmonale" and the "septum aorticum". In his text, Figures 10 and 13, in Crocodilus madasgacariensis (first described in [23] which is probably an eastern divergent from C. niloticus [24]), he describes the separation of both aortas to occur before that of the AP septum. Even in our youngest stage, the AP and IA septa are found in the same embryo, albeit at different levels. Apparently, the exact timing of these events is not strictly orchestrated. This heterochrony may indicate that the different cellular players are relatively independent of each other in the formation of the individual septum components.

3.2. Outflow Tract Separation

We decided that early in development, two OFT cushion complexes could be discerned, the dorsal-most septal cushion and the more ventrally located parietal cushion. The single septal cushion (Sc) hugs the folding septum; the latter might also be called the vertical or muscular septum [13,25] and is positioned between the left and right outflow tracts. The OFT cushions start with endocardial–mesenchymal transition of the lining endocardium but become subsequently invaded by "condensed mesenchyme", as shown in this study and also in birds [26], in human [27] and in turtles [20]. The cellular origin in chicken and mouse is established to derive from the cardiac neural crest, as demonstrated in various marker studies [28,29]. The mesenchyme of the two main semilunar valve leaflets derives likewise from the cardiac neural crest, while the second heart field, important for development of the right side of the heart including the pulmonary trunk [29,30], participates in the development of the third so-called non-facing semilunar valve leaflet, as shown by the expression of Cardiac Troponin T2 [31,32] or NKx2.5 [33]. Furthermore, a part of the septation complex does not derive from the cardiac crest [34]. This is demonstrated in quail–chicken chimeras [26] in which a narrow zone of compact chick mesenchyme remains present in an otherwise quail-dominated septation complex. This narrow strip is

also recognized between the two advancing myocardial components in the conal septum of our caiman AP septum (depicted by * in Figure 1i, Figure 2h, and Figure 3f, etc.).

The neural crest cells migrate into the septal cushion from cranial and dorsal positions [10,33,35–37], meeting the most cranial extension of the folding septum. Sumida [38] investigated the contribution of the left- and right-sided neural crest separately by transplanting a quail crest isotopically and unilaterally into a chicken host. They observed only an ipsilateral NC contribution to the pharyngeal arch arteries and to the OFT endocardial cushions, with limited crossing to the contralateral side of the AP septum. The columns of condensed mesenchyme in the OFT cushions were derived from both sides of the NC in a complementary fashion, whereas the septal cartilage presented only right-sided NC cells. Likewise, left- and right-sided columns of NC cells converging on the OFT septal complex are observed in mouse [10] after immunostaining for AP2α, a marker of neural crest cells that we employed in crocodile and turtle embryos [20], proving that also in reptiles, NC cells migrate into the AP septal complex. These studies demonstrate the existence of separate streams of NC cells, and here, we show that these streams do not mix (red and blue in Figures 1 and 2g–j). The left-sided stream is at the base of the AP septum, and the right-sided stream forms the IA septum.

This process is correlated with the persistence of two aortas in reptiles. In birds, only the right aortic arch artery persists after pharyngeal arch remodeling, whereas in mammals, the left one persists, and the right one is further downstream, incorporated into the subclavian artery. The left stream of condensed mesenchyme stays in close proximity to the folding septum and grows out to form part of the AP septum. The right stream deviates at almost 90 degrees to initiate the IA septum. The septal cushion becomes divided into three entities, each dedicated to one of the three main arterial trunks as a result from ingrowth of the two streams of condensed mesenchyme. Lineage tracing experiments in mouse and chicken have established that in these species, the single AP septal complex derives particularly from the cardiac neural crest. In the next chapter, we argue that the participation of second heart field cells in septation is restricted.

In older stages, the parietal cushions present with two long legs, the aortic (Apc) and pulmonary parietal cushion (Ppc) along the right and the left ventricular OFT. Only upon aortic separation (in Ferguson stage 20 and beyond) does the Apc divide into two bulges dedicated to one of the aortic channels each. It is worth mentioning that the pulmonary parietal cushion is not involved in the separation process, but only in the formation of a semilunar valve leaflet.

3.3. Cartilage in the OFT Cushions

A prominent developmental step in crocodiles starting in the most proximal tip of the condensed mesenchyme is the differentiation into cartilage. This is already noted deep in the ventricle in Ferguson stage 20 and occurs in both the Sc and the Apc. It increases in length and diameter and becomes a dominant feature in the distal OFT. At the base of the Sc close to the folding septum, the differentiation process of cartilage increases dramatically. The non-cartilaginous condensed mesenchyme of the IA inside the Sc protrudes towards the Apc, eventually establishing contact of the Sc with the Apc. The Apc in stage 22 and more pronouncedly differentiated in stage 24 even carries a double center of cartilage. At this point, we need to address the question about the origin of the IA and the cartilage prongs. As described above, a bona fide lineage marker is not available; therefore, we have to rely on circumstantial evidence to discuss the participation of neural crest and second heart field-derived cells. In various chicken [26,28,38] and mouse [10,39] models, the contribution of neural crest cells to the OFT septal complex has been proven unequivocally. In neural crest quail–chicken chimera, cartilage was a product of transplanted quail cells differentiating at the time of hatching [38]. Neural crest cells occupy the inner media of the aorta in an adult Wnt1-Cre mouse model, and these derive from the embryonic complete media. Taken together, we postulate that the IA derives from the cardiac NC. A consequence is that the wall of the systemic aorta, being continuous with the IA, originates

likewise from the NC [30,40]. The origin of the wall of the visceral aorta is not completely deducted by this reasoning. It can be argued that in the side facing the systemic aorta, NC-derived cells are also present as both aortas share the IA septum. The opposite side of the visceral aorta, however, is shared with the pulmonary trunk with the joining AP septum in between. In mice [30,34,41,42], it is known that the root of the pulmonary trunk is of mixed (NCC and SHF) origin. The OFT septal complex in mouse (Peterson 2018) and chicken [26,28,35,43], which we consider here as a fusion product of the crocodilian IA and AP septa, derives mainly from the cardiac NC. At this point, it is important to evaluate, again, the paper of Sumida [37] in which quail–chicken chimeras were made of the right or left half of the neural crest. These authors showed that a right and a left NC stream converged upon the chicken OFT septal complex but remained separate in the condensed mesenchyme. In particular, in our caiman material, two streams of condensed mesenchyme (Figure 2g–j) are present, each addressing only one of the septa involved. Furthermore, the stream in blue entered both the septal and parietal cushions [37] and is, therefore, responsible for cartilage formation in both cushions. In an earlier paper [20], we showed that the aortic and pulmonary flow dividers contain NC and second heart field cells in varying degrees and assumed that the IA septum might originate from the second heart field, and the AP septum from the neural crest. With the currently available material, we propose that the core of both septal components derives from the cardiac neural crest.

Cardiac cartilage is encountered in chicken [37] and in specific groups of mammals such as hamsters [44]. In adult otters [45] and various ungulates such as buffalo [46], white rhinoceros [47] and sheep [48], a "heart bone" is present in the fibrous trigone between left AV canal and aorta. A subgroup of diseased chimpanzees with myocardial fibrosis presented with trabecular bone or hyaline cartilage in the right fibrous trigone [49]. In (sub)adult alligators, a cartilage crown is present, nearly completely encircling the roots of both aortas [50,51], but penetrating not as deep into the ventricle as described by us. In our embryonic crocodiles, alligators and caimans, the cartilage elements have not fused, which was also the case in one juvenile crocodile of approximately 60 cm overall length. Other reptiles [52], terrapin [53,54] and turtle [20] present with cartilage prongs. We hypothesize that the elements, being aorta-bound, most likely develop from the left NC stream. Evidently, the NC condensed mesenchyme and ensuing cartilage are encased by fibroblasts (Figure 6), and the origin of these fibroblasts needs further investigation. To our knowledge, second heart field-derived cells do not have the capacity to differentiate into cartilage and neither do cultured pericardial cells [55]. In addition, fibroblasts or smooth muscle cells are found inside the myocardial OFT tube as an extension of the arterial walls (see Figure 3k, dashed line), the origin of which is also not clarified. We suggested earlier [20] that the aortic and pulmonary flow dividers, in which second heart field-derived cells also play a role [37], might be involved. Without proper markers, however, the participation of NCC and SHF-derived cells (see Figure 1g,h) remains an educated guess even when more or less related species are considered for comparison. With respect to the other potentially involved cell populations such as the second heart field and epicardial/pericardial cells, further research is warranted.

3.4. Bicuspid Semilunar Valves

In mammals and birds, tricuspid semilunar valves are the rule, while in reptiles, bicuspid valves are consistently present. Mammalian bicuspidy is considered a congenital malformation [32] that is often associated with a fragile wall of the ascending aorta later in life [56]. Therefore, we need to find an explanation for the bicuspid valve in our crocodilians associated with a healthy aortic wall. In development, the emerging OFT cushions present as the septal and parietal cushions. During development, these reach from a deep intraventricular position adjacent to the atrioventricular cushions distally towards the arterial pole. At the arterial pole, the septal cushion, harboring the anlage of the IA and the AP septum, becomes divided into three subcushions protruding in each arterial stem, being the pulmonary trunk, the visceral aorta and the systemic aorta. The outgrowing

interaortic septum eventually meets the aortic parietal cushion, separating this cushion into two subcushions. The pulmonary parietal cushion develops singly as it is not continuous anymore with the Apc. Finally, every artery contains two cushions, one derived from the septal cushion and one from the subdivided parietal cushion. Specifically, in the visceral aorta, a small Ap cushion remnant remains after the fusion process that could be compared to an intercalated cushion. However, this does not develop into a semilunar valve leaflet, probably because this remnant will not be filled by second heart field-derived cells as is normally the case in, e.g., mice [10]. We know from chicken and mouse studies that the two main cushions are filled by mesenchymal cells derived both from epithelium–mesenchymal transition from the endocardium, and later arriving neural crest cells. The third leaflet has a second heart field-related etiology, as demonstrated in a mouse NOS3-/-model for bicuspidy [10]. In view of the human fragile aortic wall, it is probably this third/non-coronary valve leaflet's etiology that associates with the differentiation of the outer media of the aortic wall, and that becomes prone to aneurysm formation. The inner media of the wall of the ascending aorta is NC-derived [40,57], whereas the outer media/adventita is SHF-derived [5,34]. We postulate that anomalous SHF differentiation may affect both this semilunar valve leaflet and the integrity of the ascending aorta.

3.5. Foramen of Panizza

Unique to crocodilian hearts is the foramen of Panizza [20,50,51,58]. This is a tunnel inside the septal cushion that penetrates the IA septum, providing a seemingly intracardiac shunt between the right and left circulations. Here, it is assumed that the matrix of the OFT endocardial cushions is produced by cardiomyocytes, similar to the origin of the AV cushions [59,60]. This does not mean that the whole OFT cushion remains within the myocardial border. The proximal part stays intramyocardially, while the distal part extends, without doubt, into the arterial tube at the level of the semilunar valve leaflets. Consequentially, the fully grown location of the FOP, being enclosed in the distal part of the septal cushion, is located outside the heart, connecting the facing sinus of Valsalva between the roots of both aortas. This has implications for the way we envisage semilunar valve development from the "massive" OFT cushion towards the "hollow" valve leaflets containing the sinus of Valsalva [32]. The proximal part of the cushions remains attached to the myocardial border, while the developing leaflets and commissures develop from the distal part of the cushion, which enlarges concomitantly with the expanding arterial wall.

Once the condensed mesenchyme begins to differentiate into cartilage, the surrounding mesenchyme starts to lose its integrity by degradation of the extracellular matrix. This is evident by focal absence of staining in the Alcian blue preparations. In Ferguson stage 20, the first signs of the developing sinus of Valsalva are apparent in the septal cushion followed by the appearance of endocardial strands invading the septal cushion from both aortic sides. We could not establish whether the endothelial strands sprout from the endothelium of the sinus or arise de novo from the mesenchyme of the septal cushion. By stage 21, the endothelial strands have met end to end to form a tunnel in the septal cushion penetrating the advancing IA. In stage 24, the tunnel through the septal cushion in caiman has reached an estimated diameter of about 5%–10% of the systemic aorta. We have to realize that the main intracardiac communication, the oval foramen between the right and the left atrium, is far greater, allowing much more blood shunting from right to left before hatching. With respect to the pre-hatching amounts of blood involved, we assume that the physiological function of the FOP is restricted and may even be negligible. During the adult cardiac cycle, the net flow through the FOP is also very small to non-existent [17] as the left ventricular pressure in the systemic aorta surmounts the pressure in the visceral aorta. The attributed functions of the FOP have been associated with many activities including diving or pH-related postprandial metabolism. The functions [19,61] also require the contraction of specialized muscle nodules (dubbed "cogteeth" or "cogwheels" [62,63]) in the right ventricular outflow to increase the right ventricular blood pressure over a threshold to

allow the mechanism of opening (and closing) of the foramen by the guarding septal valve leaflet in the systemic aorta [64].

Intriguingly, the cartilage prongs discussed above are spatially associated with the FOP and the ostium of the systemic aorta, but less with that of the visceral aorta. It is tempting to propose a mechanical function in maintaining the size of both these conduits when the open FOP allows right ventricular blood into the systemic aorta.

Supplementary Materials: The following are available online at https://www.mdpi.com/article/10.3390/jcdd8100132/s1, Figure S1: showing the relations in crocodilians between the cardiac chambers and the arteries, FP foramen of Panizza located between systemic (right-sided, RAo) aorta, emerging fom the left ventricle, and the vis-ceral (left-sided, LAo) aorta, emerging from the right ventricle (adapted from [9]. Cc carotid arteries, LA left atium, LV left ventricle, PA pulmonary arteries, PV pulmonary veins, RA right atrium, RV right ventricle, SC subclavian arteries, VC cardinal veins. Note the caudal connection between visceral aorta (LAo), providing the gut, and the systemic aorta (RAo).

Author Contributions: Conceptualization R.E.P., A.C.G.-d.G.; methodology C.G., M.A.G.D.B.; validation R.E.P.; Investigation R.E.P., N.G., C.G.; writing R.E.P.; visualization C.G.; Supervision R.E.P., M.K.R.; project administration M.A.G.D.B. All authors have read and agreed to the published version of the manuscript.

Funding: This research received no external funding.

Institutional Review Board Statement: Ethical review and approval were waived for this study as reptile and bird embryos are not considered experimental animals under the law. These embryos are not capable of independent life and their study does not require approval by the Institutional and National Animal Ethics Committees.

Data Availability Statement: All data are included in this manuscript.

Conflicts of Interest: The authors declare no conflict of interest.

Abbreviations

AP: aorto-pulmonary septum; Apc: aortic parietal cushion; AV: atrioventricular cushion; ca: carotid artery; dAo: dorsal aorta; FS: folding septum; ggl ganglion; IA: interaortic septum; IS: inflow septum; LA: left atrium; LV: left ventricle; LVOT: left ventricular outflow tract; MB: main bronchi; ms: membranous septum between LV and RV; myo myocardium; Oes: esophagus; p: foramen of Panizza; Ppc pulmonary parietal cushion; Pu: pulmonary trunk; RA: right atrium; RV: right ventricle; RVOT: right ventricular outflow tract; sAo: systemic aorta; sc: septal cushion; SV: sinus of Valsalva; T: trachea; vAo: visceral aorta; # ventral myocardium, part of AP septum; * (presumably) left-sided neural crest cells, part of AP septum; + (presumably) right-sided neural crest, part of IA septum; Δ dorsal myocardium, part of AP septum.

References

1. Hinton, R.B.; Yutzey, K.E. Heart valve structure and function in development and disease. *Annu. Rev. Physiol.* **2011**, *73*, 29–46. [CrossRef]
2. Grewal, N.; Girdauskas, E.; DeRuiter, M.; Goumans, M.J.; Poelmann, R.E.; Klautz, R.J.M.; Gittenberger-de Groot, A.C. The role of hemodynamics in bicuspid aortopathy: A histopathologic study. *Cardiovasc Pathol.* **2019**, *41*, 29–37. [CrossRef]
3. Michelena, H.I.; Khanna, A.D.; Mahoney, D.; Margaryan, E.; Topilsky, Y.; Suri, R.M.; Eidem, B.; Edwards, W.D.; Sundt, T.M., 3rd; Enriquez-Sarano, M. Incidence of aortic complications in patients with bicuspid aortic valves. *JAMA* **2011**, *306*, 1104–1112. [CrossRef] [PubMed]
4. Martin, P.S.; Kloesel, B.; Norris, R.A.; Lindsay, M.; Milan, D.; Body, S.C. Embryonic Development of the Bicuspid Aortic Valve. *J. Cardiovasc. Dev. Dis.* **2015**, *2*, 248–272. [CrossRef]
5. Laforest, B.; Nemer, M. GATA5 interacts with GATA4 and GATA6 in outflow tract development. *Dev. Biol.* **2011**, *358*, 368–378. [CrossRef] [PubMed]
6. Odelin, G.; Faure, E.; Coulpier, F.; Di Bonito, M.; Bajolle, F.; Studer, M.; Avierinos, J.F.; Charnay, P.; Topilko, P.; Zaffran, S. Krox20 defines a subpopulation of cardiac neural crest cells contributing to arterial valves and bicuspid aortic valve. *Development* **2018**, *145*, dev151944. [CrossRef] [PubMed]

7. Koenig, S.N.; Bosse, K.M.; Nadorlik, H.A.; Lilly, B.; Garg, V. Evidence of Aortopathy in Mice with Haploinsufficiency of Notch1 in Nos3-Null Background. *J. Cardiovasc. Dev. Dis.* **2015**, *2*, 17–30. [CrossRef] [PubMed]
8. Zhao, B.; Etter, L.; Robert, B.; Hinton, D., Jr. Woodrow Benson. BMP and FGF regulatory pathways in semilunar valve precursor cells. *Dev. Dyn.* **2007**, *236*, 971–980. [CrossRef]
9. Midgett, M.; López, C.S.; David, L.; Maloyan, A.; Rugonyi, S. Increased Hemodynamic Load in Early Embryonic Stages Alters Endocardial to Mesenchymal Transition. *Front. Physiol.* **2017**, *8*, 56. [CrossRef]
10. Peterson, J.C.; Chughtai, M.; Wisse, L.J.; Gittenberger-de Groot, A.C.; Feng, Q.; Goumans, M.T.H.; VanMunsteren, J.C.; Jong-bloed, M.R.M.; DeRuiter, M.C. Bicuspid aortic valve formation: Nos3 mutation leads to abnormal lineage patterning of neural crest cells and the second heart field. *Dis. Model Mech.* **2018**, *11*, dmm034637. [CrossRef] [PubMed]
11. Soto-Navarrete, M.T.; López-Unzu, M.Á.; Durán, A.C.; Fernández, B.; Soto-Navarrete, M.T. Embryonic development of bicuspid aortic valves. *Prog. Cardiovasc. Dis.* **2020**, *63*, 407–418. [CrossRef]
12. Poelmann, R.E.; Gittenberger-de Groot, A.C. Hemodynamics in Cardiac Development. *J. Cardiovasc. Dev. Dis.* **2018**, *5*, 54. [CrossRef]
13. Hochstetter, F. Die Entwicklung des Blutgefässsystems. In *Handbuch der Vergleichenden and Experimentellen Entwicklungslehre der Wirbeltiere*; Oscar, H., Ed.; Fischer Jena: Bryn Mawr, PA, USA, 1906; pp. 69–85.
14. Goodrich, E.S. Note on the Reptilian Heart. *J. Anat.* **1919**, *53*, 298–304. [PubMed]
15. Sandrone, S.; Riva, M. Bartolomeo Panizza (1785–1867). *J. Neurol.* **2014**, *261*, 1249–1250. [CrossRef] [PubMed]
16. Poelman, A.C. Note sur le systeme circulatoire des Crocodiliens. *Bull. Acad. Belg.* **1854**, *21*, 67–72.
17. Axelsson, M.; Holm, S.; Nilsson, S. Flow dynamics of the crocodilian heart. *Am. J. Physiol.* **1989**, *256*, R875–R879. [CrossRef]
18. Malvin, G.M.; Hicks, J.W.; Greene, E.R. Central vascular flow patterns in the alligator *Alligator mississipiensis*. *Am. J. Physiol.* **1995**, *269*, R1133–R1139. [CrossRef] [PubMed]
19. Burggren, W.; Filogonio, R.; Wang, T. Cardiovascular shunting in vertebrates: A practical integration of competing hypotheses. *Biol. Rev. Camb. Philos. Soc.* **2020**, *95*, 449–471. [CrossRef] [PubMed]
20. Poelmann, R.E.; Gittenberger-de Groot, A.C.; Biermans, M.W.M.; Dolfing, A.I.; Jagessar, A.; van Hattum, S.; Hoogenboom, A.; Wisse, L.J.; Vicente-Steijn, R.; de Bakker, M.A.G.; et al. Outflow tract sep-tation and the aortic arch system in reptiles: Lessons for understanding the mammalian heart. *Evodevo* **2017**, *8*, 9. [CrossRef]
21. Ferguson, M.W.J. Reproductive biology and embryology of the crocodilians. In *Biology of the Reptilia*; Gans, C., Billett, F., Maderson, P.F.A., Eds.; Wiley: New York, NY, USA, 1985; Volume 14, pp. 69–85.
22. Axelsson, M.; Fritsche, R.; Holmgren, S.; Grove, D.J.; Nilsson, S. Gut blood flow in the estuarine crocodile, Crocodylus porosus. *Acta Physiol. Scand.* **1991**, *142*, 509–516. [CrossRef]
23. Grandidier, A. Description de quelques reptiles nouveaux a Madagascar en 1870. *Ann. Des Sci. Nat. Cinquieme Ser. Zologie Et Paleontol.* **1872**, *15*, 6–11.
24. Hekkala, E.; Shirley, M.H.; Amato, G.; Austin, J.D.; Charter, S.; Thorbjarnarson, J.; Vliet, K.A.; Houck, M.L.; Desalle, R.; Blum, M.J. An ancient icon reveals new mysteries: Mummy DNA resurrects a cryptic species within the Nile crocodile. *Mol. Ecol.* **2011**, *20*, 4199–4215. [CrossRef] [PubMed]
25. Jensen, B.; Christoffels, V.M. Reptiles as a Model System to Study Heart Development. *Cold Spring Harb. Perspect. Biol.* **2020**, *12*, a037226. [CrossRef] [PubMed]
26. Waldo, K.; Miyagawa-Tomita, S.; Kumiski, D.; Kirby, M.L. Cardiac neural crest cells provide new insight into septation of the cardiac outflow tract: Aortic sac to ventricular septal closure. *Dev. Biol.* **1998**, *196*, 129–144. [CrossRef]
27. Bartelings, M.M.; Gittenberger-de Groot, A.C. The outflow tract of the heart–embryologic and morphologic correlations. *Int. J. Cardiol.* **1989**, *22*, 289–300. [CrossRef]
28. Kirby, M.L.; Gale, T.F.; Stewart, D.E. Neural crest cells contribute to normal aorticopulmonary septation. *Science* **1983**, *220*, 1059–1061. [CrossRef] [PubMed]
29. Kodo, K.; Shibata, S.; Miyagawa-Tomita, S.; Ong, S.G.; Takahashi, H.; Kume, T.; Okano, H.; Matsuoka, R.; Yamagishi, H. Regulation of Sema3c and the Interaction between Cardiac Neural Crest and Second Heart Field during Outflow Tract Development. *Sci. Rep.* **2017**, *7*, 6771. [CrossRef] [PubMed]
30. Zhou, Z.; Wang, J.; Guo, C.; Chang, W.; Zhuang, J.; Zhu, P.; Li, X. Temporally Distinct Six2-Positive Second Heart Field Progenitors Regulate Mammalian Heart Development and Disease. *Cell Rep.* **2017**, *18*, 1019–1032. [CrossRef]
31. Mifflin, J.J.; Dupuis, L.E.; Alcala, N.E.; Russell, L.G.; Kern, C.B. Intercalated cushion cells within the cardiac outflow tract are derived from the myocardial troponin T type 2 (Tnnt2) Cre lineage. *Dev. Dyn.* **2018**, *247*, 1005–1017. [CrossRef]
32. Henderson, D.J.; Eley, L.; Chaudhry, B. New Concepts in the Development and Malformation of the Arterial Valves. *Cardiovasc. Dev. Dis.* **2020**, *7*, 38. [CrossRef]
33. Poelmann, R.E.; Mikawa, T.; Gittenberger-de Groot, A.C. Neural crest cells in outflow tract septation of the embry-onic chicken heart: Differentiation and apoptosis. *Dev. Dyn.* **1998**, *212*, 373–384. [CrossRef]
34. Stefanovic, S.; Etchevers, H.C.; Zaffran, S. Outflow Tract Formation-Embryonic Origins of Conotruncal Congenital Heart Disease. *J. Cardiovasc. Dev. Dis.* **2021**, *8*, 42. [CrossRef] [PubMed]
35. Kirby, M.L.; Hutson, M.R. Factors controlling cardiac neural crest cell migration. *Cell Adh. Migr.* **2010**, *4*, 609–621. [CrossRef] [PubMed]

36. Bergwerff, M.; Verberne, M.E.; DeRuiter, M.C.; Poelmann, R.E.; Gittenberger-de Groot, A.C. Neural crest cell contribu-tion to the developing circulatory system: Implications for vascular morphology? *Circ. Res.* **1998**, *82*, 221–231. [CrossRef]
37. Baardman, M.E.; Zwier, M.V.; Wisse, L.J.; Gittenberger-de Groot, A.C.; Kerstjens-Frederikse, W.S.; Hofstra, R.M.; Jurdzinski, A.; Hierck, B.P.; Jongbloed, M.R.; Berger, R.M.; et al. Common arterial trunk and ventricular non-compaction in Lrp2 knockout mice indicate a crucial role of LRP2 in cardiac development. *Dis. Model Mech.* **2016**, *9*, 413–425. [CrossRef] [PubMed]
38. Sumida, H.; Akimoto, N.; Nakamura, H. Distribution of the neural crest cells in the heart of birds: A three dimen-sional analysis. *Anat. Embryol. (Berl.)* **1989**, *180*, 29–35. [CrossRef]
39. Conway, S.J.; Henderson, D.J.; Copp, A.J. Pax3 is required for cardiac neural crest migration in the mouse: Evidence from the splotch (Sp2H) mutant. *Development* **1997**, *124*, 505–514. [CrossRef]
40. Sawada, H.; Rateri, D.L.; Moorleghen, J.J.; Majesky, M.W.; Daugherty, A. Smooth Muscle Cells Derived From Second Heart Field and Cardiac Neural Crest Reside in Spatially Distinct Domains in the Media of the Ascending Aor-ta-Brief Report. *Arter. Thromb. Vasc. Biol.* **2017**, *37*, 1722–1726. [CrossRef]
41. Gittenberger-de Groot, A.C.; Peterson, J.C.; Wisse, L.J.; Roest, A.A.W.; Poelmann, R.E.; Bökenkamp, R.; Elzenga, N.J.; Hazekamp, M.; Bartelings, M.M.; Jongbloed, M.R.M.; et al. Pulmonary ductal coarctation and left pulmonary artery interruption; pathology and role of neural crest and second heart field during development. *PLoS ONE* **2020**, *15*, e0228478. [CrossRef]
42. Bajolle, F.; Zaffran, S.; Meilhac, S.M.; Dandonneau, M.; Chang, T.; Kelly, R.G.; Buckingham, M.E. Myocardium at the base of the aorta and pulmonary trunk is prefigured in the outflow tract of the heart and in subdomains of the second heart field. *Dev. Biol.* **2008**, *313*, 25–34. [CrossRef]
43. Boot, M.J.; Gittenberger-De Groot, A.C.; Van Iperen, L.; Hierck, B.P.; Poelmann, R.E. Spatiotemporally separated cardiac neural crest subpopulations that target the outflow tract septum and pharyngeal arch arteries. *Anat. Rec. A Discov. Mol. Cell Evol. Biol.* **2003**, *275*, 1009–1018. [CrossRef]
44. Durán, A.C.; López, D.; Guerrero, A.; Mendoza, A.; Arqué, J.M.; Sans-Coma, V. Formation of cartilaginous foci in the central fibrous body of the heart in Syrian hamsters (*Mesocricetus auratus*). *J. Anat.* **2004**, *205*, 219–227. [CrossRef] [PubMed]
45. Egerbacher, M.; Weber, H.; Hauer, S. Bones in the heart skeleton of the otter (*Lutra lutra*). *J. Anat.* **2000**, *196*, 485–491. [CrossRef] [PubMed]
46. Daghash, S.M.; Farghali, H.A.M. The cardiac skeleton of the Egyptian Water buffalo (*Bubalus bubalis*). *Int. J. Adv. Res. Biol. Sci.* **2017**, *4*, 1–13. [CrossRef]
47. Erdogan, S.; Lima, M.; Pérez, W. Inner ventricular structures and valves of the heart in white rhinoceros (*Ceratotherium simum*). *Anat. Sci. Int.* **2014**, *89*, 46–52. [CrossRef]
48. Frink, R.J.; Merrick, B. The sheep heart: Coronary and conduction system anatomy with special reference to the presence of an os cordis. *Anat. Rec.* **1974**, *179*, 189–200. [CrossRef] [PubMed]
49. Moittié, S.; Baiker, K.; Strong, V.; Cousins, E.; White, K.; Liptovszky, M.; Redrobe, S.; Alibhai, A.; Sturrock, C.J.; Rutland, C.S. Discovery of os cordis in the cardiac skeleton of chimpanzees (*Pan troglodytes*). *Sci. Rep.* **2020**, *10*, 9417. [CrossRef] [PubMed]
50. Cook, A.C.; Tran, V.H.; Spicer, D.E.; Rob, J.M.H.; Sridharan, S.; Taylor, A.; Anderson, R.H.; Jensen, B. Sequential segmental analysis of the crocodilian heart. *J. Anat.* **2017**, *231*, 484–499. [CrossRef]
51. White, F.N. Circulation in the reptilian heart (*Caiman sclerops*). *Anat. Rec.* **1956**, *125*, 417–431. [CrossRef] [PubMed]
52. Young, B.A. Cartilago cordis in serpents. *Anat. Rec.* **1994**, *240*, 243–247. [CrossRef]
53. López, D.; Durán, A.C.; de Andrés, A.V.; Guerrero, A.; Blasco, M.; Sans-Coma, V. Formation of cartilage in the heart of the Spanish terrapin, Mauremys leprosa (Reptilia, Chelonia). *J. Morphol.* **2003**, *258*, 97–105. [CrossRef]
54. Braz, J.K.; Freitas, M.L.; Magalhães, M.S.; Oliveira, M.F.; Costa, M.S.; Resende, N.S.; Clebis, N.K.; Silva, N.B.; Moura, C.E. His-tology and Immunohistochemistry of the Cardiac Ventricular Structure in the Green Turtle (*Chelonia mydas*). *Anat. Histol. Embryol.* **2016**, *45*, 277–284. [CrossRef]
55. Grebenik, E.A.; Gafarova, E.R.; Istranov, L.P.; Istranova, E.V.; Ma, X.; Xu, J.; Guo, W.; Atala, A.; Timashev, P.S. Mammalian Pericardium-Based Bioprosthetic Materials in Xenotransplantation and Tissue Engineering. *Biotechnol. J.* **2020**, *15*, e1900334. [CrossRef] [PubMed]
56. Grewal, N.; Gittenberger-de Groot, A.C.; Thusen, J.V.; Wisse, L.J.; Bartelings, M.M.; DeRuiter, M.C.; Klautz RJ, M.; Poelmann, R.E. The Development of the Ascending Aortic Wall in Tricuspid and Bicuspid Aortic Valve: A Process from Matu-ration to Degeneration. *J. Clin. Med.* **2020**, *9*, 908. [CrossRef] [PubMed]
57. Peterson, J.C.; Wisse, L.J.; Wirokromo, V.; van Herwaarden, T.; Smits, A.M.; Gittenberger-de Groot, A.C.; Goumans MT, H.; VanMunsteren, J.C.; Jongbloed MR, M.; DeRuiter, M.C. Disturbed nitric oxide signalling gives rise to congenital bicuspid aortic valve and aortopathy. *Dis. Model Mech.* **2020**, *13*, dmm044990. [CrossRef] [PubMed]
58. Panizza, B. Sulla struttura del cuore e sulla circolazione del sangue del Crocodilus lucius. *Biblioteca Italiana* **1833**, *70*, 87–91.
59. Eisenberg, L.M.; Markwald, R.R. Molecular regulation of atrioventricular valvuloseptal morphogenesis. *Circ. Res.* **1995**, *77*, 1–6. [CrossRef]
60. Person, A.D.; Klewer, S.E.; Runyan, R.B. Cell biology of cardiac cushion development. *Int. Rev. Cytol.* **2005**, *243*, 287–335. [CrossRef]
61. Conner, J.L.; Crossley, J.L.; Elsey, R.; Nelson, D.; Wang, T.; Crossley, D.A. Does the left aorta provide proton-rich blood to the gut when crocodilians digest a meal? *J. Exp. Biol.* **2019**, *222*, jeb201079. [CrossRef]
62. Franklin, C.E.; Axelsson, M. An actively controlled heart valve. *Nature* **2000**, *406*, 847–848. [CrossRef]

63. Syme, D.A.; Gamperl, K.; Jones, D.R. Delayed depolarization of the cog-wheel valve and pulmonary-to-systemic shunting in alligators. *J. Exp. Biol.* **2002**, *205*, 1843–1851. [CrossRef] [PubMed]
64. Axelsson, M.; Franklin, C.; Löfman, C.; Nilsson, S.; Grigg, G. Dynamic anatomical study of cardiac shunting in croco-diles using high-resolution angioscopy. *J. Exp. Biol.* **1996**, *199*, 359–365. [CrossRef] [PubMed]

Journal of
Cardiovascular
Development and Disease

MDPI

Article

Deficient Myocardial Organization and Pathological Fibrosis in Fetal Aortic Stenosis—Association of Prenatal Ultrasound with Postmortem Histology

Fleur Zwanenburg [1], Marco C. DeRuiter [2], Lambertus J. Wisse [2], Conny J. van Munsteren [2], Margot M. Bartelings [2], Marie-Jose Goumans [3], Arend D. J. Ten Harkel [4], Monique R. M. Jongbloed [2,5,†] and Monique C. Haak [1,*,†]

[1] Department of Obstetrics and Prenatal Diagnosis, Leiden University Medical Center, Albinusdreef 2, 2333 ZA Leiden, The Netherlands; f.zwanenburg@lumc.nl
[2] Department of Anatomy & Embryology, Leiden University Medical Center, Einthovenweg 20, 2333 ZC Leiden, The Netherlands; M.C.de_Ruiter@lumc.nl (M.C.D.); L.J.Wisse@lumc.nl (L.J.W.); J.C.van_Munsteren@lumc.nl (C.J.v.M.); M.M.Bartelings@lumc.nl (M.M.B.); m.r.m.Jongbloed@lumc.nl (M.R.M.J.)
[3] Department of Cell & Chemical Biology, Leiden University Medical Center, Einthovenweg 20, 2333 ZC Leiden, The Netherlands; M.J.T.H.Goumans@lumc.nl
[4] Department of Pediatric Cardiology, Leiden University Medical Center, Albinusdreef 2, 2333 ZA Leiden, The Netherlands; A.D.J.ten_Harkel@lumc.nl
[5] Department of Cardiology, Leiden University Medical Center, Albinusdreef 2, 2333 ZA Leiden, The Netherlands
* Correspondence: m.c.haak@lumc.nl; Tel.: +31-(0)71-5262896
† These authors contributed equally to this work.

Citation: Zwanenburg, F.; DeRuiter, M.C.; Wisse, L.J.; van Munsteren, C.J.; Bartelings, M.M.; Goumans, M.-J.; Ten Harkel, A.D.J.; Jongbloed, M.R.M.; Haak, M.C. Deficient Myocardial Organization and Pathological Fibrosis in Fetal Aortic Stenosis—Association of Prenatal Ultrasound with Postmortem Histology. *J. Cardiovasc. Dev. Dis.* **2021**, *8*, 121. https://doi.org/10.3390/jcdd8100121

Received: 6 August 2021
Accepted: 23 September 2021
Published: 28 September 2021

Abstract: In fetal aortic stenosis (AS), it remains challenging to predict left ventricular development over the course of pregnancy. Myocardial organization, differentiation and fibrosis could be potential biomarkers relevant for biventricular outcome. We present four cases of fetal AS with varying degrees of severity and associate myocardial deformation on fetal ultrasound with postmortem histopathological characteristics. During routine fetal echocardiography, speckle tracking recordings of the cardiac four-chamber view were performed to assess myocardial strain as parameter for myocardial deformation. After pregnancy termination, postmortem cardiac specimens were examined using immunohistochemical labeling (IHC) of key markers for myocardial organization, differentiation and fibrosis and compared to normal fetal hearts. Two cases with critical AS presented extremely decreased left ventricular (LV) strain on fetal ultrasound. IHC showed overt endocardial fibro-elastosis, which correlated with pathological fibrosis patterns in the myocardium and extremely disturbed cardiomyocyte organization. The LV in severe AS showed mildly reduced myocardial strain and less severe disorganization of the cardiomyocytes. In conclusion, the degree of reduction in myocardial deformation corresponded with high extent to the amount of pathological fibrosis patterns and cardiomyocyte disorganization. Myocardial deformation on fetal ultrasound seems to hold promise as a potential biomarker for left ventricular structural damage in AS.

Keywords: fetal aortic stenosis; prenatal ultrasound; postmortem histology; speckle tracking analysis; endocardial fibro-elastosis

1. Introduction

Fetal aortic stenosis (AS) is a rare congenital heart disease comprising 0.2–0.5 of 1000 live births. It is known for its wide spectrum of clinical severity and difficulty to predict the clinical course in pregnancy and after birth. Even the mildest forms, characterized by only a subtle flow acceleration across the aortic valve at mid-gestation, may develop into a life-threatening critical AS at birth, carrying a high risk of morbidity and mortality [1,2]. Critical AS at mid-gestation causes left ventricular dysfunction due to elevated ventricular pressure, which in turn produces left ventricular dilatation and myocardial

damage. Subsequently, blood flow through the left side of the heart diminishes, ultimately provoking progression to hypoplastic left heart syndrome (HLHS) at birth, a condition with an even worse prognosis [3–6]. Fetal aortic valvuloplasty has been introduced to relief the fetal critical AS in utero in order to prevent progression to HLHS by enhancing recovery of left ventricular function and flow patterns [7–9]. Although promising, a technically successful fetal aortic valvuloplasty still carries a 50% risk of developing into an univentricular heart [10]. Independent of prenatal treatment, it remains difficult to predict the left ventricular development in time. Possible predictors of biventricular outcome have been described previously, but a conclusive diagnostic ultrasound parameter is still lacking [11–13].

Mahtab et al. demonstrated that borderline left ventricles (BLV) with similar macroscopic appearances can show great variety in microscopic ventricular organization and differentiation. In particular, a subset of BLV hearts resembled normal hearts, containing a well-organized cardiomyocyte alignment and proper organized intercalated disks with a normal expression pattern of important myocardial differentiation markers such as cardiac troponin-I, N-cadherin, and Connexin43 (Cx43). In contrast, the remaining BLV hearts presented histologic abnormalities similar to HLHS hearts, showing disturbed cardiomyocyte and intercalated disks organization along with an almost completely absent expression of myocardial differentiation markers. Ventricular organization and differentiation could therefore be a predictor of biventricular outcome [14]. In fetal AS, the degree of prenatal endocardial fibro-elastosis is also related to the possibility of a postnatal biventricular circulation [15].

Normal myocardial organization and differentiation allows a coordinated contraction of the myocardium via effective cell–cell coupling, which is necessary for optimal cardiac function. Endocardial damage, such as endocardial fibro-elastosis, also affects myocardial contraction. A non-invasive tool to assess myocardial wall motion in vivo comprises the novel echocardiographic technique speckle tracking. Speckle tracking quantifies the deformation of the myocardial tissue by following the motion of certain myocardial regions, the so-called speckles, over sequential ultrasound frames [16].

We hypothesized that ultrasonographic myocardial deformation corresponds with the level of myocardial organization, differentiation and fibrosis and is therefore an in vivo marker of ventricular damage in fetal AS. Studies assessing the correlation between prenatal imaging and histology are extremely rare. Here, we present four cases of aortic stenosis diagnosed in utero with varying degrees of severity and compare the myocardial deformation based on prenatal ultrasound to postmortem histopathologic characteristics.

2. Materials and Methods

This study was performed in accordance with the Dutch regulation for the proper use of human tissue for medical research purposes and conducted according to the principles of the Declaration of Helsinki (version 7, October 2013) and Dutch Fetal Tissue Act. The protocol was approved by the local Ethics Committee (NL66978.058.18).

An overview flowchart of the methods is depicted in Figure 1. We included cases with a midgestational diagnosis of fetal AS who presented at our tertiary fetal cardiology service between January 2018 and January 2020. Critical AS cases were defined as eligible for fetal aortic valvuloplasty based on the criteria described by McElhinney et al.: a valvular AS with an antegrade doppler color flow jet across the aortic valve which is smaller than the valve annulus diameter, no/minimal subvalvular LV outflow tract obstruction, decreased LV function with either retrograde/bidirectional flow in the transverse aortic arch at any time during the cardiac cycle or two of the following: monophasic mitral valve (MV) inflow, left-to-right flow across the atrial septum, bidirectional flow in the pulmonary veins [11]. Severe AS was defined as valvular AS with severely increased flow velocity over the aortic valve but with preserved left ventricular function and morphology of LV and thus not eligible for fetal aortic valvuloplasty at that time. To compare speckle tracking analysis

with normal fetuses, we performed speckle tracking recordings in 2 healthy fetuses at midgestational age as well, of which informed consent was provided (NL65087.058.18).

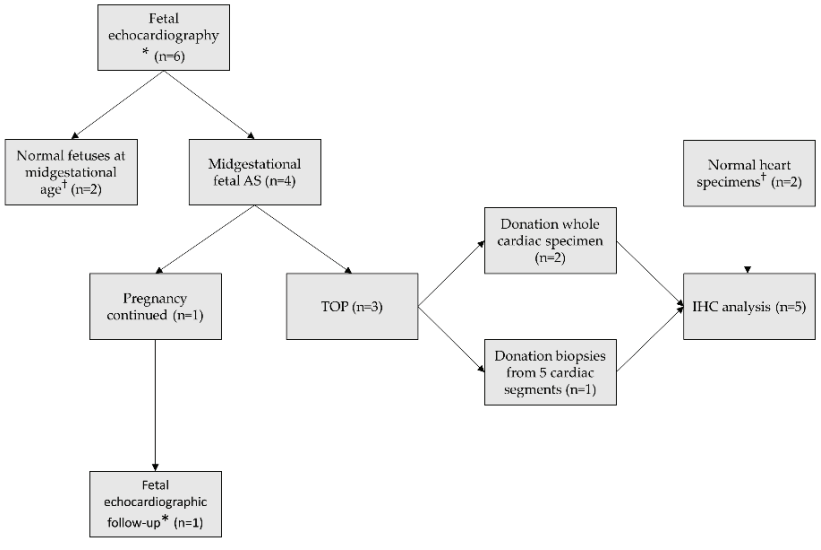

Figure 1. Overview flowchart of methods. * Offline speckle tracking analysis included; † Served as control data; AS, aortic stenosis; TOP, termination of pregnancy; IHC immunohistochemical.

Written informed consent was received from the women to perform speckle tracking recordings during routine fetal echocardiograms. The recordings were analyzed offline, weeks after the initial examination and therefore did not influence clinical decision-making. All women who decided to terminate the pregnancy (n = 3) gave signed written informed consent to donate cardiac tissue for immunohistochemical analysis. Two women donated the entire heart specimen and one woman gave permission to obtain heart biopsies taken from five segments (left ventricular apex, left ventricular base, right ventricular apex, right ventricular base, interventricular septum). The whole cardiac specimens were fixated in formaldehyde followed by storage in ethanol until use and the cardiac biopsies were immediately embedded in paraffin according to standard protocols. Two normal heart specimens (one entire heart specimen and one left ventricle (LV)) of similar gestational age served as immunohistochemical control cases, obtained from legal abortion material.

Echocardiography. All fetal echocardiograms were performed by an experienced ultrasonographer (FZ) using the Canon Aplio i-800 ultrasound machine with abdominal PVI475BX and PVT674 High Frequency convex transducers. For speckle tracking recordings, cine loops of the apical or basal cardiac four chamber-view with an insonation angle of <30° were stored in B-mode setting. We optimized settings by adjusting sector width, depth, gain and zoom box to achieve framerates between 60–120 frames/s. Each clip contained at least 4 cardiac cycles in absence of maternal and fetal movements and was repeated 3 times. A measurement software package (Canon Medical Systems) was used for offline analysis; detailed methods of the analysis have been described previously [17]. In brief, speckle tracking analysis was performed on 3 different cardiac cycles for both the LV and right ventricle (RV), with the time cursor set between complete closure of the atrioventricular (AV)-valves and just before the next AV-valves closure. Endocardial markers were placed along the endocardium in end-diastole, after which the software automatically traced the inner and outer line of the endocardium. Global and segmental longitudinal strain of each ventricle (i.e., longitudinal shortening of entire ventricular wall and longitudinal shortening of separate segments of ventricular wall, expressed as proportion to the baseline

length) were automatically calculated (Figure 2). Mean values of 3 cardiac cycles were used as definitive results.

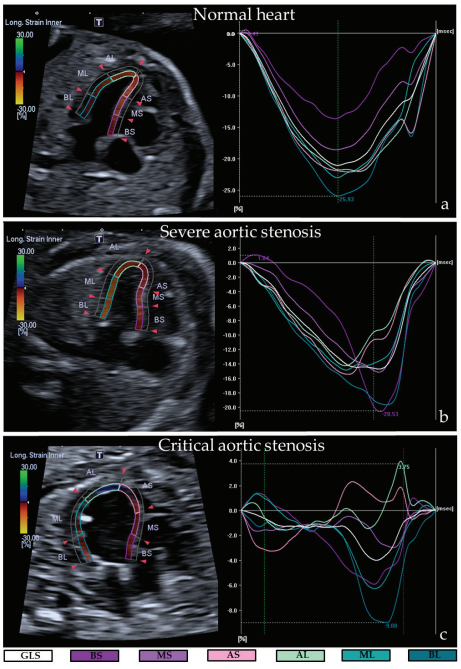

Figure 2. Decreased left ventricular myocardial deformation in cases with fetal aortic stenosis. Representative examples of global longitudinal strain and segmental longitudinal strain analysis for normal hearts (**a**), severe aortic stenosis (**b**) and critical aortic stenosis (**c**), showing the myocardial trace (**left**) and strain curves (**right**). Note that myocardial deformation is most overt in the critical aortic stenosis case. GLS, global longitudinal strain; BS, basal septal; MS, mid septal; AS, apical septal; AL, apical lateral; ML, mid lateral; BL, basal lateral.

Immunohistochemical Analysis. All cardiac specimens were embedded in paraffin according to standardized protocols. Frontal sections of 5 µm from whole hearts and 5 µm sections from the segmental biopsies were mounted on KP-Silane adhesive glass slides (Klinipath). Immunohistochemical and immunofluorescence staining was performed as described previously on the sections comprising the cardiac four chamber view and long-axis view (i.e., left ventricular outflow tract view) [14]. All used antibodies with the notation of their indication, dilution, species, clonality and source are outlined in Table 1. A cardiac troponin-I DAB (3-3′diaminobenzidine tetrahydrochloride) staining was performed to examine myocardial structure and organization. The presence of adherence junctions and gap junctions was assessed by double immunofluorescence staining with N-cadherin and Cx-43 using the suitable secondary antibodies Alexa Fluor 594-conjugated donkey anti-mouse IgG and Alexa Fluor 488-conjugated donkey anti-rabbit IgG. Cardiac fibrosis was identified using a Picro-Sirius Red staining (counterstained with Weigert's Hematoxylin). For assessment of the epicardium, we used single DAB labeling with Wilms' tumor 1 (WT-1), a marker for the epicardium and epicardial epithelial-to-mesenchymal transition (EMT). DAB staining for phosphorylated Smad2 (pSmad2) was used to examine EMT and endothelial-to-mesenchymal transition (EndMT), as both analogous processes are largely induced by the TGF-β/pSmad2 signaling pathway. EndMT was also assessed via immunofluorescence double staining of platelet endothelial cell adhesion molecule-1 (PECAM1) and α-smooth muscle actin (α-SMA) using the suitable secondary antibodies

Alexa Fluor 555-conjugated donkey anti-rabbit IgG and Alexa Fluor 488-conjugated donkey anti-mouse IgG. Lastly, we examined the presence of subepicardial nerves using βIII-tubulin (TUBB3) DAB staining, a general nerve marker. High-resolution microscopy images of all glass slides were taken at 20× or 40× magnification with the 3DHistech Pannoramic 250 Flash III digital scanner or Leica SP8 confocal microscope. To examine the slides systematically, we studied the myocardial staining pattern in 4 predefined segments (LV basal, LV apical, septum and RV) and particularly in areas in which the cardiomyocytes were cut in their longitudinal axis.

Table 1. List of antibodies used for immunohistochemical and immunofluorescence analysis.

Primary Antibodies	Indication	Species	Clonality	Dilution	Source
Cardiac troponin-I	Myocardial structure	Rabbit	Polyclonal	1:1000	Abcam; AB47003
WT-1	Epicardial cells and EEMT	Rabbit	Monoclonal	1:200	Abcam; AB89901
TUBB3	Cardiac innervation	Rabbit	Polyclonal	1:8000	Sigma-Aldrich; T3952
N-cadherin *	Adherence junctions	Mouse	Monoclonal	1:200	Sigma-Aldrich; C3865
Cx43 *	Gap junctions	Rabbit	Polyclonal	1:600	Abcam; AB11370
PECAM1 *	Endothelial cells	Rabbit	Polyclonal	1:1000	Santa Cruz; sc1506R
α-SMA *	Activated cardiac fibroblasts	Mouse	Monoclonal	1:10,000	Sigma-Aldrich; A2547
pSmad2	Activated TGF-β signaling, specific for EndMT or EMT	Rabbit	Monoclonal	1:100	Cell Signaling; 138D4
Secondary Antibodies					
Antirabbit-Biotin		Goat	Polyclonal	1:200	Vector Laboratories; BA1000
Alexa Fluor 594 anti-mouse IgG		Donkey	Polyclonal	1:200	Thermofisher Scientific; A21203
Alexa Fluor 488 anti-rabbit IgG		Donkey	Polyclonal	1:200	Thermofisher Scientific; A21206
Alexa Fluor 488 anti-mouse IgG		Donkey	Polyclonal	1:200	Thermofisher Scientific; A21202
Alexa Fluor 555 anti-rabbit IgG		Donkey	Polyclonal	1:200	Thermofisher Scientific; A31572

* Stained with immunofluorescence. WT-1, Wilms' tumor 1; eEMT, epicardial epithelial-to-mesenchymal transition; Cx-43, Connexin-43; TUBB3, βIII-tubulin; PECAM1, platelet endothelial cell adhesion molecule-1; α-SMA, alpha smooth muscle actin; pSmad2, phosphorylated Smad2.

3. Results

3.1. Case Description

Case 1 was diagnosed with a fetal critical AS at 20 + 3 weeks of gestation that met the international criteria for in utero aortic valvuloplasty (Table 2) [11]. The LV was spherical and presented poor contractility by eyeballing. After counseling, the parents opted for fetal aortic valvuloplasty one week later (21 + 2). The intervention was performed with a 2.7 mm-sized balloon inflated at 14 atmosphere. Immediately after balloon dilatation, aortic regurgitation and an increased amount of forward flow across the aortic valve was visualized. The valvuloplasty was complicated by hemopericardium with bradycardia, which resolved quickly through drainage of the hemopericardium. Three days after the procedure (21 + 5), the flow across the aortic valve had increased and the flow in the transverse aortic arch was antegrade, but the LV wall appeared thicker with no improvement in contractility. At 22 + 5, fetal echocardiography revealed LV shortening with poor contractility, scarce LV inflow and retrograde flow in the transverse aortic arch. The parents decided to terminate the pregnancy to avoid an univentricular trajectory for their child.

Table 2. Ultrasonographic baseline characteristics at first presentation.

	Case 1	Case 2	Case 3	Case 4
GA (wks) first presentation	20 + 3	19 + 5	20 + 1	21 + 1
Diagnosis	Critical AS	Critical AS	Severe AS	Severe AS
Valvuloplasty	Yes, prenatal at 21 + 1 wks	Offered but declined by parents	No	Yes, postnatal
AoV diam (Percentile [1])	2.5 (P0)	2.4 (−1.940/−2.326)	2.5 (P1)	2.9 (P4)
AoV velocity cm/s	210	250	313	301
MV diam (Percentile [2])	4.6 (P4)	4.6 (P7)	4.8 (P10)	5.5 (P24)
TV diam (Percentile [2])	5 (P17)	4.8 (P18)	5.1 (P22)	5.6 (P31)
LV length (Percentile [3])	12.8 (P44)	15.4 (P66)	13 (P47)	15.2 (P53)
RV length (Percentile [3])	11.8 (P49)	12.3 (P57)	11.4 (P48)	14.5 (P62)
LV shape	Spherical	Spherical	Normal	Normal
Aortic arch flow	Retrograde	Retrograde	Forward	Forward
EFE	Moderate	Mild	None	None
MV flow	Monophasic, regurgitation	Minimal forward, monophasic, regurgitation	Biphasic, mild regurgitation	Biphasic, mild regurgitation
FO flow	Left–right	Left–right	Right–left	Right–left
PV flow	Normal	Normal	Normal	Normal
GA of TOP (wks)	23 + 1	21 + 2	21 + 2	N/A

All measurements are performed by in vivo ultrasonography. [1] Calculation percentile using reference values of Vigneswaran et al. [18]. [2] Calculation percentile using reference values of Schneider et al. [19]. [3] Calculation percentile using reference values of Tan et al. [20]. GA, gestational age; LV, left ventricle; RV, right ventricle; MV, mitral valve; TV, tricuspid valve; diam, diameter; AoV, aortic valve; EFE, endocardial fibro-elastosis; FO, foramen ovale; PV, pulmonary veins; TOP, termination of pregnancy; AS, aortic stenosis.

Case 2 presented at our fetal cardiology service at 19 + 5 weeks of gestation, revealing a critical AS with postvalvular dilatation (Table 2). The LV was enlarged and showed poor contractility. Genetic tests, comprising Quantitative Fluorescent Polymerase Chain Reaction (QF-PCR), array and whole exome sequencing (WES) were normal. Fetal aortic valvuloplasty was offered to the parents, yet they decided to withdraw from intrauterine treatment and proceeded to termination the pregnancy.

Case 3 presented with a severe fetal AS showing seriously increased flow velocity (350 cm/s) across the aortic valve at 20 + 1 weeks gestation. The international criteria for in utero aortic valvuloplasty were not met (Table 2) as the flow in the transverse aortic arch was antegrade and the LV appeared normal in shape and function. An amniocentesis was performed and results (QF-PCR and array) were normal. The parents feared progression to HLHS later in pregnancy and therefore, decided to terminate the pregnancy.

Case 4 was referred to our fetal cardiology service with an abnormal three vessel view, based on an enlarged aorta, at 21 + 1 weeks GA. We diagnosed a severe AS with an adequate size of the aortic annulus showing increased forward flow across the valve (300 cm/s) and postvalvular dilatation with turbulent flow (Table 2). As the LV was not dilated and there was normal antegrade flow in the aortic arch and biphasic inflow across the MV, this case was not eligible for fetal aortic valvuloplasty. Amniocentesis showed normal results for QF-PCR, array and WES. Extended echocardiography was performed every 2 weeks. The first signs of deterioration were present at 27 weeks GA as the LV was slightly shorter than the RV, showed less contractility and presented mild EFE. Moreover, monophasic inflow over the MV was present with little mitral insufficiency (MI). Although the criteria for intra-uterine balloon-plasty were met at that time, the annulus of the aortic valve was too big (5 mm) to perform an antenatal procedure. One week later (28 + 1), the flow in the aortic arch appeared to be retrograde in diastole and flow over the foramen ovale was bidirectional. Fortunately, the cardiac function stayed stable thereafter. A boy of 3730 g was born at 38 + 1 weeks GA. On the first day after birth, a percutaneous balloon aortic valvulotomy was performed with a 6 mm balloon. Bilateral pulmonary arterial banding followed at 8 days postpartum as a large ASD caused a substantial left-to-right shunt leading to pulmonary overcirculation. At 16 days postpartum, MV-plasty and closure of the atrial septal defect (ASD) with a fenestrated patch was performed. The LV function

improved thereafter and debanding of the pulmonary arteries could be performed at 1 month postpartum. One year after birth, the child is doing well and develops normally.

3.2. Ultrasonographic Myocardial Deformation

Speckle tracking values of all cases are depicted in Table 3. Normal hearts showed a global longitudinal strain (GLS) and segmental longitudinal strain (SLS) between −15.5% and −22.9% for both LV and RV, which is in accordance with current literature [21]. The two cases with critical AS (case 1 and 2) presented extremely decreased left ventricular GLS and SLS values, indicating an impaired left ventricular myocardial wall deformation: mean left ventricular GLS was −2.0% and −0.9% and all mean left ventricular SLS were between −0.3% and −4.6%. The RVs showed an overall normal GLS (−19.0 and −16.0%) but the septal side, especially basal septal and mid septal, presented decreased SLS (between −4.0% and −15.3%). In contrast, the lateral sided SLS of the RV showed normal to slightly increased strain values in all cases (between −20.0% and −28.7%).

Table 3. Decreased myocardial deformation in aortic stenosis cases.

	Normal Hearts	Case 1	Case 2	Case 3	Case 4
FPS	68	115	65	60	63
Left Ventricle					
GLS	−19.6%	−2.0%	−0.9%	−11.8%	−10.5%
SLS—basal septal	−16.4%	−1.0%	−2.7%	−14.3%	−16.0%
SLS—mid septal	−18.8%	−0.6%	−1.0%	−13.7%	−13.3%
SLS—apical septal	−22.0%	−3.0%	−1.0%	−13.0%	−7.0%
SLS—basal lateral	−20.7%	−1.6%	−1.3%	−8.7%	−5.3%
SLS—mid lateral	−20.2%	−2.6%	−0.3%	−10.7%	−12.3%
SLS—apical lateral	−20.5%	−4.6%	−0.3%	−11.7 %	−11.7%
Right Ventricle					
GLS	−19.2%	−19.0%	−16.0%	−17.6%	−21.2%
SLS—basal septal	−15.5%	−4.0%	−4.0%	−9.7%	−6.0%
SLS—mid septal	−17.2%	−5.7%	−7.0%	−10.7%	−15.0%
SLS—apical septal	−18.5%	−15.3%	−14.7%	−12.7%	−29.3%
SLS—basal lateral	−20.9%	−28.7%	−20.0%	−26.3%	−25.0%
SLS—mid lateral	−22.9%	−26.0%	−24.0%	−26.3%	−23.7%
SLS—apical lateral	−18.9%	−27.3%	−24.3%	−15.3%	−30.0%

FPS, frame rate per second; GLS, global longitudinal strain; SLS, segmental longitudinal strain.

The two cases with severe AS (case 3 and 4) had normal LV appearance by eyeballing, but the left ventricular myocardial wall deformation showed a mild reduction (left ventricular GLS −11.8% and −10.5%, SLS between −5.3% and −16.0%). Right ventricular myocardial deformation was overall normal with a GLS of −17.6% and −21.2%. Again, in all severe AS cases the lateral side of the RVs showed slightly increased SLS values (SLS between −15.3% and 30.0%) and the septal side an overall mild reduction (SLS between −6% and −29.3%).

3.3. Histological Data

3.3.1. Myocardial Organization and Differentiation

In normal hearts, the cardiomyocytes of both the LV and RV were well-aligned and showed a proper banding pattern. Cx43 and N-cadherin were found as a diffuse pattern in the cytoplasm and were also expressed with more intensity at the lateral borders of the cardiomyocytes, illustrating the presence of gap and adherence junctions. Furthermore, some early intercalated disks were present at the longitudinal ends, mostly solely expressing N-cadherin but co-expression of N-cadherin and Cx43 was also found (Figure 3a–d).

In contrast, the LVs of the two cases with critical AS (case 1 and 2, Figure 3e–l) showed markedly disturbed cardiomyocyte organization and an almost completely absent banding

pattern, as was visualized by troponin-I expression. Between the cardiomyocytes, the amount of extracellular matrix was increased as compared to the normal hearts (Figure 3f,j). Regional differences were not found. A less severely disturbed cardiomyocyte structure was observed in the LV of the severe AS case (case 3, Figure 3m–p). Interestingly, all AS cases showed severely reduced expression of Cx-43 and N-cadherin compared to the normal specimens. Their expression was only present as a very diffuse pattern in the cytoplasm with barely any lateralization and formation of intercalated disks, indicating a reduced amount of gap and adherence junctions (Figure 3d,h,l,p). All RVs showed regions with normal cardiomyocyte organization but also areas with mildly disturbed alignment. Expression profiles of Cx-43 and N-cadherin were identical to the LV in all cases.

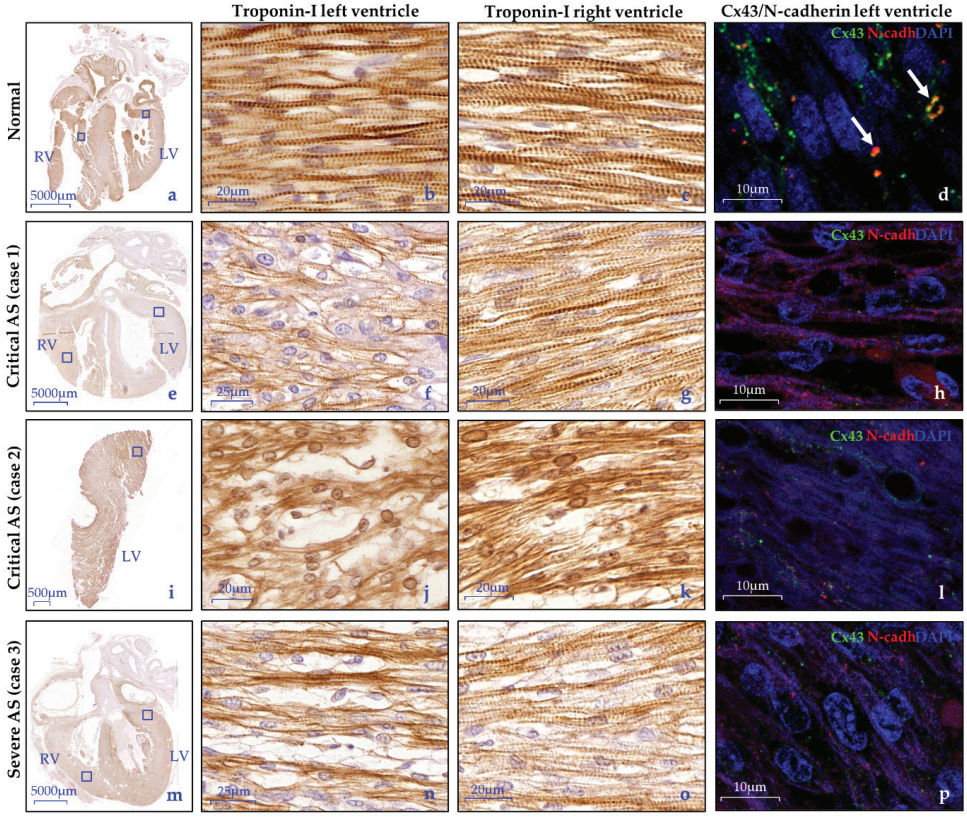

Figure 3. Disturbed alignment and altered Cx43/N-cadherin expression of the cardiomyocytes in fetal aortic stenosis. (**a**–**c**) In normal hearts, troponin-I staining shows an organized cardiomyocyte network with a proper banded pattern in the cardiomyocytes of both the LV and RV. (**d**) Cx43 (green) and N-cadherin (red) is found as a diffuse pattern in the cytoplasm as well as at the lateral borders of the cardiomyocytes, illustrating the presence of gap and adherence junctions. Some early intercalated disks are present, mostly expressing N-cadherin only but co-expression of N-cadherin and Cx43 is also seen in the intercalated disks (white arrows); (**e**–**p**) All AS hearts showed contrary findings; (**f**,**j**,**n**) The cardiomyocyte organization is disturbed in the LV with an increased amount of extracellular matrix, most apparent in case 1 and 2; (**h**,**l**,**p**) Cx43 and N-cadherin expression is markedly decreased and shows only a very scattered pattern in the cytoplasm with barely any lateralization; (**g**,**k**,**o**) The RVs of all specimens show regions with normal cardiomyocyte organization but also with mildly disturbed alignment. Negative controls are depicted in Supplementary Figure S1. Cx43, Connexin-43; *N*-cadh, N-cadherin.

3.3.2. Endocardial and Myocardial Fibrosis Patterns

In normal hearts, Picro-Sirius Red (SR) staining exposed a homogenous pattern of interstitial fibroblasts, without signs of pathological fibrosis (Figure 4a–d). The endocardium consisted of a flat layer of PECAM1 positive endothelial cells (Figure 5a–c), and underneath a subendothelial layer containing collagen (highlighted by SR staining, Figure 4a–c) and α-SMA positive cells, presumably fibroblasts (Figure 5a). In the AS hearts, the degree and patterning of myocardial and endocardial fibrosis patterns were divergent and dependent on the AS severity. The critical AS heart specimens (case 1 and 2) showed a thick compact layer of endocardial fibro-elastosis in the LV which was remarkably associated with patchy pathological fibrosis patterns in the subendocardium and myocardium (Figure 4d,e,g,h). The severe AS specimen (case 3) only presented a thin layer of endocardial fibro-elastosis, with small patchy fibrosis patterns in the subepicardium and myocardium (Figure 4j,k). Right ventricular endocardial and myocardial SR staining was similar to the normal specimens in all AS cases (Figure 4c,f,i,l). EndMT has previously been suggested as underlying mechanism for endocardial fibro-elastosis development [22]. One of the key pathways that induces EndMT is the TGF-β signaling pathway via phosphorylation of Smad2 [23]. Therefore, we also determined the expression pattern of nuclear phosphorylated Smad2 (pSmad2). In normal hearts, the expression of nuclear pSmad2 is limited in the endocardium (Figure 5b,c). In contrast, in both the critical and severe AS cases, a subset of endothelial cells showed intense expression of nuclear pSmad2 and the nucleus of part of the cells in the endocardial fibro-elastosis also stained mildly positive (Figure 5g,h,l,m), indicative of activated TGF-β signaling. During EndMT, endothelial cells lose their expression of endothelial markers, such as PECAM1, and acquire mesenchymal characteristics such as expression of α-SMA [23]. In contrast to normal hearts, the endothelial surface in all our AS cases indeed did not contain PECAM1 positive endothelial cells but only α-SMA positive cells, which supports the occurrence of EndMT resulting in fully transformed endothelial cells (Figure 5f,k).

3.3.3. Epicardium

Strikingly, in contrast to normal hearts, the subepicardium of both LV and RV was significantly thickened in all AS cases, suggesting epicardial activation. The subepicardium contained marked dilated coronary vessels which were surrounded by large TUBB3 positive nerves, while only a few nerve cells were seen in areas without vasculature (Figure 6). Next to EndMT, epicardial EMT has also been proposed as an underlying mechanism for endocardial fibro-elastosis development [24]. Unfortunately, staining of the widely used epicardial EMT and epicardial marker "WT-1" did not work on our material. EMT is largely induced by the TGF-β/pSmad2 pathway, similar to EndMT [25]. In normal hearts, in both LV and RV, nuclear pSmad2 was highly present at the epicardial site (Figure 5b–e). In contrast, the LV of the critical AS cases with the most severe endocardial fibro-elastosis demonstrated limited but more intense expression of nuclear pSmad2 in the subepicardial and myocardial cells, while the RV was similar to the normal heart specimens (Figure 5i–j). The severe AS specimen (case 3) revealed a milder reduction in nuclear pSmad2 expression at the epicardial site (Figure 5n–o).

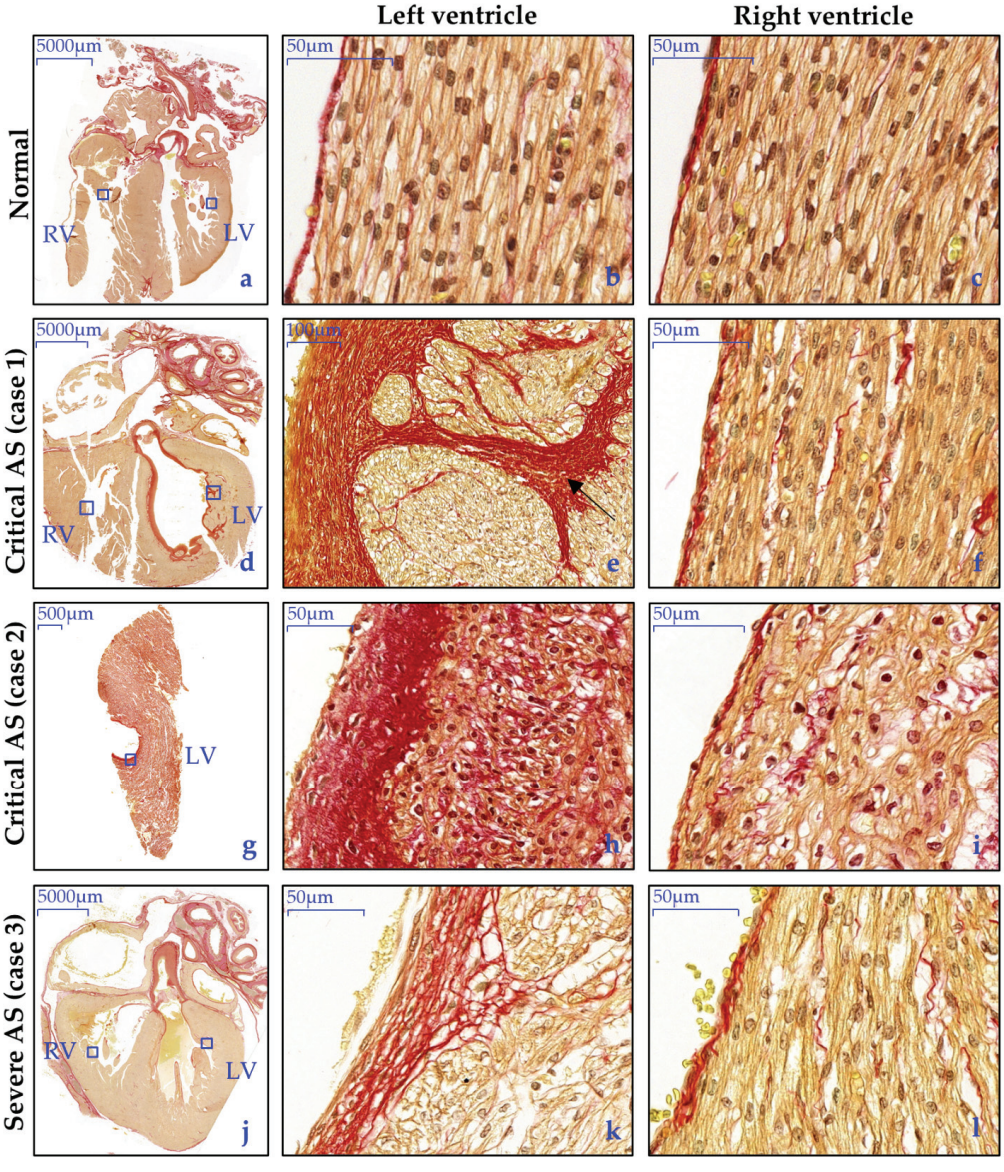

Figure 4. Overt endocardial fibro-elastosis with correlation to patchy fibrosis patterns in the myocardium in fetal AS. (**a**–**c**) In normal hearts, minimal and homogenous collagen deposition (red) is visible in the extracellular space between the cardiomyocytes and a thin layer of collagen is present in the endocardium; (**d**–**i**) the LV of the critical AS cases (case 1 and 2) shows overt EFE which is associated with patchy fibrosis patterns in the subendocardium an myocardium in case 1 (black arrow); (**j**–**l**) the severe AS case shows mild EFE with milder patchy fibrosis patterns in the subendocardium; (**c**,**f**,**i**,**l**) All RVs were similar to the normal LVs.

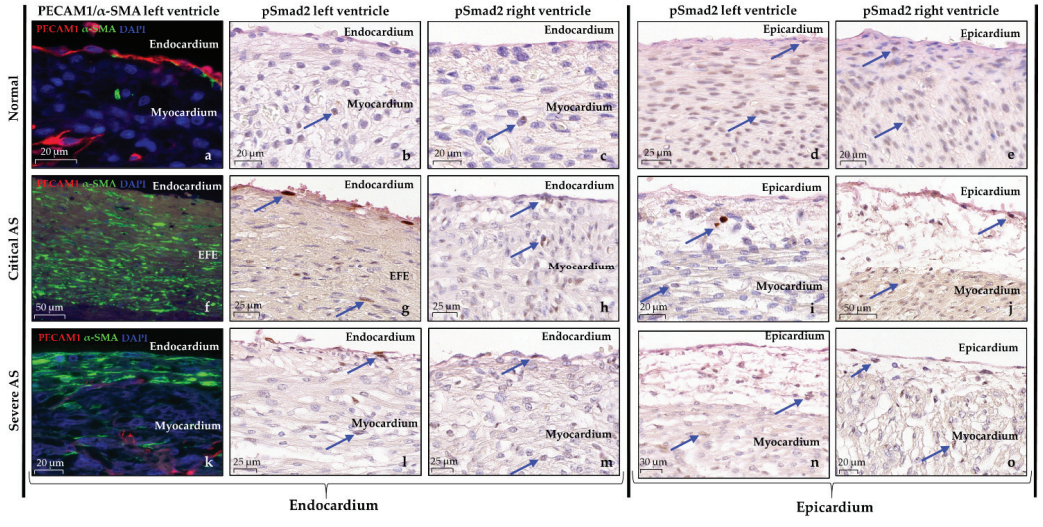

Figure 5. Altered expression markers of EndMT and EMT in cases with aortic stenosis. (**a**) In normal hearts, the endocardium consists of a flat layer of PECAM1 expressing endothelial cells (red) and a thin subendocardial connective tissue layer containing α-SMA positive cells (green). (**b**–**e**) Phospho-Smad2 (pSmad2) expression is rare at the endothelial site but highly present at the epicardial site; (**f**–**o**) Different expression profiles are seen in AS cases; (**f**,**k**) The EFE consists largely of α-SMA positive cells, representing activated fibroblasts. No PECAM1 positive endothelial cells are observed; (**g**,**h**,**l**,**m**) More expression of pSmad2 is found in the endothelial cells and cells in the EFE compared to normal hearts, which is similar between LV and RV; (**i**,**j**,**n**,**o**). At the epicardial site, the epicardium is thickened, rarely showing expression of pSmad2 in the LV of the critical AS cases while the LV of the severe AS specimen reveals a milder reduction in expression; (**j**,**o**) both RVs more closely resemble the normal hearts. PECAM1, platelet endothelial cell adhesion molecule-1; α-SMA, alpha smooth muscle actin; pSmad2, phosphorylated Smad2.

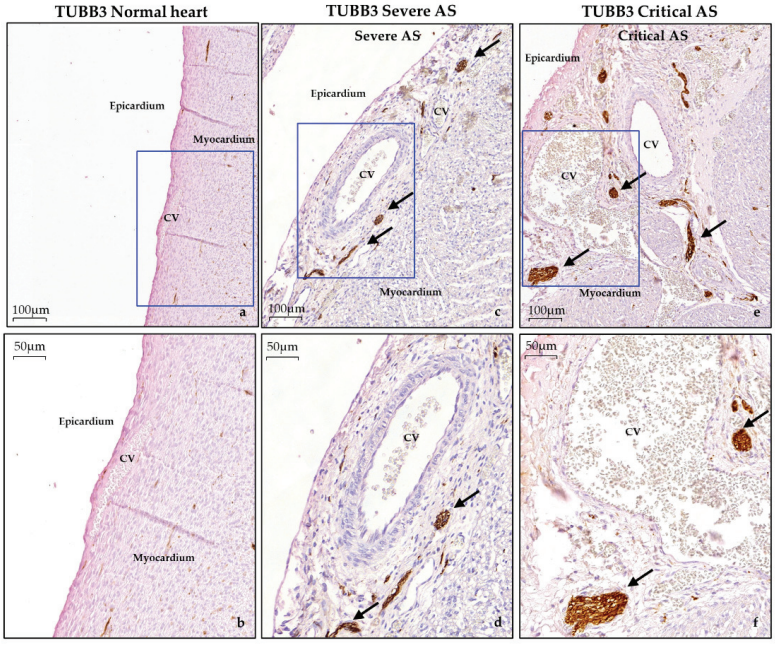

Figure 6. Abnormal epicardial thickening with dilated coronary vessels and large nerves in aortic stenosis cases. Representative images of the epicardium at two magnifications in: (**a**,**b**) normal hearts; (**c**,**d**) severe aortic stenosis; (**e**,**f**) critical aortic stenosis. Note the remarkable thickened epicardium containing dilated coronary vessels and large nerves (brown) in cases with aortic stenosis. TUBB3, βIII-tubulin; CV, coronary vessel.

4. Discussion

Fetal AS remains a challenging CHD considering its difficulty to predict left ventricular development over the course of the pregnancy and with that, the postnatal outcome. Myocardial organization, differentiation and fibrosis could be potential biomarkers, relevant for biventricular outcome [14]. The key finding of the current study is that fetal AS is associated with deficient myocardial organization, differentiation and pathological fibrosis patterns which were strongly associated with the prenatal ultrasonographic assessment of myocardial deformation (Table 4). Cx43 and N-cadherin expression, illustrating the presence of gap and adherence junctions, are altered in fetal AS cases independently of their severity. These results suggest that myocardial wall deformation on fetal ultrasound holds promise as a possible biomarker for myocardial organization and fibrosis and therewith represents the severity of left ventricular damage in cases with fetal AS. The severity of myocardial wall impairment seems unrelated to Cx43 and N-cadherin expression.

Myocardial wall deformation in relation to histopathology. In the current study, fetal AS cases with the most pronounced disturbance of the cardiomyocyte network and endocardial fibrosis patterns showed the utmost impairment of myocardial wall deformation on fetal ultrasound (Table 4). This is not surprising given that both cardiomyocyte disorganization and endocardial fibro-elastosis highly affect myocardial function. Inappropriate myocardial tissue arrangement impedes cardiac impulse propagation as well as coordinated myocardial contraction [26,27]. Likewise, endocardial fibro-elastosis is characterized by an excessive deposition of fibroblasts and accumulation of extracellular matrix, which leads to decreased ventricular diastolic compliance and impaired mechano-electric coupling of cardiomyocytes [24,28,29]. Previous studies in both adult human and animal models support the observed relationship. Adult patients with severe AS and still-preserved ejection

fraction demonstrated a reduced left ventricular GLS which correlated to the severity of myocardial fibrosis [30,31]. Adult mouse models with isolated induced subendocardial fibrotic lesions or transverse aortic constriction showed that the reduction in longitudinal myocardial wall motion corresponded to histological myocardial changes [32,33]. In our study, even the case with mild disturbance of the cardiomyocyte network and endocardial fibrosis presented a corresponding mild reduction in myocardial wall deformation while, remarkably, standard LV function parameters according to the international criteria for fetal AS appeared normal. This emphasizes that speckle tracking echocardiography not only correlates greatly with myocardial histology but is also capable of identifying early structural alterations which are not detected by other ultrasound parameters [34]. The latter is especially of interest as Ishii et al. demonstrated slightly higher strain values before prenatal valvuloplasty in fetal critical AS cases with biventricular outcome compared to cases with univentricular outcome, suggesting a pivot role of speckle tracking analysis in predicting ventricular outcome at an early stage [35].

Table 4. Summary of main ultrasound and histological findings (left ventricle).

Modality	Indication	Normal Hearts	Severe AS	Critical AS
Fetal Echocardiography	Myocardial deformation	Normal strain between −15.5% and −22.9%	Mildly decreased strain between −7.0% and −16.0%	Extremely decreased strain between −0.3% and −4.6%
Histology	Myocardial organization	Well-organized cardiomyocyte alignment	Moderate disturbed cardiomyocyte organization	Severely disturbed cardiomyocyte network
Histology	Myocardial differentiation	Proper Cx43 and N-cadh expression at lateral borders and intercalated disks	Reduced Cx43 and N-cadherin expression, mainly as diffuse intracellular pattern	Reduced Cx43 and N-cadh expression, mainly as diffuse intracellular pattern
Histology	Myocardial fibrosis	No EFE	Mild EFE	Overt EFE with patchy fibrosis patterns in myocardium

Although gap junctions and adherence junctions are important for the myocardial syncytium, the severity of myocardial dysfunction was not related to the degree of Cx43 and N-cadherin expression. In all AS cases, Cx43 and N-cadherin expression was mainly present in a very diffuse pattern in the cytoplasm with mild intensity. Vreeker et al. describes a similar expression profile in normal hearts at an earlier gestational age (approximately 15 weeks in utero), which changes gradually towards complete localization at the lateral borders and intercalated disks during prenatal and postnatal development [36]. One could hypothesize that AS hearts therefore have a delayed spatial development of Cx43 and N-cadherin. Another explanation could be a persisting altered expression, as electromechanical remodeling is known to occur in cases with left ventricular hypertrophy [37]. We demonstrated reduced Cx43 expression in all AS cases compared to normal hearts, which was independent of the severity of AS and left ventricular hypertrophy. This is in accordance with adult AS patients where similar expression levels were found between mild or severe ventricular hypertrophy [37], supporting previous reports that Cx43 is upregulated during the early stage of compensated hypertrophy followed by a downregulation in the chronic phase [38,39]. In contrast, Mahtab et al. only observed a Cx43 downregulation in the borderline left ventricles with extremely disturbed cardiomyocyte organization, while borderline left ventricles with proper cardiomyocyte organization showed normal expression levels [14]. In vitro experiments have shown that depletion of epicardial-derived cells (EPDCs) leads to downregulation of Cx43 and N-cadherin as well as dysregulation of the cardiomyocyte array [40]. An abnormal epicardial–myocardial interaction might be a possible explanation for the observed pathology.

Pathophysiology of endocardial fibro-elastosis in aortic stenosis. Altered hemodynamics in AS trigger the formation of endocardial fibro-elastosis via myocardial hypoxia [41,42]. In the current study we observed a typical endocardial fibro-elastosis appearance associated

with patchy fibrosis patterns in the subendocardium and myocardium which was most overt in the critical AS cases. These "infiltrative" fibrosis patterns have been described previously in postnatal cases with HLHS but also in cases with flow disturbances across the aortic or mitral valve without the phenotype of HLHS and were demonstrated to increase with age [22]. This suggests that the degree of pathological fibrosis increases with longer and more severe exposure to altered ventricular blood flow and/or pressure, explaining the difference in amount of endocardial fibro-elastosis at similar gestational ages between our cases and also the known progressive character of this disease.

The origin of the accumulated fibroblasts in endocardial fibro-elastosis is still debated, where both endocardium-derived cells (EndMT) or epicardial-derived cells (EMT) have been proposed [22,24]. EndMT and EMT are comparable processes during normal cardiac development and comprise a subset of either endothelial or epicardial cells that transform into mesenchymal cells, induced by common biochemical pathways such as TGF-β/pSmad2 [25,43]. After embryonic development, the epicardium of adult patients with myocardial infarction is reactivated and regains fetal characteristics such as EMT [25], whereas EndMT is described in atherosclerosis, valvular disease and cardiac fibrosis [43]. In our study, the overt pathological thickening of the epicardium in all AS cases was suggestive of epicardial activation. Unfortunately, the EMT and epicardial marker "WT-1" did not work on our material to confirm this. Additionally, nuclear pSmad2 expression seems to be less expressed in the epicardium compared to normal hearts, which could indicate that the EMT theory is incorrect, but could also be related to a different time profile since pSmad2 expression is reduced towards the end of EMT/EndMT. Instead, pSmad2 was highly expressed in a subset of endocardial cells and in cells in the endocardial fibro-elastosis areas, although in limited number. Together with the absence of PECAM1 positive endothelial cells and the presence of α-SMA positive cells at the endocardial surface, this strengthens the theory that EndMT causes excessive myofibroblast deposition.

Relation to development of HLHS. Remarkably, the degree of cardiomyocyte disorganization in the critical AS cases was identical to the HLHS specimens described by Mahtab et al. [14], which could imply that these fetal AS cases are deemed to progress towards HLHS. The exact cascade for development from AS into HLHS is still not fully understood, although this is critically important for development of a targeted therapy in order to prevent an univentricular trajectory. Altered flow patterns and pressure overload undoubtedly are key triggers for the development of left ventricular hypoplasia. Endocardial fibro-elastosis also seems to play a crucial role in this process as fetal AS cases with more extensive endocardial fibro-elastosis on fetal ultrasound are more prone to an univentricular outcome [15]. Of note, the current study observed prominent endocardial fibro-elastosis in the critical AS cases with their myocardial histopathology resembling HLHS. The role of the epicardium and endocardium via EMT or EndMT needs to be further explored. An animal model which mimics fetal aortic stenosis would be beneficial to understand the pathway of AS into HLHS better, but no such model exists nowadays as it is hard to simulate, which emphasizes that fetal AS is a multifactorial disease.

Right ventricular involvement in a left ventricular disease. The RV has long been neglected in this typical left-sided heart disease. However, there is growing evidence that typical one-sided CHDs are in fact biventricular diseases [44]. The RV in all our AS cases presented also decreased SLS at the septal side, yet this is presumably attributable to the spherical shaped LV bulging into the RV due to the pressure overload resulting from the AS, as the SLS of the lateral side appeared normal to slightly increased. Of note, the current study showed, in accordance with Mahtab et al., altered Cx43 and N-cadherin expression in the RV of all AS cases which was identical to the LV. Whether this can be related to altered hemodynamics in the RV or to a common pathophysiological pathway remains unclear at this time.

5. Perspectives, Limitations and Conclusions

Although the current study material is unique and provides relevant insights in the pathophysiology of fetal AS, the number of studied specimens is too limited for statistical evidence. However, this case series shows that prenatal myocardial function associates to high extent with myocardial histology as the degree of the reduction in myocardial wall deformation on echocardiography corresponded with the histological amount of pathological fibrosis patterns and disorganization of the cardiomyocyte network. Therefore, fetal echocardiography, in particular GLS, seems to hold promise as a potential biomarker for structural myocardial damage. Current promising sophisticated genetic techniques, such as spatiotemporal single-cell RNA sequencing [45], may provide in-depth knowledge of genetic pathways involved in myocardial development and disease. Unraveling the underlying mechanisms and determinants of disease progression is essential to optimize counseling and to timely intervene to prevent a disease course towards univentricular physiology.

Supplementary Materials: The following are available online at https://www.mdpi.com/article/10.3390/jcdd8100121/s1, Supplementary Figure S1: Representative images of negative controls. (**a**–**d**) Representative images of Troponin-I and Cx43/N-cadherin expression and their negative controls in normal hearts, and (**e**–**h**) in aortic stenosis hearts. Cx-43, Connexin-43; N-cadh, N-cadherin.

Author Contributions: Conceptualization, F.Z., M.R.M.J. and M.C.H.; methodology, F.Z., M.R.M.J. and M.C.H.; validation, F.Z., L.J.W., C.J.v.M. and M.R.M.J.; investigation, F.Z., L.J.W. and C.J.v.M.; resources, M.R.M.J.; data curation, F.Z.; writing—original draft preparation, F.Z.; writing—review and editing, F.Z., M.C.D., M.M.B., M.-J.G., A.D.J.T.H., M.R.M.J. and M.C.H.; visualization, F.Z.; supervision, M.R.M.J. and M.C.H.; project administration, F.Z.; funding acquisition, M.R.M.J. All authors have read and agreed to the published version of the manuscript.

Funding: M.R.M.J. is supported by a personal research grant from NWO ZonMw (projectnr. 91719346). M.d.R. and M.R.M.J. are supported by a grant of the Dutch Bontius Stichting. M.dR. is supported by The Netherlands Heart Foundation (project number 2019B002 OUTREACH).

Informed Consent Statement: Informed consent was obtained from all subjects involved in the study and written informed consent has been obtained from the patient(s) to publish this paper.

Data Availability Statement: Data are available upon reasonable request.

Acknowledgments: We thank Canon Medical Systems, who kindly provided technical support in hard- and software for this study.

Conflicts of Interest: The authors declare no conflict of interest. The funders had no role in the design of the study; in the collection, analyses, or interpretation of data; in the writing of the manuscript or in the decision to publish the results.

References

1. van der Linde, D.; Konings, E.E.; Slager, M.A.; Witsenburg, M.; Helbing, W.A.; Takkenberg, J.J. Birth prevalence of congenital heart disease worldwide: A systematic review and meta-analysis. *J. Am. Coll. Cardiol.* **2011**, *58*, 2241–2247. [CrossRef]
2. Freud, L.R.; Moon-Grady, A.; Escobar-Diaz, M.C.; Gotteiner, N.L.; Young, L.T.; McElhinney, D.B. Low rate of prenatal diagnosis among neonates with critical aortic stenosis: Insight into the natural history in utero. *Ultrasound Obstet. Gynecol.* **2015**, *45*, 326–332. [CrossRef]
3. Hornberger, L.K.; Sanders, S.P.; Rein, A.J.; Spevak, P.J.; Parness, I.A.; Colan, S.D. Left heart obstructive lesions and left ventricular growth in the midtrimester fetus. A longitudinal study. *Circulation* **1995**, *92*, 1531–1538. [CrossRef] [PubMed]
4. Ong, C.W.; Ren, M.; Wiputra, H.; Mojumder, J.; Chan, W.X.; Tulzer, A.; Tulzer, G.; Buist, M.L.; Matter, C.N.Z.; Lee, L.C.; et al. Biomechanics of Human Fetal Hearts with Critical Aortic Stenosis. *Ann. Biomed. Eng.* **2020**, *49*, 1364–1379. [CrossRef] [PubMed]
5. Harh, J.Y.; Paul, M.H.; Gallen, W.J.; Friedberg, D.Z.; Kaplan, S. Experimental production of hypoplastic left heart syndrome in the chick embryo. *Am. J. Cardiol.* **1973**, *31*, 51–56. [CrossRef]
6. Simpson, J.M.; Sharland, G.K. Natural history and outcome of aortic stenosis diagnosed prenatally. *Heart* **1997**, *77*, 205–210. [CrossRef] [PubMed]
7. Maxwell, D.; Allan, L.; Tynan, M.J. Balloon dilatation of the aortic valve in the fetus: A report of two cases. *Br. Heart J.* **1991**, *65*, 256–258. [CrossRef]

8. Tworetzky, W.; Wilkins-Haug, L.; Jennings, R.W.; van der Velde, M.E.; Marshall, A.C.; Marx, G.R.; Colan, S.D.; Benson, C.B.; Lock, J.E.; Perry, S.B. Balloon dilation of severe aortic stenosis in the fetus: Potential for prevention of hypoplastic left heart syndrome: Candidate selection, technique, and results of successful intervention. *Circulation* **2004**, *110*, 2125–2131. [CrossRef]
9. Freud, L.R.; McElhinney, D.B.; Marshall, A.C.; Marx, G.R.; Friedman, K.G.; del Nido, P.J.; Emani, S.M.; Lafranchi, T.; Silva, V.; Wilkens-Haug, L.E.; et al. Fetal aortic valvuloplasty for evolving hypoplastic left heart syndrome: Postnatal outcomes of the first 100 patients. *Circulation* **2014**, *130*, 638–645. [CrossRef]
10. Pickard, S.S.; Wong, J.B.; Bucholz, E.M.; Newburger, J.W.; Tworetzky, W.; Lafranchi, T.; Benson, C.B.; Wilkins-Haug, L.E.; Porras, D.; Callahan, R.; et al. Fetal Aortic Valvuloplasty for Evolving Hypoplastic Left Heart Syndrome: A Decision Analysis. *Circ. Cardiovasc. Qual. Outcomes* **2020**, *13*, e006127. [CrossRef]
11. McElhinney, D.B.; Marshall, A.C.; Wilkins-Haug, L.E.; Brown, D.W.; Benson, C.B.; Silva, V.; Marx, G.R.; Mizrahi-Arnaud, A.; Lock, J.E.; Tworetzky, W. Predictors of technical success and postnatal biventricular outcome after in utero aortic valvuloplasty for aortic stenosis with evolving hypoplastic left heart syndrome. *Circulation* **2009**, *120*, 1482–1490. [CrossRef] [PubMed]
12. Wohlmuth, C.; Wertaschnigg, D.; Wieser, I.; Arzt, W.; Tulzer, G. Tissue Doppler imaging in fetuses with aortic stenosis and evolving hypoplastic left heart syndrome before and after fetal aortic valvuloplasty. *Ultrasound Obstet. Gynecol.* **2016**, *47*, 608–615. [CrossRef] [PubMed]
13. Jantzen, D.W.; Gelehrter, S.K.; Yu, S.; Donohue, J.E.; Fifer, C.G. Echocardiographic factors discriminating biventricular versus univentricular approach in the foetus with borderline left ventricle. *Cardiol. Young* **2015**, *25*, 941–950. [CrossRef] [PubMed]
14. Mahtab, E.A.; Gittenberger-de Groot, A.C.; Vicente-Steijn, R.; Lie-Venema, H.; Rijlaarsdam, M.E.; Hazekamp, M.G.; Bartelings, M.M. Disturbed myocardial connexin 43 and N-cadherin expressions in hypoplastic left heart syndrome and borderline left ventricle. *J. Thorac. Cardiovasc. Surg.* **2012**, *144*, 1315–1322. [CrossRef] [PubMed]
15. McElhinney, D.B.; Vogel, M.; Benson, C.B.; Marshall, A.C.; Wilkins-Haug, L.E.; Silva, V.; Tworetzky, W. Assessment of left ventricular endocardial fibroelastosis in fetuses with aortic stenosis and evolving hypoplastic left heart syndrome. *Am. J. Cardiol.* **2010**, *106*, 1792–1797. [CrossRef] [PubMed]
16. Bijnens, B.; Cikes, M.; Butakoff, C.; Sitges, M.; Crispi, F. Myocardial motion and deformation: What does it tell us and how does it relate to function? *Fetal Diagn. Ther.* **2012**, *32*, 5–16. [CrossRef] [PubMed]
17. Enzensberger, C.; Achterberg, F.; Degenhardt, J.; Wolter, A.; Graupner, O.; Herrmann, J.; Axt-Fliedner, R. Feasibility and Reproducibility of Two-Dimensional Wall Motion Tracking (WMT) in Fetal Echocardiography. *Ultrasound Int. Open.* **2017**, *3*, E26–E33. [CrossRef]
18. Vigneswaran, T.; Akolekar, R.; Syngelaki, A.; Charakida, M.; Allan, L.; Nicolaides, K.; Zidere, V.; Simpson, J.M. Reference Ranges for the Size of the Fetal Cardiac Outflow Tracts From 13 to 36 Weeks Gestation: A Single-Center Study of Over 7000 Cases. *Circ. Cardiovasc. Imaging.* **2018**, *11*, e007575. [CrossRef]
19. Schneider, C.; McCrindle, B.; Carvalho, J.; Hornberger, L.; McCarthy, K.; Daubeney, P. Development of Z-scores for fetal cardiac dimensions from echocardiography. *Ultrasound Obstet. Gynecol.* **2005**, *26*, 599–605. [CrossRef]
20. Tan, J.; Silverman, N.H.; Hoffman, J.I.E.; Villegas, M.; Schmidt, K.G. Cardiac dimensions determined by cross-sectional echocardiography in the normal human fetus from 18 weeks to term. *Am. J. Cardiol.* **1992**, *70*, 1459–1467. [CrossRef]
21. van Oostrum, N.H.M.; de Vet, C.M.; van der Woude, D.A.A.; Kemps, H.M.C.; Oei, S.G.; van Laar, J. Fetal strain and strain rate during pregnancy measured with speckle tracking echocardiography: A systematic review. *Eur. J. Obstet. Gynecol. Reprod. Biol.* **2020**, *250*, 178–187. [CrossRef] [PubMed]
22. Weixler, V.; Marx, G.R.; Hammer, P.E.; Emani, S.M.; Del Nido, P.J.; Friehs, I. Flow disturbances and the development of endocardial fibroelastosis. *J. Thorac. Cardiovasc. Surg.* **2020**, *159*, 637–646. [CrossRef]
23. Yoshimatsu, Y.; Watabe, T. Roles of TGF-beta signals in endothelial-mesenchymal transition during cardiac fibrosis. *Int. J. Inflam.* **2011**, *2011*, 724080. [PubMed]
24. Zhang, H.; Huang, X.; Liu, K.; Tang, J.; He, L.; Pu, W.; Liu, Q.; Li, Y.; Tian, X.; Wang, Y. Fibroblasts in an endocardial fibroelastosis disease model mainly originate from mesenchymal derivatives of epicardium. *Cell Res.* **2017**, *27*, 1157–1177. [CrossRef]
25. Dronkers, E.; Wauters, M.M.M.; Goumans, M.J.; Smits, A.M. Epicardial TGF beta and BMP Signaling in Cardiac Regeneration: What Lesson Can We Learn from the Developing Heart? *Biomolecules* **2020**, *10*, 404. [CrossRef]
26. Pervolaraki, E.; Dachtler, J.; Anderson, R.A.; Holden, A.V. Ventricular myocardium development and the role of connexins in the human fetal heart. *Sci. Rep.* **2017**, *7*, 12272. [CrossRef]
27. Buckberg, G.; Hoffman, J.I.; Mahajan, A.; Saleh, S.; Coghlan, C. Cardiac mechanics revisited: The relationship of cardiac architecture to ventricular function. *Circulation* **2008**, *118*, 2571–2587. [CrossRef]
28. Travers, J.G.; Kamal, F.A.; Robbins, J.; Yutzey, K.E.; Blaxall, B.C. Cardiac Fibrosis: The Fibroblast Awakens. *Circ. Res.* **2016**, *118*, 1021–1040. [CrossRef]
29. Villari, B.; Campbell, S.E.; Hess, O.M.; Mall, G.; Vassalli, G.; Weber, K.T.; Krayenbuehl, H.P. Influence of collagen network on left ventricular systolic and diastolic function in aortic valve disease. *J. Am. Coll. Cardiol.* **1993**, *22*, 1477–1484. [CrossRef]
30. Fabiani, I.; Scatena, C.; Mazzanti, C.M.; Conte, L.; Pugliese, N.R.; Franceschi, S.; Lessi, F.; Menicagli, M.; De Martino, A.; Pratali, S. Micro-RNA-21 (biomarker) and global longitudinal strain (functional marker) in detection of myocardial fibrotic burden in severe aortic valve stenosis: A pilot study. *J. Transl. Med.* **2016**, *14*, 248. [CrossRef]

31. Park, S.J.; Cho, S.W.; Kim, S.M.; Ahn, J.; Carriere, K.; Jeong, D.S.; Lee, S.C.; Park, S.W.; Choe, Y.H.; Park, P.W. Assessment of Myocardial Fibrosis Using Multimodality Imaging in Severe Aortic Stenosis: Comparison with Histologic Fibrosis. *JACC Cardiovasc Imaging.* **2019**, *12*, 109–119. [CrossRef]
32. Beyhoff, N.; Brix, S.; Betz, I.R.; Klopfleisch, R.; Foryst-Ludwig, A.; Krannich, A.; Stawowy, P.; Knebel, F.; Grune, J.; Kintscher, U. Application of Speckle-Tracking Echocardiography in an Experimental Model of Isolated Subendocardial Damage. *J. Am. Soc. Echocardiogr.* **2017**, *30*, 1239–1250.e2. [CrossRef]
33. Peng, Y.; Popovic, Z.B.; Sopko, N.; Drinko, J.; Zhang, Z.; Thomas, J.D.; Penn, M.S. Speckle tracking echocardiography in the assessment of mouse models of cardiac dysfunction. *Am. J. Physiol. Heart Circ. Physiol.* **2009**, *297*, H811–H820. [CrossRef] [PubMed]
34. Day, T.G.; Charakida, M.; Simpson, J.M. Using speckle-tracking echocardiography to assess fetal myocardial deformation: Are we there yet? *Ultrasound Obstet. Gynecol.* **2019**, *54*, 575–581. [CrossRef] [PubMed]
35. Ishii, T.; McElhinney, D.B.; Harrild, D.M.; Marcus, E.N.; Sahn, D.J.; Truong, U.; Tworetzky, W. Ventricular strain in fetuses with aortic stenosis and evolving hypoplastic left heart syndrome before and after prenatal aortic valvuloplasty. *Fetal Diagn. Ther.* **2014**, *35*, 18–26. [CrossRef] [PubMed]
36. Vreeker, A.; van Stuijvenberg, L.; Hund, T.J.; Mohler, P.J.; Nikkels, P.G.; van Veen, T.A. Assembly of the cardiac intercalated disk during pre- and postnatal development of the human heart. *PLoS ONE* **2014**, *9*, e94722.
37. Vetter, C.; Zweifel, M.; Zuppinger, C.; Carrel, T.; Martin, D.; Haefliger, J.A.; Delacrétaz, E. Connexin 43 expression in human hypertrophied heart due to pressure and volume overload. *Physiol. Res.* **2010**, *59*, 35–42. [CrossRef]
38. Formigli, L.; Ibba-Manneschi, L.; Perna, A.M.; Pacini, A.; Polidori, L.; Nediani, C.; Modesti, P.A.; Nosi, D.; Tani, A.; Celli, A.; et al. Altered Cx43 expression during myocardial adaptation to acute and chronic volume overloading. *Histol. Histopathol.* **2003**, *18*, 359–369.
39. Kostin, S.; Dammer, S.; Hein, S.; Klovekorn, W.P.; Bauer, E.P.; Schaper, J. Connexin 43 expression and distribution in compensated and decompensated cardiac hypertrophy in patients with aortic stenosis. *Cardiovasc. Res.* **2004**, *62*, 426–436. [CrossRef]
40. Weeke-Klimp, A.; Bax, N.A.; Bellu, A.R.; Winter, E.M.; Vrolijk, J.; Plantinga, J.; Maas, S.; Brinker, M.; Mahtab, E.A.F.; Gittenberger-de Groot, A.C.; et al. Epicardium-derived cells enhance proliferation, cellular maturation and alignment of cardiomyocytes. *J. Mol. Cell Cardiol.* **2010**, *49*, 606–616. [CrossRef]
41. Pesevski, Z.; Kvasilova, A.; Stopkova, T.; Nanka, O.; Drobna, K.E.; Buffinton, C.; Kockova, R.; Eckhardt, A.; Sedmera, D. Endocardial Fibroelastosis is Secondary to Hemodynamic Alterations in the Chick Embryonic Model of Hypoplastic Left Heart Syndrome. *Dev. Dyn.* **2018**, *247*, 509–520. [CrossRef]
42. Shimada, S.; Robles, C.; Illigens, B.M.; Casar Berazaluce, A.M.; del Nido, P.J.; Friehs, I. Distention of the Immature Left Ventricle Triggers Development of Endocardial Fibroelastosis: An Animal Model of Endocardial Fibroelastosis Introducing Morphopathological Features of Evolving Fetal Hypoplastic Left Heart Syndrome. *Biomed. Res. Int.* **2015**, *2015*, 462469. [CrossRef] [PubMed]
43. Kovacic, J.C.; Dimmeler, S.; Harvey, R.P.; Finkel, T.; Aikawa, E.; Krenning, G.; Baker, A.H. Endothelial to Mesenchymal Transition in Cardiovascular Disease: JACC State-of-the-Art Review. *J. Am. Coll. Cardiol.* **2019**, *73*, 190–209. [CrossRef] [PubMed]
44. Schwarz, K.; Singh, S.; Dawson, D.; Frenneaux, M.P. Right ventricular function in left ventricular disease: Pathophysiology and implications. *Heart Lung Circ.* **2013**, *22*, 507–511. [CrossRef] [PubMed]
45. Mantri, M.; Scuderi, G.J.; Abedini-Nassab, R.; Wang, M.F.Z.; McKellar, D.; Shi, H.; Grodner, B.; Butcher, J.T.; De Vlaminck, I. Spatiotemporal single-cell RNA sequencing of developing chicken hearts identifies interplay between cellular differentiation and morphogenesis. *Nat. Commun.* **2021**, *12*, 1771. [CrossRef] [PubMed]

Journal of
Cardiovascular
Development and Disease

MDPI

Article

Superimposed Tissue Formation in Human Aortic Valve Disease: Differences between Regurgitant and Stenotic Valves

Boudewijn P. T. Kruithof [1,2,*], Aniek L. van Wijngaarden [1], Babak Mousavi Gourabi [3], Jesper Hjortnaes [4], Meindert Palmen [4] and Nina Ajmone Marsan [1]

[1] Department of Cardiology, Leiden University Medical Center, 2333 ZA Leiden, The Netherlands; a.l.van_wijngaarden@lumc.nl (A.L.v.W.); N.Ajmone@lumc.nl (N.A.M.)
[2] Department of Cell and Chemical Biology, Leiden University Medical Center, 2333 ZA Leiden, The Netherlands
[3] Department of Anatomy and Embryology, Leiden University Medical Center, 2333 ZA Leiden, The Netherlands; b.mousavi_gourabi@lumc.nl
[4] Department of Cardiothoracic Surgery, Leiden University Medical Center, 2333 ZA Leiden, The Netherlands; J.Hjortnaes@lumc.nl (J.H.); M.Palmen@lumc.nl (M.P.)
* Correspondence: b.p.t.kruithof@lumc.nl

Abstract: The formation of superimposed tissue (SIT), a layer on top of the original valve leaflet, has been described in patients with mitral regurgitation as a major contributor to valve thickening and possibly as a result of increased mechanical stresses. However, little is known whether SIT formation also occurs in aortic valve disease. We therefore performed histological analyses to assess SIT formation in aortic valve leaflets (n = 31) from patients with aortic stenosis (n = 17) or aortic regurgitation due to aortic dilatation (n = 14). SIT was observed in both stenotic and regurgitant aortic valves, both on the ventricular and aortic sides, but with significant differences in distribution and composition. Regurgitant aortic valves showed more SIT formation in the free edge, leading to a thicker leaflet at that level, while stenotic aortic valves showed relatively more SIT formation on the aortic side of the body part of the leaflet. SIT appeared to be a highly active area, as determined by large populations of myofibroblasts, with varied extracellular matrix composition (higher collagen content in stenotic valves). Further, the identification of the SIT revealed the presence of foldings of the free edge in the diseased aortic valves. Insights into SIT regulation may further help in understanding the pathophysiology of aortic valve disease and potentially lead to the development of new therapeutic treatments.

Keywords: aortic stenosis; aortic regurgitation; superimposed tissue; original leaflet; myofibroblasts; free edge folding

Citation: Kruithof, B.P.T.; van Wijngaarden, A.L.; Mousavi Gourabi, B.; Hjortnaes, J.; Palmen, M.; Ajmone Marsan, N. Superimposed Tissue Formation in Human Aortic Valve Disease: Differences between Regurgitant and Stenotic Valves. *J. Cardiovasc. Dev. Dis.* **2021**, *8*, 79. https://doi.org/10.3390/jcdd8070079

Received: 22 May 2021
Accepted: 5 July 2021
Published: 8 July 2021

1. Introduction

Aortic valve disease is mainly divided into aortic stenosis and aortic regurgitation [1]. Stenotic aortic valves are characterized by increased leaflet stiffness and thickening due to fibrosis and calcifications, and therefore a decreased valve opening in systole with increased transvalvular pressure gradient [2]. Regurgitant aortic valves are characterized by the lack of leaflet coaptation during diastole, secondary to aortic root or ascendens dilatation or by primary leaflet abnormalities such as myxoid degeneration or post-inflammatory fibrosis [1]. These aortic valve diseases have a very different pathophysiology, but in both cases alterations of valve stresses are believed to play an important role in the initiation of leaflet abnormalities, as well as in the propagation of leaflet remodeling [3].

The aortic valve leaflet consists of 3 layers: the fibrosa, spongiosa, and ventricularis, which are rich in collagen, proteo- and glycosaminoglycans, and elastin, respectively [4]. These layers are demarcated by the elastin layer of the ventricularis on the ventricular side and by a thin elastic lamina on the aortic side of the valve. Valvular endothelial cells

and their basement membrane surround these elastic lamina, whereas valvular interstitial cells are interspersed within the aortic valve. The hallmark of a stenotic aortic valve is the presence of calcification, which is thought to start in the fibrosa layer but might expand toward the other leaflet layers [2]. Leaflets of regurgitant aortic valves in turn typically display degeneration of the extracellular matrix, leading to a weakened leaflet [1]. Recently, the formation of superimposed tissue (SIT), an extra layer of tissue on top of the original leaflet, has been described as a major component of valve thickening and remodeling in patients with mitral valve prolapse [5,6]. Using an ex vivo animal model, SIT was suggested to be the result of increased mechanical and hemodynamic stresses [5]. SIT-like lesions, with tissue expansion outside the elastic lamina, also have been described in autoptic studies assessing early stages of aortic stenosis [7,8], but have not been systematically characterized or, more importantly, examined in advanced aortic valve disease.

We therefore hypothesized that SIT formation might frequently occur in aortic valve disease and most probably in both aortic regurgitation and stenosis, being both characterized by changes in mechanical and hemodynamic stresses. By examination of aortic valves resected from patients with significant aortic regurgitation or stenosis, we systematically observed SIT formation on both the aortic and ventricular sides of the leaflet and in both regurgitant and stenotic aortic valves. However, the distribution and composition of the SIT significantly differed between the regurgitant and stenotic valves, likely due to the difference in mechanical stresses between the two pathologies.

2. Materials and Methods

2.1. Human Aortic Valve Samples

Aortic valve samples were collected from patients (n = 20) who underwent aortic valve replacement because of moderate/severe stenosis (n = 12) or moderate/severe regurgitation due to aortic dilatation (n = 8). We selected regurgitant valves caused by aortic dilatation in order to determine specifically the effect of changed hemodynamic flow patterns on the SIT formation. From each patient, one or more aortic valve leaflets were included for analysis, resulting in a total of 17 leaflets from stenotic valves and 14 leaflets from regurgitant valves. The samples were fixed overnight in a 4% paraformaldehyde solution in phosphate buffered saline (PFA/PBS, pH 7.2). Collection and analysis of the samples were performed according to the guidelines of the Leiden University Medical Centre (Leiden, The Netherlands) and according to the Dutch regulations on the use of human tissues (rest material). Furthermore, the study was conducted according to the principles of the Declaration of Helsinki (64th WMA General Assembly, Fortaleza, Brazil, October 2013) and national and institutional guidelines, regulations, and acts.

2.2. Histological Analysis

Human valve tissue was processed as previously described [5]. Briefly, the valve samples were dehydrated through a graded series of ethanol, cleared in xylene, embedded in paraffin, and sectioned at 6 µm, producing longitudinal sections oriented from the leaflet base to the free edge. Sections were stained according to the manufacturer's protocol with Weigert's Resorcin Fuchsin (EMS, Hatfield, PA, USA) to identify elastic fibers, and counterstained with nuclear-fast red (Sigma, Zwijndrecht, The Netherlands). Sections were stained using Masson's Trichrome (Masson's trichrome kit, Klinipath, Duiven, the Netherlands) to visualize collagen fibers, and Alcian blue (Klinipath) to visualize glycosaminoglycans. For immunofluorescent staining, the slices were deparaffinized, hydrated, and boiled 35 min in antigen retrieval buffer (10 mM Tris (pH9)/1mM EDTA/0.05% Tween-20) using a pressure cooker. After blocking with 1% BSA in 0.1% Tween-PBS, sections were incubated overnight with primary antibodies against alpha-smooth muscle actin (αSMA; 1:10,000, A2547, Sigma), platelet endothelial cell adhesion molecule (PECAM-1; 1:1000, AF3628, R&D, Abingdon, UK), laminin (1:200; Z0097, Dako, Santa Clara, CA, USA), collagen IV (1:100; 1340-01, SouthernBiotech, Birmingham, AL, USA), or Ki67 (1:100, AB9260, Millipore, Amsterdam, the Netherlands), followed by incubation with an alexa-conjugated secondary

antibody (Thermo Fisher, Bleiswijk, the Netherlands). Slides were mounted using DAPI containing Prolong Gold Antifade reagent (Thermo Fisher). All slides were scanned with the Pannoramic 250 slide scanner (version 1.23, 3DHISTECH Ltd., Budapest, Hungary) and analyzed using Caseviewer (version 2.4, 3DHISTECH Ltd.).

2.3. Measurements

Measurements of original leaflet and SIT thickness were performed on sections stained for elastin at the midline or in between the midline and the commissure of the aortic valve leaflet (see indications in Figure 1A) using Caseviewer software. The surfaces of the original leaflet, of the SIT on the ventricular side of the aortic valve (ventricular SIT, vSIT) and of the SIT on the aortic side of the aortic valve (aortic SIT, aSIT), were measured at the level of the leaflet body and of the free edge, and divided by the length of the leaflet (either whole leaflet or original leaflet) to obtain the respective average thickness (Figure 1A). ImageJ software was used to determine the intensity of Masson's trichrome and Alcian blue staining and the αSMA-positive area. For each parameter, only the valve samples that allowed measurement of the complete indicated area(s) were included.

2.4. Statistical Analysis

GraphPad Prism 9 was used for statistical analysis. Data were tested for significance as indicated in each legend using analysis of variance (ANOVA) with Šidák's correction or Kruskal-Wallis with Dunn's correction for multiple groups and unpaired *t*-test or the Wilcoxon matched-pairs signed rank test for comparison of 2 groups, and correlations were determined using the Pearson's r-correlation test. Data are reported as means ± SEM. A *p*-value below 0.05 was considered significant.

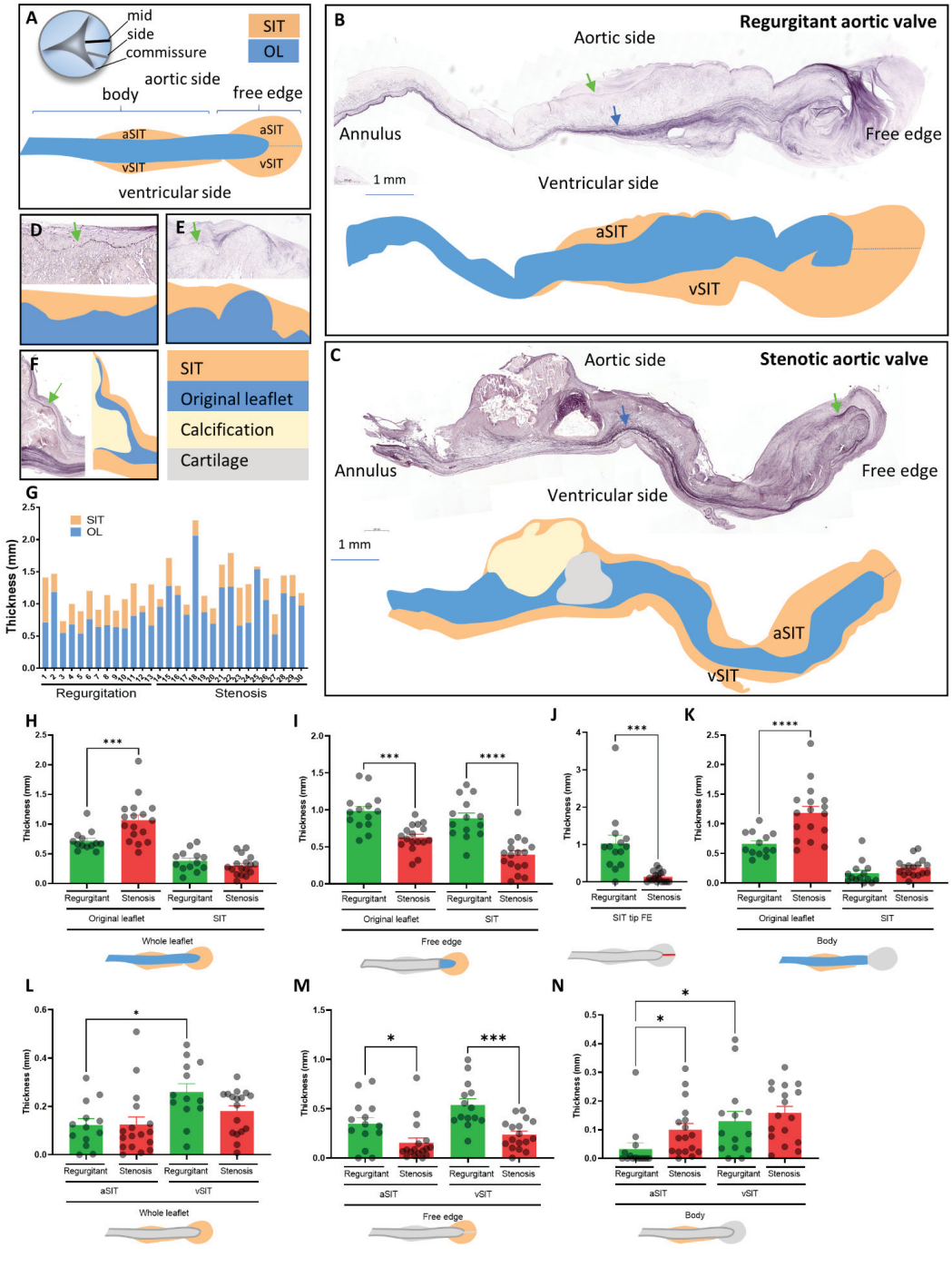

Figure 1. *Cont.*

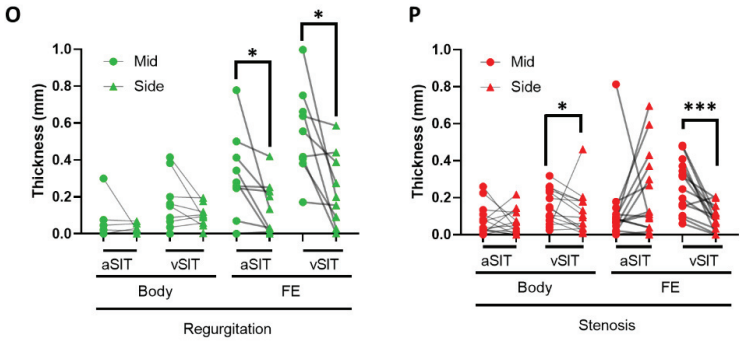

(**O**,**P**)

Figure 1. SIT distribution in regurgitant and stenotic valves. (**A**) schematic drawings indicating the defined regions of the aortic valve. (**B**–**F**) Elastin stainings indicating the borders between the original leaflet (OL) and the SIT on the ventricular (blue arrow) and aortic side (green arrow) of the aortic leaflet, and rendering of the same leaflet with blue representing the original leaflet, orange representing the SIT, yellow representing the calcific region, and gray representing the cartilaginous region. (**G**) Graph indicating the contributions of the SIT and OL to the average thickness of each leaflet. (**H**–**N**) Graphs indicating the average thicknesses of the indicated regions in the regurgitant and stenotic leaflets. (**O**,**P**) Graphs depicting the comparisons of the average thicknesses of the SIT at the midline of the aortic valve (mid) with the region closer to commissure (side) at the indicated parts of the regurgitant (**O**) and stenotic valve (**P**). Data are presented as means ± SEM. One-way ANOVA followed by Šidák's multiple comparisons test was performed for graphs (**H**,**I**,**K**–**M**), an unpaired *t*-test was performed for graph (**J**), and a Kruskal-Wallis test followed by Dunn's multiple comparisons test was performed for graph N. The Wilcoxon matched-pairs signed rank test was performed for graphs (**O**,**P**) to evaluate significant differences. * $p < 0.05$, *** $p < 0.001$, **** $p < 0.0001$. Scale bar is 1000 μm.

3. Results

3.1. SIT Distribution in Regurgitant and Stenotic Aortic Valves

To determine whether SIT contributes to the thickness of the aortic leaflet, sections from the midline of the aortic leaflet (Figure 1A) were stained for elastin to allow the visualization of the borders of the original leaflet. A thick elastin layer outlined the ventricularis of the valve (blue arrow in Figure 1B,C), which defined the border of the original leaflet at the ventricular side. The border of the original leaflet at the aortic side of the valve was in turn defined by a relatively thin elastin layer (green arrow in Figure 1B–F). In both regurgitant and stenotic aortic valves, SIT was observed on the ventricular side (vSIT) and on the aortic side (aSIT; Figure 1A–C) of the leaflet and was found to contribute up to 50% of the total average thickness of the aortic leaflet (Figure 1G). SIT distribution was variable, from rather focal (Figure 1B) to diffuse throughout the entire leaflet, and from proximal (near attachment to the annulus) to distal (free edge; Figure 1C). Additionally, SIT appeared to smoothen the irregular surface of the original leaflet (Figure 1D,E) and in stenotic valves was found to cover large parts of the calcified regions (Figure 1C,F).

Although the average thickness of the original leaflet was significantly larger in stenotic valves (Figure 1H), the average SIT thickness did not differ between regurgitant and stenotic valves (Figure 1H). However, when dividing the leaflet in a body and free edge part (Figure 1A), regurgitant valves showed a significantly thicker free edge compared to stenotic valves due partly to a thicker original leaflet, but mostly to a thicker SIT (Figure 1I). In particular, the SIT in the tip of the free edge (stippled line in Figure 1A–C) was more than 7 times thicker in regurgitant valves compared to stenotic valves (average 1.07 mm, SEM: ±0.23 for regurgitant valves, average 0.14 mm, SEM: ±0.03 for stenotic valves; Figure 1J). In turn, stenotic valves showed a thicker body part due to a thicker original leaflet but not to a thicker SIT (Figure 1K). Although the overall thickness of the aSIT and the vSIT did

not differ between regurgitant and stenotic valves (Figure 1L), the vSIT and aSIT at the level of the free edge was thicker in regurgitant valves (Figure 1M), whereas the aSIT was thicker in stenotic valves at the level of the leaflet body (Figure 1N).

The extent and types of mechanical stresses that the aortic valve experiences might be different in the regions more distant from the midline of the aortic valve [3,9,10]. To determine whether this has consequences for the extent of SIT formation, the thicknesses of the SIT at the midline of the valve (mid) were compared to the thicknesses closer to the commissure of the valve (side; Figure 1A) within each regurgitant and stenotic valve. The aSIT and vSIT at the free edges of regurgitant valves were found to be thinner closer to the commissure (Figure 1O). The vSIT of the body part and free edge part of stenotic valves was also thinner in the regions closer to the commissure (Figure 1P). Interestingly, the aSIT of the free edge appeared to be thicker closer to the commissure in the stenotic valves (Figure 1P).

The contribution of SIT to the thickness of aortic valves therefore greatly varies depending on the pathology and the specific location on the leaflet (aortic vs. ventricular; body vs free edge; midline vs. side).

3.2. Extracellular Matrix Composition of the SIT in Regurgitant and Stenotic Aortic Valves

To determine the extracellular matrix composition of SIT, stainings for elastin fibers, collagen fibers (Masson's trichrome), and glycosaminoglycans (Alcian blue) were performed (Figure 2). SIT was found to have a wide range of extracellular matrix component expression, with regions characterized by high levels of glycosaminoglycans (Figure 2(E1,E2)) or collagens (Figure 2(C2,F1,F2)) and thick layers of fragmented elastin (Figure 2(A2,D3)), and other regions in turn characterized by relatively low levels of glycosaminoglycans (Figure 2(B1,B2,E3)) or collagens (Figure 2(C1,F2,F3)) and lower amounts of elastin (Figure 2(A1)). However, on average, the collagen content in SIT was comparable to the collagen content in the original leaflet (Figure 2G), but was higher in stenotic valves as compared to regurgitant valves (Figure 2G). In turn, no significant difference in glycosaminoglycan intensity was found between stenotic and regurgitant valves (Figure 2H).

3.3. Presence and Distribution of Myofibroblasts in Regurgitant and Stenotic Aortic Valves

Diseased aortic valves are known to be characterized by an increased presence of activated valvular interstitial cells [11,12], i.e., myofibroblasts characterized by the expression of αSMA. To determine their distribution within the SIT and the original leaflet in regurgitant and stenotic valves, αSMA staining was performed and the αSMA-positive area was measured. Myofibroblasts were predominantly observed in the SIT as compared to the original leaflet in both regurgitant and stenotic aortic valves (Figure 3A–C). However, the distribution of myofibroblasts within the SIT differed between regurgitant and stenotic valves. Whereas the SIT of the body part of stenotic valves had a larger αSMA-positive area as compared to regurgitant valves (Figure 3D), the SIT at the free edge of regurgitant valves had a larger αSMA-positive area as compared to stenotic valves (Figure 3E). To determine whether the myofibroblasts in SIT proliferate [13–15], Ki67 staining was performed (Figure 3F). Single Ki67-positive myofibroblasts were observed throughout the SIT, whereas groups of Ki67-positive myofibroblasts were observed in the free edge of regurgitant valves (3 out of 4), indicating an ongoing active expansion of the SIT (yellow arrows in Figure 3(F2)).

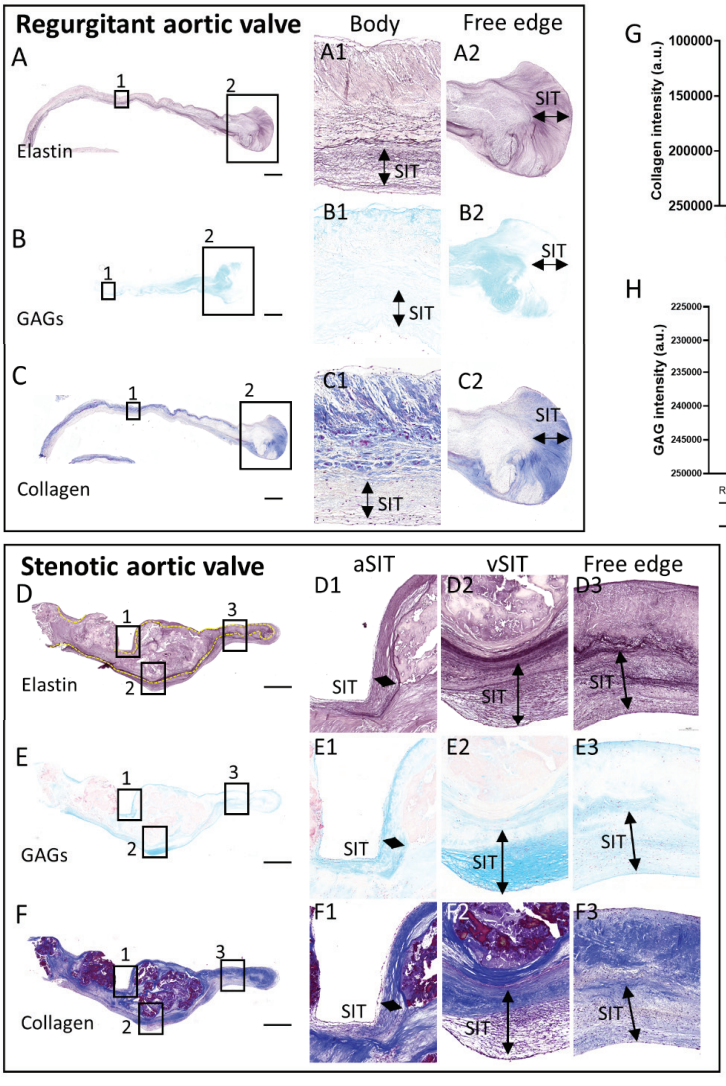

Figure 2. Extracellular matrix composition of SIT in regurgitant and stenotic valves. Stainings for elastin (**A**,**D**), glycosaminoglycans (GAGs; (**B**,**E**), and collagen (**C**,**F**) on regurgitant (**A**–**C**) and stenotic aortic leaflets (**D**–**F**). (**G**,**H**) Graphs of the collagen (**G**) and GAGs (**H**) staining intensities in the original leaflet and SIT of regurgitant and stenotic aortic leaflets. Data are presented as means ± SEM. One-way ANOVA followed by Šidák's multiple comparisons test was performed to evaluate significant differences for graphs G and H. **** $p < 0.0001$. Scale bar is 1000 µm.

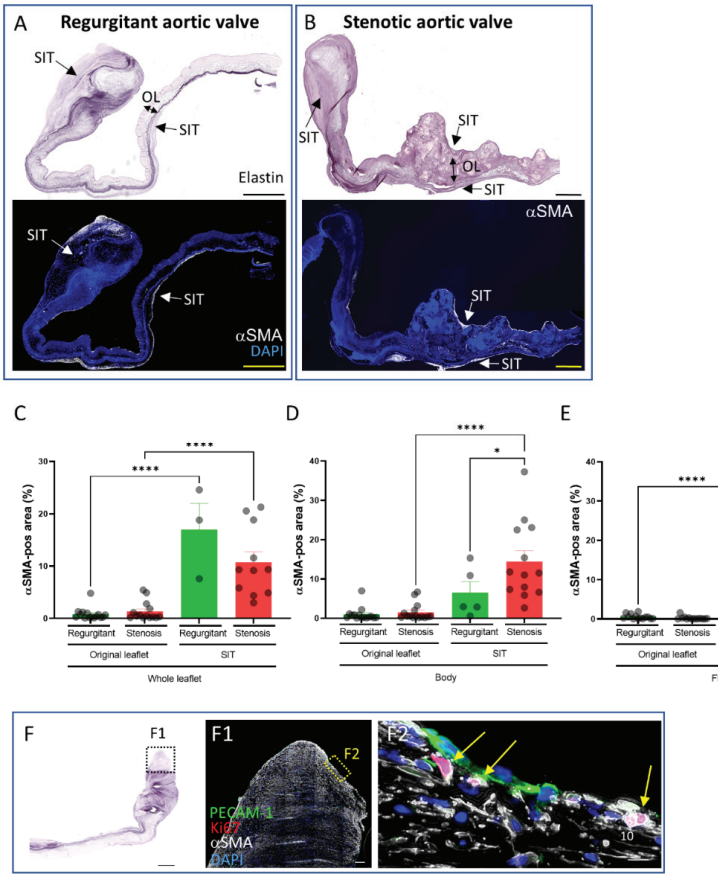

Figure 3. Presence and distribution of myofibroblasts in regurgitant and stenotic aortic valves. (**A**,**B**) Elastin and αSMA stainings on regurgitant (**A**) and stenotic (**B**) aortic valves. (**C**–**E**) Graphs indicating the αSMA-positive area of the indicated regions in the regurgitant and stenotic leaflets. (**F**) Elastin staining of a regurgitant valve (**F**) and PECAM-1, Ki67, and αSMA-co-staining (**F1**,**F2**) of the area indicated by box in F. Yellow arrows indicate Ki67-positive myofibroblasts. Data are presented as means ± SEM. One-way ANOVA followed by Šidák's multiple comparisons test was performed to evaluate significant differences for graphs (**C**–**E**). * $p < 0.05$, ** $p < 0.01$, **** $p < 0.0001$. Scale bar is 1000 μm.

3.4. Comparison of the Subendothelial Basement Membrane in Regions of Regurgitant and Stenotic Aortic Valves with and without SIT

To determine whether the SIT was located beneath or on top of the endothelial lining, stainings for endothelial cell marker PECAM-1 and for subendothelial basement membrane markers collagen IV and laminin [10] were performed (Figure 4). Differences in the expression of these markers were found in regions of regurgitant and stenotic valves with or without SIT. In the regions without SIT, collagen IV was found in both aortic and ventricular basement membranes, with lower expression on the ventricular side in regurgitant valves ($n = 4$; Figure 4(A1)), but similar expression levels in stenotic valves ($n = 5$; Figure 4(B1)), while laminin was predominantly expressed on the ventricular side in both regurgitant and stenotic valves and hardly present on the aortic side ($n = 4$ for regurgitant valves; $n = 5$ for stenotic valves; Figure 4(A1,B1)). In the regions with SIT, the expression of PECAM-1, collagen IV, and laminin was mostly observed on the luminal side of the SIT

(either ventricular or aortic), suggesting that SIT forms beneath the endothelial lining (Figure 4(A2,B2)). The laminin expression was in most parts higher than at the regions without SIT on both the aortic and ventricular sides (n = 4 for regurgitant valves; n = 6 for stenotic valves; Figure 4(A1,A2,B1,B2)). PECAM-1, collagen IV, and laminin expression were, however, also observed dispersed within the SIT mostly in the free edge of regurgitant valves (Figure 4(A3)) andat the border of the original leaflet and the SIT in the body part of the stenotic valves (Figure 4(B2,B3)).

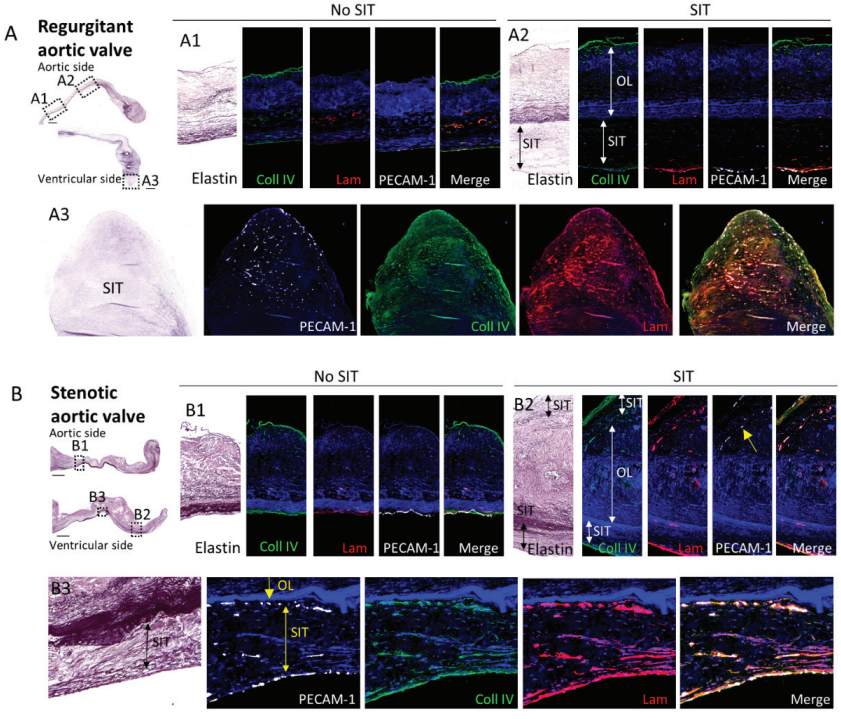

Figure 4. Comparison of the subendothelial basement membrane in regions of regurgitant and stenotic valves with and without SIT. Regurgitant (**A**) and stenotic (**B**) aortic valves stained for elastin, collagen IV (Coll IV), laminin (Lam), and PECAM-1 in regions without SIT (**A1**,**B1**) and with SIT (**A2**,**B2**). A3 and B3 indicate regions with SIT in the free edge of the regurgitant valve (**A3**) and in the ventricular SIT of the body part of the stenotic valve (**B3**), where the expression of collagen IV, laminin, and PECAM-1 is not confined to the luminal side but is present within the SIT. Yellow arrows in B2 and B3 indicate PECAM-positive cells at the border of the original leaflet and SIT. Scale bar is 1000 μm.

3.5. Characterization of Original Leaflet Folding in the Free Edge of Regurgitant and Stenotic Aortic Valves

Examination of the free edge morphology on elastin-stained sections showed that the original leaflet part of the free edge can be folded toward the ventricular side or toward the aortic side (Figure 5). However, this folding was mostly masked by the presence of SIT surrounding the original leaflet (Figure 5). We therefore defined 7 potential grades of free edge folding (Figure 5A) to describe this phenomenon and compare it between stenotic and regurgitant valves (Figure 5B). Folding of the original leaflet in the free edge was observed in most of the regurgitant leaflets (93%; all original leaflet folding grades except grade 0) and the direction in 83% of the cases was toward the ventricular side with different grades (folding scores 1,2, and 3; Figure 5B,C). In 17% of the cases the tip of the original leaflet

was folded to the aortic side (folding scores −1, −2, and −3; Figure 5B,C). On the other hand, stenotic valves did not show folding of the original leaflet in the free edge in 38% of the cases (folding grade 0), and only 1 sample showed a slight folding to the aortic side (Figure 5B,C).

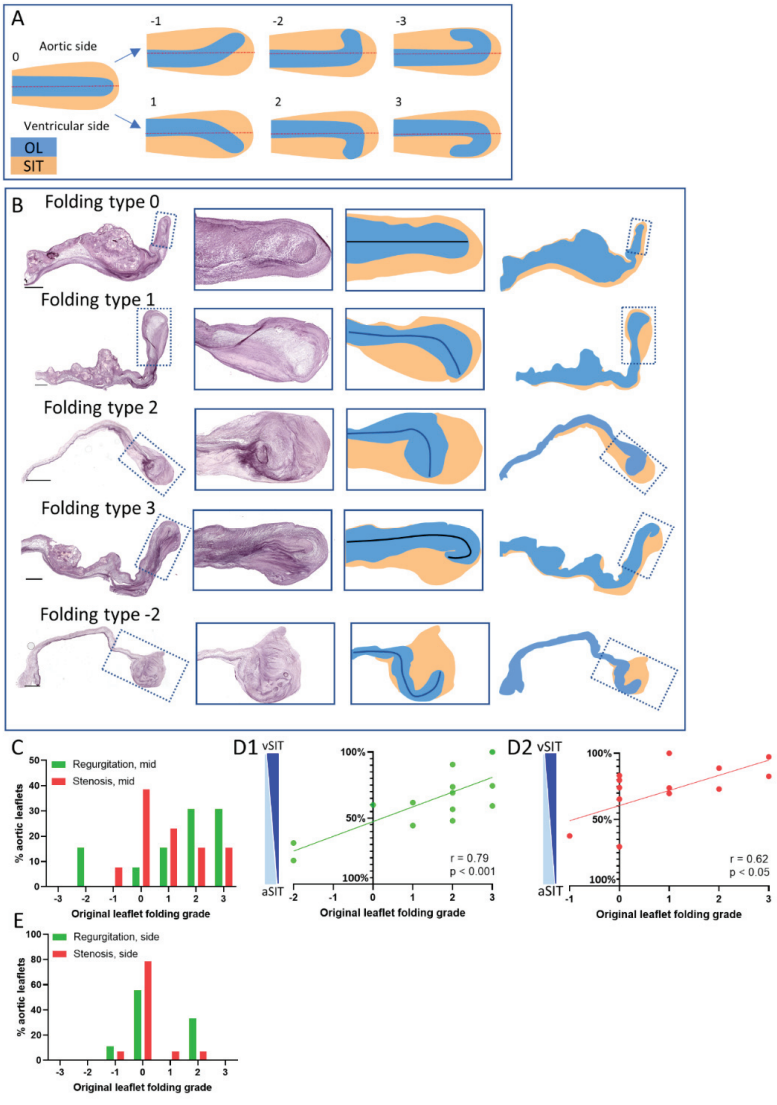

Figure 5. Characterization of the original leaflet folding in the free edge of regurgitant and stenotic valves. (**A**) Schematic drawings depicting the original leaflet folding types. The grade is based on the direction and the extent that the original leaflet deviates from the course of the free edge part of the leaflet, which is indicated by the red line. A grade 0 indicates no folding, whereas values above 0 indicate folding toward the ventricular side and values below 0 indicate folding toward the aortic side. The red line also indicates the border between the ventricular SIT (vSIT) and aortic SIT (aSIT).

(**B**) Elastin stainings of aortic valves displaying the different folding types and the rendering of these leaflets, with blue representing the original leaflet and orange representing the SIT. (**C**) Graph showing the relative distribution of the original leaflet folding grades at the midline of regurgitant and stenotic aortic valves. (**D**) Graphs depicting the relative contribution of the vSIT and aSIT to the total SIT of the free edge in regurgitant (**D1**) and stenotic (**D2**) valves per original leaflet folding grade. (**E**) Graph showing the relative distribution of the original leaflet folding grades on the side region of regurgitant and stenotic aortic valves. Correlations between the relative contribution of the vSIT and aSIT to the total SIT and the original leaflet folding grade was determined using the Pearson's r-correlation test. Scale bar is 1000 μm.

In addition, the type and grade of folding of the original leaflet was correlated with the relative contribution of the SIT to the ventricular or aortic side of the free edge. The vSIT and aSIT in each folding type was defined as indicated by a red stippled line in Figure 5A along the line of the leaflet. A strong correlation was found for the regurgitant valves, with relative larger vSIT when the original leaflet was folded toward the ventricular side (Figure 5(D1)), and larger aSIT when the original leaflet was folded toward the aortic side (Figure 5(D1)). For the stenotic valves in turn, only a weak correlation was found (Figure 5(D2)).

The folding was less and often absent in the regions closer to the commissure (Figures 1A and 5E) compared to the midline location in both the regurgitant and stenotic aortic valves (Figure 5C), suggesting that hemodynamic stresses are likely involved in the regulation of original leaflet folding in the free edge.

4. Discussions

In this study, we reported for the first time the systematic presence of SIT in both regurgitant and stenotic aortic valves. Differences in the extent, location, and composition of SIT were found between stenotic and regurgitant aortic valves, suggesting the involvement of mechanical and hemodynamic stresses in the initiation and progression of SIT formation.

4.1. Aortic Valve SIT Formation

The healthy aortic valve is demarcated by the aortic and ventricular elastin lamina, which are only separated from the aortic and ventricular lumen by a layer of valvular endothelial cells and their basement membrane. In cases of aortic valve pathology, most leaflet alterations (such as calcification or myxoid degeneration) occur within the elastic lamina, leading to an expansion of leaflet layers and valve thickening. However, observations of tissue expansion outside the elastic lamina also were made by Otto et al. [8] in sclerotic and stenotic aortic valves on the aortic side, being considered subendothelial lesions with a displacement and/or reduplication of the elastic lamina. Similar observations were made by Kuusisto et al. [7], who observed atherosclerosis-like lesions on the aortic side of the aortic valve of non-stenotic young and elderly patients after necropsy. Interestingly, the subendothelial lesions that were observed on the aortic surface of non-stenotic aortic valves were characterized by inflammatory cell infiltration, lipid deposition, and micro-calcifications, indicating these regions as potential initiation points of the disease. The presence of tissue outside the elastin lamina has recently also been observed on the ventricular side of early stenotic aortic valves [11]. Therefore, the presence of an additional tissue superimposed on the original leaflet, i.e., SIT, has been already suggested, especially in the early phase of aortic stenosis, but has not been systematically assessed and characterized in patients with advanced stenotic valves or in aortic valve regurgitation.

In this study, which included a large sample of aortic valves of patients with moderate or severe stenosis or regurgitation (secondary to aortic dilatation), we observed in every sample the presence of SIT formation on either the aortic, the ventricular, or both sides of the leaflet. Although no significant difference was found in the average SIT thickness between regurgitant and stenotic valves, the distribution of the SIT differed between the two pathologies. Regurgitant aortic valves showed more SIT formation in the free edge,

leading to a thicker leaflet at that level, while stenotic aortic valves had relatively more SIT formation on the aortic side of the body part of the leaflet. These findings might be explained by the different mechanical stresses that stenotic and regurgitant valves are subjected to, and which are responsible for SIT formation [5]. The regurgitation etiology of the aortic valves used in the current study was aortic dilatation (and not a primary defect of the aortic valve). Leaflet remodeling of these regurgitant aortic valves, including the formation of SIT, was therefore likely caused by the hemodynamic stresses related to the dilatation and (central) regurgitation. The observed relatively high levels of SIT formation on the leaflet free edge, which was mostly subjected to the regurgitant flow, supports this hypothesis. The examined stenotic aortic valves had in turn a primary leaflet alteration (calcifications and fibrosis) causing pathologic remodeling of specifically the body part of the valve. This remodeling has been shown to change the mechanical properties of the valve and therefore the hemodynamic and mechanical stresses that the valve experiences [3]. SIT formation at this level might therefore also be initiated by hemodynamic and mechanical stress, which could explain the differential distribution of SIT between stenotic and regurgitant aortic valves. The presence of overall less SIT in the valvular regions closer to commissures also indicates the involvement of hemodynamics in SIT formation, as these regions are exposed to lower hemodynamic stresses [16,17]. Only the aSIT of the stenotic valves at the free edge part showed more SIT formation, which might suggest exposure to a different type of mechanical stress compared to the regurgitant valves.

4.2. Aortic Valve SIT Composition

The extracellular matrix composition of SIT greatly differed between and within the aortic leaflets, which was likely due to the "age" of the SIT and to the different mechanical and molecular stimuli each region was exposed to, as suggested by for the SIT formation in the mitral valve [5]. Some regions were shown to be highly cellular and consisted mostly of glycosaminoglycans, whereas other regions had a lower cell density and consisted mostly of collagen. Of interest, we observed a relatively higher expression of collagen in the SIT of the stenotic valves as compared to regurgitant ones, which might indicate that fibrosis in the SIT contributes to overall leaflet fibrosis and therefore to the mechanical properties of stenotic aortic valves.

Myofibroblasts are known to be present in diseased aortic valves and are thought to be the main cell type that actively remodels the extracellular matrix by the degradation and secretion of extracellular matrix components [12]. Both in stenotic and regurgitant valves, we observed that myofibroblasts, as identified by αSMA expression, are highly present in SIT but not in the original leaflet, indicating that the SIT is the more active area of the leaflet in terms of extracellular matrix remodeling in end-stage diseased aortic valves. Proliferation of these myofibroblasts in some regions of the valve at the time of isolation suggests that expansion of the SIT is still occurring in end-stage diseased aortic valves. Interestingly, αSMA cells were hardly observed in the SIT-like subendothelial lesions in stenotic aortic valves in the early disease stage [7,8].

4.3. Mechanisms of Aortic SIT Formation

To obtain more insights into the mechanisms of SIT formation in aortic valves, stainings for the basement membrane markers collagen IV and laminin were performed. In most regions, SIT was present underneath the basement membrane, which had increased levels of laminin compared to the regions without SIT. However, we also observed regions where valvular endothelial cells and the basement membrane markers were present at the border between the original leaflet and the SIT or dispersed throughout the part of the SIT area with αSMA expression (presumably with active remodeling). These observations in the aortic valve support the hypothesis formulated on the basis of the mitral valve ex vivo mouse model [5], that migration of activated valvular interstitial cells (αSMA-positive) and resident macrophages through breakages in the endothelial lining are responsible for SIT

formation on top of the endothelial cell layer. The fact that most regions with SIT were also covered by valvular endothelial cells might indicate that these cells migrate (possibly from the sides) on top of the newly formed SIT, whereas the valvular endothelial cells within or underneath the SIT disappear over time. Future in vivo and ex vivo studies should focus on SIT formation at different time points to gain more insight into the precise mechanisms.

4.4. Aortic Valve Free Edge Folding

While examining the free edges of the diseased aortic valves, we frequently observed folding of the original leaflet of various degrees toward either the ventricular or aortic side. This characteristic has never been reported before and was not visible by gross examination due to the formation of SIT around the folding. The folding occurred more frequently in the regurgitant valves and was mostly directed toward the ventricular side, suggesting that the regurgitant flow caused the folding of the original leaflet. In the regions closer to the commissure, the folding was reduced or absent, supporting the involvement of the flow in the formation of the folding.

4.5. Limitations

Our study suggests that SIT formation is driven by hemodynamic and mechanical stresses; therefore, differences in SIT distribution and composition were expected between the aortic valve samples from patients with moderate or severe regurgitation or stenosis. The number of samples with moderate stenosis or regurgitation in our study was, however, too small to perform a robust comparison, which will therefore be included in future studies. In addition, to further characterize the composition of the SIT and substantiate differences between SIT formation in regurgitant and stenotic aortic valves, additional stainings for different extracellular matrix components are needed. In our study, αSMA staining was used to identify myofibroblasts; smooth muscle cells, however, also express αSMA and have been shown to be present in normal aortic valves and more abundant in calcified aortic valves [18,19]. Expression studies using smooth muscle cell-specific markers should be performed to distinguish the two cell types.

5. Conclusions

Overall, we have shown that SIT is a major feature of stenotic and regurgitant valves, contributing greatly to the thickness of the leaflets. The SIT appeared to be a highly active area with various extracellular matrix compositions potentially modifying the mechanical properties and therefore the function of the valves. The distribution and composition of the SIT differed between stenotic and regurgitant valves, indicating disease-specific regulation of SIT formation. Understanding the mechanisms underlying SIT formation is crucial to understand the initiation and progression of aortic valve disease and might open new pathways to the development of new therapeutic treatments.

Author Contributions: Conceptualization, B.P.T.K. and N.A.M.; formal analysis, B.P.T.K.; investigation, B.P.T.K. and B.M.G.; resources, A.L.v.W., M.P. and J.H.; writing—original draft preparation, B.P.T.K.; writing—review and editing, N.A.M.; visualization, B.P.T.K.; supervision, B.P.T.K. and N.A.M. All authors have read and agreed to the published version of the manuscript.

Funding: This work was supported by grants received from GE Healthcare, Lantheus medical imaging, St. Jude Medical, Medtronic, Boston Scientific, Biotronik, and Edwards Lifesciences, by the Dutch Heart Foundation AHA grant number 2013T093 awarded to the BAV consortium, and by the partners of Regenerative Medicine Crossing Borders (www.regmedxb.com, accessed on 1 January 2020).

Institutional Review Board Statement: The study was conducted according to the guidelines of the Declaration of Helsinki. Collection and analysis of the samples were performed according to the guidelines of the Leiden University Medical Centre (Leiden, The Netherlands) and Dutch regulations on the use of human tissues (rest material).

Informed Consent Statement: Patient consent was waived as tissues were handed over anonymously, without any patient-specific information. According to the Dutch medical scientific research with human subjects act (WMO), secondary use of patient material does not require review by a Medical Ethics Examination Committee.

Data Availability Statement: No report of any data.

Conflicts of Interest: The authors declare no conflict of interest.

References

1. Fishbein, G.A.; Fishbein, M.C. Pathology of the Aortic Valve: Aortic Valve Stenosis/Aortic Regurgitation. *Curr. Cardiol. Rep.* **2019**, *21*, 81. [CrossRef] [PubMed]
2. Yutzey, K.E.; Demer, L.L.; Body, S.C.; Huggins, G.S.; Towler, D.A.; Giachelli, C.M.; Hofmann-Bowman, M.A.; Mortlock, D.P.; Rogers, M.B.; Sadeghi, M.M.; et al. Calcific aortic valve disease: A consensus summary from the Alliance of Investigators on Calcific Aortic Valve Disease. *Arter. Thromb. Vasc. Biol.* **2014**, *34*, 2387–2393. [CrossRef] [PubMed]
3. Gould, S.T.; Srigunapalan, S.; Simmons, C.A.; Anseth, K.S. Hemodynamic and cellular response feedback in calcific aortic valve disease. *Circ. Res.* **2013**, *113*, 186–197. [CrossRef] [PubMed]
4. Schoen, F.J. Evolving concepts of cardiac valve dynamics: The continuum of development, functional structure, pathobiology, and tissue engineering. *Circulation* **2008**, *118*, 1864–1880. [CrossRef] [PubMed]
5. Kruithof, B.P.T.; Paardekooper, L.; Hiemstra, Y.L.; Goumans, M.J.; Palmen, M.; Delgado, V.; Klautz, R.J.M.; Ajmone Marsan, N. Stress-induced remodelling of the mitral valve: A model for leaflet thickening and superimposed tissue formation in mitral valve disease. *Cardiovasc. Res.* **2019**. [CrossRef] [PubMed]
6. Roberts, W.C.; Vowels, T.J.; Ko, J.M.; Hebeler, R.F., Jr. Gross and histological features of excised portions of posterior mitral leaflet in patients having operative repair of mitral valve prolapse and comments on the concept of missing (=ruptured) chordae tendineae. *J. Am. Coll. Cardiol.* **2014**, *63*, 1667–1674. [CrossRef] [PubMed]
7. Kuusisto, J.; Rasanen, K.; Sarkioja, T.; Alarakkola, E.; Kosma, V.M. Atherosclerosis-like lesions of the aortic valve are common in adults of all ages: A necropsy study. *Heart* **2005**, *91*, 576–582. [CrossRef] [PubMed]
8. Otto, C.M.; Kuusisto, J.; Reichenbach, D.D.; Gown, A.M.; O'Brien, K.D. Characterization of the early lesion of 'degenerative' valvular aortic stenosis. Histological and immunohistochemical studies. *Circulation* **1994**, *90*, 844–853. [CrossRef] [PubMed]
9. Back, M.; Gasser, T.C.; Michel, J.B.; Caligiuri, G. Biomechanical factors in the biology of aortic wall and aortic valve diseases. *Cardiovasc. Res.* **2013**, *99*, 232–241. [CrossRef] [PubMed]
10. Sacks, M.S.; David Merryman, W.; Schmidt, D.E. On the biomechanics of heart valve function. *J. Biomech.* **2009**, *42*, 1804–1824. [CrossRef] [PubMed]
11. Goody, P.R.; Hosen, M.R.; Christmann, D.; Niepmann, S.T.; Zietzer, A.; Adam, M.; Bonner, F.; Zimmer, S.; Nickenig, G.; Jansen, F. Aortic Valve Stenosis: From Basic Mechanisms to Novel Therapeutic Targets. *Arter. Thromb. Vasc. Biol.* **2020**, *40*, 885–900. [CrossRef] [PubMed]
12. Liu, A.C.; Joag, V.R.; Gotlieb, A.I. The emerging role of valve interstitial cell phenotypes in regulating heart valve pathobiology. *Am. J. Pathol.* **2007**, *171*, 1407–1418. [CrossRef] [PubMed]
13. Nagaraju, C.K.; Robinson, E.L.; Abdesselem, M.; Trenson, S.; Dries, E.; Gilbert, G.; Janssens, S.; Van Cleemput, J.; Rega, F.; Meyns, B.; et al. Myofibroblast Phenotype and Reversibility of Fibrosis in Patients with End-Stage Heart Failure. *J. Am. Coll. Cardiol.* **2019**, *73*, 2267–2282. [CrossRef] [PubMed]
14. Halfter, W.; Candiello, J.; Hu, H.; Zhang, P.; Schreiber, E.; Balasubramani, M. Protein composition and biomechanical properties of in vivo-derived basement membranes. *Cell Adhes. Migr.* **2013**, *7*, 64–71. [CrossRef]
15. Gomez-Stallons, M.V.; Tretter, J.T.; Hassel, K.; Gonzalez-Ramos, O.; Amofa, D.; Ollberding, N.J.; Mazur, W.; Choo, J.K.; Smith, J.M.; Kereiakes, D.J.; et al. Calcification and extracellular matrix dysregulation in human postmortem and surgical aortic valves. *Heart* **2019**. [CrossRef] [PubMed]
16. Markl, M.; Draney, M.T.; Miller, D.C.; Levin, J.M.; Williamson, E.E.; Pelc, N.J.; Liang, D.H.; Herfkens, R.J. Time-resolved three-dimensional magnetic resonance velocity mapping of aortic flow in healthy volunteers and patients after valve-sparing aortic root replacement. *J. Thorac. Cardiovasc. Surg.* **2005**, *130*, 456–463. [CrossRef] [PubMed]
17. Hope, M.D.; Hope, T.A.; Meadows, A.K.; Ordovas, K.G.; Urbania, T.H.; Alley, M.T.; Higgins, C.B. Bicuspid aortic valve: Four-dimensional MR evaluation of ascending aortic systolic flow patterns. *Radiology* **2010**, *255*, 53–61. [CrossRef] [PubMed]
18. Latif, N.; Sarathchandra, P.; Chester, A.H.; Yacoub, M.H. Expression of smooth muscle cell markers and co-activators in calcified aortic valves. *Eur. Heart J.* **2015**, *36*, 1335–1345. [CrossRef] [PubMed]
19. Bairati, A.; DeBiasi, S. Presence of a smooth muscle system in aortic valve leaflets. *Anat. Embryol.* **1981**, *161*, 329–340. [CrossRef] [PubMed]

Journal of
Cardiovascular
Development and Disease

MDPI

Article

Surgical Aortic Valve Replacement with Concomitant Aortic Surgery in Patients with Purely Bicuspid Aortic Valve and Associated Aortopathy

Mevlüt Çelik, Edris A. F. Mahtab * and Ad J. J. C. Bogers

Department of Cardiothoracic Surgery, Erasmus University Medical Center,
3015 GD Rotterdam, The Netherlands; m.celik@erasmusmc.nl (M.Ç.); a.j.j.c.bogers@erasmusmc.nl (A.J.J.C.B.)
* Correspondence: e.mahtab@erasmusmc.nl

Abstract: The bicuspid aortic valve (BAV) is the most common congenital cardiac malformation associated with aortopathy. The current study provides surgical clinical data on the patient characteristics and long-term survival of this less common adult purely BAV population undergoing surgical aortic valve replacement (SAVR) with concomitant aortic surgery. Adult patients with purely BAV who underwent SAVR and concomitant aortic surgery were included. Prevalence, predictors of survival, and outcomes for this patient population were analyzed. A total of 48 patients (mean age 58.7 ± 13.2 years, 33% female) with purely BAV underwent SAVR and concomitant aortic surgery between 1987 and 2016. The majority (62%) of the patients had pure aortic stenosis (AS). A total of 12 patients died. Survival was 92%, 73%, and 69% at 1, 5, and 20 years of follow-up. At 15 years of follow-up, the survival was close to that of the Dutch population, with a relative survival of 77%. Adult patients with a purely bicuspid aortic valve morphology undergoing SAVR and concomitant aortic root and/or ascending aorta present with excellent survival.

Keywords: aortic valve replacement; surgical; aortic surgery; bicuspid aortic valve; Bentall

Citation: Çelik, M.; Mahtab, E.A.F.; Bogers, A.J.J.C. Surgical Aortic Valve Replacement with Concomitant Aortic Surgery in Patients with Purely Bicuspid Aortic Valve and Associated Aortopathy. *J. Cardiovasc. Dev. Dis.* **2021**, *8*, 16. https://doi.org/10.3390/jcdd8020016

Academic Editor: Monique R.M. Jongbloed
Received: 31 December 2020
Accepted: 5 February 2021
Published: 10 February 2021

1. Introduction

Bicuspid aortic valve (BAV) disease is the most prevalent congenital heart defect, with approximately 1% prevalence in the general population [1,2]. A classification system for BAV from 304 surgical specimens showed an incidence of only 7% purely BAV in an autopsied population [3]. Although much data are present in patients with BAV and a raphe, data in patients with the less common purely bicuspid aortic valve are still relatively limited [3].

BAV is associated with aortopathies that lead to clinical manifestations such as aortic dilation, aneurysm, and dissection [4]. In the adult population, BAV patients undergoing aortic valve surgery are younger than the tricuspid aortic valve population. Patients with BAV present earlier with aortic stenosis (AS) and tend to undergo more frequent concomitant aortic surgery due to aortopathy [5].

Studies assessing the clinical profiles of BAV patients with a purely bicuspid aortic valve undergoing surgical aortic valve replacement (SAVR) and concomitant aortic surgery remain scarce. Therefore, the purpose of this study is to (i) describe the clinical characteristics of purely BAV patients undergoing SAVR with concomitant aortic surgery and (ii) assess the long-term survival and predictors of survival in this subpopulation of BAV patients.

2. Methods

2.1. Study Design

Patients older than 18 years of age undergoing SAVR between 1987 and 2016 at the Erasmus Medical Centre, Rotterdam, were included. In this SAVR population (total

n = 4404), 16% of the patients who had undergone SAVR had purely BAV (n = 711), and only 7% of these purely BAV patients underwent concomitant aortic surgery (n = 48, as shown in Figure 1). Patients without pure BAV were excluded (Sievers 0) [3]. Likewise, patients without concomitant aortic surgery were excluded. Patients who did not receive a biological or mechanical aortic valve prosthesis were also excluded. The valvular morphology was classified during the operation and defined by the attending surgeon. Electronic medical records were used to obtain patient and procedural characteristics. For inclusion in this study, the bicuspid aortic valve was classified as a purely bicuspid aortic valve according to the Sievers classification (Sievers 0). All of the authors vouch for the validity of the data and adherence to the protocol.

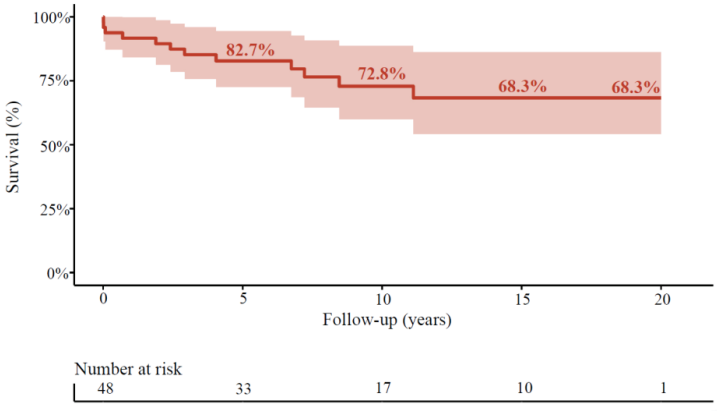

Figure 1. Long-term survival after surgical aortic valve replacement (SAVR) with aortic surgery. Survival in overall cohort. The shaded area represents the 95% confidence interval.

2.2. Endpoints and Definitions

The primary aim was to assess the characteristics of patients with purely BAV requiring surgery. A further aim was to assess the survival after surgery of patients with purely BAV. The primary indication for operation (AS, aortic regurgitation (AR), or combined AS and AR) was determined based on the initial echocardiogram and according to the clinical guidelines in use at the time of the surgery.

2.3. Statistical Analysis

Discrete variables are presented as numbers, percentages, or proportions and compared with either the chi-square test or the Fisher exact test, where appropriate. Continuous variables are presented as means ± standard deviation or medians with the interquartile range (IQR) if there was evidence of skewed data according to the Kolmogorov–Smirnov test, and values were compared with either the two-sample t-test or Wilcoxon rank-sum test, where appropriate.

The relative survival can be used as an estimate of cause-specific mortality. It is defined as the ratio between the observed survival rates and the expected survival rates in the general population [6]. The Human Mortality Database was used to obtain the age-, sex-, and calendar year-matched expected survival data of the general population in The Netherlands [7]. The Human Mortality Database is continuously updated and includes mortality data from The Netherlands up until 2016. Relative survival was estimated through the Ederer II method [8,9]. Predictors of mortality were identified in a Cox proportional hazards model. Significant variables on univariable analyses were included in a multivariable Cox proportional hazards model. Sensitivity analysis was performed for isolated SAVR. Two-sided p-values < 0.05 were considered to be statistically significant. Data analyses were done using SPSS 25.0 (SPSS Inc, Chicago, IL, USA) and R software, version 3.5 (R

Foundation, Vienna, Austria). Figures were generated using Microsoft Excel (Microsoft, Redmond, WA, USA) and R software, version 3.5 (R Foundation, Vienna, Austria).

3. Results

3.1. Characteristics of Patients with Bicuspid Aortic Valves

A total of 48 purely BAV patients underwent SAVR with concomitant aortic surgery (Figure 2). The mean age of operated patients was 58.7 ± 13.2, with 9 patients younger than 50 and 10 patients being 70 or older. The prevalence of comorbidities such as hypertension (32%), hypercholesterolemia (10%), and diabetes mellitus (4%) is shown in Table 1.

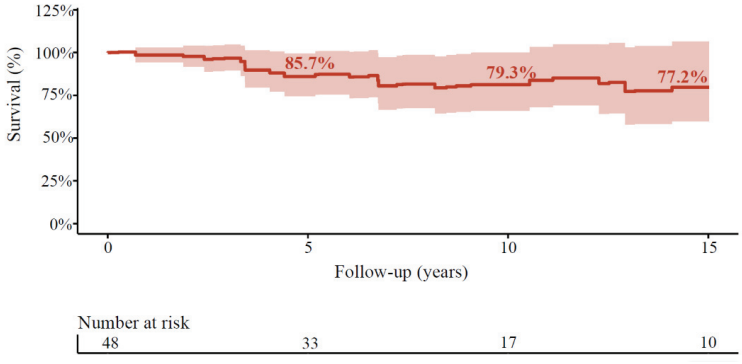

Figure 2. Long-term relative survival after SAVR with aortic surgery compared to the Dutch population. Relative survival compared to the age-, gender-, and year-matched population in the overall cohort. The shaded area represents the 95% confidence interval.

Table 1. Baseline and procedural characteristics in the overall cohort.

	Overall Cohort
Age at operation	58.7 ± 13.2
Gender (female)	16 (33.3)
Indication	-
AS	30 (62)
AR	9 (19)
Combined	9 (19)
Previous cardiac operation	6 (13)
Creatinine	0.93 (0.86–1.07)
≥2 mg/dL	0
Atrial fibrillation	5 (10)
Diabetes mellitus	2 (4)
Decompensation cordis	4 (8)
Hypertension	15 (32)
Hypercholesterolemia	5 (10)
Previous myocardial infarction	3 (6)
Previous PCI	1 (2)
COPD	1 (2)
Endocarditis	2 (4)
History of cancer	3 (6)
Stroke/TIA	2 (4)
Stroke	1 (2)
TIA	2 (4)
Arterial disease	3 (6)

Table 1. *Cont.*

	Overall Cohort
Carotid	1 (2)
Peripheral	2 (4)
Concomitant CABG	8 (17)
Aortic surgery	-
Aortic root replacement	10 (21)
Supracoronay ascendens replacement	38 (79)
Ascendens + Hemi(arch)	13 (27)
Valve size	24.8 ± 2.3
Urgency	-
Emergent	3 (7)
Not emergent	42 (93)
LVEF	-
Preserved	35 (76)
Mildly reduced	3 (7)
Moderately reduced	6 (13)
Severely reduced	2 (4)
Valve (mechanical)	29 (60)

AR, aortic regurgitation; AS, aortic stenosis; CABG, coronary artery bypass graft; COPD, chronic obstructive pulmonary disease; LVEF, left ventricular ejection fraction; PCI, percutaneous coronary intervention; TIA, transient ischemic attack.

3.2. Procedural Characteristics

The indication for surgery was mainly AS (62%), followed by AR (19%) or combined AS and AR (19%). The type of aortic surgery was aortic root replacement in 21% of the patients and supracoronary ascendens replacement in 79% of the patients. Additionally, in 13 patients (27%), on top of the aortic root and/or ascending aorta, concomitant (hemi-)arch replacement was performed. Further concomitant surgery included coronary artery bypass graft (CABG) in 17% of the patients. The diameter of the implanted valve prosthesis was 24.8 ± 2.3. Further concomitant surgeries and characteristics are shown in Table 1.

3.3. Long-Term Outcomes after Surgery

A total of 12 patients died during follow-up. Survival was 92%, 90%, 83%, 73%, and 68% at 1, 2, 5, 10, and 20 years of follow-up in the overall cohort for patients with purely BAV (Figure 1). In age-, sex-, and year-matched Dutch controls, the relative survival in patients with purely BAV was 99%, 96% 86%, 79%, and 77%, at 1, 2, 5, 10, and 15 years of follow-up, respectively (Figure 3).

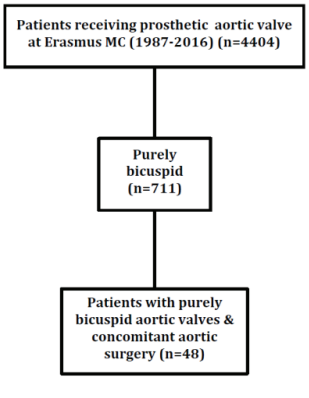

Figure 3. Flowchart of included patients.

3.4. Factors Associated with Survival during Follow-Up in the Age-Matched Population

In univariable analyses, the presence of COPD was a predictor of survival ($p = 0.02$). However, cardiovascular risk factors such as increasing age ($p = 0.20$), atrial fibrillation ($p = 0.80$), and concomitant CABG ($p = 0.64$) were not predictors of survival (Table 2).

Table 2. Predictors of survival after SAVR with concomitant aortic surgery.

Characteristics	Univariable HR (95% CI); *p*-Value
Age	1.04 (1.00–1.10); $p = 0.20$
Sex (female)	1.7 (0.5–5.4); $p = 0.37$
AS	1.7 (0.4–6.1); $p = 0.44$
AR	0.2 (0.01–3.3); $p = 0.25$
Hypertension	1.1 (0.3–3.7); $p = 0.86$
Hypercholesterolemia	1.0 (0.8–1.1); $p = 0.29$
Diabetes mellitus	1.4 (0.9–2.1); $p = 0.14$
Arterial disease	2.3 (0.3–18.4); $p = 0.44$
Renal failure	1.3 (0.6–3.0); $p = 0.49$
Previous MI	3.1 (0.7–14.3); $p = 0.14$
Previous PCI	1.1 (0.6–2.1); $p = 0.74$
Decompensated heart failure	0.8 (0.1–6.1); $p = 0.82$
LVEF < 50%	1.8 (0.5–6.2); $p = 0.35$
Atrial fibrillation	0.7 (0.1–6.0); $p = 0.80$
Previous stroke or TIA	2.0 (0.2–15.3); $p = 0.52$
COPD	1.9 (1.3–2.8); $p = 0.002$
Concomitant CABG	1.4 (0.4–5.1); $p = 0.64$
Emergent SAVR versus non-emergent	1.7 (0.2–13.5); $p = 0.62$
Mechanical prosthesis	1.0 (0.2–4.3); $p = 0.97$

AR, aortic regurgitation; AS, aortic stenosis; CABG, coronary artery bypass graft; COPD, chronic obstructive pulmonary disease; LVEF, left ventricular ejection fraction; MI, myocardial infarction; PCI, percutaneous coronary intervention; SAVR, surgical aortic valve replacement; TIA, transient ischemic attack.

4. Discussion

This study describes patients' characteristics and outcomes with purely bicuspid aortic valves that underwent aortic root, ascendens, and arch replacement as concomitant surgery to SAVR as the long-term survival and predictors of survival in this population. We found that the purely BAV population requiring SAVR and concomitant aortic surgery (i) mostly consists of young patients, (ii) has few cardiovascular risk factors that were not found predictive for their survival, and (iii) has excellent long-term survival.

The mechanisms leading to the development of BAV and the associated aortopathies are a matter of ongoing discussion. Adriana C. Gittenberger-de Groot and her team have performed an extensive number of indispensable studies on the spectrum of BAV disease and associated aortic anomalies over the past three decades. This contribution includes several developmental, histopathological, and anatomical studies on animal as well as human tissue, such as the meticulous explanation of cardiac development in congenital malformations [10], anatomical description of BAV and the aortic root [11], and the contribution of several cell lineages to the development of BAV and the associated aortic root anomalies [12–14]. In addition, other groups have reported that patient-specific factors such as aortic valve stenosis (AS), in combination with the specific leaflet morphology (the type of BAV) and the resultant shear stress, were associated with dilatation of the aorta [15,16].

Our cohort consisted of relatively young patients with purely BAV, a minority of the BAV population [3,17]. Our patients often presented with aortic stenosis, yet aortic regurgitation incidence was close to 40%. This prevalence of aortic regurgitation was higher than the standard surgical aortic valve replacement population, which could be partly due to aortic root or proximal aorta dilatation [4]. A bicuspid aortic valve indicates abnormal leaflet modeling, subsequently leading to turbulence downstream and upstream of the aortic valve [18]. This turbulence increases the aortic wall shear stress and abnormal helical

flow in the ascending aorta, as shown with previous 4D magnetic resonance imaging [19,20]. In addition, increased matrix metalloproteinase activity in the aorta of BAV patients can affect the structural flexibility by altered elastin, collagen, and smooth muscle composition of the elastic laminae (aortic media) and can therefore lead to reduced compliance and increased aortic stiffness [4,21]. Therefore, BAV is associated with an increased prevalence of aortic root dilatation and ascending aortic aneurysms [22], even in patients without developed valvular dysfunction [23]. Moreover, gender differences in the aortic dimension of the patients with BAV were associated with aortopathy. Male patients more often present with larger aortic annulus and sinotubular junction dimensions [24]. The majority of our patients (two-thirds) described in this study were male. This finding is similar to previous studies [4]. Patients with bicuspid valves also present with fewer cardiovascular risk factors compared to patients with tricuspid aortic morphology and at an earlier age. This is partly due to accelerated calcification [25]. Aside from aortopathy and subsequent aortic dissection, endocarditis was prevalent in 4% of our cohort. This rate is lower than the previously noted higher prevalence [26].

In our cohort, the majority of the patients received mechanical valvular prostheses. Mechanical prostheses are undoubtedly superior regarding long-term durability and survival in the younger population [27]. However, a mechanical prosthesis might affect the patient's quality of life due to anticoagulant medication and known bleeding risks, especially in an aging population [28,29]. Nevertheless, our cohort's overall survival was exceptionally high, with 68% of the population surviving at 20 years of follow-up. The relative survival of this population (79%) is close to that of the Dutch general population. This could be partly explained by the lower prevalence in the cardiovascular risk profile of those patients.

Limitations

Given its retrospective and nonrandomized nature, our study could be subject to shortcomings related to data capture and inherent confounders. Second, our study evaluated patient characteristics and long-term mortality as outcomes. Other aspects of clinical outcome and specific valve-related outcomes, including symptom improvement, quality of life, and structural valve dysfunction at long-term follow-up, were not assessed and should be assessed in further studies. In our study, we only included patients with purely BAV (Type 0) to create a homogenous BAV morphology. However, we are missing other BAV types with associated raphe and a comparison between our population and the TAV population in terms of the prevalence of aortopathy, clinical patient characteristics, and survival.

5. Conclusions

Patients with purely BAV undergoing SAVR with concomitant aortic surgery present with excellent survival rates. Additional studies are needed to examine the exact effect of the intervention on other endpoints, such as quality of life.

Author Contributions: M.Ç., E.A.F.M. and A.J.J.C.B. conceived and planned the study. M.Ç. and E.A.F.M. drafted the manuscript and designed the figures. All authors discussed the results and commented on the final version of the manuscript.

Funding: This study was performed without funding.

Institutional Review Board Statement: This study was approved by the Institutional Review Board of the Erasmus Medical Center.

Informed Consent Statement: Patient informed consent was waived.

Data Availability Statement: Data will not be made available.

Conflicts of Interest: The authors declare no conflict of interest.

References

1. Nistri, S.; Basso, C.; Marzari, C.; Mormino, P.; Thiene, G. Frequency of bicuspid aortic valve in young male conscripts by echocardiogram. *Am. J. Cardiol.* **2005**, *96*, 718–721. [CrossRef]
2. Braverman, A.C.; Guven, H.; Beardslee, M.A.; Makan, M.; Kates, A.M.; Moon, M.R. The bicuspid aortic valve. *Curr. Probl. Cardiol.* **2005**, *30*, 470–522. [CrossRef]
3. Sievers, H.H.; Schmidtke, C. A classification system for the bicuspid aortic valve from 304 surgical specimens. *J. Thorac. Cardiovasc. Surg.* **2007**, *133*, 1226–1233. [CrossRef]
4. Fedak, P.W.; Verma, S.; David, T.E.; Leask, R.L.; Weisel, R.D.; Butany, J. Clinical and pathophysiological implications of a bicuspid aortic valve. *Circulation* **2002**, *106*, 900–904. [CrossRef]
5. Mordi, I.; Tzemos, N. Bicuspid aortic valve disease: A comprehensive review. *Cardiol. Res. Pract.* **2012**, *2012*, 196037. [CrossRef] [PubMed]
6. Perme, M.P.; Pavlic, K. Nonparametric Relative Survival Analysis with the R Package relsurv. *J. Stat. Softw.* **2018**, *87*, 1–27. [CrossRef]
7. Database, H.M. The Human Mortality Database. 2019. Available online: https://www.mortality.org/ (accessed on 29 January 2021).
8. Pohar, M.; Stare, J. Relative survival analysis in R. *Comput. Methods Programs Biomed.* **2006**, *81*, 272–278. [CrossRef]
9. Pohar, M.; Stare, J. Making relative survival analysis relatively easy. *Comput. Biol. Med.* **2007**, *37*, 1741–1749. [CrossRef]
10. Gittenberger-de Groot, A.C.; Bartelings, M.M.; Deruiter, M.C.; Poelmann, R.E. Basics of cardiac development for the understanding of congenital heart malformations. *Pediatr. Res.* **2005**, *57*, 169–176. [CrossRef] [PubMed]
11. Bartelings, M.M.; Bogers, A.J.; Galantowicz, M.E.; Gittenberger-De Groot, A.C. Anatomy of the aortic and pulmonary roots. *Semin. Thorac. Cardiovasc. Surg.* **1998**, *1*, 157–164. [CrossRef]
12. Peterson, J.C.; Wisse, L.J.; Wirokromo, V.; Van Herwaarden, T.; Smits, A.M.; Groot, A.C.G.-D.; Goumans, M.-J.T.H.; VanMunsteren, J.C.; Jongbloed, M.R.M.; DeRuiter, M.C. Disturbed nitric oxide signalling gives rise to congenital bicuspid aortic valve and aortopathy. *Dis. Model. Mech.* **2020**, *13*, dmm044990. [CrossRef]
13. Bergwerff, M.; Verberne, M.E.; DeRuiter, M.C.; Poelmann, R.E.; Gittenberger-de Groot, A.C. Neural crest cell contribution to the developing circulatory system: Implications for vascular morphology? *Circ. Res.* **1998**, *82*, 221–231. [CrossRef] [PubMed]
14. Kappetein, A.P.; Gittenberger-de Groot, A.C.; Zwinderman, A.H.; Rohmer, J.; Poelmann, R.E.; Huysmans, H.A. The neural crest as a possible pathogenetic factor in coarctation of the aorta and bicuspid aortic valve. *J. Thorac. Cardiovasc. Surg.* **1991**, *102*, 830–836. [CrossRef]
15. Kimura, N.; Nakamura, M.; Komiya, K.; Nishi, S.; Yamaguchi, A.; Tanaka, O.; Misawa, Y.; Adachi, H.; Kawahito, K. Patient-specific assessment of hemodynamics by computational fluid dynamics in patients with bicuspid aortopathy. *J. Thorac. Cardiovasc. Surg.* **2017**, *153*, S52–S62. [CrossRef]
16. Youssefi, P.; Gomez, A.; He, T.; Anderson, L.; Bunce, N.; Sharma, R.; Figueroa, C.A.; Jahangiri, M. Patient-specific computational fluid dynamics-assessment of aortic hemodynamics in a spectrum of aortic valve pathologies. *J. Thorac. Cardiovasc. Surg.* **2017**, *153*, 8–20. [CrossRef]
17. Hayman, S.; Wright, G.; West, C.; Burstow, D.; Scalia, G.M. True Bicuspid Aortic Valves are Rare Compared with Functionally Bicuspid Aortic Valves. *Heart Lung Circ.* **2008**, *17*, S63. [CrossRef]
18. Robicsek, F.; Thubrikar, M.J.; Cook, J.W.; Fowler, B. The congenitally bicuspid aortic valve: How does it function? Why does it fail? *Ann. Thorac. Surg.* **2004**, *77*, 177–185. [CrossRef]
19. Hope, M.D.; Hope, T.A.; Meadows, A.K.; Ordovas, K.G.; Urbania, T.H.; Alley, M.T.; Higgins, C.B. Bicuspid aortic valve: Four-dimensional MR evaluation of ascending aortic systolic flow patterns. *Radiology* **2010**, *255*, 53–61. [CrossRef]
20. Barker, A.J.; Markl, M.; Bürk, J.; Lorenz, R.; Bock, J.; Bauer, S.; Schulz-Menger, J.; Von Knobelsdorff-Brenkenhoff, F. Bicuspid aortic valve is associated with altered wall shear stress in the ascending aorta. *Circ. Cardiovasc. Imaging* **2012**, *5*, 457–466. [CrossRef]
21. Verma, S.; Siu, S.C. Aortic dilatation in patients with bicuspid aortic valve. *N. Engl. J. Med.* **2014**, *370*, 1920–1929. [CrossRef]
22. Tadros, T.M.; Klein, M.D.; Shapira, O.M. Ascending aortic dilatation associated with bicuspid aortic valve: Pathophysiology, molecular biology, and clinical implications. *Circulation* **2009**, *119*, 880–890. [CrossRef] [PubMed]
23. Nkomo, V.T.; Enriquez-Sarano, M.; Ammash, N.M.; Melton, L.J.; Bailey, K.R.; Desjardins, V.; Horn, R.A.; Tajik, A.J. Bicuspid aortic valve associated with aortic dilatation: A community-based study. *Arterioscler. Thromb. Vasc. Biol.* **2003**, *23*, 351–356. [CrossRef] [PubMed]
24. Kong, W.K.; Regeer, M.V.; Ng, A.C.; McCormack, L.; Poh, K.K.; Yeo, T.C.; Shanks, M.; Parent, S.; Enache, R.; Popescu, B.A.; et al. Sex Differences in Phenotypes of Bicuspid Aortic Valve and Aortopathy: Insights From a Large Multicenter, International Registry. *Circ. Cardiovasc. Imaging.* **2017**, *10*, e005155. [CrossRef]
25. Wallby, L.; Janerot-Sjoberg, B.; Steffensen, T.; Broqvist, M. T lymphocyte infiltration in non-rheumatic aortic stenosis: A comparative descriptive study between tricuspid and bicuspid aortic valves. *Heart* **2002**, *88*, 348–351. [CrossRef]
26. Ward, C. Clinical significance of the bicuspid aortic valve. *Heart* **2000**, *83*, 81–85. [CrossRef] [PubMed]
27. Goldstone, A.B.; Chiu, P.; Woo, Y.J. Prosthesis Type for Aortic- and Mitral-Valve Replacement. *N. Engl. J. Med.* **2018**, *378*, 778–779. [PubMed]

28. Aicher, D.; Holz, A.; Feldner, S.; Kollner, V.; Schafers, H.J. Quality of life after aortic valve surgery: Replacement versus reconstruction. *J. Thorac. Cardiovasc. Surg.* **2011**, *142*, e19–e24. [CrossRef] [PubMed]
29. Panduranga, P.; Al-Mukhaini, M.; Al-Muslahi, M.; Haque, M.A.; Shehab, A. Management dilemmas in patients with mechanical heart valves and warfarin-induced major bleeding. *World J. Cardiol.* **2012**, *4*, 54–59. [CrossRef] [PubMed]

Journal of
Cardiovascular
Development and Disease

MDPI

Article

Asymptomatic Patients with Severe Aortic Stenosis and the Impact of Intervention

Mevlüt Çelik, Milan Milojevic, Andras P. Durko, Frans B. S. Oei, Edris A. F. Mahtab * and Ad J. J. C. Bogers

Department of Cardiothoracic Surgery, Erasmus University Medical Center,
3015 GD Rotterdam, The Netherlands; m.celik@erasmusmc.nl (M.Ç.); mln.milojevic@gmail.com (M.M.);
andras.durko@gmail.com (A.P.D.); f.oei@erasmusmc.nl (F.B.S.O.); a.j.j.c.bogers@erasmusmc.nl (A.J.J.C.B.)
* Correspondence: e.mahtab@erasmusmc.nl

Abstract: Objectives the exact timing of aortic valve replacement (AVR) in asymptomatic patients with severe aortic stenosis (AS) remains a matter of debate. Therefore, we described the natural history of asymptomatic patients with severe AS, and the effect of AVR on long-term survival. **Methods:** Asymptomatic patients who were found to have severe AS between June 2006 and May 2009 were included. Severe aortic stenosis was defined as peak aortic jet velocity Vmax $\geq$ 4.0 m/s or aortic valve area (AVA) $\leq$ 1 cm^2. Development of symptoms, the incidence of AVR, and all-cause mortality were assessed. **Results:** A total of 59 asymptomatic patients with severe AS were followed, with a mean follow-up of 8.9 $\pm$ 0.4 years. A total of 51 (86.4%) patients developed AS related symptoms, and subsequently 46 patients underwent AVR. The mean 1-year, 2-year, 5-year, and 10-year overall survival rates were higher in patients receiving AVR compared to those who did not undergo AVR during follow-up (100%, 93.5%, 89.1%, and 69.4%, versus 92.3%, 84.6%, 65.8%, and 28.2%, respectively; $p < 0.001$). Asymptomatic patients with severe AS receiving AVR during follow-up showed an incremental benefit in survival of up to 31.9 months compared to conservatively managed patients ($p = 0.002$). **Conclusions:** The majority of asymptomatic patients turn symptomatic during follow-up. AVR during follow-up is associated with better survival in asymptomatic severe AS patients.

Keywords: aortic valve replacement; aortic stenosis; asymptomatic; early surgery; watchful waiting

Citation: Çelik, M.; Milojevic, M.; Durko, A.P.; Oei, F.B.S.; Mahtab, E.A.F.; Bogers, A.J.J.C. Asymptomatic Patients with Severe Aortic Stenosis and the Impact of Intervention. *J. Cardiovasc. Dev. Dis.* **2021**, *8*, 35. https://doi.org/10.3390/jcdd8040035

Academic Editors: Monique R.M. Jongbloed and Robert Poelmann

Received: 26 February 2021
Accepted: 28 March 2021
Published: 31 March 2021

1. Introduction

Aortic stenosis (AS) is the most common valvular heart disease, with a prevalence of approximately 5% in adults above the age of 65 years [1]. The prevalence is expected to grow exponentially in the coming decades due to the aging population in developed countries [2]. Patients with symptomatic severe AS currently hold a class IB recommendation for surgical aortic valve replacement (SAVR) treatment, due to the dismal prognosis once symptoms are present [3,4]. Yet, up to 50% of the patients with severe AS report no symptoms at initial diagnosis [5].

Due to the low risk of sudden cardiac death, which is believed to be approximately 1%, a conservative approach is currently the treatment of choice in the asymptomatic population. New evidence challenges this belief, and the incidence of sudden death might be higher than previously expected [6]. In addition, the majority of these patients develop AS related symptoms and require intervention within the first 2 years of follow-up [7]. In the present study, we aimed to study the natural history of a cohort of consecutive asymptomatic patients with severe AS, and to evaluate the implications of aortic valve intervention (AVR) on long-term survival.

2. Methods

2.1. Patient Population

This retrospectively analyzed, prospective multicenter study enrolled asymptomatic adult (≥18 years) patients diagnosed with severe AS at seven Cardiology clinics in the Rotterdam area between June 2006 and May 2009. Patients were deemed asymptomatic if they had no cardiac symptoms at baseline visit (angina, shortness of breath, or syncope). In accordance with the European Society of Cardiology and American College of Cardiology/American Heart Association Guidelines for the Management of Patients With Valvular Heart Disease, severe AS was defined as aortic jet maximal velocity Vmax $\geq$ 4.0 m/s or aortic valve area (AVA) $\leq$ 1 cm^2 [8,9]. Patients had a normal left ventricular ejection fraction (≥50%). After inclusion in the present cohort, asymptomatic patients were invited for exercise testing at baseline. A positive exercise test was defined according to the ACC/AHA guidelines [10]. The study was approved by the medical ethics committee of the Erasmus University Medical Center, and patient informed consent was waived. All authors vouch for the validity of the data and adherence to the protocol.

2.2. Endpoints and Definitions

The primary endpoint was all-cause mortality. The secondary endpoints were the development of AS related symptoms and the need for AVR with either SAVR or transcatheter aortic valve implantation (TAVI). SAVR within 24 h of establishing the indication was classified as urgent.

2.3. Statistical Analysis

Discrete variables are presented as numbers, percentages, or proportions. Continuous variables are presented as means ± standard deviation, and presented as median with the interquartile range (IQR) if there was evidence of skewed data according to the Kolmogorov–Smirnov test. Discrete variables were compared with either the Chi Square test or the Fisher exact test, where appropriate. Continuous variables were compared with either the two-sample t-test or Wilcoxon rank-sum test, where appropriate.

Cumulative incidences were assessed using Kaplan–Meier curves to estimate the probability of: (i) symptom development, (ii) AVR, (iii) all-cause mortality in the overall cohort, and (iv) all-cause mortality in patients separated by whether they underwent AVR during follow-up. The incidence of AVR during follow-up was calculated and expressed as the number of AVRs per 1000 patient-years.

Predictors of (i) all-cause mortality and (ii) AVR were identified by a Cox proportional hazards model. Significant variables on univariable analyses were included in a multivariable Cox proportional hazards model. Furthermore, the restricted mean survival time at 10-years of follow-up was calculated to substantiate the overall treatment effect. Two-sided p-values < 0.05 were considered to be statistically significant. Data analyses were performed using SPSS 25.0 (SPSS Inc., Chicago, IL, USA) and R software, version 3.4 (R Foundation, Vienna, Austria).

3. Results

3.1. Baseline Characteristics

The final study population consisted of 59 asymptomatic patients with severe AS (Supplementary Materials, Figure S1). The mean age of the patients was 68.2 ± 10.7 years. Patients receiving AVR during follow-up were younger compared to patients with a conservative approach, 66.5 ± 10.6 versus 74.1 ± 8.9; $p = 0.022$, respectively. Asymptomatic patients with AVR during follow-up had a trend toward being female (30.4% versus 7.7%, $p = 0.096$) and had less diabetes mellitus (13.0% versus 46.2%, $p = 0.009$). No difference in baseline severity of AS was noted, based on AVA (0.85 ± 0.27 versus 0.80 ± 0.30, $p = 0.536$) and Vmax (4.23 ± 0.68 versus 4.28 ± 0.70, $p = 0.823$). Further baseline characteristics for the overall cohort and patients undergoing AVR and no AVR during follow-up are shown in Table 1.

Table 1. Baseline characteristics of the asymptomatic population.

	All (n = 59)	Conservative Treatment (n = 13)	AVR (n = 46)	p-Value
Age (years)	68.8 ± 10.6	74.1 ± 8.9	66.5 ± 10.6	0.022
Female	15 (25.4)	1 (7.7)	14 (30.4)	0.096
BMI	27.1 ± 3.7	27.5 ± 3.9	26.9 ± 3.7	0.661
BSA	1.93 ± 0.20	2.00 ± 0.12	1.91 ± 0.21	0.226
Previous CABG	2 (3.4)	0	2 (4.3)	0.444
Smoking	42 (71.2)	10 (76.9)	32 (69.6)	0.605
Atrial fibrillation	4 (7.0)	2 (15.4)	2 (4.5)	0.179
Carotid disease	1 (1.7)	1 (7.7)	0	0.058
Coronary artery disease	4 (6.8)	0	4 (8.7)	0.271
COPD	6 (10.2)	2 (15.4)	4 (8.7)	0.481
Diabetes	12 (20.3)	6 (46.2)	6 (13.0)	0.009
Hyperlipidemia	29 (49.2)	8 (61.5)	21 (45.7)	0.312
Hypertension	29 (49.2)	5 (38.5)	24 (52.2)	0.383
Myocardial infarction	4 (6.8)	0	4 (8.7)	0.271
Peripheral arterial disease	5 (8.5)	0	5 (10.9)	0.214
Stroke	12 (20.3)	3 (23.1)	9 (19.6)	0.781
NT-proBNP (pmol/l)	32.0 (18.0–97.0)	33.0 (12.8–149.3)	32.0 (18.0–89.0)	0.976
Baseline positive stress test	15 (25.4)	4 (30.8)	11 (24.4)	0.646
Logistic EuroSCORE	4.0 (2.1–6.9)	4.7 (3.2–8.1)	3.9 (2.1–5.5)	0.485
STS score	3.8 (2.0–6.0)	5.2 (2.2–8.6)	3.6 (2.0–5.0)	0.403
No medication	13 (22.0)	2 (15.4)	11 (23.9)	0.512
Diuretics	11 (18.6)	3 (23.1)	8 (17.4)	0.642
Ace Inhibitor	14 (23.7)	4 (30.8)	10 (21.7)	0.499
A2 antagonist	11 (18.6)	5 (38.5)	6 (13.0)	0.038
B blocker	15 (25.4)	1 (7.7)	14 (30.4)	0.096
Calcium antagonist	8 (13.6)	2 (15.4)	6 (13.0)	0.828
Digoxine	4 (6.8)	0	4 (8.7)	0.271
Echocardiographic Parameters				
Vmax (m/s)	4.24 ± 0.68	4.28 ± 0.70	4.23 ± 0.68	0.823
AVA (cm^2)	0.85 ± 0.28	0.80 ± 0.30	0.85 ± 0.27	0.536
iAVA (cm^2/m^2)	0.44 ± 0.15	0.41 ± 0.16	0.44 ± 0.14	0.423
MAG (mmHg)	42.8 ± 15.0	44.3 ± 17.4	42.3 ± 14.4	0.684
PAG (mmHg)	73.2 ± 23.6	75.3 ± 24.1	72.6 ± 23.7	0.720
AR grade I/II	29 (50.0)	6 (46.2)	23 (51.1)	0.753
MR grade I/II	12 (20.7)	4 (30.8)	8 (17.8)	0.308
LVEF	62.5 ± 5.9	61.1 ± 5.9	62.7 ± 5.7	0.374
LF/LG AS (%)	5 (8.5)	0	5 (10.9)	0.214
LVH (%)	14 (25.5)	2 (16.7)	12 (27.9)	0.429
TAPSE (mm)	25.1 ± 3.7	23.6 ± 2.8	25.5 ± 3.9	0.104

Table 1. *Cont.*

	All (n = 59)	Conservative Treatment (n = 13)	AVR (n = 46)	p-Value
LVEDD (mm)	49.0 ± 6.0	49.6 ± 5.1	25.5 ± 3.9	0.687
LVESD (mm)	31.4 ± 6.2	30.3 ± 5.7	31.7 ± 6.4	0.466
LVFS (%)	36.1 ± 8.8	38.6 ± 11.0	35.4 ± 8.1	0.248
LA (mm)	41.3 ± 6.4	42.2 ± 6.8	41.0 ± 6.3	0.563
IVSd (mm)	12.6 ± 2.7	12.5 ± 2.0	12.6 ± 2.9	0.834
IVCd (mm)	17.4 ± 3.6	16.4 ± 2.7	17.7 ± 3.8	0.252
PWd (mm)	10.8 ± 2.0	11.5 ± 1.7	10.7 ± 2.1	0.161
E′ (cm/s)	79.5 ± 23.6	69.1 ± 29.9	82.0 ± 21.4	0.103
A′ (cm/s)	89.9 ± 37.2	104.2 ± 59.9	86.0 ± 27.9	0.134
E′A′ ratio	1.0 ± 0.57	0.8 ± 0.5	1.1 ± 0.6	0.120
LVET (ms)	322.1 ± 32.2	312.6 ± 43.9	324.8 ± 28.4	0.296
DT (ms)	239.4 ± 63.3	217.5 ± 52.6	245.3 ± 65.2	0.198

Values are presented as mean ± SD or n (%). A′, peak velocity of diastolic mitral annular motion; AR, aortic regurgitation; AVA, aortic valve area; BMI, body mass index; BSA, body surface area; COPD, chronic obstructive pulmonary disease; DT, deceleration time; iAVA, indexed aortic valve area; E′, peak velocity of early diastolic mitral annular motion; E′A′ ratio, ratio of E′ to A′; IVCd, inferior vena cava dimension; IVSd, interventricular septum dimension; LA, left atrium; LF/LG AS, low-flow/low-grade AS; LVEDD, left ventricular end diastolic diameter; LVEF, left ventricular ejection fraction; LVESD, left ventricular end systolic diameter; LVET, left ventricular ejection time; LVFS, left ventricular fractional shortening; LVH, left ventricular hypertrophy; MAG, mean aortic gradient; MR, mitral regurgitation; PAD, peripheral arterial disease; PAG, peak aortic gradient; PWd, posterior wall dimension; TAPSE, tricuspid annular plane systolic excursion; Vmax, maximal velocity.

3.2. Natural Course of Asymptomatic Severe Stenosis

Forty-seven out of the 59 patients underwent an exercise stress test at baseline. Of these 47 patients, 15 (32%) tested positive and 32 (68%) patients tested negative. The other twelve patients were unable to undergo an exercise stress test. Nearly half of the patients had their symptoms unmasked by baseline exercise test or eventually developed symptoms within the first year after initial diagnosis (n = 26; 44%), but the vast majority of patients had symptoms (n = 51/59, 86.4%) before AVR or death (Figure 1). Mean time to symptom onset was 2.6 ± 0.4 years. During follow-up, 46 patients required AVR, of whom 11 (24.4%) had a positive exercise test at baseline. Three patients underwent TAVI. Eight patients died before undergoing AVR. Cumulative incidence of AVR was 13.6% and 91.4% at 1-year and 10-years, respectively (Figure 1). The linearized incidence rate of AVR was 95.5 per 1000 patient-years. Baseline characteristics of patients who did not undergo AVR according to survival status is shown in Table S1.

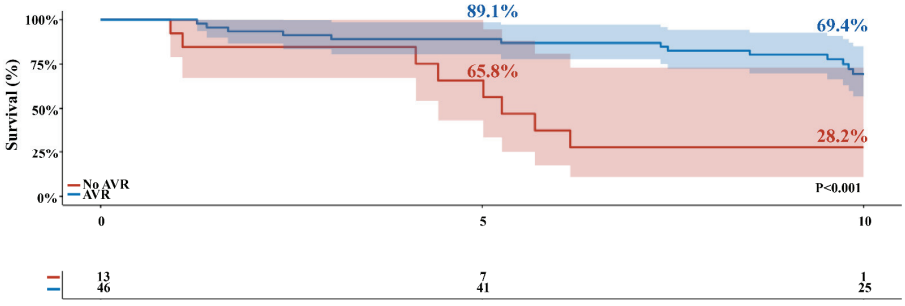

Figure 1. Survival during follow-up. Actual survival of asymptomatic patients according to having received AVR during follow-up. Blue line represents patients who underwent AVR during follow-up. Red line represents patients who did not undergo AVR during follow-up. Shaded region represents the 95% confidence interval. AVR, aortic valve replacement.

3.3. Survival

During the mean follow-up time of 8.9 ± 0.4 years, 35 patients (59.3%) died. Early (30-day) mortality after AVR occurred in 0 patients. The incidence of all-cause mortality was 38.9% at 10-years in the overall cohort (Figure 2C). The mean 1-year, 2-year, 5-year, and 10-year overall survival rates was higher in patients receiving AVR compared to conservatively managed patients (100%, 93.5%, 89.1%, and 69.4% versus 92.3%, 84.6%, 65.8%, and 28.2% respectively; $p < 0.001$) (Figure 2). Patients receiving AVR during follow-up had a 31.9-month survival benefit over 10 years of follow-up (95% confidence interval (CI): 13.27–58.44, $p = 0.002$) compared to conservatively managed patients (Table 2).

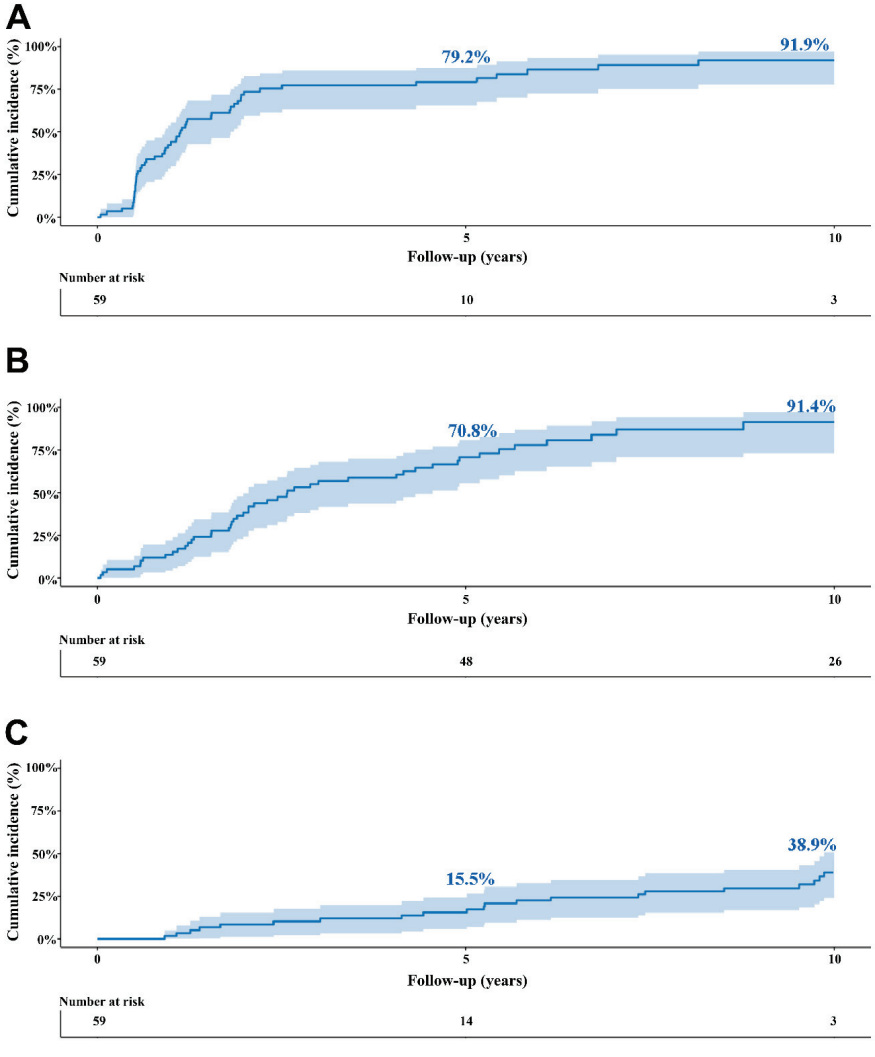

Figure 2. Cumulative incidence rates in the overall cohort. (**A**) symptom development, (**B**) aortic valve replacement (either surgical or transcatheter), and (**C**) all-cause mortality. Shaded region represents the 95% confidence interval.

Table 2. Between-group differences in mortality among treatment strategies (conservative versus AVR).

Overall Cohort			
Restricted Mean Survival Time at 10 Years		**95% CI**	***p*-Value**
Difference—months	31.85	13.27–58.44	0.002
Ratio	1.51	1.11–2.05	0.008
Ratio of restricted mean time lost	0.28	0.13–0.60	0.001

AVR, aortic valve replacement; CI, confidence interval.

3.4. Predictors of Outcome

In univariable analyses, being older (HR 1.11, 95% CI 1.06–1.17), having higher NT-proBNP levels (HR 1.002, 95% CI 1.001–1.004), having diabetes mellitus (HR = 4.57, 95% CI 1.91–10.96), atrial fibrillation (HR 4.98, 95% CI 1.40–17.72), and AVR during follow-up (HR 0.24, 95% CI 0.10–0.58) were predictors of all-cause mortality (Table 3). Age remained the only predictor after multivariable analysis (HR 1.08, 1.01–1.16, $p = 0.026$). Univariate predictors of AVR in asymptomatic patients are shown in Table S2.

Table 3. Predictors of all-cause mortality in the overall cohort during follow-up.

	Univariable HR (95% CI), *p*-Value	**Multivariable HR (95% CI), *p*-Value**
Age	1.11 (1.06–1.17), $p < 0.001$	1.08 (1.01–1.16), $p = 0.026$
Gender (female)	0.43 (0.16–1.37), $p = 0.125$	
Atrial fibrillation	4.98 (1.40–17.72), $p = 0.013$	3.10 (0.68–14.26), $p = 0.146$
Coronary artery disease	0.62 (0.08–4.59), $p = 0.639$	
COPD	1.60 (0.48–5.39), $p = 0.446$	
Diabetes mellitus	4.57 (1.91–10.96), $p < 0.001$	2.36 (0.87–6.44), $p = 0.094$
Hyperlipidemia	1.65 (0.72–3.78), $p = 0.234$	
Hypertension	1.50 (0.66–3.37), $p = 0.332$	
Myocardial infarction	1.14 (0.27–4.86), $p = 0.862$	
Peripheral arterial disease	1.58 (0.46–5.34), $p = 0.466$	
Stroke	2.11 (0.90–4.92), $p = 0.086$	
Exercise test (positive)	0.74 (0.27–1.98) $p = 0.543$	
NT-proBNP	1.002 (1.001–1.004) $p < 0.001$	1.002 (1.00–1.003), $p = 0.053$
STS score	1.06 (0.99–1.14), $p = 0.098$	
Logistic EuroSCORE	1.22 (1.09–1.35), $p < 0.001$	0.98 (0.81–1.18), $p = 0.830$
AVR	0.24 (0.10–0.58) $p = 0.002$	1.17 (0.31–4.36), $p = 0.820$
LVEF	0.96 (0.90–1.04), $p = 0.315$	
Vmax	0.95 (0.53–1.70), $p = 0.851$	
AVA	0.19 (0.03–1.11), $p = 0.065$	
iAVA	0.05 (0.00–1.141), $p = 0.078$	
MAG	1.01 (0.99–1.03), $p = 0.460$	
PAG	1.00 (0.98–1.10), $p = 0.817$	

AVA, aortic valve area; AVR, aortic valve replacement; COPD: chronic obstructive pulmonary disease; iAVA, indexed aortic valve area; LVEF, left ventricular ejection fraction; MAG, mean aortic gradient; PAG, peak aortic gradient; STS, Society of Thoracic Surgery; Vmax, maximal jet velocity.

4. Discussion

This study describes the natural history of asymptomatic patients with severe AS and the impact of intervention in this patient population. We found that (i) the majority of the patients eventually develop AS related symptoms, (ii) subsequently requiring AVR, and that (iii) patients who received AVR had a survival benefit of close to three years compared to conservatively managed patients.

Adriana C. Gittenberger-de Groot and her team have performed an extensive number of indispensable studies on the spectrum of aortic valvular disease over the past decades, including histopathological, anatomical, and developmental studies on animal, as well as human, tissue [10].

The majority of asymptomatic patients developed symptoms within the first 3 years after initial diagnosis [11], with up to 86.4% at 10-years in our cohort. The asymptomatic patient might be "falsely" labelled as asymptomatic. In our cohort 79.7% underwent exercise stress testing at baseline, of whom 31.9% of the patients had a positive test. Abnormal exercise test is associated with impaired 2-year event-free survival [12–14], and is a clear indication of AVR [3,4]; especially in elderly patients who are subconsciously adapting their exercise to their tolerance and underrepresent their symptoms. It is still concerning that relatively few asymptomatic patients in practice undergo routine stress testing [15]. Several difficulties with exercise testing exist in the elderly population, including (1) its lower predictive value compared to a younger population, (2) limited exercise capability in the elderly due to non-cardiac conditions limiting mobility, and (3) the differences in exercise protocol and definition of an abnormal exercise test [16,17]. The relevancy and accuracy of exercise testing is therefore still a debated topic.

The majority of the asymptomatic population with severe AS who develop symptoms underwent AVR (91.4%). Our rate was higher in comparison with earlier reports, wherein approximately 57% of the patients underwent AVR at 10-years of follow-up [11]. This discrepancy could be caused by the recommendation of the physician. The current asymptomatic patient with severe AS does not have a formal indication for intervention, unless the patient has (1) depressed LVEF, or (2) is undergoing concomitant cardiac surgery [3,4]. Yet, it is expected that the degree of AS will gradually increase, and the initially asymptomatic patient eventually will develop symptoms due to disease progression, and subsequently requiring the guideline recommended AVR. The upfront gain obtained by delaying surgery might not outweigh the risk of AVR being delayed with conservative treatment. This is especially the case in patients who are older, and subsequently have increased operative risk [18]. In those patients the long-term hemodynamic consequences might outweigh the positive outcomes of an early interventional strategy [19,20].

Asymptomatic patients with severe AS undergoing AVR during follow-up had better survival compared to conservatively managed patients. In the first randomized controlled trial, a total of 145 asymptomatic patients with very severe AS were randomized to early surgery (n = 73) and conservative care (n = 72) [21]. Early surgery resulted in improved survival at 8-years of follow-up compared to patients treated with a conservative approach (90% versus 74%, p = 0.003, respectively). However, this study only provides a perspective on patients with very severe AS. Initial data in asymptomatic patients with severe AS on all-cause mortality at 5-year from the CURRENT AS registry indicate a survival benefit for patients undergoing surgery within 3-months compared to conservative treatment, 26.4% vs. 15.4%; p = 0.009, respectively [20]. While a pre-emptive strategy seems superior in those with (very) severe AS [21], the exact timing and benefit of AVR in asymptomatic patients with severe AS remains to be defined. The exact timing may be refined with improvements in imaging modalities. Measuring the aortic valve calcium score through computed tomography has emerged as a strategy to assess the severity and progression of aortic stenosis, especially in asymptomatic patients with echocardiographic discordance [22]. With the advent of TAVI, conservative treatment is a solution that almost nobody still considers. The role of minimally invasive techniques and imaging modalities in the asymptomatic cohort with severe AS will need to be substantiated in the future (NCT03094143 and NCT03042104, Table S3).

5. Limitations

Several limitations need to be acknowledged. First, this is an retrospective study, with the inherent shortcomings. Second, the number of patients and subsequent events was relatively low, with shortcomings related to overfitting of multivariable analyses. Given the fact that patients were not randomized into early surgical management and conservative treatment, potential selection bias cannot be eliminated, wherein an older patient was less likely to undergo AVR, as the indication for treatment was left to the discretion of the treating physician.

6. Conclusions

The vast majority of asymptomatic patients with severe AS develop symptoms during follow-up and subsequently require intervention. Intervention during follow-up is associated with better long-term survival, and early intervention is likely to improve survival. Close clinical follow-up is warranted for all patients, and pre-emptive elective aortic valve procedures may be considered in selected elderly patients at low procedural risk. Further results from the currently ongoing clinical trials will give us more insight into the role of early intervention in asymptomatic patients with severe AS.

Supplementary Materials: The following are available online at https://www.mdpi.com/article/10.3390/jcdd8040035/s1, Figure S1. Flowchart of the patients during follow-up. A total of 59 asymptomatic patients with severe AS were included. Total of 51 patients did develop symptoms and 8 did not. Of whom who did develop symptoms underwent 42 AVR, and 15 patients died after AVR. Of whom who did not develop symptoms 3 underwent AVR, and 1 died after AVR. Five patients died after symptoms without undergoing AVR. Four patients died with no symptoms without undergoing AVR.

Author Contributions: Conceptualization, M.Ç. and A.J.J.C.B.; methodology, M.Ç. and A.J.J.C.B.; formal analysis, M.Ç., M.M. and A.J.J.C.B.; investigation, M.Ç., M.M., A.P.D., F.B.S.O., E.A.F.M. and A.J.J.C.B.; writing—original draft preparation, M.Ç., E.A.F.M., and A.J.J.C.B.; writing—review and editing, M.Ç., M.M., A.P.D., F.B.S.O., E.A.F.M. and A.J.J.C.B.; visualization, M.Ç., M.M., A.P.D., F.B.S.O., E.A.F.M. and A.J.J.C.B.; supervision, A.J.J.C.B.; All authors have read and agreed to the published version of the manuscript.

Funding: This research received no external funding.

Institutional Review Board Statement: This study was approved by the Institutional Review Board of the Erasmus Medical Center.

Informed Consent Statement: Patient informed consent was waived.

Data Availability Statement: Not applicable.

Conflicts of Interest: The authors declare no conflict of interest.

Abbreviations

A′	peak velocity of diastolic mitral annular motion
AR	aortic regurgitation
AS	aortic stenosis
AVA	aortic valve area
AVR	aortic valve replacement
BMI	body mass index
BSA	body surface area
CI	confidence interval
COPD	chronic obstructive pulmonary disease
E′	peak velocity of early diastolic mitral annular motion
E′A′ ratio	ratio of E′ to A
EuroSCORE	European system for cardiac operative risk evaluation
HR	hazard ratio
iAVA	indexed aortic valve area
IVCd	inferior vena cava dimension
IVSd	interventricular septum dimension
LA	left atrium
LF/LG AS	low-flow/low-grade AS
LVEDD	left ventricular end diastolic diameter
LVEF	left ventricular ejection fraction
LVET	left ventricular ejection time

LVESD	left ventricular end systolic diameter
LVFS	left ventricular fractional shortening
LVH	left ventricular hypertrophy
MAG	mean aortic gradient
MR	mitral regurgitation
PAD	peripheral arterial disease
PAG	peak aortic gradient
PWd	posterior wall dimension
RCT	randomized controlled trial
SAVR	surgical aortic valve replacement
STS	society of thoracic surgery
TAPSE	tricuspid annular plane systolic excursion
TAVI	transcatheter aortic valve implantation
Vmax	maximal velocity

References

1. Go, A.S.; Mozaffarian, D.; Roger, V.L.; Benjamin, E.J.; Berry, J.D.; Blaha, M.J.; Dai, S.; Ford, E.S.; Fox, C.S.; Franco, S.; et al. Heart Disease and Stroke Statistics—2014 Update: A Report from the American Heart Association. *Circulation* **2013**, *129*, e28–e292. [CrossRef] [PubMed]
2. Nkomo, V.T.; Gardin, J.M.; Skelton, T.N.; Gottdiener, J.S.; Scott, C.G.; Enriquez-Sarano, M. Burden of valvular heart diseases: A population-based study. *Lancet* **2006**, *368*, 1005–1011. [CrossRef]
3. Baumgartner, H.; Falk, V.; Bax, J.J.; De Bonis, M.; Hamm, C.; Holm, P.J.; Iung, B.; Lancellotti, P.; Lansac, E.; Muñoz, D.R.; et al. 2017 ESC/EACTS Guidelines for the management of valvular heart disease. *Eur. Heart J.* **2017**, *38*, 2739–2791. [CrossRef] [PubMed]
4. Nishimura, R.A.; Otto, C.M.; Bonow, R.O.; Carabello, B.A.; Erwin, J.P.; Fleisher, L.A.; Jneid, H.; Mack, M.J.; McLeod, C.J.; O'Gara, P.T.; et al. 2017 AHA/ACC Focused Update of the 2014 AHA/ACC Guideline for the Management of Patients with Valvular Heart Disease: A Report of the American College of Cardiology/American Heart Association Task Force on Clinical Practice Guidelines. *Circulation* **2017**, *135*, e1159–e1195. [CrossRef] [PubMed]
5. Généreux, P.; Stone, G.W.; O'Gara, P.T.; Marquis-Gravel, G.; Redfors, B.; Giustino, G.; Pibarot, P.; Bax, J.J.; Bonow, R.O.; Leon, M.B. Natural History, Diagnostic Approaches, and Therapeutic Strategies for Patients with Asymptomatic Severe Aortic Stenosis. *J. Am. Coll. Cardiol.* **2016**, *67*, 2263–2288. [CrossRef]
6. Taniguchi, T.; Morimoto, T.; Shiomi, H.; Ando, K.; Kanamori, N.; Murata, K.; Kitai, T.; Kawase, Y.; Izumi, C.; Kato, T.; et al. Sudden Death in Patients with Severe Aortic Stenosis: Observations from the CURRENT AS Registry. *J. Am. Heart Assoc.* **2018**, *7*. [CrossRef]
7. Heuvelman, H.J.; Van Geldorp, M.W.A.; Kappetein, A.P.; Geleijnse, M.L.; Galema, T.W.; Bogers, A.J.J.C.; Takkenberg, J.J.M. Clinical course of patients diagnosed with severe aortic stenosis in the Rotterdam area: Insights from the AVARIJN study. *Neth. Heart J.* **2012**, *20*, 487–493. [CrossRef]
8. Bonow, R.O.; Carabello, B.A.; Kanu, C.; de Leon, A.C.; Faxon, D.P.; Freed, M.D.; Gaasch, W.H.; Lytle, B.W.; Nishimura, R.A.; O'Gara, P.T.; et al. ACC/AHA 2006 guidelines for the management of patients with valvular heart disease: A report of the American College of Cardiology/American Heart Association Task Force on Practice Guidelines (writing committee to revise the 1998 Guidelines for the Management of Patients With Valvular Heart Disease): Developed in collaboration with the Society of Cardiovascular Anesthesiologists: Endorsed by the Society for Cardiovascular Angiography and Interventions and the Society of Thoracic Surgeons. *Circulation* **2006**, *114*, e84–e231.
9. Vahanian, A.; Baumgartner, H.; Bax, J.; Butchart, E.; Dion, R.; Filippatos, G.; Flachskampf, F.; Hall, R.; Iung, B.; Kasprzak, J.; et al. Guidelines on the management of valvular heart disease: The Task Force on the Management of Valvular Heart Disease of the European Society of Cardiology. *Eur. Heart J.* **2006**, *28*, 230–268. [CrossRef]
10. Gibbons, R.J. ACC/AHA 2002 Guideline Update for Exercise Testing: Summary Article: A Report of the American College of Cardiology/American Heart Association Task Force on Practice Guidelines (Committee to Update the 1997 Exercise Testing Guidelines). *Circulation* **2002**, *106*, 1883–1892.
11. Pellikka, P.A.; Sarano, M.E.; Nishimura, R.A.; Malouf, J.F.; Bailey, K.R.; Scott, C.G.; Barnes, M.E.; Tajik, A.J. Outcome of 622 Adults with Asymptomatic, Hemodynamically Significant Aortic Stenosis During Prolonged Follow-Up. *Circulation* **2005**, *111*, 3290–3295. [CrossRef] [PubMed]
12. Lancellotti, P.; Lebois, F.; Simon, M.; Tombeux, C.; Chauvel, C.; Pierard, L.A. Prognostic importance of quantitative exercise Doppler echocardiography in asymptomatic valvular aortic stenosis. *Circulation* **2005**, *112*, I377–I382. [PubMed]
13. Peidro, R.; Brión, G.; Angelino, A. Exercise Testing in Asymptomatic Aortic Stenosis. *Cardiology* **2006**, *108*, 258–264. [CrossRef] [PubMed]
14. Rafique, A.M.; Biner, S.; Ray, I.; Forrester, J.S.; Tolstrup, K.; Siegel, R.J. Meta-Analysis of Prognostic Value of Stress Testing in Patients with Asymptomatic Severe Aortic Stenosis. *Am. J. Cardiol.* **2009**, *104*, 972–977. [CrossRef]

15. Iung, B.; Baron, G.; Butchart, E.G.; Delahaye, F.; Gohlke-Bärwolf, C.; Levang, O.W.; Tornos, P.; Vanoverschelde, J.-L.; Vermeer, F.; Boersma, E.; et al. A prospective survey of patients with valvular heart disease in Europe: The Euro Heart Survey on Valvular Heart Disease. *Eur. Heart J.* **2003**, *24*, 1231–1243. [CrossRef]
16. Das, P.; Rimington, H.; Chambers, J. Exercise testing to stratify risk in aortic stenosis. *Eur. Heart J.* **2005**, *26*, 1309–1313. [CrossRef]
17. Redfors, B.; Pibarot, P.; Gillam, L.D.; Burkhoff, D.; Bax, J.J.; Lindman, B.R.; Bonow, R.O.; O'Gara, P.T.; Leon, M.B.; Généreux, P. Stress Testing in Asymptomatic Aortic Stenosis. *Circulation* **2017**, *135*, 1956–1976. [CrossRef]
18. Hussain, A.I.; Auensen, A.; Brunborg, C.; Beitnes, J.O.; Gullestad, L.; Pettersen, K.I. Age-dependent morbidity and mortality outcomes after surgical aortic valve replacement. *Interact. Cardiovasc. Thorac. Surg.* **2018**, *27*, 650–656. [CrossRef]
19. Everett, R.J.; Clavel, M.-A.; Pibarot, P.; Dweck, M.R. Timing of intervention in aortic stenosis: A review of current and future strategies. *Heart* **2018**, *104*, 2067–2076. [CrossRef]
20. Taniguchi, T.; Morimoto, T.; Shiomi, H.; Ando, K.; Kanamori, N.; Murata, K.; Kitai, T.; Kawase, Y.; Izumi, C.; Miyake, M.; et al. Initial Surgical Versus Conservative Strategies in Patients with Asymptomatic Severe Aortic Stenosis. *J. Am. Coll. Cardiol.* **2015**, *66*, 2827–2838. [CrossRef]
21. Kang, D.-H.; Park, S.-J.; Lee, S.-A.; Lee, S.; Kim, D.-H.; Kim, H.-K.; Yun, S.-C.; Hong, G.-R.; Song, J.-M.; Chung, C.-H.; et al. Early Surgery or Conservative Care for Asymptomatic Aortic Stenosis. *N. Engl. J. Med.* **2020**, *382*, 111–119. [CrossRef] [PubMed]
22. Park, S.-J.; Dweck, M.R. Multimodality Imaging for the Assessment of Severe Aortic Stenosis. *J. Cardiovasc. Imaging* **2019**, *27*, 235–246. [CrossRef] [PubMed]

Journal of
Cardiovascular
Development and Disease

MDPI

Article

A Systematic Histopathologic Evaluation of Type-A Aortic Dissections Implies a Uniform Multiple-Hit Causation

Nimrat Grewal [1,2,*,†], Bart J. J. Velders [1,†], Adriana C. Gittenberger-de Groot [2,3], Robert Poelmann [4], Robert J. M. Klautz [1], Thomas J. Van Brakel [1] and Jan H. N. Lindeman [5]

[1] Department of Cardiothoracic Surgery, Leiden University Medical Center, 2333 ZA Leiden, The Netherlands; b.j.j.velders@lumc.nl (B.J.J.V.); r.j.m.klautz@lumc.nl (R.J.M.K.); t.j.van_brakel@lumc.nl (T.J.V.B.)
[2] Department of Anatomy and Embryology, Leiden University Medical Center, 2333 ZA Leiden, The Netherlands; a.c.gitten@lumc.nl
[3] Department of Cardiology, Leiden University Medical Center, 2333 ZA Leiden, The Netherlands
[4] Institute of Biology, Animal Sciences and Health, Leiden University, 2333 BE Leiden, The Netherlands; R.E.Poelmann@lumc.nl
[5] Department of Vascular Surgery, Leiden University Medical Center, 2333 ZA Leiden, The Netherlands; J.H.N.lindeman@lumc.nl
* Correspondence: N.Grewal@lumc.nl; Tel.: +31-715264022
† Both authors contributed equally to this manuscript.

Abstract: (1) Background: The pathophysiologic basis of an acute type A aortic dissection (TAAD) is largely unknown. In an effort to evaluate vessel wall defects, we systematically studied aortic specimens in TAAD patients. (2) Methods: Ascending aortic wall specimens (n = 58, mean age 63 years) with TAAD were collected. Autopsy tissues (n = 17, mean age 63 years) served as controls. All sections were studied histopathologically. (3) Results: Pathomorphology in TAAD showed predominantly moderate elastic fiber fragmentation/loss, elastic fiber thinning, elastic fiber degeneration, mucoid extracellular matrix accumulation, smooth muscle cell nuclei loss, and overall medial degeneration. The control group showed significantly fewer signs of those histopathological features (none-mild, p = 0.00). It was concluded that the dissection plane consistently coincides with the vasa vasorum network, and that TAAD associates with a significantly thinner intimal layer p = 0.005). (4) Conclusions: On the basis of the systematic evaluation and the consistent presence of diffuse, pre-existing medial defects, we hypothesize that TAAD relates to a developmental defect of the ascending aorta and is caused by a triple-hit mechanism that involves (I) an intimal tear; and (II) a diseased media, which allows (III) propagation of the tear towards the plane of the vasa vasorum where the dissection further progresses.

Keywords: acute aortic syndrome; cardiovascular disease; aorta

Citation: Grewal, N.; Velders, B.J.J.; Gittenberger-de Groot, A.C.; Poelmann, R.; Klautz, R.J.M.; Van Brakel, T.J.; Lindeman, J.H.N. A Systematic Histopathologic Evaluation of Type-A Aortic Dissections Implies a Uniform Multiple-Hit Causation. *J. Cardiovasc. Dev. Dis.* **2021**, *8*, 12. https://doi.org/10.3390/jcdd8020012

Received: 19 December 2020
Accepted: 22 January 2021
Published: 27 January 2021

1. Introduction

An acute aortic dissection is a medical catastrophe [1] with an estimated mortality of 26% in patients undergoing acute surgery and up to 58% in patients not receiving surgical treatment [2]. Reported incidences of an aortic dissection vary between 3 and 9 per 100,000 person-years [1–4], but with an aging population further increases are anticipated for the future.

An aortic dissection is hallmarked by a tear in the intimal layer, which allows blood to access the middle layer of the wall, causing the vascular layers to separate (dissect) from one another, resulting in formation of a ''false" lumen. One or multiple re-entry tears down- or upstream allow flow in the false lumen. Pressure build-up in the false lumen may result in compression of the aortic side branches. Depending on the degree of occlusion, and the side branches involved, this may result in life-threatening ischemia.

The large majority of dissections are continuous with the actual arterial lumen via one or more intimal ''entry tears", yet some dissections may present without an apparent

continuity with the actual lumen [1]. Based on their location and extent, an aortic dissection is classified as Stanford type-A (TAAD) dissections (dissections involving the aortic root and/or ascending aorta, which can propagate to the aortic arch and further into the descending aorta), and type-B dissections (dissections that do not involve the ascending aorta) [5]. The focus of this study is on TAAD.

The pathophysiologic basis of TAAD is poorly understood. Although the disease is associated with hypertension [1–3], the great majority of patients with hypertension will not develop a dissection. Observed associations between sporadic TAAD and genetic disorders that associate with structural aortic defects such as Marfan-, Ehlos-Danlos-, and Turner's syndrome [1,3] imply impaired aortic wall integrity as a predisposing factor for TAAD.

A role for (an) underlying aortic defect(s) as predisposing factor for TAAD is further supported by a number of histological evaluations [6–8]. Unfortunately, while diffuse medial defects are consistently reported in the literature, the published studies are extremely heterogeneous with respect to the histopathological descriptions and the nomenclature used [9]. Moreover, most evaluations so far are based on conventional Haematoxylin and Eosin (H&E) staining, a staining that while highly useful for obtaining a gross overview of cell shape and cellular density lacks the level of information required for the appreciation of putative matrix defects.

With the aim of harmonizing the histomorphological characterization of degenerative vascular pathologies, the Society for Cardiovascular Pathology along with the Association for European Cardiovascular Pathology recently issued a consensus statements with an unambiguous nomenclature [9]. This nomenclature allows for a systematic and uniform description of the histomorphology of non-inflammatory degenerative vascular pathologies [9]. In order to systematically map and describe putative aortic wall defects in TAAD, we now applied the consensus scoring and nomenclature on histological sections of 58 successive TAAD patients that underwent ascending aortic replacement for a type-A dissection. In order to optimally map putative matrix defects, H&E staining was combined with MOVAT pentachrome and Resorcin Fuchsin (elastin) stainings.

2. Materials and Methods

2.1. Ethics

Our study complies with the Declaration of Helsinki. Approval for this study was granted by the Medial Ethical Committee of Leiden University Medical Center (LUMC), Leiden. All control specimens were obtained post mortem. Obduction has been performed according the guidelines of the pathology department. Tissue collection was performed according to the regulations and protocols for secondary tissue use of the dept. of pathology at the Leiden University Medical Center. We have obtained permission to include the specimens in our study and obduction.

2.2. Patients and Tissue Samples

Ascending aortic wall samples were obtained from the aortotomy site as residual aortic wall material during an ascending aortic replacement in patients with acute TAAD. Seventeen control aortas were obtained during post-mortem autopsies. The wall samples were formalin-fixed, decalcified using Kristensens solution, and paraffin-embedded.

Successive 4 μm sections were, respectively, Haematoxylin-Eosin (HE)-, Resorcin-Fuchsin (RF)-, and MOVAT-pentachrome-stained. Vasa vasorum were visualized by CD31 staining (M0823, Agilent, Amsterdam, the Netherlands), 1/1000 after Tris EDTA (0.01 M, pH 8) heat retrieval. The anti-mouse Envision+ System HRP (K4007, Agilent) and DAB solution (K3468, Agilent) were used for visualization.

2.3. Morphology

Histomorphological grading was performed according to the consensus classification for degenerative aorta pathology [9]. Elastic fiber fragmentation/loss, elastic fiber thinning,

elastic fiber disorganisation, mucoid extracellular matrix accumulation, smooth muscle cell nuclei loss, and overall medial degeneration were described as none (0), mild (1), moderate (2), or severe (3). Standard H&E staining was used to examine smooth muscle cell nuclei loss; elastic fiber fragmentation/loss, elastic fiber thinning, and elastic fiber disorganisation were graded by RF staining, and mucoid extracellular matrix accumulation and medial degeneration were scored in the MOVAT pentachrome staining. Scoring was performed by two independent researchers. Inter-observer variation was estimated with Cohen's kappa coefficient [10]. Excellent (>0.8) Cohen's kappas [10] were observed for all parameters (Table 1).

Table 1. Morphological aspects included in the Pathology Consensus Score with the calculated kappa coefficient.

Morphological Feature	Kappa
Elastic fiber fragmentation/Loss	0.915
Elastic fiber thinning	0.880
Elastic fiber degeneration	0.801
Mucoid extra cellular matrix accumulation	0.938
Smooth muscle cell nuclei loss	0.978
Overall medial degeneration	0.879

2.4. Anatomical Location of Dissection Plane

The relative position of the dissection plane in the media was estimated as the ratio of the distance from the first major internal elastic lamella (lamina elastica interna) to the dissection plane over the full medial thickness (i.e., inner to outer elastic lamina (lamina elastica externa) (Figure 1). For the relative position of the vasa vasorum, the ratio of the distance from the lamina elastica interna to the vasa vasorum and the full medial thickness were calculated (Figure 2). Distance ratios were assessed for three different fields using Philips Standalone Viewer software (Philips, Eindhoven, The Netherlands), and the average relative position was used.

2.5. Statistical Analysis

Statistical analysis was performed using the IBM SPSS statistics software, version 26. Chi-square test was used to compare the morphology between the dissection and the control group. Independent samples *t*-test was used to compare the ratio of the dissection plane to ratio of the vasa vasorum plexus.

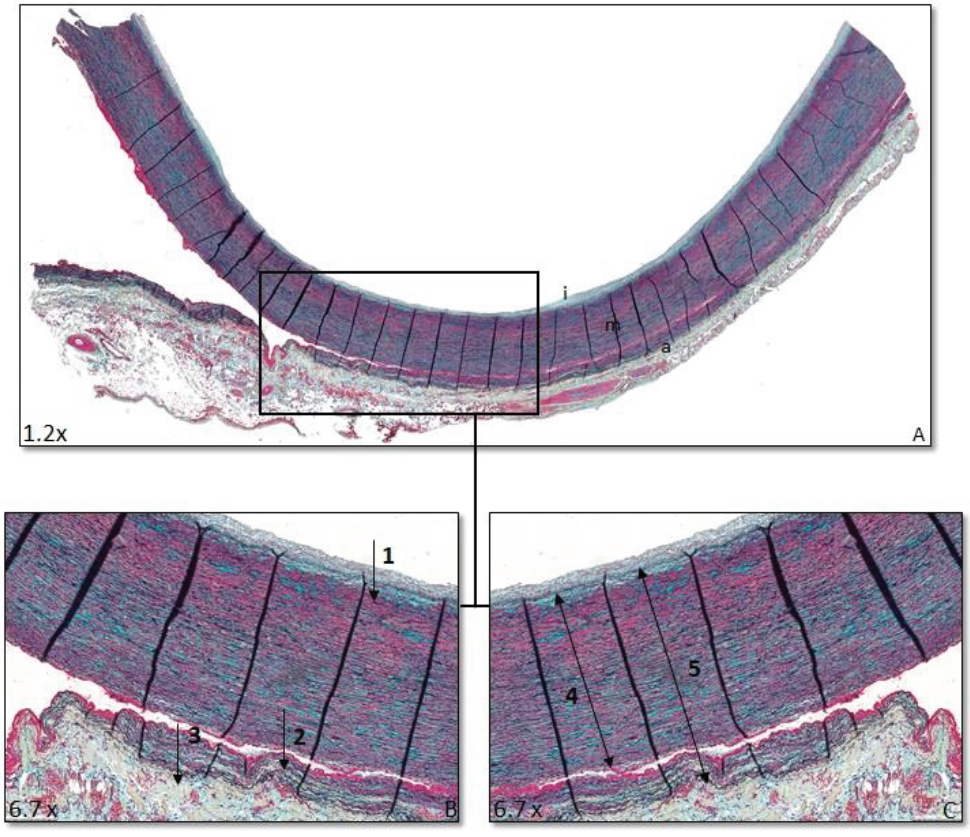

Figure 1. Ratio dissection plane. Transverse histologic sections of the ascending aorta 4 μm stained with MOVAT pentachrome staining. (**A**) Overview ascending aorta I = intima, m = media, a = adventitia. (**B**) 1: Lamina elastica interna (LEI), 2: dissection plane (DP), and 3: lamina elastica externa (LEE). (**C**) 4: Distance between LEI and DP, 5: distance between LEI and LEE. Ratio dissection plane is defined as distance 4 divided by distance 5.

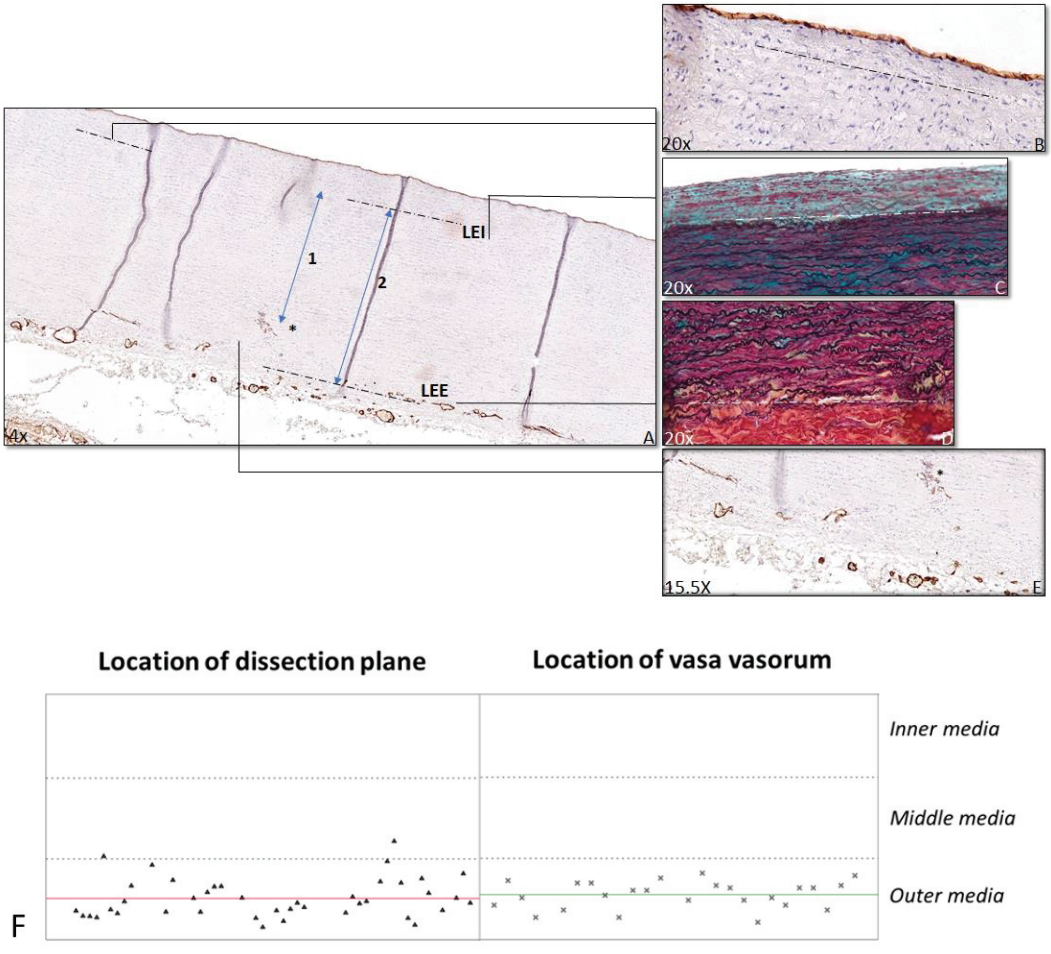

Figure 2. Ratio vasa vasorum. Transverse histologic sections 4 μm stained for CD31 (**A**,**B**,**E**) and MOVAT (**C**,**D**) in a control patient (**A**–**E**). **A** shows an overview of the ascending aorta, with the dashed lines indicating the lamina elastica interna (LEI), with a detailed view of the LEI in **B** in a CD31 stained section and in **C** in a MOVAT stained section. The second dashed line (**A**) indicates the lamina elastica externa (LEE), with a detailed view in the MOVAT stained section (**D**). The asterisk indicates the nearest vasa vasorum (**A**,**E**). The ratio of the vasa vasorum is calculated by dividing the distance between LEI and nearest vasa vasorum (indicated by 1 in **A**) by the distance between LEI and LEE (indicated by 2 in **A**). The location of the dissection plane is shown on the left and the vasa vasorum on the right in graph **F**. Each triangle and asterisk (**F**) represents one TAAD patient. The red line represents the median location of the dissection plane, and the green line represents the median location of vasa vasorum. The dashed lines are the borders between the inner, middle, and outer media.

3. Results

3.1. Patient Characteristics

This study includes 58 successive TAAD patients and 17 control patients. Baseline characteristics of the patients are shown in Table 2.

Table 2. Baseline characteristics.

Variable	Type A Aortic Dissection Group n = 58	Control Group n = 17
Age, years	63 ± 10.36	63 ± 5.46
Gender		
- Female	- 26 (45%)	- 9 (53%)
- Male	- 31 (53%)	- 8 (47%)
- Unknown	- 1 (2%)	- 0 (0%)
Arterial hypertension		
- Yes	- 28 (48%)	- 5 (29%)
- No	- 29 (50%)	- 5 (29%)
- Unknown	- 1 (2%)	- 7 (42%)
Peripheral arterial disease		
- Yes	- 0 (0%)	- 0 (0%)
- No	- 57 (98%)	- 0 (0%)
- Unknown	- 1 (2%)	- 17 (100%)
Valve Morphology		
- Tricuspid aortic valve	- 52 (90%)	- 17 (100%)
- Bicuspid aortic valve	- 4 (7%)	- 0 (0%)
- Unknown	- 2 (3%)	- 0 (0%)
Connective tissue disorder		
- Marfan syndrome	- 2 (4%)	- 0 (0%)
Diabetes Mellitus		
- Yes	- 1 (2%)	- 1 (6%)
- No	- 57 (98%)	- 9 (53%)
- Unknown	- 0 (0%)	- 7 (41%)

3.2. Histopathology of the Vascular Wall

Putative aortic wall abnormalities in TAAD were mapped according to the revised, consensus nomenclature for noninflammatory, degenerative aortic histopathologies [9]. Conclusions for this systematic evaluation of TAAD wall and control aorta are summarized in Table 3 and Figure 3. While all degenerative aspects covered in the consensus classification were classified moderately severe in TAAD, in the control group predominantly mild degenerative aspects were observed, with a significant difference between both groups (Table 3) (Figure 3). After excluding the BAV and MFS patients from the TAAD group, the observed differences remained significant.

Wall thicknesses in TAAD and control were similar, but the intimal thickness was consistently less in the TAAD group (mean thickness 131 ± 122 µm (mean ± sd) vs. 193 ± 132 µm (mean ± sd) in the control group (p = 0.044) (Figure 4). Intimal thickness of the 6 patients with Marfan syndrome or BAV disease included in this study was 47 ± 29 µm (mean ± sd). After excluding the BAV and MFS patients from the TAAD group, the intima was still significantly thinner than in the control group.

Table 3. Histomorphological features in the aortic dissection and control group.

Morphological Feature	Score	Type A Aortic Dissection Group N (%)	Control Group N (%)	*p*-Value
Elastic fiber fragmentation/loss	- None	- 0 (0)	- 2 (12)	0.000
	- Mild	- 19 (33)	- 14 (82)	
	- Moderate	- 29 (50)	- 1 (6)	
	- Severe	- 10 (17)	- 0 (0)	
Elastic fiber thinning	- None	- 0 (0)	- 2 (12)	0.000
	- Mild	- 12 (21)	- 15 (88)	
	- Moderate	- 41 (71)	- 0 (0)	
	- Severe	- 5 (8)	- 0 (0)	
Elastic fiber disorganization	- None	- 0 (0)	- 2 (12)	0.000
	- Mild	- 13 (23)	- 13 (76)	
	- Moderate	- 28 (48)	- 2 (12)	
	- Severe	- 17 (29)	- 0 (0)	
Overall medial degeneration	- None	- 0 (0)	- 0 (0)	0.000
	- Mild	- 6 (10)	- 16 (94)	
	- Moderate	- 27 (47)	- 1 (6)	
	- Severe	- 25 (43)	- 0 (0)	
Mucoid extracellular matrix accumulation	- None	- 0 (0)	- 0 (0)	0.000
	- Mild	- 8 (10)	- 15 (88)	
	- Moderate	- 32 (55)	- 2 (12)	
	- Severe	- 18 (31)	- 0 (0)	
Smooth muscle cell nuclei loss	- None	- 0 (0)	- 0 (0)	0.023
	- Mild	- 10 (17)	- 8 (47)	
	- Moderate	- 33 (57)	- 9 (53)	
	- Severe	- 14 (24)	- 0 (0)	

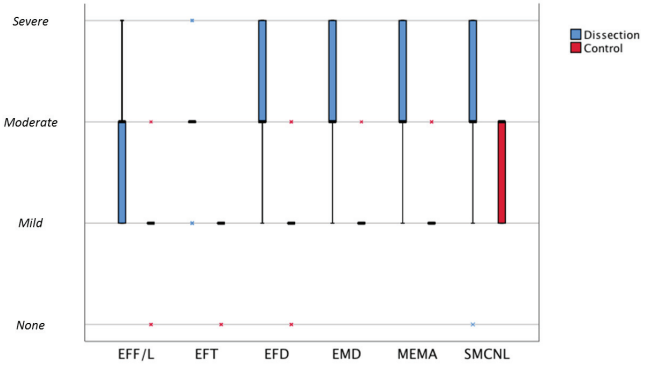

Figure 3. Graph of median morphology scores comparing the dissection and control group. Boxplot of median morphological scores comparing the dissection and control group. Boxes represent median morphological score (bold horizontal lines) and interquartile ranges (75%; 25%). Extremes are presented as asterisks. Blue corresponds to the dissection group and red to the control group. EFF/L: elastic fiber fragmentation/loss; EFT: elastic fiber thinning; EFD: elastic fiber degeneration; OMD: overall medial degeneration; MEMA: mucoid extracellular matrix accumulation; SMCNL: smooth muscle cell nuclei loss.

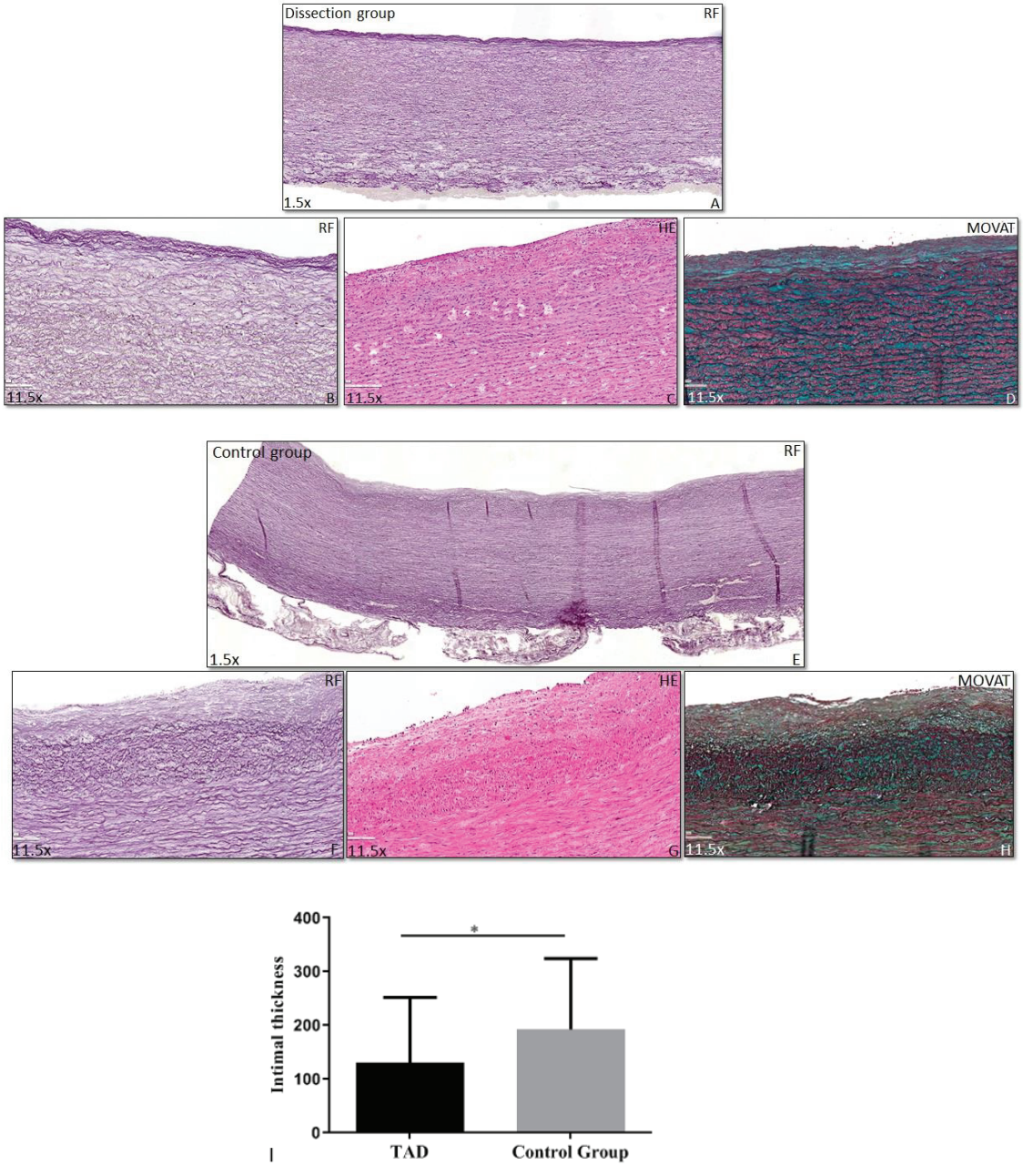

Figure 4. Intimal thickness. Transverse histologic sections (4 μm) stained for Resorcin Fuchsin (RF), Haematoxylin Eosin (HE), and MOVAT. The intimal layer, indicated with the dashed line, is significantly thinner in the dissection group (a patient without Marfan or a bicuspid aortic valve) (**A**–**D**) than in the control group (**E**–**H**) (Graph **I**). Magnification (**A**,**E**) 1.5×, (**B**–**D**,**F**–**H**) 11.5×, *: $p < 0.05$.

3.3. Dissection Plane

From the histological evaluation, the picture emerged of a uniform dissection plane for all TAAD specimens in the study. We therefore evaluated the level of the dissection plane for the 41 cases for which full-thickness aortic wall samples were available. For the remaining 17 samples, the adventitial aspect of the media was either lost or fully separated from the media in the process of tissue procurement. In the available full thickness samples, the dissection plane was consistently located in the outer aspect of the media (at 83% (SD 0.08) of the full medial thickness), a level that coincides with the aortic vasa vasorum network (Figure 2). The level of the vasa vasorum was calculated in the specimen with an intact vasa vasorum network in the outer media (n = 25).

4. Discussion

This systematic histological evaluation of aorta segments of type A dissections shows universal presence of diffuse, moderately-severe medial defects, a thinner intima, and a dissection plane that is consistently located at the level of the vasa vasorum network in the outer media. On basis of these observations, the picture emerges of aortic dissection being the consequence of a multi-hit process that involves a potentially more vulnerable (thinner) intima, a pre-existing incompetent media that is unable to withstand the tear forces exerted by the blood following an intimal tear, thereby allowing the blood access to an area of least resistance (the actual dissection plane) at the level of the vasa vasorum network in the outer medial layer.

Histological evaluation indicated universal presence of medial defects in all TAAD cases included in this evaluation. Medial defects were systematically inventoried by applying the recently issued consensus grading from the Society for Cardiovascular Pathology and the Association For European Cardiovascular Pathology [9]. This consensus grading system was developed in order to harmonize the nomenclature for histopathology of vascular diseases. The ultimate aim of the nomenclature is to facilitate data integration of results obtained from different groups or from different diseases [11]. Evaluation of the grading performance showed excellent Cohen's kappas for all parameters in the consensus grading.

This is the first study to apply the consensus classification to TAAD wall samples. Based on this grading, it was concluded that TAAD universally associates with moderately severe elastic fiber pathology, overall medial degeneration, mucoid extracellular matrix accumulation, and smooth muscle cell nuclei loss. Additionally, MOVAT staining implied further pathological changes not included in the consensus classification [11] such as extensive (micro) fibrotic changes [12] and adventitial remodeling in subset of cases.

Apart from the consistent presence of the moderately severe medial defects, this systematic histological inventory also revealed a remarkably thin intima, and the existence of uniform dissection plane, as consistent findings in the 58 TAAD cases.

Although one could speculate that the observed thin intima in TAAD constitutes the primary defect, with thin intima's being more prone to dissection and the medial defects reflecting a bystander phenomenon, such a theory is not compliant with the clinical observations that intimal tears or medial injuries in a healthy vessel do not result in dissection. Localized intimal tears are observed as incidental findings in elderly patients or after trauma [13]. Similarly, iatrogenic medial injuries following aortic cannulation [14], subintimal angioplasty [15], and end-atherectomy [16] do not associate clinically with dissection. Consequently, a healthy, competent media is able to fully resist exposure to perpendicular dissecting forces that develop when directly exposed to the blood stream. Mechanistically, this stability resides in the tissue's network behavior that allows forces to be evenly distributed over the wall, and that prevents dissection of the individual layers [17,18].

An alternative explanation for the thin intima is that it reflects an underlying developmental and/or differentiation defect of the mesenchymal cell population [19]. Relative thin intima's are present in Marfan Syndrome and in aortas from patients with bicuspid valve

disease [20,21], conditions with clear developmental aortic maturation defects [22]. The universal finding of a reduced intimal thickness and the diffuse, moderately severe medial pathology suggest that TAAD relates to some form of underlying developmental defect in the ascending aorta.

A further remarkable observation was the uniform localization of the dissection plane (a preferential position in the outer media was reported in two earlier reports) [23,24]. The more detailed analysis herein shows that the dissection plane consistently co-localizes with the plane of the vasa vasorum network in the outer media.

One could speculate that the level harboring this vascular network structure is an inherently mechanically weak plane that is less able to resist the wedge forces exhibited by the blood than the other segments of the media, thereby creating an inherently weak plane within the aortic wall along which the dissection progresses. Considering the fact that the mean blood pressure in the vasa vasorum network is lower than the central blood pressure, we consider it unlikely that TAADs that present without an apparent continuity with the actual lumen relate to a bleeding from the vasa vasorum plexus.

In conclusion: this systematic histological evaluation of 58 successive TAAD shows that TAAD uniformly associates with pre-existing ascending aortic wall defects and consistently proceeds along a plane that coincides with the vascular plexus in the outer media. On this basis, a picture emerges of a TAAD-susceptible phenotype that relates to an inherently mechanically incompetent media, and a common final pathway reflecting propagation of the dissection along the plane of least resistance (the vasa vasorum network).

This is an observational study. As such, the study comes with several limitations: the evaluation is based on histological evaluation surgical specimens obtained at the time of aorta replacement, hence information on non-operated patients is missing. Moreover, information on the natural history of the medial changes, and on the molecular aspects of TAAD, is missing.

Author Contributions: Conceptualization, N.G., A.C.G.-d.G., and J.H.N.L.; methodology, J.H.N.L. and R.P.; software, B.J.J.V. and J.H.N.L.; validation, all; formal analysis, N.G., B.J.J.V., and J.H.N.L.; investigation N.G., B.J.J.V., J.H.N.L., and A.C.G.-d.G.; resources, N.G., B.J.J.V., J.H.N.L., and A.C.G.-d.G.; data curation, N.G., B.J.J.V., and J.H.N.L.; writing—original draft preparation, N.G., B.J.J.V., and J.H.N.L.; writing—review and editing: N.G., B.J.J.V., A.C.G.-d.G., R.P., R.J.M.K., T.J.V.B., J.H.N.L.; visualization, N.G., B.J.J.V., and J.H.N.L.; supervision, A.C.G.-d.G., R.P., and J.H.N.L.; project administration, N.G., B.J.J.V.; funding acquisition, J.H.N.L. and R.J.M.K. All authors have read and agreed to the published version of the manuscript.

Funding: This research received no external funding.

Institutional Review Board Statement: The study was conducted according to the guidelines of the Declaration of Helsinki and approved by the Institutional Review Board (or Ethics Committee) of The Leiden University Medical Center (protocol code G19.113 and date of approval: 25-05-2019).

Informed Consent Statement: Patient consent was waived due to use of ascending aortic material, which was considered as surgical waste material.

Data Availability Statement: The data presented in this study are available on request from the corresponding author. The data are not publicly available due to ethical reasons.

Acknowledgments: This paper is dedicated to Adriana Gittenberger-de Groot, who contributed largely to the paper and sadly passed away in the final phases of the writing process.

Conflicts of Interest: The authors declare no conflict of interest.

References

1. Erbel, R.; Aboyans, V.; Boileau, C.; Bossone, E.; Bartolomeo, R.D.; Eggebrecht, H.; Evangelista, A.; Falk, V.; Frank, H.; Gaemperli, O.; et al. 2014 ESC Guidelines on the diagnosis and treatment of aortic diseases: Document covering acute and chronic aortic diseases of the thoracic and abdominal aorta of the adult. The Task Force for the Diagnosis and Treatment of Aortic Diseases of the European Society of Cardiology (ESC). *Eur. Heart J.* **2014**, *35*, 2873–2926.
2. Wu, J.; Zafar, M.; Qiu, J.; Huang, Y.; Chen, Y.; Yu, C.; Elefteriades, J.A. A systematic review and meta-analysis of isolated abdominal aortic dissection. *J. Vasc. Surg.* **2019**, *70*, 2046–2053.e6. [CrossRef]
3. Nienaber, C.A.; Clough, R.E. Management of acute aortic dissection. *Lancet* **2015**, *385*, 800–811. [CrossRef]
4. Smedberg, C.; Steuer, J.; Leander, K.; Hultgren, R. Sex differences and temporal trends in aortic dissection: A population-based study of incidence, treatment strategies, and outcome in Swedish patients during 15 years. *Eur. Heart J.* **2020**, *41*, 2430–2438. [CrossRef] [PubMed]
5. Daily, P.O.; Trueblood, H.W.; Stinson, E.B.; Wuerflein, R.D.; Shumway, N.E. Management of Acute Aortic Dissections. *Ann. Thorac. Surg.* **1970**, *10*, 237–247. [CrossRef]
6. Kita, Y.; Nakamura, K.; Itoh, A.H. Histologic and Histometric Study of the Aortic Media in Dissecting Aneurysm Comparison with True Aneurysm and Age-matched Controls. *Pathol. Int.* **1990**, *40*, 408–416. [CrossRef] [PubMed]
7. Osada, H.; Kyogoku, M.; Matsuo, T.; Kanemitsu, N. Histopathological evaluation of aortic dissection: A comparison of congenital versus acquired aortic wall weakness. *Interact. Cardiovasc. Thorac. Surg.* **2018**, *27*, 277–283. [CrossRef]
8. Dingemans, K.P.; Teeling, P.; van der Wal, A.C.; Becker, A.E. Ultrastructural pathology of aortic dissections in patients with Marfan syndrome: Comparison with dissections in patients without Marfan syndrome. *Cardiovasc. Pathol.* **2006**, *15*, 203–212. [CrossRef]
9. Halushka, M.K.; Angelini, A.; Bartoloni, G.; Basso, C.; Batoroeva, L.; Bruneval, P.; Buja, L.M.; Butany, J.; D'Amati, G.; Fallon, J.T.; et al. Consensus statement on surgical pathology of the aorta from the Society for Cardiovascular Pathology and the Association For European Cardiovascular Pathology: II. Noninflammatory degenerative diseases—nomenclature and diagnostic criteria. *Cardiovasc. Pathol.* **2016**, *25*, 247–257. [CrossRef]
10. Cohen, J. A Coefficient of Agreement for Nominal Scales. *Educ. Psychol. Meas.* **1960**, *20*, 37–46. [CrossRef]
11. Hiratzka, L.F.; Creager, M.A.; Isselbacher, E.M.; Svensson, L.G.; Nishimura, R.A.; Bonow, R.O. Surgery for Aortic Dilatation in Patients With Bicuspid Aortic Valves: A Statement of Clarification From the American College of Cardiology/American Heart Association Task Force on Clinical Practice Guidelines. *Circulation* **2016**, *133*, 680–686. [PubMed]
12. Wang, L.; Zhang, J.; Fu, W.; Guo, D.; Jiang, J.; Wang, Y. Association of smooth muscle cell phenotypes with extracellular matrix disorders in thoracic aortic dissection. *J. Vasc. Surg.* **2012**, *56*, 1698–1709. [CrossRef] [PubMed]
13. Wilson, W.C.; Grande, C.M.; Hoyt, D.B. *Trauma: Emergency Resuscitation, Perioperative Anesthesia, Surgical Management*; CRC Press: Boca Raton, FL, USA, 2007; Volume II.
14. Taylor, P.C.; Groves, L.K.; Loop, F.D.; Effler, D. Cannulation of the ascending aorta for cardiopulmonary bypass. Experience with 9,000 cases. *J. Thorac. Cardiovasc. Surg.* **1976**, *71*, 255–258. [CrossRef]
15. Met, R.; Van Lienden, K.P.; Koelemay, M.J.W.; Bipat, S.; Legemate, D.A.; Reekers, J.A. Subintimal Angioplasty for Peripheral Arterial Occlusive Disease: A Systematic Review. *Cardiovasc. Interv. Radiol.* **2008**, *31*, 687–697. [CrossRef]
16. Bergamini, T.M.; Seabrook, G.R.; Bandyk, D.F.; Towne, J.B. Symptomatic recurrent carotid stenosis and aneurysmal degeneration after endarterectomy. *Surgenry* **1993**, *113*, 580–586.
17. Lindeman, J.H.; Ashcroft, B.A.; Beenakker, J.W.; van Es, M.; Koekkoek, N.B.; Prins, F.A.; Tielemans, J.F.; Abdul-Hussien, H.; Bank, R.A. Distinct defects in collagen microarchi-tecture underlie vessel-wall failure in advanced abdominal aneurysms and aneurysms in Marfan syndrome. *Proc. Natl. Acad. Sci. USA* **2010**, *107*, 862–865. [CrossRef]
18. Niestrawska, J.A.; Haspinger, D.C.; Holzapfel, G.A. The influence of fiber dispersion on the mechanical response of aortic tissues in health and disease: A computational study. *Comput. Methods Biomech. Biomed. Eng.* **2018**, *21*, 99–112. [CrossRef]
19. Maleki, S.; Kjellqvist, S.; Paloschi, V.; Magné, J.; Branca, R.M.M.; Du, L.; Hultenby, K.; Petrini, J.; Fuxe, J.; Consortium, M.L.; et al. Mesenchymal state of intimal cells may explain higher propensity to ascending aortic aneurysm in bicuspid aortic valves. *Sci. Rep.* **2016**, *6*, 35712. [CrossRef]
20. Grewal, N.; Franken, R.; Mulder, B.J.; Goumans, M.J.; Lindeman, J.H.; Jongbloed, M.R.; De Ruiter, M.C.; Klautz, R.J.M.; Bogers, A.J.C.C.; Poelmann, R.E.; et al. Histopathology of aortic complications in bicuspid aortic valve versus Marfan syndrome: Relevance for therapy? *Heart Vessels* **2015**, *31*, 795–806. [CrossRef]
21. Grewal, N.; Groot, A.C.G.-D.; Poelmann, R.; Klautz, R.J.M.; Lindeman, J.H.; Goumans, M.-J.; Palmen, M.; Mohamed, S.A.; Sievers, H.-H.; Bogers, A.J.; et al. Ascending aorta dilation in association with bicuspid aortic valve: A maturation defect of the aortic wall. *J. Thorac. Cardiovasc. Surg.* **2014**, *148*, 1583–1590. [CrossRef]
22. Grewal, N.; Groot, A.C.G.-D.; Von Der Thüsen, J.H.; Wisse, L.J.; Bartelings, M.M.; DeRuiter, M.C.; Klautz, R.J.M.; Poelmann, R. The Development of the Ascending Aortic Wall in Tricuspid and Bicuspid Aortic Valve: A Process from Maturation to Degeneration. *J. Clin. Med.* **2020**, *9*, 908. [CrossRef] [PubMed]

23. Osada, H.; Kyogoku, M.; Ishidou, M.; Morishima, M.; Nakajima, H. Aortic dissection in the outer third of the media: What is the role of the vasa vasorum in the triggering process? European journal of cardio-thoracic surgery: Official journal of the European. *Assoc. Cardio-Thoracic Surg.* **2013**, *43*, e82–e88. [CrossRef] [PubMed]
24. Angouras, D.; Sokolis, D.P.; Dosios, T.; Kostomitsopoulos, N.; Boudoulas, H.; Skalkeas, G.; Karayannacos, P.E. Effect of impaired vasa vasorum flow on the structure and mechanics of the thoracic aorta: Implications for the pathogenesis of aortic dissection. *Eur. J. Cardio-Thoracic Surg.* **2000**, *17*, 468–473. [CrossRef]

Journal of
Cardiovascular
Development and Disease

MDPI

Review

Pathology of the Aorta and Aorta as Homograft

Gaetano Thiene *, Cristina Basso and Mila Della Barbera

Department of Cardiac, Thoracic, Vascular Sciences and Public Health, Cardiovascular Pathology, University of Padua Medical School, Via A. Gabelli, 61, 35121 Padua, Italy; cristina.basso@unipd.it (C.B.); mila.dellabarbera@unipd.it (M.D.B.)
* Correspondence: gaetano.thiene@unipd.it; Tel.: +39-049-827-2283

Abstract: The aorta is not a rigid tube, it is an "organ" with lamellar units, consisting of elastic fibers, extracellular matrix and smooth muscle cells in between as parenchyma. Several diseases may occur in the natural history of the aorta, requiring replacement of both semilunar cusps and ascending aorta. They may be congenital defects, such as bicuspid aortic valve and isthmal coarctation with aortopathy; genetically determined, such as Marfan and William syndromes; degenerative diseases, such as atherosclerosis and medial necrosis with aortic dilatation, valve incompetence and dissecting aneurysm; inflammatory diseases such as Takayasu arteritis, syphilis, giant cell and IgM4 aortitis; neoplasms; and trauma. Aortic homografts from cadavers, including both the sinus portion with semilunar cusps and the tubular portion, are surgically employed to replace a native sick ascending aorta. However, the antigenicity of allograft cells, in the lamellar units and interstitial cells in the cusps, is maintained. Thus, an immune reaction may occur, limiting durability. After proper decellularization and 6 months' implantation in sheep, endogenous cell repopulation was shown to occur in both the valve and aortic wall, including the endothelium, without evidence of inflammation and structural deterioration/calcification in the mid-term. The allograft was transformed into an autograft.

Keywords: aorta; homograft; semilunar valves

Citation: Thiene, G.; Basso, C.; Della Barbera, M. Pathology of the Aorta and Aorta as Homograft. *J. Cardiovasc. Dev. Dis.* **2021**, *8*, 76. https://doi.org/10.3390/jcdd8070076

Academic Editor: Robert Poelmann

Received: 6 May 2021
Accepted: 21 June 2021
Published: 29 June 2021

1. Introduction

Along with natural history, the aorta, the highway of our body, transforms from a smooth, pliable vessel in children into a rigid tube in the elderly (Figure 1) [1,2]. If normal or nearly normal, it may be donated at the time of death to serve as an arterial allograft for repair of both congenital and acquired diseases.

Figure 1. (**a**) Normal thoracic aorta in a child; (**b**) Severe atherosclerosis of the aorta in an old man.

Here we will review gross and histologic features of normal and diseased aorta. Moreover, we will summarize the results of an experimental investigation, showing endogenous repopulation of decellularized aortic allografts implanted in juvenile sheep.

2. Normal Anatomy

The aorta is a smooth great vessel consisting of intima, media and adventitia. It is an elastic artery with variations in diameter during ventricular systole and diastole ("compliance"), thanks to elastic fibers of the tunica media (Figure 2a). They appear parallel with smooth muscle cells in between (Figure 2b). The number of elastic fibers varies from 56 in the ascending aorta and gradually decreases to 28 in the abdominal aorta. The intima is lined with endothelium and with time appears as a myointimal layer.

There are lamellar units in the media consisting of elastic fibers, smooth muscle cells and extracellular matrix (Figure 2c). The biological concept of the lamellar unit was put forward by Glagov in 1967 [3]. The aorta was considered as an organ with smooth muscle cells as parenchyma. The precise role of smooth muscle cells, whether synthetic, contractile or both, is still a matter under investigation [4,5]. The tunica adventitia consists of collagen fibers, nerves and vasa vasorum. The latter supplies the outer part of the tunica media in the thoracic aorta and not in the abdominal aorta, which is thinner because there are fewer lamellar units.

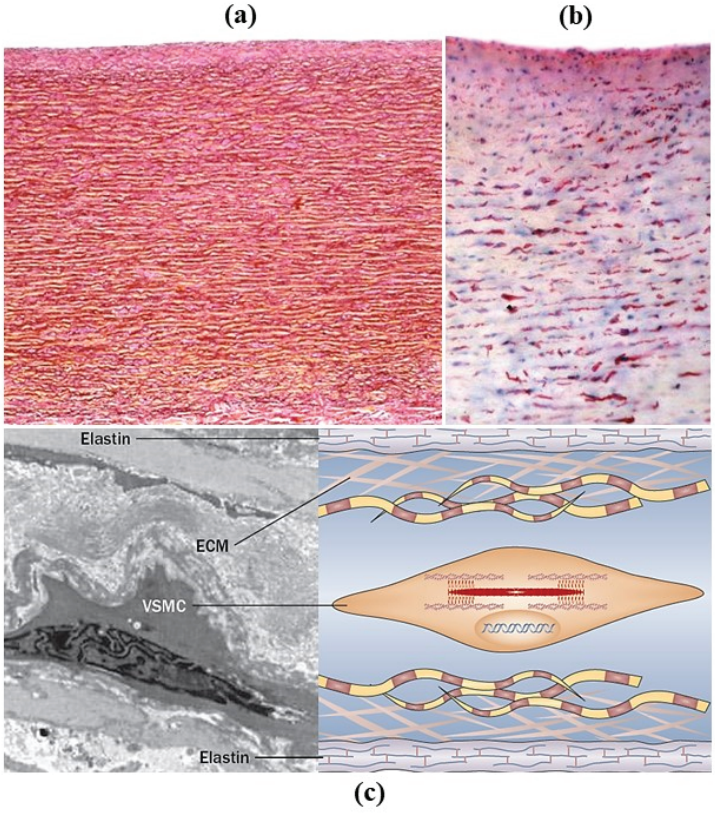

Figure 2. Histology of thoracic aorta. (**a**) The media consists of lamellar units with parallel elastic fibers. Weigert Van Gieson stain. (**b**) Smooth muscle cells, dark stained by anti-SMC immunohistochemistry, are the "parenchyma". (**c**) The lamellar unit consists of elastic fibers, with vascular smooth muscle cells (VSMCs) and extracellular matrix (ECM) in between. Adapted from [4].

3. Pathology

The pathology may be congenital (structural defect present at birth), genetically determined with onset during childhood or even later, or acquired (inflammatory, degenerative, neoplastic, traumatic).

3.1. Congenital Malformations

Congenital malformations may affect the aortic valve, the ascending aorta and the aortic arch [6].

Bicuspid aortic valve (BAV) is a congenital defect with an incidence of 0.5–0.8% by echo in children (Figure 3) [7,8]. One of the two sinuses shows a raphe, most probably an aborted commissure during embryonic development.

	Author, Year	N.	BAV	Prevalence %
(a)	Basso et al. Am J Cardiol 2004	817	4	0.5
(b)	Nistri et al. Am J Cardiol 2005	20,946	167	0.8

(c)

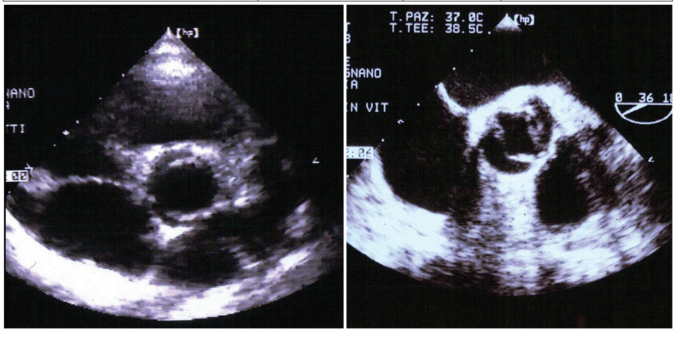

Figure 3. Prevalence of BAV in children (**a**) and conscript soldiers (**b**,**c**) by echo. Adapted from [7,8], with permission.

In BAV type I the cusps appear antero-posterior (ventro-dorsal) with the raphe in the anterior sinus, due to embryonic fusion of anterior right and left cushions [9]. Both the coronary arteries originate from the anterior (ventral) sinus. In BAV type II the cusps appear side by side (latero-lateral) and the raphe the fusion of right and posterior cushions, with coronary arteries originating each from the opposite sinus. Under the raphe there is no interleaflet triangle (Figure 4). Rare cases of BAV without raphe do exist.

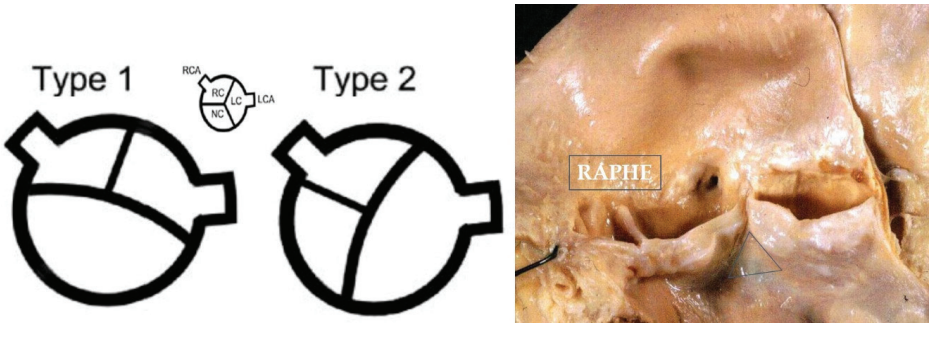

Figure 4. Bicuspid aortic valve, type 1 and 2. Note the raphe without the interleaflet triangle underneath.

Natural history of BAV is characterized by progressive calcification of the cusps with aortic valve stenosis [10] and by aortopathy (Figure 5) with dilatation of the ascending aorta, valve incompetence and aortic dissection (Figure 6) [11–13].

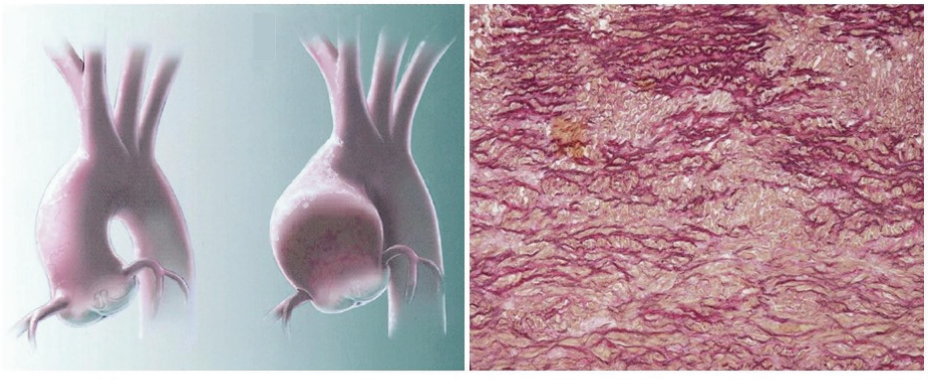

Figure 5. Aortopathy in the bicuspid valve. Note normal (**a**) vs. dilated (**b**) ascending aorta with loss of lamellar units at histology (**c**). (Weigert Van Gieson stain).

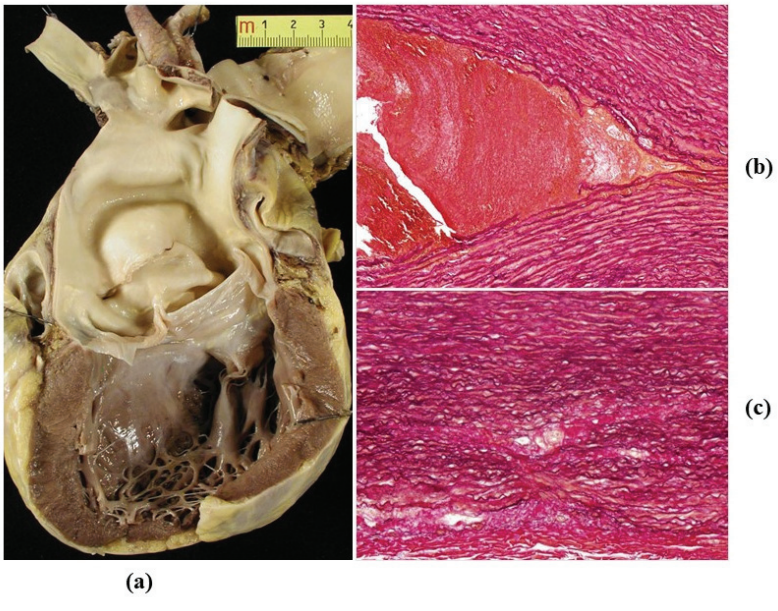

Figure 6. (**a**) Dissection of dilated ascending aorta in the bicuspid aortic valve, with intimal tear just above the commissures. (**b**,**c**) On histology, wave front propagation of the dissecting hematoma and medial necrosis. (Weigert Van Gieson stain).

BAV represents a well-known risk factor for infective endocarditis (Figure 7a,b). It is a cardiovascular risk factor in which antibiotic prophylaxis is recommended, for instance, in case of dental procedures.

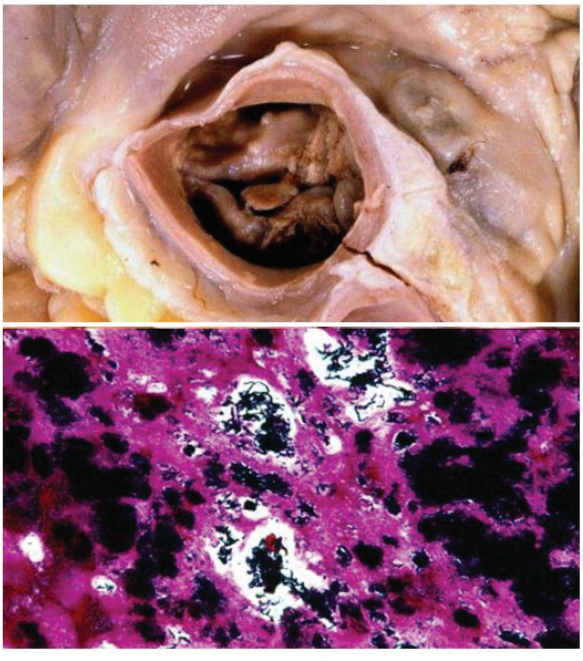

Figure 7. Infective endocarditis (**a**) with cocci (**b**) in a young drug addict with bicuspid aortic valve. (Gram stain).

Calcification of BAV is similar to senile calcific aortic stenosis and requires interventional repair with transcatheter aortic valve implantation (TAVI) or surgical repair-replacement. It occurs in adults and the elderly, usually ten years earlier than calcific senile.

Aortopathy develops with time in nearly 50% of BAV patients. Disruption of elastic fibers in the tunica media explains loss of wall elasticity as well as aneurysmal dilatation of both sinusal and tubular portions of the ascending aorta, with valve incompetence and even aortic dissection (Figure 6). Surgical replacement of the aorta, with repair of the valve, is indicated when the diameter of the aorta exceeds 5 cm [14]. Both increased aortic diameter and impaired elasticity of the stiffened wall can be assessed by 2D echo [15]. A hereditary Mendelian transmission with scanty penetrance has been advanced, but a definitive molecular genetic background, such as in Marfan syndrome, has not been proven so far.

The role of neurocrest in the development of BAV aortopathy has been conjectured since BAV is frequently (40–50%) associated with isthmic coarctation (Figure 8) [16].

Non-infective aneurysm of the sinuses of Valsalva represent a curious congenital malformation of the aortic root [17].

3.2. Genetically Determined Diseases of Thoracic Aorta

William's syndrome is a dominant hereditary disease, due to molecular deletion of the elastic gene located in chromosome 7, accounting for increased wall thickness and stiffness of the ascending aorta [18,19]. The number of elastic fibers may be increased. Supravalvular aortic stenosis occurs in the shape of an hour-glass (Figure 9) in the diaphragm or hypoplastic ascending aorta. The aortic valve may be also involved with cusp thickening. Insulation of the coronary ostia may be observed because of the fusion of the cusps with sinus aortic wall.

Figure 8. Isthmic aortic coarctation. (**a**) Plication at the aortic arch. (**b**) Corresponding histology. (Weigert Van Gieson stain).

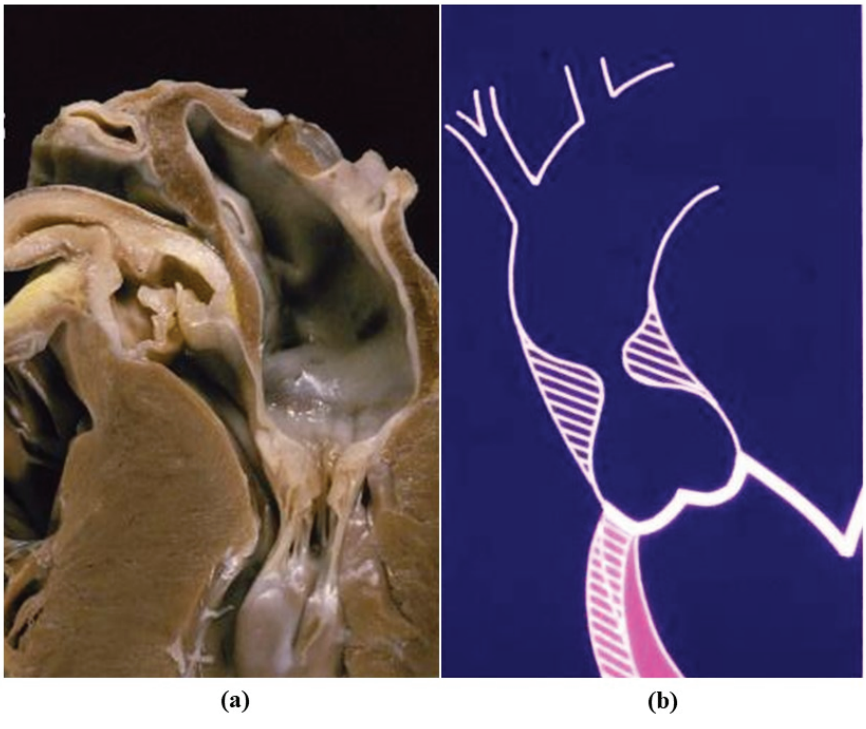

Figure 9. Long-axis (**a**) and hour-glass appearance (**b**) of supravalvular aortic stenosis in William's syndrome.

In Marfan syndrome, the molecular defect consists in a mutation of the gene coding fibrillin 1, a protein connecting smooth muscle cells with elastic fibers of lamellar units in the tunica media [20]. The disease is hereditary dominant, frequently has de novo mutation, and involves joints, lens and the cardiovascular system. It is associated with aortopathy,

similar to that of BAV, with disruption and loss of elastic fibers, medial necrosis, aortic dilatation and aortic and mitral valve incompetence. Loss of elastic fibers accounts for weakness and fragility of the aorta to such a degree that aortic dissection may occur, with risk of premature sudden death (Figure 10).

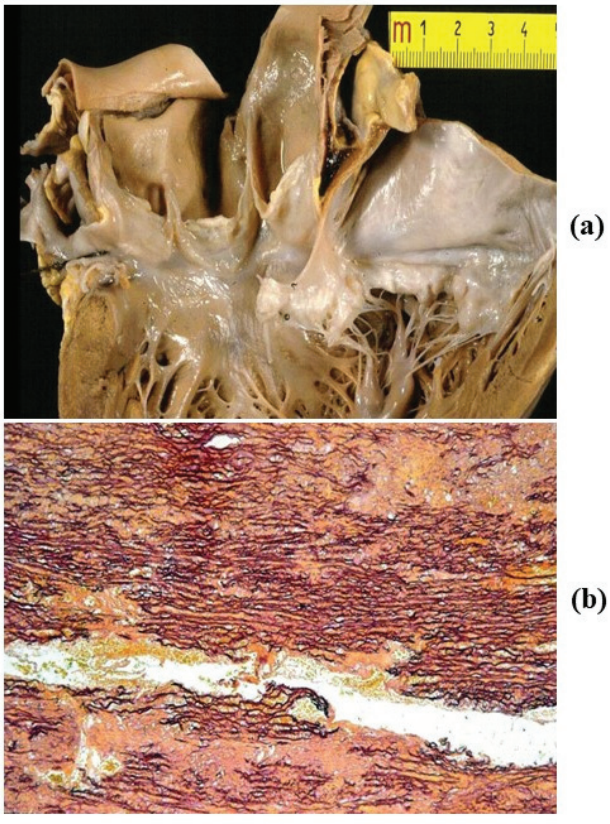

Figure 10. Aortic dissection in Marfan syndrome and sudden death. (**a**) Gross view: intimal tear in the tubular ascending aorta and mitral valve prolapse. (**b**) Histology of the aortic wall: severe elastic fibers frequent in aortic dissection. (Weigert Van Gieson stain).

Recently, a new syndrome (Loeys-Dietz) has been reported, with an autosomal dominant pattern showing aortic lesions (Figure 11) similar to Marfan. It is due to mutations of genes coding transforming growth factor beta receptor (TGF BR) 1 or 2 [21]. The pathogenetic pathways in Marfan and Loeys-Dietz are similar [22]. Mutations of fibrillin 1 and TGF BR 1 and 2 all result in dysregulated TGB signaling. The main clinical characteristics are hypertelorism, cleft palate and bifid uvula, besides aortic tortuosity prone to dissection.

Ehlers-Danlos syndrome is a soft connective tissue disease, secondary to mutations in one of the genes coding collagen fiber or enzymes involved in collagens synthesis [23]. Six different forms of disease have been recognized. Pathological manifestations in the cardiovascular system are aortic aneurysm and dissection [24].

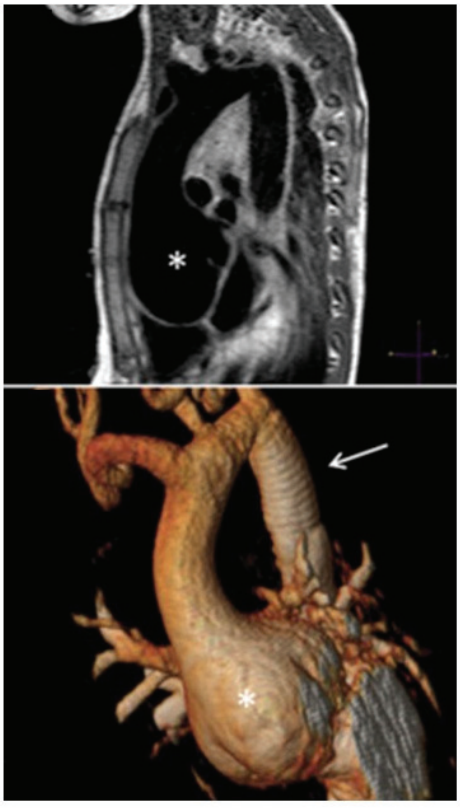

Figure 11. The aorta in Loeys-Dietz syndrome. Notice the large anuloaortic ectasia (**a**,**b**) by tomography. From Rizzo S et al. Ann Thorac Surg. 2016 Mar; 101(3):1193-5, with permission.

Turner syndrome is characterized by the absence of one X chromosome in a female. Aneurysmal dilatation of the aorta, BAV and isthmic coarctation are the phenotype, prone to aortic dissection [25].

3.3. Degenerative Diseases of the Aorta

Atherosclerosis is the "malignant" disease of the cardiovascular system, mostly related to aging and life style risk factors (smoke, lipid-rich foods . . .). Premature atherosclerosis is promoted by genetic hypercholesterolemia, the most frequent hereditary cardiovascular disorder (1:500). The disease starts in the intima with atherosclerotic plaque as an elementary lesion, which may complicate with rupture of the fibrous cap and thrombosis (atherothrombosis), a source of peripheral embolism and cause of stroke (Figure 12). The ulcer of an aortic plaque may penetrate into the media and create a local dissection with mural hematoma and false aneurysm at risk of external rupture (Figure 13). Moreover. the ulcerated plaque may be a site of microorganism settlement in the case of bacteremia, with development of mycotic aneurysm.

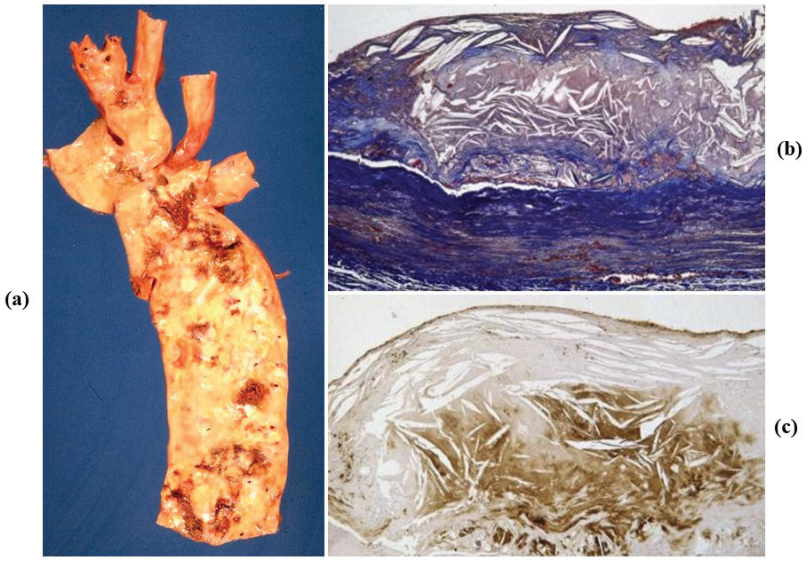

Figure 12. (**a**) Atherothrombosis of the thoracic aorta, gross view. (**b**,**c**) Histology of atherosclerotic plaque. (Weigert Van Gieson and C-68 immuno stains).

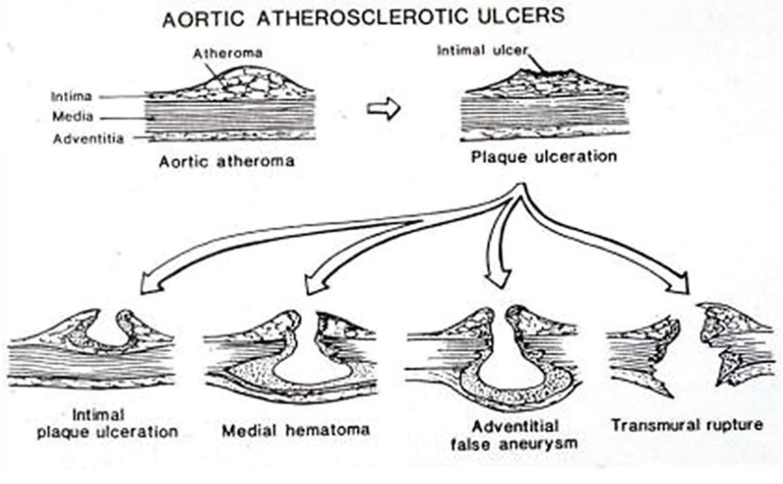

Figure 13. Ulcer of atherosclerotic plaque with intramural hematoma, false aneurysm and external rupture.

Atherosclerotic aneurysm is the complication of progressive thinning of the tunica media due to the release of proteases (elastase included) by monocytes, which play a pivotal role in the onset and progression of atherosclerosis [26]. Release of proteases in the intima may lead to thinning and rupture of the fibrous cap with thrombus deposition. On the outer side of the media, the release accounts for progressive thinning of the aortic wall with aneurysm formation (Figure 14). The occurrence of aortic atherosclerotic aneurysm is more frequent in the abdominal aorta, where the wall is thinner and the number of elastic lamellae is much lower.

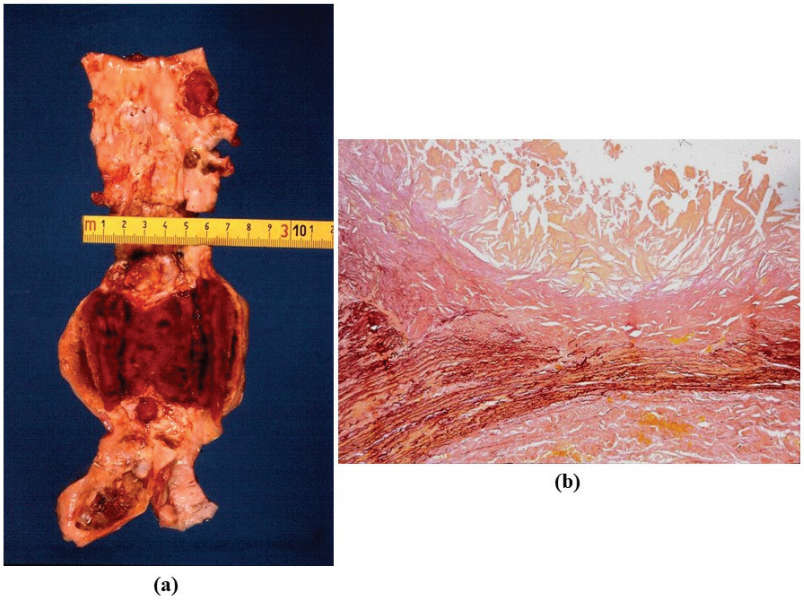

(a) **(b)**

Figure 14. Atherosclerotic saccular aneurysm of the abdominal aorta. (**a**) Gross features. (**b**) Histology with atheroma disrupting the tunica media, with loss of elastic fibers and thinning. (Weigert Van Gieson stain).

Degenerative disease may primarily affect the tunica media with medionecrosis, elastic fiber fragmentation and an increase in extracellular ground substance in the lamellar units, even in the absence of a genetically determined disorder (Figure 15). It may account for aortic dilatation of the ascending aorta and aortic valve regurgitation, nowadays the most frequent cause of aortic incompetence. Both sinusal [27,28] and tubular portions appear dilated (Figures 16 and 17). It was Currigan of Dublin who first recognized in 1832 the existence of a non-inflammatory cause of aortic incompetence, besides syphilis, rheumatism and infective endocarditis. It represents a fragile substrate favoring aortic dissection, which is featured by intimal tear and dissecting hematoma, triggered by mechanical stress [29] (Figure 18). Hypertensive attack is the main precipitating factor of dissecting aneurysm (Figure 19), which may originate either from the ascending or descending aorta. A more benign form does exist (so-called intramural hematoma), which lacks an intimal tear and is located in the thoracic aorta with the blood source from the vasa vasorum [30] (Figure 20). Hypertension is largely the more frequent risk factor (85%) of aorta dissection [31,32], followed by BAV and Marfan syndrome. Cases have been reported with familiarity (2–3%), distinct from Marfan [33–35].

Classic aortic dissection starts from an intimal tear and proceeds forward (antegrade dissection) in the outer tunica media, with risk of external rupture, hemopericardium and cardiac tamponade in the case of the ascending aorta or left hemothorax in the case of the descending aorta. The dissection transforms the aorta into two lumens (true and false) and may involve vital arteries, such as carotid and renal, with organ ischemic injury. Reentry may occur with distal intimal tears, leading a double barrel chronic dissection of the aorta (Figure 21) [36]. Retrograde dissection towards the aortic root may be responsible for commissural dehiscence with aortic valve incompetence and coronary stems dissection with myocardial infarction. (Figure 22). Hemorrhagic infiltration of the aorto-atrial space and atrial septum may account for av block due to atrio-nodal discontinuity.

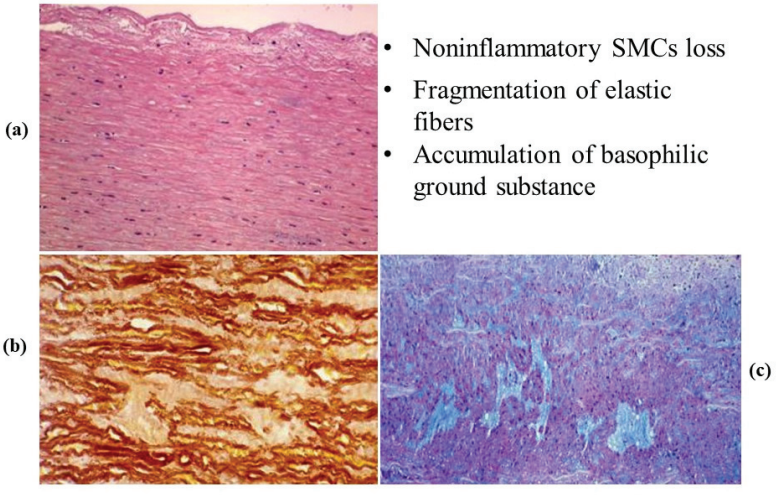

Figure 15. Elementary degenerative lesions in the tunica media of the aorta. (**a**) Non-inflammation loss (medionecrosis) of smooth muscle cells (SMCs). (**b**) Elastic fragmentation. (**c**) Cystic medial necrosis. (Hematoxylin-eosin (**a**), Weigert Van Gieson (**b**), and Alcian PAS (**c**) stains).

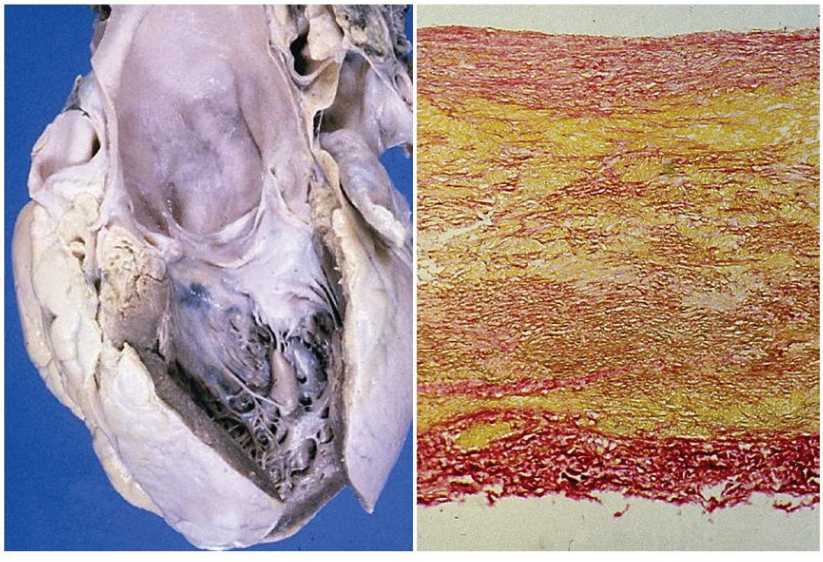

Figure 16. (**a**) Gross view of a dilated ascending aorta with aortic valve incompetence (anuloaortic-ectasia), due to degenerative disease of the aortic tunica media, not genetically determined. (**b**) Severe disruption of the elastic fibers in the tunica media. (Weigert Van Gieson stain).

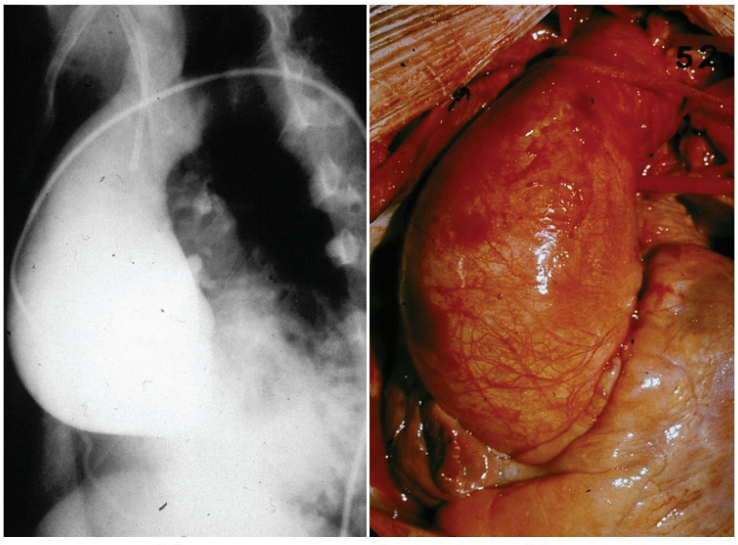

(a) **(b)**

Figure 17. Angiographic (**a**) and intraoperative (**b**) gross views of non-inflammatory anuuloaortic ectasia with valve incompetence.

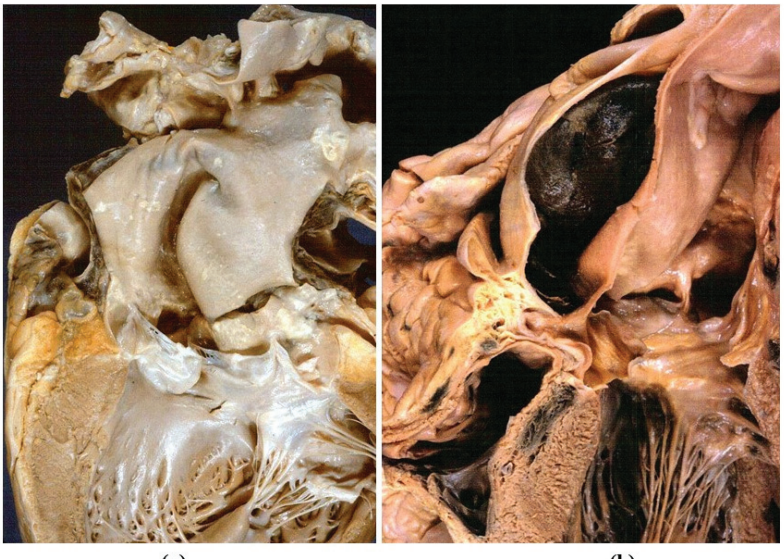

(a) **(b)**

Figure 18. Aortic dissection with intimal tear (**a**) and dissection of the ascending aorta (**b**).

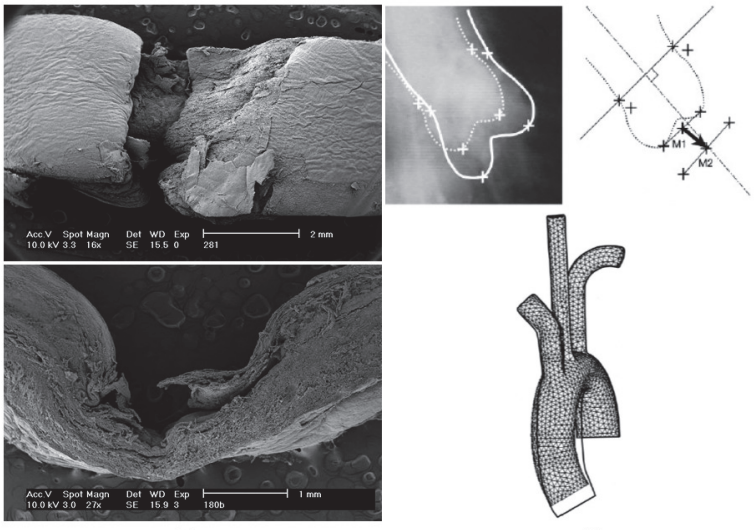

Figure 19. (**a**) Scanning electron microscopy views of an intimal tear in aortic dissection. (**b**) Stretch of the aorta during hypertension attack, accounting for intimal tear and aortic dissection. Adapted from [29], with permission.

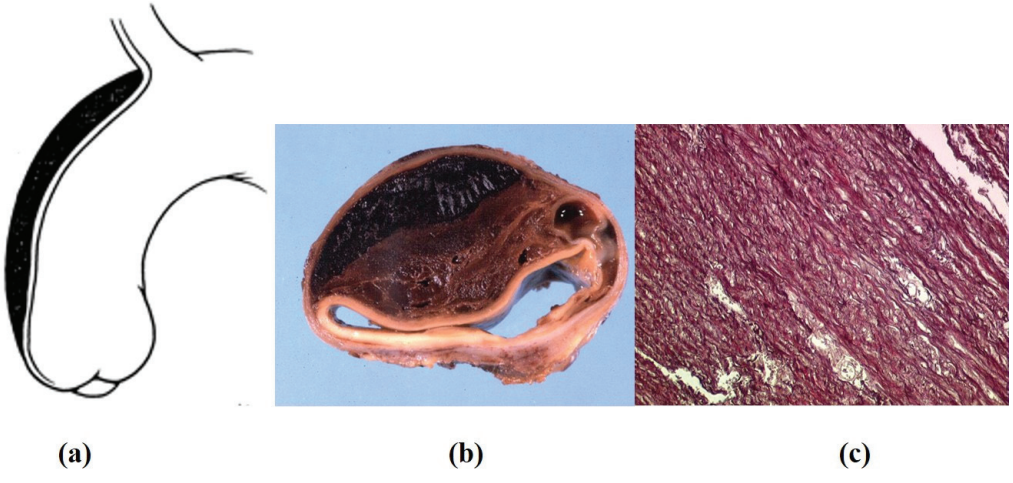

Figure 20. Intramural hematoma in the absence of intimal tear. (**a**) Schematic drawing. (**b**) Gross cross section of the aorta, with intramural hematoma. (**c**) Scattered elastic disruption. (Weigert Van Gieson stain). (**a**) Adapted from [30].

Figure 21. Double barrel aorta in chronic aortic dissection. (**a**) Gross view. (**b**) Corresponding histology. (Weigert Van Gieson stain).

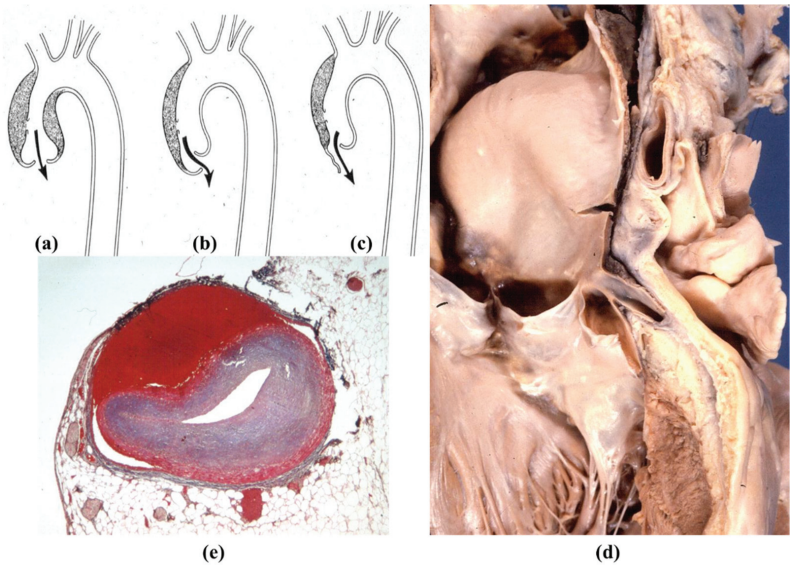

Figure 22. (**a**–**c**) Drawing of aortic incompetence due to retrograde aortic dissection. (**d**,**e**) Retrograde dissection involves and occludes the left coronary artery main stem (Azan Mallory stain).

3.4. Inflammatory Diseases of the Aorta

Inflammatory diseases of the aorta may be infectious or immune-mediated [37–39].

Syphilitic aortitis occurs late in the third stage of the disease [40]. The setting of Treponema pallidum in the tunica media triggers colliquative necrosis (gumma) with giant cells, and disruption of the tunica media (mesoaortitis). The sequela is the development of sacciform aneurysm of the ascending aorta and aortic arch, the rupture of which may

precipitate sudden death (Figure 23a). Scarring with retraction of the tunica intima accounts for the specific pavement-like feature and superimposed atherosclerotic plaques (Figure 23b). An alternative theory for mesoaortitis is an obstructive disease of the vasa vasorum of the adventitia with plasma cell infiltrates (Figure 23c,d) causing ischemic damage to the lamellar units of the tunica media. This would explain the absence of syphilitic mesoaortitis in the abdominal aorta, where no vasa vasorum do exist. The mesoaortitis may involve also the sinus portion of the ascending aorta, with valve incompetence, coronary ostia stenosis and angina pectoris.

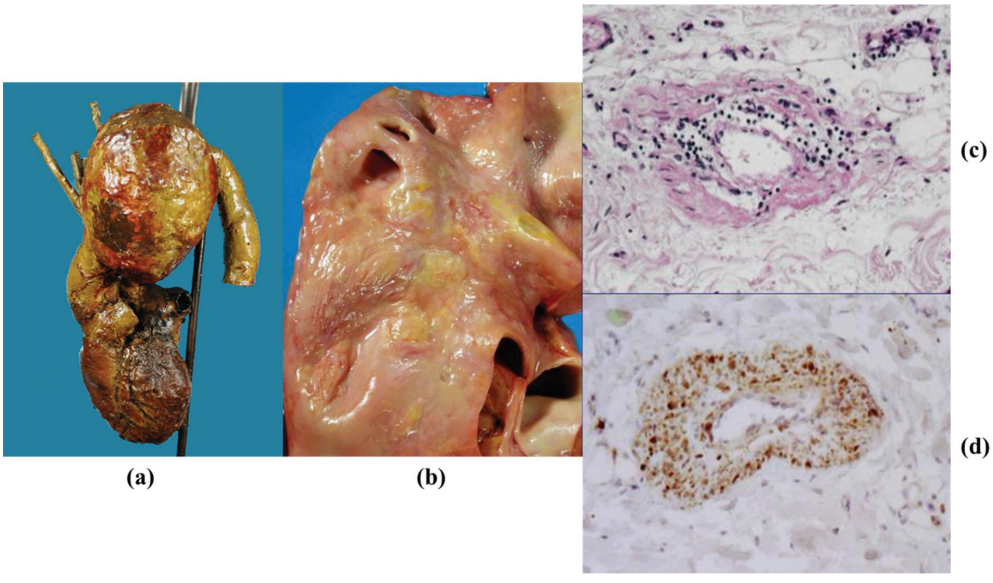

Figure 23. (**a**) Huge saccular syphilitic aneurysm of the aortic arch (from the Morgagni Museum of the Institute of Pathological Anatomy, University of Padua, with permission). (**b**) Syphilitic ascending aorta with pavement-like appearance of the intima. (**c**,**d**) Plasma cell inflammatory infiltrates in the obstructed vasa vasorum. (Hematoxylin-eosin and anti-CD79 immuno stain).

Infective endocarditis of the aortic valve may involve the annulus, accounting for abscesses and aneurysms in the Valsalva sinus. Optimal repair requires replacement of both valves and the ascending aorta using a homograft [41,42].

Mycotic aneurysm is another infectious disease of the aorta. The adjective refers to the look of the aneurysm, similar to a mushroom (or to a nuclear bomb). It develops as the consequence of microorganisms settling in the tunica media, usually cocci bacteriemia via the vasa vasorum, with a neutrophil inflammatory reaction, abscess and transmural necrosis, wall weakening, pseudo-aneurysm and external rupture (Figure 24). Atherosclerotic ulcers are an ideal nidus for bacteria implantation, directly from the aortic blood.

Giant cell angiitis involves non-infectious inflammation of the systemic arteries, with giant cell infiltrates in the absence of epithelioid granuloma. It usually affects the temporal artery in adult-elderly people (Horton arteritis). The involvement of the thoracic aorta, whether isolated or in association with the temporal artery, can be complicated with an aneurysm when the tunica media is extensively affected [43] (Figure 25). The diagnosis may come as a surprise at the time of surgical pathology examination since, clinically, it had been considered atherosclerotic.

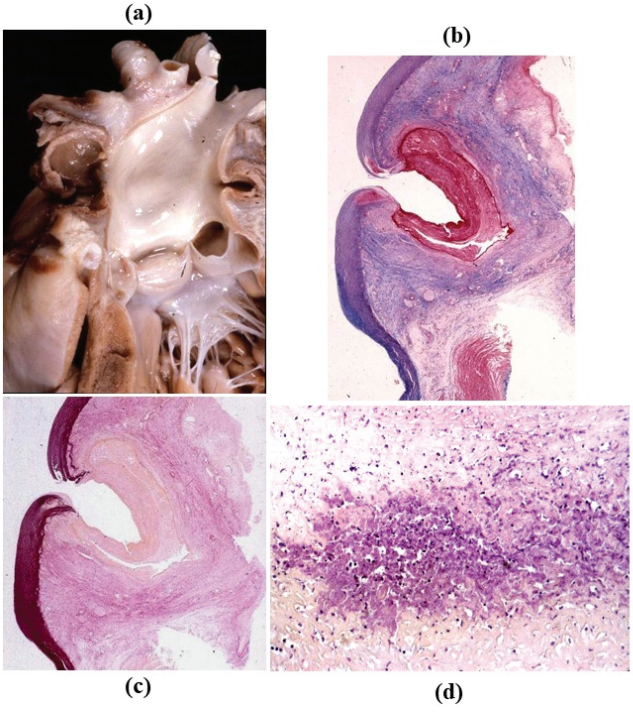

Figure 24. Mycotic aneurysm of the ascending aorta. (**a**) Gross appearance. (**b**) Histology: through and through laceration of the aortic wall with false aneurysm (Alcian PAS stain). (**c**) Same as (**b**) (Weigert Van Gieson stain). (**d**) Abscess by cocci in the aortic wall (hematoxylin-eosin stain).

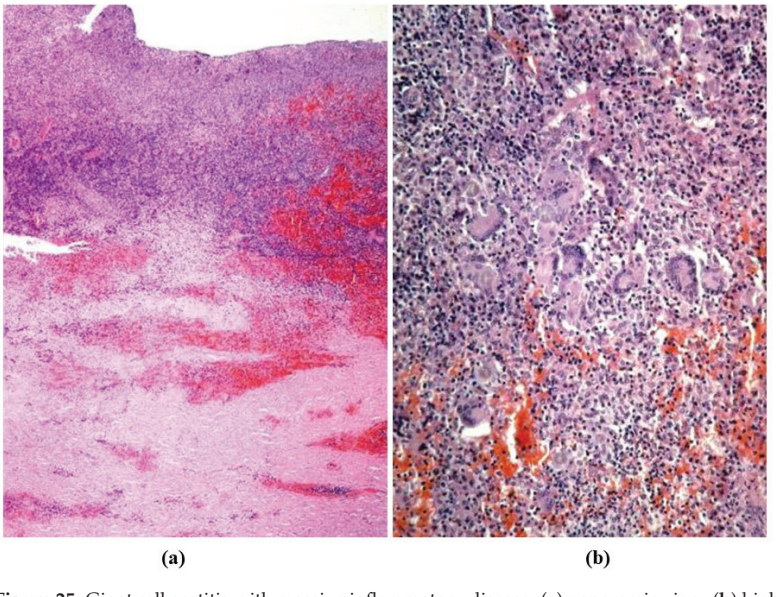

Figure 25. Giant cell aortitis with massive inflammatory disease: (**a**) panoramic view; (**b**) high-power view: note the giant cells (hematoxylin-eosin stain).

Takayasu angiitis is a necrotizing arteritis typically involving the ascending aorta, the aortic arch and brachiocephalic arteries, with non-granuloma giant cells inflammation and elastic fiber disruption [44]. It affects mostly the young and is associated with intimal proliferation of brachiocephalic arteries and coronary stems (Figure 26) as well as fibrotic thickness of the adventitia, hindering aneurysm formation.

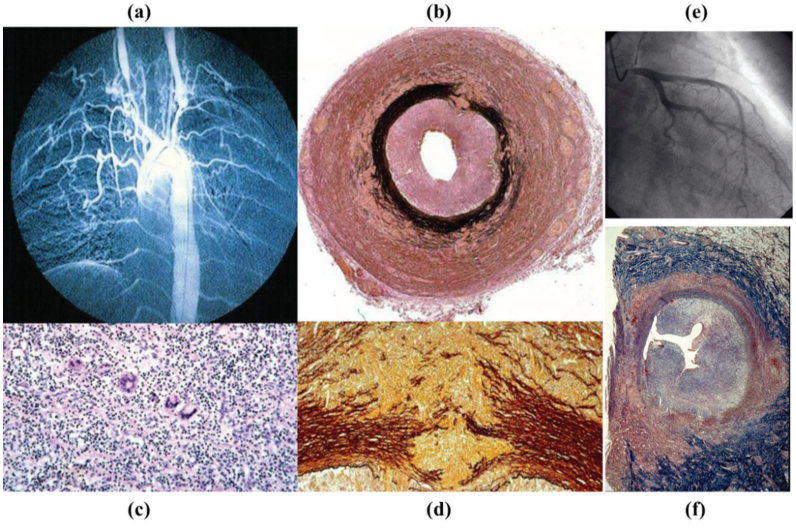

Figure 26. Takayasu arteritis in a 17-year-old girl. (**a**) Angiogram with typical obstruction of the brachiocephalic arteries. (**b**) Cross-section of the left carotid artery: note the severe stenosis of the lumen and the thickness of the adventitia (Weigert Van Gieson stains). (**c**) Giant cell inflammatory infiltrates (hematoxylin-eosin stain). (**d**) Necrotizing angiitis with disruption of the tunica media (close up of (**b**)). (**e**) Left coronary artery stem stenosis by selective coronary angiography with obstructed ostium. (**f**) Corresponding histology (Weigert Van Gieson stain).

IgG4 aortitis-periaortitis occurs in 8% of IgG4-related systemic arteritis [45]. It involves more frequently the abdominal rather than thoracic aorta and is characterized by wall thickening and inflammatory infiltrates, consisting of IgGM-positive plasma cells and lymphocytes (Figure 27). When the ascending aorta is involved, coronary ostia may become stenotic as to require stenting.

Ankylosing spondylitis frequently affects the aorta, both thoracic and abdominal, in the form of aortitis [46–49].

Rheumatoid aortitis [48,50], Reiter's Syndrome [51], Beçhet's Disease [52–54] and Wegener's granulomatosis [55,56] represent other systemic morbid entities with inflammatory involvement of the aorta.

3.5. Neoplasms

Malignant neoplasms of the aorta may be primary or secondary [57].

As far as primary sarcoma, they arise from the intima and appear at clinical imaging as a focal mass protruding into the aortic lumen, mimicking atherothrombosis (Figure 28).

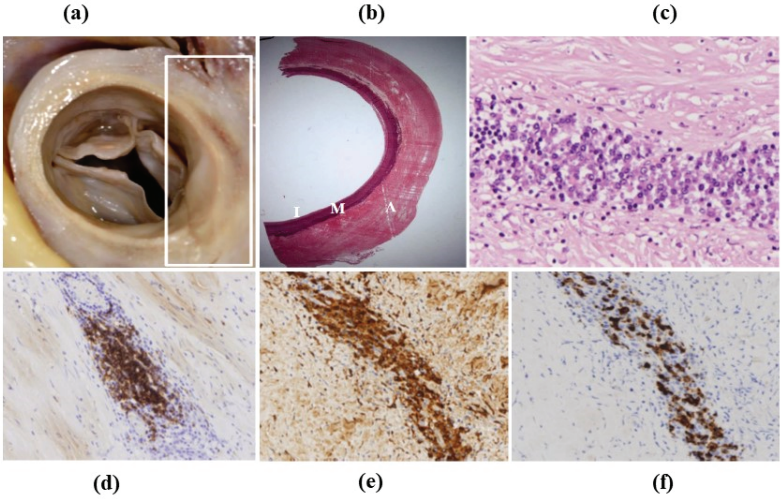

Figure 27. IgG4 aortitis. (**a**) Ascending aorta with increased thickness of the wall. (**b**) Histology: the thickness is located in the adventitia. Weigert Van Gieson stain. (**c**–**f**) Inflammatory infiltrates consist mostly of plasma cells. (**c**) Hematoxylin-Eosin. (**d**) CD79a immunohistochemistry for plasma cells. (**e**) Immunohistochemistry for any IgG. (**f**) Immunohistochemistry for IgG4.

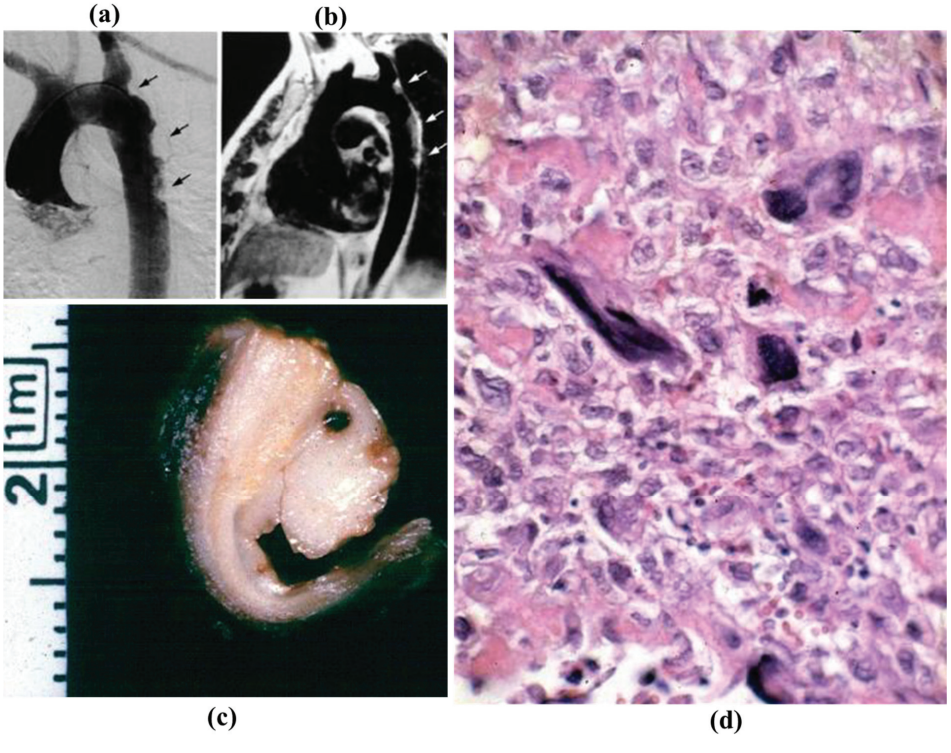

Figure 28. Intimal masses protruding into the lumen of the descending thoracic aorta at selective (**a**) and at tomography angiography (**b**). (**c**) Gross appearance of the specimens removed at surgery. (**d**) Malignant histiocytoma at histology (hematoxylin-eosin).

As far as secondary malignancies, carcinoma of the esophagus (close to the aorta) may infiltrate and penetrate the aortic wall up to the aortic lumen (Figure 29). Massive gastrointestinal hemorrhage may occur, with blood leaking from the mouth like a fountain.

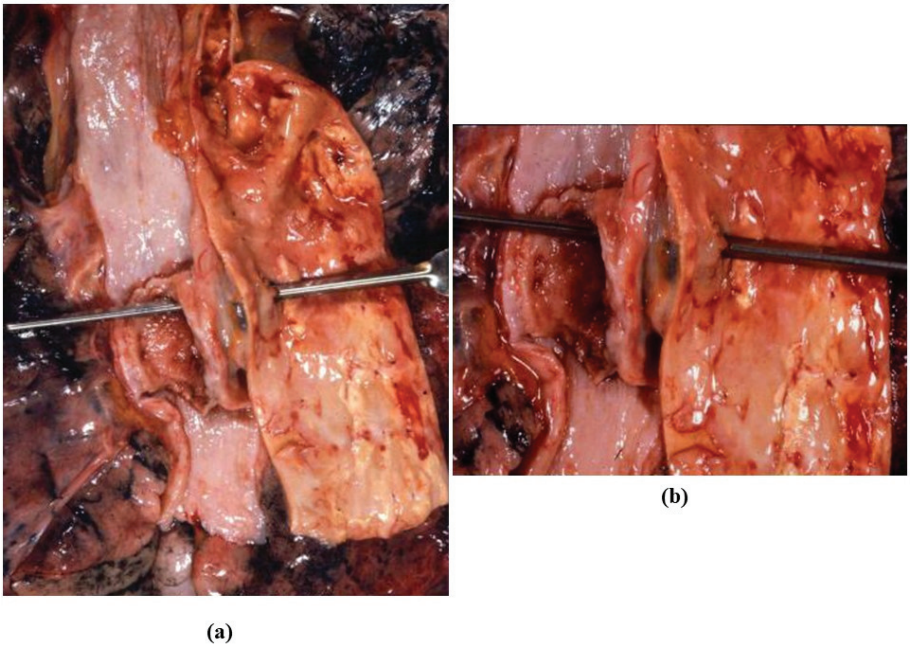

(a) **(b)**

Figure 29. Carcinoma of the esophagus, infiltrating the adjacent aorta and penetrating in the aortic lumen, with massive hematemesis (**a**) Gross view. (**b**) Close up.

3.6. Thoracic Trauma

Penetrating or blunt trauma of the thorax may lead to aortic rupture, usually located in the region of the aortic arch, where the aorta is fixed to the pulmonary artery by the arterial ligament [58]. Traumatic torsion with stretching creates a transmural tear accounting for pseudoaneurysm and external rupture. (Figure 30). An overt aortic dissection is rare.

In conclusion, the aorta is like an organ, with smooth muscle cells of lamellar units as the "parenchyma". Several diseases may affect the thoracic aorta: congenital, genetically determined, degenerative, inflammatory (both infectious and immune), neoplastic and traumatic. In several morbid entities, the aortic valve, ascending aorta and aortic arch represent an anatomo-pathological unit. Surgical replacement, of both the native aortic valve and ascending aorta, with an aortic homograft is an attractive therapeutic option (see below).

Figure 30. Fatal case of traumatic transmural aortic rupture at isthmic level by blunt trauma.

4. Aorta as Homograft

Aortic homograft from a cadaver, including both tubular and sinus portions with valves, is surgically employed to replace the native ascending aorta and aortic valve in several of the above-mentioned morbid conditions [59]. However, the ideal graft has not been accomplished so far; the antigenicity of the wall and valve cells triggers an immune cellular reaction.

Tissue engineering techniques can provide a valid approach to solve the problem.

So far, the main common techniques to realize bioengineered grafts are (1) in vitro cell seeding on biodegradable synthetic scaffolds, (2) in vitro cell seeding of decellularized natural scaffolds and (3) in vivo repopulation of decellularized natural scaffolds by circulating endogenous cells [60]. The last choice, however, can be the best to investigate cell repopulation and interaction with the extracellular matrix (ECM), which seems to play a pivotal role in tissue maintenance and regeneration, and modulates cell adhesion and migration, growth factor storage and release, stem cell activation and differentiation [61]. The decellularized homograft appears to be the best scaffold to realize the ideal graft with in vivo self-repopulation [62,63] because it can preserve regeneration capabilities, while the recipient child grows up.

Decellularization of natural scaffold-like aorta (or pulmonary) allografts represents the first step to remove immunogenic cells from both valve and lamellar units [64–66].

With this purpose, we carried out an investigation based on the hypothesis that decellularized homograft may serve as a scaffold for endogenous self-repopulation, thus

preventing immune reaction and dystrophic calcification, which is a nightmare with current homografts. The research was carried out in healthy juvenile sheep (35–45 kg) by achieving complete decellularization in unimplanted aortic homograft through 0.5% sodium deoxycholate and 0.5% sodium dodecylsulphate and then implanted in allograft recipients, with a follow up of 14–18.5 months. The morphological study was performed in both aortic cusps and wall, with gross, X-ray, histology, immunohistochemistry, transmission electron microscopy and spectroscopy examinations. Results in detail have been reported elsewhere [67]. In summary:

1. Decellularization in unimplanted allografts appeared complete, both in the lamellar units of the tunica media and valvular interstitium with disappearance of endothelial lining (Figure 31);
2. Cellular repopulation was observed in the outer part of implanted homograft wall by novel smooth muscle cells in the lamellar units (Figure 32a,b) and in the intima with a novel myointimal layer; this layer was noticed also in small animals such as rodents [68]. Novel endothelial cells appeared to line both the aortic wall intima and inflow/outflow at the cusp surface, as well as vasa vasorum, and valve spongiosa appeared repopulated by interstitial cells (Figure 32c,d);
3. The ultrastructure of the wall revealed that novel smooth muscle cells have immature aspects, with a central oval nucleus, few contractile filaments and focal densities mainly located close to cytoplasmic membrane and in the paranuclear region; repopulated cells of the cusps are scarcely differentiated cells, in some case showing short intercellular junctions, rough endoplasmic reticulum and focal basal lamina (Figure 33), whereas others exhibited a fibroblast-like morphology;
4. The undifferentiated nature of the repopulated cells is demonstrated by colocalization of some biomarkers. Novel wall cells showed positivity both for α-SMA and vimentin and novel cusp cells for SMA, vWF, VEGF, VEGF R2, α-SMA and CD57 (HNK-1), which is a neural crest marker;
5. The origin of repopulated cells may be vasa vasorum for the homograft outer wall and the blood stream itself for cusps. Recently it has been demonstrated in a GFP rodent model that all novel cells belong to the recipient [68]. Bone marrow may be a source of progenitor cells (endothelial and mesenchymal cells) contributing to recruitment of smooth muscle-like cells [69,70]. Circulating bone-marrow-derived endogenous cells can be recruited in vivo by adhering to the intimal surface [71,72] and then recruited, undergoing an endothelial-to-mesenchymal transition (EMT) within the valve, followed by differentiation into interstitial cells that ultimately synthesize and remodel the ECM;
6. Cell density, when compared to non-decellularized control allografts, showed 20% repopulation both in the aortic wall and at the cusp level (Figure 34);
7. Mean calcium content by spectroscopy in aortic homografts at 14 months from implant was scanty: 4.24 ± 2.17 mg/g dry weight in the wall vs. 0.530 in controls and 5505 ± 2.04 in the cusps vs. 0.936 in the controls.

In conclusion, cell endogenous repopulation of decellularized homografts occurs at both aortic wall and cusps and persists after implantation, thus providing biological compatibility. An immune inflammatory reaction was not observed. The aortic cusps and wall showed no structural deterioration with negligible mineralization. Decellularized homograft may serve as ideal scaffold for self-repopulation from the recipient, transforming homograft into autograft, even if changes in the ECM constitution were found as compared to native tissue, which could lead to problems in cell growth and migration [63].

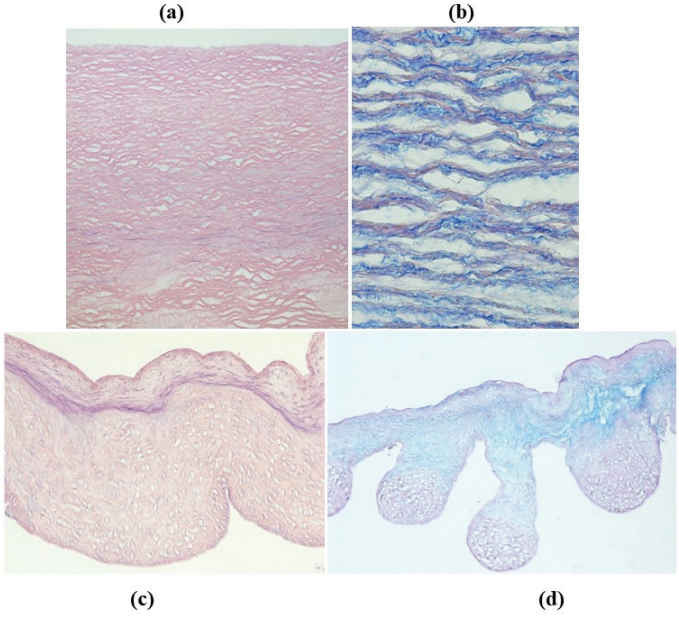

Figure 31. Decellularization of unimplanted aortic homograft: wall (**a**,**b**) and cusps (**c**,**d**). Elastic fibers and ground substance of extracellular matrix are preserved (hematoxylin-eosin, Heidenhein and Alcian PAS stain). From [67], with permission.

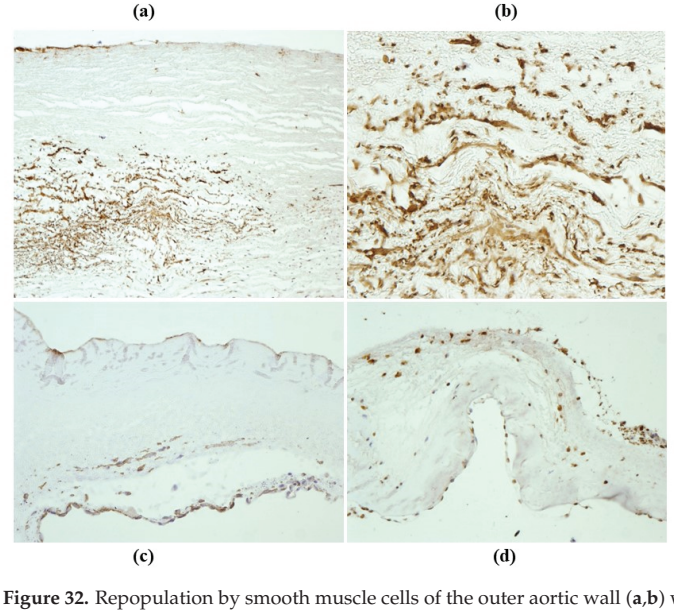

Figure 32. Repopulation by smooth muscle cells of the outer aortic wall (**a**,**b**) with neo endothelial lining (**a**) of a decellularized homograft, 14 months from implant (anti-α-SMA). (**c**,**d**) Repopulation after 14 months of implantation of decellularized homograft aortic cusps by smooth muscle cells and endothelial cells (anti-α-SMA and VWF). From [67], with permission.

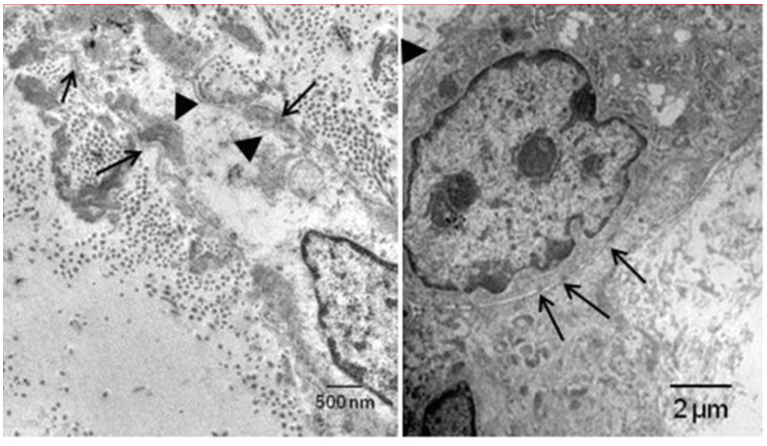

Figure 33. (**a**) Repopulating smooth muscle cells with basal lamina (arrows) and few contractile filaments with focal densities, close to the cytoplasmic membrane and in the paranuclear region (arrowheads). (**b**) Implanted pulmonary homograft cusps: poorly differentiated cells with intercellular junctions (arrows), rough endoplasmic reticulum, and focal basal lamina (arrowhead). From [67].

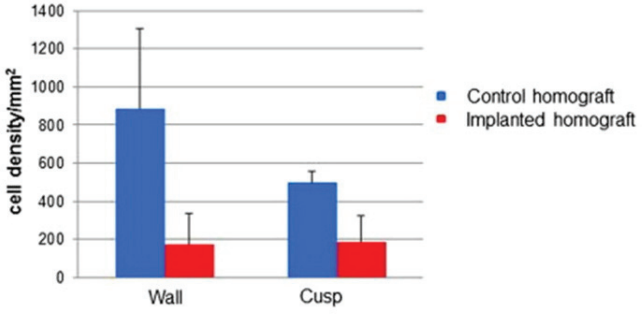

	Wall cell density/mm²	Cusp cell density/mm²
Control homograft	885.4±424.38*	495.96±63.92^
Implanted homograft	172.64±160.33*	184.66±140.74^

*p< 0.01; ^ p<0.01. Values are expressed as mean±SD

Figure 34. Histogram displaying cell density per millimeter squared in native vs. implanted decellularized conduit wall and cusps. A 20% repopulation occurred. All values are expressed as mean ± S.D. From [67].

These results, however, represent a significant advancement when compared with cryopreserved homografts, which retain allografts cells as a target for immune inflammatory rejection and early calcification.

Finally, investigation of other more specific immunoreactive precursor cell markers is mandatory to study the repopulation cell phenotype and their proliferation modality, especially for the poorly differentiated elements found in the cusps.

Funding: This study was supported by the Registry for Cardio-cerebro-vascular Pathology, Veneto Region, Italy.

Acknowledgments: We thank the technical staff of Cardiovascular Pathology Unit of the University of Padua for the excellent collaboration.

Conflicts of Interest: The authors declare no conflict of interest.

References

1. Isselbacher, E.; Eagle, K.; Desanctis, R. Disease of the aorta. In *Heart Disease: A Textbook of Cardiovascular Medicine*; Braunwald, E., Ed.; W.B. Saunders Co.: Philadelphia, PA, USA, 1997; pp. 1546–1581.
2. Buja, L.M.; Butany, J. *Cardiovascular Pathology*, 4th ed.; Academic Press; Elsevier: London, UK, 2016; ISBN 978-0-12-420219-1.
3. Wolinsky, H.; Glagov, S. A Lamellar Unit of Aortic Medial Structure and Function in Mammals. *Circ. Res.* **1967**, *20*, 99–111. [CrossRef]
4. El-Hamamsy, I.; Yacoub, M.H. Cellular and molecular mechanisms of thoracic aortic aneurysms. *Nat. Rev. Cardiol.* **2009**, *6*, 771–786. [CrossRef] [PubMed]
5. Majesky, M.W. Developmental Basis of Vascular Smooth Muscle Diversity. *Arter. Thromb. Vasc. Biol.* **2007**, *27*, 1248–1258. [CrossRef]
6. Thiene, G.; Corrado, D.; Basso, C. *Sudden Cardiac Death in the Young and Athletes: Text Atlas of Pathology and Clinical Correlates*; Springer: Milan, Italy, 2016.
7. Basso, C.; Boschello, M.; Perrone, C.; Mecenero, A.; Cera, A.; Bicego, D.; Thiene, G.; De Dominicis, E. An echocardiographic survey of primary school children for bicuspid aortic valve. *Am. J. Cardiol.* **2004**, *93*, 661–663. [CrossRef] [PubMed]
8. Nistri, S.; Basso, C.; Marzari, C.; Mormino, P.; Thiene, G. Frequency of bicuspid aortic valve in young male conscripts by echo-cardiogram. *Am. J. Cardiol.* **2005**, *96*, 718–721. [CrossRef] [PubMed]
9. Fernandes, S.M.; Khairy, P.; Sanders, S.; Colan, S.D. Bicuspid Aortic Valve Morphology and Interventions in the Young. *J. Am. Coll. Cardiol.* **2007**, *49*, 2211–2214. [CrossRef] [PubMed]
10. Sabet, H.Y.; Edwards, W.D.; Tazelaar, H.D.; Daly, R.C. Congenitally Bicuspid Aortic Valves: A Surgical Pathology Study of 542 Cases (1991 through 1996) and a Literature Review of 2715 Additional Cases. In *Mayo Clinic Proceedings*; Elsevier BV: Amsterdam, The Netherlands, 1999; Volume 74, pp. 14–26.
11. McKusick, V.A. Association of congenital bicuspid aortic valve and Erdheim's cystic medial necrosis. *Lancet* **1972**, *1*, 1026–1027. [CrossRef]
12. Roberts, C.S.; Roberts, W.C. Dissection of the aorta associated with congenital malformation of the aortic valve. *J. Am. Coll. Cardiol.* **1991**, *17*, 712–716. [CrossRef]
13. Verma, S.; Siu, S.C. Aortic Dilatation in Patients with Bicuspid Aortic Valve. *New Engl. J. Med.* **2014**, *370*, 1920–1929. [CrossRef] [PubMed]
14. El-Hamamsy, I.; Yacoub, M.H. A measured approach to managing the aortic root in patients with bicuspid aortic valve dis-ease. *Curr. Cardiol. Rep.* **2009**, *11*, 94–100. [CrossRef]
15. Nistri, S.; Grande-Allen, J.; Noale, M.; Basso, C.; Siviero, P.; Maggi, S.; Crepaldi, G.; Thiene, G. Aortic elasticity and size in bicuspid aortic valve syndrome. *Eur. Heart J.* **2007**, *29*, 472–479. [CrossRef] [PubMed]
16. Kappetein, A.P.; Gittenberger-de Groot, A.C.; Zwinderman, A.H.; Rohmer, J.; Poelmann, R.E.; Huysmans, H.A. The neural crest as a possible pathogenetic factor in coarctation of the aorta and bicuspid aortic valve. *J. Thorac. Cardiovasc. Surg.* **1991**, *102*, 830–836. [CrossRef]
17. Sakakibara, S.; Konno, S. Congenital aneurysm of the sinus of Valsalva Anatomy and classification. *Am. Heart J.* **1962**, *63*, 405–424. [CrossRef]
18. Morris, C.A.; Loker, J.; Ensing, G.; Stock, A.D. Supravalvular aortic stenosis cosegregates with a familial 6;7 translocation which disrupts the elastin gene. *Am. J. Med. Genet.* **1993**, *46*, 737–744. [CrossRef] [PubMed]
19. Williams, J.C.P.; Barratt-Boyes, B.G.; Lowe, J.B. Supravalvular Aortic Stenosis. *Circulation* **1961**, *24*, 1311–1318. [CrossRef] [PubMed]
20. Dietz, H.C.; Cutting, C.R.; Pyeritz, R.E.; Maslen, C.L.; Sakai, L.Y.; Corson, G.M.; Puffenberger, E.; Hamosh, A.; Nanthakumar, E.J.; Curristin, S.M.; et al. Marfan syndrome caused by a recurrent de novo missense mutation in the fibrillin gene. *Nat. Cell Biol.* **1991**, *352*, 337–339. [CrossRef] [PubMed]
21. Loeys, B.L.; Schwarze, U.; Holm, T.; Callewaert, B.L.; Thomas, G.H.; Pannu, H.; De Backer, J.F.; Oswald, G.L.; Symoens, S.; Manouvrier, S.; et al. Aneurysm syndromes caused by mutations in the TGF-beta receptor. *N. Engl. J. Med.* **2006**, *355*, 788–798. [CrossRef]
22. Neptune, E.R.; Frischmeyer, P.A.; Arking, D.E.; Myers, L.; Bunton, T.E.; Gayraud, B.; Ramirez, F.; Sakai, L.Y.; Dietz, H.C. Dysregulation of TGF-beta activation contributes to pathogenesis in Marfan syndrome. *Nat. Genet.* **2003**, *33*, 407–411. [CrossRef] [PubMed]
23. De Paepe, A.; Malfait, F. The Ehlers-Danlos syndrome.; a disorder with many faces. *Clin. Genet.* **2012**, *82*, 1–11. [CrossRef] [PubMed]
24. Wenstrup, R.J.; A Meyer, R.; Lyle, J.S.; Hoechstetter, L.; Rose, P.S.; Levy, H.P.; A Francomano, C. Prevalence of aortic root dilation in the Ehlers-Danlos syndrome. *Genet. Med.* **2002**, *4*, 112–117. [CrossRef]
25. Turtle, E.J.; A Sule, A.; Webb, D.J.; E Bath, L. Aortic dissection in children and adolescents with Turner syndrome: Risk factors and management recommendations. *Arch. Dis. Child.* **2015**, *100*, 662–666. [CrossRef] [PubMed]

26. Thompson, R.W.; Parks, W.C. Role of Matrix Metalloproteinases in Abdominal Aortic Aneurysms. *Ann. N. Y. Acad. Sci.* **1996**, *800*, 157–174. [CrossRef] [PubMed]
27. Cooley, D.A. Annuloaortic Ectasia. *Ann. Thorac. Surg.* **1979**, *28*, 303–304. [CrossRef]
28. Ellis, P.R.; Cooley, D.A.; De Bakey, M.E. Clinical considerations and surgical treatment of annulo-aortic ectasia. *J. Thorac. Cardiovasc. Surg.* **1961**, *42*, 363–370. [CrossRef]
29. Beller, C.J.; Labrosse, M.; Thubrikar, M.J.; Robicsek, F. Role of Aortic Root Motion in the Pathogenesis of Aortic Dissection. *Circulation* **2004**, *109*, 763–769. [CrossRef] [PubMed]
30. Evangelista, A.; Mukherjee, D.; Mehta, R.H.; O'Gara, P.T.; Fattori, R.; Cooper, J.V.; Smith, D.E.; Oh, J.K.; Hutchison, S.; Sechtem, U.; et al. International Registry of Aortic Dissection (IRAD) Investigators. Acute in-tramural hematoma of the aorta: A mystery in evolution. *Circulation* **2005**, *111*, 1063–1070. [CrossRef]
31. Larson, E.W.; Edwards, W.D. Risk factors for aortic dissection: A necropsy study of 161 cases. *Am. J. Cardiol.* **1984**, *53*, 849–855. [CrossRef]
32. Goldfinger, J.Z.; Halperin, J.L.; Marin, M.L.; Stewart, A.S.; Eagle, K.A.; Fuster, V. Thoracic Aortic Aneurysm and Dissection. *J. Am. Coll. Cardiol.* **2014**, *64*, 1725–1739. [CrossRef] [PubMed]
33. Jondeau, G.; Boileau, C. Familial thoracic aortic aneurysms. *Curr. Opin. Cardiol.* **2014**, *29*, 492–498. [CrossRef] [PubMed]
34. Ladich, E.; Butany, J.; Virmani, R. 5-Aneurysms of the Aorta: Ascending, Thoracic and Abdominal and Their Management. In *Cardiovascular Pathology*, 4th ed.; Buja, L.M., Butany, J., Eds.; Academic Press: Cambridge, MA, USA, 2016; pp. 169–211. ISBN 9780124202191.
35. Pyeritz, R.E. Heritable thoracic aortic disorders. *Curr. Opin. Cardiol.* **2014**, *29*, 97–102. [CrossRef] [PubMed]
36. Vaideeswar, P.; Dixit, V.; Butany, J.; David, T.E.; Feindel, C. Surgical pathology of chronic ascending aortic dissections. *Pathology* **2008**, *40*, 505–512. [CrossRef]
37. Gornik, H.L.; Creager, M.A. Aortitis. *Circulation* **2008**, *117*, 3039–3051. [CrossRef]
38. Virmani, R.; Burke, A.P. Pathologic features of aortitis. *Cardiovasc. Pathol.* **1994**, *3*, 205–216. [CrossRef]
39. Virmani, R.; McAllister, H. Pathology of the aorta and major arteries. In *Aortitis: Clinical, Pathologic, and Radiographic Aspects*; Lande, A., Borkman, Y., McAllister, H., Eds.; Raven Press: New York, NY, USA, 1986; pp. 7–53.
40. Heggtveit, H.A. Syphilitic aortitis. A clinicopathologic autopsy study of 100 cases, 1950 to 1960. *Circulation* **1964**, *29*, 346–355. [CrossRef]
41. Musci, M.; Weng, Y.; Hübler, M.; Amiri, A.; Pasic, M.; Kosky, S.; Stein, J.; Siniawski, H.; Hetzer, R. Homograft aortic root replacement in native or prosthetic active infective endocarditis: Twenty-year single-center experience. *J. Thorac. Cardiovasc. Surg.* **2010**, *139*, 665–673. [CrossRef]
42. Yanagawa, B.; Mazine, A.; Tam, D.Y.; Jüni, P.; Bhatt, D.L.; Spindel, S.; Puskas, J.D.; Verma, S.; Friedrich, J.O. Homograft Versus Conven-tional Prosthesis for Surgical Management of Aortic Valve Infective Endocarditis: A Systematic Review and Meta-analysis. *Innovations* **2018**, *13*, 163–170. [CrossRef]
43. Evans, J.M.; Bowles, C.A.; Bjornsson, J.; Mullany, C.J.; Hunder, G.G. Thoracic aortic aneurysm and rupture in giant cell arteritis. a descriptive study of 41 cases. *Arthritis Rheum.* **1994**, *37*, 1539–1547. [CrossRef]
44. Lupi-Herrera, E.; Sánchez-Torres, G.; Marcushamer, J.; Mispireta, J.; Horwitz, S.; Vela, J.E. Takayasu's arteritis. Clinical study of 107 cases. *Am. Heart. J.* **1977**, *93*, 94–103. [CrossRef]
45. Stone, J.H.; Khosroshahi, A.; Deshpande, V.; Stone, J.R. IgG4-related systemic disease accounts for a significant proportion of thoracic lymphoplasmacytic aortitis cases. *Arthritis Rheum.* **2010**, *62*, 316–322. [CrossRef]
46. Ansell, B.M.; Bywaters, E.G.L.; Doniach, I. The aortic lesion of ankylosing spondylitis. *Br. Heart J.* **1958**, *20*, 507–515. [CrossRef]
47. Bulkley, B.H.; Roberts, W.C. Ankylosing spondylitis and aortic regurgitation. Description of the characteristic cardiovascular lesion from study of eight necropsy patients. *Circulation* **1973**, *48*, 1014–1027. [CrossRef]
48. Arnason, J.A.; Patel, A.K.; Rahko, P.S.; Sundstrom, W.R. Transthoracic and transesophageal echocardiographic evaluation of the aortic root and subvalvular structures in ankylosing spondylitis. *J. Rheumatol.* **1996**, *23*, 120–123. [PubMed]
49. Palazzi, C.; D' Angelo, S.; Lubrano, E.; Olivieri, I. Aortic involvement in ankylosing spondylitis. *Clin. Exp. Rheumatol.* **2008**, *26* (Suppl. 49), S131–S134.
50. Reimer, K.A.; Rodgers, R.F.; Oyasu, R. Rheumatoid Arthritis With Rheumatoid Heart Disease and Granulomatous Aortitis. *JAMA* **1976**, *235*, 2510–2512. [CrossRef]
51. Paulus, H.E.; Pearson, C.M.; Pitts, W., Jr. Aortic insufficiency in five patients with Reiter's syndrome. A detailed clinical and pathologic study. *Am. J. Med.* **1972**, *53*, 464–472. [CrossRef]
52. Chajek, T.; Fainaru, M. Behcet's disease. Report of 41 cases and a review of the literature. *Medicine* **1975**, *54*, 179–196. [CrossRef]
53. Hamza, M. Large artery involvement in Behcet's disease. *J. Rheumatol.* **1987**, *14*, 554–559.
54. Tuzun, H.; Besirli, K.; Sayin, A.; Vural, F.S.; Hamuryudan, V.; Hizli, N.; Yurdakul, S.; Yazici, H. Management of aneurysms in Behcet's syndrome: An analysis of 24 patients. *Surgery* **1997**, *121*, 150–156. [CrossRef]
55. Blockmans, D.; Baeyens, H.; Van Loon, R.; Lauwers, G.; Bobbaers, H. Periaortitis and aortic dissection due to Wegener's granu-lomatosis. *Clin. Rheumatol.* **2000**, *19*, 161–164. [CrossRef]
56. Unlü, C.; Willems, M.; Ten Berge, I.J.; Legemate, D.A. Aortitis with aneurysm formation as a rare complication of Wegener's granulomatosis. *J. Vasc. Surg.* **2011**, *54*, 1485–1487. [CrossRef]

57. Chiche, L.; Mongrédien, B.; Brocheriou, I.; Kieffer, E. Primary Tumors of the Thoracoabdominal Aorta: Surgical Treatment of 5 Patients and Review of the Literature. *Ann. Vasc. Surg.* **2003**, *17*, 354–364. [CrossRef]
58. Neschis, D.G.; Scalea, T.M.; Flinn, W.R.; Griffith, B.P. Blunt Aortic Injury. *N. Eng. J. Med.* **2008**, *359*, 1708–1716. [CrossRef] [PubMed]
59. Eugene, H.B.; Frank, L.H.; James, K.K.; Nicholas, T. *Kouchoukos Kirklin/Barratt-Boyes. Cardiac Surgery*; Expert Consult. Saunders: Milan, Italy, 2012; ISBN 9781416063919.
60. Mendelson, K.; Schoen, F.J. Heart valve tissue engineering: Concepts, approaches, progress, and challenges. *Ann. Biomed. Eng.* **2006**, *34*, 1799–1819. [CrossRef]
61. Flaumenhaft, R.; Moscatelli, D.; Saksela, O.; Rifkin, D.B. Role of extracellular matrix in the action of basic fibroblast growth factor: Ma-trix as a source of growth factor for long-term stimulation of plasminogen activator production and DNA synthesis. *J. Cell. Physiol.* **1989**, *140*, 75–81. [CrossRef] [PubMed]
62. Baraki, H.; Tudorache, I.; Braun, M.; Höffler, K.; Görler, A.; Lichtenberg, A.; Bara, C.; Calistru, A.; Brandes, G.; Hewicker-Trautwein, M.; et al. Orthotopic replacement of the aortic valve with decellularized allograft in a sheep model. *Biomaterials* **2009**, *30*, 6240–6246. [CrossRef]
63. Grauss, R.W.; Hazekamp, M.G.; Oppenhuizen, F.; Van Munsterena, C.J.; Groot, A.C.G.-D.; DeRuiter, M.C. Histological evaluation of decellularised porcine aortic valves: Matrix changes due to different decellularisation methods. *Eur. J. Cardio-Thorac. Surg.* **2005**, *27*, 566–571. [CrossRef]
64. Cebotari, S.; Lichtenberg, A.; Tudorache, I.; Hilfiker, A.; Mertsching, H.; Leyh, R.; Breymann, T.; Kallenbach, K.; Maniuc, L.; Batrinac, A.; et al. Clinical application of tissue engineered human heart valves using autolo-gous progenitor cells. *Circulation* **2006**, *114*, I132–I137. [CrossRef]
65. Cebotari, S.; Tudorache, I.; Jaekel, T.; Hilfiker, A.; Dorfman, S.; Ternes, W.; Haverich, A.; Lichtenberg, A. Detergent Decellularization of Heart Valves for Tissue Engineering: Toxicological Effects of Residual Detergents on Human Endothelial Cells. *Artif. Organs* **2010**, *34*, 206–210. [CrossRef]
66. Tudorache, I.; Theodoridis, K.; Samir, S.; Bara, C.; Meyer, T.; Höffler, K.; Hartung, D.; Hilfiker, A.; Haverich, A.; Cebotari, S. Decellular-ized aortic allograft vs pulmonary autograft for aortic valve replacement in growing sheep model: Haemodynamic and morphological results after implantation for 20 months. *Circulation* **2014**, *130*, A20027.
67. Della Barbera, M.; Valente, M.; Basso, C.; Thiene, G. Morphologic studies of cell endogenous repopulation in decellularized aortic and pulmonary homografts implanted in sheep. *Cardiovasc Pathol.* **2015**, *24*, 102–109. [CrossRef]
68. Dedja, A.; Padalino, M.A.; Della Barbera, M.; Rasola, C.; Pesce, P.; Milan, A.; Pozzobon, M.; Sacerdoti, D.; Thiene, G.; Stellin, G. Heterotopic Implantation of Decellularized Pulmonary Artery Homografts In A Rodent Model: Technique Description and Preliminary Report. *J. Investig. Surg.* **2017**, *31*, 282–291. [CrossRef]
69. Sata, M.; Fukuda, D.; Tanaka, K.; Kaneda, Y.; Yashiro, H.; Shirakawa, I. The role of circulating precursors in vascular repair and lesion formation. *J. Cell. Mol. Med.* **2005**, *9*, 557–568. [CrossRef]
70. Frid, M.G.; Kale, V.A.; Stenmark, K.R. Mature vascular endothelium can give rise to smooth muscle cells via endotheli-al-mesenchymal transdifferentiation: In vitro analysis. *Circ. Res.* **2002**, *90*, 1189–1196. [CrossRef]
71. Deb, A.; Wang, S.H.; Skelding, K.; Miller, D.; Simper, D.; Caplice, N. Bone marrow-derived myofibroblasts are present in adult human heart valves. *J. Heart Valve Dis.* **2005**, *14*, 674–678.
72. Armstrong, E.J.; Bischoff, J. Heart valve development: Endothelial cell signaling and differentiation. *Circ. Res.* **2004**, *95*, 459–470. [CrossRef]

Journal of
Cardiovascular
Development and Disease

MDPI

Case Report

The Clinical Spectrum of Kommerell's Diverticulum in Adults with a Right-Sided Aortic Arch: A Case Series and Literature Overview

Philippe J. van Rosendael [1,2], J. Lauran Stöger [3], Philippine Kiès [1,2], Hubert W. Vliegen [1,2], Mark G. Hazekamp [1,4], David R. Koolbergen [1,4], Hildo J. Lamb [3], Monique R. M. Jongbloed [1,2,5,†] and Anastasia D. Egorova [1,2,*,†]

[1] Center for Congenital Heart Disease Amsterdam-Leiden (CAHAL), Leiden University Medical Center, 2333 ZA Leiden, The Netherlands; p.j.van_rosendael@lumc.nl (P.J.v.R.); p.kies@lumc.nl (P.K.); H.W.Vliegen@lumc.nl (H.W.V.); M.G.Hazekamp@lumc.nl (M.G.H.); D.R.Koolbergen@lumc.nl (D.R.K.); M.R.M.Jongbloed@lumc.nl (M.R.M.J.)
[2] Department of Cardiology, Heart Lung Centre, Leiden University Medical Centre, 2333 ZC Leiden, The Netherlands
[3] Department of Radiology, Leiden University Medical Center, 2333 ZA Leiden, The Netherlands; J.L.Stoger@lumc.nl (J.L.S.); h.j.lamb@lumc.nl (H.J.L.)
[4] Department of Cardiothoracic Surgery, Leiden University Medical Center, 2333 ZC Leiden, The Netherlands
[5] Department of Anatomy and Embryology, Leiden University Medical Center, 2333 ZC Leiden, The Netherlands
* Correspondence: a.egorova@lumc.nl; Tel.: +31715262020; Fax: +31715266809
† These authors contributed equally.

Abstract: Background: Kommerell's diverticulum is a rare vascular anomaly characterized as an outpouch at the onset of an aberrant subclavian artery. In the variant of a right-sided aortic arch, the trachea and esophagus are enclosed dorsally by the arch. In the configuration of an aberrant left subclavian artery, a Kommerell's diverticulum and persisting ductus arteriosus or ductal ligament enclose the lateral side, forming a vascular ring which may result in (symptomatic) esophageal or tracheal compression. Spontaneous rupture of an aneurysmatic Kommerell's diverticulum has also been reported. Due to the rarity of this condition and underreporting in the literature, the clinical implications of a Kommerell's diverticulum are not well defined. Case summary: We describe seven consecutive adult patients with a right-sided aortic arch and an aberrant course of the left subclavian artery (arteria lusoria), and a Kommerell's diverticulum, diagnosed in our tertiary hospital. One patient had severe symptoms related to the Kommerell's diverticulum and underwent surgical repair. In total, two of the patients experienced mild non-limiting dyspnea complaints and in four patients the Kommerell's diverticulum was incidentally documented on a computed tomography (CT) scan acquired for a different indication. The size of the Kommerell's diverticulum ranged from 19 × 21 mm to 30 × 29 mm. In the six patients that did not undergo surgery, a strategy of periodic follow-up with structural imaging was pursued. No significant growth of the Kommerell's diverticulum was observed and none of the patients experienced an acute aortic syndrome to date. Discussion: Kommerell's diverticulum in the setting of a right-sided aortic arch with an aberrant left subclavian artery is frequently associated with tracheal and esophageal compression and this may result in a varying range of symptoms. Guidelines on management of Kommerell's diverticulum are currently lacking. This case series and literature overview suggests that serial follow-up is warranted in adult patients with a Kommerell's diverticulum with small dimensions and no symptoms, however, that surgical intervention should be considered when patients become symptomatic or when the diameter exceeds 30 mm in the absence of symptoms.

Keywords: Kommerell's diverticulum; right sided aortic arch; anomalous left subclavian artery; arteria lusoria; tracheal compression; esophageal compression

Citation: van Rosendael, P.J.; Stöger, J.L.; Kiès, P.; Vliegen, H.W.; Hazekamp, M.G.; Koolbergen, D.R.; Lamb, H.J.; Jongbloed, M.R.M.; Egorova, A.D. The Clinical Spectrum of Kommerell's Diverticulum in Adults with a Right-Sided Aortic Arch: A Case Series and Literature Overview. *J. Cardiovasc. Dev. Dis.* **2021**, *8*, 25. https://doi.org/10.3390/jcdd8030025

Received: 11 January 2021
Accepted: 22 February 2021
Published: 26 February 2021

1. Introduction: From Embryology to Clinical Presentation

A Kommerell's diverticulum is a rare vascular anomaly and is characterized by an aneurysmatic onset of an aberrant left or right subclavian artery [1]. A Kommerell's diverticulum was first described by the radiologist Burckhard Kommerell in 1936 in a patient with dysphagia due to esophageal compression that was related to an aneurysmatic onset of an aberrant right subclavian artery from a left-sided aortic arch [2,3]. Currently, the definition also includes an aneurysmatic origin of an aberrant left subclavian artery from a right-sided aortic arch, and it may also be present in patients with a double aortic arch [4]. From surgical and radiology series, it has been estimated that the prevalence of a left-sided aortic arch with an aberrant right subclavian artery ranges between 0.7–2.0% and between 0.04–0.4% for a right-sided aortic arch with an aberrant left subclavian artery [3,5]. Overall, it is reported that 20–60% of the aberrant subclavian arteries are associated with a Kommerell's diverticulum, defined as an offset diameter being more than 50% larger than the diameter of the distal segment of the aberrant subclavian artery [3,5,6]. Recently, Erben et al. reported a retrospective analysis of the radiological database of Yale from the years 1999 to 2006. Of the 75 patients with a Kommerell's diverticulum 63% had a left-sided arch with aberrant right subclavian artery and 37% had a right-sided arch with left subclavian artery [7]. In contrast, a retrospective analysis of the radiology database of the Mayo clinic of the years 1990 to 2014 by Poterucha et al. (Congress abstract data, American Cardiology College 2015) showed that in 863 patients who were identified with an aberrant subclavian artery, that a Kommerell's diverticulum was observed in 14% (n = 121), and of those patients 60% (n = 73) had a right-sided aortic arch and aberrant left subclavian artery [8]. The discrepancies between the data of Erben et al. and Poterucha et al. may in part be explained by differences in the used criteria to define a Kommerell's diverticulum or due to diagnostic underreporting.

From an embryological perspective and based on extensive studies in animal models, a Kommerell's diverticulum has been suggested to result from incomplete regression of the 4th pharyngeal arch artery (PAA) [6,9,10]. The embryological vascular system is initially bilateral, and both a right and left-sided aortic arch can be identified (Figure 1A). In the right and left aortic arches several different segments can be recognized (Figure 1A), that are partly derived from the PAAs, embryological bilateral vascular structures that during early development arise from the aortic sac, the first part of the developing aorta that can be recognised. Part of the left and right aortic arches are derived from the right and the left 4th PAA [9–12]. The right and left 4th PAAs give rise to the aortic segment in between the carotid and subclavian arteries (also referred to as the aortic B segment) and connect distally via so-called beta- and alpha-segments to the descending aorta (Figure 1A) [9–12].

During development of a normal left aortic arch (Figure 1B), the right alpha-segment (i.e., the part connecting the right arch to the descending aorta, after the offset of the right common carotid and the right subclavian artery) regresses [10]. In this case the left 4th PAA will persist to form the normal left aortic arch, that is connected via the left beta- and alpha-segment to the descending aorta. The aortic arch tributaries are also largely derived from the embryonic PAAs. The left and right third PAA will contribute to the left and right common carotid arteries. The subclavian arteries are derived from the 7th intersegmental arteries, and will eventually connect to the aortic arch at the level of the beta-segment (Figure 1A,B). During normal development, the right 4th PAA and beta-segment will eventually form the origin of the right subclavian artery (Figure 1B), connecting it to the aorta via the brachiocephalic trunk [13]. If, however, the right 4th PAA shows an abnormal regression, this connection cannot be established resulting in an aberrant, more distal origin of the right subclavian artery from the descending aorta, via a persisting right alpha-segment [3] (Figure 1C). This aberrant subclavian artery courses posteriorly to the esophagus and trachea, to supply the right arm [9,10].

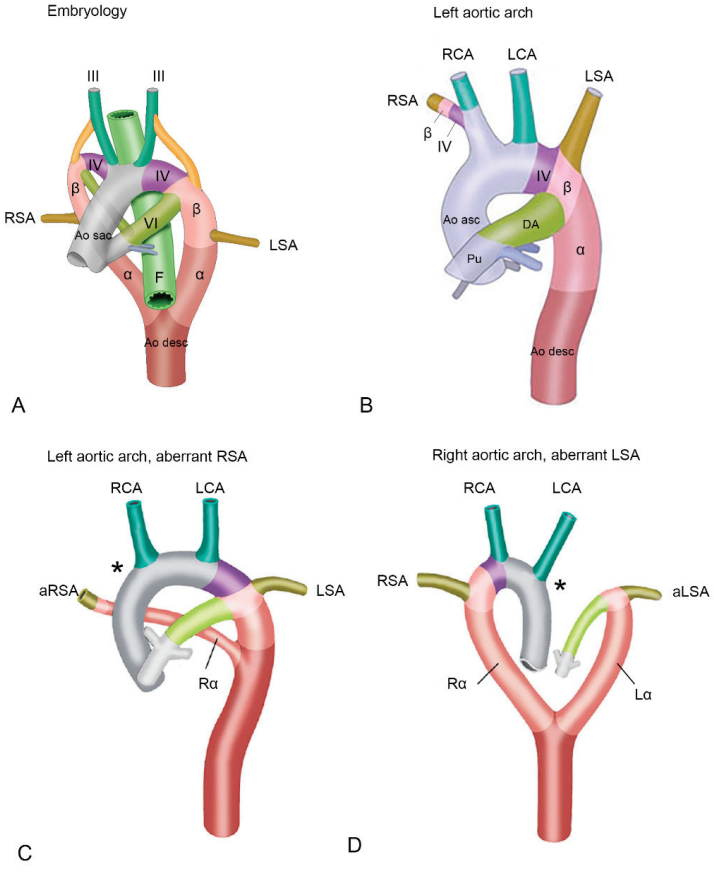

Figure 1. (**A**) Schematic overview of early development. Embryological segments are superimposed on the developing vascular system of the cardiac outflow tract. The vascular system evolves from an initially almost symmetrical bilateral system, into an asymmetrical system. Structures relevant to development of the outflow tract arteries are indicated. (**B**) Left sided aortic arch. The right 4th pharyngeal arch artery (PAA) and beta-segment now form the base of the right subclavian artery, connecting it to the aorta via the brachiocephalic artery. The right alpha-segment has regressed. (**C**) Left aortic arch with an aberrant right subclavian artery. Due to deficiency of the right 4th PAA (asterisk *), the proximal part of the right subclavian artery is deficient, and an aberrant right subclavian artery is connected distally to the aorta descendens via a persisting right alpha-segment. (**D**) Right aortic arch with an aberrant right subclavian artery. In this case, the left 4th PAA is deficient (asterisk *) and the aberrant left subclavian artery is connected to the aorta descendens via a persisting left alpha-segment. Abbreviations in the figure: α, alpha-segment; aLSA, aberrant left subclavian artery; Ao desc, descending aorta; Ao sac, aortic sac; aRSA, aberrant right subclavian artery; β, beta-segment; DA, ductus arteriosus; F, foregut (will later form a.o. esophagus and trachea); Lα, left alpha-segment, LCA, left carotid artery; LSA, left subclavian artery; Pu, pulmonary trunk; Rα, right alpha-segment; RCA, right carotid artery; RSA, right subclavian artery. III, IV and VI, 3rd, 4th and 6th pharyngeal arch arteries (PAA) respectively. Color coding: Grey, ascending aorta; green, carotid arteries, derived form 3rd PAA; purple, aortic B segment (in between carotid and subclavian artery, derived from 4th PAA, olive green, left subclavian arteries (derived from 7th intersegmental arteries); dark brown, descending aorta; dark pink, alpha-segment; light pink, beta-segment. Figures are modified with permission from Molin et al. Cardiovasc Res. 2002 [11] and Molin et.al Birth Defects Res A Clin Mol Teratol. 2004 [12].

In case of development of a right (instead of a left) aortic arch, a complete mirror image of the arch arteries can be encountered: the right arch first gives rise to a left brachiocephalic trunk, and subsequently a right carotid and right subclavian artery arising directly from the aortic arch. The right aortic arch in this case connects to the descending aorta via a persisting right alpha-segment, whereas the left alpha-segment has regressed. If in case of a right aortic arch, the left 4th PAA (partially) regresses, an aberrant left subclavian artery will connect to the descending aorta via a persisting left alpha-segment, and will course dorsally to the esophagus and trachea to supply the left arm [9,10] (Figure 1D). One could hypothesize that a Kommerell's diverticulum results from an only partial regression of the 4th PAA, thus still forming part of the base of the left subclavian artery together with the beta-segment, but lacking a connection to the proximal part of the aorta (Figure 2). The arterial duct connects to the aorta in this area, and will thus complete the vascular ring formed by the right aortic arch. After closure of the duct, traction by the arterial ligament is considered to be an important factor in growth of the Kommerell's diverticulum.

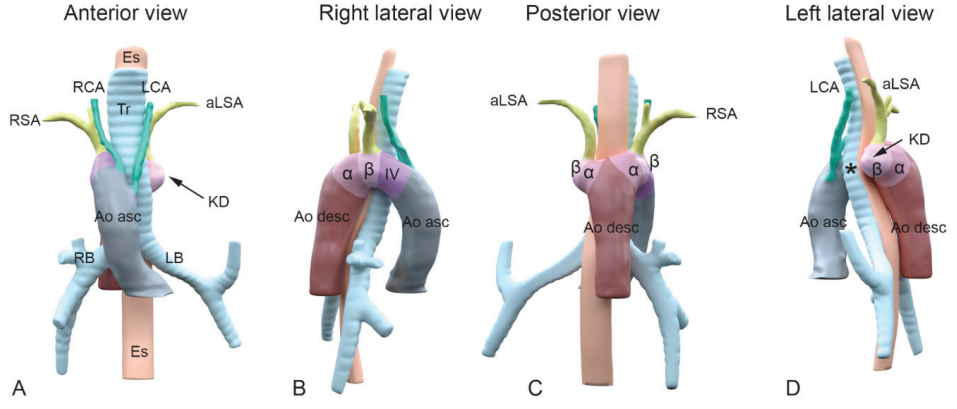

Figure 2. A schematic representation of the embryological aortic segments involved in development of a Kommerell's diverticulum. Panel (**A**–**D**): Different views of 3D reconstructions based on computed tomography angiography (CTA) images of a patient with a right-sided aortic arch and an aberrant left subclavian artery. Colors superimposed on the figures indicate segments derived from the embryological pharyngeal arch arteries (PAA) and other embryological aortic segments. Color coding: Grey: ascending aorta; green: carotid arteries, derived from 3rd PAA; purple: aortic B segment (in between carotid and subclavian artery, derived from 4th PAA); olive green: subclavian arteries (derived from 7th intersegmental arteries); dark brown: descending aorta; dark pink: alpha-segment; light pink: beta-segment. Colors and segments are derived from Molin et al. Cardiovasc Res. 2002 [11], and Molin et al. Birth Defects Res A Clin Mol Teratol. 2004 [12]. (**A**) Anterior view. Note the right-sided position of the arch in relation to trachea and esophagus. Upstream in the aorta, the following aortic arch tributaries can be encountered: left carotid artery (LCA), right carotid artery (RCA), right subclavian artery (RSA) and an aberrant left subclavian artery (aLSA). (**B**) Right lateral view indicating the embryonic aortic segments of the right aortic arch. (**C**) Posterior view and (**D**) left lateral view. The aLSA connects to a dilated embryonic beta-segment (arrow), that forms the base of a Kommerell's diverticulum (KD). The asteriks * indicates where the location of the left 4th PAA (that is missing here) would have been in case of a double aortic arch. As the 4th PAA borders the beta-segment, the the segment indicating the dilated beta-segment, may also comprisee part of an incompletely regressed left 4th PAA. α, alpha-segment; Ao asc, ascending aorta; Ao desc, descending aorta; aLSA, aberrant left subclavian artery; β, beta-segment; Es, esophagus; LB, left bronchus; LCA, left carotid artery; LSA, left subclavian artery; KD, Komerell's diverticulum; RB, right bronchus; RCA, right carotid artery; RSA, right subclavian artery; Tr, trachea.

The configuration of a right-sided aortic arch and left-sided aberrant subclavian artery in the presence of a Kommerell's diverticulum and ductal ligament (or persistent ductus arteriosus) forms a vascular ring around the esophagus and trachea. This may result in symptoms related to esophageal and tracheal compression, depending on location and

degree of compression. For the trachea of an adult, it is estimated that exertional dyspnea occurs when the tracheal luminal diameter is less than 8mm and that symptoms in rest occur when the diameter is less than 6 mm [14]. The progression to symptomatic esophageal and tracheal compression varies and may partly explain the wide spectrum of clinical manifestations of a Kommerell's diverticulum, that range from severely symptomatic cases requiring surgical intervention during the early years of life, to an incidental finding in asymptomatic adult patients. The latter type is probably underreported in literature. Additionally, Kommerell's diverticulum may be associated with an increased risk of acute aortic/vascular syndromes. Cina and colleagues reported an aortic dissection rate ranging between 19 to 53% in the 32 case reports available at time of publishing [15]. However, this rate seems inconsistent with clinical experience and is likely based on significant (over) reporting bias [7].

As there is currently no clear consensus with regards to the clinical management of Kommerell's diverticulum or defined indicators to justify surgery, we discuss the clinical presentation, diagnosis and management, and follow-up of 7 consecutive patients from our academic referral center. The current series explores the relation between the anatomy and the occurrence and severity of symptoms in patients with a right-sided aortic arch, left aberrant subclavian artery and a Kommerell's diverticulum considering this configuration as a distinct entity rather than also including patients with a left-sided aortic arch.

2. Case Presentation

2.1. Patient 1

A 40-year old male patient was evaluated at the cardiology outpatient clinic prior to renal transplantation. His history included Ewing's sarcoma, left nephrectomy due to metastatic disease five years earlier and subsequent right kidney failure. The initial Computed Tomography (CT) Angiography (CTA, Figure 3) showed a Kommerell's diverticulum of 22 $\times$ 20 mm (319 mm^2) from a right-sided aortic arch with aberrant left subclavian artery. In addition, the brachiocephalic vein had an aberrant course ventral to the trachea and in this case, this structure contributed to the mild tracheal compression. The ductus arteriosus had regressed (ductal ligament) leading to an incomplete vascular ring. The patient experienced no pulmonary complaints. Echocardiography showed normal biventricular function and no hemodynamically significant valvular disease. Scintigraphy revealed reversible ischemia of the anterior segments and coronary angiography confirmed a significant stenosis in the proximal left anterior descending artery, which was treated with percutaneous coronary intervention and stenting. Patient routinely undergoes chest and abdominal CT surveillance to exclude recurrence of malignant disease. His most recent exam, performed five years after initial documentation of the Kommerell's diverticulum, showed stable dimensions of the vascular structures.

2.2. Patient 2

A 40-year old male presented to the emergency department with partial paraplegia due to multiple traumatic cervical fractures after an accident. As an incidental finding, the CTA (Figure 4) showed a right-sided aortic arch with an aberrant left subclavian artery and a Kommerell's diverticulum of 22 $\times$ 21 mm (357 mm^2) with partial compression of the trachea due to bowing of the posterior tracheal membrane. This configuration formed an incomplete vascular ring. He experienced no complaints related to the Kommerell's diverticulum, hence a watchful waiting strategy is pursued with periodic CTA follow-up.

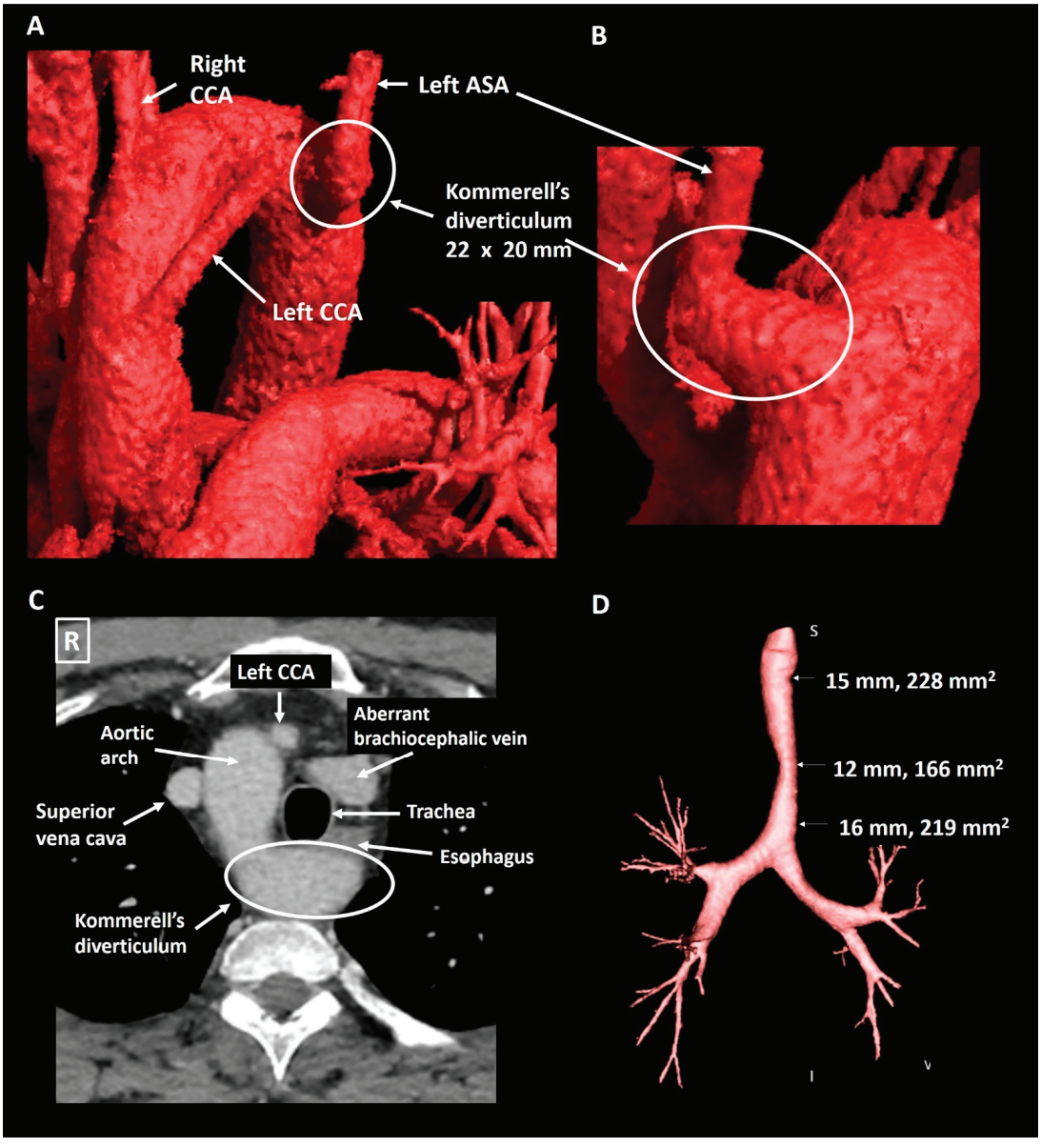

Figure 3. Patient 1. Panel (**A**) shows a CT-image reconstructed with global illumination rendering (iGIR) (Vitrea®, Vital Images) in a anterolateral orientation depicting a right-sided aortic arch with an aberrant left subclavian artery. Panel (**B**) shows a close up of the oblique posterior view of a Kommerell's diverticulum as the onset of the aberrant left subclavian artery. Panel (**C**) is an axial reconstruction depicting the anatomical relationship between the aortic arch, Kommerell's diverticulum and an aberrant brachiocephalic vein which encircle the trachea resulting in mild compression. Panel (**D**) is a minimum intensity projection of the trachea showing mild external compression. ASA, aberrant subclavian artery; CCA, common carotid artery.

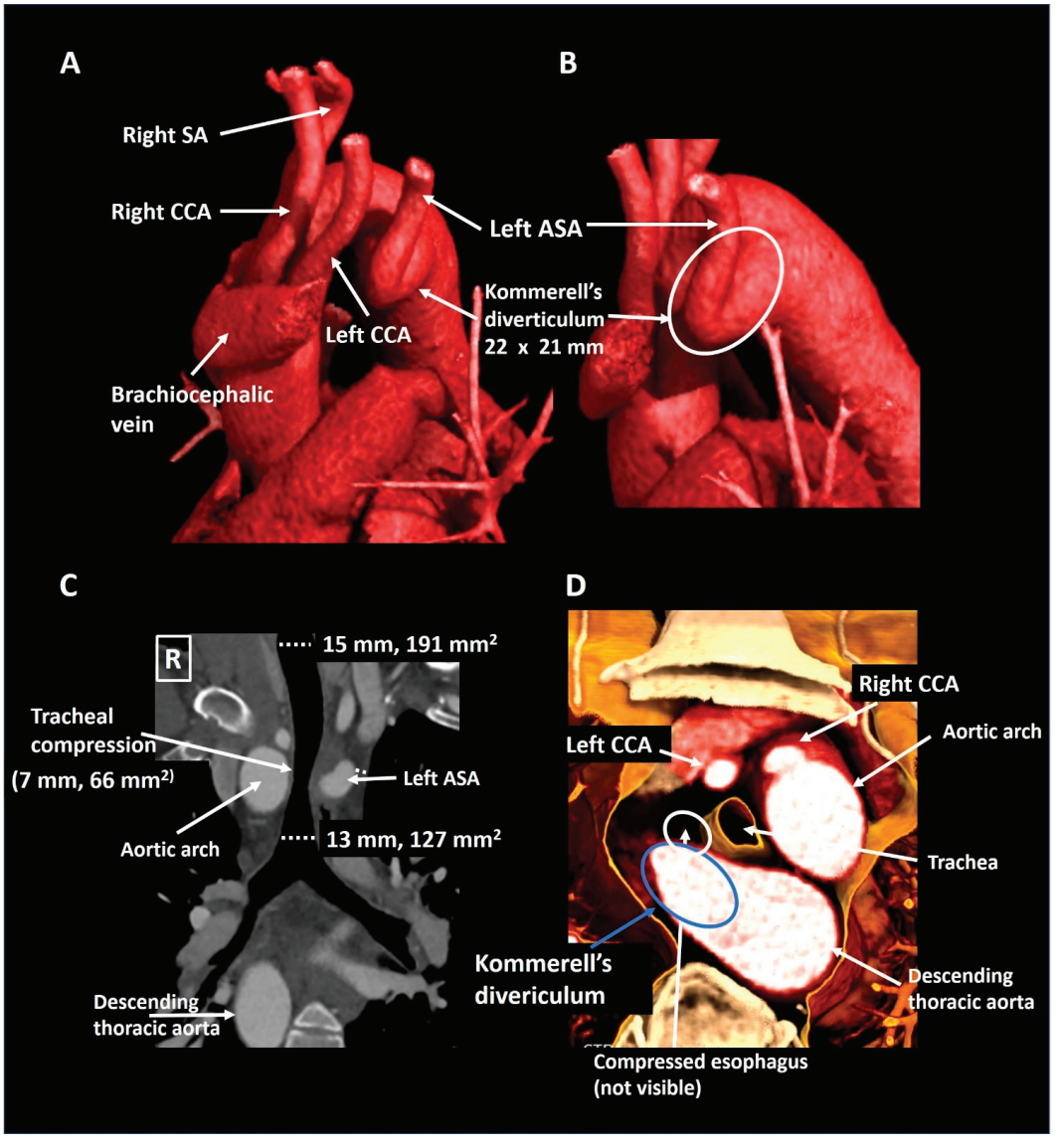

Figure 4. Patient 2. Panel (**A**) shows a lateral computed tomography reconstruction depicting a right-sided aortic arch with an aberrant left subclavian artery. The zoomed posterolateral reconstruction in panel (**B**) shows that the aberrant left subclavian artery is arising from a Kommerell's diverticulum. Panel (**C**) is a coronal reconstruction that reveals tracheal compression. The axial 3D cross-section (panel (**D**)) shows partial posterior compression of the trachea which was secondary to tracheal bowing and not directly to compression by the vascular structures. ASA, aberrant subclavian artery; CCA, common carotid artery; SA, subclavian artery.

2.3. Patient 3

A 50-year old woman was referred by the pulmonologist with progressive symptoms of dysphagia since the last three years. The forced expiratory volume during spirometry was reduced (2.76 L, 90% of predicted) and she had recently developed an inspiratory

stridor. Chest X-ray revealed a right-sided aortic arch. Further investigation with a CTA (Figure 5) showed an aberrant left subclavian artery with a Kommerell's diverticulum of 30 × 29 mm. At the level of the Kommerell's diverticulum, there was significant tracheal (transverse luminal diameter, 7 mm) and esophageal compression (without any upper gastrointestinal tract complaints). The patient underwent surgical resection of the Kommerell's diverticulum with the subsequent placement of a Vascutek prosthetic aortic patch and re-implantation of the left subclavian artery within a branch of the patch. The surgery was uneventful and patient's symptoms resolved. Postoperatively the patient developed mild symptoms of vocal cord dysfunction, which improved after speech therapy. Follow-up CTA after 6 and 12 months showed recovery of the tracheal (transverse luminal diameter 10 mm) and esophageal dimensions. The patient is under periodic follow-up.

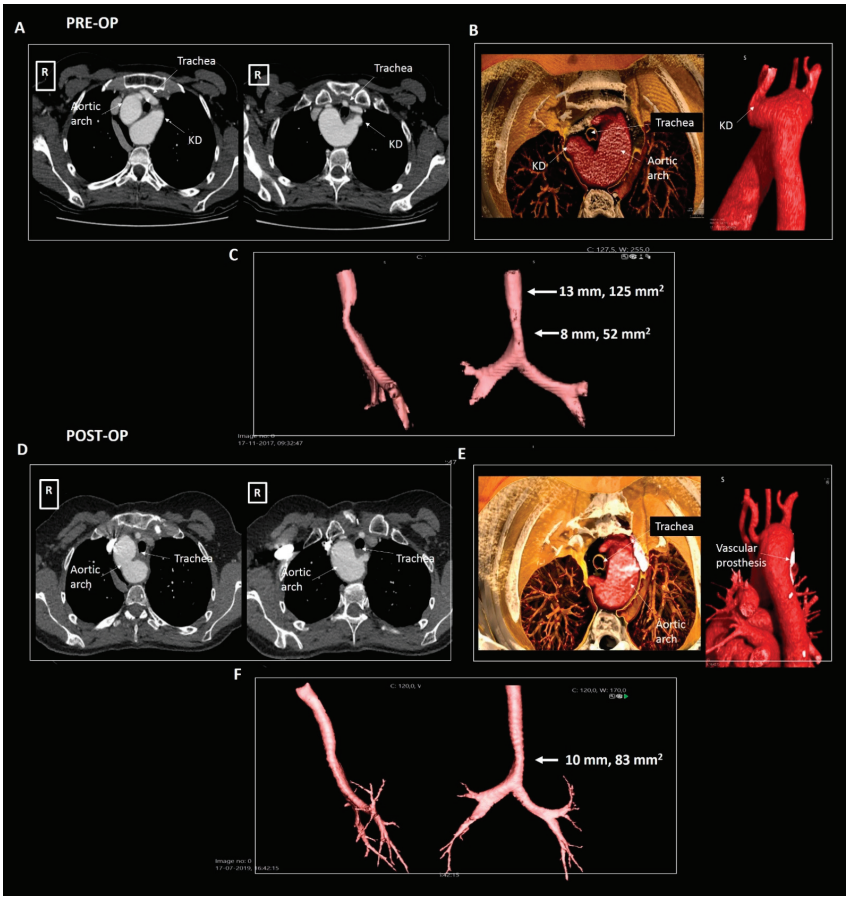

Figure 5. Patient 3. Panels (**A**–**C**) pre-operative imaging, panels (**D**–**F**) post-operative imaging. Panel (**A**) shows the axial reconstructions illustrating a right-sided aortic arch, aberrant left subclavian artery and a Kommerell's diverticulum compressing the trachea and esophagus. Panel (**B**) shows the volume rendering images and panel (**C**) depicts the compressed trachea. Panel (**D**) shows the post-operative result after surgical resection of the Kommerell's diverticulum in axial reconstructions and panel (**E**) in volume rendered reconstructions. Panel (**F**) depicts the trachea, illustrating some increase in tracheal dimensions. KD, Kommerell's diverticulum.

2.4. Patient 4

A 55-year old male was evaluated by his general practitioner due to mild complaints of dyspnea upon exertion, whilst training for a triathlon. A chest X-ray showing a right-sided aorta and a reduced maximal expiratory peak flow during spirometry testing prompted further investigation. Subsequent CTA (Figure 6) showed an aberrant left subclavian artery with a Kommerell's diverticulum of 25 × 23 mm (575 mm^2) that caused mild tracheal compression in the absence of a persisting ductus arteriosus. As Kommerell's diverticulum carries a risk of rupture, caution was advised with regard to peak and maximal exercise efforts. CTA was repeated 1 year after diagnosis, revealing stable dimensions of the Kommerell's diverticulum. The patient is under periodic follow-up.

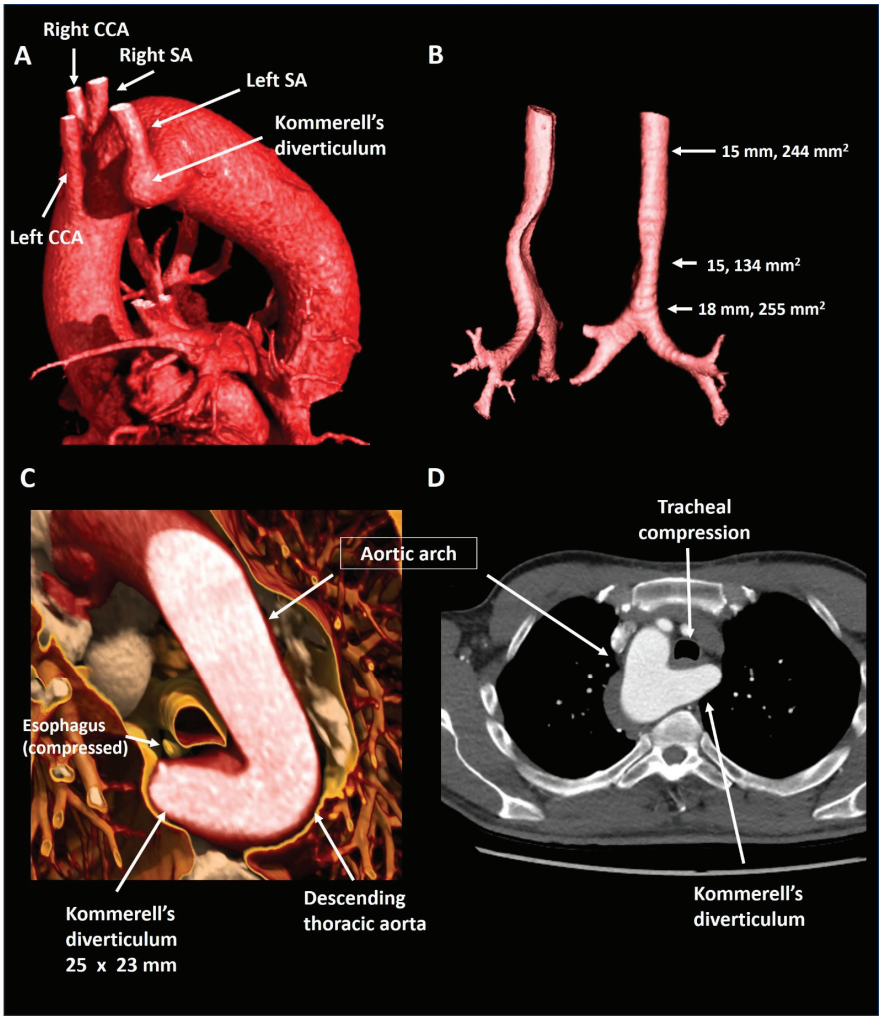

Figure 6. Patient 4. Panel (**A**) shows a lateral reconstruction depicting a right-sided aorta and an aberrant left subclavian artery with Kommerell's diverticulum. Panel (**B**) shows the tracheal compression in isolation. Panel (**C**) provides a volume rendered axial reconstruction and panel (**D**) a standard axial reconstruction. CCA, common carotid artery; SA, subclavian artery.

2.5. Patient 5

A 63-year old male underwent curative surgery for colorectal carcinoma with hepatic metastases and underwent 6-monthly CT follow-up to screen for potential recurrence of malignancy. The first chest CT (Figure 7) revealed a right-sided aortic arch and an aberrant left subclavian artery arising from a Kommerell's diverticulum of 24 × 19 mm (343 mm^2) that resulted in asymptomatic esophageal compression. Given the lack of symptoms and known metastatic disease, it was decided to refrain from intervention and opt for CTA follow-up. During the subsequent 3 years, diverticular dimensions have remained stable.

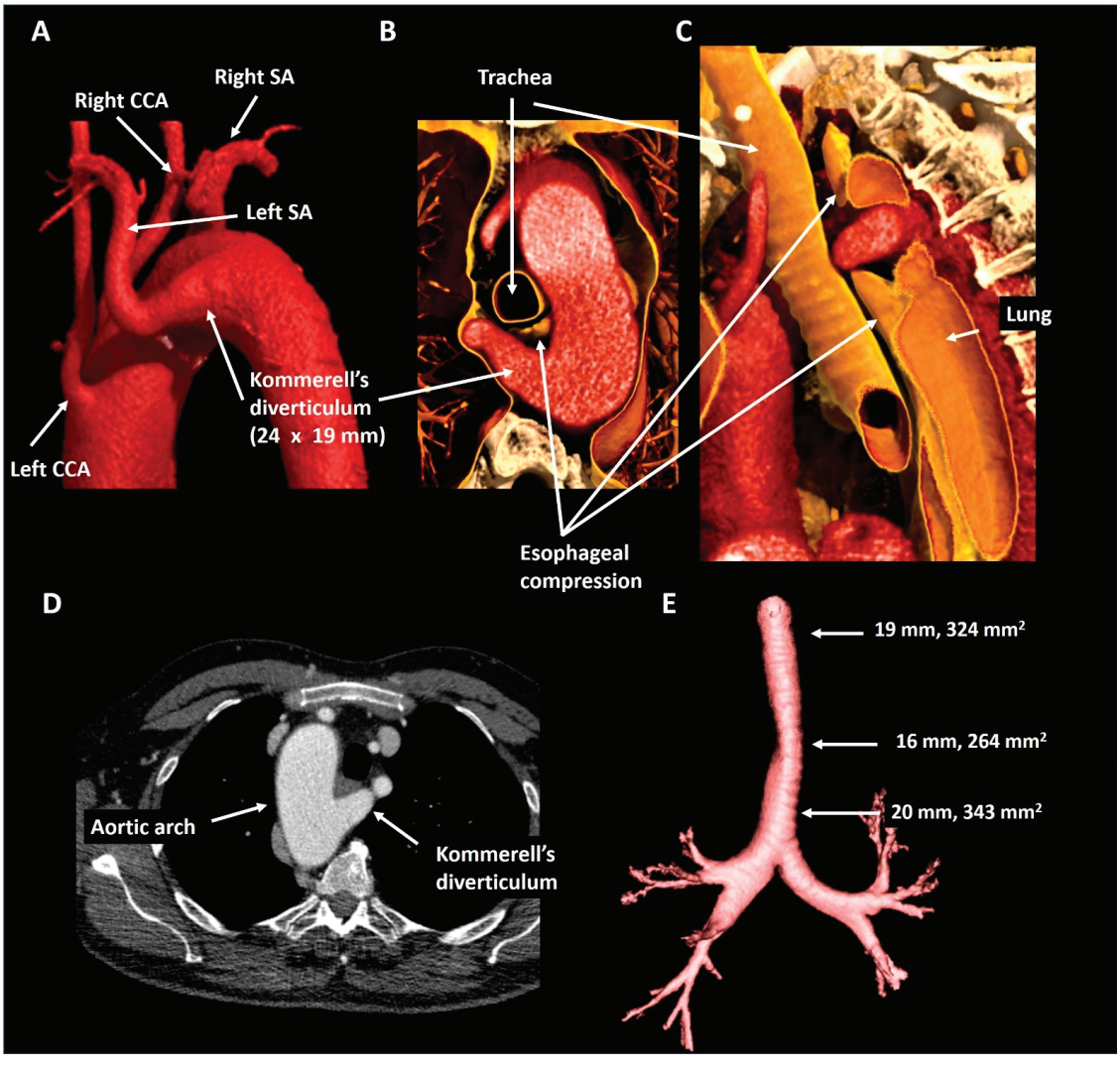

Figure 7. Patient 5. Panel (**A**) shows a posterolateral view depicting a right-sided aortic arch and an aberrant left subclavian artery with a Kommerell's diverticulum. The axial (panel (**B**)) and oblique sagittal (panel (**C**)) lateral 3D volume rendering reconstructions reveal that the Kommerell's diverticulum causes esophageal compression. Panel (**D**) shows the axial reconstruction and in panel (**E**) the mild tracheal compression is viewed in isolation. CCA, common carotid artery; SA, subclavian artery.

2.6. Patient 6

A 23-year old male who was referred by a general practitioner after analysis for suspected asthma revealed a right-sided aortic arch on a chest X-ray. Subsequent CTA (Figure 8) showed mirror image branching of the aortic arch arteries and an isolated Kommerell's diverticulum of 27 × 21 mm (440 mm^2), likely due to traction of an arterial ligament. This anomaly resulted in mild tracheal and esophageal compression. As the patient had an excellent exercise capacity (375 Watt at bicycle exercise testing) after the initiation of bronchodilator therapy, and a relatively small size of Kommerell's diverticulum, a strategy of watchful waiting with periodic CTA follow-up was pursued. In addition, caution was advised with regards to peak and maximal exercise efforts. The patient is under periodic follow-up.

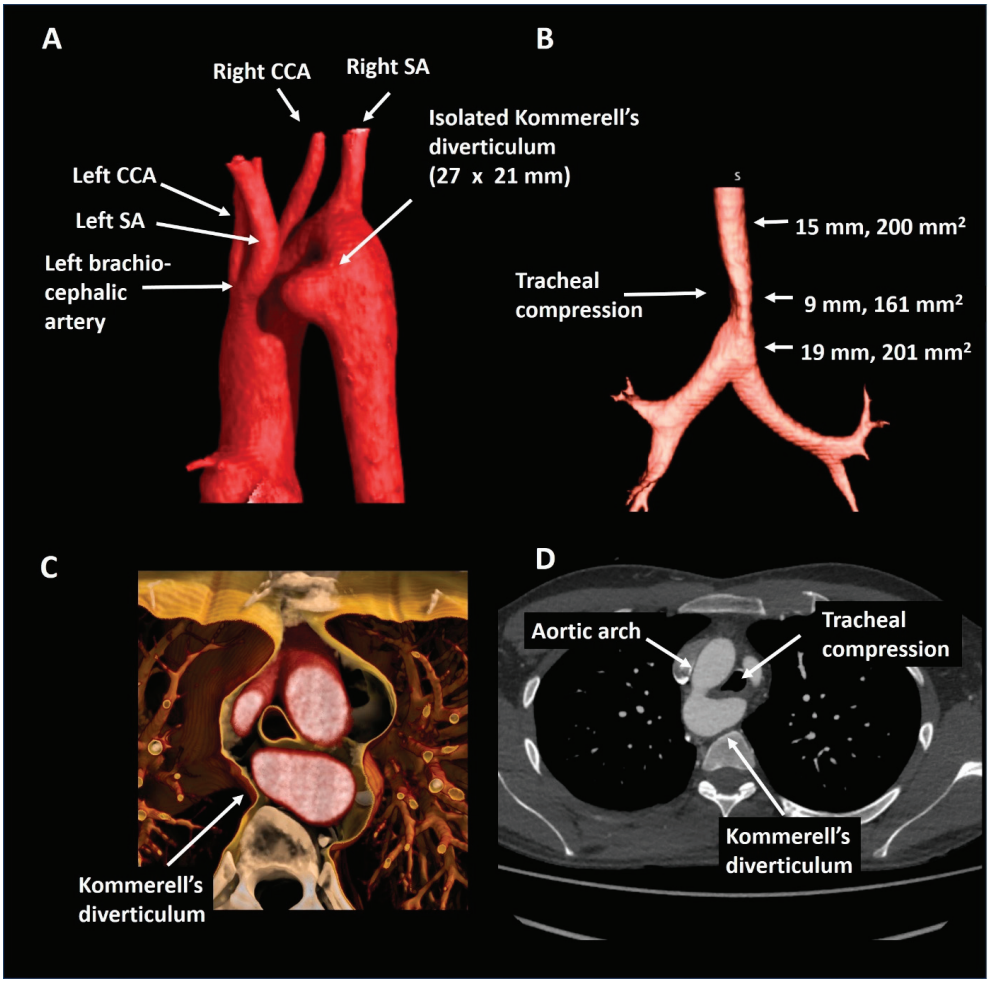

Figure 8. Patient 6. Panel (**A**) shows a posterolateral view of a right-sided aortic arch with mirror imaging branching and an isolated Kommerell's diverticulum compressing the trachea (panel (**B**)) by the formation of a vascular ring (panel (**C**)). Panel (**D**) shows the axial reconstruction. CCA, common carotid artery; SA, subclavian artery.

2.7. Patient 7

A 25-year old female with the Noonan syndrome and a right-sided aortic arch, was referred for cardiac screening due to an active pregnancy wish. Echocardiography showed a structurally normal heart. For better visualization of the thoracic aorta she underwent CTA (Figure 9) that confirmed the right-sided aortic arch and showed a left aberrant subclavian artery and a Kommerell's diverticulum of 19 × 21 mm. The trachea and esophagus were only mildly compressed. In the absence of symptoms and a good exercise capacity (160 Watt at bicycle exercise testing) a watchful waiting strategy was pursued and the patient was advised to avoid maximal exercise. The patient is under periodic follow-up.

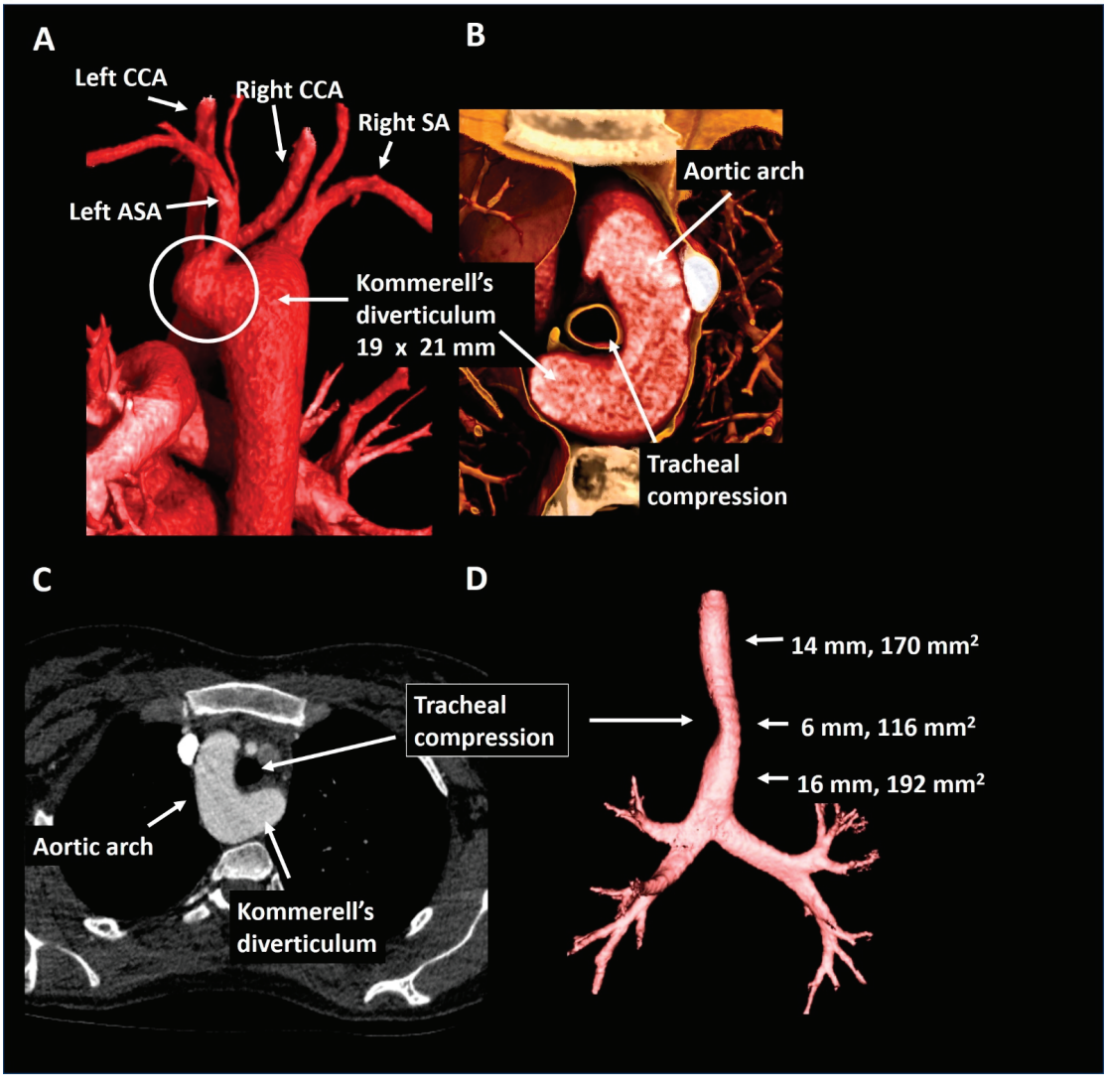

Figure 9. Patient 7. Panel (**A**) shows a posterior view of the descending thoracic aorta, right-sided aortic arch and Kommerell's diverticulum as offset for an aberrant left subclavian artery. In panel (**B**) the short axis configuration is depicted showing mild tracheal compression. Panel (**C**) shows the axial reconstruction and panel (**D**) provides the trachea in isolation. ASA, aberrant subclavian artery; CCA, common carotid artery; SA, subclavian artery.

3. Discussion: Clinical Implications

Due to its incidental nature and presumed underreporting in the literature, the natural history and exact clinical consequences of Kommerell's diverticulum are unknown. Consequently, there are currently no guidelines that specifically address how patients with Kommerell's diverticulum should be managed. We report our experience with 7 consecutive adult patients with the anatomic variant of an aberrant left subclavian artery with Kommerell's diverticulum and a right-sided aortic arch.

From the current case-series (Table 1), 1 of the 7 patients had significant symptoms related to extrinsic esophageal and tracheal compression and underwent successful surgical repair. The Kommerell's diverticulum of the operated patient (patient 3) was the largest of the current series (30 mm). Nonetheless, it should be appreciated that Kommerell's diverticulum is frequently an incidental finding. In total, six patients from the current series had only slight esophageal or tracheal compression on CT that was not associated with significant symptoms and in these patients a strategy of watchful waiting with serial CTA follow-up was pursued. Bearing in mind the risk of acute complications, we advised these patients to avoid peak exercise to reduce the shear stress and vascular strain on the diverticulum.

Table 1. An overview of the anatomical and clinical characteristics of patients 1–7.

	Age at Diagnosis (Years)	Gender	Anatomy	Compression	Dimensions of KD	Symptoms	Management
Patient 1	40	Male	Right-sided arch, aberrant LSA and KD	Mild tracheal compression	22 × 20 mm, 319 mm^2	Incidental finding	Structural imaging follow-up
Patient 2	40	Male	Right-sided arch, aberrant LSA and KD	Partial tracheal compression	22 × 21 mm, 357 mm^2	Incidental finding	Structural imaging follow-up
Patient 3	50	Female	Right-sided arch, aberrant LSA and KD	Symptomatic tracheal and esophageal compression	30 × 29 mm, 870 mm^2	Dysphagia and dyspnea	Surgical resection
Patient 4	55	Male	Right-sided arch, aberrant LSA and KD	Mild tracheal compression	25 × 23 mm, 575 mm^2	Mild dyspnea, although excellent objective exercise capacity	Structural imaging follow-up
Patient 5	63	Male	Right-sided arch, aberrant LSA and KD	Asymptomatic esophageal compression	24 × 19 mm, 343 mm^2	Incidental finding	Structural imaging follow-up
Patient 6	23	Male	Right-sided arch, mirror imaging branching and KD	Mild tracheal and esophageal compression	27 × 21 mm, 440 mm^2	Dyspnea, although excellent objective exercise capacity	Structural imaging follow-up
Patient 7	25	Female	Right-sided arch, aberrant LSA and KD	Mild tracheal and esophageal compression	19 × 21 mm, 399 mm^2	Incidental finding	Structural imaging follow-up

LSA, left subclavian artery; KD, Kommerell's diverticulum.

Colleagues from the Radiology department of the Yale University showed that the majority (63%) of 75 patients with Kommerell's diverticulum had a left-sided aortic arch [7], whereas in the 121 patients reported by Poterucha et al. [8] 60% had a right-sided aortic arch. Bogerijen et al. observed a left-sided aortic arch in 73% of a surgical cohort

of 22 patients [1]. However, data from larger populations is lacking, particularly from individuals without symptoms or surgical intervention. The combination of Kommerell's diverticulum, an aberrant left subclavian artery, a right-sided aortic arch and persistent arterial duct may form a vascular ring around the trachea and esophagus. Depending on the size of the diverticulum, the local anatomy and presence of concomitant (vascular) anomalies, this variant may more frequently result in symptoms than the combination of a Kommerell's diverticulum and an aberrant right subclavian artery which has a retroesophageal course. Nowadays, non-invasive 3D imaging techniques such as CT or magnetic resonance have largely replaced the need for bronchoscopy or barium swallow testing in adult patients [3].

Some groups advocate an aggressive intervention strategy in patients with Kommerell's diverticulum based on the reported high rupture rate of up to 53% [15]. Kim and colleagues recommend surgical resection of a Kommerell's diverticulum even in asymptomatic patients and reported the retrospective results of 19 adult patients who underwent surgical correction independent of the size of the Kommerell's diverticulum, that ranged from 15–45 mm [16]. In this series, the surgical procedure was complicated by an perioperative type A dissection (5.3%), laryngeal and phrenic nerve injury (10.5%), and transient neurologic dysfunction (5.3%). Patient 3 in our series had mild symptoms of vocal cord dysfunction due to perioperative laryngeal nerve injury. Other single centers' recommendations include an indication for surgery when the Kommerell's diverticular dimension exceeds 50 mm in the long-axis [17] or if the maximal orifice diameter exceeds 30 mm [18]. In our center, we consider operative treatment in adult patients with a diverticular orifice diameter of 30 mm or more due to the risk of dissection or rupture, irrespective of complaints. The lack of international consensus and the periprocedural risks advocate the importance of anatomical and clinical criteria with regards to patient selection for surgical management in adults.

There may be factors beyond the absolute diverticular size when it comes to risk of dissection or rupture. A recent systematic review described 210 patients with a Kommerell's diverticulum (mean age 42 years) and reported a ruptured diverticulum and aortic dissection as presentation in 4 and 11% of the patients, respectively [3]. Interestingly, in this population the vast majority (84%) of the patients underwent surgical intervention [3]. The size of the Kommerell's diverticulum ranged from 15 to 80 mm (mean 38 $\pm$ 18 mm) in the overall population, from 20 to 60 mm in the ruptured cases and 25 to 70 mm in those with an aortic dissection [3]. Backer et al. showed that patients who undergo surgical repair because of a symptomatic Kommerell's diverticulum (n = 20) had more frequently a right-sided aortic arch (n = 16), probably because this configuration is more likely to lead to symptomatic esophageal or tracheal enclosure [19]. Due to increased shear stress, it is hypothesized that the curvature of a right-sided aorta and a larger absolute size of the Kommerell's diverticulum may be associated with an increased risk of rupture [20]. The potential role of primary vascular pathology or premature atherosclerosis in this population remains to be established.

To conclude, Kommerell's diverticulum is characterized by an aneurysmatic onset (the diverticulum) of an aberrant left or right subclavian artery. The configuration of a Kommerell's diverticulum from an aberrant left subclavian artery from a right-sided aorta is often associated with some degree of tracheal and esophageal compression, and this may result in a range of associated symptoms. Although frequently an incidental finding in asymptomatic adults, one should be aware of the intricate anatomic characteristics and potential vascular complications of such diverticulum and its presence should always warrant further investigation. Serial follow-up is warranted in cases with small dimensions and no symptoms, however, surgical intervention should be considered when patients become symptomatic, or if the diameter exceeds 30 mm in the absence of symptoms, or when there is rapid growth. Based on the current literature, defining patients at risk of acute and potentially life-threatening vascular complications remains a challenge.

Author Contributions: Conceptualization, P.J.v.R., M.R.M.J., and A.D.E.; methodology, P.J.v.R., J.L.S., M.R.M.J., M.G.H. and A.D.E.; software, P.J.v.R., and J.L.S.; validation, P.J.v.R., J.L.S., M.R.M.J., and A.D.E.; formal analysis, P.J.v.R. and A.D.E.; investigation, P.J.v.R., M.R.M.J. and A.D.E.; resources, P.J.v.R., M.R.M.J. and A.D.E.; data curation, P.J.v.R., J.L.S., and A.D.E.; writing—original draft preparation, P.J.v.R., J.L.S., H.J.L., M.R.M.J., and A.D.E.; writing—review and editing, P.J.v.R., J.L.S., P.K., H.W.V., M.G.H., D.R.K., H.J.L., M.R.M.J., and A.D.E.; visualization, P.J.v.R., J.L.S., M.R.M.J., A.D.E.; supervision, H.J.L., D.R.K., M.G.H.; project administration, A.D.E. All authors have read and agreed to the published version of the manuscript.

Funding: The work was funded by the general funds of the Department of Cardiology of the Leiden University Medical Center, Leiden, The Netherlands. ADE received additional funding support from the Johanna Zaaijer Foundation of the Leiden University Medical Center. MRMJ is funded by Organization for Scientific Research (NWO) [project nr. 91719346].

Institutional Review Board Statement: All tests and procedures performed involving human participants were in accordance with the ethical standards of the institutional and/or national research committee and with the 2013 Helsinki declaration or comparable ethical standards.

Informed Consent Statement: The patients provided consent for registration of their data and publication.

Data Availability Statement: All data relevant to the study are included in the article or uploaded as supplementary information. Additional data are available on reasonable request.

Acknowledgments: The authors would like to thank Ronald Slagter and Friso Jansen (Department of Anatomy and Embryology, Leiden University Medical Center, Leiden, the Netherlands) for their help in creating Figures 1 and 2, respectively. In respectful memory of Adriana C. Gittenberger-de Groot, whose work continues to inspire us.

Conflicts of Interest: The authors declare that they have no competing interests.

References

1. Van Bogerijen, G.H.; van Bogerijen, G.H.; Patel, H.J.; Eliason, J.L.; Criado, E.; Williams, D.M.; Knepper, J.; Yang, B.; Deeb, G.M. Evolution in the Management of Aberrant Subclavian Arteries and Related Kommerell Diverticulum. *Ann. Thorac. Surg.* **2015**, *100*, 47–53. [CrossRef]
2. Kommerell, B. Verlagerung des osophagus durch eine abnorm verlaufende arteria subclavia dextra (arteria lusoria). *Fortschr Roentgenstrahlen* **1936**, *54*, 590–595.
3. Tanaka, A.; Milner, R.; Ota, T. Kommerell's diverticulum in the current era: A comprehensive review. *Gen. Thorac. Cardiovasc. Surg.* **2015**, *63*, 245–259. [CrossRef] [PubMed]
4. Backer, C.L.; Bharadwaj, S.N.; Eltayeb, O.M.; Forbess, J.M.; Popescu, A.R.; Mongé, M.C. Double Aortic Arch With Kommerell Diverticulum. *Ann. Thorac. Surg.* **2019**, *108*, 161–166. [CrossRef] [PubMed]
5. Yang, C.; Shu, C.; Li, M.; Li, Q.; Kopp, R. Aberrant Subclavian Artery Pathologies and Kommerell's Diverticulum: A Review and Analysis of Published Endovascular/Hybrid Treatment Options. *J. Endovasc. Ther.* **2012**, *19*, 373–382. [CrossRef] [PubMed]
6. Hanneman, K.; Newman, B.; Chan, F. Congenital Variants and Anomalies of the Aortic Arch. *Radiographics* **2017**, *37*, 32–51. [CrossRef] [PubMed]
7. Erben, Y.; Brownstein, A.J.; Velasquez, C.A.; Li, Y.; Rizzo, J.A.; Mojibian, H.; Tanweer, M.; Zafar, M.A.; Ziganshin, B.A.; Elefteriades, J.A. Natural history and management of Kommerell's diverticulum in a single tertiary referral center. *J. Vasc. Surg.* **2020**, *71*, 2004–2011. [CrossRef] [PubMed]
8. Poterucha, J.; Anavekar, N.; Niaz, T.; Agarwal, A.; Young, P.; Dearani, J.; Ammash, N.; Warnes, C.; Connolly, H. Incidence and clinical presentation of kommerell diverticulum and aneurysm. *J. Am. Coll. Cardiol.* **2015**, *65*, A524. [CrossRef]
9. Stewart, J.R.; Kindcaid, O.W.; Edwards, J.E. *An Atlas of Vascular Rings and Related Malformations of the Aortic Arch System*; Thomas: Springfield, IL, USA, 1964.
10. Gittenberger-de Groot, A.C.; Azhar, M.; Molin, D.G. Transforming growth factor beta-SMAD2 signaling and aortic arch development. *Trends Cardiovasc. Med.* **2006**, *16*, 1–6. [CrossRef] [PubMed]
11. Molin, D.G.; DeRuiter, M.C.; Wisse, L.J.; Azhar, M.; Doetschman, T.; Poelmann, R.E.; Gittenberger-de Groot, A.C. Altered apoptosis pattern during pharyngeal arch artery remodelling is associated with aortic arch malformations in Tgfbeta2 knock-out mice. *Cardiovasc. Res.* **2002**, *56*, 312–322. [CrossRef]
12. Molin, D.G.; Roest, P.A.; Nordstrand, H.; Wisse, L.J.; Poelmann, R.E.; Eriksson, U.J.; Gittenberger-De Groot, A.C. Disturbed morphogenesis of cardiac outflow tract and increased rate of aortic arch anomalies in the offspring of diabetic rats. *Birth Defects Res. A Clin. Mol. Teratol.* **2004**, *70*, 927–938. [CrossRef] [PubMed]
13. Bergwerff, M.; DeRuiter, M.C.; Hall, S.; Poelmann, R.E.; Groot, A.C.G.-D. Unique vascular morphology of the fourth aortic arches: Possible implications for pathogenesis of type-B aortic arch interruption and anomalous right subclavian artery. *Cardiovasc. Res.* **1999**, *44*, 185–196. [CrossRef]

14. Ernst, A.; Feller-Kopman, D.; Becker, H.D.; Mehta, A.C. Central Airway Obstruction. *Am. J. Respir. Crit. Care Med.* **2004**, *169*, 1278–1297. [CrossRef] [PubMed]
15. Cinà, C.; Althani, H.; Pasenau, J.; Abouzahr, L. Kommerell's diverticulum and right-sided aortic arch: A cohort study and review of the literature. *J. Vasc. Surg.* **2004**, *39*, 131–139. [CrossRef] [PubMed]
16. Kim, K.M.; Cambria, R.P.; Isselbacher, E.M.; Baker, J.N.; Lamuraglia, G.M.; Stone, J.R.; MacGillivray, T.E. Contemporary Surgical Approaches and Outcomes in Adults With Kommerell Diverticulum. *Ann. Thorac. Surg.* **2014**, *98*, 1347–1354. [CrossRef] [PubMed]
17. Ota, T.; Okada, K.; Takanashi, S.; Yamamoto, S.; Okita, Y. Surgical treatment for Kommerell's diverticulum. *J. Thorac. Cardiovasc. Surg.* **2006**, *131*, 574–578. [CrossRef] [PubMed]
18. Idrees, J.; Keshavamurthy, S.; Subramanian, S.; Clair, D.G.; Svensson, L.G.; Roselli, E.E. Hybrid repair of Kommerell diverticulum. *J. Thorac. Cardiovasc. Surg.* **2014**, *147*, 973–976. [CrossRef] [PubMed]
19. Backer, C.L.; Russell, H.M.; Wurlitzer, K.C.; Rastatter, J.C.; Rigsby, C.K. Primary Resection of Kommerell Diverticulum and Left Subclavian Artery Transfer. *Ann. Thorac. Surg.* **2012**, *94*, 1612–1617. [CrossRef] [PubMed]
20. Vinnakota, A.; Idrees, J.J.; Rosinski, B.F.; Tucker, N.J.; Roselli, E.E.; Pettersson, G.B.; Vekstein, A.M.; Stewart, R.D.; Raja, S.; Svensson, L.G. Outcomes of Repair of Kommerell Diverticulum. *Ann. Thorac. Surg.* **2019**, *108*, 1745–1750. [CrossRef] [PubMed]

Journal of
Cardiovascular
Development and Disease

MDPI

Perspective

Coronary Anatomy in Congenital Heart Disease: The Important Contributions of Professor Dr. Adriana Gittenberger-de Groot

Mark Hazekamp

Department of Cardiothoracic Surgery, D6-26, Leiden University Medical Center, Albinusdreef 2, 2333ZA Leiden, The Netherlands; M.G.Hazekamp@lumc.nl

Abstract: The contributions of Professor Dr. Adriana Gittenberger-de Groot in relation to coronary artery development and classification are described from the viewpoint of a pediatric cardiac surgeon.

Keywords: transposition great arteries coronary anatomy

Citation: Hazekamp, M. Coronary Anatomy in Congenital Heart Disease: The Important Contributions of Professor Dr. Adriana Gittenberger-de Groot. *J. Cardiovasc. Dev. Dis.* **2021**, *8*, 27. https://doi.org/10.3390/jcdd8030027

Academic Editor: Andy Wessels

Received: 11 January 2021
Accepted: 6 March 2021
Published: 9 March 2021

Professor Dr. Adriana Gittenberger-de Groot has contributed in many ways to the vast field of congenital heart disease. Her research in this area comprises many different topics and is too extensive to summarize in one paper.

As a surgeon who is specialized in congenital heart disease, I will focus on one field where Adriana Gittenberger-de Groot has made contributions that have been of especially great value to me and to my fellow pediatric cardiac surgeons. I here refer to her work on coronary development and anatomy in congenital heart disease. This has ultimately resulted in the so-called Leiden Convention, a coronary coding system where the origin and location of the coronary arteries in hearts with congenital heart disease, such as transposition of the great arteries (TGA), is described in a way that is both simple and unequivocal. The strength of the system lies in that it is independent of the relative anatomical position of the great arteries, which can vary in different forms of congenital heart disease. This classification greatly facilitates communication between pediatric cardiologists and pediatric heart surgeons when they speak on how the coronary arteries are distributed in a patient with TGA. Its simplicity and the fact that it is always applicable underlines the beauty of the Leiden Convention coronary coding system [1].

The first arterial switch operation in Leiden was performed in 1977, shortly after Jatene had done his first successful arterial switch in Sao Paulo in 1975 [2]. The most critical part of this surgical procedure was (and still is) the translocation of the coronary arteries from their original position in the aorta to their new place in the pulmonary truncus, which will function as the new aorta after the arterial switch operation. Variations in the origin and course of the coronary arteries are common, especially when TGA is combined with a ventricular septal defect. As specific variations significantly increase the risk of the arterial switch operation, it is of great importance to know the coronary anatomy before surgery is started. A classification that is both simple and comprehensive was therefore desperately needed with the evolution of this surgical technique.

The classification that Adriana Gittenberger-de Groot proposed was independent of the spatial relation between the great arteries and was based on the observation that the coronary arteries always arise from the facing sinuses. In short, an observer is positioned in the non-facing sinus of the aorta and looks towards the pulmonary artery. The sinus on the right-hand side is called "sinus 1", and the sinus on the left-hand side is called "sinus 2". Then the three main coronary arteries are each named with the observer looking in a counterclockwise fashion, starting in sinus 1. Thus, the most common anatomy in TGA will be 1LCx-2R, where 1 and 2 denote the sinuses, L is left anterior descending artery, Cx is the circumflex artery, and R stands for the right coronary artery. The nomenclature was elegantly described by the Leiden pediatric cardiac surgeon Jan Quaegebeur after

studying many clinical and autopsy cases of TGA [3]. The Leiden Convention is for all reasons mentioned above more understandable than other classifications, such as Yacoub type A–D [4,5].

The embryological aspects of coronary artery development have always been a topic of interest for Prof. Dr. Gittenberger-de Groot, as demonstrated by several studies that have led to the refutation of previous theories [6,7]. This work has shown that coronary arteries do not grow from the aorta towards the periphery, but on the contrary, coronary arteries grow toward the aorta. This provides explanations for coronary artery variations in TGA, in common arterial trunk but for also the occurrence of aberrant coronary arteries that arise from the pulmonary artery [8,9]. All this is of importance to the congenital cardiac surgeon.

Many years later, the same topic resurfaced when Adriana Gittenberger-de Groot started looking at coronary artery anatomy in relation to bicuspid aortic valve [10,11]. Ultimately, this led to a modification of the Leiden Convention that encompasses coronary arterial origin and branching not only in hearts with TGA or double outlet right ventricle but also in hearts with normally related great arteries, hearts with different types of bicuspid aortic valve, or hearts that have coronary arteries that arise from another aortic sinus. In bicuspid aortic valve, the Leiden Convention is applicable in 99% of cases (not in the very rare cases where there is no raphe). Furthermore, the Leiden Convention can be used to determine which leaflets are fused. The newly modified Leiden Convention stands for a simple coronary coding system that is broadly applicable (Figure 1).

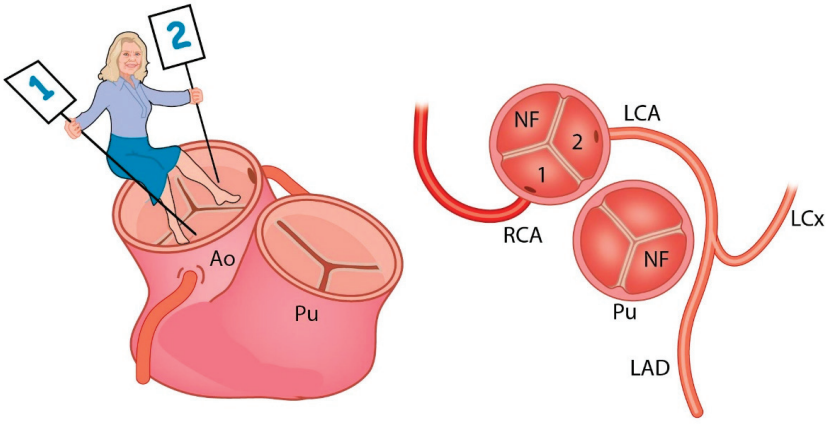

Figure 1. Ao: aorta, Pu: Pulmonary artery, NF: Non Facing sinus, RCA: Right Coronary Artery, LCA: Left Coronary Artery, LAD: Left Anterior Descending artery, LCx: Left Circumflex artery. The observer sits in the non-facing sinus of the aorta and looks towards the facing sinuses. Sinus 1 is on her right-hand side, while sinus 2 is on her left-hand side. The coronary arteries are described in a counterclockwise fashion: 1RCA-2LAD LCx. (Adapted with permission from: Gittenberger de Groot et al. J Thorac Cardiovasc Surg. 2018 Dec;156(6):2260–2269).

In summary, the contributions of Adriana Gittenberger-de Groot have helped to advance new theories and change the way of thinking in the field of coronary artery development and coronary artery variations in TGA and bicuspid aortic valve. The Leiden Convention and the more recently modified Leiden Convention provide a simple, unambiguous coding system of coronary artery origin and branching that is of great help to surgeons who dedicate their efforts to the treatment of congenital heart disease.

Funding: This research received no external funding.

Institutional Review Board Statement: Not applicable.

Informed Consent Statement: Not applicable.

Conflicts of Interest: The authors declare no conflict of interest.

References

1. Gittenberger-de Groot, A.C.; Sauer, U.; Oppenheimer-Dekker, A.; Quaegebeur, J. Coronary arterial anatomy in transposition of the great arteries: A morphologic study. *Pediatr. Cardiol.* **1983**, *4*, 15–24.
2. Jatene, A.D.; Fontes, V.F.; Paulista, P.P.; Souza, L.C.B.; Neger, F.; Galantier, M.; Sousa, J.E. Anatomic correction of transposition of the great vessels. *J. Thorac. Cardiovasc. Surg.* **1976**, *72*, 364–370. [CrossRef]
3. Quaegebeur, J. The Arterial Switch Operation- Rationale, Results, Perspectives. Ph.D. Thesis, Leiden University, Leiden, The Netherlands, 1986.
4. Yacoub, M.H.; Radley-Smith, R. Anatomy of the coronary arteries in transposition of the great arteries and methods for their transfer in anatomical correction. *Thorax* **1978**, *33*, 418–424. [CrossRef] [PubMed]
5. Tsang, V. Always keep an open mind. *J. Thorac. Cardiovasc. Surg.* **2018**, *56*, 2270. [CrossRef] [PubMed]
6. Bogers, A.J.J.C.; Gittenberger-de Groot, A.C.; Dubbeldam, J.A.; Huysmans, H.A. The inadequacy of existing theories on development of the proximal coronary arteries and their connexions with the arterial trunks. *Int. J. Cardiol.* **1988**, *20*, 117–123. [CrossRef]
7. Bogers, A.J.; Gittenberger-de Groot, A.C.; Poelmann, R.E.; Peault, B.M.; Huysmans, H.A. Development of the origin of the coronary arteries, a matter of ingrowth or outgrowth? *Anat. Embryol.* **1989**, *180*, 437–441. [CrossRef] [PubMed]
8. Bogers, A.J.; Bartelings, M.M.; Bökenkamp, R.; Stijnen, T.; van Suylen, R.J.; Poelmann, R.E.; Gittenberger-de Groot, A.C. Common arterial trunk, uncommon coronary arterial anatomy. *J. Thorac. Cardiovasc. Surg.* **1993**, *106*, 1133–1137. [CrossRef]
9. Eralp, I.; Lie-Venema, H.; DeRuiter, M.C.; van den Akker, N.M.S.; Bogers, A.J.J.C.; Mentink, M.M.T.; Poelmann, R.E.; Gittenberger-de Groot, A.C. Coronary artery and orifice development is associated with proper timing of epicardial outgrowth and correlated fas ligand associated apoptosis patterns. *Circ. Res.* **2005**, *96*, 526–534. [CrossRef] [PubMed]
10. Gittenberger-de Groot, A.C.; Koenraadt, W.M.C.; Bartelings, M.M.; Bokenkamp, R.; DeRuiter, M.C.; Hazekamp, M.G.; Bogers, A.J.J.C.; Quaegebeur, J.; Schalij, M.J.; Vliegen, H.W.; et al. Coding of coronary arterial origin and branching in congenital heart disease: The modified Leiden Convention. *J. Thorac. Cardiovasc. Surg.* **2018**, *156*, 2260–2269. [CrossRef] [PubMed]
11. Koppel, C.J.; Vliegen, H.W.; Bökenkamp, R.; Ten Harkel, A.D.J.; Kiès, P.; Egorova, A.D.; Jukema, J.W.; Hazekamp, M.G.; Schalij, M.J.; Groot, A.C.G.; et al. The Leiden Convention coronary coding system: Translation from the surgical to the universal view. *Eur. Heart J. Cardiovasc. Imaging* **2021**, jeab012. [CrossRef] [PubMed]

Journal of
Cardiovascular
Development and Disease

MDPI

Article

Applicability of the Leiden Convention and the Lipton Classification in Patients with a Single Coronary Artery in the Setting of Congenital Heart Disease

Diana Isabel Katekaru-Tokeshi [1], Moisés Jiménez-Santos [2], Claire J. Koppel [3], Hubert W. Vliegen [3], Mariana Díaz-Zamudio [2], Francisco Castillo-Castellón [2], Monique R. M. Jongbloed [3,4] and Eric Kimura-Hayama [2,*]

[1] Service of Cardiology, Hospital Nacional Dos de Mayo, Lima 150101, Peru; diakatekaru@hotmail.com
[2] Departament of Radiology, Service of Computed Tomography, Instituto Nacional de Cardiologia Ignacio Chavez, Juan Badiano 1, Col. Seccion XVI, Mexico City 14080, Mexico; mjimenez@ctcardiomexico.com (M.J.-S.); diazzmariana@gmail.com (M.D.-Z.); fcastillo@ctcardiomexico.com (F.C.-C.)
[3] Department of Cardiology, Leiden University Medical Center, Albinusdreef 2, Postal Zone B-04-P, 2300 RC Leiden, The Netherlands; C.J.Koppel@lumc.nl (C.J.K.); h.w.vliegen@lumc.nl (H.W.V.); M.R.M.Jongbloed@lumc.nl (M.R.M.J.)
[4] Department of Anatomy and Embryology, Leiden University Medical Center, Einthovenweg 20, Postal Zone S-1-P, 2300 RC Leiden, The Netherlands
* Correspondence: erickimura@ctcardiomexico.com; Tel.: +52-55732911

Citation: Katekaru-Tokeshi, D.I.; Jiménez-Santos, M.; Koppel, C.J.; Vliegen, H.W.; Díaz-Zamudio, M.; Castillo-Castellón, F.; Jongbloed, M.R.M.; Kimura-Hayama, E. Applicability of the Leiden Convention and the Lipton Classification in Patients with a Single Coronary Artery in the Setting of Congenital Heart Disease. *J. Cardiovasc. Dev. Dis.* **2021**, *8*, 93. https://doi.org/10.3390/jcdd8080093

Academic Editor: Andy Wessels

Received: 27 June 2021
Accepted: 29 July 2021
Published: 4 August 2021

Abstract: Abstract: BackgroundIn single coronary artery (SCA) anatomy, all coronary tributaries arise from a single ostium, providing perfusion to the entire myocardium. Coronary classification systems can facilitate the description of SCA anatomy. **Aim:** Evaluation of the applicability of Lipton classification and the Leiden Convention coronary coding system in SCA. **Methods:** All patients (n = 6209) who underwent computed tomography (CT) scanning between 2014 and 2018 were retrospectively examined for the presence of SCA and classified, according to Lipton classification and the Leiden Convention coronary coding system. **Results:** The prevalence of SCA was 0.51% (32/6209). Twenty-eight patients (87.5%) had coexisting congenital heart disease (CHD), most frequently pulmonary atresia (9/32, 28.1%). Ten patients (10/32, 31.25%) could not be classified with either the Leiden Convention or Lipton classification (pulmonary atresia n = 9, common arterial trunk (CAT) n = 1). In one case with CAT, Lipton classification, but not the Leiden Convention, could be applied. In two cases with the transposition of the great arteries and in two cases of double outlet right ventricle, the Leiden Convention, but not the Lipton classification, could be applied. **Conclusions:** Both classifications are useful to detail information about SCA. As Lipton classification was not developed for structural heart disease cases, in complex CHD with abnormal position of the great arteries, the Leiden Convention is better applicable. The use of both systems is limited in pulmonary atresia. In this scenario, it is better to provide a precise description of the coronary origin and associated characteristics that might affect treatment and prognosis.

Keywords: single coronary artery; Leiden Convention coronary coding system; Lipton classification; coronary artery anatomy; congenital heart disease

1. Introduction

In single coronary artery (SCA) anatomy, all coronary tributaries arise from a single ostium, providing perfusion to the entire myocardium [1,2]. The prevalence reported in the general population is 0.024% to 0.066%, diagnosed by invasive coronary angiography [1]. SCA has been associated with other congenital heart disease (CHD) in 40% of cases [2].

As variations in origin and course are common, classification systems have been developed to facilitate anatomical description.

In 1979, Lipton described a SCA classification system based on the origin, branching pattern, and course of the coronary artery [2]. The classification system describes coronary anatomy according to predefined patterns. In 1990, the system was modified by Yamanaka and Hobbs to include a septal course [3] (Figure 1). SCAs originating from the anatomical right or left sinus are indicated by an R and L, respectively, followed by the numerical category of the branching pattern (I–III). In Lipton classification, an origin of the coronary artery from the posterior sinus is not included. The classification was not primarily developed, however, for CHD with abnormally aligned great vessels.

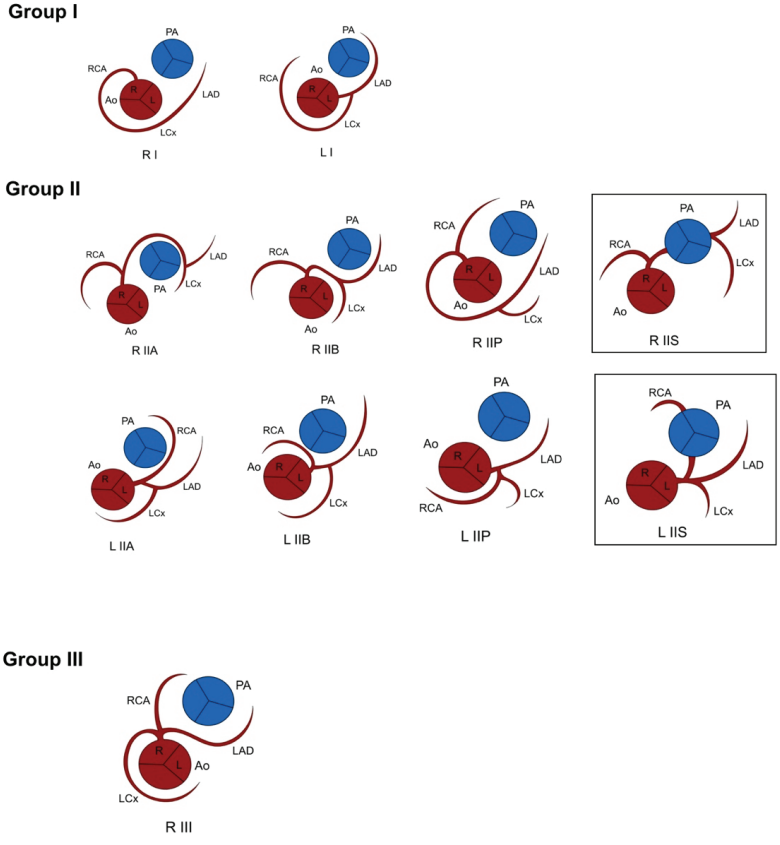

Figure 1. Classification of SCA by Lipton and modified by Yamanaka and Hobbs (marked). Viewed from caudal to cranial, "imaging view". Ao: Aorta. L: Left sinus of Valsalva. LAD: Left anterior descending artery. LCx: Left circumflex artery. PA: Pulmonary artery. R: Right sinus of Valsalva. RCA: Right coronary artery.

The imaging Leiden Convention coronary is a coronary coding system that was developed in the 1980s by Prof. Dr. Adriana Gittenberger-de Groot [4,5]. It can be used in cases with variable and complicated coronary patterns and has the advantage that it can be used irrespective of the position of the great arteries. The system approaches the coronary anatomy based on the fact that both great arteries have, in principle, two "facing" sinuses (Figure 2). Therefore, it applies in structurally normal hearts as well as in CHD, including bicuspid aortic valves. The system avoids using terms related to the spatial orientation of the arterial origin from the aorta in the description, and designates the aortic sinuses as "left or right facing" or "non-facing" relative to the pulmonary valve sinuses. This is based

on the principle that the non-facing sinus (corresponding to the posterior sinus in the case of a normal position of the great arteries), will never carry a coronary artery. Originally, the system was developed for use by cardiac surgeons but was recently extended to provide its use by interventional and imaging (pediatric) cardiologists as well [5,6]. To correct for the different angles at which the coronary arteries are viewed by surgeons and imaging cardiologists, the methods to acquire the same annotation are slightly different for the imaging than for the surgical perspective of the Leiden Convention coding system. For the imaging view, the physician positions themselves in the non-facing sinus of the aortic valve, looking out from the sinus. Positioned in this way, the right-hand sinus is sinus 1, and the left-hand sinus is sinus 2. Then, the branches are described in the order in which they are encountered when adopting a clockwise rotation starting at sinus 1 [5,6] (Figure 2). To our knowledge, there are no studies that evaluate the applicability of the two classification systems (i.e., Lipton classification and the Leiden Convention coronary coding system) for classification of single coronary arteries in the setting of complex congenital heart disease. The aims of the present study are (1) to report the prevalence of cases of SCA diagnosed by coronary computed tomography angiography (CCTA) in a tertiary healthcare cardiovascular center and (2) to evaluate the applicability of Lipton classification and the imaging Leiden Convention coronary coding system to annotate the SCA anatomy.

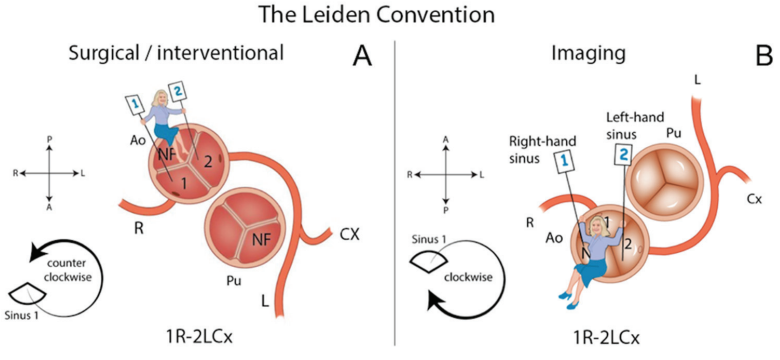

Figure 2. The Leiden Convention considers a surgical/interventional or an imaging perspective (Figure derived with permission from Koppel et al. [6]). (**A**) Surgical/Interventional Leiden Convention. In this method, the coronary anatomy is examined from above, as a surgeon would see it during surgery. The physician sits in the non-facing sinus, facing the pulmonary valve. In that position, the sinus on the right is sinus 1 and the sinus on the left is sinus 2. Starting from sinus 1, the coronary branches are named in the order that they are encountered when following a *counterclockwise* rotation. (**B**) Imaging Leiden Convention. The physician's view on the coronary anatomy is from the base of the aorta upward. The physician sits in the non-facing sinus of the aortic valve, facing outward from the sinus. From this position, the right-hand sinus is again sinus 1, and the left-hand sinus is sinus 2. Following a *clockwise rotation*, starting at sinus 1, the encountered coronary branches are annotated. A: Anterior. Ao: Aorta. L: Left. NF: Non-facing sinus. P: Posterior. Pu: Pulmonary. R: Right.

2. Materials and Methods

Consecutive patients that were scanned between March 2014 and January 2018 in a tertiary referral center were evaluated for the presence of SCA. We employed a dual-source 256-MDCT scanner (Definition Flash, Siemens Healthineers, Erlangen, Germany) with a sectional collimation of $2 \times 128 \times 0.6$. Either ECG-gated or non–ECG-gated high-pitch protocols were used (pitch factor of 0.17 and 3.4 respectively), at the discretion of the attending physician, taking into account the patient's ability to follow instructions, clinical condition and request. The indication for the CCTA in pediatric patients (24/32, 75%) was to further investigate previously diagnosed CHD. The indication for the CCTA in the adult patients (8/32, 25%) was to rule out coronary artery disease. In cardiac-gated scans,

a prospective acquisition was triggered in systole (40–45% of R-R interval). X-ray tube parameters of voltage and current were adjusted to patient's weight as follows: 80 kV if less than 20 kg and 100 kV if BMI < 25 or weight 20–80 kg, with a current of 10 mA/kg (up to 9 kg) and 5 mA for each additional kg. A current *z*-modulation technique (CARE-Dose, Siemens Healthinneers) was used in all patients. The FOV extended from the carina to the lower portion of the heart. The contrast transit time was determined with the use of a bolus tracking technique by placing the region of interest in the ascending aorta. Images were reconstructed in 0.75 mm thickness and interval reconstruction with a B25f kernel filter.

We used non-ionic contrast material (iobitridol, Guerbet, Roissy, France) at a volume of 1–1.5 mL/kg of body weight for non-gated scans or 1.5–2 mL/kg for ECG-gated acquisitions. All images were analyzed by an imaging cardiologist with 8 years of experience in adult and pediatric cardiovascular imaging (MJS). Afterwards, the coronary anatomy was also reviewed and annotated by CJK. Dedicated cardiac workstations were used (Syngo Via v2.0, Siemens Healthineers, Forcheim, Germany and Vitrea, Vital images, Inc., Minnetonka, MN, USA., resp.), capable of multiplanar and volume rendering reformations. An institutional review board (IRB) consent form was obtained at the time that CCTA was performed. The average dose length product (DLP) was 142.5 mGy-cm (16–426 mGy-cm).

3. Results

The prevalence of SCA diagnosed by CCTA was 0.51% (32/6209) in this tertiary cardiovascular referral center. Twenty patients were female (62.5%); the median age was 16 years and 7 months (range 1 month to 78 years) (Table 1).

Ten patients (31.25%) presented with a concomitant coronary anatomy anomaly (CAA), including an anomalous origin of a right coronary artery (RCA) from the left anterior descending coronary artery (LAD) (Figure 3) (6/32, 18.75%) and an absent RCA (4/32, 12.5%). Of the 32 included patients, 4 (12.5%) showed an interarterial course.

Table 1. Patients' demographics, associated congenital heart disease, imaging Leiden Convention and Lipton classification.

Patient Number	Gender	Age	Associated Anomalies	Anatomical Relationship of the Ao to the PA	Leiden Convention	Lipton Classification	Concomitant Coronary Anomaly
1	M	1M	Double-outlet right ventricle	Right anterior	2LCx	LI	Absent RCA
2	F	2M	Truncus arteriosus Van Praagh type A4	NA	NA	NI*	None
3	F	6M	Pulmonary atresia. Single outlet right ventricle. Right aortic arch.	NA	NA	NI*	None
4	F	6M	Pulmonary atresia. Single outlet right ventricle.	NA	NA	NI*	None
5	F	8M	Transposition of the great arteries	Left anterior	2CxRL	NI*	None
6	F	3Y	Tetralogy of Fallot	Clockwise rotation of the aortic root	2RLCx	LIIA	Anomalous origin of RCA from LAD
7	M	3Y	Double-outlet right ventricle. Common atrioventricular canal type C of Rastelli. Right aortic arch	Left anterior	1LCxR	NI*	None
8	F	4Y	Stenosis left ventricular outflow tract by fibromuscular protrusion	Right posterior	2LCx	LI	Absent RCA
9	M	4Y	Tetralogy of Fallot	Clockwise rotation of the aortic root	2RLCx	LIIA	Anomalous origin of RCA from LAD

Table 1. *Cont.*

Patient Number	Gender	Age	Associated Anomalies	Anatomical Relationship of the Ao to the PA	Leiden Convention	Lipton Classification	Concomitant Coronary Anomaly
10	M	4Y	Pulmonary atresia. Ambiguous atrioventricular connection. Right aortic arch	NA	NA	NI*	None
11	F	5Y	Truncus arteriosus Van Praagh type A1. Right aortic arch	NA	NA	RIII	None
12	F	5Y	Syndrome Noonan	Right posterior	2RLCx	LIIA	None
13	F	6Y	Double-outlet right ventricle	Right anterior	2LCxR	NI*	None
14	F	8Y	Isolated	Right posterior	1RLCx	RIIS	None
15	F	9Y	Double-outlet right ventricle. Pulmonary atresia	NA	NA	NI*	None
16	M	10Y	Tetralogy of Fallot	Clockwise rotation of the aortic root	1RLCx	RIIA	None
17	F	10Y	Pulmonary agenesis. Common atrioventricular connection. Single outlet right ventricle	NA	NA	NI*	None
18	F	11Y	Pulmonary atresia	NA	NA	NI*	None
19	M	12Y	Pulmonary agenesis. Single outlet right ventricle. Right aortic arch	NA	NA	NI*	None
20	F	13Y	Mitral valve prolapse	Right posterior	1RL*Cx	RIII	None
21	M	14Y	Transposition of the great arteries	Left anterior	1LCxR	RIIP	None
22	M	15Y	Supravalvular aortic stenosis	Right posterior	2R*LCx	LIIB	None
23	M	15Y	Tetralogy of Fallot	Clockwise rotation of the aortic root	2RLCx	LIIA	Anomalous origin of RCA from LAD
24	M	16Y	Transposition of the great arteries	Right anterior	1RLCx	NI*	None
25	F	18Y	Pulmonary atresia	NA	NA	NI*	None
26	F	25Y	Pulmonary atresia. Double inlet left ventricle. Right aortic arch	NA	NA	NI*	None
27	F	37Y	Atrial septal defect. Ventricular septal defect	Right posterior	2R*LCx	LIIB	Anomalous origin of RCA from LAD
28	F	51Y	Left ventricular non-compaction	Right posterior	2RLCx	LIIA	Anomalous origin of RCA from LAD
29	M	52Y	Isolated	Right posterior	2LCx	LI	Absent RCA
30	M	53Y	Dysplastic aortic valve	Right posterior	2LCx	LI	Absent RCA
31	M	58Y	Coronary artery disease. Rupture of right sinus of Valsalva aneurysm	Right posterior	2LCxR	LIIP	None
32	F	78Y	Isolated	Right posterior	2RLCx	LIIA	Anomalous origin of RCA from LAD

Ao: Aorta. PA: Pulmonary artery. NA: Not applicable. NI*: Not included in the classification.

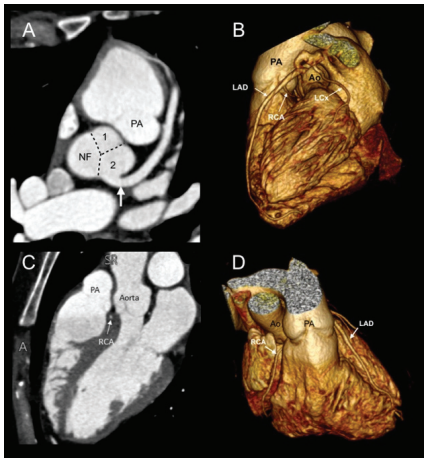

Figure 3. Case 27. CCTA in a 37-year-old woman undergoing preoperative evaluation for an atrial septal defect. (**A**) Axial image depicting the origin of the SCA (arrow) from sinus 2. (**B**) A 3D volume-rendered image showing that the RCA originates from the middle segment of the LAD with an interarterial course. According to the Imaging Leiden Convention, the anatomy is 2R*LCx; by Lipton classification, it is LIIB. (**C**,**D**) The RCA follows a course between the aorta and pulmonary artery (level of right ventricular outflow tract). Ao: Aorta. LAD: Left anterior descending coronary artery. LCx: Left circumflex. NF: Non-facing sinus. PA: Pulmonary artery. RCA: Right coronary artery.

Twenty-eight patients (87.5%) had coexisting CHD (Table 1). The most frequent were pulmonary atresia/agenesis (9/32, 28.1%), one of which also had a double-outlet right ventricle, right aortic arch (6/32, 18.75%), double-outlet right ventricle (4/32, 12.5%), tetralogy of Fallot (4/32, 12.5%), and transposition of great arteries (3/34, 9.4%).

In our cohort, six patients (18.75%) had an anomalous position of the great arteries in which the anatomical relationship of the aorta in relation to the pulmonary trunk was as follows: right anterior 3 (9.4%) and left anterior 3 (9.4%). Additionally, four patients with tetralogy of Fallot had clockwise rotation of the aortic root (Figure 4).

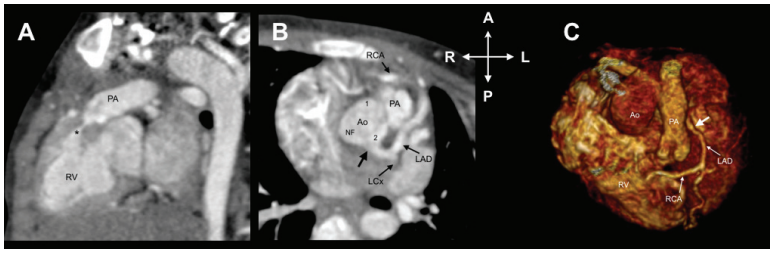

Figure 4. Case 9. A 4-year-old child with tetralogy of Fallot. (**A**) Oblique image showing infundibular pulmonary stenosis (*). (**B**) Axial image reveals coronary origins clockwise rotated along with the aortic root. According to the Leiden Convention, it is 2RLCx and by Lipton classification, it is LIIA. (**C**) A 3D volume-rendered image shows an anomalous origin of the RCA from the LAD. A: Anterior. Ao: Aorta. LAD: Left anterior descending coronary artery. L: Left. LCx: Left circumflex. P: Posterior. R: Right. RV: Right ventricle. NF: Non-facing sinus. PA: Pulmonary artery. RCA: Right coronary artery.

Of the adult patients, (8/32, 25%) the mean calcium score was 11.38 Agatston units (AU) (0–63.4 AU).

3.1. Lipton Classification

The most common origin of the SCA was from the left anterior sinus of Valsalva (13/32, 50%), followed by an origin from the right anterior sinus of Valsalva (5/32, 15.6%), as observed from the anatomical position of the heart in the thorax. According to this system, these 18 patients were classified as LI (n = 4, 22.2%), LIIA (n = 6, 33.3%), LIIB (n = 2, 11%), LIIP (n = 1, 5.5%), RIIA (n = 1, 5.5%), RIIP (n = 1, 5.5%), RIIS (n = 1, 5.5%) and RIII (n = 2, 11%). However, 9 patients with CHD and abnormally aligned great vessels had a SCA origin from the anatomically posterior sinus and 4 with pulmonary atresia, and 1 patient with a common arterial trunk Van Praagh type A4 did not have a course around the pulmonary artery or right ventricular outflow tract, so could not be included in any category of the Lipton classification (Figure 5, Table 2).

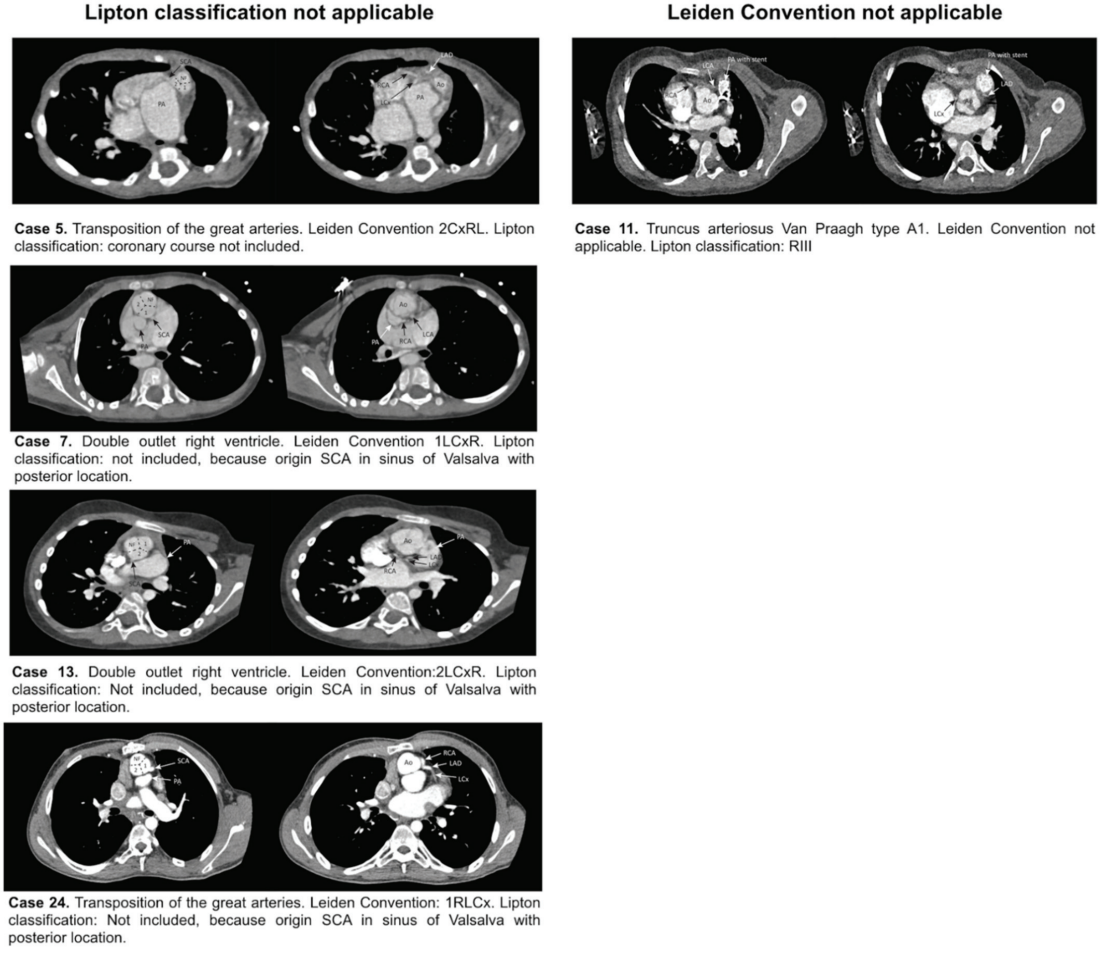

Figure 5. Overview of cases that could be classified only with the Lipton classification or the Leiden Convention. Ao: Aorta. LAD: Left anterior descending coronary artery. LCx: Left circumflex. R: Right. NF: Non-facing sinus. PA: Pulmonary artery. RCA: Right coronary artery. SCA: Single coronary artery.

Table 2. Overview of cases not assessable by either classification.

	Lipton Classification	Leiden Convention
Patient Number	**Associated Anomaly Preventing Use of Both Classification Systems**	
2	Posterior sinus	Truncus arteriosus type A4
3	Posterior sinus	Pulmonary atresia
4	Course not included	Pulmonary atresia
10	Course not included	Pulmonary atresia
15	Posterior sinus	Pulmonary atresia
17	Posterior sinus	Pulmonary atresia
18	Posterior sinus	Pulmonary atresia
19	Course not included	Pulmonary atresia
5	Course not included	Pulmonary atresia
26	Posterior sinus	Pulmonary atresia
	Lipton classification applicable, Leiden Convention not applicable (Figure 5)	
11	RIII	Truncus arteriosus type A1
	Lipton classification not applicable, Leiden Convention applicable (Figure 5)	
5	Course not included	2CxRL
7	Posterior sinus	1LCxR
13	Posterior sinus	2LCxR
24	Posterior sinus	1RLCx

3.2. Leiden Convention Coronary Coding System

According to the imaging Leiden Convention, the origin of the SCA was from the left-hand sinus (sinus 2) in 15 patients (71.4%). In 13 patients, these single coronary arteries were also designated as originating from the left sinus in the Lipton classification; 2 could not be classified with Lipton. The origin of the SCA was from the right-hand sinus (sinus 1) in 6 cases (28.5%), according to the Leiden Convention. This corresponded to the right sinus in the Lipton classification in 4 of these patients; 2 could not be classified according to Lipton. The imaging Leiden Convention could not be used in 11/32 patients (34%): nine patients had pulmonary atresia/agenesis, and 2 patients had a common arterial trunk (1 Van Praagh type A1 and 1 with Van Praagh type A4 [7]) (Table 2). As these conditions do not allow to determine facing and non-facing sinuses, the Leiden Convention coronary coding system could not be used for these cases.

In summary, 10 patients (10/32, 31.25%) could not be classified with either the imaging Leiden Convention or Lipton classification (Table 2). Nine had pulmonary atresia, 1 had a truncus arteriosus Van Praagh type 4A, and in 6 of these, the origin of the SCA was from the anatomically posterior sinus, near the interatrial septum (Figure 6). Four patients, 2 with TGA and 2 with double outlet right ventricle, could be classified by the Leiden Convention, but not by Lipton classification, and 1 patient could be classified by Lipton classification, but not by the Leiden Convention (Figure 5, Table 2). This was a patient with a truncus arteriosus Van Praagh type A1.

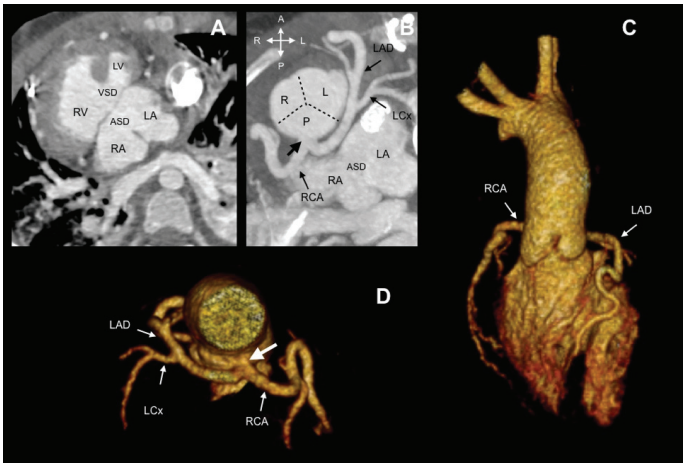

Figure 6. Case 17. A 10-year-old child with pulmonary atresia and common atrioventricular canal type C of Rastelli. (**A**) Oblique axial view showing atrial situs inversus, common atrioventricular connection, atrial and ventricular septal defect. (**B**) The SCA (thick arrow) arises from the posterior sinus, which gives origin to the RCA and left main stem. (**C**,**D**) A 3D volume-rendered image showing a posterior SCA. Ao: Aorta. ASD: Atrial septal defect. LA: Left atrium. LAD: Left anterior descending coronary artery. LCx. Left circumflex. LV: Left ventricle. NF: Non-facing sinus. RA: Right atrium. RCA: Right coronary artery. RV: Right ventricle. VSD: Ventricular septal defect.

4. Discussion

We present a case series of SCA diagnosed with CCTA in a tertiary referral center. To our knowledge, this represents the largest cohort of SCA reported based on CT. The CCTA allows accurate non-invasive evaluation of the coronary ostial morphology, course, and distribution area of the coronary arteries. This might be a result of the type of institution we represent, i.e., a nationwide cardiovascular referral center for complex congenital heart disease, that may show a higher prevalence of SCA as compared to the population without structural cardiac defects. In addition, the higher prevalence of the anomaly when compared to invasive angiography might be the result of the multiplanar capabilities of CT when compared to a biplanar method with limited visualization of spatial relationships.

Coronary artery anomalies are potentially relevant findings during surgery and for coronary intervention planning. In terms of clinical diagnosis, in our series, this finding was incidental in all cases. Although none of the adult patients in this study had significant atherosclerotic disease, the detection of atherosclerosis in an SCA is important because of the potential clinical implications of significant coronary artery disease in a single vessel providing the entire myocardial blood flow. In addition, relevance of its diagnosis also lies in the fact that this anomaly may cause myocardial ischemia by different mechanisms: due to angulations or abnormal courses that may affect the distribution of blood flow, even in the absence of atherosclerotic coronary lesions [2,8–10].

Of the 32 patients included, only 4 (12.5%) showed an interarterial course. This variation might increase the risk of a major cardiac event, due to potential hemodynamic compromise. This prevalence is similar to previous reports [10,11]. Additionally, it is worthwhile to notice that approximately one third of the patients had an additional anomalous coronary branching pattern. In our series, associated CHD was found in almost 87.5% of cases, and concomitant anomalies in coronary arterial branching patterns were present in 31.25% of the patients.

Knowledge of anatomical variations in the origin and course of the coronary arteries in patients with CHD is essential to achieve optimal surgical preparation and follow up.

Coronary classification systems are useful tools to detail important information about coronary anomalies to cardiologists, radiologists and cardiac surgeons.

Lipton classification was originally designed for patients with normal cardiac anatomy without additional congenital cardiac anomalies and is based on classifying the coronary artery as left or right, based on the spatial position (i.e., left or right) of the sinuses of Valsalva from which they emerge. To assign the branching pattern to a group, the system takes into account the coronary artery course relative to the pulmonary artery [2,3], which one might extend to the course around the right ventricular outflow tract for practical reasons. However, this limits their use in hearts with a rotated orientation of the great arteries (described as a general feature in congenital malformation of the outflow tract [12]) or pulmonary atresia. Another limitation of Lipton classification is that it contains a pre-set array of variations, leaving no room for anatomical variations outside this set. However, for many cases, the variations described by Lipton et al. are sufficient. An advantage with respect to the Leiden Convention is that posterior, anterior and septal courses of the coronary artery are directly included in the annotation and not only an interarterial course.

The Leiden Convention coronary coding system was developed to avoid using terms referring to the spatial anatomical position, such as left, right, posterior and anterior, which might be ambiguous in cases with malposition of the great arteries; herein lies its strength for use in (complex) CHD. In Lipton classification, the posterior sinus would, in many cases, correspond to the non-facing sinus in the Leiden Convention, which does not carry a coronary artery. However, especially in malrotation of the great arteries, this correspondence of the posterior sinus to the non-facing sinus is not obligatory.

The nomenclature of the sinuses of the Leiden Convention allows its use also in cases with congenital heart disease and malposition of the great arteries, regardless of the position of the great arteries and the spatial position of the sinuses of Valsalva. As the recognition of facing and non-facing sinuses is a prerequisite of the Leiden Convention coronary coding system, in principle, it cannot be used in cases of common arterial trunk, pulmonary atresia, cases with uni/quadri/pentacuspid valves or if the valve morphology cannot be distinguished [4,5]. The Leiden Convention also cannot be used if the coronary artery arises from the non-facing sinus. We have, to date, not encountered this situation in humans.

Neither the Leiden Convention nor Lipton classification could be applied in 10 patients (Table 2). Nine patients had pulmonary atresia and one patient had a common trunk Van Praagh type A4. For application of the Lipton classification, the SCA has to course around the pulmonary trunk or right ventricular outflow tract, so in the absence of a pulmonary trunk, such as in cases of pulmonary atresia, Lipton classification cannot be used. In addition, cases with the SCA originating from the posterior sinus make Lipton classification inapplicable. A coronary artery originating from a non-facing sinus is extremely rare, and we, therefore, do not consider the posterior sinus to be the equivalent of the non-facing sinus in these cases.

In some cases of pulmonary atresia where a small pulmonary trunk can be visualized, the Leiden Convention might still be applicable. However, we believe that in highly complex CHD where the coronary anatomy cannot be adequately described according to a classification system, it is better to provide a detailed description, including the origin, course (especially important in the case of the interarterial course), coronary artery dominance, the relationship relative to the position of the great vessels, as well as, in particular cases, the shape of the coronary orifice, acute angle take-off, or presence of myocardial bridging of a coronary artery. This corresponds to the "associated anomalies" step of the Leiden Convention coronary coding system.

5. Study Limitations

This a retrospective study including patients for whom CCTA was performed on a variety of indications. Therefore, not all scans were made in an ECG triggered way that would be optimal for evaluation of the coronary anatomy. This may have hampered an optimal evaluation in some of the cases described.

6. Conclusions

Both Lipton classification and the Leiden Convention are useful to present important information about coronary anomalies. In complex CHD with an abnormal position of the great arteries, the Leiden Convention is better applicable. As expected, Lipton classification, which was principally developed for cases without structural heart disease, is less suitable for complex CHD with abnormal position of the great arteries. In pulmonary atresia, the use of both systems is limited. In such cases, it is recommended to provide a detailed description of the coronary anatomy as well as associated characteristics that might affect treatment planning and prognosis.

Author Contributions: Conceptualization, D.I.K.-T., M.J.-S., E.K.-H.; methodology, D.I.K.-T., M.J.-S., C.J.K., M.R.M.J. and E.K.-H.; validation, D.I.K.-T., C.J.K., M.R.M.J. and H.W.V.; formal analysis, D.I.K.-T. and C.J.K.; investigation, D.I.K.-T. and C.J.K.; data curation, D.I.K.-T., C.J.K. and M.R.M.J.; writing—original draft preparation, D.I.K.-T., M.J.-S., F.C.-C., M.D.-Z. and E.K.-H.; writing—review and editing, D.I.K.-T., M.J.-S., C.J.K., M.R.M.J. and E.K.-H.; visualization, D.I.K.-T. and C.J.K. All authors have read and agreed to the published version of the manuscript.

Funding: This research received no external funding.

Institutional Review Board Statement: Ethical review and approval were waived, due to the design of the study. However, it is worth mentioning that all patients in our institution signed a consent form that includes an approval to use their imaging information for academic purposes in those cases where retrospective studies are performed.

Informed Consent Statement: Informed consent was obtained from all subjects involved in the study.

Conflicts of Interest: All authors declare no conflict of interest. This research did not receive any specific grant from funding agencies in the public, commercial, or not-for-profit sectors.

References

1. Aldana-Sepulveda, N.; Restrepo, C.S.; Kimura-Hayama, E. Single coronary artery: Spectrum of imaging findings with multidetector CT. *J. Cardiovasc. Comput. Tomogr.* **2013**, *7*, 391–399. [CrossRef] [PubMed]
2. Lipton, M.J.; Barry, W.H.; Obrez, I.; Silverman, J.F.; Wexler, L. Isolated single coronary artery: Diagnosis, angiographic classification, and clinical significance. *Radiology* **1979**, *130*, 39–47. [CrossRef] [PubMed]
3. Yamanaka, O.; Hobbs, R.E. Coronary artery anomalies in 126,595 patients undergoing coronary arteriography. *Catheter. Cardiovasc. Diagn.* **1990**, *21*, 28–40. [CrossRef] [PubMed]
4. Gittenberger-de Groot, A.C.; Sauer, U.; Oppenheimer-Dekker, A.; Quaegebeur, J. Coronary arterial anatomy in transposition of the great arteries: A morphologic study. *Pediatr. Cardiol.* **1983**, *4*, 15–24.
5. Gittenberger-de Groot, A.C.; Koenraadt, W.M.C.; Bartelings, M.M.; Bökenkamp, R.; DeRuiter, M.C.; Hazekamp, M.G.; Bogers, A.; Quaegebeur, J.M.; Schalij, M.J.; Vliegen, H.W.; et al. Coding of coronary arterial origin and branching in congenital heart disease: The modified Leiden Convention. *J. Thorac. Cardiovasc. Surg.* **2018**, *156*, 2260–2269. [CrossRef] [PubMed]
6. Koppel, C.J.; Vliegen, H.W.; Bökenkamp, R.; Ten Harkel, A.D.J.; Kiès, P.; Egorova, A.D.; Jukema, J.W.; Hazekamp, M.G.; Schalij, M.J.; Gittenberger-de Groot, A.C.; et al. The Leiden Convention coronary coding system: Translation from the surgical to the universal view. *Eur. Heart J. Cardiovasc. Imaging* **2021**. [CrossRef] [PubMed]
7. Van Praagh, R.; Van Praagh, S. The anatomy of common aorticopulmonary trunk (truncus arteriosus communis) and its embryologic implications. A study of 57 necropsy cases. *Am. J. Cardiol.* **1965**, *16*, 406–425. [CrossRef]
8. De Agustín, J.A.; Marcos-Alberca, P.; Manzano Mdel, C.; Fernández-Golfín, C.; Pérez de Isla, L.; Hernández Antolín, R.; Macaya, C.; Zamorano, J. Percutaneous Intervention in a single coronary artery: Evaluation of multislice tomography and its feasibility. *Rev. Esp. Cardiol.* **2010**, *63*, 607–611. [CrossRef]
9. Mandal, S.; Tadros, S.S.; Soni, S.; Madan, S. Single coronary artery anomaly: Classification and evaluation using multidetector computed tomography and magnetic resonance angiography. *Pediatr. Cardiol.* **2014**, *35*, 441–449. [CrossRef] [PubMed]
10. Villa, A.; Sammut, E.; Nair, A.; Rajani, R.; Bonamini, R.; Chiribiri, A. Coronary artery anomalies overview: The normal and the abnormal. *World J. Radiol.* **2016**, *8*, 537–555. [CrossRef] [PubMed]

11. Zhou, Z.; Xu, L.; Zhang, N.; Wang, H.; Liu, W.; Sun, Z.; Fan, Z. CT coronary angiography findings in non-atherosclerotic coronary artery diseases. *Clin. Radiol.* **2018**, *73*, 205–213. [CrossRef] [PubMed]
12. Houyel, L.; Bajolle, F.; Capderou, A.; Laux, D.; Parisot, P.; Bonnet, D. The pattern of the coronary arterial orifices in hearts with congenital malformations of the outflow tracts: A marker of rotation of the outflow tract during cardiac development? *J. Anat.* **2013**, *222*, 349–357. [CrossRef] [PubMed]

Journal of
Cardiovascular
Development and Disease

MDPI

Systematic Review

The Coronary Arteries in Adults after the Arterial Switch Operation: A Systematic Review

Leo J. Engele [1,2], Barbara J. M. Mulder [1,2], Jan W. Schoones [3,†], Philippine Kiès [4], Anastasia D. Egorova [4], Hubert W. Vliegen [4], Mark G. Hazekamp [5], Berto J. Bouma [1,2,‡] and Monique R. M. Jongbloed [4,6,*,‡]

1 Center for Congenital Heart Disease Amsterdam-Leiden (CAHAL), Department of Clinical and Experimental Cardiology, Amsterdam Cardiovascular Sciences, Heart Centre, Amsterdam UMC, University of Amsterdam, 1105 AZ Amsterdam, The Netherlands; l.j.engele@amsterdamumc.nl (L.J.E.); b.j.mulder@amsterdamumc.nl (B.J.M.M.); b.j.bouma@amsterdamumc.nl (B.J.B.)
2 Netherlands Heart Institute, 3511 EP Utrecht, The Netherlands
3 Directorate of Research Policy, Leiden University Medical Center, 2333 ZA Leiden, The Netherlands; j.w.schoones@lumc.nl
4 Center for Congenital Heart Disease Amsterdam-Leiden (CAHAL), Department of Cardiology, Leiden University Medical Center, 2333 ZA Leiden, The Netherlands; p.kies@lumc.nl (P.K.); a.egorova@lumc.nl (A.D.E.); h.w.vliegen@lumc.nl (H.W.V.)
5 Center for Congenital Heart Disease Amsterdam-Leiden (CAHAL), Department of Cardiothoracic Surgery, Leiden University Medical Center, 2333 ZA Leiden, The Netherlands; m.g.hazekamp@lumc.nl
6 Center for Congenital Heart Disease Amsterdam-Leiden (CAHAL), Department of Anatomy and Embryology, Leiden University Medical Center, 2333 ZA Leiden, The Netherlands
* Correspondence: m.r.m.jongbloed@lumc.nl
† Directorate of Research Policy (Formerly: Walaus Library).
‡ These authors contributed equally to the manuscript.

Citation: Engele, L.J.; Mulder, B.J.M.; Schoones, J.W.; Kiès, P.; Egorova, A.D.; Vliegen, H.W.; Hazekamp, M.G.; Bouma, B.J.; Jongbloed, M.R.M. The Coronary Arteries in Adults after the Arterial Switch Operation: A Systematic Review. *J. Cardiovasc. Dev. Dis.* **2021**, *8*, 102. https://doi.org/10.3390/jcdd8090102

Academic Editor: Andy Wessels

Received: 6 July 2021
Accepted: 21 August 2021
Published: 26 August 2021

Publisher's Note: MDPI stays neutral with regard to jurisdictional claims in published maps and institutional affiliations.

Abstract: Coronary artery status in adults long after the arterial switch operation (ASO) is unclear. We conducted a systematic review to provide an overview of coronary complications during adulthood and to evaluate the value of routine coronary imaging in adults after ASO, in light of current guidelines. Articles were screened for the inclusion of adult ASO patients and data on coronary complications and findings of coronary imaging were collected. A total of 993 adults were followed with a median available follow-up of only 2.0 years after reaching adulthood. Myocardial ischemia was suspected in 17/192 patients (8.9%). The number of coronary interventions was four (0.4%), and coronary death was reported in four (0.4%) patients. A lack of ischemia-related symptoms cannot be excluded because innervation studies indicated deficient cardiac innervation after ASO, although data is limited. Anatomical high-risk features found by routine coronary computed tomography (cCT) included stenosis (4%), acute angle (40%), kinking (24%) and inter-arterial course (11%). No coronary complications were reported during pregnancy (n = 45), although, remarkably, four (9%) patients developed heart failure. The 2020 European Society of Cardiology (ESC) guidelines state that routine screening for coronary pathologies is questionable. Based on current findings and in line with the 2018 American ACC/AHA guidelines a baseline assessment of the coronary arteries in all ASO adults seems justifiable. Thereafter, an individualized coronary follow-up strategy is advisable at least until significant duration of follow-up is available.

Keywords: transposition of the great arteries; arterial switch operation; coronary artery; coronary complications; imaging

1. Introduction

Transposition of the great arteries (TGA) is a congenital heart defect with a prevalence of approximately 4.7 per 10,000 newborns and represents 5% to 7% of all congenital heart disease (CHD) [1,2]. Today, the arterial switch operation (ASO) is the operation of choice for anatomical correction in newborns with TGA and selected cases of double outlet right

ventricle (DORV). The ASO is also part of the double switch in congenitally corrected TGA (ccTGA) patients. The ASO was performed successfully for the first time by Jatene and colleagues in 1975 [3,4], and after a transition period in the 1980s, it has now replaced the atrial switch procedures in the vast majority of cases. Translocation of the coronary arteries is the most critical step during the arterial switch procedure. The coronary arteries are excised from the aorta (neo-pulmonary trunk) after which the coronary artery is sutured into the pulmonary artery (neo-aorta) (Figure 1). Several factors contribute to a successful coronary transfer, including a sufficient length of the coronary artery and the coronary anatomy. Coronary events are an important cause of death and most often occur early after ASO; previous studies reported a prevalence of coronary obstruction after ASO from 2% to 11% in children [5,6].

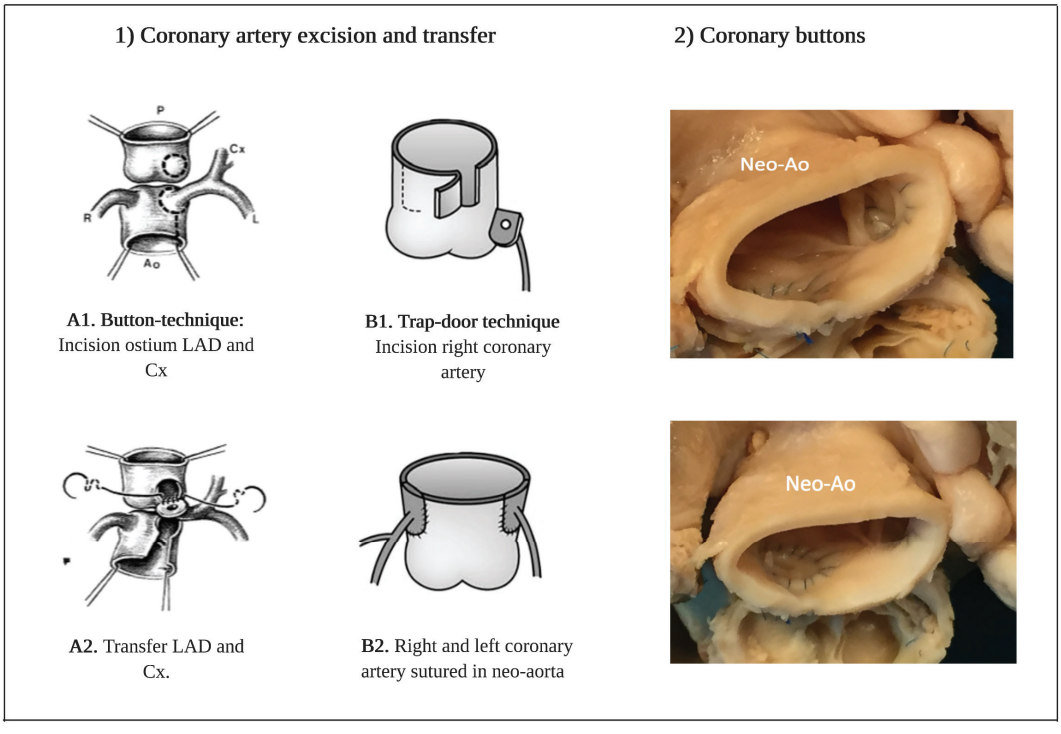

Figure 1. (**1**) Operation techniques for translocation of the coronary arteries during the arterial switch operation. (**A1**,**A2**) Button-technique of coronary artery excision and transfer to the neo-aorta in most common type (1R-2LCx). (**B1**,**B2**) Trap-door technique of coronary artery excision and transfer to the neo-aorta. (**2**) Coronary buttons in the neo-aorta in a patient with transposition of the great arteries after arterial switch. Abbreviations: LAD = left anterior descending artery, Cx = circumflex artery, Neo-Ao = Neo-aorta. Note. Images A1 and A2-1D adapted with approval of the author from the thesis: 'The Arterial Switch Operation–Rationale, Results, Perspectives, by J.M. Quaegebeur, 1986, Chapter IV, p127, ISBN 90-9001327. Images B1 and B2 are adapted from 'The importance of neo-aortic root geometry in the arterial switch operation with the trap-door technique in the subsequent development of aortic valve regurgitation', by Jhang et al. European Journal of Cardio-thoracic Surgery, 2012 Nov; 42(5): 794–92013; 96: 1390–1397. Copyright 2021 by Copyright Clearance Center.

Less is known about the long-term patency of the translocated coronary arteries and the occurrence of myocardial ischemia during adulthood. Potential mechanisms for myocardial ischemia after translocation of the coronary arteries include coronary kinking, anatomical distortion, stretching, and extrinsic compression. Furthermore, growth of the

neo-aorta and proximal coronary arteries during lifetime may result in an increased risk for anatomical high-risk features of the coronary arteries including acute angle, mechanical kinking or stretching [7–9]. Patients with an unusual anatomical coronary pattern may be at higher risk for the occurrence of late coronary complications [10]. Due to cardiac denervation after dissecting the cardiac plexus during ASO, patients with a coronary artery stenosis may be asymptomatic. Previous long-term follow-up studies in children reported significant coronary stenosis after ASO in asymptomatic patients [6,7].

Due to the lifelong risk of coronary complications after the ASO, periodic surveillance of the coronary arteries is recommended by current guidelines [11,12]. Non-invasive examinations for detecting myocardial ischemia with ECG, stress echocardiography, exercise testing, and perfusion scintigraphy have shown low sensitivity for detecting significant coronary stenosis [6]. However, Cardiovascular Magnetic Resonance (CMR) and coronary computed tomography (cCT) can be of value in timely detection of coronary complications. There is currently no consensus regarding the optimal follow-up interval and imaging modality for surveillance of the translocated coronary arteries.

Currently, the group of young adult ASO patients is growing. Although many studies reported coronary complications during childhood, a structured overview of available literature concerning coronary status in adults is lacking. Therefore, we performed a systematic review to provide an overview of currently available literature reporting on the incidence of coronary complications specifically during adulthood and the value of coronary imaging in adults after ASO. Besides, the effects of pregnancy on coronary outcomes and studies on cardiac innervation, given the potential relevance for symptomatology, were analysed. Findings will be discussed in light of current coronary follow-up recommendations after the ASO.

2. Materials and Methods

This systematic review was conducted according to the Preferred Reporting Items for Systematic Reviews and Meta Analyses (PRISMA) checklist [11]. Quality assessment of included long-term follow–up cohort studies was performed with the Newcastle Ottawa Scale (NOS) [13]. Studies were scored on the following two domains: (1) selection, including representativeness of the exposed cohort, ascertainment of exposure, and demonstration that the outcome of interest was not present at the start of the study; (2) outcome, including assessment of outcome, follow-up period, and adequacy of follow-up. The maximum number of awarded stars was six.

2.1. Search Strategy

A comprehensive literature search was performed in PubMed, Embase, Web of Science, Cochrane Library and Emcare. Language was restricted to English and German. Because we focused on the outcomes in adults, only articles which were published between 1994 (18 years after introduction of the ASO) and August 2020 were selected. The search strategy was carried out by using key words for arterial switch, transposition of the great arteries, coronary outcome, long-term outcome, and ischemia. (For complete query: see Appendix A). Duplicate articles were removed.

2.2. Selection Criteria

Cohort studies with TGA, DORV or ccTGA patients after ASO were included. Long-term outcome on coronary interventions or coronary death in adults ($\geq$18 years) was retrieved. Because the purpose was to evaluate the long-term coronary status after arterial switch, patients with one-stage repair, two-stage repair, and late arterial switch were all included in analysis. Furthermore, cross-sectional coronary imaging studies investigating coronary anatomy or myocardial perfusion with any imaging modality were considered eligible for the review. Finally, studies reporting cardiac outcomes during pregnancy, cardiac innervation, and case reports on coronary complications were included. Studies reporting other than coronary outcome in adults after ASO, description of outcome exclusively in

children (<18 year), or patients with a non-identifiable age were excluded. In addition, reviews, editorials and articles in which the full-text could not be retrieved were excluded. Reference lists of reviews were searched for eligible articles which were not identified in the literature search.

2.3. Definitions

The literature search was restricted to adults (18 years or older) because the purpose was to evaluate the long-term patency of the coronary arteries without focusing on the early and midterm outcome. Coronary complications were defined as percutaneous coronary intervention, coronary surgery or coronary death. The following causes of death were interpreted as coronary related: (aborted) sudden cardiac death or death related to proven or possible ischemic heart failure. All imaging techniques performed in adults to assess coronary anatomy or coronary function were considered eligible for systematic review. When duplication of patient data in studies from the same institutions were suspected, the study with the highest number of ASO adults with description of coronary complications was included.

2.4. Data Extraction and Appraisal

All abstracts were screened for eligibility by two independent observers (LJE and MRMJ). In case of disagreement, differences between the observers' judgements were discussed to seek consensus. In each of the included long-term follow-up papers, data were collected on the number of included adults, the number of coronary complications, and the follow-up time, using data derived from full-text, tables, and overall Kaplan–Meier curves. One observer (LJE) performed a quality assessment of the included papers using the NOS. In patients with coronary complications, data were collected on NYHA class and presence of chest pain when available. Data on the number of adults and duration of follow-up collected from Kaplan–Meier curves were categorized into the following age groups: 18–20 years, 20–25 years, 25–30 years, older than 30 years. It was not possible to identify the censored age for each patient from the Kaplan–Meier curves. Therefore, we were not able to include patients who were censored at the age of 18 and 19 years. Mean follow-up was calculated with the follow-up time derived from Kaplan–Meier curves.

In cross-sectional anatomical and physiological imaging studies, data on the imaging technique, the number of patients with anatomical high-risk features, perfusion defects, ischemia, and coronary intervention were retrieved. In addition, data of patients with suspicion of myocardial ischemia were collected. Anatomical high-risk features of the proximal coronary arteries following ASO were defined as: acute angle take-off ($\leq$30 degree), interarterial course, ostial stenosis, and/or kinking. These coronary features have been associated with myocardial ischemia in CHD cohorts [14,15].

Suspicion of myocardial ischemia was based on symptoms or ST-segment deviation during exercise tests. Inclusion of imaging studies was based on the median or mean age ($\geq$18 years) of the ASO cohort; therefore, the potential presence of individual patients in this cohort with an age under 18 years could not be excluded. The following data were extracted from case reports: type of examination, type of intervention, presence of chest pain. From pregnancy studies, data on the number of coronary complications, ventricular rhythm disorders, and left ventricular function were collected. The technique and outcome were retrieved from cardiac innervation studies.

3. Results

3.1. Study Selection

A total of 893 studies were identified (Figure 2). The number of excluded studies by abstract screening was 658; most of these reported outcome exclusively in children (<18 years) or focused on atrial switch procedures. The remaining 235 articles were assessed for eligibility by full-text screening. After full-text assessment, 46 studies were included with the following study designs: 27 long-term follow-up cohort studies, 3 cross-sectional

imaging studies, and 4 case reports. In addition, studies focusing on the following aspects were included: late arterial switch studies (n = 4), double switch studies (n = 2), pregnancy studies (n = 4), and sympathetic innervation studies (n = 2).

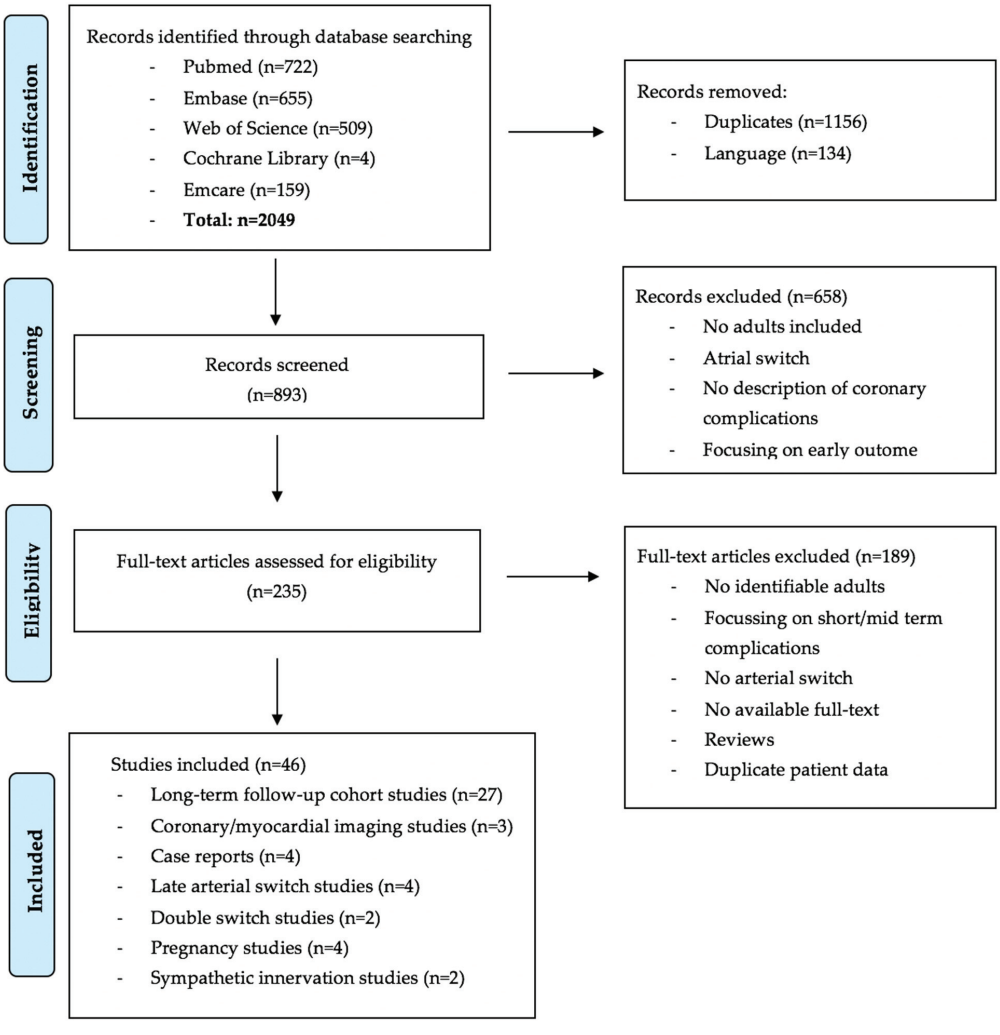

Figure 2. Prisma flow diagram.

3.2. Long-Term Follow-Up Cohort Studies

A total number of 993 ASO patients were followed for at least 18 years in the long-term follow-up cohort studies [16–41] (Table 1). Figure 3A shows the freedom from coronary complications; the number at risk at 18 years is 993 patients. However, at the age of 25 years the number at risk is only 130 patients, which is explained by the relatively young age of the adult patients described in the included papers. The median follow-up duration into adulthood was 2.0 years (mean 2.8 years). Of the 993 adult ASO patients that were included, a total of 8 (0.8%) coronary-related events were reported. Specifically, four patients (0.4%) underwent a coronary intervention (percutaneous coronary intervention (PCI) or coronary artery bypass grafting (CABG)) for coronary stenosis (n = 2) or occlusion (n = 2). One

patient (0.1%) who underwent coronary intervention was asymptomatic. Coronary death was reported in four patients (0.4%): three patients died due to sudden cardiac death, and one patient was found in asystole. All coronary complications are summarized in Table 2. Seventeen out of 192 (8.9%) patients [19,27,42] were suspected to have myocardial ischemia based on symptoms or exercise testing; after additional examinations, 3 out of 17 patients underwent coronary intervention (PCI or CABG).

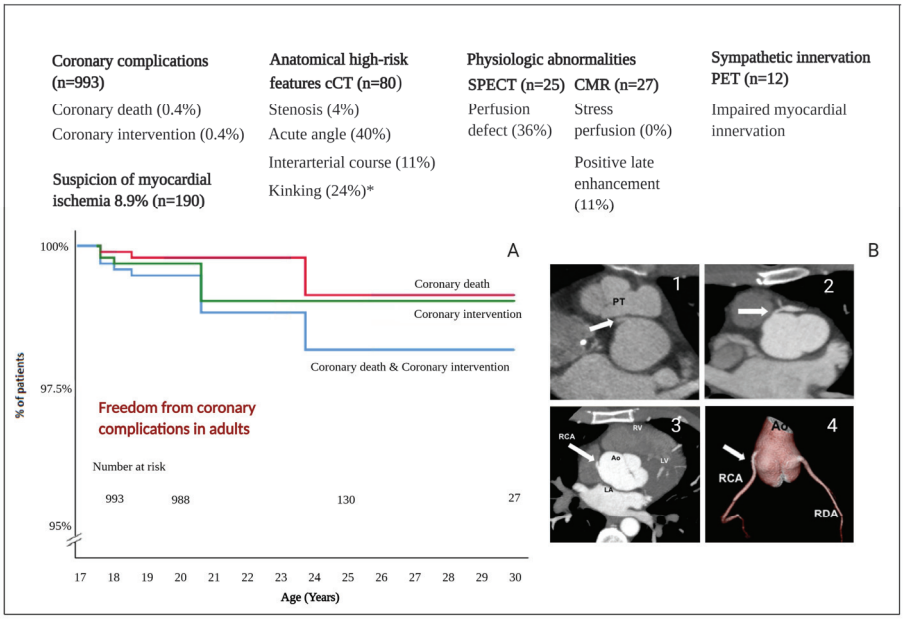

Figure 3. Coronary artery status in adults after ASO. Legend: (**A**). Freedom from coronary complications in adults after ASO. (**B**). Anatomical high-risk features on coronary computed tomography. (B1) Interarterial course of the right coronary artery. (B2) A significant proximal left anterior descending coronary artery stenosis. (B3) Acute angle right coronary artery (axial slice). (B4) Acute angle right coronary artery (three-dimensional reconstruction). Abbreviations: cCT = coronary computer tomography, SPECT = single-photon emission computer tomography, CMR = cardiovascular magnetic resonance, PET = position emission tomography, RDA = Ramus Descendens anterior, RCA = Right Coronary Artery. * only 1 study did describe the presence of kinking (n = 50). Note. CT images B1 and B2 are adapted from 'Variation in Coronary Anatomy in Adult Patients Late After Arterial Switch Operation: A Computed Tomography Coronary Angiography Study', by Veltman et al. Ann Thorac Surg, 2013; 96: 1390–1397. Copyright 2021 by Copyright Clearance Center.

3.3. Coronary Imaging Studies

Two studies [9,42] examined coronary anatomy in adults using routine cCT. The combined results of both studies demonstrated that 4 out of 80 (5%) patients were suspected of coronary stenosis. Three of these patients had no anginal complaints and did not have ischemia at functional testing with single-photon emission computed tomography (SPECT); therefore, no further investigations were performed. In the fourth patient, an angiogram was performed which showed significant proximal luminal narrowing caused by a fibrotic lesion, after which a percutaneous intervention with stent implantation was performed. Other anatomical high-risk features identified by cCT included the following: presence of an acute angle (40%), interarterial course (11%) and proximal kinking (24%). Additional stress SPECT did not show a correlation between perfusion defects and the presence of these high-risk features. Another imaging study in a cohort of 27 ASO adults compared cardiovascular magnetic resonance (CMR) and SPECT under identical physiological circumstances [43]. Nine out of 25 patients (36%) were reported as having perfusion defects

on SPECT; however, CMR stress perfusion with dipyridamole was visually normal in all these patients. A summary of coronary abnormalities of all imaging studies (n = 3) is provided in Table 3 and Figure 3.

Table 1. Overview of the extracted studies on coronary complications across different age groups in ASO adults.

			Age Groups (Years)				
			18–20	20–25	25–30	>30	
Author	**Patients ≥ 18 Year**	**Maximum Follow-Up in Adulthood (Yr)**	**Event/n. at Risk**	**Event/n. at Risk**	**Event/n. at Risk**	**Event/n. at Risk**	**Newcastle Ottawa Scale**
Fricke et al. [16]	183	2	0/183	-	-	-	★★★★★★
Khairy et al. [17]	148	7	0/148	1/28	-	-	★★★★★
Moll et al. [18]	136	7	0/136	0/4	-	-	★★★★★
Kempny et al. [19]	112	20	3/112	1/67	0/20	1/1	★★★★★★
Tobler et al. [20]	60	7	1/60	0/10	-	-	★★★★★★
Santens et al. [21]	52	12	0/52	0/4	0/4	-	★★★★★★
Baruteau et al. [22]	47	7	0/47	0/6	-	-	★★★★★★
Lo Rito et al. [23].	44	2	0/44	-	-	-	★★★★★★
Vida et al. [24]	44	12	0/44	0/1	0/1	-	★★★★★
Oda et al. [25]	40	2	0/40	-	-	-	★★★★
Raissadati et al. [26]	34	12	0/34	0/1	0/1	-	★★★★★★
Ruys et al. [27]	21	2	0/21	-	-	-	★★★★★★
Hörer et al. [19]	17	2	0/17	-	-	-	★★★★★
Shivaram et al. [29]	13	12	0/13	0/3	0/1	-	★★★★★
Lalezari et al. [44]	11	7	0/11	0/2	-	-	★★★★★★
Lim et al. [30]	9	2	0/9	-	-	-	★★★★
Choi et al. [31]	5	7	0/5	0/3	-	-	★★★★★★
Rudra et al. [32]	4	2	0/4	-	-	-	★★★★★★
Gerelli et al. [33]	2	2	0/2	-	-	-	★★★★★★
De Praetere et al. [34]	3	7	0/3	0/1	-	-	★★★★★★
Hayes et al. [45]	2	2	0/2	-	-	-	★★★★★
Hutter et al. [36]	1	2	0/1	-	-	-	★★★★★
Manso et al. [37]	1	2	0/1	-	-	-	★★★★★★
El-Segaier et al. [38]	1	0	1/1	-	-	-	★★★★★★
Gorler et al. [39]	1	2	0/1	-	-	-	★★★★★
Arnaz et al. [40]	1	2	0/1	-	-	-	★★★★
Shim et al. [41]	1	2	0/1	-	-	-	★★★★★
Total	993	median 2.0	5/993	2/130	0/27	1/1	

Table 2. Clinical data of ASO patients with coronary complication during adulthood.

Author	**Age at ASO**	**Age at Event (y)**	**Coronary Anatomy**	**Chest Pain**	**NYHA Class**	**Details**
Kempny et al. [19]	-	18	-	-	-	PCI/CABG
Kempny et al. [19]	-	18	-	-	-	PCI/CABG
Tobler et al. [20]	6 days	18	Usual	-	-	Sudden cardiac death
El-Sagaier et al. [38]	4 days	18	Usual	No	-	PCI LCA
Kempny et al. [19]	7 months	19	Cx from RCA	-	III	Sudden cardiac death
Kempny et al. [19]	-	21	-	-	-	PCI/CABG
Khairy et al. [17]	-	24	Single RCA	-	-	Asystole
Kempny et al. [19]	10 y	38	Usual	-	IV	Sudden cardiac death

Abbreviations: NYHA = New York Heart Association, CABG = coronary artery bypass graft, ASO = arterial switch operation, PCI = percutaneous coronary intervention, y = years, LCA = left coronary artery RCA = right coronary. artery, Cx = circumflex.

Table 3. Description of findings in cardiac imaging studies in adults after ASO.

						cCT		SPECT		CMR	Angiogram	
Author	**N**	**Age**	**Common Coronary Anatomy n (%)**	**Coronary Stenosis n (%)**	**Inter-Arterialn (%)**	**Acute Anglen (%)**	**Kinkingn (%)**	**Perfusion Defectn (%)**	**Ischemia n (%)**	**Ischemia n/Total n**	**Coronary Stenosis n/Total n**	**Coronary Interven-tion(%)**
Michalak [40]	50	23	-	3 (6%)	4 (8%)	25 (50%)	12 (24%)	3 (6%)	0 (0%)	-	-	0 (0%)
Veltman [8]	30	22.0	24 (80)	1 (3%)	5 (17%)	7 (23%)	-	3 (14%)	0 (0%)	-	1/1	1 (3.3%)
Tobler [39]	27	21	18 (67)	-	-	-	-	13 (52%)	8 (32%)	0/27	0/1	0 (0%)

Abbreviations: CAD = coronary artery disease, n = number of patients, total n = total number of examined patients, CT = computer tomography, SPECT = single photon emission computed tomography, CMR = cardiovascular magnetic resonance.

3.4. Case Reports

The literature search identified four case reports [46–49] (Table 4) in which a successful coronary intervention was reported in adults with a significant coronary lesion. Two patients were diagnosed with a significant stenosis of the left main stem. One patient

presented an acute coronary syndrome due to compression of the left main stem. The final patient had subtotal RCA occlusion after pulmonary artery surgery. The presence of chest pain was described in three patients; one patient was asymptomatic.

Table 4. Case reports reporting coronary intervention in ASO adults.

Author	Age	Reason for Intervention	Examination	Chest Pain	Intervention
Quarrie et al. [45]	18 yr	Left main stenosis	SPECT Angio	No	Surgery LIMA-LAD
Stoll et al. [46]	27 yr	ACS due to left main stem compression	CT	Yes	Surgery: defect was reroofed
Ueki et al. [47]	18 yr	subtotal occlusion RCA after patch plasty for PA stenosis	Angiography	Yes	Drug eluting stent
Hamada et al. [48]	24 yr	Ostial stenosis of the left main	CMR & angiography	Yes	Surgery: patch extension

Abbreviations: ACS = acute coronary syndrome, SPECT = single photon emission computed tomography, CMR = cardiovascular magnetic resonance, CT = computer tomography, y = years, LIMA = left internal mammary artery, LAD = left artery descending, PA = pulmonary artery.

3.5. Pregnancy Studies

Four studies described the outcome in patients during pregnancy [50–53] (Table 5). 45 patients were followed peri- and post-partum during 73 pregnancies. During these pregnancies, no coronary events were reported. However, two patients (4.4%) had decrease in LV function, and in four patients (9%), heart failure requiring diuretics treatment was reported. Nonsustained ventricular tachycardia was described in four (9%) patients. These outcomes were not associated with coronary events but could partly be attributed to valvular heart disease. Risk factor for adverse outcome included older age at ASO and higher maternal age [50–53].

Table 5. Cardiovascular outcome peri- and post-partum in ASO adults.

				Peripartum			Postpartum		
Author	All pt	Number of Pregnancies	Age	Coronary Event, n	Heart Failure, n	nsVT, n	nsVT, n	Decrease LV Function, n	Heart Failure, n
Stoll, V.M., et al. [49]	15	25	23	0					
Tobler, D., et al. [50]	9	17	22	0			1	2	
Fricke, T.A., et al. [51]	11	17	29	0	1				
Horiuchi, C., et al. [52]	10	14	29	0	0	2	3	0	3

Abbreviations: pt = patient, nsVT = non sustained ventricular tachycardia, n = number of patients, LV = left ventricular.

3.6. Late Arterial Switch and Double Switch

In 12 patients, a late arterial switch operation was performed during adulthood [54–57] (Table 6). Eleven patients were free from coronary complications during follow-up (range: three months to five years). One patient died five days post-operatively because of low cardiac output syndrome. The outcome of double switch was reported in two adult patients with ccTGA [58,59] (Table 7). Both patients, operated at the age of 14 years and within the first year of life, were free from coronary complications at 5- and 20-year follow-up, respectively.

Table 6. Coronary complications during adulthood in patients after late arterial switch.

Author	n. of Adult Patients	Age at ASO	Follow-Up	Coronary Complications
Cetta et al. [53]	1	36 yr	3 m	no
Padalino et al. [55]	1	23 yr	1 yr	no
Watanabe et al. [56]	8	>20 yr	5 yr	no
Maeda et al. [54]	2	18.6 yr & 32.4 yr	-	1 patient died 5 days after ASO due to low cardiac ouput syndrome

Abbreviations: n = number, ASO = arterial switch operation, m = months, yr = year.

Table 7. Coronary complications in adults after double switch.

Author	n. of Adult Patients	Age at ASO	Follow-Up	Coronary Complications
Uno et al. [57]	1	14 yr	5 yr	no
Konstantinov et al. [58]	1	within the first year	20 yr	no

Abbreviations: n = number, ASO = arterial switch operation, yr = year.

3.7. Cardiac Sympathetic Innervation

Two studies [60,61] were found on cardiac sympathetic innervation exclusively in adults. Possner and colleagues [60] demonstrated that cardiac sympathetic innervation, measured by [^{11}C] meta-hydroxyephedrine uptake, was significantly lower in 12 ASO patients compared to 10 healthy individuals, indicating impaired myocardial innervation long-term after ASO. Furthermore, there was no difference in myocardial blood flow (MBF) response after the cold pressor test; however, when corrected for heart rate, the MBF response was lower in ASO patients. This may be explained by an increased release of catecholamines compensating the deficient innervation. The second study [61] investigated myocardial sympathetic innervation in nine ASO patients and nine Rastelli patients by measuring ^{11}C epinephrine (EPI) retention with positron-emission tomography (PET). In eight ASO patients signs of reinnervation were found, one patient was suspected to have complete denervation (EPI-retention < 7%/min). An association was found between reduced EPI retention and patients undergoing more than one cardiothoracic operation. A summary of findings is provided in Table 8.

Table 8. Description of findings in cardiac innervation studies in adults after ASO.

				cCT	H2O PET			PET	
				(Ostial)	Myocardial Blood Flow (mL/min/g)			EPI Retention	
Author	All pt	Age	Examination	Stenosis	Rest	Adenosine	Cold Pressor Test	Mean (%/min)	<7%/min
Possner et al. [60]	12	22.5	PET & cTA	0	0.66 ± 0.08	2.23 ± 1.19	0.99 ± 0.20	-	-
Kuehn et al. [61]	9	20.8	PET	-	-	-	-	12.83 ± 1.42	n = 1

Abbreviations: cCT = coronary computed tomography, PET = positron-emission tomography, pt = patient, EPI = epinephrine.

4. Discussion

This systematic review shows that the number of reported coronary complications in 993 ASO adults is low (0.8%), but the follow-up period after reaching the age of 18 years is limited with a median of only 2.0 years. In our opinion, the limited follow-up duration demonstrates the relevance of this systematic review to provide an overview of current available literature on coronary arterial status of the young adult ASO population because the evidence for current guideline recommendations for coronary follow-up remains limited. Compared to most previous ASO studies in children, the unique aspect of the current systematic review is that it is focused on the coronary status solely in the adult ASO population with a description of late coronary complications, including an overview of both anatomical and physiological coronary imaging studies.

4.1. Coronary Imaging Strategy

The review focused on the adult population of each cohort; however, similarly low numbers of coronary interventions in children are reported in two included long-term follow-up cohort studies with a routine coronary imaging strategy and a strategy where coronary imaging was performed on clinical indication. Baruteau and colleagues [22] reported the outcome of a routine coronary imaging strategy with catheterization or cCT in 200 ASO patients; this examination was performed every five years, starting from their fifth year. During a median follow-up of 17 years, coronary stenosis or occlusion was found in 4 patients (2%) at a median age of 9.7 years. Khairy et al. [17] described the coronary outcome in 400 ASO patients during a median follow-up of 18.7 years and

reported myocardial infarction in 4 children (1%). In these ASO patients, coronary imaging was performed not on a routine basis but only when clinically indicated.

4.2. Imaging Techniques

SPECT can be performed to detect myocardial perfusion defects in patients after ASO. In comparison with the specificity, the sensitivity for detecting coronary stenosis is low [6]. Clinical significance of perfusion abnormalities is unclear and might be related to the operation itself rather than reflecting coronary flow determined by myocardial perfusion [62]. Despite radiation exposure, cCT is a good non-invasive imaging technique alternative for detecting ostial and proximal coronary stenosis compared to gold standard coronary angiography [63]. In the current review, two anatomical imaging studies in adults (n = 80) after ASO demonstrated that anatomical high-risk features, including acute angle, inter-arterial course and kinking were frequently observed at routine cCT. However, additional physiological examination by SPECT at rest and during exercise demonstrated that most of these high-risk features were not associated with significant perfusion defects. A recent systematic review from Morfaw et al. [64] reported a prevalence of any coronary anomaly of 23.0% in ASO patients older than 20 years, although it was not specified how these coronary anomalies were defined. In this review, we focused specifically on the occurrence of coronary complications and coronary high-risk features. The presence of high-risk features may be related to the technical approach of the coronary transfer and not necessarily the original coronary anatomy. This is consistent with Michalak et al. [42] who did not find an association between coronary anomaly and the presence of high-risk features. In their analysis, a proximal coronary stenosis was significantly correlated with a history of complex coronary transfer. Although, the presence of an acute angle was not associated with surgical technique.

Contradictory literature results about the association between coronary features and mortality exists. A meta-analysis by Pasquali and colleagues reported that in almost 2000 ASO patients, all operated before 1999, both an intramural course and single coronary artery anatomy were associated with a higher all-cause mortality rate. However, in a recent study [16], these abnormalities were not found to be a risk factor for death, which may be explained by the improved surgical experience with coronary high-risk features. Data regarding the impact of anatomical high-risk features on myocardial flow is limited, and further investigation is needed [65].

Existing literature on the anomalous aortic origin of a coronary artery (AAOCA) demonstrated that the presence of a high orifice, ostial stenosis, intramural course and length, inter-arterial course, acute angulation and a slit like orifice have been associated with myocardial ischemia [14,15]. The current 2020 ESC guideline for coronary anomalies recommends physical-stress-induced ischemia testing to examine the presence of myocardial ischemia [12]. The clinical significance of the anatomical high-risk features in the ASO population is still undetermined. Progressive neo-aortic root dilatation has been reported in adults after ASO [66]. Due to dilatation of the neo-aortic root in both radial and longitudinal directions, the angle between the coronary artery and aortic wall could decrease progressively during adulthood and may result in coronary stenosis during adult life. Veltman and colleagues [9] reported an association between larger neo-aortic root dimensions and higher coronary take-off in patients with an acute angle, suggesting that individual patient root geometry might play an additional role.

4.3. Follow-Up Strategy and Current Findings in Relation to Guidelines Recommendations

To determine the long-term patency of the coronary arteries in this population of young adults, a lifelong follow-up is required. Currently, the 2018 ACC and AHA guidelines for the management of adults with congenital heart disease [11] recommend at least single baseline investigation of the coronary arteries by catheter angiography or cCT. Thereafter, the decision is made on clinical indication. The 2020 ESC guidelines on ACHD [12] recommend cCT when a stenosis is suspected, and they state that a routine non-invasive

imaging of coronary arteries with cCT is questionable. Although the current systematic review shows a low number of reported coronary complications, it also exposes that the amount of long-term follow-up data concerning coronary status in adults is still limited. The impact of suture induced fibrosis and atherosclerotic disease on the translocated coronary arties is unclear, and patients with coronary stenosis may be less symptomatic due to decreased innervation post-cardiac surgery. Based on the number of anatomical high-risk features detected by coronary imaging, it seems justified that ASO patients should have at least a baseline assessment of the coronary anatomy with non-invasive CT angiography during young adulthood with additional physiological imaging in patients with high-risk anatomical features or clinical signs of myocardial ischemia.

4.4. Limitations

The number of adults extracted from the Kaplan–Meier curves is underestimated because most studies reported the number of patients at risk at 20 years. However, the number of patients censored at the age of 18 and 19 were not reported and therefore could not be included in this systematic review. One explanation for the low number of coronary complications reported during adulthood might be that coronary complications may occur prior to adulthood. In our analysis, these patients were not included because the event occurred during childhood, and these patients were censored before the age of 18 in Kaplan–Meier figures. Secondly, all reported data regarding anatomical high-risk features of the coronary arteries were analysed; however, not all studies described the same coronary features. Thirdly, strategies for coronary follow-up were different between studies. As a consequence of this heterogeneity, coronary interventions may have been performed more frequently in centers with a routine coronary imaging protocol. Finally, all patients after ASO including TGA, DORV and late arterial switch were included in our review because it was not possible to identify individual patients for subgroup analyses.

5. Conclusions

The number of reported coronary complications in 993 ASO adults during a median follow-up of 2 years is low (0.8%). Anatomical high-risk features were frequently found by routine coronary imaging with cCT in ASO adults; however, the number of interventions in these patients is low, and the clinical significance of these high-risk features at longer term follow up remains unclear. Based on current findings and in line with the 2018 ACC and AHA guidelines on ACHD, we suggest a baseline assessment of the coronary arteries. Thereafter, an individualized coronary follow-up strategy seems appropriate in young adult patients after the ASO.

Author Contributions: Conceptualization: L.J.E., B.J.M.M., J.W.S., M.R.M.J.; methodology, J.W.S., L.J.E., M.R.M.J.; formal analysis, L.J.E.; resources, J.W.S., L.J.E.; writing—original draft preparation, L.J.E., B.J.M.M., J.W.S., M.R.M.J., B.J.B.; writing—review and editing, L.J.E., B.J.M.M., J.W.S., P.K., A.D.E., H.W.V., M.G.H., B.J.B., M.R.M.J.; visualization, L.J.E., M.R.M.J.; supervision, B.J.M.M., B.J.B., M.R.M.J.; funding acquisition, B.J.M.M., B.J.B., M.R.M.J. All authors have read and agreed to the published version of the manuscript.

Funding: This research was funded by the Netherlands Heart Institute (NLHI-308), grant Outreach, grant number CVON2019-002.

Acknowledgments: In respectful memory of Adriana Gittenberger-de Groot, who passionately studied coronary arterial anatomy in congenital heart disease during her life and laid the foundation of much of our knowledge on this subject.

Conflicts of Interest: The authors declare no conflict of interest.

Appendix A

Literature Search

Pubmed: ((((“Arterial Switch Operation”[Mesh] OR “Arterial Switch Operation”[tw] OR “Arterial Switch Operations”[tw] OR “arterial switch procedure”[tw] OR “arterial switch procedures”[tw] OR “arterial switch repair”[tw] OR “arterial switch surgery”[tw] OR “arterial switch”[tw] OR “Arterial Switch Technique”[tw] OR “Double Switch Operation”[tw] OR “Double Switch Operations”[tw] OR “Double Switch Procedure”[tw] OR “Double Switch Procedures”[tw] OR “Double Switch Technique”[tw] OR “Double Switch”[tw] OR “Jatene Operation”[tw] OR “Jatene Procedure”[tw] OR “Jatene Technique”[tw]) AND (“coronary complications”[tw] OR “coronary complication”[tw] OR “Coronary Disease”[mesh] OR “Coronary Aneurysm”[tw] OR “Coronary Aneurysms”[tw] OR “Coronary Artery Disease”[tw] OR “Coronary Artery Diseases”[tw] OR “Coronary Disease”[tw] OR “Coronary Diseases”[tw] OR “Coronary Occlusion”[tw] OR “Coronary Occlusions”[tw] OR “Coronary Restenosis”[tw] OR “Coronary Restenoses”[tw] OR “Coronary Stenosis”[tw] OR “Coronary Stenoses”[tw] OR “Coronary Thrombosis”[tw] OR “Coronary Thromboses”[tw] OR “Coronary Vasospasm”[tw] OR “Coronary Vasospasms”[tw] OR “Coronary-Subclavian Steal Syndrome”[tw] OR “ischemic event”[tw] OR “ischemic events”[tw] OR “ischaemic event”[tw] OR “ischaemic events”[tw] OR “Myocardial Ischemia”[Mesh] OR “Acute Coronary Syndrome”[tw] OR “Angina Pectoris”[tw] OR “Cardiogenic Shock”[tw] OR “Kounis Syndrome”[tw] OR “Microvascular Angina”[tw] OR “Myocardial Infarct”[tw] OR “Myocardial Infarction”[tw] OR “Myocardial Infarctions”[tw] OR “Myocardial Infarcts”[tw] OR “Myocardial Ischaemia”[tw] OR “Myocardial Ischemia”[tw] OR “Myocardial Reperfusion Injuries”[tw] OR “Myocardial Reperfusion Injury”[tw] OR “Stable Angina”[tw] OR “Unstable Angina”[tw] OR “ischemic disease”[tw] OR “ischemic diseases”[tw] OR “ischaemic disease”[tw] OR “ischaemic diseases”[tw] OR “coronary surgery”[tw] OR “coronary artery surgery”[tw] OR “Coronary Artery Bypass”[Mesh] OR “Coronary Artery Bypass”[tw] OR “Coronary Vessels/surgery”[Mesh] OR “Catheterization”[Mesh] OR “Catheterization”[tw] OR “Catheterisation”[tw] OR Catheter*[tw] OR “Death, Sudden, Cardiac”[Mesh] OR “sudden cardiac death”[tw] OR “Cardiac Sudden Death”[tw] OR “Sudden Cardiac Arrest”[tw] OR “Karoshi Death”[tw] OR “coronary artery anatomy”[tw] OR “coronary artery pattern”[tw] OR “coronary artery patterning”[tw] OR “coronary artery patterns”[tw] OR “coronary outcome”[tw] OR “coronary outcomes”[tw] OR “Chest Pain”[Mesh] OR “thoracic pain*”[tw] OR “thorax pain*”[tw] OR “chest pain*”[tw] OR “Neuralgia”[Mesh] OR “nerve pain*”[tw] OR “neuronal pain*”[tw] OR “neuralg*”[tw] OR “atypical pain*”[tw] OR “Denervation”[Mesh] OR “Denervat*”[tw] OR “reinnervation”[tw] OR “reinnervat*”[tw] OR “re innervat*”[tw] OR “innervation” [Subheading] OR “innervation”[tw] OR “innervat*”[tw] OR “coronary anatom*”[tw] OR “Coronary Vessels/anatomy and histology”[mesh] OR “myocardial perfusion”[tw] OR “Myocardial Perfusion Imaging”[Mesh]) AND (english[la] OR german[la]) AND (“1994/01/01”[PDAT]: “3000/12/31”[PDAT])) OR ((“Arterial Switch Operation”[majr] OR “Arterial Switch Operation”[ti] OR “Arterial Switch Operations”[ti] OR “arterial switch procedure”[ti] OR “arterial switch procedures”[ti] OR “arterial switch repair”[ti] OR “arterial switch surgery”[ti] OR “arterial switch”[ti] OR “Arterial Switch Technique”[ti] OR “Double Switch Operation”[ti] OR “Double Switch Operations”[ti] OR “Double Switch Procedure”[ti] OR “Double Switch Procedure*”[ti] OR “Double Switch Technique”[ti] OR “Double Switch”[ti] OR “Jatene Operation”[ti] OR “Jatene Procedure”[ti] OR “Jatene Technique”[ti]) AND (“outcomes”[tiab] OR “outcome”[tiab] OR “long term”[tiab] OR “longterm”[tiab] OR “experience”[tiab]) AND (english[la] OR german[la]) AND (“1994/01/01”[PDAT]: “3000/12/31”[PDAT]))) NOT (“ablation”[tw] OR “prenatal”[tw] OR “neonates”[ti] OR “neonate”[ti] OR “newborn”[ti] OR “newborns”[ti])

Embase: (((*”Arterial Switch Operation”/OR “Arterial Switch Operation”.ti,ab OR “Arterial Switch Operations”.ti,ab OR “arterial switch procedure”.ti,ab OR “arterial switch procedures”.ti,ab OR “arterial switch repair”.ti,ab OR “arterial switch surgery”.ti,ab OR “arterial switch”.ti,ab OR “Arterial Switch Technique”.ti,ab OR “Double Switch Operation”.ti,ab OR “Double Switch Operations”.ti,ab OR “Double Switch Procedure”.ti,ab OR “Double Switch Procedures”.ti,ab OR “Double Switch Technique”.ti,ab OR “Double Switch”.ti,ab

OR “Jatene Operation”.ti,ab OR “Jatene Procedure”.ti,ab OR “Jatene Technique”.ti,ab) AND (“coronary complications”.ti,ab OR “coronary complication”.ti,ab OR exp *”Coronary Artery Disease”/OR “Coronary Aneurysm”.ti,ab OR “Coronary Aneurysms”.ti,ab OR “Coronary Artery Disease”.ti,ab OR “Coronary Artery Diseases”.ti,ab OR “Coronary Disease”.ti,ab OR “Coronary Diseases”.ti,ab OR “Coronary Occlusion”.ti,ab OR “Coronary Occlusions”.ti,ab OR “Coronary Restenosis”.ti,ab OR “Coronary Restenoses”.ti,ab OR “Coronary Stenosis”.ti,ab OR “Coronary Stenoses”.ti,ab OR “Coronary Thrombosis”.ti,ab OR “Coronary Thromboses”.ti,ab OR “Coronary Vasospasm”.ti,ab OR “Coronary Vasospasms”.ti,ab OR “Coronary-Subclavian Steal Syndrome”.ti,ab OR “ischemic event”.ti,ab OR “ischemic events”.ti,ab OR “ischaemic event”.ti,ab OR “ischaemic events”.ti,ab OR exp *”Ischemic Heart Disease”/OR “Acute Coronary Syndrome”.ti,ab OR “Angina Pectoris”.ti,ab OR “Cardiogenic Shock”.ti,ab OR “Kounis Syndrome”.ti,ab OR “Microvascular Angina”.ti,ab OR “Myocardial Infarct”.ti,ab OR “Myocardial Infarction”.ti,ab OR “Myocardial Infarctions”.ti,ab OR “Myocardial Infarcts”.ti,ab OR “Myocardial Ischaemia”.ti,ab OR “Myocardial Ischemia”.ti,ab OR “Myocardial Reperfusion Injuries”.ti,ab OR “Myocardial Reperfusion Injury”.ti,ab OR “Stable Angina”.ti,ab OR “Unstable Angina”.ti,ab OR “ischemic disease”.ti,ab OR “ischemic diseases”.ti,ab OR “ischaemic disease”.ti,ab OR “ischaemic diseases”.ti,ab OR “coronary surgery”.ti,ab OR “coronary artery surgery”.ti,ab OR *”Coronary Artery Bypass Graft”/OR “Coronary Artery Bypass”.ti,ab OR exp *”coronary artery surgery”/OR exp *”Catheterization”/OR “Catheterization”.ti,ab OR “Catheterisation”.ti,ab OR Catheter*.ti,ab OR *”Sudden Cardiac Death”/OR “sudden cardiac death”.ti,ab OR “Cardiac Sudden Death”.ti,ab OR “Sudden Cardiac Arrest”.ti,ab OR “Karoshi Death”.ti,ab OR “coronary artery anatomy”.ti,ab OR “coronary artery pattern”.ti,ab OR “coronary artery patterning”.ti,ab OR “coronary artery patterns”.ti,ab OR “coronary outcome”.ti,ab OR “coronary outcomes”.ti,ab OR *”Thorax Pain”/OR “thoracic pain*”.ti,ab OR “thorax pain*”.ti,ab OR “chest pain*”.ti,ab OR exp *”Neuralgia”/OR “nerve pain*”.ti,ab OR “neuronal pain*”.ti,ab OR “neuralg*”.ti,ab OR “atypical pain*”.ti,ab OR exp *”Denervation”/OR “Denervat*”.ti,ab OR “reinnervation”.ti,ab OR “reinnervat*”.ti,ab OR “re innervat*”.ti,ab OR exp “innervation”/OR “innervation”.ti,ab OR “innervat*”.ti,ab OR “coronary anatom*”.ti,ab OR “myocardial perfusion”.ti,ab OR *”heart muscle perfusion”/OR *”Myocardial Perfusion Imaging”/) AND (english.la OR german.la)) OR ((*”Arterial Switch Operation”/OR “Arterial Switch Operation”.ti OR “Arterial Switch Operations”.ti OR “arterial switch procedure”.ti OR “arterial switch procedures”.ti OR “arterial switch repair”.ti OR “arterial switch surgery”.ti OR “arterial switch”.ti OR “Arterial Switch Technique”.ti OR “Double Switch Operation”.ti OR “Double Switch Operations”.ti OR “Double Switch Procedure”.ti OR “Double Switch Procedures”.ti OR “Double Switch Technique”.ti OR “Double Switch”.ti OR “Jatene Operation”.ti OR “Jatene Procedure”.ti OR “Jatene Technique”.ti) AND (“outcomes”.ti,ab OR “outcome”.ti,ab OR “long term”.ti,ab OR “longterm”.ti,ab OR “experience”.ti,ab) AND (english.la OR german.la))) NOT (“ablation”.ti,ab OR “prenatal”.ti,ab OR “neonates”.ti OR “neonate”.ti OR “newborn”.ti OR “newborns”.ti)

Web of Science: ((ti=(“Arterial Switch Operation” OR “Arterial Switch Operation” OR “Arterial Switch Operations” OR “arterial switch procedure” OR “arterial switch procedures” OR “arterial switch repair” OR “arterial switch surgery” OR “arterial switch” OR “Arterial Switch Technique” OR “Double Switch Operation” OR “Double Switch Operations” OR “Double Switch Procedure” OR “Double Switch Procedures” OR “Double Switch Technique” OR “Double Switch” OR “Jatene Operation” OR “Jatene Procedure” OR “Jatene Technique”) AND ts=(“coronary complications” OR “coronary complication” OR “Coronary Artery Disease” OR “Coronary Aneurysm” OR “Coronary Aneurysms” OR “Coronary Artery Disease” OR “Coronary Artery Diseases” OR “Coronary Disease” OR “Coronary Diseases” OR “Coronary Occlusion” OR “Coronary Occlusions” OR “Coronary Restenosis” OR “Coronary Restenoses” OR “Coronary Stenosis” OR “Coronary Stenoses” OR “Coronary Thrombosis” OR “Coronary Thromboses” OR “Coronary Vasospasm” OR “Coronary Vasospasms” OR “Coronary-Subclavian Steal Syndrome” OR “ischemic event” OR “ischemic events” OR “ischaemic event” OR “ischaemic events” OR “Ischemic Heart Disease” OR “Acute Coronary Syndrome” OR “Angina Pectoris” OR “Cardiogenic Shock”

OR “Kounis Syndrome” OR “Microvascular Angina” OR “Myocardial Infarct” OR “Myocardial Infarction” OR “Myocardial Infarctions” OR “Myocardial Infarcts” OR “Myocardial Ischaemia” OR “Myocardial Ischemia” OR “Myocardial Reperfusion Injuries” OR “Myocardial Reperfusion Injury” OR “Stable Angina” OR “Unstable Angina” OR “ischemic disease” OR “ischemic diseases” OR “ischaemic disease” OR “ischaemic diseases” OR “coronary surgery” OR “coronary artery surgery” OR *”Coronary Artery Bypass Graft” OR “Coronary Artery Bypass” OR “coronary artery surgery” OR “Catheterization” OR “Catheterization” OR “Catheterisation” OR Catheter* OR *”Sudden Cardiac Death” OR “sudden cardiac death” OR “Cardiac Sudden Death” OR “Sudden Cardiac Arrest” OR “Karoshi Death” OR “coronary artery anatomy” OR “coronary artery pattern” OR “coronary artery patterning” OR “coronary artery patterns” OR “coronary outcome” OR “coronary outcomes” OR *”Thorax Pain” OR “thoracic pain*” OR “thorax pain*” OR “chest pain*” OR “Neuralgia” OR “nerve pain*” OR “neuronal pain*” OR “neuralg*” OR “atypical pain*” OR “Denervation” OR “Denervat*” OR “reinnervation” OR “reinnervat*” OR “re innervat*” OR “innervation” OR “innervation” OR “innervat*” OR “coronary anatom*” OR “myocardial perfusion” OR *”heart muscle perfusion” OR “Myocardial Perfusion Imaging”) AND la=(english OR german)) OR (ts=(“Arterial Switch Operation” OR “Arterial Switch Operation” OR “Arterial Switch Operations” OR “arterial switch procedure” OR “arterial switch procedures” OR “arterial switch repair” OR “arterial switch surgery” OR “arterial switch” OR “Arterial Switch Technique” OR “Double Switch Operation” OR “Double Switch Operations” OR “Double Switch Procedure” OR “Double Switch Procedures” OR “Double Switch Technique” OR “Double Switch” OR “Jatene Operation” OR “Jatene Procedure” OR “Jatene Technique”) AND ti=(“coronary complications” OR “coronary complication” OR “Coronary Artery Disease” OR “Coronary Aneurysm” OR “Coronary Aneurysms” OR “Coronary Artery Disease” OR “Coronary Artery Diseases” OR “Coronary Disease” OR “Coronary Diseases” OR “Coronary Occlusion” OR “Coronary Occlusions” OR “Coronary Restenosis” OR “Coronary Restenoses” OR “Coronary Stenosis” OR “Coronary Stenoses” OR “Coronary Thrombosis” OR “Coronary Thromboses” OR “Coronary Vasospasm” OR “Coronary Vasospasms” OR “Coronary-Subclavian Steal Syndrome” OR “ischemic event” OR “ischemic events” OR “ischaemic event” OR “ischaemic events” OR “Ischemic Heart Disease” OR “Acute Coronary Syndrome” OR “Angina Pectoris” OR “Cardiogenic Shock” OR “Kounis Syndrome” OR “Microvascular Angina” OR “Myocardial Infarct” OR “Myocardial Infarction” OR “Myocardial Infarctions” OR “Myocardial Infarcts” OR “Myocardial Ischaemia” OR “Myocardial Ischemia” OR “Myocardial Reperfusion Injuries” OR “Myocardial Reperfusion Injury” OR “Stable Angina” OR “Unstable Angina” OR “ischemic disease” OR “ischemic diseases” OR “ischaemic disease” OR “ischaemic diseases” OR “coronary surgery” OR “coronary artery surgery” OR *”Coronary Artery Bypass Graft” OR “Coronary Artery Bypass” OR “coronary artery surgery” OR “Catheterization” OR “Catheterization” OR “Catheterisation” OR Catheter* OR *”Sudden Cardiac Death” OR “sudden cardiac death” OR “Cardiac Sudden Death” OR “Sudden Cardiac Arrest” OR “Karoshi Death” OR “coronary artery anatomy” OR “coronary artery pattern” OR “coronary artery patterning” OR “coronary artery patterns” OR “coronary outcome” OR “coronary outcomes” OR *”Thorax Pain” OR “thoracic pain*” OR “thorax pain*” OR “chest pain*” OR “Neuralgia” OR “nerve pain*” OR “neuronal pain*” OR “neuralg*” OR “atypical pain*” OR “Denervation” OR “Denervat*” OR “reinnervation” OR “reinnervat*” OR “re innervat*” OR “innervation” OR “innervation” OR “innervat*” OR “coronary anatom*” OR “myocardial perfusion” OR *”heart muscle perfusion” OR “Myocardial Perfusion Imaging”)) OR (ti=(*”Arterial Switch Operation” OR “Arterial Switch Operation” OR “Arterial Switch Operations” OR “arterial switch procedure” OR “arterial switch procedures” OR “arterial switch repair” OR “arterial switch surgery” OR “arterial switch” OR “Arterial Switch Technique” OR “Double Switch Operation” OR “Double Switch Operations” OR “Double Switch Procedure” OR “Double Switch Procedures” OR “Double Switch Technique” OR “Double Switch” OR “Jatene Operation” OR “Jatene Procedure” OR “Jatene Technique”) AND ts=(“outcomes” OR “outcome” OR “long term” OR “longterm” OR “experience”))) NOT (ts=(“ablation”

OR "prenatal") OR ti=("neonates" OR "neonate" OR "newborn" OR "newborns")) AND la=(english OR german)

Cochrane Library: (("Arterial Switch Operation" OR "Arterial Switch Operation" OR "Arterial Switch Operations" OR "arterial switch procedure" OR "arterial switch procedures" OR "arterial switch repair" OR "arterial switch surgery" OR "arterial switch" OR "Arterial Switch Technique" OR "Double Switch Operation" OR "Double Switch Operations" OR "Double Switch Procedure" OR "Double Switch Procedures" OR "Double Switch Technique" OR "Double Switch" OR "Jatene Operation" OR "Jatene Procedure" OR "Jatene Technique"):ti,ab,kw AND ("coronary complications" OR "coronary complication" OR "Coronary Disease" OR "Coronary Aneurysm" OR "Coronary Aneurysms" OR "Coronary Artery Disease" OR "Coronary Artery Diseases" OR "Coronary Disease" OR "Coronary Diseases" OR "Coronary Occlusion" OR "Coronary Occlusions" OR "Coronary Restenosis" OR "Coronary Restenoses" OR "Coronary Stenosis" OR "Coronary Stenoses" OR "Coronary Thrombosis" OR "Coronary Thromboses" OR "Coronary Vasospasm" OR "Coronary Vasospasms" OR "Coronary-Subclavian Steal Syndrome" OR "ischemic event" OR "ischemic events" OR "ischaemic event" OR "ischaemic events" OR "Myocardial Ischemia" OR "Acute Coronary Syndrome" OR "Angina Pectoris" OR "Cardiogenic Shock" OR "Kounis Syndrome" OR "Microvascular Angina" OR "Myocardial Infarct" OR "Myocardial Infarction" OR "Myocardial Infarctions" OR "Myocardial Infarcts" OR "Myocardial Ischaemia" OR "Myocardial Ischemia" OR "Myocardial Reperfusion Injuries" OR "Myocardial Reperfusion Injury" OR "Stable Angina" OR "Unstable Angina" OR "ischemic disease" OR "ischemic diseases" OR "ischaemic disease" OR "ischaemic diseases" OR "coronary surgery" OR "coronary artery surgery" OR "Coronary Artery Bypass" OR "Coronary Artery Bypass" OR "Catheterization" OR "Catheterization" OR "Catheterisation" OR Catheter* OR "Death, Sudden, Cardiac" OR "sudden cardiac death" OR "Cardiac Sudden Death" OR "Sudden Cardiac Arrest" OR "Karoshi Death" OR "coronary artery anatomy" OR "coronary artery pattern" OR "coronary artery patterning" OR "coronary artery patterns" OR "coronary outcome" OR "coronary outcomes" OR "Chest Pain" OR "thoracic pain*" OR "thorax pain*" OR "chest pain*" OR "Neuralgia" OR "nerve pain*" OR "neuronal pain*" OR "neuralg*" OR "atypical pain*" OR "Denervation" OR "Denervat*" OR "reinnervation" OR "reinnervat*" OR "re innervat*" OR "innervation" OR "innervation" OR "innervat*" OR "coronary anatom*" OR "coronary anatom*" OR "myocardial perfusion" OR *"heart muscle perfusion" OR "Myocardial Perfusion Imaging"):ti,ab,kw OR (ti=(*"Arterial Switch Operation" OR "Arterial Switch Operation" OR "Arterial Switch Operations" OR "arterial switch procedure" OR "arterial switch procedures" OR "arterial switch repair" OR "arterial switch surgery" OR "arterial switch" OR "Arterial Switch Technique" OR "Double Switch Operation" OR "Double Switch Operations" OR "Double Switch Procedure" OR "Double Switch Procedures" OR "Double Switch Technique" OR "Double Switch" OR "Jatene Operation" OR "Jatene Procedure" OR "Jatene Technique"):ti AND ts=("outcomes" OR "outcome" OR "long term" OR "longterm" OR "experience"):ti,ab,kw))

Emcare: see Embase.

References

1. Centers for Disease Control and Prevention (CDC). Improved national prevalence estimates for 18 selected major birth defects–United States, 1999–2001. *MMWR Morb. Mortal. Wkly. Rep.* **2006**, *54*, 1301–1305.
2. Martins, P.; Castela, E. Transposition of the great arteries. *Orphanet J. Rare Dis.* **2008**, *3*, 27. [CrossRef] [PubMed]
3. Jatene, A.D.; Fontes, V.F.; Paulista, P.P.; Souza, L.C.; Neger, F.; Galantier, M.; Sousa, J.E. Anatomic correction of transposition of the great vessels. *J. Thorac. Cardiovasc. Surg.* **1976**, *72*, 364–370. [CrossRef]
4. Jatene, A.D.; Fontes, V.F.; Paulista, P.P.; de Souza, L.C.; Neger, F.; Galantier, M.; Souza, J.E. Successful anatomic correction of transposition of the great vessels. A preliminary report. *Arq. Bras. Cardiol.* **1975**, *28*, 461–464. [PubMed]
5. Prêtre, R.; Tamisier, D.; Bonhoeffer, P.; Mauriat, P.; Pouard, P.; Sidi, D.; Vouhé, P. Results of the arterial switch operation in neonates with transposed great arteries. *Lancet* **2001**, *357*, 1826–1830. [CrossRef]
6. Legendre, A.; Losay, J.; Touchot-Koné, A.; Serraf, A.; Belli, E.; Piot, J.D.; Lambert, V.; Capderou, A.; Planche, C. Coronary events after arterial switch operation for transposition of the great arteries. *Circulation* **2003**, *108* (Suppl. 1), Ii186–Ii190. [CrossRef]

7. Tanel, R.E.; Wernovsky, G.; Landzberg, M.J.; Perry, S.B.; Burke, R.P. Coronary artery abnormalities detected at cardiac catheterization following the arterial switch operation for transposition of the great arteries. *Am. J. Cardiol.* **1995**, *76*, 153–157. [CrossRef]
8. Bonnet, D.; Bonhoeffer, P.; Piéchaud, J.F.; Stümper, O.; Kachaner, J.; Sidi, D.; Vouhé, P.R. Coronary obstructions after reimplantation of the two coronary ostia in a single orifice during arterial switch operation for transposition of the great arteries. *Eur. J. Cardiothorac. Surg.* **1996**, *10*, 482. [CrossRef]
9. Veltman, C.E.; Beeres, S.; Kalkman, D.N.; Kelder, T.P.; Kiès, P.; Vliegen, H.W.; Hazekamp, M.G.; Delgado, V.; Kroft, L.J.M.; van der Wall, E.E.; et al. Variation in coronary anatomy in adult patients late after arterial switch operation: A computed tomography coronary angiography study. *Ann. Thorac. Surg.* **2013**, *96*, 1390–1397. [CrossRef]
10. Bonhoeffer, P.; Bonnet, D.; Piéchaud, J.F.; Stümper, O.; Aggoun, Y.; Villain, E.; Kachaner, J.; Sidi, D. Coronary artery obstruction after the arterial switch operation for transposition of the great arteries in newborns. *J. Am. Coll. Cardiol.* **1997**, *29*, 202–206. [CrossRef]
11. Stout, K.K.; Daniels, C.J.; Aboulhosn, J.A.; Bozkurt, B.; Broberg, C.S.; Colman, J.M.; Crumb, S.R.; Dearani, J.A.; Fuller, S.; Gurvitz, M.; et al. 2018 AHA/ACC Guideline for the Management of Adults with Congenital Heart Disease: A Report of the American College of Cardiology/American Heart Association Task Force on Clinical Practice Guidelines. *J. Am. Coll. Cardiol.* **2019**, *73*, e81–e192. [CrossRef] [PubMed]
12. Baumgartner, H.; De Backer, J.; Babu-Narayan, S.V.; Budts, W.; Chessa, M.; Diller, G.P.; Lung, B.; Kluin, J.; Lang, I.M.; Meijboom, F.; et al. 2020 ESC Guidelines for the management of adult congenital heart disease. *Eur. Heart J.* **2020**, *42*, 563–645. [CrossRef] [PubMed]
13. Stang, A. Critical evaluation of the Newcastle-Ottawa scale for the assessment of the quality of nonrandomized studies in meta-analyses. *Eur. J. Epidemiol.* **2010**, *25*, 603–605. [CrossRef] [PubMed]
14. Opolski, M.P.; Pregowski, J.; Kruk, M.; Witkowski, A.; Kwiecinska, S.; Lubienska, E.; Demkow, M.; Hryniewiecki, T.; Michalek, P.; Ruzyllo, W.; et al. Prevalence and characteristics of coronary anomalies originating from the opposite sinus of Valsalva in 8,522 patients referred for coronary computed tomography angiography. *Am. J. Cardiol.* **2013**, *111*, 1361–1367. [CrossRef] [PubMed]
15. Jegatheeswaran, A.; Devlin, P.J.; McCrindle, B.W.; Williams, W.G.; Jacobs, M.L.; Blackstone, E.H.; DeCampli, W.M.; Caldarone, C.A.; Gaynor, J.W.; Kirklin, J.K.; et al. Features associated with myocardial ischemia in anomalous aortic origin of a coronary artery: A Congenital Heart Surgeons' Society study. *J. Thorac. Cardiovasc. Surg.* **2019**, *158*, 822–834.e3. [CrossRef]
16. Fricke, T.A.; Bell, D.; Daley, M.; d'Udekem, Y.; Brizard, C.P.; Alphonso, N.; Konstantinov, I.E. The influence of coronary artery anatomy on mortality after the arterial switch operation. *J. Thorac. Cardiovasc. Surg.* **2020**, *160*, 191–199.e1. [CrossRef] [PubMed]
17. Khairy, P.; Clair, M.; Fernandes, S.M.; Blume, E.D.; Powell, A.J.; Newburger, J.W.; Landzberg, M.J.; Mayer, J.E., Jr. Cardiovascular outcomes after the arterial switch operation for D-transposition of the great arteries. *Circulation* **2013**, *127*, 331–339. [CrossRef]
18. Moll, M.; Moll, J.A.; Moll, J.J.; Łubisz, M.; Michalak, K.W. Intramural coronary pattern in patients with transposition: Incidence and impact on follow-up. *Eur. J. Cardiothorac. Surg.* **2020**, *58*, 145–152. [CrossRef] [PubMed]
19. Kempny, A.; Wustmann, K.; Borgia, F.; Dimopoulos, K.; Uebing, A.; Li, W.; Chen, S.S.; Piorkowski, A.; Radley-Smith, R.; Yacoub, M.H.; et al. Outcome in adult patients after arterial switch operation for transposition of the great arteries. *Int. J. Cardiol.* **2013**, *167*, 2588–2593. [CrossRef]
20. Tobler, D.; Williams, W.G.; Jegatheeswaran, A.; Van Arsdell, G.S.; McCrindle, B.W.; Greutmann, M.; Oechslin, E.N.; Silversides, C.K. Cardiac outcomes in young adult survivors of the arterial switch operation for transposition of the great arteries. *J. Am. Coll. Cardiol.* **2010**, *56*, 58–64. [CrossRef]
21. Santens, B.; Van De Bruaene, A.; De Meester, P.; Gewillig, M.; Troost, E.; Claus, P.; Bogaert, J.; Budts, W. Outcome of arterial switch operation for transposition of the great arteries. A 35-year follow-up study. *Int. J. Cardiol.* **2020**, *316*, 94–100. [CrossRef] [PubMed]
22. Baruteau, A.E.; Vergnat, M.; Kalfa, D.; Delpey, J.G.; Ly, M.; Capderou, A.; Lambert, V.; Belli, E. Long-term outcomes of the arterial switch operation for transposition of the great arteries and ventricular septal defect and/or aortic arch obstruction. *Interact. Cardiovasc. Thorac. Surg.* **2016**, *23*, 240–246. [CrossRef] [PubMed]
23. Lo Rito, M.; Fittipaldi, M.; Haththotuwa, R.; Jones, T.J.; Khan, N.; Clift, P.; Brawn, W.J.; Barron, D.J. Long-term fate of the aortic valve after an arterial switch operation. *J. Thorac. Cardiovasc. Surg.* **2015**, *149*, 1089–1094. [CrossRef] [PubMed]
24. Vida, V.L.; Zanotto, L.; Zanotto, L.; Triglia, L.T.; Bellanti, E.; Castaldi, B.; Padalino, M.A.; Gasperetti, A.; Battista, F.; Varnier, M.; et al. Arterial switch operation for transposition of the great arteries: A single-centre 32-year experience. *J. Card. Surg.* **2019**, *34*, 1154–1161. [CrossRef]
25. Oda, S.; Nakano, T.; Sugiura, J.; Fusazaki, N.; Ishikawa, S.; Kado, H. Twenty-eight years' experience of arterial switch operation for transposition of the great arteries in a single institution. *Eur. J. Cardiothorac. Surg.* **2012**, *42*, 674–679. [CrossRef] [PubMed]
26. Raissadati, A.; Nieminen, H.; Sairanen, H.; Jokinen, E. Outcomes after the Mustard, Senning and arterial switch operation for treatment of transposition of the great arteries in Finland: A nationwide 4-decade perspective. *Eur. J. Cardiothorac. Surg.* **2017**, *52*, 573–580. [CrossRef]
27. Ruys, T.P.; van der Bosch, A.E.; Cuypers, J.A.; Witsenburg, M.; Helbing, W.A.; Bogers, A.J.; van Domburg, R.; McGhie, J.S.; Geleijnse, M.L.; Henrichs, J.; et al. Long-term outcome and quality of life after arterial switch operation: A prospective study with a historical comparison. *Congenit. Heart Dis.* **2013**, *8*, 203–210. [CrossRef]
28. Hörer, J.; Schreiber, C.; Cleuziou, J.; Vogt, M.; Prodan, Z.; Busch, R.; Holper, K.; Lange, R. Improvement in long-term survival after hospital discharge but not in freedom from reoperation after the change from atrial to arterial switch for transposition of the great arteries. *J. Thorac. Cardiovasc. Surg.* **2009**, *137*, 347–354. [CrossRef]

29. Shivaram, P.; Padiyath, A.; Bai, S.; Gossett, J.M.; Collins, R.T. Utility of Follow-Up Annual Echocardiograms in Patients With Complete Transposition of the Great Arteries After Arterial Switch Operations. *Am. J. Cardiol.* **2018**, *122*, 1972–1976. [CrossRef]
30. Lim, H.G.; Kim, W.H.; Lee, J.R.; Kim, Y.J. Long-term results of the arterial switch operation for ventriculo-arterial discordance. *Eur. J. Cardiothorac. Surg.* **2013**, *43*, 325–334. [CrossRef]
31. Choi, B.S.; Kwon, B.S.; Kim, G.B.; Bae, E.J.; Noh, C.I.; Choi, J.Y.; Yun, Y.S.; Kim, W.H.; Lee, J.R.; Kim, Y.J. Long-term outcomes after an arterial switch operation for simple complete transposition of the great arteries. *Korean Circ. J.* **2010**, *40*, 23–30. [CrossRef]
32. Rudra, H.S.; Mavroudis, C.; Backer, C.L.; Kaushal, S.; Russell, H.; Stewart, R.D.; Webb, C.; Sullivan, C. The arterial switch operation: 25-year experience with 258 patients. *Ann. Thorac. Surg.* **2011**, *92*, 1742–1746. [CrossRef]
33. Gerelli, S.; Pontailler, M.; Rochas, B.; Angeli, E.; Van Steenberghe, M.; Bonnet, D.; Vouhé, P.; Raisky, O. Single coronary artery and neonatal arterial switch operation: Early and long-term outcomes. *Eur. J. Cardiothorac. Surg.* **2017**, *52*, 90–95. [CrossRef] [PubMed]
34. De Praetere, H.; Vandesande, J.; Rega, F.; Daenen, W.; Marc, G.; Eyskens, B.; Heying, R.; Cools, B.; Meyns, B. 20 years of arterial switch operation for simple TGA. *Acta Chir. Belg.* **2014**, *114*, 92–98. [CrossRef]
35. Hayes, D.A.; Jones, S.; Quaegebeur, J.M.; Richmond, M.E.; Andrews, H.F.; Glickstein, J.S.; Chen, J.M.; Bacha, E.; Liberman, L. Primary arterial switch operation as a strategy for total correction of Taussig-Bing anomaly: A 21-year experience. *Circulation* **2013**, *128*, S194–S198. [CrossRef] [PubMed]
36. Hutter, P.A.; Kreb, D.L.; Mantel, S.F.; Hitchcock, J.F.; Meijboom, E.J.; Bennink, G.B. Twenty-five years' experience with the arterial switch operation. *J. Thorac. Cardiovasc. Surg.* **2002**, *124*, 790–797. [CrossRef] [PubMed]
37. Manso, P.H.; Amaral, F.T.; Júnior, T.J.; Jurca, M.C.; Haddad, J.; Vicente, W.V.; Sgarbieri, R.N.; Carmona, F. Outcomes of Patients After Arterial Switch Operation: 18 Years of Experience in a Single Medium-Volume Center. *Pediatr. Cardiol.* **2015**, *36*, 1657–1661. [CrossRef] [PubMed]
38. El-Segaier, M.; Lundin, A.; Hochbergs, P.; Jögi, P.; Pesonen, E. Late coronary complications after arterial switch operation and their treatment. *Catheter. Cardiovasc. Interv.* **2010**, *76*, 1027–1032. [CrossRef] [PubMed]
39. Görler, H.; Ono, M.; Thies, A.; Lunkewitz, E.; Westhoff-Bleck, M.; Haverich, A.; Breymann, T.; Boethig, D. Long-term morbidity and quality of life after surgical repair of transposition of the great arteries: Atrial versus arterial switch operation. *Interact. Cardiovasc. Thorac. Surg.* **2011**, *12*, 569–574. [CrossRef]
40. Arnaz, A.; Sarioglu, T.; Yalcinbas, Y.; Erek, E.; Turkoz, R.; Oktay, A.; Saygili, A.; Altun, D.; Sarioglu, A. Coronary artery bypass grafting in children. *J. Card. Surg.* **2018**, *33*, 29–34. [CrossRef]
41. Shim, M.S.; Jun, T.G.; Yang, J.H.; Park, P.W.; Kang, I.S.; Huh, J.; Song, J.Y. Current expectations of the arterial switch operation in a small volume center: A 20-year, single-center experience. *J. Cardiothorac. Surg.* **2016**, *11*, 34. [CrossRef]
42. Michalak, K.W.; Sobczak-Budlewska, K.; Moll, J.J.; Szymczyk, K.; Moll, J.A.; Niwald, M.; Dryżek, P.; Moll, M. Can we predict potentially dangerous coronary patterns in patients with transposition of the great arteries after an arterial switch operation? *Cardiol. Young* **2019**, *29*, 1350–1355. [CrossRef] [PubMed]
43. Tobler, D.; Motwani, M.; Wald, R.M.; Roche, S.L.; Verocai, F.; Iwanochko, R.M.; Greenwood, J.P.; Oechslin, E.N.; Crean, A.M. Evaluation of a comprehensive cardiovascular magnetic resonance protocol in young adults late after the arterial switch operation for d-transposition of the great arteries. *J. Cardiovasc. Magn. Reson.* **2014**, *16*, 98. [CrossRef]
44. Lalezari, S.; Bruggemans, E.F.; Blom, N.A.; Hazekamp, M.G. Thirty-year experience with the arterial switch operation. *Ann. Thorac. Surg.* **2011**, *92*, 973–979. [CrossRef] [PubMed]
45. Hayes, A.M.; Baker, E.J.; Kakadeker, A.; Parsons, J.M.; Martin, R.P.; Radley-Smith, R.; Qureshi, S.A.; Yacoub, M.; Maisey, M.N.; Tynan, M. Influence of anatomic correction for transposition of the great arteries on myocardial perfusion: Radionuclide imaging with technetium-99m 2-methoxy isobutyl isonitrile. *J. Am. Coll. Cardiol.* **1994**, *24*, 769–777. [CrossRef]
46. Quarrie, R.; Kopf, G.S.; Hashim, S. Left main coronary artery occlusion in an asymptomatic patient: Late complication after arterial switch operation. *J. Card. Surg.* **2016**, *31*, 599–600. [CrossRef] [PubMed]
47. Stoll, V.M.; Hudsmith, L.E.; Drury, N.E.; Barron, D.J. Late complication of intramural coronary transfer during the arterial switch operation. *Interact. Cardiovasc. Thorac. Surg.* **2019**, *28*, 638–639. [CrossRef]
48. Ueki, Y.; Kadner, A.; Gräni, C.; Räber, L. ST-Segment Elevation Myocardial Infarction Due to Optical Coherence Tomography-Detected Coronary Artery Compression Following Supravalvular Pulmonary Artery Patchplasty 18 Years after Switch Procedure. *JACC Cardiovasc. Interv.* **2018**, *11*, e149–e151. [CrossRef]
49. Hamada, S.; Frick, M.; Marx, N.; Brehmer, K.; Manka, R. Severe myocardial ischaemia after neonatal arterial switch operation. *Eur. Heart J.* **2015**, *36*, 3214. [CrossRef]
50. Stoll, V.M.; Drury, N.E.; Thorne, S.; Selman, T.; Clift, P.; Chong, H.; Thompson, P.J.; Morris, R.K.; Hudsmith, L.E. Pregnancy Outcomes in Women with Transposition of the Great Arteries after an Arterial Switch Operation. *JAMA Cardiol.* **2018**, *3*, 1119–1122. [CrossRef] [PubMed]
51. Tobler, D.; Fernandes, S.M.; Wald, R.M.; Landzberg, M.; Salehian, O.; Siu, S.C.; Colman, J.M.; Sermer, M.; Silversides, C.K. Pregnancy outcomes in women with transposition of the great arteries and arterial switch operation. *Am. J. Cardiol.* **2010**, *106*, 417–420. [CrossRef]
52. Fricke, T.A.; Konstantinov, I.E.; Grigg, L.E.; Zentner, D. Pregnancy Outcomes in Women after the Arterial Switch Operation. *Heart Lung Circ.* **2019**, *29*, 1087–1092. [CrossRef]

53. Horiuchi, C.; Kamiya, C.A.; Ohuchi, H.; Miyoshi, T.; Tsuritani, M.; Iwanaga, N.; Neki, R.; Niwa, K.; Kurosaki, K.; Ichikawa, H.; et al. Pregnancy outcomes and mid-term prognosis in women after arterial switch operation for dextro-transposition of the great arteries—Tertiary hospital experiences and review of literature. *J. Cardiol.* **2019**, *73*, 247–254. [CrossRef] [PubMed]
54. Cetta, F.; Bonilla, J.J.; Lichtenberg, R.C.; Stasior, C.; Troman, J.E.; Deleon, S.Y. Anatomic correction of dextrotransposition of the great arteries in a 36-year-old patient. *Mayo Clin. Proc.* **1997**, *72*, 245–247. [CrossRef] [PubMed]
55. Maeda, T.; Sakamoto, T.; Nagashima, M.; Hiramatsu, T.; Yamazaki, K. Long-Term Outcome of Arterial Switch Operation Conversion After Failed Senning/Mustard Procedure. *Ann. Thorac. Surg.* **2016**, *102*, 1573–1579. [CrossRef] [PubMed]
56. Padalino, M.A.; Stellin, G.; Brawn, W.J.; Fasoli, G.; Daliento, L.; Milanesi, O.; Casarotto, D. Arterial switch operation after left ventricular retraining in the adult. *Ann. Thorac. Surg.* **2000**, *70*, 1753–1757. [CrossRef]
57. Watanabe, N.; Mainwaring, R.D.; Carrillo, S.A.; Lui, G.K.; Reddy, V.M.; Hanley, F.L. Left Ventricular Retraining and Late Arterial Switch for D-Transposition of the Great Arteries. *Ann. Thorac. Surg.* **2015**, *99*, 1655–1661. [CrossRef] [PubMed]
58. Uno, Y.; Morita, K.; Ko, Y.; Kinouchi, K. Double switch operation for congenitally corrected transposition of the great arteries after two-staged pulmonary artery banding. *Jpn. J. Thorac. Cardiovasc. Surg.* **2006**, *54*, 40–43. [CrossRef]
59. Konstantinov, I.E.; Fricke, T.A.; d'Udekem, Y.; Radford, D.J. Translocation of a single coronary artery from the nonfacing sinus in the arterial switch operation: Long-term patency of the interposition graft. *J. Thorac. Cardiovasc. Surg.* **2010**, *140*, 1193–1194. [CrossRef]
60. Possner, M.; Buechel, R.R.; Vontobel, J.; Mikulicic, F.; Gräni, C.; Benz, D.C.; Clerc, O.F.; Fuchs, T.A.; Tobler, D.; Stambach, D.; et al. Myocardial blood flow and cardiac sympathetic innervation in young adults late after arterial switch operation for transposition of the great arteries. *Int. J. Cardiol.* **2020**, *299*, 110–115. [CrossRef]
61. Kuehn, A.; Vogt, M.; Schwaiger, M.; Ewert, P.; Hauser, M. Ventricular sympathetic innervation in patients with transposition of the great arteries after arterial switch operation and Rastelli procedure: Impact of arterial dissection and coronary reimplantation. *Circ. J.* **2014**, *78*, 1717–1722. [CrossRef] [PubMed]
62. Vogel, M.; Smallhorn, J.F.; Gilday, D.; Benson, L.N.; Ash, J.; Williams, W.G.; Freedom, R.M. Assessment of myocardial perfusion in patients after the arterial switch operation. *J. Nucl. Med.* **1991**, *32*, 237–241. [PubMed]
63. Ou, P.; Celermajer, D.S.; Marini, D.; Agnoletti, G.; Vouhé, P.; Brunelle, F.; Le Quan Sang, K.H.; Thalabard, J.C.; Sidi, D.; Bonnet, D. Safety and accuracy of 64-slice computed tomography coronary angiography in children after the arterial switch operation for transposition of the great arteries. *JACC Cardiovasc. Imaging* **2008**, *1*, 331–339. [CrossRef] [PubMed]
64. Morfaw, F.; Leenus, A.; Mbuagbaw, L.; Anderson, L.N.; Dillenburg, R.; Thabane, L. Outcomes after corrective surgery for congenital dextro-transposition of the arteries using the arterial switch technique: A scoping systematic review. *Syst. Rev.* **2020**, *9*, 231. [CrossRef]
65. Koppel, C.J.; Driesen, B.W.; de Winter, R.J.; van den Bosch, A.E.; van Kimmenade, R.; Wagenaar, L.J.; Jukema, J.W.; Hazekamp, M.G.; van der Kley, F.; Jongbloed, M.R.M.; et al. The first multicentre study on coronary anomalies in the Netherlands: MuSCAT. *Neth. Heart J.* **2021**, *29*, 311–317. [CrossRef]
66. Van der Bom, T.; van der Palen, R.L.; Bouma, B.J.; van Veldhuisen, S.L.; Vliegen, H.W.; Konings, T.C.; Zwinderman, A.H.; Blom, N.A.; Koolbergen, D.R.; Hazekamp, M.G.; et al. Persistent neo-aortic growth during adulthood in patients after an arterial switch operation. *Heart* **2014**, *100*, 1360–1365. [CrossRef]

Journal of
Cardiovascular
Development and Disease

MDPI

Article

Transcriptome Analysis Reveals Differential Gene Expression between the Closing Ductus Arteriosus and the Patent Ductus Arteriosus in Humans

Junichi Saito [1], Tomoyuki Kojima [1,2], Shota Tanifuji [1], Yuko Kato [1], Sayuki Oka [1], Yasuhiro Ichikawa [3], Etsuko Miyagi [2], Tsuyoshi Tachibana [3], Toshihide Asou [3] and Utako Yokoyama [1,*]

[1] Department of Physiology, Tokyo Medical University, 6-1-1 Shinjuku, Shinjuku-ku, Tokyo 160-8402, Japan; junichi.saito@yale.edu (J.S.); kojimat@tokyo-med.ac.jp (T.K.); tanifuji@tokyo-med.ac.jp (S.T.); yukato@tokyo-med.ac.jp (Y.K.); s120052@tokyo-med.ac.jp (S.O.)
[2] Department of Obstetrics and Gynecology, Yokohama City University, 3-9 Fukuura, Kanazawa-ku, Yokohama, Kanagawa 236-0004, Japan; emiyagi@yokohama-cu.ac.jp
[3] Department of Cardiovascular Surgery, Kanagawa Children's Medical Center, 2-138-4 Mutsukawa, Minami-ku, Yokohama, Kanagawa 232-8555, Japan; yas1lll@yahoo.co.jp (Y.I.); tachi.t@icloud.com (T.T.); toshisurgeonfamily@live.jp (T.A.)
* Correspondence: uyokoyam@tokyo-med.ac.jp; Tel.: +81-3-3351-6141

Abstract: The ductus arteriosus (DA) immediately starts closing after birth. This dynamic process involves DA-specific properties, including highly differentiated smooth muscle, sparse elastic fibers, and intimal thickening (IT). Although several studies have demonstrated DA-specific gene expressions using animal tissues and human fetuses, the transcriptional profiles of the closing DA and the patent DA remain largely unknown. We performed transcriptome analysis using four human DA samples. The three closing DA samples exhibited typical DA morphology, but the patent DA exhibited aorta-like elastic lamellae and poorly formed IT. A cluster analysis revealed that samples were clearly divided into two major clusters, the closing DA and patent DA clusters, and showed distinct gene expression profiles in IT and the tunica media of the closing DA samples. Cardiac neural crest-related genes such as *JAG1* were highly expressed in the tunica media and IT of the closing DA samples compared to the patent DA sample. Abundant protein expressions of jagged 1 and the differentiated smooth muscle marker calponin were observed in the closing DA samples but not in the patent DA sample. Second heart field-related genes such as *ISL1* were enriched in the patent DA sample. These data indicate that the patent DA may have different cell lineages compared to the closing DA.

Keywords: ductus arteriosus; neointima; tunica media; congenital heart disease; transcriptome; neural crest

Citation: Saito, J.; Kojima, T.; Tanifuji, S.; Kato, Y.; Oka, S.; Ichikawa, Y.; Miyagi, E.; Tachibana, T.; Asou, T.; Yokoyama, U. Transcriptome Analysis Reveals Differential Gene Expression between the Closing Ductus Arteriosus and the Patent Ductus Arteriosus in Humans. *J. Cardiovasc. Dev. Dis.* **2021**, *8*, 45. https://doi.org/10.3390/jcdd8040045

Academic Editors: Monique R.M. Jongbloed and Robert Poelmann

Received: 8 March 2021
Accepted: 14 April 2021
Published: 16 April 2021

1. Introduction

The ductus arteriosus (DA) is a fetal vascular shunt that connects the pulmonary artery and the aorta, and it is essential for maintaining fetal circulation. The DA begins to close immediately after birth. This closing process is characterized by several DA-specific features including differentiated contractile smooth muscle cells (SMCs), fragmentation of internal elastic laminae, sparse elastic fiber formation in the tunica media, and intimal thickening (IT) formation [1–6]. Histological analyses of human DA samples and several animal models indicated that these DA-specific features gradually develop throughout the fetal and neonatal periods [7]. Patent DA is a condition where the DA does not close properly after birth. Patent DA occurs in approximately 1 in 2000 full-term infants and occurs more frequently in premature neonates [8]. PDA samples exhibit fewer DA-specific structural features [9]. Comprehensive analysis of gene expression comparing the closing DA and the patent DA is necessary in order to better understand DA-specific remodeling and to explore methods to regulate patency of the DA.

Several research groups have previously reported the gene expression profiles of mouse, rat, and ovine DAs [10–17]. However, transcriptome analyses of human DA tissues are limited [18,19]. Yarboro et al. performed RNA sequencing using human DA tissues of 21 weeks gestation and identified genes that were distinctly expressed in the DA tissue compared to the aorta [18]. Additionally, they compared their human RNA sequencing data with previously reported rodent microarray data and demonstrated transcriptional commonalities between human and rodent DAs [18]. A report by Mueller et al. [19] is presently the only published study that demonstrated the differences of transcriptional profiles using postnatal human DAs. They compared gene expression between stent-implanted open DAs on postnatal days 222 and 239, closed ligamentous DAs on day 147, and an open unstented DA on day 1. To the best of our knowledge, transcriptomic comparisons of the closing DA and the patent DA in human infants have not been previously reported.

Using four postnatal human DA tissues, we performed an unbiased transcriptome analysis using the IT and the tunica media of each DA tissue. We found differential gene expression between the tunica media of the closing DA and that of the patent DA. Additionally, we investigated genes enriched in the IT or the tunica media of closing DA tissues to identify genes that potentially contribute to DA-specific remodeling.

2. Materials and Methods

2.1. Study Subjects and Ethics Statements

The protocol for using human DA tissues was approved by the Research Ethics Committees at Tokyo Medical University and Kanagawa Children's Medical Center (reference numbers: T2020-0238 and 1502-05, respectively). The protocol conformed to the principles outlined in the Declaration of Helsinki. After receiving written informed parental consent, human DA tissues were obtained from four patients with congenital heart diseases, during cardiac surgeries in Kanagawa Children's Medical Center. The patient information for each of the four cases included in this study is summarized in Table 1.

Table 1. A summary of the patient profiles for the four cases included in this study.

Case Number	Diagnosis	Gestational Age (Weeks)	Birth Weight (g)	Age at Operation (Days)	Duration of PGE_1 Administration (Days)	Closing Tendency of the DA
1	Polysplenia, intermediate AVSD, CoA, TAPVC (cardiac type), PDA, IVC interruption (azygos connection)	38	2714	17	0	No
2	DORV (subpulmonary VSD), hypoplastic distal arch, CoA, PFO	41	2948	5	5	Yes
3	HLHS, TR, cor triatriatum, PLSVC	40	3352	24	24	Yes
4	HLHS (MA, AA), PLSVC	37	2654	98	98	Yes

Abbreviations: PGE_1, prostaglandin E1; DA, ductus arteriosus; AVSD, atrioventricular septal defect; CoA, coarctation of the aorta; TAPVC, total anomalous pulmonary venous connection; PDA, patent ductus arteriosus; IVC, inferior vena cava; DORV, double outlet right ventricle; VSD, ventricular septal defect; PFO, patent foramen ovale; HLHS, hypoplastic left heart syndrome; TR, tricuspid regurgitation; PLSVC, persistent left superior vena cava; MA, mitral atresia; AA, aortic atresia.

2.2. Total RNA Preparation and Microarray Analysis

Four human DA tissues were subjected to tissue staining and transcriptome analysis. Each DA tissue was divided into two pieces. One piece was fixed with 10% buffered formalin (FUJIFILM Wako Pure Chemical Corporation, Osaka, Japan) for tissue staining. The other piece of tissue was prepared for microarray analysis as follows. After the

adventitia was removed, each DA tissue was divided into two parts: the inner part and the outer part, which mainly contained IT and the tunica media, respectively, as indicated by the yellow dotted lines in Figure 1A. The tissues were immediately frozen in liquid nitrogen and stored at −80 °C until all patient samples were collected. Total RNA preparation and microarray analysis were performed as described previously [10,11]. Briefly, the frozen tissues were disrupted by a multi-bead shocker instrument (Yasui Kikai, Osaka, Japan). After buffer RLT with β-mercaptoethanol was added to the tissues, they were sonicated to ensure the samples were uniformly homogeneous. Total RNA was isolated using a RNeasy Mini Kit (Qiagen, Venlo, The Netherlands). Microarray experiments were carried out using a SurePrint G3 Human GE 8 × 60 K v2 Microarray (Agilent, Santa Clara, CA, USA) according to the manufacturer's protocol.

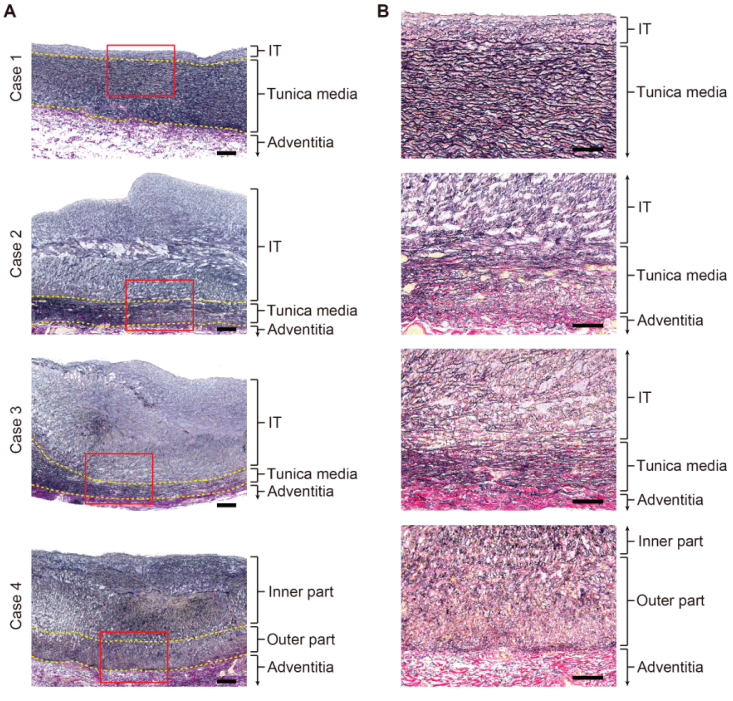

Figure 1. Histological analysis of the human ductus arteriosus (DA) tissues. (**A**) Lower magnification images of the Elastica van Gieson stain of the human DA tissues. The yellow dotted lines indicate the border between the intimal thickening (IT) and the tunica media and the border between the tunica media and the adventitia. Scale bars: 200 μm. (**B**) Magnified images of red boxes in (**A**). Scale bars: 100 μm.

2.3. Generation of a Dendrogram, Venn Diagrams, and a Heatmap

The dendrogram was generated with Ward's method using the hclust and dendrogram functions in R. The packages gplots and genefilter in R were used to create a heatmap in which data was normalized into a *z*-score. The mapping grids were subsequently colored according to their *z*-score. Venn diagrams of the number of differentially expressed genes in each sample group were generated using the gplots package in R.

2.4. Gene Set Enrichment Analyses (GSEAs)

Gene set enrichment analyses (GSEAs) were conducted to investigate the functions of genes that significantly correlated with each sample group. GSEAs ranked the gene list by the correlation between genes and phenotype, and an enrichment score was calculated to as-

sess the gene distribution. Each analysis was carried out with 1000 permutations. Gene sets were considered significantly enriched if the false discovery rate (FDR) q-value < 0.25 [20].

2.5. Tissue Staining and Immunohistochemistry

Paraffin-embedded blocks containing the human DA tissues were cut into 4 μm thick sections and placed on glass slides. Elastica van Gieson staining was performed for morphological analysis to evaluate IT and the tunica media, as described previously [21,22]. Immunohistochemistry was performed using primary antibodies for jagged 1 (sc-390177, Santa Cruz Biotechnology, Dallas, TX, USA) and calponin (M3556, DakoCytomation, Glostrup, Denmark). Biotinylated rabbit antibody (Vectastain Elite ABC IgG kit, Vector Labs, Burlingame, CA, USA) was used as a secondary antibody, and the presence of targeted proteins was determined by 3,3′-diaminobenzidine tetrahydrochloride (DAB) (DakoCytomation, Glostrup, Denmark). Negative staining of immunohistochemistry was confirmed by the omission of primary antibodies.

3. Results

3.1. DA-Related Clinical Course of Each Participant

Four patients with congenital heart diseases were analyzed in this study. Patient profiles are presented in Table 1. Case 1 was considered a patent DA case because the DA did not exhibit closing tendency throughout the clinical course. The DA tissue was isolated during an operation for an atrioventricular septal defect closure and repairs of the aortic arch and pulmonary venous returns. The other three cases (Cases 2–4) exhibited complex congenital heart diseases that required DA patency to maintain systemic circulation. Cases 2–4 were administered prostaglandin E1 (PGE_1) because they exhibited closing tendency of the DA.

In Case 2, lipo-PGE_1 (1 ng/kg/min) was administered 8 h after birth when an echocardiography indicated narrowing of the DA. Case 2 continued lipo-PGE_1 treatment until the operation. The patient had an aortic repair and pulmonary artery banding (PAB) conducted on postnatal day 5.

Case 3 showed closing tendency of the DA soon after birth and was administrated lipo-PGE_1 (2 ng/kg/min). The dose of lipo-PGE_1 was increased (4 ng/kg/min) 8 h after birth due to further closing tendency. The patient had PAB conducted on postnatal day 3. The closing tendency of the DA remained and required PGE_1-cyclodextrin (30 ng/kg/min) on postnatal day 4. The patient received PGE_1-cyclodextrin until the Norwood operation was conducted on postnatal day 24.

Case 4 showed closing tendency of the DA at 9 h after birth and received a lipo-PGE_1 infusion (1 ng/kg/min). The patient underwent PAB on postnatal day 3. The DA was gradually narrowed and required an increased dose of lipo-PGE_1 (5 ng/kg/min) on postnatal day 70. The patient underwent the Norwood operation on postnatal day 98. On the basis of their clinical courses, Cases 2–4 were considered as closing DAs.

3.2. Histological Differences between the Patent DA and the Closing DA Tissues

The Elastica van Gieson stain demonstrated that Case 1 had well-organized layered elastic fibers in the tunica media and a poorly formed IT (Figure 1A, upper panel). In Case 1, there was no overt fragmentation of the internal elastic laminae (Figure 1B, upper panel). Case 2 and Case 3 showed prominent IT formation that protruded into the lumen (Figure 1A, middle panels). Circumferentially oriented layered elastic fibers in the tunica media were sparsely formed and the internal elastic laminae were highly fragmented (Figure 1B, middle panels). Similarly, Case 4, who received PGE_1 administration for more than 3 months, had a prominent IT (Figure 1A, lower panel). However, the entire tunica media consisted of sparse elastic fibers radially oriented toward the internal lumen, and circumferentially oriented elastic fibers were not recognized (Figure 1B, lower panel). These findings indicated that the closing DA had well-recognized, DA-specific morphological features, including prominent IT formation, fragmented internal elastic laminae, and

less elastic fibers in the tunica media, which seemed to reflect a normal closing process. On the other hand, the patent DA tissue (Case 1) was devoid of these structures and exhibited aortification of the vascular wall, which was consistent with previously reported morphological characteristics of the patent DA [9].

3.3. Microarray Analysis of the IT and the Tunica Media of Human DA Tissues

To elucidate a differential gene expression profile between the patent DA (Case 1) and the closing DA tissues (Cases 2–4), we performed an unbiased transcriptomic analysis using these human DA tissues. Each DA sample was divided into the IT and the tunica media in Cases 1–3. In Case 4, circumferentially oriented SMCs and layered elastic laminae could not be identified; therefore, the IT-like wall was divided into the inner part and the outer part (Figure 1A, lower). These samples were subjected to microarray analysis.

The dendrogram demonstrated that the human DA tissues were clearly divided into two major clusters, A and B (Figure 2). Cluster A consisted of both the IT and the tunica media from Case 1. Cluster B consisted of the samples from Cases 2–4, and this cluster was further divided into two subgroups, B1 and B2. Cluster B1 consisted of the IT tissues from Cases 2 and 3 and both the inner and outer IT-like parts from Case 4. Cluster B2 consisted of the tunica media samples from Cases 2 and 3. These data suggested that the patent DA tissue (Case 1) had a distinct gene expression pattern compared to the other closing DA samples (Cases 2–4). In Cases 2 and 3, the gene expression patterns of the tunica media samples were relatively similar. Additionally, the IT samples showed similar gene expression profiles, which were distant from the tunica media samples of Cases 2 and 3. In agreement with histological analysis showing that two parts of the DA tissue from Case 4 (inner and outer parts) exhibited an IT-like structure, these two samples of Case 4 showed similar gene patterns, which were close to that of the IT of Cases 2 and 3.

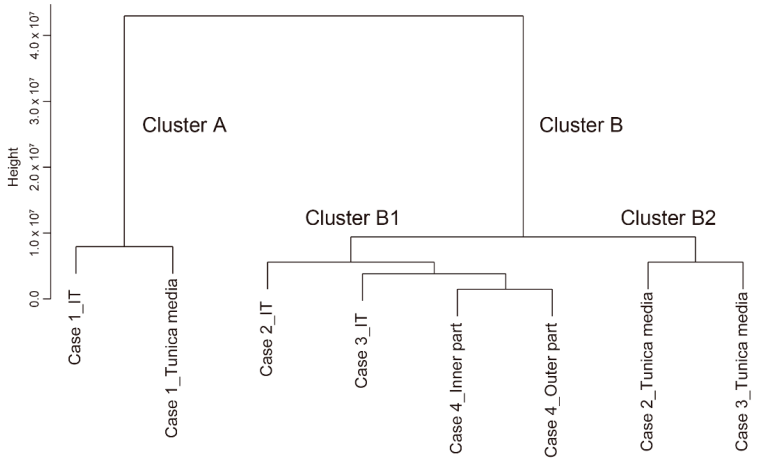

Figure 2. A dendrogram of the gene expressions from human ductus arteriosus tissues. IT: intimal thickening.

3.4. Transcriptomic Differences between the Tunica Media of Closing DA Tissues and the Patent DA Tissue

Both the histological assessment and the cluster analysis of DA tissues demonstrated that the gene expression profile of the tunica media of the patent DA tissue (Case 1) was markedly different from that of the closing DA tissues (Cases 2 and 3). We, thus, compared gene expressions between the tunica media of the patent DA and closing DA tissues.

The GSEAs between the tunica media of the closing DA and the patent DA tissues, using all gene sets related to biological processes in the Gene Ontology (GO) (size > 300), revealed that the closing DA tissues were significantly correlated to 87 biological processes

(FDR < 0.25, Table 2). Notably, vascular development-related gene sets (GO_REGULATION_OF_VASCULATURE_DEVELOPMENT and GO_BLOOD_VESSEL_ MORPHOGENESIS) were highly enriched in the tunica media of closing DA tissues (Figure 3). Kinase activation-related gene sets (GO_REGULATION_OF_MAP_KINASE_ ACTIVITY, GO_ACTIVATION_OF_PROTEIN_KINASE_ACTIVITY, and GO_POSITIVE_ REGULATION_OF_PROTEIN_SERINE_THREONINE_KINASE_ACTIVITY) and three catabolic process-related gene sets, including GO_REGULATION_OF_PROTEIN_CATABOLIC_PROCESS, were positively correlated with the closing DA tunica media tissue. This suggested that intracellular signaling was more actively regulated in the closing DA tissues compared to the patent DA tissue. Protein secretion-related gene sets (GO_POSITIVE_REGULATION_OF_SECRETION and GO_GOLGI_VESICLE_TRANSPORT) and adhesion-related gene sets (GO_POSITIVE_ REGULATION_OF_CELL_ADHESION, GO_REGULATION_OF_CELL_CELL_ADHESION, and GO_CELL_SUBSTRATE_ ADHESION) were also enriched in the closing DA tissues, which support previous reports which found that multiple extracellular matrices and cell–matrix interactions play roles in DA-specific physiological remodeling [5,21,22]. The gene set GO_RESPONSE_TO_OXYGEN_ LEVELS was positively correlated to the closing DA tissues (Figure 3). In this gene set, *EGR1*, which was previously shown to increase immediately after birth in rat DA tissues [10], was upregulated in the tunica media of the closing DA tissues. Enrichment of the gene set GO_ACTIN_FILAMENT_ORGANIZATION in the closing DA tissues (Figure 3) contained the Rho GTPase *RHOD*, which regulates directed cell migration [23]. This may support the migratory feature of SMCs in the closing DA tissue.

Table 2. Gene Ontology biological process terms (size > 300) that were significantly upregulated (FDR < 0.25) in the tunica media of the closing human DA tissues (Cases 2 and 3) compared to that of the patent DA tissue (Case 1).

Gene Set Name	Size	NES	FDR *q*-Value	Rank at Max
GO_REGULATION_OF_VASCULATURE_DEVELOPMENT	310	1.61	0.000	6660
GO_BLOOD_VESSEL_MORPHOGENESIS	564	1.61	0.000	6712
GO_GOLGI_VESICLE_TRANSPORT	350	1.61	0.000	8448
GO_REGULATION_OF_HEMOPOIESIS	441	1.60	0.000	6338
GO_NCRNA_PROCESSING	340	1.59	0.000	5889
GO_VIRAL_LIFE_CYCLE	315	1.58	0.000	7537
GO_REGULATION_OF_MAP_KINASE_ACTIVITY	332	1.55	0.000	6500
GO_LEUKOCYTE_CELL_CELL_ADHESION	339	1.54	0.000	5082
GO_NEGATIVE_REGULATION_OF_IMMUNE_SYSTEM_PROCESS	405	1.54	0.000	4982
GO_NEGATIVE_REGULATION_OF_PHOSPHORYLATION	424	1.53	0.000	5671
GO_POSITIVE_REGULATION_OF_CELL_ADHESION	410	1.53	0.000	4942
GO_NEGATIVE_REGULATION_OF_CELL_CYCLE_PROCESS	312	1.53	0.000	5276
GO_NUCLEAR_TRANSPORT	337	1.52	0.000	7197
GO_T_CELL_ACTIVATION	458	1.51	0.000	5293
GO_IN_UTERO_EMBRYONIC_DEVELOPMENT	372	1.47	0.000	6660
GO_REGULATION_OF_INFLAMMATORY_RESPONSE	348	1.47	0.000	5237
GO_PEPTIDYL_LYSINE_MODIFICATION	353	1.46	0.000	8228
GO_REGULATION_OF_PROTEIN_CATABOLIC_PROCESS	372	1.45	0.000	6333
GO_IMMUNE_RESPONSE_REGULATING_SIGNALING_PATHWAY	385	1.40	0.000	7472
GO_CELLULAR_RESPONSE_TO_EXTERNAL_STIMULUS	305	1.40	0.000	7120
GO_REGULATION_OF_CELL_CELL_ADHESION	406	1.39	0.000	5082
GO_RNA_SPLICING	423	1.39	0.000	7328
GO_ACTIVATION_OF_PROTEIN_KINASE_ACTIVITY	321	1.39	0.000	5553

Table 2. *Cont.*

Gene Set Name	Size	NES	FDR *q*-Value	Rank at Max
GO_REGULATION_OF_CELLULAR_RESPONSE_TO_STRESS	690	1.39	0.000	6338
GO_RAS_PROTEIN_SIGNAL_TRANSDUCTION	330	1.39	0.000	7040
GO_POSITIVE_REGULATION_OF_PROTEIN_SERINE_THREONINE_KINASE_ACTIVITY	329	1.38	0.000	6543
GO_AMEBOIDAL_TYPE_CELL_MIGRATION	386	1.38	0.000	7624
GO_REGULATION_OF_DNA_BINDING_TRANSCRIPTION_FACTOR_ACTIVITY	415	1.37	0.000	6196
GO_REGULATION_OF_LYMPHOCYTE_ACTIVATION	420	1.35	0.000	5268
GO_RNA_SPLICING_VIA_TRANSESTERIFICATION_REACTIONS	341	1.35	0.000	7328
GO_REGULATION_OF_T_CELL_ACTIVATION	316	1.35	0.000	5256
GO_LYMPHOCYTE_DIFFERENTIATION	354	1.34	0.000	5436
GO_ORGANELLE_FISSION	414	1.34	0.000	4640
GO_POSITIVE_REGULATION_OF_CATABOLIC_PROCESS	430	1.34	0.000	4648
GO_EPITHELIAL_CELL_PROLIFERATION	379	1.33	0.011	6543
GO_REGULATION_OF_PROTEIN_SERINE_THREONINE_KINASE_ACTIVITY	495	1.33	0.010	6256
GO_MRNA_PROCESSING	477	1.33	0.010	7113
GO_EMBRYO_DEVELOPMENT_ENDING_IN_BIRTH_OR_EGG_HATCHING	644	1.32	0.010	6259
GO_NEGATIVE_REGULATION_OF_INTRACELLULAR_SIGNAL_TRANSDUCTION	475	1.32	0.009	7981
GO_PROTEIN_POLYUBIQUITINATION	327	1.31	0.014	6212
GO_RIBONUCLEOPROTEIN_COMPLEX_BIOGENESIS	405	1.31	0.013	6510
GO_MAINTENANCE_OF_LOCATION	305	1.31	0.013	5837
GO_LEUKOCYTE_DIFFERENTIATION	514	1.31	0.013	7110
GO_POSITIVE_REGULATION_OF_CELL_CYCLE	357	1.31	0.013	5009
GO_POSTTRANSCRIPTIONAL_REGULATION_OF_GENE_EXPRESSION	554	1.29	0.012	6212
GO_RESPONSE_TO_OXYGEN_LEVELS	370	1.29	0.012	6459
GO_POSITIVE_REGULATION_OF_ESTABLISHMENT_OF_PROTEIN_LOCALIZATION	371	1.28	0.012	6982
GO_REGULATION_OF_METAL_ION_TRANSPORT	363	1.28	0.012	4661
GO_PROTEASOMAL_PROTEIN_CATABOLIC_PROCESS	455	1.28	0.011	5596
GO_NEGATIVE_REGULATION_OF_PHOSPHORUS_METABOLIC_PROCESS	530	1.26	0.011	5671
GO_POSITIVE_REGULATION_OF_GTPASE_ACTIVITY	375	1.26	0.011	7037
GO_REGULATION_OF_GTPASE_ACTIVITY	447	1.26	0.011	7095
GO_POSITIVE_REGULATION_OF_RESPONSE_TO_EXTERNAL_STIMULUS	496	1.25	0.010	6529
GO_COVALENT_CHROMATIN_MODIFICATION	436	1.25	0.010	6473
GO_NEURON_DEATH	338	1.25	0.010	7040
GO_POSITIVE_REGULATION_OF_PROTEOLYSIS	340	1.24	0.010	6359
GO_POSITIVE_REGULATION_OF_CELLULAR_PROTEIN_LOCALIZATION	307	1.24	0.010	6982
GO_POSITIVE_REGULATION_OF_CYTOKINE_PRODUCTION	432	1.24	0.010	5082
GO_PROCESS_UTILIZING_AUTOPHAGIC_MECHANISM	495	1.23	0.009	5327
GO_VESICLE_ORGANIZATION	315	1.23	0.009	7253
GO_POSITIVE_REGULATION_OF_CELL_ACTIVATION	324	1.23	0.009	7094
GO_POST_TRANSLATIONAL_PROTEIN_MODIFICATION	352	1.23	0.009	7885
GO_LEUKOCYTE_MIGRATION	428	1.22	0.009	7094
GO_ESTABLISHMENT_OF_ORGANELLE_LOCALIZATION	397	1.22	0.009	6914
GO_CANONICAL_WNT_SIGNALING_PATHWAY	315	1.20	0.009	5210
GO_REGULATION_OF_CELLULAR_AMIDE_METABOLIC_PROCESS	385	1.19	0.008	6376
GO_REGULATION_OF_AUTOPHAGY	327	1.18	0.008	4699
GO_REGULATION_OF_CHROMOSOME_ORGANIZATION	321	1.17	0.014	6695
GO_REGULATION_OF_SMALL_GTPASE_MEDIATED_SIGNAL_TRANSDUCTION	312	1.16	0.024	7040
GO_REPRODUCTIVE_SYSTEM_DEVELOPMENT	428	1.16	0.026	3453
GO_REGULATION_OF_SUPRAMOLECULAR_FIBER_ORGANIZATION	339	1.15	0.028	6891
GO_POSITIVE_REGULATION_OF_DEFENSE_RESPONSE	360	1.14	0.048	5237
GO_POSITIVE_REGULATION_OF_NERVOUS_SYSTEM_DEVELOPMENT	513	1.14	0.047	4697
GO_REGULATION_OF_APOPTOTIC_SIGNALING_PATHWAY	383	1.13	0.047	5796
GO_MYELOID_CELL_DIFFERENTIATION	375	1.12	0.061	6268
GO_RESPONSE_TO_VIRUS	315	1.12	0.060	5563
GO_ACTIN_FILAMENT_ORGANIZATION	400	1.11	0.077	6891
GO_RESPONSE_TO_MOLECULE_OF_BACTERIAL_ORIGIN	326	1.10	0.097	6178

Table 2. *Cont.*

Gene Set Name	Size	NES	FDR *q*-Value	Rank at Max
GO_REGULATION_OF_PROTEIN_CONTAINING_COMPLEX_ASSEMBLY	408	1.10	0.098	6574
GO_OSSIFICATION	378	1.10	0.106	6790
GO_POSITIVE_REGULATION_OF_SECRETION	358	1.09	0.109	6953
GO_EPITHELIAL_TUBE_MORPHOGENESIS	326	1.09	0.126	6477
GO_ACTIVATION_OF_IMMUNE_RESPONSE	433	1.09	0.138	7472
GO_CELL_SUBSTRATE_ADHESION	342	1.08	0.172	8285
GO_REGULATION_OF_BINDING	349	1.08	0.178	6143
GO_REGULATION_OF_DEVELOPMENTAL_GROWTH	324	1.08	0.178	4701
GO_CELLULAR_RESPONSE_TO_CHEMICAL_STRESS	329	1.07	0.229	4800

Abbreviations: NES, normalized enrichment score; FDR, false discovery rate.

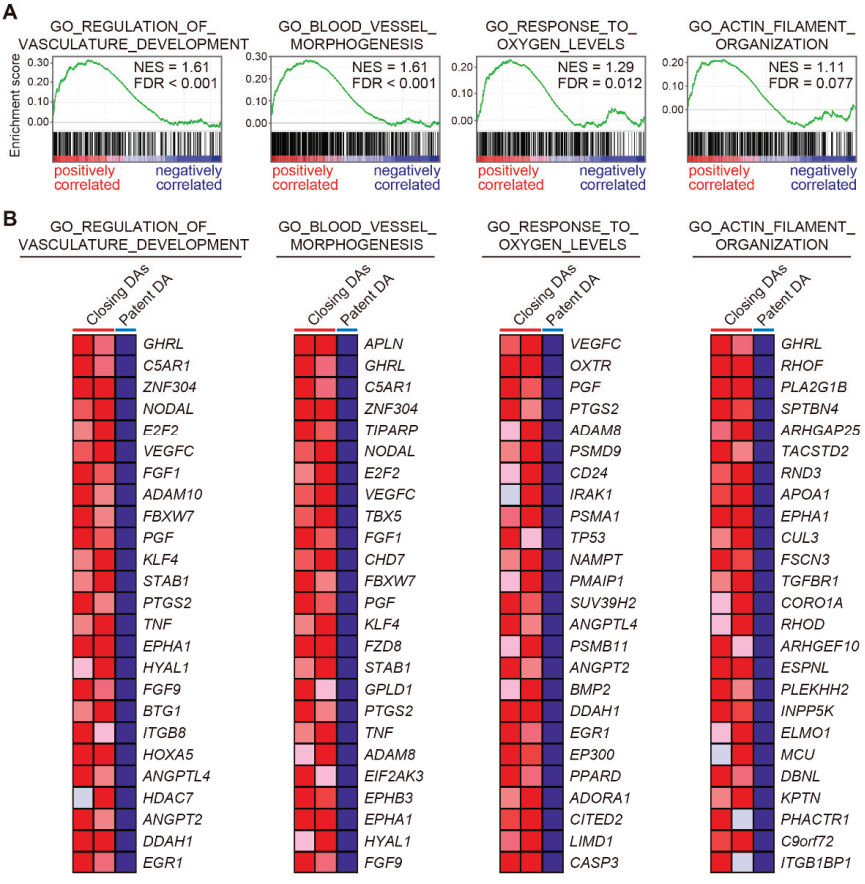

Figure 3. Gene set enrichment analyses (GSEAs) of the tunica media of the closing human ductus arteriosus (DA) and the patent DA tissues. (**A**) GSEAs revealed positive correlations between the tunica media of the closing human DA tissues and vascular development–related genes, oxygen level response-related genes, and actin filament organization-related genes. On the *x*-axis, the genes in each gene set are ranked from the left side (positively correlated) to the right side (negatively correlated). The vertical black lines that look like barcodes indicate each gene in the gene set. The *y*-axis displays the calculated enrichment score of each gene (green color). NES, normalized enrichment score; FDR, false discovery rate. (**B**) The top 25 genes that comprise the leading edge of the enrichment score in (**A**) are shown in each heatmap.

Although we demonstrated several genes that were highly expressed in the tunica media of the closing DAs compared to that of the patent DA (Figure 3, and Tables 2 and 3), postnatal PGE_1 administration possibly affected these gene expressions of the tunica media. To address this issue, we compared gene expressions of the tunica media between shorter-term PGE_1-treated DAs (less than one month of administration, Cases 2 and 3) and a longer-term PGE_1-treated DA (more than three months of administration, Case 4). The GSEAs revealed that the outer part of longer-term PGE_1-treated DA was significantly correlated to eight biological processes related to cell-cycle regulation (FDR < 0.25, Table S1 and Figure S1A,B, Supplementary Materials) compared to the tunica media of shorter-term PGE_1-treated DAs. Among these gene sets, the gene sets GO_ORGANELLE_FISSION and GO_NEGATIVE_REGULATION_OF_CELL_CYCLE_PROCESS belonged to gene sets that were highly expressed in the tunica media of the closing DAs (Table 2). These two gene sets may be associated with PGE_1 administration, but not with specific features of the closing DA. However, the remaining 85 gene sets in Table 2 seemed to be independent of duration of PGE_1 administration.

Table 3. Sixteen genes that overlapped and were enriched (>8-fold) in the tunica media of the closing DA tissues (Cases 2 and 3) compared to that of the patent DA tissue (Case 1).

Gene Name	Description	Fold Change	
		Case 2 vs. Case 1	Case 3 vs. Case 1
CD83	*CD83* molecule	29.9	29.9
AP1S3	adaptor-related protein complex 1 subunit sigma 3	26.5	18.0
GSTT1	glutathione *S*-transferase theta 1	21.6	10.7
BCL2L13	*BCL2*-like 13	12.9	13.1
NEDD9	neural precursor cell expressed, developmentally downregulated 9	12.1	13.6
HLA-DMA	major histocompatibility complex, class II, DM alpha	9.1	16.3
GHRL	ghrelin and obestatin prepropeptide	13.1	12.2
FLCN	folliculin	12.2	9.1
TCF7	transcription factor 7, T-cell-specific	11.0	9.0
ELOVL5	*ELOVL* fatty-acid elongase 5	9.0	9.9
APLN	apelin	9.2	9.6
MAFF	*MAF* bZIP transcription factor F	9.5	8.8
AURKAPS1	aurora kinase A pseudogene 1	9.7	8.4
MIS12	*MIS12* kinetochore complex component	9.5	8.3
CEMIP2	cell migration inducing hyaluronidase 2	8.4	9.1
GMCL1	germ cell-less 1, spermatogenesis associated	8.5	8.5

3.5. Vascular Development-Related Genes in Human DA Tissues

The vascular development-related gene sets noted above (Table 2 and Figure 3) contain cardiovascular cell lineage-related genes. A heatmap composed of cardiovascular cell lineage-related genes demonstrated distinct gene expression patterns between the closing DA tissues (Cases 2 and 3) and the patent DA tissue (Case 1) (Figure 4A). The genes *SEMA5A*, *SFRP1*, *NRG1*, *CTNNB1*, *PHACTR4*, and *JAG1* were highly expressed in the ITs of the closing DA tissues. Among these genes, the expression of *PHACTR4* and *JAG1*, which are cardiac neural crest-related genes, was greater in the tunica media of the closing DA tissues than the patent DA tissue. The expression levels of *CFL1*, *TWIST1*, *EDNRB*, *SMO*, and *MAPK1* were greater in the tunica media of the patent DA tissue compared to the closing DA tissues. Similarly, expressions of *SEMA4F*, *NRP1*, *LTBP3*, *EDN3*, and *FGF8* were enriched in the tunica media of the patent DA tissue. *SEMA3G*, *ALX1*, *SOX8*, *ALDH1A2*, and *SEMA7A* were relatively highly expressed in the entire tissue of the patent DA. *WNT8A*, *KLHL12*, *FBXL17*, and *ISL1*, which is a second heart field-related gene, were relatively enriched in the patent DA tissue, and the expression levels of these genes were higher in the IT than in the tunica media.

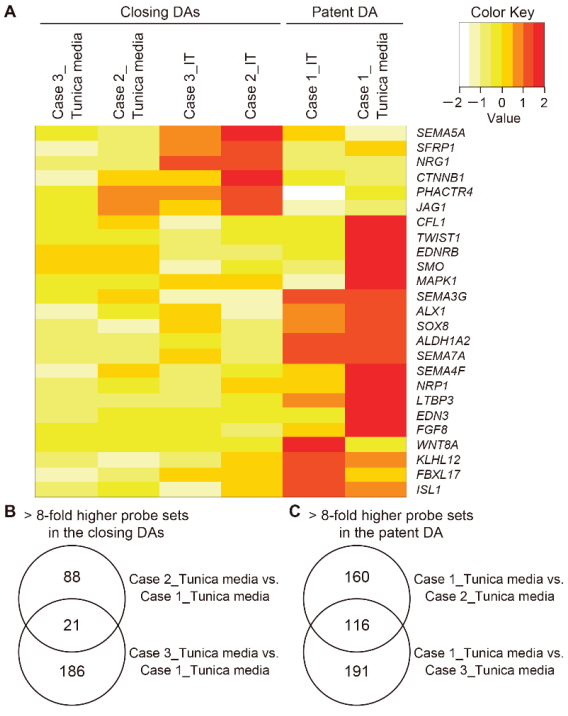

Figure 4. Differential gene expression between the tunica media of the closing human ductus arteriosus (DA) tissues and that of the patent DA tissue. (**A**) A heatmap of vascular cell lineage-related genes is depicted. (**B**) A Venn diagram shows the number of probe sets that were highly expressed (>8-fold) in the tunica media of closing DA tissues (Cases 2 and 3) compared to that of the patent DA tissue (Case 1). (**C**) A Venn diagram shows the number of probe sets highly expressed (>8-fold) in the tunica media of the patent DA tissue (Case 1) compared to that of the closing DA tissues (Cases 2 and 3). IT, intimal thickening.

3.6. The Closing or Patent DA Tissue-Specific Gene Expression

Figure 4B presents a Venn diagram that shows probe sets that were upregulated (>8-fold) in the tunica media of the closing DA tissues (Cases 2 and 3) compared to the patent DA tissue (Case 1). Twenty-one overlapped probe sets consisted of 16 genes (Table 3). *APLN*, *CEMIP2*, and *GHRL* are related to vascular development [24–26]. There were several genes related to adhesion and protein secretion such as *APLN*, *CD83*, *FLCN*, and *NEDD9* [27–30]. *GHRL* and *NEDD9* were reported to regulate actin filament organization [31,32]. *APLN* was reported to promote proliferation and migration of vascular SMCs, as well as promote SMC contraction [27]. *NEDD9* is involved in embryonic neural crest cell development and promotes cell migration, cell adhesion, and actin fiber formation [31]. To examine the effect of PGE_1 administration on the human DAs, we compared gene expressions of the tunica media between shorter-term PGE_1-treated DAs (Cases 2 and 3) and a longer-term PGE_1-treated DA (Case 4) using a Venn diagram (Figure S1C, Supplementary Materials). We identified 20 probe sets that overlapped and were enriched in the outer part of a longer-term PGE_1-treated DA compared to the IT of shorter-term PGE_1-treated DAs (Table S2, Supplementary Materials). These genes did not belong to the genes in Table 3, suggesting that the genes presented in Table 3 did not seem to have been strongly influenced by PGE_1 administration.

In the Venn diagram in Figure 4C, 116 probe sets are presented, which were upregulated (>8-fold) in the tunica media of the patent DA tissue (Case 1) compared to the

closing DA tissues (Cases 2 and 3). These probe sets contained 52 genes (Table 4). Latent transforming growth factor beta-binding protein 3 (*LTBP3*) was upregulated in the tunica media of the patent DA tissue. *LTBP3* is related to extracellular matrix constituents [33] and second heart field-derived vascular SMCs [34]. Expression of *PRSS55*, identified as an aorta-dominant gene in rodent microarray data [11], was elevated in the patent DA tissue.

Table 4. Fifty-two genes that overlapped and were enriched (>8-fold) in the tunica media of the patent DA tissue (Case 1) compared to that of the closing DA tissues (Cases 2 and 3).

Gene Name	Description	Fold Change	
		Case 1 vs. Case 2	Case 1 vs. Case 3
MYH16	myosin heavy chain 16 pseudogene	70.1	68.9
PRDM12	PR/SET domain 12	69.8	68.5
CXXC4	*CXXC* finger protein 4	62.8	61.5
VENTXP1	*VENT* homeobox pseudogene 1	60.4	57.3
MKRN3	makorin ring finger protein 3	70.9	43.7
CLEC3A	C-type lectin domain family 3 member A	26.1	251.3
TEX43	testis expressed 43	51.3	26.7
SCN11A	sodium channel, voltage-gated, type XI, alpha subunit 11	38.0	26.5
CYP3A43	cytochrome P450 family 3 subfamily A member 43	24.5	22.3
MROH2A	maestro heat-like repeat family member 2A	21.1	21.4
MUC12	mucin 12, cell-surface-associated	30.5	15.3
MS4A6A	membrane-spanning 4-domains subfamily A member 6A	46.8	11.7
RBFOX3	RNA-binding fox-1 homolog 3	15.5	20.4
SLC2A1	solute carrier family 2 member 1	30.4	10.7
CFAP299	cilia- and flagella-associated protein 299	15.4	15.8
PSG5	pregnancy-specific beta-1-glycoprotein 5	16.3	14.6
LTBP3	latent transforming growth factor beta-binding protein 3	13.7	16.9
ZFP57	zinc finger protein 57	21.8	11.0
MFSD4	major facilitator superfamily domain-containing 4A	13.8	13.8
HOXA11	homeobox A11	10.2	19.1
ALLC	allantoicase	24.8	8.8
SLC6A14	solute carrier family 6 member 14	13.1	12.1
SLC44A4	solute carrier family 44 member 4	12.7	11.7
MAS1	*MAS1* proto-oncogene, G-protein-coupled receptor	12.2	12.2
CARD18	caspase recruitment domain family member 18	12.9	11.5
LCE1C	late cornified envelope protein 1C	12.2	10.6
PAMR1	peptidase domain-containing associated with muscle regeneration 1	8.1	18.7
PRSS55	serine protease 55	11.4	10.5
RUNDC3B	*RUN* domain-containing 3B	10.0	11.8
LINC00114	long intergenic non-protein-coding RNA 114	8.9	13.8
TFAP4	transcription factor AP-4	11.2	10.1
PLIN2	perilipin 2	9.8	11.1
CCR2	C–C motif chemokine receptor 2	11.7	9.3
CDKN2B-AS	*CDKN2B* antisense RNA 1	10.0	9.8
MYO7A	myosin VIIA	10.4	9.3
PDILT	protein disulfide isomerase like, testis expressed	9.6	9.6
SPA17	sperm autoantigenic protein 17	10.8	8.5
SLITRK2	*SLIT* and *NTRK*-like family member 2	9.5	9.5
SLC9B1	solute carrier family 9 member B1	9.3	9.7
PANX2	pannexin 2	11.4	8.0
PLPPR1	phospholipid phosphatase-related 1	10.1	8.8
ASTE1	asteroid homolog 1	9.2	9.4
MUC16	mucin 16, cell-surface-associated	9.5	8.7
OR51B2	olfactory receptor family 51 subfamily B member 2	9.2	8.6
ARHGAP36	Rho GTPase-activating protein 36	8.8	8.7
KRTAP4-8	keratin-associated protein 4-8	8.8	8.5
METTL21CP1	methyltransferase-like 21E, pseudogene	9.1	8.3
BPIFB6	BPI fold-containing family B member 6	8.9	8.4
HABP2	hyaluronan-binding protein 2	9.0	8.2
DUSP13	dual-specificity phosphatase 13	8.9	8.2
CXorf51A	chromosome X open reading frame 51A	8.2	8.0
MTM1	myotubularin 1	8.2	8.1

3.7. Jagged 1 Was Highly Expressed in the Closing DA Tissues

Previous reports using genetically modified mice clearly demonstrated that SMCs of the DA are derived from cardiac neural crest cells, and these cells contribute to SMC differentiation in the DA [35,36]. Since the transcriptome analysis revealed that the neural crest cell-related gene *JAG1* was abundantly expressed in the closing DA tissues compared to the patent DA tissue (Figure 4A), we performed immunohistochemistry to examine protein expression of jagged 1. In agreement with the transcriptome data, jagged 1 was highly expressed in the closing DA tissues (Cases 2–4) (Figure 5A). Calponin is well recognized as a differentiated SMC marker [1], and it was decreased in the DA tissues of *Jag1*-deficient mice [37]. A strong immunoreaction for calponin was observed in the closing DA tissues but was not as strong in the patent DA tissue (Figure 5B).

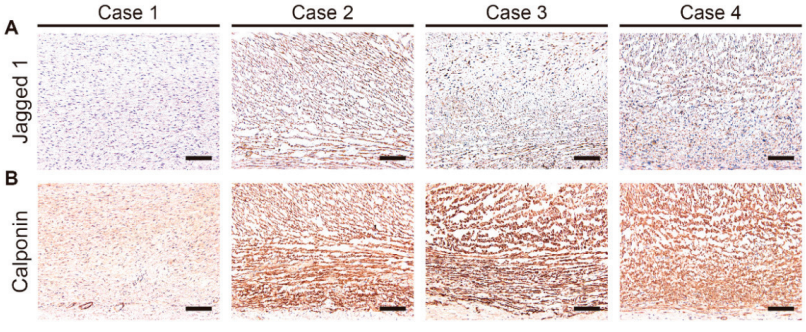

Figure 5. Immunohistochemistry for jagged 1 (**A**) and calponin (**B**) in the human ductus arteriosus tissues from Cases 1–4. A brown color indicates positive immunostaining. Scale bars: 100 μm.

3.8. Transcriptomic Characteristics of the IT and the Tunica Media in the Closing DA Tissues

Lastly, we investigated the difference in gene expression between the IT and the tunica media in the closing DA tissues. IT formation is partly attributed to migration and proliferation of the tunica media-derived SMCs [2–5,7]. Gene expression analysis indicated that there were different transcriptomic characteristics between the IT and the tunica media in the closing DA tissues (Clusters B1 and B2 in Figure 2). We, thus, compared the expression of genes between the IT and the tunica media of the closing DA tissues (Cases 2 and 3).

The GSEAs between the IT and the tunica media, using all gene sets which related to biological processes in the Gene Ontology (GO) (size > 300), were performed. The analyses revealed that the IT was significantly correlated to 89 biological processes (FDR < 0.25, Table 5), and that the tunica media correlated to 81 biological processes (FDR < 0.25, Table 6). The IT of the closing DAs was significantly correlated to more than 10 migration- and proliferation-related gene sets (GO_MICROTUBULE_CYTOSKELETON_ORGANIZATION and GO_CELL_DIVISION, etc.) (Figure 6A,B). Wnt signaling-related gene sets (GO_ REGULATION_OF_WNT_SIGNALING_PATHWAY, GO_CANONICAL_WNT_SIGNALING_PATHWAY, and GO_CELL_CELL_SIGNALING_BY_WNT) were also enriched in the IT of the closing DA tissues. The tunica media of the closing DAs was significantly correlated to vascular development-related gene sets (GO_REGULATION_OF VASCULATURE_DEVELOPMENT, GO_BLOOD_VESSEL_MORPHOGENESIS, GO_VASCULAR_DEVELOPMENT, and GO_CIRCULATORY_SYSTEM_DEVELOPMENT) (Figure 6C,D). Five adhesion-related gene sets, including GO_BIOLOGICAL_ADHESION, were enriched in the tunica media compared to the IT in the closing DA tissues.

Table 5. Gene Ontology biological process terms (size > 300) that were significantly upregulated (FDR < 0.25) in the intimal thickening compared to the tunica media of the closing DA tissues (Cases 2 and 3).

Gene Set Name	Size	NES	FDR *q*-Value	Rank at Max
GO_MICROTUBULE_CYTOSKELETON_ORGANIZATION	526	1.67	0.000	6797
GO_MICROTUBULE_BASED_PROCESS	757	1.59	0.000	6797
GO_CELL_DIVISION	549	1.58	0.000	6799
GO_PROTEIN_POLYUBIQUITINATION	327	1.56	0.000	7778
GO_MITOTIC_CELL_CYCLE	954	1.54	0.000	6055
GO_MODIFICATION_DEPENDENT_MACROMOLECULE_CATABOLIC_PROCESS	604	1.51	0.000	6933
GO_NEGATIVE_REGULATION_OF_CELL_CYCLE	566	1.51	0.000	6548
GO_NEGATIVE_REGULATION_OF_CELL_CYCLE_PROCESS	312	1.50	0.001	6055
GO_MRNA_PROCESSING	477	1.50	0.001	6995
GO_RNA_SPLICING_VIA_TRANSESTERIFICATION_REACTIONS	341	1.48	0.001	6758
GO_ESTABLISHMENT_OF_ORGANELLE_LOCALIZATION	397	1.47	0.001	6823
GO_REGULATION_OF_MRNA_METABOLIC_PROCESS	326	1.47	0.001	9158
GO_ORGANELLE_LOCALIZATION	602	1.46	0.001	6823
GO_RNA_SPLICING	423	1.45	0.002	6007
GO_CELL_CYCLE	1681	1.44	0.002	6059
GO_ORGANELLE_FISSION	414	1.44	0.002	5836
GO_CELL_CYCLE_PROCESS	1251	1.43	0.002	6470
GO_REGULATION_OF_MITOTIC_CELL_CYCLE	600	1.43	0.002	6548
GO_MUSCLE_TISSUE_DEVELOPMENT	368	1.42	0.003	4069
GO_CELLULAR_PROTEIN_CATABOLIC_PROCESS	733	1.41	0.005	6933
GO_REGULATION_OF_CELL_CYCLE_PROCESS	706	1.41	0.005	6450
GO_CELL_CYCLE_PHASE_TRANSITION	578	1.40	0.005	6055
GO_REGULATION_OF_CELL_CYCLE	1110	1.40	0.004	6548
GO_MICROTUBULE_BASED_MOVEMENT	321	1.37	0.007	5942
GO_PROTEIN_MODIFICATION_BY_SMALL_PROTEIN_CONJUGATION_OR_REMOVAL	1033	1.36	0.008	6585
GO_PROTEIN_CATABOLIC_PROCESS	876	1.36	0.008	7607
GO_PROTEASOMAL_PROTEIN_CATABOLIC_PROCESS	455	1.34	0.011	7536
GO_POST_TRANSLATIONAL_PROTEIN_MODIFICATION	352	1.33	0.013	4520
GO_VESICLE_ORGANIZATION	315	1.33	0.013	6530
GO_PROTEIN_MODIFICATION_BY_SMALL_PROTEIN_CONJUGATION	864	1.32	0.014	7634
GO_PROTEIN_CONTAINING_COMPLEX_DISASSEMBLY	310	1.32	0.014	6434
GO_CHROMOSOME_ORGANIZATION	1059	1.32	0.015	6004
GO_RNA_PROCESSING	1149	1.31	0.016	7021
GO_REGULATION_OF_CHROMOSOME_ORGANIZATION	321	1.29	0.024	7299
GO_REGULATION_OF_CELL_CYCLE_PHASE_TRANSITION	424	1.29	0.024	6055
GO_MRNA_METABOLIC_PROCESS	789	1.28	0.026	7021
GO_REGULATION_OF_INTRACELLULAR_TRANSPORT	325	1.28	0.026	6449
GO_MUSCLE_SYSTEM_PROCESS	423	1.28	0.028	3948
GO_CELLULAR_MACROMOLECULE_CATABOLIC_PROCESS	1100	1.26	0.034	7104
GO_REGULATION_OF_AUTOPHAGY	327	1.25	0.041	6901
GO_CELLULAR_PROTEIN_CONTAINING_COMPLEX_ASSEMBLY	909	1.25	0.041	6799
GO_REGULATION_OF_WNT_SIGNALING_PATHWAY	347	1.25	0.042	3438
GO_RIBONUCLEOPROTEIN_COMPLEX_BIOGENESIS	405	1.24	0.042	8496
GO_PROCESS_UTILIZING_AUTOPHAGIC_MECHANISM	495	1.23	0.049	6585
GO_ANATOMICAL_STRUCTURE_HOMEOSTASIS	426	1.23	0.048	6332
GO_ORGANOPHOSPHATE_BIOSYNTHETIC_PROCESS	526	1.23	0.049	3613
GO_REGULATION_OF_CELLULAR_CATABOLIC_PROCESS	812	1.23	0.051	6913
GO_PROTEIN_CONTAINING_COMPLEX_SUBUNIT_ORGANIZATION	1716	1.23	0.052	5624
GO_REGULATION_OF_SYSTEM_PROCESS	571	1.22	0.057	3069
GO_GLYCEROPHOSPHOLIPID_METABOLIC_PROCESS	325	1.22	0.055	2842
GO_ORGANELLE_ASSEMBLY	780	1.22	0.055	5055
GO_MUSCLE_CONTRACTION	339	1.20	0.070	3948
GO_REGULATION_OF_CELLULAR_LOCALIZATION	939	1.20	0.073	6537
GO_CYTOSKELETON_ORGANIZATION	1278	1.20	0.072	5064
GO_REGULATION_OF_CATABOLIC_PROCESS	960	1.20	0.075	7638
GO_MACROMOLECULE_CATABOLIC_PROCESS	1319	1.19	0.077	7614

Table 5. *Cont.*

Gene Set Name	Size	NES	FDR *q*-Value	Rank at Max
GO_ORGANONITROGEN_COMPOUND_CATABOLIC_PROCESS	1233	1.19	0.080	6337
GO_CANONICAL_WNT_SIGNALING_PATHWAY	315	1.18	0.084	3438
GO_DIVALENT_INORGANIC_CATION_TRANSPORT	443	1.18	0.087	2865
GO_MUSCLE_STRUCTURE_DEVELOPMENT	606	1.18	0.094	4139
GO_POSITIVE_REGULATION_OF_ESTABLISHMENT_OF_PROTEIN_LOCALIZATION	371	1.18	0.092	5436
GO_DNA_METABOLIC_PROCESS	822	1.18	0.091	7381
GO_CELL_CELL_SIGNALING_BY_WNT	488	1.17	0.102	3490
GO_INTRACELLULAR_TRANSPORT	1599	1.16	0.108	6629
GO_MUSCLE_ORGAN_DEVELOPMENT	360	1.16	0.108	4772
GO_REGULATION_OF_PEPTIDE_TRANSPORT	641	1.16	0.109	5020
GO_SECOND_MESSENGER_MEDIATED_SIGNALING	412	1.15	0.125	3308
GO_PEPTIDE_SECRETION	495	1.15	0.125	3880
GO_REGULATION_OF_CYTOSKELETON_ORGANIZATION	513	1.15	0.128	3944
GO_SIGNAL_RELEASE	577	1.14	0.130	3898
GO_DNA_REPAIR	480	1.14	0.132	6578
GO_MUSCLE_CELL_DIFFERENTIATION	338	1.14	0.131	4061
GO_NEGATIVE_REGULATION_OF_PROTEIN_MODIFICATION_PROCESS	565	1.14	0.132	5343
GO_NEGATIVE_REGULATION_OF_PHOSPHORYLATION	424	1.14	0.138	5364
GO_MITOCHONDRION_ORGANIZATION	459	1.14	0.138	7936
GO_NEGATIVE_REGULATION_OF_PHOSPHORUS_METABOLIC_PROCESS	530	1.13	0.144	5394
GO_HORMONE_TRANSPORT	309	1.12	0.165	3880
GO_REGULATION_OF_PROTEIN_CATABOLIC_PROCESS	372	1.12	0.176	7675
GO_REGULATION_OF_PROTEIN_LOCALIZATION	905	1.11	0.184	6577
GO_RIBOSE_PHOSPHATE_METABOLIC_PROCESS	373	1.11	0.183	4526
GO_OSSIFICATION	378	1.11	0.180	5020
GO_REGULATION_OF_DNA_METABOLIC_PROCESS	314	1.11	0.192	7720
GO_NUCLEOBASE_CONTAINING_SMALL_MOLECULE_METABOLIC_PROCESS	545	1.11	0.196	3618
GO_PHOSPHOLIPID_METABOLIC_PROCESS	420	1.10	0.215	5395
GO_REGULATION_OF_ORGANELLE_ORGANIZATION	1209	1.10	0.220	5212
GO_ORGANOPHOSPHATE_METABOLIC_PROCESS	950	1.09	0.238	3618
GO_REGULATION_OF_CELLULAR_RESPONSE_TO_STRESS	690	1.09	0.235	6943
GO_CELLULAR_RESPONSE_TO_DNA_DAMAGE_STIMULUS	761	1.09	0.246	6578
GO_GLYCEROLIPID_METABOLIC_PROCESS	409	1.09	0.246	5591

Abbreviations: NES, normalized enrichment score; FDR, false discovery rate.

Table 6. Gene Ontology biological process terms (size > 300) that were significantly upregulated (FDR < 0.25) in the tunica media compared to the intimal thickening of the closing DA tissues (Cases 2 and 3).

Gene Set Name	Size	NES	FDR *q*-Value	Rank at Max
GO_EXTRACELLULAR_STRUCTURE_ORGANIZATION	376	1.67	0.002	5349
GO_SKELETAL_SYSTEM_DEVELOPMENT	494	1.55	0.012	5310
GO_REGULATION_OF_VASCULATURE_DEVELOPMENT	310	1.49	0.030	7236
GO_EMBRYONIC_ORGAN_DEVELOPMENT	443	1.49	0.023	6270
GO_PATTERN_SPECIFICATION_PROCESS	442	1.48	0.021	6393
GO_INFLAMMATORY_RESPONSE	706	1.45	0.029	7279
GO_TAXIS	612	1.45	0.027	7278
GO_NEGATIVE_REGULATION_OF_CELL_DEVELOPMENT	311	1.44	0.030	6296
GO_BLOOD_VESSEL_MORPHOGENESIS	564	1.43	0.030	7164
GO_NEGATIVE_REGULATION_OF_CELL_DIFFERENTIATION	668	1.42	0.032	6377
GO_POSITIVE_REGULATION_OF_NERVOUS_SYSTEM_DEVELOPMENT	513	1.42	0.036	6270
GO_REGIONALIZATION	347	1.40	0.043	6393
GO_VASCULATURE_DEVELOPMENT	676	1.39	0.050	6711
GO_EMBRYONIC_MORPHOGENESIS	578	1.39	0.050	5668
GO_POSITIVE_REGULATION_OF_CELL_DEVELOPMENT	528	1.38	0.052	5938
GO_REGULATION_OF_NERVOUS_SYSTEM_DEVELOPMENT	888	1.37	0.058	6409
GO_BIOLOGICAL_ADHESION	1379	1.37	0.062	7362

Table 6. *Cont.*

Gene Set Name	Size	NES	FDR *q*-Value	Rank at Max
GO_EPITHELIAL_TUBE_MORPHOGENESIS	326	1.36	0.069	6392
GO_TUBE_MORPHOGENESIS	808	1.35	0.075	6726
GO_REGULATION_OF_NEURON_DIFFERENTIATION	631	1.35	0.073	4480
GO_POSITIVE_REGULATION_OF_DEVELOPMENTAL_PROCESS	1298	1.35	0.071	6726
GO_REGULATION_OF_INFLAMMATORY_RESPONSE	348	1.34	0.074	6671
GO_POSITIVE_REGULATION_OF_CELL_DIFFERENTIATION	939	1.34	0.072	6708
GO_AMEBOIDAL_TYPE_CELL_MIGRATION	386	1.34	0.070	3718
GO_POSITIVE_REGULATION_OF_MULTICELLULAR_ORGANISMAL_PROCESS	1662	1.34	0.067	6427
GO_REGULATION_OF_CELL_ADHESION	682	1.34	0.071	7361
GO_CELL_MORPHOGENESIS_INVOLVED_IN_NEURON_DIFFERENTIATION	585	1.33	0.075	6775
GO_NEGATIVE_REGULATION_OF_DEVELOPMENTAL_PROCESS	905	1.33	0.075	6377
GO_AXON_DEVELOPMENT	512	1.32	0.079	7161
GO_TUBE_DEVELOPMENT	998	1.32	0.080	6726
GO_NEUROGENESIS	1571	1.32	0.079	6708
GO_REGULATION_OF_ANATOMICAL_STRUCTURE_MORPHOGENESIS	1032	1.32	0.079	6334
GO_REGULATION_OF_CELL_DIFFERENTIATION	1729	1.31	0.086	6377
GO_REGULATION_OF_T_CELL_ACTIVATION	316	1.31	0.084	5912
GO_POSITIVE_REGULATION_OF_CELL_ADHESION	410	1.31	0.083	6893
GO_REGULATION_OF_CELL_DEVELOPMENT	904	1.31	0.086	6400
GO_REGULATION_OF_CELL_MORPHOGENESIS	474	1.30	0.102	6663
GO_REGULATION_OF_CELL_CELL_ADHESION	406	1.29	0.105	6811
GO_ANATOMICAL_STRUCTURE_FORMATION_INVOLVED_IN_MORPHOGENESIS	1044	1.29	0.106	7374
GO_EPITHELIAL_CELL_PROLIFERATION	379	1.28	0.119	6725
GO_POSITIVE_REGULATION_OF_NEURON_DIFFERENTIATION	356	1.28	0.120	6270
GO_REGULATION_OF_PEPTIDASE_ACTIVITY	419	1.28	0.118	6411
GO_LEUKOCYTE_CELL_CELL_ADHESION	339	1.28	0.116	6889
GO_CELL_CELL_ADHESION	826	1.28	0.119	7362
GO_CELL_MORPHOGENESIS	996	1.27	0.118	6775
GO_MORPHOGENESIS_OF_AN_EPITHELIUM	539	1.27	0.125	6433
GO_CIRCULATORY_SYSTEM_DEVELOPMENT	1018	1.27	0.127	6433
GO_POSITIVE_REGULATION_OF_HYDROLASE_ACTIVITY	719	1.26	0.132	6562
GO_CELLULAR_PROCESS_INVOLVED_IN_REPRODUCTION_IN_MULTICELLULAR_ORGANISM	330	1.26	0.131	6092
GO_GLAND_DEVELOPMENT	436	1.26	0.143	6386
GO_NEGATIVE_REGULATION_OF_MULTICELLULAR_ORGANISMAL_PROCESS	1145	1.25	0.147	6749
GO_REGULATION_OF_CELLULAR_COMPONENT_SIZE	360	1.25	0.152	3939
GO_SENSORY_ORGAN_DEVELOPMENT	560	1.25	0.155	5533
GO_NEURON_DIFFERENTIATION	1327	1.25	0.155	6400
GO_REPRODUCTIVE_SYSTEM_DEVELOPMENT	428	1.25	0.154	4925
GO_CELL_PART_MORPHOGENESIS	680	1.24	0.155	6775
GO_NEURON_DEVELOPMENT	1080	1.24	0.155	6705
GO_T_CELL_ACTIVATION	458	1.24	0.154	7224
GO_POSITIVE_REGULATION_OF_CELL_PROJECTION_ORGANIZATION	366	1.24	0.169	6270
GO_ANIMAL_ORGAN_MORPHOGENESIS	1048	1.24	0.168	6373
GO_ORGANIC_ANION_TRANSPORT	491	1.22	0.168	6889
GO_CELL_MORPHOGENESIS_INVOLVED_IN_DIFFERENTIATION	728	1.22	0.168	6775
GO_ANION_TRANSMEMBRANE_TRANSPORT	303	1.22	0.191	8857
GO_ALCOHOL_METABOLIC_PROCESS	362	1.22	0.192	7136
GO_G_PROTEIN_COUPLED_RECEPTOR_SIGNALING_PATHWAY	1235	1.22	0.195	9098
GO_EMBRYO_DEVELOPMENT	1018	1.22	0.194	6690
GO_ANION_TRANSPORT	628	1.21	0.204	6889
GO_REGULATION_OF_NEURON_PROJECTION_DEVELOPMENT	486	1.21	0.202	4480
GO_REGULATION_OF_CELL_PROJECTION_ORGANIZATION	652	1.21	0.203	6334
GO_LIPID_CATABOLIC_PROCESS	327	1.21	0.203	6013
GO_UROGENITAL_SYSTEM_DEVELOPMENT	325	1.20	0.233	6411
GO_TISSUE_MORPHOGENESIS	639	1.20	0.233	6433
GO_REGULATION_OF_HEMOPOIESIS	441	1.20	0.236	7164
GO_REGULATION_OF_HYDROLASE_ACTIVITY	1205	1.20	0.236	6564
GO_REGULATION_OF_IMMUNE_SYSTEM_PROCESS	1387	1.20	0.235	7164
GO_LYMPHOCYTE_DIFFERENTIATION	354	1.19	0.243	8193
GO_EPITHELIUM_DEVELOPMENT	1261	1.19	0.240	6313
GO_HEAD_DEVELOPMENT	765	1.19	0.238	7239
GO_ENDOCYTOSIS	541	1.19	0.238	5944
GO_TRANSMEMBRANE_RECEPTOR_PROTEIN_TYROSINE_KINASE_SIGNALING_PATHWAY	695	1.19	0.245	7173
GO_REGULATION_OF_CELL_ACTIVATION	538	1.19	0.247	7342

Abbreviations: NES, normalized enrichment score; FDR, false discovery rate.

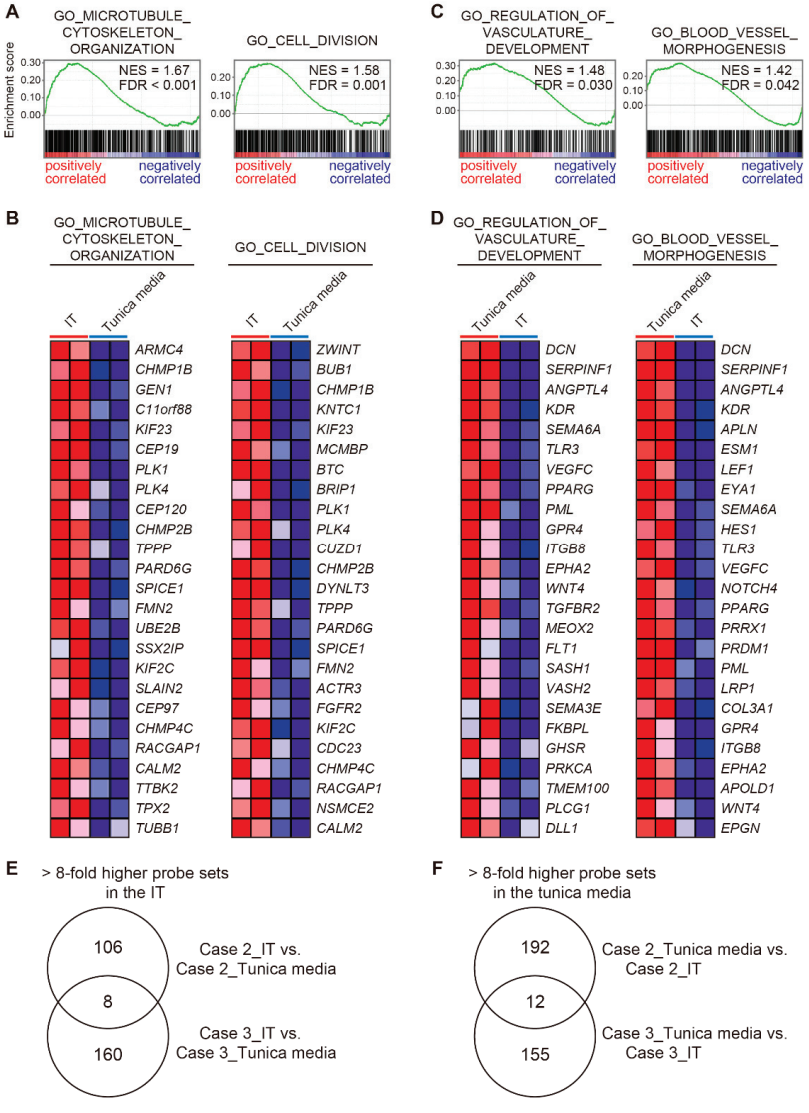

Figure 6. Differential gene expression between the intimal thickening (IT) and the tunica media of the closing human ductus arteriosus (DA) tissues. (**A**) Gene set enrichment analyses (GSEAs) revealed positive correlations between the IT of closing DA tissues and migration- and proliferation–related genes. (**B**) The top 25 genes that comprise the leading edge of the enrichment score in (**A**) are shown as a heatmap. (**C**) GSEAs revealed positive correlations between the tunica media of the closing DA tissues and vascular morphogenesis-related genes. (**D**) The top 25 genes that comprise the leading edge of the enrichment score in (**B**) are shown as a heatmap. (**E**) A Venn diagram shows the number of probe sets that were highly expressed (>8-fold) in the IT compared to the tunica media of closing DA tissues (Cases 2 and 3). (**F**) A Venn diagram shows the numbers of probe sets that were highly expressed (>8-fold) in the tunica media compared to the IT of closing DA tissues (Cases 2 and 3). NES, normalized enrichment score; FDR, false discovery rate.

Figure 6E presents a Venn diagram that shows probe sets that were upregulated (>8-fold) in the IT of closing DA tissues compared to the tunica media of the same DA tissues (Cases 2 and 3). Eight overlapped probe sets consisted of eight genes (Figure 6E and Table 7). *POU4F1*, *FGF1*, and *PROCR* are related to cell division and cell cycle [38–40]. *FGF1* is reportedly involved in proliferation and migration of vascular SMCs [39]. A Venn diagram in Figure 6F shows 12 probe sets that were commonly upregulated (>8-fold) in the tunica media of the closing DA tissues compared to the IT of the same DA tissues (Cases 2 and 3), which consisted of eight genes (Figure 6F and Table 8). There were several genes related to muscle structure development such as *BDKRB2*, *MSC*, and *DCN* [41–43]. *DCN* is also involved in extracellular constituents and stabilizes collagen and elastic fibers [44,45].

Table 7. Eight genes that overlapped and were enriched (>8-fold) in the intimal thickening (IT) compared to the tunica media of the closing DA tissues (Cases 2 and 3).

Gene Name	Description	Fold Change IT vs. the Tunica Media	
		Case 2	Case 3
POU4F1	*POU* class 4 homeobox 1	22.1	16.4
BMX	*BMX* non-receptor tyrosine kinase	10.6	29.2
FGF1	fibroblast growth factor 1	15.9	9.0
MPZL2	myelin protein zero-like 2	18.8	10.2
FMO3	flavin-containing dimethylaniline monooxygenase 3	12.8	10.0
PROCR	protein C receptor	13.0	8.6
DSP	desmoplakin	9.3	11.7
NR1I2	nuclear receptor subfamily 1 group I member 2	9.7	10.7

Table 8. Eight genes that overlapped and were enriched (>8-fold) in the tunica media compared to the intimal thickening (IT) of the closing DA tissues (Cases 2 and 3).

Gene Name	Description	Fold Change the Tunica Media vs. IT	
		Case 2	Case 3
GAS7	growth arrest-specific 7	52.4	9.8
H19	*H19* imprinted maternally expressed transcript	14.2	18.5
BTNL9	butyrophilin-like 9	8.4	17.9
SELENOP	selenoprotein P	14.8	13.4
BDKRB2	bradykinin receptor B2	11.3	11.6
CHRDL1	chordin-like 1	9.2	23.6
MSC	musculin	11.7	8.4
DCN	decorin	9.0	9.4

4. Discussion

The present study demonstrated that neonatal closing DAs exhibited prominent IT and sparse elastic fiber formation, which are typical human DA characteristics. Postnatal closing DA tissues had abundant expression of cardiac neural crest-related protein jagged 1 and the differentiated smooth muscle marker calponin compared to the patent DA tissue. On the other hand, the patent DA tissue had a distinct morphology (e.g., aorta-like elastic lamellae and a poorly formed IT) and gene profiles, such as second heart field-related genes, compared to the closing DA tissues.

The DA is originally derived from the sixth left aortic artery and has a unique cell-lineage [46]. SMCs of the DA are derived from cardiac neural crest cells [35,47,48] and the DA endothelial cells (ECs) are from second heart field [48,49], while both SMCs and ECs of the adjacent pulmonary artery are derived from second heart field [48,49]. In the ascending aorta, ECs are derived from second heart field, and SMCs of the inner medial layer and outer layer are derived from neural crest cells and second heart field, respectively [47,48]. The heatmap of transcriptome data indicated that these cell lineage-related genes were differentially expressed between the closing DA tissues and the patent DA tissue. Although it was difficult to clearly classify these genes into each lineage due to some overlap, cardiac

neural crest-related genes such as *JAG1* were highly expressed in the closing DA tissues. In contrast, second heart field-related genes, such as *ISL1*, were enriched in the patent DA tissue.

The DA has been reported to have differentiated SMCs compared to the adjacent great arteries [1,50]. Slomp et al. demonstrated high levels of calponin expression in the tunica media of the fetal human DA [1]. Similarly, Kim et al. reported the presence of highly differentiated SMCs in the fetal rabbit DA, according to *SM2* expression [50]. These differentiated SMCs have a high contractile apparatus, which makes them compatible with the postnatal potent DA contraction [1,50]. Additionally, several mutant mice with the patent DA had less differentiated SMCs [35–37]. Ivey et al. reported that mice lacking *Tfap2β*, which is a neural crest-enriched transcription factor, had decreased expression of calponin on embryonic day 18.5 [36]. Huang et al. utilized mice that harbored a neural crest-restricted deletion of the myocardin gene and demonstrated that decreased SMC contractile proteins were present on embryonic day 16.5 [35]. In addition, SMC-specific *Jag1*-deficient mice had a limited expression of SMC contractile proteins, even at postnatal day 0 [37]. The transcriptome data of the human DA tissues in the present study exhibited decreased protein levels of Jagged 1 and calponin in the patent DA tissue compared to the closing DA tissues. These altered SMC differentiation markers may contribute to postnatal DA patency in humans.

Prematurity and several genetic syndromes are reported to increase the incidence of the patent DA [51], and the patent DA can be classified into three groups, i.e., (1) patent DA in preterm infants, (2) patent DA as a part of a clinical syndrome, and (3) non-syndromic patent DA. This study included only one case with patent DA who had heterotaxy syndrome (polysplenia), which is a major study limitation. Indeed, in the present study, the expression of *Nodal*, which plays a primary role in the determination of left–right asymmetry, was positively correlated to the closing DAs compared to the patent DA with heterotaxy (Figure 3B). Therefore, it was not able to conclude that differentially expressed genes between in the closing DAs and the patent DA were associated with DA patency, but not with heterotaxy.

There are several syndromes (mutated genes) associated with the patent DA, such as Cantú (*ABCC9*), Char (*TFAP2B*), DiGeorge (*TBX1*), Holt-Oram (*TBX5*), and Rubinstein–Taybi (*CREBBP*) syndromes [52–54]. In addition to these syndromes, heterotaxy syndrome was reported to have a higher incidence of patent DA [55]. Notch signaling pathways have been reported to play a role in the establishment of left–right asymmetry via regulating *Nodal* expression [56,57]. Mutant for the Notch ligand *Dll1* or double mutants for *Notch1* and *Notch2* exhibited defects in left–right asymmetry [56,57]. *Dll1*-null mutants die at early embryonic days due to severe hemorrhages [58], and it is not yet elucidated whether this *Dll1*-mediated Notch signaling is involved in the pathogenesis of patent DA. It has been reported that combined SMC-specific deletion of *Notch2* and heterozygous deletion of *Notch3* in mice showed the patent DA, but not heterotaxy [59]. In this study, we delineated the low levels of *JAG1*, which is a Notch ligand, in the patent DA with heterotaxy syndrome. Mice with *Jag1*-null mutant are early embryonic lethal due to hemorrhage [60], and SMC-specific *Jag1*-deleted mice are postnatal lethal due to patent DA [37]. These *Jag1* mutants were not reported to exhibit heterotaxy. In humans, there is no obvious relationship between Alagille syndrome (*JAG1*) and patent DA or heterotaxy [61,62]. In mice, phenotypes of patent DA or heterotaxy seem to depend on ligands and isoforms of receptors of Notch signaling. In addition, there are differences in phenotypes caused by genetic mutations between in mice and humans. Analysis of non-syndromic patent DA would provide further insights into molecular mechanisms of closing and patency of the human DA.

Yarboro et al. performed RNA sequencing to determine genes that were differentially expressed in the preterm human DA and aorta at 21 weeks gestation [18], which was a much earlier time point than we used in our study. They found that several previously recognized DA-dominant genes in rodent studies [11,14,15,17] (e.g., *ABCC9*, *PTGER4*, and *TFAP2B*) were also upregulated in the preterm human DA tissues compared to the

aorta [18]. Some DA-dominant genes (e.g., *ERG1* and *SFRP1*) in the preterm human DA [18] were upregulated in the closing DAs compared to the patent DA in the present study. In addition, some aorta-dominant genes, including *ALX1* [18], were upregulated in the patent DA compared to the closing DA, which might partly support the aortification phenotype of the patent DA. *Jag1* was reported to be the term DA dominant gene rather than the preterm DA dominant gene in rats [10], suggesting that *Jag1* contributes to normal DA development. In addition to these previously reported genes, the gene profiles in our study potentially provide novel candidate genes (e.g., *APLN* and *LTBP3*) that may contribute to vascular SMC development and function [27,34]. Further study is needed to understand the roles of these genes in DA development.

Mueller et al. performed DNA microarray analysis using postnatal human DAs [19]. Their DA samples were composed of two stent-implanted DAs, one ligamentous DA, and one un-stented open DA [19]. We compared our data to their un-stented open DA dominant genes; however, we could not find obvious overlapped genes among them. One possible reason is that Mueller et al. compared the un-stented open DA on postnatal day 1 to the stented DAs on postnatal days 222 and 239. The stent implantation and time-course of sampling might affect the gene expressions.

This study elucidated the transcriptomic difference between the closing DA tissues and the patent DA tissue in humans. However, one of the limitations in this study pertains to the different durations of PGE_1 administration. In utero, the DA is dilated by prostaglandin E2 (PGE_2), which is mainly derived from the placenta [63]. After birth, the loss of the placenta and the increased flow of the lung, which is the major site of PGE catabolism, cause a decline in circulating PGE_2 [64]. This decline in PGE_2 contributes to a postnatal DA contraction [64]. We previously reported PGE_2-induced structural DA remodeling via the prostaglandin receptor EP4 (e.g., IT formation [4,5,22] and attenuation of elastic laminae in the tunica media [6]). In humans, Mitani et al. reported that lipo-PGE_1 administration increased IT formation in the DA [65]. Gittenberger-de Groot et al. reported that PGE_1 treatment induced histopathologic changes (e.g., edema) in the human DA [66]. In this study, Case 4 who received the longest PGE_1 administration, for 98 days, had prominent IT formation and less visible layered elastic fibers. This study demonstrated that the duration of PGE_1-treatment affected gene expressions such as cell-cycle process-related genes. On the basis of these findings, postnatal PGE_1 administration was thought to influence not only structural changes but also gene expression in the postnatal DA.

In 1977, Gittenberger-de Groot et al. performed histological analysis of 42 specimens of postnatal human DAs ranging in age from 12 h after premature delivery to 32 years [9]. An abnormal wall structure of the DA was found in all 14 patients that were over 4 months of age, and the most prominent feature was an aberrant distribution of elastic material, such as unfragmented subendothelial elastic lamina [9]. Three of the 14 patients also showed countable elastic laminae in the tunica media, namely, an aortification [9]. The histological finding of patent DA (Case 1) in the present study was consistent with this aortification type, showing aberrant distribution of elastic materials.

As mentioned above, a major limitation of this study is the use of only one sample of the patent DA, which could not represent the whole entity of patent DA. It is difficult to obtain large numbers of samples with a variety of different congenital heart diseases because isolation of the DA is possible only in the case of a limited number of surgical procedures (e.g., aortic arch repair). However, transcriptome comparisons of different types of patent DA tissues would be more informative to elucidate the pathogenesis of the human patent DA.

5. Conclusions

Transcriptome analysis using the IT and the tunica media of human DA tissue revealed different gene profiles between the patent DA and the closing DA tissues. Cardiac neural crest-related genes such as *JAG1* were highly expressed in the tunica media and IT of the closing DA tissues compared to the patent DA. Second heart field-related genes, such as

ISL1, were enriched in the patent DA. The data from this study indicate that patent DA tissue may have different cell lineages from closing DA tissue.

Supplementary Materials: The following are available online at https://www.mdpi.com/article/10.3390/jcdd8040045/s1: Figure S1. Differential gene expression between the longer-term PGE_1-treated human ductus arteriosus (DA) tissue (Case 4) and the shorter-term PGE_1-treated DA tissues (Cases 2 and 3); Table S1. Gene Ontology biological process terms (size > 300) that were significantly upregulated (FDR < 0.25) in the outer part of long-term PGE_1-treated human ductus arteriosus (DA) tissue (Case 4) compared to the tunica media of short-term PGE_1-treated DA tissues (Case 2 and Case 3); Table S2. Twenty genes that overlapped and were enriched (>8-fold) in the outer part of a longer-term PGE_1-treated DA tissue (Case 4) compared to the IT of shorter-term PGE_1-treated DA tissues (Cases 2 and 3).

Author Contributions: Conceptualization, J.S. and U.Y.; methodology, U.Y.; validation, J.S., T.K., S.T., Y.K., and U.Y.; formal analysis, J.S., T.K., S.T., Y.K., and U.Y.; investigation, J.S., T.K., S.T., Y.K., S.O., Y.I., and U.Y.; resources, T.T. and T.A.; data curation, J.S., T.K., S.T., Y.K., and U.Y.; writing—original draft preparation, J.S. and U.Y.; writing—review and editing, J.S., T.K., S.T., Y.K., E.M., and U.Y.; visualization, J.S.; supervision, E.M.; project administration, U.Y.; funding acquisition, J.S., S.T., Y.K., and U.Y. All authors have read and agreed to the published version of the manuscript.

Funding: This work was supported by the Japan Society for the Promotion of Science (JSPS) KAKENHI (J.S., JP18K15681, JP16H07107; S.T., JP20K17730; Y.K., JP17K08976, JP21K07352; U.Y., JP20H03650, JP20K21638, JP18K08767), the Japan Agency for Medical Research and Development (AMED) (U.Y., 20ek0210117h0002), the Lydia O'Leary Memorial Pias Dermatological Foundation (Y.K.), and the Miyata Cardiac Research Promotion Foundation (U.Y.).

Institutional Review Board Statement: The study was conducted according to the guidelines of the Declaration of Helsinki, and approved by the Institutional Ethics Committee of Tokyo Medical University and Kanagawa Children's Medical Center (protocol codes: T2020-0238 and 1502-05; date of approval: 16-November-2020 and 9-July-2015).

Informed Consent Statement: Informed consent was obtained from all subjects involved in the study.

Data Availability Statement: The data presented in this study are available within the article.

Acknowledgments: The authors are grateful to Yuka Sawada for excellent technical assistance.

Conflicts of Interest: The authors declare no conflict of interest. The funders had no role in the design, execution, interpretation, or writing of this study.

References

1. Slomp, J.; de Groot, A.C.G.; Glukhova, M.A.; van Munsteren, J.C.; Kockx, M.M.; Schwartz, S.M.; Kote-liansky, V.E. Differentiation, dedifferentiation, and apoptosis of smooth muscle cells during the development of the human ductus arteriosus. *Arterioscler. Thromb. Vasc. Biol.* **1997**, *17*, 1003–1009. [CrossRef]
2. Yokoyama, U.; Minamisawa, S.; Ishikawa, Y. Regulation of vascular tone and remodeling of the ductus arteriosus. *J. Smooth Muscle Res.* **2010**, *46*, 77–87. [CrossRef] [PubMed]
3. Yokoyama, U.; Minamisawa, S.; Katayama, A.; Tang, T.; Suzuki, S.; Iwatsubo, K.; Iwasaki, S.; Kurotani, R.; Okumura, S.; Sato, M.; et al. Differential Regulation of Vascular Tone and Remodeling via Stimulation of Type 2 and Type 6 Adenylyl Cyclases in the Ductus Arteriosus. *Circ. Res.* **2010**, *106*, 1882–1892. [CrossRef] [PubMed]
4. Yokoyama, U.; Minamisawa, S.; Quan, H.; Akaike, T.; Suzuki, S.; Jin, M.; Jiao, Q.; Watanabe, M.; Otsu, K.; Iwasaki, S.; et al. Prostaglandin e2-activated epac promotes neointimal formation of the rat ductus arteriosus by a process distinct from that of camp-dependent protein kinase A. *J. Biol. Chem.* **2008**, *283*, 28702–28709. [CrossRef] [PubMed]
5. Yokoyama, U.; Minamisawa, S.; Quan, H.; Ghatak, S.; Akaike, T.; Segi-Nishida, E.; Iwasaki, S.; Iwamoto, M.; Misra, S.; Tamura, K.; et al. Chronic activation of the prostaglandin receptor ep4 promotes hyaluronan-mediated neointimal formation in the ductus arteriosus. *J. Clin. Investig.* **2006**, *116*, 3026–3034. [CrossRef]
6. Yokoyama, U.; Minamisawa, S.; Shioda, A.; Ishiwata, R.; Jin, M.H.; Masuda, M.; Asou, T.; Sugimoto, Y.; Aoki, H.; Nakamura, T.; et al. Prostaglandin E2 Inhibits Elastogenesis in the Ductus Arteriosus via EP4 Signaling. *Circulation* **2014**, *129*, 487–496. [CrossRef]
7. Yokoyama, U. Prostaglandin E-mediated molecular mechanisms driving remodeling of the ductus arteriosus. *Pediatr. Int.* **2015**, *57*, 820–827. [CrossRef]
8. Forsey, J.T.; Elmasry, O.A.; Martin, R.P. Patent arterial duct. *Orphanet J. Rare Dis.* **2009**, *4*, 17–19. [CrossRef]

9. De Groot, A.C.G. Persistent ductus arteriosus: Most probably a primary congenital malformation. *Br. Heart J.* **1977**, *39*, 610–618. [CrossRef]
10. Yokoyama, U.; Sato, Y.; Akaike, T.; Ishida, S.; Sawada, J.; Nagao, T.; Quan, H.; Jin, M.; Iwamoto, M.; Yokota, S.; et al. Maternal vitamin A alters gene profiles and structural maturation of the rat ductus arteriosus. *Physiol. Genom.* **2007**, *31*, 139–157. [CrossRef]
11. Jin, M.H.; Yokoyama, U.; Sato, Y.; Shioda, A.; Jiao, Q.; Ishikawa, Y.; Minamisawa, S. DNA microarray profiling identified a new role of growth hormone in vascular remodeling of rat ductus arteriosus. *J. Physiol. Sci.* **2011**, *61*, 167–179. [CrossRef]
12. Liu, N.M.; Yokota, T.; Maekawa, S.; Lu, P.; Zheng, Y.W.; Taniguchi, H.; Yokoyama, U.; Kato, T.; Minamisawa, S. Transcription profiles of endothelial cells in the rat ductus arteriosus during a perinatal period. *PLoS ONE* **2013**, *8*, e73685. [CrossRef]
13. Goyal, R.; Goyal, D.; Longo, L.D.; Clyman, R.I. Microarray gene expression analysis in ovine ductus arteriosus during fetal development and birth transition. *Pediatr. Res.* **2016**, *80*, 610–618. [CrossRef]
14. Bokenkamp, R.; van Brempt, R.; van Munsteren, J.C.; van den Wijngaert, I.; de Hoogt, R.; Finos, L.; Goeman, J.; Groot, A.C.; Poelmann, R.E.; Blom, N.A.; et al. Dlx1 and rgs5 in the ductus arteriosus: Vessel-specific genes identified by transcriptional profiling of laser-capture microdissected endothelial and smooth muscle cells. *PLoS ONE* **2014**, *9*, e86892. [CrossRef]
15. Shelton, E.L.; Ector, G.; Galindo, C.L.; Hooper, C.W.; Brown, N.; Wilkerson, I.; Pfaltzgraff, E.R.; Paria, B.C.; Cotton, R.B.; Stoller, J.Z.; et al. Transcriptional profiling reveals ductus arteriosus-specific genes that regulate vascular tone. *Physiol. Genom.* **2014**, *46*, 457–466. [CrossRef]
16. Costa, M.; Barogi, S.; Socci, N.D.; Angeloni, D.; Maffei, M.; Baragatti, B.; Chiellini, C.; Grasso, E.; Coceani, F. Gene expression in ductus arteriosus and aorta: Comparison of birth and oxygen effects. *Physiol. Genom.* **2006**, *25*, 250–262. [CrossRef] [PubMed]
17. Hsieh, Y.T.; Liu, N.M.; Ohmori, E.; Yokota, T.; Kajimura, I.; Akaike, T.; Ohshima, T.; Goda, N.; Minamisawa, S. Transcription profiles of the ductus arteriosus in brown-norway rats with irregular elastic fiber formation. *Circ. J.* **2014**, *78*, 1224–1233. [CrossRef] [PubMed]
18. Yarboro, M.T.; Durbin, M.D.; Herington, J.L.; Shelton, E.L.; Zhang, T.; Ebby, C.G.; Stoller, J.Z.; Clyman, R.I.; Reese, J. Transcriptional profiling of the ductus arteriosus: Comparison of rodent microarrays and human RNA sequencing. *Semin. Perinatol.* **2018**, *42*, 212–220. [CrossRef]
19. Mueller, P.P.; Drynda, A.; Goltz, D.; Hoehn, R.; Hauser, H.; Peuster, M. Common signatures for gene expression in postnatal patients with patent arterial ducts and stented arteries. *Cardiol. Young* **2009**, *19*, 352–359. [CrossRef] [PubMed]
20. Subramanian, A.; Tamayo, P.; Mootha, V.K.; Mukherjee, S.; Ebert, B.L.; Gillette, M.A.; Paulovich, A.; Pomeroy, S.L.; Golub, T.R.; Lander, E.S.; et al. Gene set enrichment analysis: A knowledge-based approach for interpreting genome-wide expression profiles. *Proc. Natl. Acad. Sci. USA* **2005**, *102*, 15545–15550. [CrossRef] [PubMed]
21. Saito, J.; Yokoyama, U.; Nicho, N.; Zheng, Y.-W.; Ichikawa, Y.; Ito, S.; Umemura, M.; Fujita, T.; Ito, S.; Taniguchi, H.; et al. Tissue-type plasminogen activator contributes to remodeling of the rat ductus arteriosus. *PLoS ONE* **2018**, *13*, e0190871. [CrossRef]
22. Ito, S.; Yokoyama, U.; Nakakoji, T.; Cooley, M.A.; Sasaki, T.; Hatano, S.; Kato, Y.; Saito, J.; Nicho, N.; Iwasaki, S.; et al. Fibulin-1 Integrates Subendothelial Extracellular Matrices and Contributes to Anatomical Closure of the Ductus Arteriosus. *Arterioscler. Thromb. Vasc. Biol.* **2020**, *40*, 2212–2226. [CrossRef]
23. Blom, M.; Reis, K.; Heldin, J.; Kreuger, J.; Aspenstrom, P. The atypical Rho GTPase RhoD is a regulator of actin cytoskeleton dynamics and directed cell migration. *Exp. Cell Res.* **2017**, *352*, 255–264. [CrossRef] [PubMed]
24. Kang, Y.; Kim, J.; Anderson, J.P.; Wu, J.; Gleim, S.R.; Kundu, R.K.; McLean, D.L.; Kim, J.D.; Park, H.; Jin, S.W.; et al. Apelin-APJ signaling is a critical regulator of endothelial MEF2 activation in cardiovascular development. *Circ. Res.* **2013**, *113*, 22–31. [CrossRef] [PubMed]
25. Shimoda, M.; Yoshida, H.; Mizuno, S.; Hirozane, T.; Horiuchi, K.; Yoshino, Y.; Hara, H.; Kanai, Y.; Inoue, S.; Ishijima, M.; et al. Hyaluronan-Binding Protein Involved in Hyaluronan Depolymerization Controls Endochondral Ossification through Hyaluronan Metabolism. *Am. J. Pathol.* **2017**, *187*, 1162–1176. [CrossRef]
26. Benso, A.; Broglio, F.; Marafetti, L.; Lucatello, B.; Seardo, M.A.; Granata, R.; Martina, V.; Papotti, M.; Muccioli, G.; Ghigo, E. Ghrelin and Synthetic Growth Hormone Secretagogues are Cardioactive Molecules with Identities and Differences. *Semin. Vasc. Med.* **2004**, *4*, 107–114. [CrossRef]
27. Luo, X.; Liu, J.; Zhou, H.; Chen, L. Apelin/APJ system: A critical regulator of vascular smooth muscle cell. *J. Cell. Physiol.* **2018**, *233*, 5180–5188. [CrossRef]
28. Scholler, N.; Hayden-Ledbetter, M.; Hellstrom, K.E.; Hellstrom, I.; Ledbetter, J.A. Cd83 is an i-type lectin adhesion receptor that binds monocytes and a subset of activated cd8+ t cells [corrected]. *J. Immunol.* **2001**, *166*, 3865–3872. [CrossRef] [PubMed]
29. Khabibullin, D.; Medvetz, D.A.; Pinilla, M.; Hariharan, V.; Li, C.; Hergrueter, A.; Contreras, M.L.; Zhang, E.; Parkhitko, A.; Yu, J.J.; et al. Folliculin regulates cell-cell adhesion, AMPK, and mTORC1 in a cell-type-specific manner in lung-derived cells. *Physiol. Rep.* **2014**, *2*, e12107. [CrossRef] [PubMed]
30. Alba, G.A.; Samokhin, A.O.; Wang, R.S.; Zhang, Y.Y.; Wertheim, B.M.; Arons, E.; Greenfield, E.A.; Slingsby, M.H.L.; Ceglowski, J.R.; Haley, K.J.; et al. NEDD9 is a Novel and Modifiable Mediator of Platelet-Endothelial Adhesion in the Pulmonary Circulation. *Am. J. Respir. Crit. Care Med.* **2021**. [CrossRef]
31. Aquino, J.B.; Lallemend, F.; Marmigere, F.; Adameyko, I.; Golemis, E.A.; Ernfors, P. The retinoic acid inducible Cas-family signaling protein Nedd9 regulates neural crest cell migration by modulating adhesion and actin dynamics. *Neuroscience* **2009**, *162*, 1106–1119. [CrossRef] [PubMed]

32. Dieci, E.; Casati, L.; Pagani, F.; Celotti, F.; Sibilia, V. Acylated and unacylated ghrelin protect MC3T3-E1 cells against tert-butyl hydroperoxide-induced oxidative injury: Pharmacological characterization of ghrelin receptor and possible epigenetic involvement. *Amino Acids* **2014**, *46*, 1715–1725. [CrossRef] [PubMed]
33. Robertson, I.B.; Horiguchi, M.; Zilberberg, L.; Dabovic, B.; Hadjiolova, K.; Rifkin, D.B. Latent tgf-beta-binding proteins. *Matrix Biol.* **2015**, *47*, 44–53. [CrossRef]
34. Zhou, Y.; Cashman, T.J.; Nevis, K.R.; Obregon, P.; Carney, S.A.; Liu, Y.; Gu, A.; Mosimann, C.; Sondalle, S.; Peterson, R.E.; et al. Latent tgf-beta binding protein 3 identifies a second heart field in zebrafish. *Nature* **2011**, *474*, 645–648. [CrossRef] [PubMed]
35. Huang, J.; Cheng, L.; Li, J.; Chen, M.; Zhou, D.; Lu, M.M.; Proweller, A.; Epstein, J.A.; Parmacek, M.S. Myocardin regulates expression of contractile genes in smooth muscle cells and is required for closure of the ductus arteriosus in mice. *J. Clin. Investig.* **2008**, *118*, 515–525. [CrossRef]
36. Ivey, K.N.; Sutcliffe, D.; Richardson, J.; Clyman, R.I.; Garcia, J.A.; Srivastava, D. Transcriptional regulation during development of the ductus arteriosus. *Circ. Res.* **2008**, *103*, 388–395. [CrossRef]
37. Feng, X.; Krebs, L.T.; Gridley, T. Patent ductus arteriosus in mice with smooth muscle-specific Jag1 deletion. *Development* **2010**, *137*, 4191–4199. [CrossRef]
38. Hohenauer, T.; Berking, C.; Schmidt, A.; Haferkamp, S.; Senft, D.; Kammerbauer, C.; Fraschka, S.; Graf, S.A.; Irmler, M.; Beckers, J.; et al. The neural crest transcription factor brn3a is expressed in melanoma and required for cell cycle progression and survival. *EMBO Mol. Med.* **2013**, *5*, 919–934. [CrossRef]
39. Mi, S.; Wang, P.; Lin, L. Mir-188-3p inhibits vascular smooth muscle cell proliferation and migration by targeting fibro-blast growth factor 1 (fgf1). *Med. Sci. Monit.* **2020**, *26*, e924394. [CrossRef] [PubMed]
40. Heng, W.; Huang, J.A.; Wang, Z.Y. Inhibition of Cellular Growth and Migration by Suppression of Endothelial Protein C Receptor (EPCR) in Lung Carcinoma Cells. *Oncol. Res.* **2012**, *20*, 231–240. [CrossRef]
41. Robb, L.; Hartley, L.; Wang, C.C.; Harvey, R.P.; Begley, C.G. Musculin: A murine basic helix-loop-helix transcription factor gene expressed in embryonic skeletal muscle. *Mech. Dev.* **1998**, *76*, 197–201. [CrossRef]
42. Järveläinen, H.; Vernon, R.B.; Gooden, M.D.; Francki, A.; Lara, S.; Johnson, P.Y.; Kinsella, M.G.; Sage, E.H.; Wight, T.N. Overexpression of Decorin by Rat Arterial Smooth Muscle Cells Enhances Contraction of Type I Collagen In Vitro. *Arterioscler. Thromb. Vasc. Biol.* **2004**, *24*, 67–72. [CrossRef]
43. Figueroa, C.D.; Marchant, A.; Novoa, U.; Forstermann, U.; Jarnagin, K.; Scholkens, B.; Muller-Esterl, W. Differential distribution of bradykinin b(2) receptors in the rat and human cardiovascular system. *Hypertension* **2001**, *37*, 110–120. [CrossRef]
44. Danielson, K.G.; Baribault, H.; Holmes, D.F.; Graham, H.; Kadler, K.E.; Iozzo, R.V. Targeted Disruption of Decorin Leads to Abnormal Collagen Fibril Morphology and Skin Fragility. *J. Cell Biol.* **1997**, *136*, 729–743. [CrossRef] [PubMed]
45. Reinboth, B.; Hanssen, E.; Cleary, E.G.; Gibson, M.A. Molecular interactions of biglycan and decorin with elastic fiber components: Biglycan forms a ternary complex with tropoelastin and microfibril-associated glycoprotein 1. *J. Biol. Chem.* **2002**, *277*, 3950–3957. [CrossRef]
46. Schussler, O.; Gharibeh, L.; Mootoosamy, P.; Murith, N.; Tien, V.; Rougemont, A.L.; Sologashvili, T.; Suuronen, E.; Lecarpentier, Y.; Ruel, M. Cardiac Neural Crest Cells: Their Rhombomeric Specification, Migration, and Association with Heart and Great Vessel Anomalies. *Cell. Mol. Neurobiol.* **2020**, *41*, 403–429. [CrossRef] [PubMed]
47. Sawada, H.; Rateri, D.L.; Moorleghen, J.J.; Majesky, M.W.; Daugherty, A. Smooth Muscle Cells Derived From Second Heart Field and Cardiac Neural Crest Reside in Spatially Distinct Domains in the Media of the Ascending Aorta—Brief Report. *Arterioscler. Thromb. Vasc. Biol.* **2017**, *37*, 1722–1726. [CrossRef]
48. Zhou, Z.; Wang, J.; Guo, C.; Chang, W.; Zhuang, J.; Zhu, P.; Li, X. Temporally Distinct Six2 -Positive Second Heart Field Progenitors Regulate Mammalian Heart Development and Disease. *Cell Rep.* **2017**, *18*, 1019–1032. [CrossRef]
49. Wang, X.; Chen, D.; Chen, K.; Jubran, A.; Ramirez, A.; Astrof, S. Endothelium in the pharyngeal arches 3, 4 and 6 is derived from the second heart field. *Dev. Biol.* **2017**, *421*, 108–117. [CrossRef] [PubMed]
50. Kim, H.S.; Aikawa, M.; Kimura, K.; Kuroo, M.; Nakahara, K.; Suzuki, T.; Katoh, H.; Okamoto, E.; Yazaki, Y.; Nagai, R. Ductus arteriosus. Advanced differentiation of smooth muscle cells demonstrated by myosin heavy chain isoform expression in rabbits. *Circulation* **1993**, *88*, 1804–1810. [CrossRef]
51. Schneider, D.J.; Moore, J.W. Patent ductus arteriosus. *Circulation* **2006**, *114*, 1873–1882. [CrossRef]
52. Bokenkamp, R.; DeRuiter, M.C.; van Munsteren, C.; de Groot, A.C.G. Insights into the pathogenesis and genetic background of patency of the ductus arteriosus. *Neonatology* **2010**, *98*, 6–17. [CrossRef] [PubMed]
53. Hajj, H.; Dagle, J.M. Genetics of Patent Ductus Arteriosus Susceptibility and Treatment. *Semin. Perinatol.* **2012**, *36*, 98–104. [CrossRef] [PubMed]
54. Lewis, T.R.; Shelton, E.L.; Van Driest, S.L.; Kannankeril, P.J.; Reese, J. Genetics of the patent ductus arteriosus (PDA) and pharmacogenetics of PDA treatment. *Semin. Fetal Neonatal Med.* **2018**, *23*, 232–238. [CrossRef]
55. Rose, V.; Izukawa, T.; Moes, C.A. Syndromes of asplenia and polysplenia. A review of cardiac and non-cardiac malformations in 60 cases withspecial reference to diagnosis and prognosis. *Br. Heart J.* **1975**, *37*, 840–852. [CrossRef]
56. Raya, A.; Kawakami, Y.; Rodriguez-Esteban, C.; Buscher, D.; Koth, C.M.; Itoh, T.; Morita, M.; Raya, R.M.; Dubova, I.; Bessa, J.G.; et al. Notch activity induces nodal expression and mediates the establishment of left-right asymmetry in vertebrate embryos. *Genes. Dev.* **2003**, *17*, 1213–1218. [CrossRef] [PubMed]

57. Krebs, L.T.; Iwai, N.; Nonaka, S.; Welsh, I.C.; Lan, Y.; Jiang, R.; Saijoh, Y.; O'Brien, T.P.; Hamada, H.; Gridley, T. Notch signaling regulates left-right asymmetry determination by inducing nodal expression. *Genes. Dev.* **2003**, *17*, 1207–1212. [CrossRef]
58. De Angelis, M.H.; McIntyre, J., 2nd; Gossler, A. Maintenance of somite borders in mice requires the delta homologue dii1. *Nature* **1997**, *386*, 717–721. [CrossRef]
59. Baeten, J.T.; Jackson, A.R.; McHugh, K.M.; Lilly, B. Loss of Notch2 and Notch3 in vascular smooth muscle causes patent ductus arteriosus. *Genesis* **2015**, *53*, 738–748. [CrossRef] [PubMed]
60. Xue, Y.; Gao, X.; Lindsell, C.E.; Norton, C.R.; Chang, B.; Hicks, C.; Gendron-Maguire, M.; Rand, E.B.; Weinmaster, G.; Gridley, T. Embryonic Lethality and Vascular Defects in Mice Lacking the Notch Ligand Jagged1. *Hum. Mol. Genet.* **1999**, *8*, 723–730. [CrossRef] [PubMed]
61. Kamath, B.M.; Spinner, N.B.; Emerick, K.M.; Chudley, A.E.; Booth, C.; Piccoli, D.A.; Krantz, I.D. Vascular anomalies in alagille syndrome: A significant cause of morbidity and mortality. *Circulation* **2004**, *109*, 1354–1358. [CrossRef]
62. Spinner, N.B.; Colliton, R.P.; Crosnier, C.; Krantz, I.D.; Hadchouel, M.; Meunier-Rotival, M. Jagged1 mutations in alagille syndrome. *Hum. Mutat.* **2001**, *17*, 18–33. [CrossRef]
63. Clyman, R.I.; Mauray, F.; Roman, C.; Rudolph, A.M.; Heymann, M.A.; Maury, F. Circulating prostaglandin E2 concentrations and patent ductus arteriosus in fetal and neonatal lambs. *J. Pediatr.* **1980**, *97*, 455–461. [CrossRef]
64. Smith, G.C. The pharmacology of the ductus arteriosus. *Pharmacol. Rev.* **1998**, *50*, 35–58.
65. Mitani, Y.; Takabayashi, S.; Sawada, H.; Ohashi, H.; Hayakawa, H.; Ikeyama, Y.; Imanaka-Yoshida, K.; Maruyama, K.; Shimpo, H.; Komada, Y. Fate of the "opened" arterial duct: Lessons learned from bilateral pulmonary artery banding for hypoplastic left heart syndrome under the continuous infusion of prostaglandin E1. *J. Thorac. Cardiovasc. Surg.* **2007**, *133*, 1653–1654.e2. [CrossRef]
66. De Groot, A.C.G.; Strengers, J.L. Histopathology of the arterial duct (ductus arteriosus) with and without treatment with prostaglandin E1. *Int. J. Cardiol.* **1988**, *19*, 153–166. [CrossRef]

Journal of
Cardiovascular
Development and Disease

MDPI

Article

Isolated Dissection of the Ductus Arteriosus Associated with Sudden Unexpected Intrauterine Death

Marny Fedrigo [1], Silvia Visentin [2], Paola Veronese [2], Ilaria Barison [1], Alessia Giarraputo [1], Erich Cosmi [2], Gaetano Thiene [1], Maria Teresa Gervasi [2], Cristina Basso [1] and Annalisa Angelini [1,*]

[1] Department of Cardiac, Thoracic, Vascular Sciences, and Public Health, University of Padua, 35128 Padua, Italy; marny.fedrigo@aopd.veneto.it (M.F.); ilaria.barison@unipd.it (I.B.); alessia.giarraputo@studenti.unipd.it (A.G.); gaetano.thiene@unipd.it (G.T.); cristina.basso@unipd.it (C.B.)
[2] Department of Woman and Children Health, University of Padua, 35128 Padua, Italy; silvia.visentin.1@unipd.it (S.V.); paola.veronese@aopd.veneto.it (P.V.); erich.cosmi@unipd.it (E.C.); mariateresa.gervasi@aopd.veneto.it (M.T.G.)
* Correspondence: annalisa.angelini@unipd.it; Tel.: +39-049-8272260

Abstract: We report five cases of sudden intrauterine death due to premature closure of the ductus arteriosus. In four cases, this was caused by dissecting the hematoma of the ductus arteriosus with intimal flap and obliteration of the lumen. In one case, the ductus arteriosus was aneurysmatic, with lumen occlusion caused by thrombus stratification. No drug therapy or free medication consumption were reported during pregnancy. The time of stillbirth ranged between 26 and 33 gestational weeks. We performed TUNEL analysis for apoptosis quantification. The dissecting features were intimal tears with flap formation in four of the cases, just above the origin of the ductus arteriosus from the pulmonary artery. The dissecting hematoma of the ductus arteriosus extended downward to the descending aorta and backward to the aortic arch with involvement of the left carotid and left subclavian arteries. TUNEL analysis showed a high number of apoptotic smooth muscle cells in the media in two cases. Abnormal ductal remodeling with absence of subintimal cushions, lacunar spaces rich in glycosaminoglycans (cystic medial necrosis), and smooth muscle cell apoptosis were the pathological substrates accounting for failure of remodeling process and dissection.

Keywords: ductus arteriosus; remodeling; dissection of ductus arteriosus; sudden unexpected intrauterine death

Citation: Fedrigo, M.; Visentin, S.; Veronese, P.; Barison, I.; Giarraputo, A.; Cosmi, E.; Thiene, G.; Gervasi, M.T.; Basso, C.; Angelini, A. Isolated Dissection of the Ductus Arteriosus Associated with Sudden Unexpected Intrauterine Death. *J. Cardiovasc. Dev. Dis.* **2021**, *8*, 91. https://doi.org/10.3390/jcdd8080091

Academic Editors: Monique R. M. Jongbloed and Robert Poelmann

Received: 30 June 2021
Accepted: 27 July 2021
Published: 31 July 2021

1. Introduction

Sudden intrauterine death is a socio-epidemiological problem. It accounts for 4–5/1000 births. The causes of unexpected death are mostly related to placenta injury in terms of placenta insufficiency, maternal malperfusion vascularization, inadequate fetal vascularization, or umbilical cord causes, such as nodal cord, rupture, marginal insertion, etc. [1,2]. Most of the studies in the literature show a high percentage of cases reported as unexplained causes, ranging from 20% to 50% [3].

Premature closure of the ductus arteriosus is a rare condition, which is difficult to diagnose. The incidence is not well defined [4–8]. Since 2013, our center has acted as a tertiary referral center in Northeast Italy for sudden unexpected intrauterine death. Among 375 cases collected since then, from 25 weeks of gestation to term, we identified five cases (1.3%) of abrupt ductus arteriosus closure caused by dissection of the ductus with hematoma of the parietal wall and obliteration of the lumen. These cases prompted us to review the literature on the topic of the ductus arteriosus and its remodeling process during fetal life to understand the structural abnormalities that could be at the base of these fatal events.

During fetal life, the ductus arteriosus, with its patency, guarantees blood flow from the right ventricle into the descending aorta bypassing the lungs since the role of blood oxygenation is played by the placenta.

The fetal ductus arteriosus is a large muscular artery originating from the 6th aortic arch [9–11], composed of three layers, the intima, the media with smooth muscle cells (SMCs), separated by elastic fibers, and the adventitia [12–14]. The intima is represented by a flat endothelium adherent to the internal elastic lamina or separated by intimal cushions. The intimal cushions are constituted by SMCs, usually longitudinally oriented with interposed thin elastic and collagen fibers and an extracellular matrix. By the end of gestation, they progressively become thicker. They are constantly present in all the ducts and preferentially located at the pulmonary extreme. The internal elastic lamina is a thick, continuous elastic layer, intact if adherent to the endothelium or fragmented, absent, or reduplicated when interposition of the intimal cushions occurs. The media are composed of many layers of SMCs, both contractile and synthetic, which are usually oriented circularly in the outer media but longitudinally in the inner media, favoring the postnatal contraction and shortening of the duct. Muscle cell layers are separated by fine reticulin fibers and thin elastic fibers. Mucopolysaccharides are interposed between the muscle and the elastic lamellae. Vasa vasorum are present in the outer layer of the media. During the second trimester of pregnancy, the media start to remodel, and the number of smooth muscle cells and extracellular matrix increases with gestational age. The ductal smooth muscle cells, longitudinally oriented, are inserted between the ending of the two great arteries' elastic lamellae in the junctional zone. At this level, the elastic fibers of the pulmonary arteries interdigit with the SMCs of the ductal media. The ductal adventitia consists of fibroelastic connective tissue containing small blood vessels, nerves, and ganglia. The elastic fibers are most abundant adjacent to the media but do not form an external elastic lamina [13,15].

Two different conditions can affect the ductus arteriosus before birth: excessive patency with aneurysm formation and premature closure with lumen obstruction [16,17].

Aneurysm of the ductus arteriosus, a relatively rare lesion detected mostly in children and adults, can be incidental and asymptomatic but can evolve to spontaneous dissection, rupture, thrombosis, and embolism of the aorta and pulmonary arteries, leading to death [18–25]. Nowadays, thanks to routine diagnostic imaging modalities, these conditions can also be detected during fetal life.

Aneurysms of the ductus arteriosus can be congenital (present at birth) or acquired. Congenital ductus arteriosus aneurysms are reported to be more common than originally thought postnatal and can remain asymptomatic at birth [26–28].

Several theories have been postulated to explain the mechanism of congenital aneurysm formation of the ductus arteriosus [12,29,30]. The ductal aneurysm can resolve spontaneously without complications through the normal physiological constriction of the parietal wall of the duct at birth and or through a thrombus stratification inside the lumen with organization and incorporation of the thrombotic material and fibrotic occlusion [25]. However, during fetal life, the process of ductus arteriosus remodeling, which should allow postnatal closure, can fail and lead to aneurysm formation or persistent ductus arteriosus patency after birth [15,31–33].

The persistent ductus arteriosus has been associated with chromosomal abnormalities in 10% of the cases and TGFBeta signaling abnormalities, as in Marfan or Loeys Dietz, to TFAP2B in Char syndrome and to TFAP2B, TNF-RAF1, prostacyclin synthase in premature and term infants [31,34].

Few case reports present dissecting aneurysms of the ductus arteriosus as a cause of sudden unexpected intrauterine death.

The purpose of our study was to report the clinical and pathological characteristics of five cases of unexpected and sudden intrauterine death due to dissection of the ductus arteriosus and to elucidate the possible mechanism leading to this severe complication and ultimately to death.

2. Materials and Methods

Since 2013, our center at Padua University has acted as a tertiary referral center in the Veneto region for sudden intrauterine death. All the unexpected and sudden intrauterine

deaths of the Veneto region are referred to Padua for autopsy, which are performed by two expert cardiovascular pathologists on rotation (AA, MF). The autopsy was a complete autopsy performed according to a standard adopted protocol for fetal autopsy inclusive of radiographic and photographic documentation. Clinical data from the mother and the pregnancy are reported in the clinical information protocol attached to the autopsy request. This protocol includes the metabolic and infective profile of the mother together with the family history and the documentation of the pregnancy. Routinely, the standard protocol for autopsy foresees histology of all the organs and if the maceration is not too advanced, we store fresh tissues for genetic studies when requested.

Among 375 cases collected since then, from 25 weeks of gestation to term, we have identified at autopsy, 5 cases (1.3%) of abrupt ductus arteriosus closure caused by dissection of the ductus with hematoma of the parietal wall and ab extrinseco compression of the lumen. We removed the thoracic block including the heart and the lungs and further evaluated them under a stereomicroscope. We used the sequential segmental approach for categorization. We opened the heart according to the blood flow. For histology, we sampled all the thoracic and abdominal organs. For the heart, we made a transverse cut to include the right ventricle, septum, and the left ventricle.

The ductus was sectioned with a serial transverse cut every 3 mm from the pulmonary junction to the aortic end, with a mean of three paraffin blocks per case. For each macroscopic block, we performed hematoxylin–eosin, elastic fiber–van Gieson, and Alcian–PAS staining. For apoptosis assessment, we performed TUNEL staining.

The protocol for sudden intrauterine death includes also the evaluation of the placenta according to the international guidelines "Sampling and definitions of placental lesions: Amsterdam placental workshop group consensus statement" [35].

3. Results

We present five cases of ductus arteriosus dissection, all male, as a cause of death (1.3%) from our registry of sudden intrauterine death since 2013. We used ReCoDe classification for causes of death [36] and according to this classification, we identified the 5 cases, which represent 7% of the causes in the fetus group (Group A). In Table 1, we present some information related to the mother. Unfortunately, we do not have any further information related to events following pregnancies.

Table 1. Clinical data.

Case	Sex	GA	Ethnicity	Risk Factors of Mother	Pregnancy	Medications during Pregnancy	Reported Symptoms during Pregnancy
1	M	33	Caucasian	Smoking during pregnancy	First	None	None
2	M	32	Caucasian	No risk factors	Second	None	None
3	M	32	Caucasian	Hypertension, smoking during pregnancy	First	None	Hypertension
4	M	26	Caucasian	No risk factors	First	None	None
5	M	33	Caucasian	Pre-eclampsia	First	None	Hypertension

GA: gestational age.

Postmortem examination of the five cases.

At autopsy, the external examination showed a normally developed fetus for the gestational week (see Table 2). All the anthropometric indexes were in keeping with the gestational age. In four of the cases, the maceration of the fetus was severe.

Table 2. Autopsy major findings.

Case	Body Weight	Heart Weight	Wall Thickness RV/S/LV mm	GM	DA Anatomical Macroscopic Description	Foramen Ovale
1	1750 g	8.7 g	2.5/2.8/2.8	III	Dissecting DA	Restrictive
2	1650 g	8.5 g	2.4/2.5/2.5	III	Dissecting DA	Patent
3	1300 g	7 g	2/2/2.2	III	Dissecting DA	Patent
4	810 g	5 g	1.2/1.3/1.8	III	Dissecting DA	Patent
5	1670 g	9 g	2.3/2.5/2.5	I	Dissecting DA	Patent

RV: right ventricle; S: septum; LV: left ventricle; GM: grade of maceration; DA: ductus arteriosus.

Examination of the thorax and abdomen also showed normally related organs with a preserved normal laterality and no associated pathologies. No congenital defects were observed anywhere. In the thorax, after opening the pericardium, in four cases, adventitial hemorrhagic imbibition/hematoma at the level of the ductus arteriosus, giving an appearance of dilatation exceeding the diameter of the aorta and the pulmonary trunk, suggestive of dissection/hematoma was identified. Such hematoma started at the pulmonary end of the ductus arteriosus, partially involving the pulmonary trunk, the entire length of the ductus arteriosus, and extending into the descending aorta but stopped immediately after the junction with the ductus arteriosus. There was also the involvement of the origin of the left subclavian and left common carotid arteries (Figures 1 and 2). The heart was located on the left side of the thorax, with the apex pointing to the left. The sequential segmental analysis showed situs solitus, concordant atrioventricular and ventriculoarterial connections, patent foramen ovale; only for one case (case 1), foramen ovale was restrictive, normally developed atrioventricular and semilunar valves. The coronary arteries were regular. No macroscopic abnormalities of the heart or great vessels were identified. The heart was opened according to the blood flow, and the pulmonary trunk showed a normal trifurcation, giving origin to the right and left pulmonary arteries and the ductus arteriosus. A serial transverse cut showed an intimal flap just above the junction of the ductus arteriosus with pulmonary vessels with a semi-circumferential involvement and dissection of the media-adventitia layer, which accounted for the adventitia hematoma detected from outside in four of the cases. In the other case, a ductal aneurysm was evident from the outside. A parietal hematoma completely occluded the lumen of the ductus arteriosus.

The lungs were normally located, the right trilobed, supplied by short, epi-arterial bronchus, and the left bilobed, supplied by a long, hypoarterial bronchus. The sectioning of the lung revealed, as expected, a compacted parenchyma, which, at histology, showed a saccular pattern in cases 1, 2, 3, and 5 and a canalicular pattern in case 4, in keeping with the gestational age. No vascular intraparenchymal abnormalities were present.

No emboli or infarcts were evident in the downstream circulation.

The placenta was available in four of the five cases. We could not detect any sign of infections; in two cases (case 4 and 5), we identified multifocal small infarcts. In another case (case 2), we recognized maternal vascular malperfusion. The last placenta (case 1) was unremarkable.

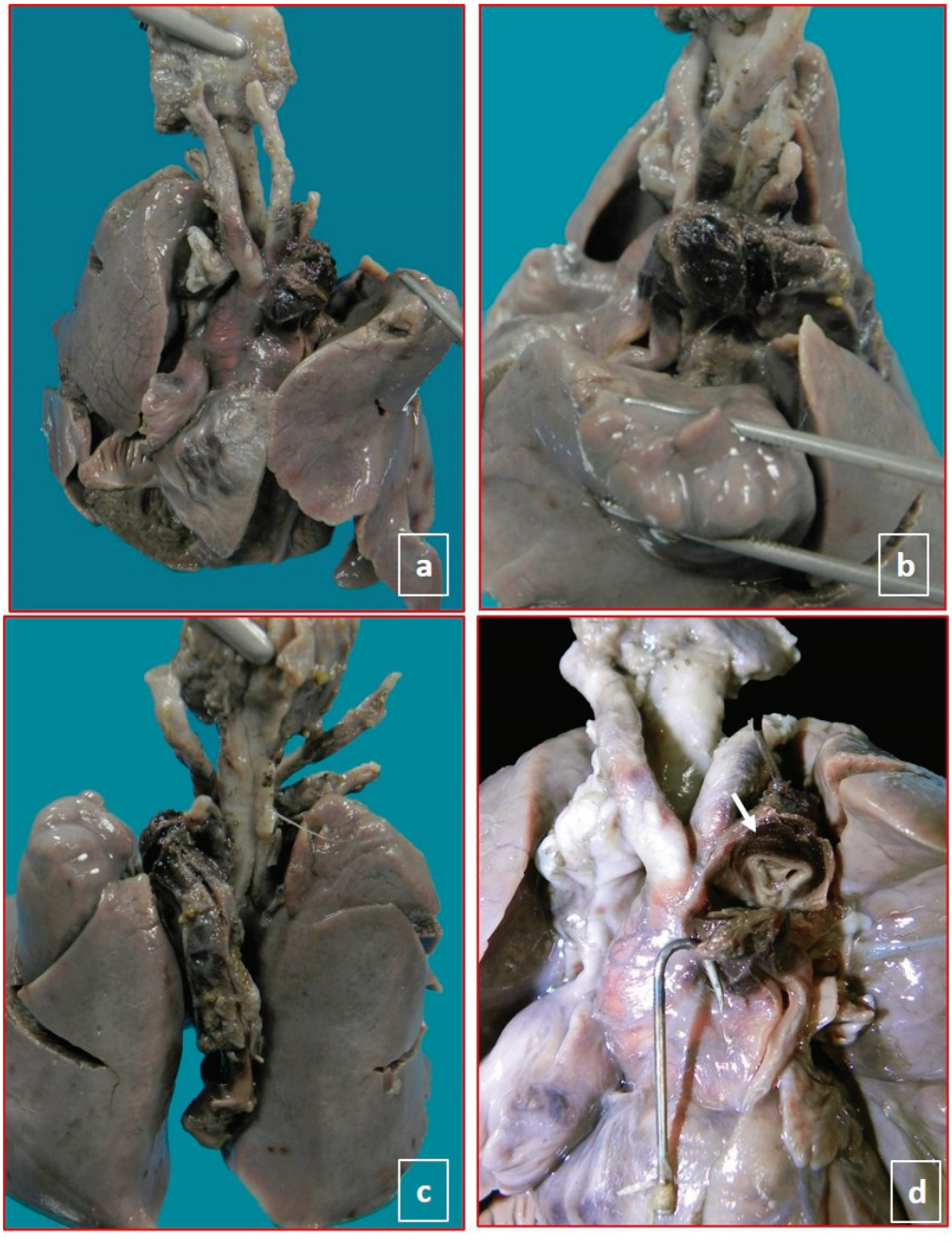

Figure 1. Male fetus, 32 gestation weeks (case 2), without congenital anomalies and slight intrauterine growth restriction. The placenta showed a fetal vascular malperfusion. No maternal pathology during this second pregnancy. (**a**–**c**), the localization and extension of peri-adventitial hematoma involving ductus arteriosus, aortic arch, brachiocephalic vessels, and descending aorta. (**d**), ab extrinseco compression of the aorta (white arrow).

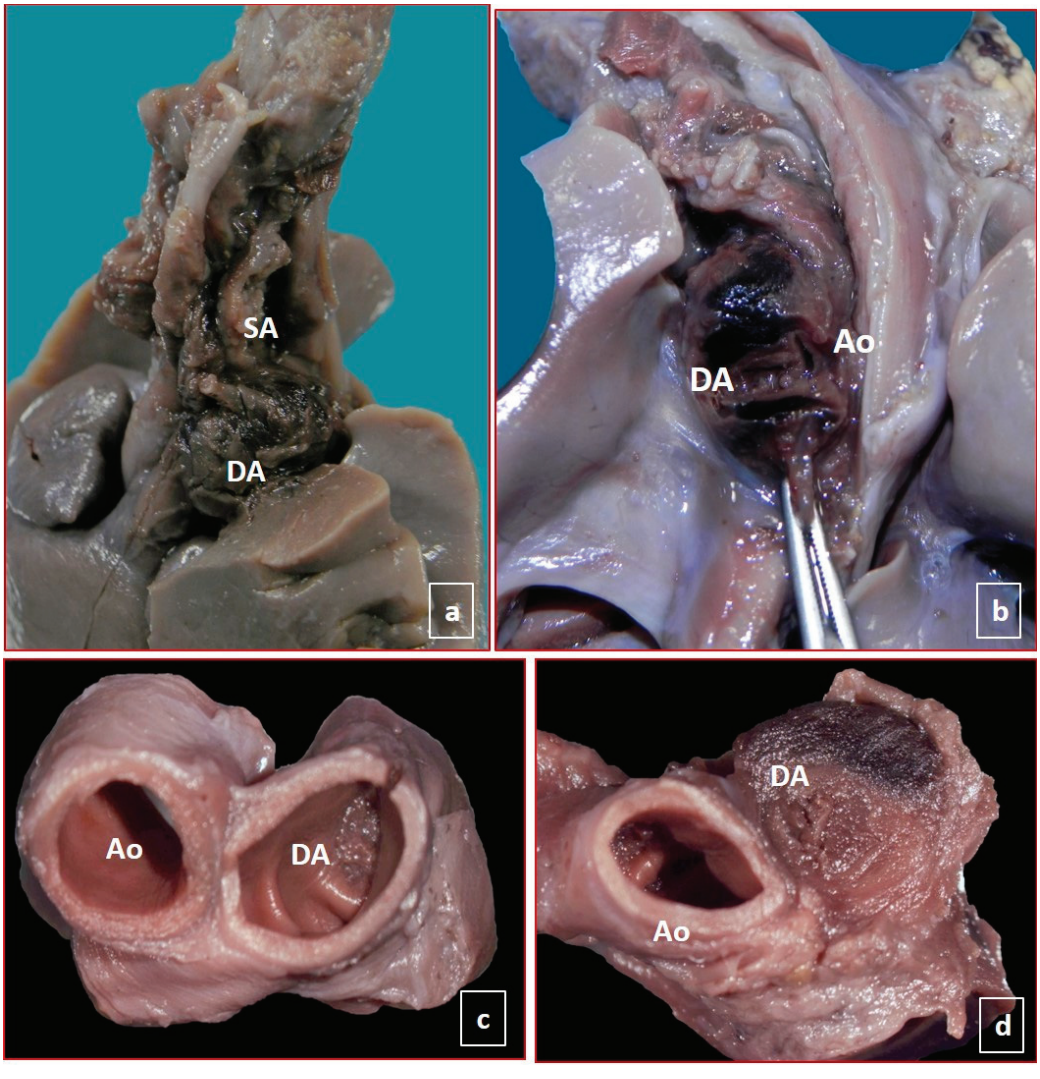

Figure 2. Male fetus, 33 gestation weeks (case 5), without congenital anomalies and slight intrauterine growth restriction. The placenta showed a high maternal vascular malperfusion. The mother had a positive history for hypertension and smoking during pregnancy. In (**a**,**b**), the localization and extension of peri-adventitia hematoma involved the ductus arteriosus, aortic arch, and brachiocephalic vessels. In (**c**,**d**), the complete closure of the ductus by thrombus. Ao: aorta; DA: ductus arteriosus.

The microscopic examination of the ductus arteriosus showed absence of subendothelial intimal cushions with intact internal elastic lamina in three cases. In three cases, the presence of cystic medial necrosis (lacunar spaces in the media) were the prominent abnormalities (Table 3). Apoptosis in the media was present in two cases. In none of our cases, we identified inflammatory cell infiltration in the ductus arteriosus. In particular, each of our five cases presented a different association of the pathological substrates of the ductus arteriosus. In case 1, there was complete absence of intimal cushions, no media hematoma but aneurysm of the parietal ductal wall with thrombotic occlusion of the lumen, and no

adventitia hematoma. In case 2, no subendothelial cushions, intimal flap with dissection of the outer media involving the adventitia, congestion of the vasa vasorum, large lacunar spaces, and apoptosis of SMCs in the media were identified (Figure 3). In case 3, we identified an intimal flap with thrombus stratification and lumen occlusion, and outer media dissection, adventitial hematoma and subendothelial cushion and medial large lacunar spaces with accumulation of glycosaminoglycans. In case 4, the youngest for gestational age, the ductus arteriosus was still without the remodeling of the subendothelial cushions as expected for the gestational age. Moreover, we identified an absence of lacunar space but a high rate of SMCs apoptosis in the media. An intimal flap with dissection of the outer media and hematoma of the adventitia was also present. In the fifth case, the substrate was characterized by large lacunar space in the presence of subendothelial cushions and intimal flap and parietal dissection and adventitial hematoma (Figures 4 and 5).

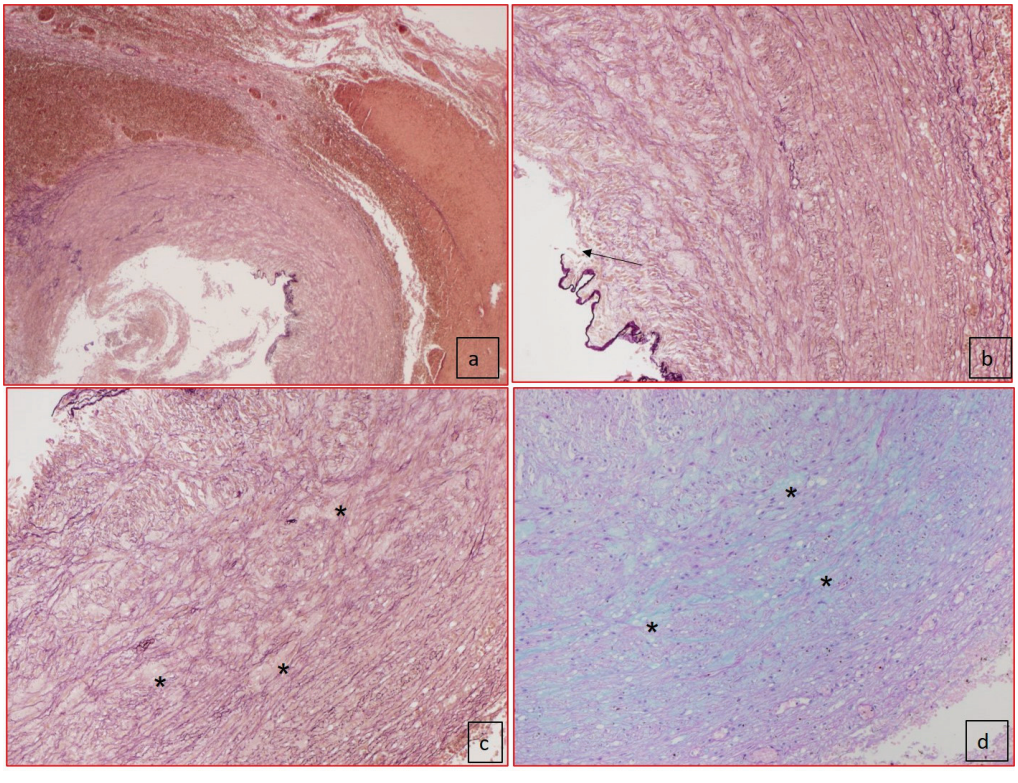

Figure 3. Histology of the ductus arteriosus (case 2). (**a**) Panoramic view of ductus arteriosus with elastic fiber–van Gieson staining showed the dissection of media (50× of magnification) and the absence of intimal cushions. (**b**) Elastic fiber–van Gieson staining at higher magnification showed the disorganization of elastic fibers and rupture of internal elastic lamina (black arrow). (**c**) Elastic fiber–van Gieson (100× magnification) staining showing disorganization of elastic fibers and presence of lacunar spaces, cystic medial necrosis (*), without SMCs replaced by mucopolysaccharides as shown in (**d**) with Alcian–PAS staining (100× magnification).

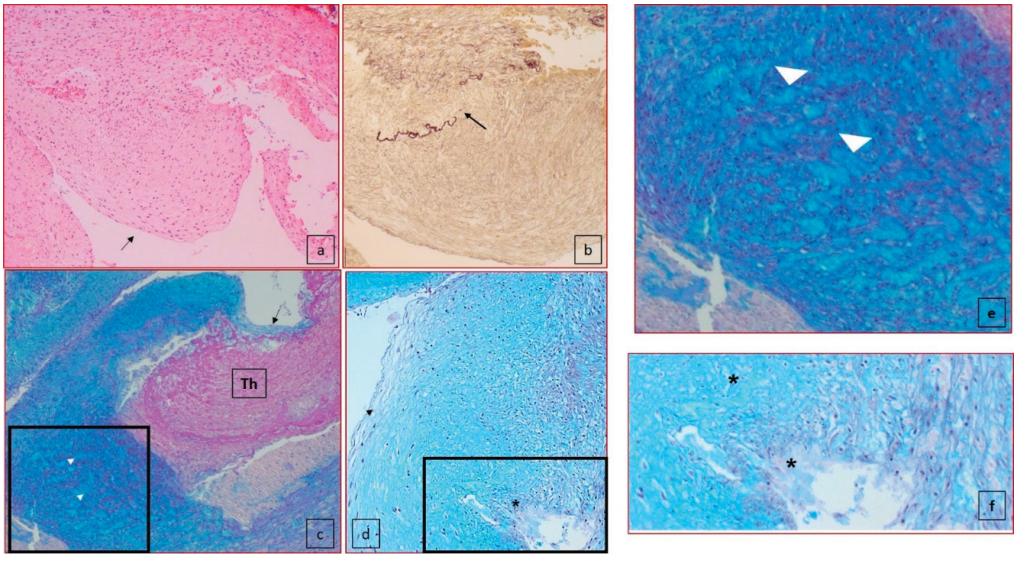

Figure 4. Histology of the ductus arteriosus. (**a**) Subendothelial intimal cushion (case 5) (50× magnification, black arrow); (**b**) elastic fiber–van Gieson (50× magnification) showed the interruption of the internal elastic lamina (black arrow); (**c**) presence of lacunar spaces (white arrow head) in the media closed to dissection (black arrow) (100× magnification) with thrombus formation (Th); (**d**) lacunar spaces, cystic medial necrosis (*) in the media, under the intimal proliferation (black arrow head) (100×). (**e**) High-power view of the insert highlighted in (**c**). (**f**) High-power view of the insert highlighted in (**d**).

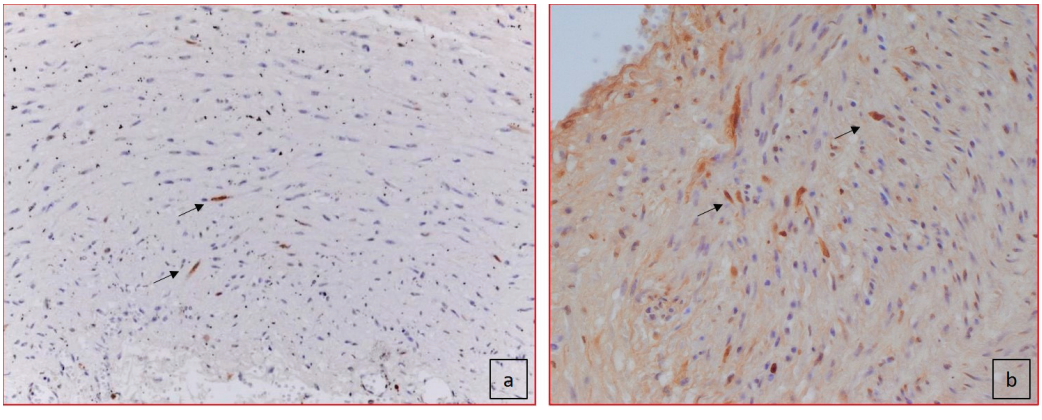

Figure 5. Apoptosis. Two different cases of TUNEL nuclear staining positivity for apoptosis of SMCs within the parietal wall (black arrows). (**a**) Case 2 (100×): apoptotic cells in the media without clear signs of proliferation; (**b**) case 4: diffuse apoptotic cells in the media (100×).

Table 3. Microscopic features of the ductus arteriosus.

Case	Intimal Flap	Intima	Media-Adventitia	Inflammation	Apoptosis (TUNEL)
1	Absent	No subendothelial cushions, thrombotic lumen occlusion	Outer dissecting hematoma, no cystic medial necrosis	Absent	+
2	Present	No subendothelial cushions	Outer dissecting hematoma, cystic medial necrosis	Absent	+++
3	Present	Subendothelial cushions, thrombus stratification	Outer dissecting hematoma, cystic medial necrosis	Absent	+
4	Present	No subendothelial cushions	Outer dissecting hematoma, no cystic medial necrosis	Absent	+++
5	Present	Subendothelial cushions	Dissecting hematoma, cystic medial necrosis	Absent	+

4. Discussion

The results of our morphological study on five cases of stillbirth babies due to dissecting aneurysm of the ductus arteriosus showed that the dissection is similar to that affecting the aorta and the great vessel and other muscular arteries such as the coronary and cerebral arteries. We were able to identify an intima tear at the junction between the pulmonary trunk and the ductus with an intima-media flap and hematoma dissection through the media and the adventitia without any re-entry mechanisms in four of the five cases. This led to occlusion of the lumen by the flap segment and circumferential hematoma. In all the four cases, the hematoma dissection involved the descending aorta and the retrograde aortic arch. In only one case, we were unable to identify an intimal tear or parietal dissection, but the lesion was ascribed to ductal aneurysm and occlusive thrombus stratification.

There are no differences in terms of morphological substrates if we compare the dissection of the aorta or the coronary arteries with the dissection of the ductus arteriosus [37,38]. In both elastic and muscular arteries, an intimal tear/laceration can be identified with the blood entering the parietal wall and producing the intima-media or medial-adventitia detachment and creating a false lumen filled with blood, which determines the further progression of the dissection. The dissection can be either circumferential or semi-circumferential for the muscular arteries, while it is usually spiraliform for the aorta, according to the main longitudinal direction of the vessel and the orientation of the parietal wall SMCs of collateral vessels. Degenerative lesions such as mucoid pools, known as cystic medial necrosis, fragmentation of the elastic components and fragmentation and duplication of internal elastic lamina, and loss of SMCs are common features of the dissecting phenomena. In three of our cases, these lacunar spaces filled by extracellular mucoid matrix were the pathological substrates. Of relevance, in all of our cases, no inflammatory cell infiltration was present both at the site of intimal laceration and along the ductus, aorta, aortic arch, and the pulmonary trunk, excluding a possible vasculitis as a pathogenic mechanism of dissection. A thorough evaluation of the autopsy substrates as well as of the placenta also excluded the concomitant presence of other associated congenital anomalies, both cardiac and extracardiac, and confirmed the negativity of inflammatory status of the fetuses. Only in two of our cases, hypertension during pregnancy in the mother was reported and in one of them at preeclampsia range. We are aware that hypertension in the mother or preeclampsia status could affect the placenta causing vascular malperfusion and fetal growth restriction, with the evidence of parietal wall stiffness as an indirect sign of intravascular stress [39]. However, we do not know if this mechanism could have played a role in our cases. In the history of the mother, we did not find other risk factors traditionally recognized for dissection in adults. We cannot exclude a genetic background accounting for connective tissue disorders, dissection, and aneurysm formation since we could not

perform genetic studies on these cases, mainly in relation to the severe maceration in four of them. We plan to carry out a genetic assessment for the most frequent gene involved in collagen disease in the case with more preserved conditions [31,40].

During pregnancy, the ductus arteriosus remains open, and during the second trimester, the proliferation of intimal cushions with lumen reduction will prepare for ductus arteriosus closure. The lumen is stellate in the closing duct and is reduced in size, mainly in the pulmonary extremity [9–13,15,24,25].

Remodeling for the preparation of ductus arteriosus closure at birth with immediate contraction of the parietal wall implies differentiation of vascular SMCs and endothelial cells, production of the extracellular matrix, vascular SMCs proliferation and migration, and finally, a decrease in elastic fibers and an increase in fibrous connective tissue [12,25]. The sequence of events can be summarized as follows: endothelial detachment from the internal elastic lamina with an accumulation of extracellular matrix in the subendothelial space, migration of SMCs from the media into the intima through the fenestration of the elastic lamina, growth of endothelial cushions, occlusion of the lumen by contraction and overgrowth of cushions and the necrosis of the inner layer of the media, and degeneration of the ductus arteriosus into a fibrous ligament at birth through apoptosis and necrosis [9,13,15,24,25]. In preterm infants, the ductus arteriosus usually remains open because there is a lack of intimal cushions. In the case of persistent ductus arteriosus or patent ductus arteriosus in a full-term fetus, the intimal cushions are not so well formed. They are encircled by an additional subendothelial elastic lamina.

In the congenital aortic arch aneurysm, the ductus arteriosus is usually tortuous, saccular, and dilated and elongated, and characterized microscopically by a lack of intimal cushion formation and defective elastic lamellae formation, enhancement of necrosis, and mucoid degeneration of the inner part of the media [12,15]. This remodeling process occurs in the third trimester of pregnancy. They are often associated with connective tissue disorders such as Marfan syndrome or Ehlers Danlos syndrome [34]. They can resolve or evolve with fatal complications such as thromboembolic extension into the main pulmonary artery or the aorta, spontaneous rupture, erosion or compression of adjacent structures, and infection [24,25,41–43].

In all the other 370 cases of our registry, we did not identify the presence of aneurysms of the ductus arteriosus. Dissecting aneurysm of ductus arteriosus can be regarded as the end of the spectrum of the patent ductus arteriosus (PDA), a congenital cardiac abnormality that can be a single cardiac abnormality or can be part of other associated congenital heart diseases. PDA is characterized by the lack of closure at the time of birth with the persistence of patency, allowing shunting of blood between the systemic and the pulmonary circulations [31].

At a histomorphological analysis, the patent ductus arteriosus is characterized by the absence of the features at the base of remodeling for closure after birth, which are the intimal cushions, pads of proliferating SMCs migrating from the media into the intima, and thickening of the medial wall as a consequence of longitudinal SMCs fascicles arrangement in the subintimal space [15,30,31]. The absence of intimal cushions in three of our dissecting cases supports the theory of abnormal remodeling for postnatal ductus arteriosus closure, with the weakening of the parietal wall, which can favor secondary dissection. If the dissection were not occurring, the result would be eventual patency of the ductus arteriosus. Moreover, the presence of large lacunar spaces rich in glycosaminoglycans is recognized as the cystic medial necrosis substrate in aortic dissection.

Dissecting aneurysm is an acute event that has led to fetal death. Since this was an unexpected and sudden event, we do not know the exact time frame for the dissection of the parietal wall, occlusion of the ductus arteriosus, and death. The barrage at the ductus arteriosus would have caused a redirection of flow toward the pulmonary arteries and an increase in blood shunt from the right atrium to the left atrium. The dimension of the foramen ovale would play a crucial role in the hemodynamics of these fetuses. Very few papers have reported dissection of the ductus arteriosus as the cause of sudden unexpected

deaths in single-center experiences or as anecdotal cases without an accurate and detailed description of the parietal dissected wall [21,41,42].

One point should be discussed as well in relation to the terminology adopted in the literature. As in adults with aortic dissection, in which we are not utilizing anymore the term dissecting aneurysm, since the dissection has been recognized to occur in the absence of ectasia or aneurysm formation, it would be more appropriate to adopt the term dissection of ductus arteriosus rather than dissecting aneurysm. The dilatation is not a prerequisite for dissection, but dissection can manifest without an increase in the diameter of the vessel.

On the other hand, an aneurysm of the ductus arteriosus can be present and be detected accidentally during the fetal ultrasound and resolved spontaneously after birth with closure without complications [44].

Several theories have been proposed for the development of an aneurysm of the ductus arteriosus. At the time of birth, delayed closure of the aortic end of the ductus would expose the ductal wall to high pressure with related dilatation. During the third trimester, as detected by ultrasound, dilatation and aneurysm development has been ascribed to the weakening of the parietal wall with a reduction of intimal cushion formation or deposition of elastin. Aneurysm development in some reported cases was associated with defective fibrillin or collage [34,41] or vascular SMCs dysregulation [31,34]. In our cases, we could not carry out a genetic study to unravel the possible genetic defects associated with dissection. However, no associated cardiac or extracardiac anomalies during the autopsy were present in our cases. Aneurysms of the non-patent ductus arteriosus have been reported by Falcone et al. to affect patients at different ages but all after birth from infants to adults and related to death in 31% of the reported cases [20].

To the best of our knowledge, a ductal aneurysm has never been described in the stillborn fetus.

Spontaneous premature closure of the fetal ductus can be a cause of fetal demise. However, in the cases reported in the literature, no morphological description of the mechanism of closure has been described [4,16,45,46]. Much attention in those cases was driven toward the hemodynamic consequence of the closure, with an ultrasound description at the ductus level, with right heart failure, pulmonary overflow, and persistent pulmonary hypertension after birth in case of successful delivery. The mechanism of premature closure is still ill-defined. We cannot exclude that in some of these cases, a dissecting aneurysm could be responsible per se for the lumen occlusion.

Some other aspects are puzzling in our five cases. All of them were males. However, we do not know if this is by chance or it implies any male gender propensity to dissection. All of them except one occurred at around 32 gestational weeks, which is the time of the remodeling process of the arterial duct, with intimal cushion formation in preparation for physiological closure occurring at birth. This could imply failure of the remodeling process.

5. Study Limitation

The main limitation is represented by the poor quality of the autoptic material on which we performed the histological and genetic assessments, in part due to the severe maceration of four of the five cases. As a consequence of the high level of degradation of DNA, it was not possible to detect possible genetic collagenopathies. Indeed, these genes are characterized by long nucleotide sequences.

6. Conclusions

In case of sudden unexpected intrauterine death, a thorough autopsy should be performed to identify rare conditions such as dissecting ductus arteriosus as the cause of death. Histological examination should be performed for the detection of pathological substrates accounting for intimal tears, dissection, hematoma, apoptosis, and absence of inflammatory infiltrate. Further genetic studies should be carried out to confirm or exclude the genetic background.

Author Contributions: Conceptualization, A.A. and M.F.; methodology, formal analysis, and investigation, M.F. and A.A.; resources, G.T. and C.B.; data curation, S.V., P.V., A.G., M.T.G. and E.C.; writing—original draft preparation, M.F., I.B. and A.A.; writing—review and editing, M.F., S.V., P.V., I.B., A.G., E.C., M.T.G., G.T., C.B. and A.A.; supervision, G.T.; funding acquisition, C.B. and G.T. All authors have read and agreed to the published version of the manuscript.

Funding: This study was supported by the Registry of Cardio-Cerebral-Vascular Pathology, Veneto Region, Italy; and BIRD191520/19, BIRD204045/20, BIRD191573/19 and BIRD170215/17, University of Padua.

Institutional Review Board Statement: The study was conducted according to the guidelines of the Declaration of Helsinki, the present work fulfills the ethical requirements of autopsy study on sudden intrauterine unexpected death of the Ministry of Health in Italy.

Informed Consent Statement: Informed consent was obtained from all the parents of the stillborn fetuses according to the Italian legislation.

Data Availability Statement: Not applicable.

Acknowledgments: We thank the Registry of Cardio-Cerebral-Vascular Pathology, Veneto Region, Italy, for supporting our research and the centers Sacro Cuore-Don Calabria Hospital (Negrar, Verona), Santorso Hospital (Thiene, Vicenza), Verona Hospital (Verona), Treviso Hospital (Treviso), and Bussolengo Hospital (Bussolengo, Verona), which provided the cases discussed.

Conflicts of Interest: The authors declare no conflict of interest.

References

1. Blythe, C.; Vazquez, R.E.Z.; Cabrera, M.S.; Zekic Tomas, S.; OC Anumba, D.; Cohen, M.C. Results of full postmortem examination in a cohort of clinically unexplained stillbirths: Undetected fetal growth restriction and placental insufficiency are prevalent findings. *J. Perinatol.* **2019**, *39*, 1196–1203. [CrossRef] [PubMed]
2. Frøen, J.F.; Cacciatore, J.; McClure, E.M.; Kuti, O.; Jokhio, A.H.; Islam, M.; Shiffman, J. Stillbirths: Why they matter. *Lancet* **2011**, *377*, 1353–1366. [CrossRef]
3. Reinebrant, H.E.; Leisher, S.H.; Coory, M.; Henry, S.; Wojcieszek, A.M.; Gardener, G.; Lourie, R.; Ellwood, D.; Teoh, Z.; Allanson, E.; et al. Making stillbirths visible: A systematic review of globally reported causes of stillbirth. *BJOG An. Int. J. Obstet. Gynaecol.* **2018**, *125*, 212–224. [CrossRef] [PubMed]
4. Gewillig, M.; Brown, S.C.; De Catte, L.; Debeer, A.; Eyskens, B.; Cossey, V.; Van Schoubroeck, D.; Van Hole, C.; Devlieger, R. Premature foetal closure of the arterial duct: Clinical presentations and outcome. *Eur. Heart J.* **2009**, *30*, 1530–1536. [CrossRef]
5. Tynan, M. The ductus arteriosus and its closure. *N. Engl. J. Med.* **1993**, *329*, 1570–1572. [CrossRef]
6. Leal, S.D.; Cavallé-Garrido, T.; Ryan, G.; Farine, D.; Heilbut, M.; Smallhorn, J.F. Isolated ductal closure in utero diagnosed by fetal echocardiography. *Am. J. Perinatol.* **1997**, *14*, 205–210. [CrossRef] [PubMed]
7. Ishida, H.; Kawazu, Y.; Kayatani, F.; Inamura, N. Prognostic factors of premature closure of the ductus arteriosus in utero: A systematic literature review. *Cardiol. Young* **2017**, *27*, 634–638. [CrossRef]
8. Operle, M.; Anderson, S. Premature Closure of the Ductus Arteriosus in an Otherwise Healthy Fetus. *J. Diagnostic Med. Sonogr.* **2019**, *35*, 235–239. [CrossRef]
9. Gittenberger-De Groot, A.C.; Peterson, J.C.; Wisse, L.J.; Roest, A.A.W.; Poelmann, R.E.; Bökenkamp, R.; Elzenga, N.J.; Hazekamp, M.; Bartelings, M.M.; Jongbloed, M.R.M.; et al. Pulmonary ductal coarctation and left pulmonary artery interruption; pathology and role of neural crest and second heart field during development. *PLoS ONE* **2020**, *15*, e0228478. [CrossRef]
10. Scherptong, R.W.C.; Jongbloed, M.R.M.; Wisse, L.J.; Vicente-steijn, R.; Bartelings, M.M.; Poelmann, R.E.; Schalij, M.J.; Groot, A.C.G. Morphogenesis of Outflow Tract Rotation During Cardiac Development: The Pulmonary Push Concept. *Dev. Dyn.* **2012**, *241*, 1413–1422. [CrossRef]
11. Bergwerff, M.; Deruiter, M.C.; Gittenberger-deGroot, A.C. Comparative anatomy and ontogeny of the ductus arteriosus, a vascular outsider. *Anat. Embryol.* **1999**, *200*, 559–571. [CrossRef]
12. Gittenberger-De Groot, A.C. Persistent ductus arteriosus: Most probably a primary congenital malformation. *Br. Heart J.* **1977**, *39*, 610–618. [CrossRef] [PubMed]
13. Yen Ho, S.; Anderson, R.H. Anatomical closure of the ductus arteriosus: A study in 35 specimens. *J. Anat.* **1979**, *128*, 829–82936.
14. Gittenberger-de Groot, A.C.; Strengers, J.L.M.; Mentink, M.; Poelmann, R.E.; Patterson, D.F. Histologic studies on normal and persistent ductus arteriosus in the dog. *J. Am. Coll. Cardiol.* **1985**, *6*, 394–404. [CrossRef]
15. Silver, M.M.; Freedom, R.M.; Silver, M.D.; Olley, P.M. The morphology of the human newborn ductus arteriosus: A reappraisal of its structure and closure with special reference to prostaglandin E1 therapy. *Hum. Pathol.* **1981**, *12*, 1123–1136. [CrossRef]
16. Weichert, J.; Hartge, D.R.; Axt-Fliedner, R. The fetal ductus arteriosus and its abnormalities—A review. *Congenit. Heart Dis.* **2010**, *5*, 398–408. [CrossRef] [PubMed]

17. Hofstadler, G.; Tulzer, G.; Altmann, R.; Schmitt, K.; Danford, D.; Huhta, J.C. Spontaneous closure of the human fetal ductus arteriosus—A cause of fetal congestive heart failure. *Am. J. Obstet. Gynecol.* **1996**, *174*, 879–883. [CrossRef]
18. Cruickshank, B.; Marquis, R.M. Spontaneous Aneurysm of the Ductus Arteriosus. A review and report of the tenth adult case. *Am. J. Med.* **1958**, *25*, 140–149. [CrossRef]
19. Tutassaura, H.; Goldman, B.; Moes, C.A.; Mustard, W.T. Spontaneous aneurysm of the ductus arteriosus in childhood. *J. Thorac. Cardiovasc. Surg.* **1969**, *57*, 180–184. [CrossRef]
20. Falcone, M.W.; Perloff, J.K.; Roberts, W.C. Aneurysm of the Nonpatent Ductus Arteriosus in the Newborn. *Am. J. Cardiol.* **1971**, *29*, 422–426. [CrossRef]
21. Ithuralde, M.; Halloran, K.H.; Fishbone, G.; Brill, S.; Downing, S.E. Dissecting Aneurysm of the Ductus Arteriosus in the Newborn Infant. *Am. J. Dis. Child.* **1971**, *122*, 165–169. [CrossRef] [PubMed]
22. Lund, J.T.; Jensen, M.B.; Hielms, E. Aneurysm of the ductus arteriosus. A review of the literature and the surgical implications. *Eur. J. Cario-Thorac. Surg.* **1991**, *5*, 566–570. [CrossRef]
23. Lund, J.T.; Hansen, D.; Brocks, V.; Jensen, M.B.; Jacobsen, J.R. Aneurysm of the ductus arteriosus in the neonate: Three case reports with a review of the literature. *Pediatr. Cardiol.* **1992**, *13*, 222–226. [CrossRef]
24. Dyamenahalli, U.; Smallhorn, J.F.; Geva, T.; Fouron, J.C.; Cairns, P.; Jutras, L.; Hughes, V.; Rabinovitch, M.; Mason, C.A.E.; Hornberger, L.K. Isolated ductus arteriosus aneurysm in the fetus and infant: A multi-institutional experience. *J. Am. Coll. Cardiol.* **2000**, *36*, 262–269. [CrossRef]
25. Jan, S.L.; Hwang, B.; Fu, Y.C.; Chai, J.W.; Chi, C.S. Isolated neonatal ductus arteriosus aneurysm. *J. Am. Coll. Cardiol.* **2002**, *39*, 342–347. [CrossRef]
26. Fukuta, M.; Horita, T.; Seko-Nakamura, Y.; Kato, H.; Kanno, S.; Monma-Otaki, J.; Aoki, Y. Sudden Death Caused by Rupture of Spontaneous Ductus Arteriosus Aneurysm in an Adult. *J. Forensic Sci.* **2020**, *65*, 1004–1008. [CrossRef]
27. Komai, H.; Naito, Y.; Fujiwara, K. Ductal aneurysm of adult patients. *Jpn. J. Thorac. Cardiovasc. Surg.* **2000**, *48*, 139–141. [CrossRef]
28. Pastuszko, P.; Eisenberg, J.A.; Diehl, J.T. Ductus arteriosus aneurysm in an adult patient presenting with hoarseness. *J. Card. Surg.* **2005**, *20*, 386–388. [CrossRef]
29. Ardhanari, M.; Swaminathan, S. Congenital ductus arteriosus aneurysm in association with MYH11 mutation: A case report. *Cardiol. Young* **2020**, *30*, 123–125. [CrossRef]
30. Gittenberger-de Groot, A.C.; van Ertbruggen, I.; Moulaert, A.J.M.G.; Harinck, E. The ductus arteriosus in the preterm infant: Histologic and clinical observations. *J. Pediatr.* **1980**, *96*, 88–93. [CrossRef]
31. Bökenkamp, R.; Deruiter, M.C.; Van Munsteren, C.; Gittenberger-De Groot, A.C. Insights into the pathogenesis and genetic background of patency of the ductus arteriosus. *Neonatology* **2010**, *98*, 6–17. [CrossRef]
32. Gittenberger-De Groot, A.C. Influence of Prostaglandin E_1 on the Histology of the Normal and the Persistent Ductus Arteriosus. In Proceedings of the Selected Topics in Cardiac Surgery, Symposium Hel, Padova, Italy, 25–26 May 1979; Gallucci, V., Bini, R.M., Thiene, G., Eds.; Patron Editore Bologna: Bologna, Italy, 1979; pp. 159–168.
33. Matsui, H.; McCarthy, K.; Ho, S. Morphology of the patent arterial duct: Features relevant to treatment. *Images Paediatr. Cardiol.* **2008**, *10*, 27–38.
34. Dagle, J.M.; Lepp, N.T.; Cooper, M.E.; Schaa, K.L.; Kelsey, K.J.P.; Orr, K.L.; Caprau, D.; Zimmerman, C.R.; Steffen, K.M.; Johnson, K.J.; et al. Determination of Genetic Predisposition to Patent Ductus Arteriosus in Preterm Infants. *Pediatrics* **2009**, *123*, 1116–1123. [CrossRef] [PubMed]
35. Khong, T.Y.; Mooney, E.E.; Ariel, I.; Balmus, N.C.M.; Boyd, T.K.; Brundler, M.A.; Derricott, H.; Evans, M.J.; Faye-Petersen, O.M.; Gillan, J.E.; et al. Sampling and definitions of placental lesions Amsterdam placental workshop group consensus statement. *Arch. Pathol. Lab. Med.* **2016**, *140*, 698–713. [CrossRef]
36. Gardosi, J.; Kady, S.M.; McGeown, P.; Francis, A.; Tonks, A. Classification of stillbirth by relevant condition at death (ReCoDe): Population based cohort study. *Br. Med. J.* **2005**, *331*, 1113–1117. [CrossRef] [PubMed]
37. Schlatmann, T.J.M.; Becker, A.E. Pathogenesis of dissecting aneurysm of aorta. Comparative histopathologic study of significance of medial changes. *Am. J. Cardiol.* **1977**, *39*, 21–26. [CrossRef]
38. Halushka, M.K.; Angelini, A.; Bartoloni, G.; Basso, C.; Batoroeva, L.; Bruneval, P.; Buja, L.M.; Butany, J.; D'Amati, G.; Fallon, J.T.; et al. Consensus statement on surgical pathology of the aorta from the Society for Cardiovascular Pathology and the Association for European Cardiovascular Pathology: II. Noninflammatory degenerative diseases-Nomenclature and diagnostic criteria. *Cardiovasc. Pathol.* **2016**, *25*, 247–257. [CrossRef] [PubMed]
39. Visentin, S.; Londero, A.P.; Calanducci, M.; Grisan, E.; Bongiorno, M.C.; Marin, L.; Cosmi, E. Fetal Abdominal Aorta: Doppler and Structural Evaluation of Endothelial Function in Intrauterine Growth Restriction and Controls. *Ultraschall Med.* **2019**, *40*, 55–63. [CrossRef]
40. Zhu, L.; Vranckx, R.; Van Kien, P.K.; Lalande, A.; Boisset, N.; Mathieu, F.; Wegman, M.; Glancy, L.; Gasc, J.M.; Brunotte, F.; et al. Mutations in myosin heavy chain 11 cause a syndrome associating thoracic aortic aneurysm/aortic dissection and patent ductus arteriosus. *Nat. Genet.* **2006**, *38*, 343–349. [CrossRef]
41. Tongsong, T.; Chanprapaph, P.; Sittiwangkul, R.; Sirichotiyakul, S. Rupture of Fetal Ductus Arteriosus Aneurysm. *Am. Coll. Obstet. Gynecol.* **2005**, *105*, 1275–1278. [CrossRef]

42. Stewart, A.; Dyamenahalli, U.; Greenberg, S.B.; Drummond-Webb, J. Ductus arteriosus aneurysm with community-acquired methicillin-resistant Staphylococcus aureus infection and spontaneous rupture: A potentially fatal quandary. *Pediatrics* **2006**, *117*, e1259–e1262. [CrossRef] [PubMed]
43. Muthialu, N.; Robertson, A.; Mortensen, K.; Khambadkone, S. Case report on surgical repair of unusual dissection of arterial duct involving main pulmonary artery in a child with vein of Galen malformation. *Eur. Hear. J. Case Rep.* **2018**, *2*, 1–4. [CrossRef] [PubMed]
44. Tseng, J.J.; Jan, S.L. Fetal echocardiographic diagnosis of isolated ductus arteriosus aneurysm: A longitudinal study from 32 weeks of gestation to term. *Ultrasound Obstet. Gynecol.* **2005**, *26*, 50–56. [CrossRef] [PubMed]
45. Luchese, S.; Mânica, J.L.; Zielinsky, P. Intrauterine ductus arteriosus constriction: Analysis of a historic cohort of 20 cases. *Arq. Bras. Cardiol.* **2003**, *81*, 405–410. [CrossRef]
46. Mielke, G.; Steil, E.; Breuer, J.; Goelz, R. Circulatory changes following intrauterine closure of the ductus arteriosus in the human fetus and newborn. *Prenat. Diagn.* **1998**, *18*, 139–145. [CrossRef]

MDPI
St. Alban-Anlage 66
4052 Basel
Switzerland
Tel. +41 61 683 77 34
Fax +41 61 302 89 18
www.mdpi.com

Journal of Cardiovascular Development and Disease Editorial Office
E-mail: jcdd@mdpi.com
www.mdpi.com/journal/jcdd

MDPI
St. Alban-Anlage 66
4052 Basel
Switzerland

Tel: +41 61 683 77 34

www.mdpi.com

ISBN 978-3-0365-4048-1